



**HAL**  
open science

# Estimation of the thermal performance of building walls and thermal bridges using active infrared thermography and inverse techniques

Adrien François

► **To cite this version:**

Adrien François. Estimation of the thermal performance of building walls and thermal bridges using active infrared thermography and inverse techniques. Other. Université Paris-Est, 2020. English. NNT : 2020PESC0040 . tel-03392202

**HAL Id: tel-03392202**

**<https://theses.hal.science/tel-03392202>**

Submitted on 21 Oct 2021

**HAL** is a multi-disciplinary open access archive for the deposit and dissemination of scientific research documents, whether they are published or not. The documents may come from teaching and research institutions in France or abroad, or from public or private research centers.

L'archive ouverte pluridisciplinaire **HAL**, est destinée au dépôt et à la diffusion de documents scientifiques de niveau recherche, publiés ou non, émanant des établissements d'enseignement et de recherche français ou étrangers, des laboratoires publics ou privés.

# THESE DE DOCTORAT

Spécialité : Sciences de l'ingénieur

Ecole doctorale : S.I.E - Sciences, Ingénierie et Environnement

réalisée au

**Centre d'Etudes et de Recherche en Thermique,  
Environnement et Systèmes**

sous la direction de Laurent IBOS

Présentée par

**Adrien FRANÇOIS**

Sujet de la thèse :

**Estimation of the thermal performance of building walls  
and thermal bridges using active infrared thermography  
and inverse techniques**

(Estimation des performances thermiques de parois de bâtiment et de ponts  
thermiques par thermographie infrarouge active et méthodes inverses)

Soutenue le 15 décembre 2020

devant le jury composé de :

M <sup>me</sup>	Monika WOLOSZYN	Université Savoie Mont-Blanc	Présidente du Jury
M.	Thomas OLOFSSON	Umeå University (SE)	Rapporteur
M.	Benjamin RÉMY	Université de Lorraine	Rapporteur
M.	Christopher GORSE	Leeds Beckett University (UK)	Examineur
M <sup>me</sup>	Tingting VOGT WU	Université de Bordeaux	Examinatrice
M.	Laurent IBOS	Université Paris-Est Créteil	Directeur de thèse
M.	Vincent FEUILLET	Université Paris-Est Créteil	Encadrant
M.	Johann MEULEMANS	Saint-Gobain Research Paris	Encadrant
M.	Mario MARCHETTI	Université Gustave Eiffel	Invité



# Contents

<b>Abstract</b>	<b>1</b>
<b>Résumé</b>	<b>3</b>
<b>Acknowledgments</b>	<b>5</b>
<b>List of Figures</b>	<b>6</b>
<b>List of Tables</b>	<b>16</b>
<b>1. Introduction</b>	<b>21</b>
1.1. General introduction . . . . .	21
1.2. Types of thermal bridges . . . . .	24
1.3. Plan of the manuscript . . . . .	26
<b>2. Literature review on <i>in situ</i> characterization of building walls and thermal bridge</b>	<b>29</b>
2.1. Key Performance Indicators (KPI) . . . . .	32
2.1.1. Wall thermal transmittance $U$ and resistance $R$ . . . . .	32
2.1.2. Thermal bridge transmittance $\psi$ or $\chi$ . . . . .	32
2.1.3. Thermal bridge Incidence (or Impact) factor $I_{tb}$ . . . . .	33
2.1.4. The temperature factor $f_{Rsi}$ . . . . .	34
2.2. Detection and quantification of thermal bridges . . . . .	36
2.2.1. Detection of thermal bridges . . . . .	36
2.2.1.1. Passive IRT . . . . .	37
2.2.1.2. Active IRT . . . . .	38
2.2.2. Laboratory characterization . . . . .	40
2.2.2.1. Tests in Hot box facilities without IRT . . . . .	40
2.2.2.2. Tests in Hot box facilities with IRT . . . . .	41
2.2.3. <i>In situ</i> characterization . . . . .	42
2.2.4. Methods combining measurements and calculations . . . . .	45
2.2.4.1. Combining measurement and simulations to assess thermal performance of building façades . . . . .	46
2.2.4.2. Validation of a thermal modeling . . . . .	48
2.2.5. Numerical modeling . . . . .	50
2.2.5.1. Determination of an equivalent wall method . . . . .	50
2.2.5.2. Other numerical studies on thermal bridges . . . . .	54
2.2.6. Conclusion . . . . .	55

2.3.	Quantification of a wall thermal transmittance . . . . .	59
2.3.1.	Steady-state methods . . . . .	59
2.3.1.1.	Heat flux meter methods (standard methods) . . . . .	59
2.3.1.2.	Thermometric methods . . . . .	60
2.3.1.3.	IRT methods . . . . .	61
2.3.2.	Dynamic methods . . . . .	65
2.3.2.1.	Gray-box approaches . . . . .	65
2.3.2.2.	Black-box approaches . . . . .	66
2.3.2.3.	Other approaches . . . . .	67
2.3.3.	Active methods . . . . .	68
2.3.4.	Conclusion . . . . .	70
2.4.	Conclusion . . . . .	73

**3. Experimental aspects 75**

3.1.	Contact thermal measurements . . . . .	78
3.1.1.	Thermocouples . . . . .	78
3.1.1.1.	Presentation . . . . .	78
3.1.1.2.	Calibration: one-junction configuration . . . . .	79
3.1.1.3.	Bad cold junction compensation . . . . .	80
3.1.1.4.	Calibration: two-junction configuration . . . . .	81
3.1.2.	Heat flux meters . . . . .	82
3.1.2.1.	Presentation . . . . .	82
3.1.2.2.	Calibration . . . . .	84
3.2.	Infrared thermography . . . . .	87
3.2.1.	Basics on radiant intensity . . . . .	87
3.2.2.	Basics on radiative heat flux . . . . .	88
3.2.2.1.	Theory on radiative heat flux . . . . .	88
3.2.2.2.	Radiative heat flux linearization . . . . .	91
3.2.2.3.	Total heat flux . . . . .	91
3.2.3.	Thermography equation . . . . .	93
3.2.4.	Infrared camera properties . . . . .	95
3.2.4.1.	Types of sensor . . . . .	95
3.2.4.2.	Camera calibration . . . . .	96
3.2.4.3.	Non-uniformity correction (NUC) . . . . .	97
3.2.4.4.	Noise Equivalent Temperature Difference (NETD) . . . . .	97
3.2.4.5.	Instantaneous Field of View (IFOV) . . . . .	98
3.2.5.	Temperature measurement with IRT . . . . .	101
3.2.5.1.	Measurement of absolute temperatures . . . . .	101
3.2.5.2.	Measurement of temperature differences . . . . .	103
3.2.6.	Heat flux measurement with IRT . . . . .	104
3.2.6.1.	Method . . . . .	104
3.2.6.2.	Numerical application . . . . .	105
3.2.7.	Geometrical corrections . . . . .	107
3.2.7.1.	Fisheye correction . . . . .	107
3.2.7.2.	Camera angle correction . . . . .	107
3.2.8.	IR Camera used . . . . .	110

3.3.	Conclusion . . . . .	112
<b>4.</b>	<b>Presentation of experimental campaigns</b>	<b>113</b>
4.1.	Overview . . . . .	115
4.2.	CERTES 1 setup . . . . .	117
4.2.1.	Presentation . . . . .	117
4.2.2.	Sensor instrumentation . . . . .	118
4.3.	CERTES 2 setup . . . . .	122
4.4.	CEREMA . . . . .	124
4.4.1.	Presentation of the wall . . . . .	124
4.4.2.	Sensor instrumentation . . . . .	127
4.4.3.	About infrared measurements . . . . .	127
4.4.4.	Detail of experimental campaign . . . . .	131
4.5.	SGR . . . . .	133
4.5.1.	Presentation . . . . .	133
4.5.2.	Sensor instrumentation . . . . .	133
4.5.3.	Infrared measurements . . . . .	134
4.5.4.	Detail of experimental campaign . . . . .	135
4.6.	Conclusion . . . . .	139
<b>5.</b>	<b>Measurement of wall heat transfer coefficient</b>	<b>141</b>
5.1.	Motivation . . . . .	144
5.2.	Literature review on total $h$ -coefficient evaluation . . . . .	146
5.3.	Measurement setup and methods . . . . .	149
5.3.1.	Experimental setup . . . . .	149
5.3.2.	Double measurement method 1 (DM1) . . . . .	150
5.3.3.	Double measurement method 2 (DM2) . . . . .	151
5.3.4.	Operative temperature measurement method 1 (OT1) . . . . .	152
5.3.5.	Operative temperature measurement method 2 (OT2) . . . . .	153
5.3.6.	Harmonic excitation measurement method (HE) . . . . .	155
5.4.	Focus on Harmonic Excitation method (HE) . . . . .	157
5.4.1.	Influence of the oscillation period . . . . .	157
5.4.2.	Influence of the oscillation amplitude . . . . .	158
5.4.3.	Theoretical model . . . . .	160
5.5.	Uncertainty calculations . . . . .	162
5.5.1.	Type-A uncertainty . . . . .	162
5.5.2.	Type-B uncertainty . . . . .	163
5.6.	Results . . . . .	164
5.6.1.	Steady-state results . . . . .	164
5.6.2.	Transient results . . . . .	165
5.6.2.1.	DM1 method . . . . .	165
5.6.2.2.	DM2 method . . . . .	166
5.6.2.3.	OT1 method . . . . .	167
5.6.2.4.	OT2 method . . . . .	167
5.6.2.5.	HE method . . . . .	169
5.7.	Discussion . . . . .	173
5.7.1.	Comparison of methods . . . . .	173

5.7.2.	Comparison to empirical correlations . . . . .	174
5.7.3.	Heat flux reconstruction . . . . .	175
5.8.	Conclusion . . . . .	177
<b>6.</b>	<b>Steady-state characterization of a wall and a thermal bridge</b>	<b>179</b>
6.1.	Methodologies . . . . .	183
6.1.1.	Characterization of a homogenous wall: $R$ and $U$ values . . . . .	183
6.1.1.1.	Method presentation . . . . .	183
6.1.1.2.	Measurement uncertainties . . . . .	184
6.1.2.	Characterization of a thermal bridge: “ $I_{tb}$ method” . . . . .	184
6.1.2.1.	Method presentation . . . . .	184
6.1.2.2.	“Standard approach” for $I_{tb}$ measurement . . . . .	185
6.1.2.3.	Proposed approach for $I_{tb}$ measurement . . . . .	186
6.1.2.4.	Measurement uncertainties . . . . .	187
6.1.3.	Characterization of a thermal bridge: “ $h$ method” . . . . .	189
6.1.3.1.	Method presentation . . . . .	189
6.1.3.2.	Measurement uncertainties . . . . .	190
6.1.4.	Conclusion . . . . .	191
6.2.	Results on the CERTES 1 setup . . . . .	192
6.2.1.	Contact measurements and $R$ estimation . . . . .	192
6.2.2.	Infrared measurements . . . . .	193
6.2.3.	Numerical simulations . . . . .	194
6.2.4.	Results for the “ $I_{tb}$ method” . . . . .	196
6.2.5.	Results for the “ $h$ method” . . . . .	197
6.2.6.	Conclusion . . . . .	198
6.3.	Results on CEREMA experiments . . . . .	199
6.3.1.	Contact measurements and $R$ estimation . . . . .	199
6.3.2.	Measurement of $h$ . . . . .	200
6.3.3.	Infrared measurements . . . . .	201
6.3.4.	Numerical simulations . . . . .	202
6.3.5.	Results of $\psi$ -value calculation . . . . .	202
6.3.6.	Robustness assessment . . . . .	205
6.3.7.	Conclusion . . . . .	205
6.4.	Results on SGR experiments . . . . .	207
6.4.1.	Contact measurements and $R$ estimation . . . . .	207
6.4.2.	Measurement of $h$ . . . . .	208
6.4.3.	Infrared measurements . . . . .	209
6.4.4.	Numerical simulation . . . . .	209
6.4.5.	Results of $\psi$ -values calculation . . . . .	210
6.4.6.	Conclusion . . . . .	211
6.5.	Conclusion . . . . .	214
<b>7.</b>	<b>Theory on Inverse methods</b>	<b>217</b>
7.1.	Direct model definition with thermal quadrupole formalism . . . . .	220
7.1.1.	Thermal quadrupole formalism from 1D slab equations . . . . .	220
7.1.2.	Parameterization . . . . .	222
7.1.3.	Application to a multilayer building wall . . . . .	223

7.1.4.	Numerical Laplace inversion . . . . .	224
7.1.4.1.	Gaver-Stehfest algorithm . . . . .	225
7.1.4.2.	De Hoog algorithm . . . . .	226
7.1.4.3.	Limitation of numerical Laplace inversion algorithms	227
7.1.5.	Test case: a two-layer wall subjected to internal air heating . .	228
7.2.	Inverse method with “white-box” models . . . . .	232
7.2.1.	Presentation . . . . .	232
7.2.2.	Solving . . . . .	235
7.2.2.1.	Cost function minimization . . . . .	235
7.2.2.2.	Levenberg-Marquardt algorithm . . . . .	237
7.2.2.3.	Expectancy of the estimator . . . . .	237
7.2.3.	Tools to estimate parameters estimability . . . . .	238
7.2.3.1.	Reduced sensitivity coefficients and sensitivity matrix	238
7.2.3.2.	Variance of the estimator . . . . .	239
7.2.3.3.	Rank of the sensitivity matrix and number of degrees of freedom . . . . .	241
7.2.3.4.	Residual analysis . . . . .	243
7.2.4.	Conclusion . . . . .	243
7.3.	System identification: “black-box” ARX models . . . . .	246
7.3.1.	Presentation . . . . .	246
7.3.1.1.	The deconvolution problem . . . . .	246
7.3.1.2.	Non-parametric methods . . . . .	247
7.3.1.3.	Parametric methods . . . . .	248
7.3.1.4.	Presentation of ARX models . . . . .	249
7.3.2.	Solving . . . . .	250
7.3.2.1.	Estimation of model parameters . . . . .	250
7.3.2.2.	Thermal impedance and estimate of a wall thermal resistance . . . . .	251
7.3.3.	Tools to assess the quality of estimation . . . . .	252
7.3.3.1.	Variance of the estimator . . . . .	253
7.3.3.2.	Residuals analysis . . . . .	253
7.3.3.3.	Choice of number of parameters . . . . .	255
7.3.4.	Conclusion . . . . .	255
7.4.	Conclusion . . . . .	258
<b>8.</b>	<b>Active characterization of a homogeneous wall</b>	<b>259</b>
8.1.	Presentation of the active methodology . . . . .	263
8.1.1.	Definition of model inputs and output . . . . .	263
8.1.2.	Theoretical study: justification of thermal load . . . . .	263
8.1.2.1.	Common thermal loads . . . . .	263
8.1.2.2.	Step-heating vs Square-heating . . . . .	265
8.1.3.	Experimental protocol . . . . .	267
8.1.4.	Conclusion . . . . .	269
8.2.	Presentation of the white-box approach . . . . .	270
8.2.1.	Overview of the method . . . . .	270
8.2.2.	Analytical expressions of the inputs . . . . .	271



8.2.3.	Direct model definition . . . . .	272
8.2.3.1.	Model reduction . . . . .	272
8.2.3.2.	Decomposition of inputs and model nomenclature . . . . .	274
8.2.3.3.	The heavyweight wall case . . . . .	276
8.2.4.	Conclusion . . . . .	277
8.3.	Application to CEREMA experimental campaign . . . . .	278
8.3.1.	Measurements on one example . . . . .	278
8.3.2.	White-box method . . . . .	279
8.3.2.1.	Analytical expression of the input . . . . .	279
8.3.2.2.	Direct model definition . . . . .	279
8.3.2.3.	Sensitivity analysis and estimation of uncertainties . . . . .	281
8.3.2.4.	Parameter estimation . . . . .	282
8.3.2.5.	Robustness of the method . . . . .	283
8.3.3.	Black-box ARX method . . . . .	284
8.3.3.1.	Presentation of the model . . . . .	284
8.3.3.2.	Choice of number of parameters . . . . .	285
8.3.3.3.	Residuals analysis . . . . .	286
8.3.3.4.	Impact of time horizon . . . . .	287
8.3.4.	Test of the methods on different configurations . . . . .	287
8.3.4.1.	Constant external conditions . . . . .	288
8.3.4.2.	Varying external conditions . . . . .	289
8.3.5.	Conclusion . . . . .	291
8.4.	Application to SGR experiments . . . . .	293
8.4.1.	All active measurements . . . . .	293
8.4.2.	White-box method . . . . .	294
8.4.2.1.	Analytical expressions of the inputs . . . . .	294
8.4.2.2.	Direct model definition . . . . .	295
8.4.2.3.	Sensitivity analysis and estimation of uncertainties . . . . .	295
8.4.2.4.	Parameter estimation . . . . .	296
8.4.2.5.	Robustness of the method . . . . .	296
8.4.3.	Test of the method on different configurations . . . . .	297
8.4.4.	Conclusion . . . . .	299
8.5.	Conclusion . . . . .	301

**9. Active characterization of a non-homogeneous wall 303**

9.1.	Presentation of the method . . . . .	305
9.1.1.	General method . . . . .	305
9.1.1.1.	Homogenization for model reduction . . . . .	305
9.1.1.2.	General active method for the estimation of $\psi$ and $\chi$ coefficients . . . . .	306
9.1.2.	Theoretical study: Two-step and Single-step approaches . . . . .	308
9.1.2.1.	Presentation . . . . .	308
9.1.2.2.	Two-step approach . . . . .	310
9.1.2.3.	Single-step approach . . . . .	312
9.1.2.4.	Comparison and choice of approach . . . . .	313
9.1.3.	Conclusion . . . . .	314

9.2. Results on CEREMA experiments . . . . .	315
9.2.1. Detailed results on one example . . . . .	315
9.2.1.1. Temperature and heat flux extrapolation . . . . .	315
9.2.1.2. Parameter estimation . . . . .	317
9.2.2. Results for different configurations . . . . .	320
9.2.3. Conclusion . . . . .	323
9.3. Results on SGR experiments . . . . .	324
9.3.1. Detailed results on one example . . . . .	324
9.3.1.1. Temperature and heat flux extrapolation . . . . .	324
9.3.1.2. Parameter estimation . . . . .	326
9.3.2. Results for all experiments . . . . .	326
9.3.3. Conclusion . . . . .	327
9.4. Conclusion . . . . .	330
<b>10. Conclusion</b>	<b>333</b>
10.1. Context and objectives . . . . .	333
10.2. Summary of developments . . . . .	334
10.3. Limitations . . . . .	335
10.4. Next steps . . . . .	336
<b>References</b>	<b>339</b>
<b>A. Appendices of Chap 3</b>	<b>359</b>
A.1. Emissivity (IR spectrometer) . . . . .	359
A.1.1. Principle of the method . . . . .	359
A.1.2. Results: examples . . . . .	361
A.2. Thermal conductivity and diffusivity (Hot Disk) . . . . .	362
A.2.1. Principle of the method . . . . .	362
A.2.2. Example of results . . . . .	363
A.3. Thermal effusivity (Photothermal method) . . . . .	365
A.3.1. Principle of the method . . . . .	365
A.3.2. Results: examples . . . . .	366
A.4. Conclusion . . . . .	367
<b>B. Appendices of Chap 5</b>	<b>369</b>
B.1. Type-A uncertainty calculation of the HE method . . . . .	369
B.1.1. 5Amplitude and phase uncertainty of a Fourier transform . . . . .	369
B.1.2. Uncertainty on $h$ calculation . . . . .	370
<b>C. Appendices of Chap 6</b>	<b>373</b>
C.1. $\psi$ uncertainty calculation . . . . .	373
C.1.1. Partial derivatives for the “ $I_{tb}$ ” method . . . . .	373
C.1.2. Partial derivatives for the “ $h$ ” method . . . . .	374
C.2. Details on FE simulations (CERTES 1 setup) . . . . .	375
C.2.1. Geometry and boundary conditions . . . . .	375
C.2.2. Equations and numerical scheme . . . . .	375
C.2.3. Mesh . . . . .	376

C.3. Detailed uncertainty analysis (CERTES 1 setup, “ $I_{tb}$ method”) . . . . .	378
<b>D. Appendices of Chap 7</b>	<b>379</b>
D.1. Details on the Levenberg-Marquardt algorithm . . . . .	379
D.2. ARX MISO case . . . . .	381
D.2.1. Formulation . . . . .	381
D.2.2. Estimation of a wall thermal resistance . . . . .	381
D.2.3. Discussion of results . . . . .	382
<b>E. Appendices of Chap 8</b>	<b>383</b>
E.1. Theoretical study: signal normalization . . . . .	383
E.2. CEREMA, estimation of $R_3$ & $b_3$ (concrete block thermal properties)	385
E.2.1. Time-domain method . . . . .	385
E.2.2. Harmonic method . . . . .	387
E.3. CEREMA, impact of a bias on the values of $R_3$ and $b_3$ on the esti- mated thermal resistance . . . . .	390
E.4. CEREMA experiments, residuals after parameter estimation . . . . .	392
E.5. SGR, residuals after parameter estimation . . . . .	398
<b>F. Appendices of Chap 9</b>	<b>401</b>
F.1. CEREMA experiments, residuals after parameter estimation . . . . .	401
F.2. SGR experiments, residuals after parameter estimation . . . . .	415
<b>G. Appendix: Personal references</b>	<b>419</b>
G.1. Scientific papers . . . . .	419
G.2. International conferences . . . . .	419
G.3. National conferences . . . . .	420

## Abstract

The building sector has a major role to play in the mitigation of greenhouse gas emissions. Indeed, residential and non-residential buildings account for 40% total energy consumption in the European union. In addition, given that 80% of building energy demand come from heating, thermal insulation is a domain with great potential for energy savings.

The estimation of the thermal performance of a building usually relies on theoretical calculations. When in situ measurements are performed, the results often show some discrepancies with predictions: this is the so-called “performance gap”. Thus, it is important to distinguish the contribution of each element of the building envelope to the overall energy losses. In particular, “thermal bridges” (insulation irregularities) generate locally additional heat losses. They may also alter the thermal comfort of inhabitants as well as lead to mould growth issues.

This thesis proposes several methods for the in situ estimation of heat losses in a building wall or in a thermal bridge. The methodology consists in applying an artificial thermal load to the wall and to analyze its transient response. This “active” approach is usually faster and less sensitive to weather conditions than standard steady-state methods. In practice, the indoor air is heated, and both the temperature and heat flux are measured on the wall surface. An inverse method then estimates the thermal resistance of the wall by fitting a model (direct model) to these transient measurements. The well-posedness of the inverse problem is assessed thanks to several mathematical tools. Some model reduction steps are required for the parameters of the direct model to be estimable with the desired uncertainty.

In the case of a homogeneous wall, temperatures and heat fluxes are measured with contact sensors at one specific location. For a non-homogeneous wall or a thermal bridge, these local contact measurements are extrapolated to the rest of the wall thanks to infrared thermography and the quantification of the total heat transfer coefficient. For this purpose, several methods were developed to measure this coefficient in situ. Thanks to this extrapolation procedure, the inverse method can estimate the thermal resistance (or thermal transmittance) of an equivalent homogeneous wall having the same behavior as the real wall.

The methods developed were validated on four experimental campaigns. Measurements were carried out in laboratory, in a climate chamber, and in situ. Different types of wall (heavyweight internally insulated wall, lightweight insulated wall) were tested. Several types of material-related thermal bridges were also investigated (mainly high-conductive materials in insulation systems). The results were compared to reference values obtained from steady-state measurements. Indeed, several methods for the characterization of thermal bridges in steady-state were compared: some are inspired from the literature, others are original.



## Résumé

Le secteur du bâtiment a un rôle majeur à jouer dans la réduction des émissions de gazes à effet de serre. En effet, les bâtiments (résidentiels et non-résidentiels) représentent 40% de la consommation d'énergie totale en Europe. De plus, étant donné que 80% des besoins énergétiques des bâtiments proviennent du chauffage, l'isolation thermique représente un grand potentiel d'économies d'énergie.

L'estimation des performances thermiques d'un bâtiment repose la plupart du temps sur des calculs théoriques. Quand des mesures de terrain sont réalisées, les résultats montrent souvent des écarts par rapport aux prédictions. Ainsi, il est important de pouvoir distinguer les contributions de chaque élément de l'enveloppe du bâtiment aux déperditions totales. En particulier, les « ponts thermiques » (irrégularités et défauts dans l'isolation), génèrent localement des pertes supplémentaires. De plus, ils peuvent altérer le confort des habitants et engendrer de problèmes de développement de moisissures.

Cette thèse propose plusieurs méthodes permettant de mesurer sur le terrain les déperditions thermiques à travers une paroi de bâtiment ou un pont thermique. La méthode consiste à chauffer artificiellement le mur et à analyser sa réponse transitoire à cette sollicitation. Cette approche, dite « active », est en général plus rapide et moins sensible aux conditions météorologiques que les méthodes en régime stationnaire habituelles. En pratique, l'air intérieur est chauffé, et la température et le flux thermique sont tous les deux mesurés à la surface du mur. Une méthode inverse estime ensuite la résistance thermique de la paroi en calant un modèle sur ces mesures (modèle direct). Le caractère bien-posé du problème inverse est évalué grâce à divers outils mathématiques. Des étapes de réduction de modèle sont nécessaires pour que les paramètres inconnus du modèle direct utilisés puissent être estimés avec une incertitude correcte.

Dans le cas d'une paroi courante homogène, les températures et les flux sont mesurés à un endroit spécifique, supposé représentatif de l'ensemble du mur. Pour une paroi non-homogène ou un pont thermique, ces mesures locales par contact sont extrapolées au reste du mur grâce des mesures infrarouges et à la quantification du coefficient d'échange total en surface. A ces fins, plusieurs méthodes ont été développées pour mesurer ce coefficient sur le terrain. Grâce à cette procédure d'extrapolation, les méthodes inverses peuvent estimer la résistance (ou la transmittance) thermique d'un mur homogène équivalent ayant le même comportement que le mur réel.

Les méthodes développées ont été validées sur quatre campagnes expérimentales. Des mesures ont été réalisées en laboratoire, en chambre climatique, puis en conditions réelles. Différents types de parois (mur porteur isolé par l'intérieur, paroi légère) ont été testés. Plusieurs types de ponts thermiques intégrés ont également été étudiés. Les résultats ont été comparés à des valeurs de référence obtenues grâce à des mesures en régime stationnaire. En effet, plusieurs méthodes pour la caractérisation des ponts thermiques en régime permanent ont été comparées : certaines proviennent de la littérature, d'autres ont été développées pendant cette thèse.



## Acknowledgments

Foremost, I would like to express my sincere gratitude to my three supervisors: Johann Meulemans, Laurent Ibos and Vincent Feuillet. I warmly thank them for their continuous support, their knowledge, their advice, their availability, as well as their thorough proof-reading of this manuscript and all my papers. It has been a pleasure working with them during these three years.

Besides my supervisors, I would like to thank the rest of my thesis committee for accepting to review my work. A special thank you for Benjamin Remy and Thomas Olofsson for being the reviewers (“rapporteurs”) of my PhD thesis, as well as for Monika Woloszyn for chairing this (remote) committee. I also thank Christopher Gorse, Tingting Vogt Wu and Mario Marchetti.

I want to thank people at CEREMA Nancy for making available their climate chamber, building the wall, and checking on my experiments when I was away.

I thank my colleagues at Saint-Gobain Research Paris and at CERTES laboratory for their presence.

I would like to express my special thanks of gratitude to my family, my friends, and especially my wife, for their support during these three years.

Last but not least, I thank the COVID-19 pandemic for striking only during the third year of my PhD thesis, when most of the experimental work was finished.





# List of Figures

1.1.	World primary energy supply by source (source: IEA, www.iea.org). Gtoe = Giga tonne of oil equivalent. . . . .	21
1.2.	Illustration of heat losses in a building (Eq 1.1). . . . .	23
1.3.	Example of thermal bridges (thermal image from [9]). . . . .	23
1.4.	Examples of thermal bridges in buildings, from [16, 10]. . . . .	25
1.5.	Illustration of “repeating” and “non-repeating” thermal bridges, from [17]. . . . .	25
1.6.	Illustration of thesis plan. . . . .	26
2.1.	Illustration of thesis plan. . . . .	29
2.2.	Illustration of heat losses in a building wall. . . . .	33
2.3.	Histogram of thermal image and threshold definition from Asdrubali <i>et al.</i> [43]. . . . .	37
2.4.	Automatic detection of thermal bridges from Garrido <i>et al.</i> [45]. . . . .	38
2.5.	Empirical orthogonal functions and their associated principal compo- nents after Singular Value Decomposition (SVD) of thermal images, from Douguet <i>et al.</i> [58]. . . . .	39
2.6.	General view of the hot box apparatus from Asdrubali and Baldinelli [59]. . . . . .	40
2.7.	Sample IR image of a component with linear thermal bridge from O’Grady <i>et al.</i> [64]. . . . .	41
2.8.	Pillar thermal bridge (TB1): thermogram (a) and temperature trends (b) from Baldinelli <i>et al.</i> [22]. . . . .	43
2.9.	Photo and thermal image of the slab joints of the building structure studied in Benko [67]. . . . .	43
2.10.	Example of an angular thermal bridge and relative thermogram out- put from Asdrubali <i>et al.</i> [19]. . . . .	44
2.11.	Instrumented window (with heat flux meters) from Asdrubali <i>et al.</i> [19]. . . . . .	45
2.12.	Picture of the test-room facility used in Bianchi <i>et al.</i> [20]. . . . .	45
2.13.	Measurements and numerical simulations of eaves from Taylor <i>et al.</i> [24]. . . . . .	46
2.14.	Experimental setup to detect missing insulation panel from Taylor <i>et al.</i> [57]. . . . . .	47
2.15.	Comparison of heat flux values through measurements and the model from Cuce <i>et al.</i> [69]. . . . .	48
2.16.	Different types of defects studied in Aïssani <i>et al.</i> [70]. . . . .	49
2.17.	Electric circuit model for three layers equivalent wall from Martin <i>et al.</i> [81]. . . . . .	51

2.18. Comparison of the heat flux between the Equivalent Slab and thermal bridge for 3 different configurations from Xianoa and Yi [88]. . . . .	53
2.19. Comparison of heat flux computed by the real model and the equivalent wall for two thermal bridges, from Quinten and Feldheim [89]. . . . . .	57
2.20. Experimental protocol for application of ISO 9869-2 [102]. . . . .	62
2.21. Picture (left) and 2D map of $U$ -value (right) on a heavyweight wall, from Tejedor <i>et al.</i> [110]. . . . .	63
2.22. Running example illustrating Rouchier [124] (R2C model). . . . .	65
2.23. Evolution of temperatures, heating power and heat flux density during a 4-hour QUB/e test. The red, blue and black solid lines correspond to the heating phase, the free cooling phase and the linear regressions used to derive the quantities used in the QUB formula, respectively. From Meulemans <i>et al.</i> [149]. . . . .	69
2.24. Control system and working principles of the Excitation Pulse Method from Rasooli <i>et al.</i> [151]. . . . .	70
2.25. Experimental setup and example of unit-pulses response, from Yang <i>et al.</i> [154]. . . . .	71
2.26. Schematic view of the experimental setup of Larbi Youcef <i>et al.</i> [155].	72
2.27. Normalized measurements and simulated curves for an <i>in situ</i> concrete wall experiment, from Chaffar <i>et al.</i> [156]. . . . .	72
3.1. Illustration of thesis plan. . . . .	75
3.2. Illustration of thermocouple working principle: One (a) and Two (b) junction configurations. . . . .	78
3.3. Example of thermocouple calibration in water. . . . .	79
3.4. Example of difference between true temperature and measured temperature without and with correction (before and after thermocouple calibration). . . . .	80
3.5. Example of measured hot junction temperatures with a bad (a) and a good (b) cold junction compensation. . . . .	81
3.6. Working principle of a heat flux meter. . . . .	83
3.7. A $100 \times 100$ mm <sup>2</sup> heat flux meter from Captec <sup>®</sup> fixed on a wall. . . .	84
3.8. Electrical assembly used to automatically switch the HFM terminals on the data logger inputs. . . . .	85
3.9. Measured heat flux during the offset-calibration procedure (sampling period: 7 s). . . . .	86
3.10. Planck law. . . . .	87
3.11. Illustration of elementary radiative heat flux. . . . .	88
3.12. Example of of different materials at ambient temperature, from [165].	90
3.13. Exact and linearized radiative heat flux as a function of the temperature difference for $T_1 = 300$ K and $T_2 \in [300; 400]$ K . . . . .	92
3.14. Illustration of infrared thermography. . . . .	93
3.15. Transmittance of the atmosphere, from [166]. . . . .	96
3.16. Planck law and spectral bandwidths of infrared cameras. . . . .	97

---

3.17. Example of calibration curves for a Jade III camera with a 4 $\mu\text{m}$ monochromatic filter, from Rémy <i>et al.</i> [167]. . . . .	98
3.18. Impact of Non-Uniformity Correction (NUC) on recorded thermal images. . . . .	99
3.19. Example of camera NETD computation from response histogram of pixels, from [166]. . . . .	99
3.20. Illustration of FOV and IFOV of a camera (IFOV = 1 mrad). . . . .	100
3.21. Measured radiative intensity as a function of apparent temperature and fit with a power-four function. . . . .	101
3.22. Convective heat transfer coefficient $h^c$ calculated with Eckert and Jackson empirical correlation [170] as a function of the altitude. . . . .	106
3.23. Uncertainties on the measured surface heat flux: Approach 1= true temperature-based. Approach 2= apparent temperature-based. . . . .	107
3.24. Example of fisheye correction. . . . .	108
3.25. Scheme of the situation. . . . .	108
3.26. Illustration of camera angle correction. . . . .	109
3.27. Example of camera angle correction. . . . .	110
3.28. Photography of the infrared camera (SC7000 from FLIR <sup>®</sup> ). . . . .	110
3.29. Example of measured spectral emissivities. . . . .	111
4.1. Illustration of thesis plan. . . . .	113
4.2. CERTES 1: Front view of the setup without the gypsum board (dimensions in mm). . . . .	117
4.3. CERTES 1: Cut out of the setup (dimensions in mm). . . . .	118
4.4. CERTES 1: Heating resistance. . . . .	119
4.5. CERTES 1: Picture of the setup without the gypsum board. . . . .	119
4.6. CERTES 1: Picture of the setup in working conditions. . . . .	120
4.7. CERTES 1: Infrared image in steady-state. . . . .	120
4.8. CERTES 1: Picture of heat flux meters with their prolongation cables. . . . .	121
4.9. CERTES 1: Location of the thermocouples and HFMs instrumented inside and on the experimental set-up. . . . .	121
4.10. CERTES 2: Picture of the setup without the gypsum layer. . . . .	122
4.11. CERTES 2: Picture of the instrumented setup (see Chap 5 for a description of each device). . . . .	123
4.12. CEREMA: Climate chamber modules at CEREMA, Nancy. . . . .	124
4.13. CEREMA: Wall before installation of the glass wool and gypsum boards. . . . .	125
4.14. CEREMA: Wall before the installation of the gypsum boards. . . . .	125
4.15. CEREMA: Illustration of wall layout and position of thermal bridges (dimensions in mm). . . . .	126
4.16. CEREMA: Pictures of metal rails used to hold the insulation system (thermal bridges). . . . .	126
4.17. CEREMA: Detail of sensor instrumentation: double referenced thermocouple symbols means that there are two sensors on the given location at a different altitude. . . . .	127
4.18. CEREMA: Scheme of the climate chamber: view from above. . . . .	128

4.19. CEREMA: Schemes of the climate chamber: side view. . . . .	129
4.20. CEREMA: Picture of the finished wall with the cantilever structure above. . . . .	129
4.21. CEREMA: Example of two consecutive thermograms captured during a steady-state experiment. . . . .	130
4.22. CEREMA: Thermogram of the wall in steady-state with geometrical correction. . . . .	130
4.23. CEREMA: Example of internal and external temperatures for consecutive active tests (configuration 5). . . . .	132
4.24. SGR: Picture of the test cell. . . . .	133
4.25. SGR: Scheme and picture of the wall layout. . . . .	134
4.26. SGR: Picture of the North wall insulation system. . . . .	135
4.27. SGR: Scheme of the test cell (top view). . . . .	136
4.28. SGR: Scheme of thermal bridges (focus on North-East corner). . . . .	137
4.29. SGR: Example of two consecutive thermograms captured during a steady-state experiment (Left = North wall, Right = East wall). . . . .	137
4.30. SGR: Measured air and surface (North wall) temperatures during pseudo-steady-state measurements. . . . .	138
4.31. SGR: Internal room air temperature during and between the six active tests. . . . .	138
5.1. Illustration of thesis plan. . . . .	141
5.2. Schematic front view of the studied experimental wall within its insulating frame and location of all the devices used (labeled by letters: devices having the same letter are identical). . . . .	149
5.3. Picture of the instrumented setup. . . . .	150
5.4. Measured air and wall temperature during an experiment. . . . .	150
5.5. Device A: simple HFM directly fixed on the wall (used in DM1 and DM2 methods). . . . .	151
5.6. Device B: a HFM mounted on a heating resistance fixed on the wall (used in the DM1, OT1 and OT2 methods). . . . .	152
5.7. Device C: a HFM mounted on a piece of extruded polystyrene fixed on the wall (used in the DM2 method). . . . .	153
5.8. Device D: a thermocouple sandwiched between a copper plate and extruded polystyrene (used in the OT1 method). . . . .	154
5.9. Device E: a HFM mounted on an array of Thermoelectric coolers fixed on the wall (used in the OT2 and HE methods). . . . .	155
5.10. Measured heat flux (up) and temperature (down) on $h$ -meter surface for several oscillation periods (variations around mean value). . . . .	157
5.11. Influence of oscillation period on phase lag between $\varphi$ and $T$ . . . . .	158
5.12. Influence of oscillation period on estimated $h$ -value. . . . .	158
5.13. Measured $h$ -coefficient according to the amplitude of temperature oscillations $A_T$ in natural convection. . . . .	159
5.14. Measured $h$ -coefficient according to the amplitude of temperature oscillations $A_T$ in forced convection. . . . .	159
5.15. Simplified scheme of the $h$ -meter. . . . .	160

---

5.16. Electrical analogy of the modeled layer. . . . .	160
5.17. Steady-state $h$ measurements. . . . .	164
5.18. Evolution of the air temperature, measured 15 cm away from the wall. . . . .	165
5.19. DM1 method: surface heat flux and temperature measurements. . . . .	166
5.20. DM1 method: measured $h$ -coefficient against time. . . . .	167
5.21. DM2 method: surface heat flux and temperature measurements. . . . .	168
5.22. DM2 method: linear regressions. . . . .	169
5.23. OT2 method: measured surface heat fluxes and TEC voltage command. . . . .	170
5.24. OT2 method: comparison of measured temperatures. . . . .	170
5.25. OT2 method: linear regressions. . . . .	171
5.26. HE method: air heating phase. . . . .	171
5.27. HE method: air free-cooling phase. . . . .	172
5.28. HE method: measured $h$ -coefficient value against time. . . . .	172
5.29. Comparison of $h$ measurement methods: heating period (full markers) and free-cooling period (empty markers). The colors correspond to the methods. . . . .	173
5.30. Estimated $h$ -value from empirical correlations. . . . .	175
5.31. Heat flux extrapolation using measured $h$ -coefficient. . . . .	176
6.1. Illustration of thesis plan. . . . .	179
6.2. Illustration of wall instrumentation for steady-state measurements. . . . .	183
6.3. Illustration of thermal bridge dimensions (simulated thermal images). . . . .	185
6.4. Scheme of apparent temperatures used in $I_{tb}$ calculation. . . . .	188
6.5. Illustration of a linear thermal bridge contribution to the overall sur- face heat flux. . . . .	189
6.6. Measured temperature elevations and heat fluxes inside the setup during transient state and steady-state (reached when temperature and heat fluxes are less than 1% away from their final value). . . . .	192
6.7. Thermal image of the CERTES 1 setup in steady-state, with ROIs (two per thermal bridge, “M”=metal rail, “P”=metal pin, and “W”=wood stud). . . . .	193
6.8. Time averaged apparent temperature profiles on thermal bridges in steady-state ( $T_{tb}^{app} > T_{1D}^{app}$ because the setup is heated from behind). . . . .	194
6.9. Domain and Boundary Conditions (BC) used in FE simulations (wood stud example). . . . .	195
6.10. Isothermal lines in the vicinity of each thermal bridge in steady-state for a unit temperature difference. . . . .	195
6.11. Results of thermal bridge transmission coefficient estimations, “ $I_{tb}$ method”. . . . .	196
6.12. Results of thermal bridge transmission coefficient estimations, “ $h$ method”. . . . .	197
6.13. Measured temperatures heat fluxes during transient and steady states (see Fig 6.14 for nomenclature). . . . .	199
6.14. Scheme of main contact sensors for thermal resistance measurements. . . . .	199
6.15. Measured temperature and heat flux difference between the wall sur- face and the surface of a piece of polystyrene fixed on the wall (“ $h$ - meter 1”). . . . .	201

6.16. Reconstructed thermogram of the setup in steady-state, with ROIs. . . . .	202
6.17. Measured apparent temperature profiles on thermal bridges in steady-state. . . . .	203
6.18. Isothermal lines in the vicinity of the thermal bridges in steady-state for a unit temperature difference. . . . .	204
6.19. Impact of $L_{tb}$ on measured $I_{tb}$ and $\psi$ for each thermal bridge. . . . .	205
6.20. Impact of altitude $z$ on measured $\psi$ coefficient and thermal image. . . . .	206
6.21. Internal/external surface temperature difference $\Delta T_{sie}$ and internal surface heat flux $\varphi_{si}$ measured during three consecutive cloudy nights of a pseudo-steady-state experiment. . . . .	208
6.22. Concatenated night-time measurement data. . . . .	209
6.23. Estimation of walls thermal resistance from cumulated data as a function of dataset upper limit. . . . .	210
6.24. Sample of surface heat transfer coefficient measured on the north wall during the first night. . . . .	211
6.25. Thermograms of thermal bridges in steady-state with ROIs (average of 120 frame capture during 2 h of pseudo-steady-state). . . . .	212
6.26. Measured apparent temperature profiles on thermal bridges in steady-state. . . . .	212
6.27. Section of the computational domain and temperature iso-contours in the vicinity of the thermal bridge. . . . .	213
7.1. Illustration of thesis plan. . . . .	217
7.2. Scheme of a simple slab (1D problem). . . . .	220
7.3. A 1D uniform wall is thermally characterized by any two of the four parameters $R$ , $C$ , $\tau$ and $b$ which are derived from $e$ , $k$ and $a$ . . . . .	222
7.4. Electrical analogy of a 1D wall exchanging heat with the surrounding environments. . . . .	224
7.5. Time-domain functions obtained from application of the Gaver-Stehfest algorithm on function in Eq 7.28 for several orders $N$ . . . . .	226
7.6. Time-domain functions obtained from application of the Gaver-Stehfest algorithm on function in Eq 7.28 for several tolerances $tol$ and $\alpha = 0$ . . . . .	227
7.7. Numerical Laplace inversions of a cosine function ( $N = 20$ for Gaver-Stehfest algorithm, $tol = 10^{-20}$ and $\alpha = 0$ for De Hoog algorithm). . . . .	228
7.8. Model used for the generation of synthetic measurements. . . . .	229
7.9. Exponential function fitted on measurement data (operative temperature). . . . .	230
7.10. Synthetic data generated from the model of a two-layer wall subjected to internal air heating. . . . .	231
7.11. Illustration of inverse problems. . . . .	232
7.12. Components of the estimation error, inspired from [205]. . . . .	234
7.13. Reduced sensitivity coefficients for the test case (section 7.1.5). . . . .	239
7.14. Example of linear combination between three reduced sensitivity coefficients. . . . .	242
7.15. Example of unbiased estimation from noised synthetic data (unsigned residuals). . . . .	244

7.16. Example of biased estimation from noised synthetic data (signed residuals). . . . .	245
7.17. Illustration of parameter identification according to the model representation. . . . .	249
7.18. Theoretical and estimated impedances (inverse of transfer function) from ARX model applied to the test case with $n_a = n_b = 20$ and $n_k = 0$ . . . . .	252
7.19. Residuals of ARX estimation (test case), with $n_a = n_b = 20$ and $n_k = 0$ . . . . .	255
7.20. Normalized autocorrelation and correlation coefficients for the test case. They are of small magnitude. . . . .	256
7.21. Estimated thermal resistance as a function of hyperparameters $n_a$ and $n_b$ (test case). . . . .	257
8.1. Illustration of thesis plan. . . . .	259
8.2. Definition of model inputs and output. . . . .	263
8.3. Model used for the generation of synthetic measurements. . . . .	265
8.4. Internal surface temperature and heat flux for the Step and Square heating strategies (test case). . . . .	266
8.5. Reduced sensitivity coefficients for the Step and Square heating strategies (test case). . . . .	266
8.6. Flow chart of experimental aspects for active measurements. . . . .	268
8.7. Flow chart of inverse technique for application of the white-box approach. . . . .	271
8.8. Illustration the real (top) and reduced (bottom) thermal problems: surface resistances and operative temperatures are excluded from the model. Measured quantities are written in red. . . . .	273
8.9. Decomposition of internal and external surface temperatures (superimposition theorem). . . . .	274
8.10. Internal and external air temperatures during an active test (the heaters are turned on at $t = 0$ ). . . . .	279
8.11. Surface heat flux and temperature measured on the internal wall surface during an active test, as well as wall internal temperature. . . . .	280
8.12. Function fit on model input $\theta_{si}^+$ (from CEREMA experiment, $n = 7$ ). . . . .	281
8.13. Reduced sensitivities of white-box model $A_2$ for the given example. . . . .	283
8.14. Comparison between measurements and model after parameter estimation (model $A_2$ ). . . . .	284
8.15. Impact of experiment duration (upper limit of time horizon) on thermal resistance estimation (model $A_2$ ). . . . .	285
8.16. Impact of ARX model number of parameters on the estimated thermal resistance (model $A'$ ). The sampling period is 30 s. . . . .	286
8.17. Residual analysis with $n_a = n_b = 25$ and $n_k = 0$ . . . . .	286
8.18. Impact of experiment duration on thermal resistance estimation (ARX approach, with model $A'$ ). . . . .	287
8.19. Example of internal and external temperatures for consecutive active tests (configuration 5). . . . .	291



8.20. Presentation of active measurements for the SGR experimental campaign. The active tests are highlighted in red. . . . .	293
8.21. Function fitted on model inputs. . . . .	294
8.22. Illustration of model reduction: the three-layer wall is modeled with a two-layer model. . . . .	295
8.23. Reduced sensitivities of model $A_2$ (Experiment 1). . . . .	296
8.24. Comparison between measurements and model after parameter estimation. . . . .	297
8.25. Impact of experiment duration (upper limit of time horizon) on thermal resistance estimation. . . . .	298
8.26. Summary of wall thermal resistance estimations for every model. . . . .	299
8.27. Contribution of each term in the calculation of $\varphi_{\text{mo}}$ . . . . .	299
9.1. Illustration of thesis plan. . . . .	303
9.2. Illustration of homogenization of surface heat flux. . . . .	305
9.3. Illustration of the homogenization procedure on a three-layer wall: it turns one 2D or 3D thermal problem into two 1D problems. . . . .	306
9.4. Flow chart of the active method for the characterization of a thermal bridge. . . . .	307
9.5. Illustration of Two-step and Single-step approaches for the characterization of a thermal bridge. . . . .	309
9.6. Two-layer model used for the comparison of the Two-step and Single-step approaches. . . . .	310
9.7. Synthetic measurements for the Two-step approach. . . . .	311
9.8. Reduced sensitivity coefficients for the Two-step approach. . . . .	311
9.9. Example of concatenated measurement vector $\varphi = [\varphi_{1D}, \varphi_{\text{tb}}]$ for the Single-step approach (synthetic measurements). . . . .	312
9.10. Reduced sensitivity coefficients for the Single-step approach. . . . .	313
9.11. Example of internal and external temperatures for consecutive active tests (configuration 5). . . . .	315
9.12. Evolution of temperature differences between thermal bridges and sound area (from IRT) during an active test (configuration 2). . . . .	316
9.13. Thermal image captured during an active test (configuration 2, after 4 h of heating) and ROIs used for temperature and heat flux extrapolation. The HFM is on the sound area. . . . .	317
9.14. Evolution of wall surface temperature and heat flux extrapolated from the sound area to the thermal bridges (configuration 2). . . . .	318
9.15. Comparison of measurements and model output after parameter estimation (model $A_2$ ). . . . .	319
9.16. Summary of estimated $\psi$ coefficients for each thermal bridge. . . . .	322
9.17. Presentation of active measurements for the SGR experimental campaign. The active tests are highlighted in red. . . . .	324
9.18. Thermal images captured during an active test (Experiment 1, after 4 h of heating) and ROIs used for temperature and heat flux extrapolation. HFMs are the sound areas. . . . .	325

9.19. Evolution of temperature difference and surface heat flux extrapolated from the sound area to thermal bridges N2 and E2 during an active test. . . . .	326
9.20. Comparison of measurements and model output after parameter estimation (Experiment 1). . . . .	329
10.1. Illustration of thesis plan. . . . .	333
A.1. Photography of the IR spectrometer. . . . .	359
A.2. Samples used for emissivity measurements. . . . .	361
A.3. Example of measured spectral emissivities. . . . .	361
A.4. Example of a hot disk sensor. . . . .	362
A.5. Two configurations for measurement with the “Hot Disk”. . . . .	363
A.6. Example of measured temperature and residuals after estimation of the sample material properties with the Hot Disk method. . . . .	364
A.7. Measured thermal conductivity $k$ and diffusivity $a$ as a function of temperature for two samples made of wood and gypsum. . . . .	364
A.8. Description of the experimental setup used to characterize the thermal effusivity of materials. . . . .	365
A.9. Surface temperature evolutions of the gypsum sample and the reference plastic plate as a function time and square root of time. . . . .	366
A.10. Surface temperature evolutions of the insulating material samples and the reference plastic plate as a function time and square root of time. . . . .	367
C.1. Parts of computational domains and boundary conditions of FE models (note: the computational domains are much taller: only a fraction of them is shown). . . . .	375
C.2. Meshes used in the FE simulations. Zoom on thermal bridge. . . . .	376
C.3. Mesh convergence: the internal surface heat flux is measured on several simulations of increasing mesh refinement and the simulation with the finest mesh is used as a benchmark. . . . .	377
C.4. Relative uncertainty of each parameter in $\psi$ coefficient calculation (metal rail). . . . .	378
E.1. Reduced sensitivity coefficients of the non-normalized and normalized models. . . . .	383
E.2. External surface measurements during one period (experiment of configuration 5). . . . .	385
E.3. Fit of a polynomial function (order 7) to the external surface temperature $T_{se}$ . . . . .	387
E.4. Reduced sensitivity coefficients (calculated for $\beta = \hat{\beta}$ ). . . . .	388
E.5. Comparison model/measurements and residuals. . . . .	389
E.6. Elements of $\mathbf{y} - \mathbf{y}_{mo}(\beta)$ vector and cost junction $J$ plotted in the parameter space. . . . .	389
E.7. Isocontours of relative bias on $\hat{R}$ as a function of relative bias on $R_3$ and $b_3$ for experiments 17, 19, 21 and 23. . . . .	391

E.8. Summary of relative biases on $\hat{R}$ as a function of relative bias on $R_3$ and $b_3$ for experiments 17, 19, 21 and 23. . . . .	391
E.9. Configuration 1, model $A_2$ , $1/2$ . . . . .	392
E.10. Configuration 1, model $A_2$ , $2/2$ (Experiment 5). . . . .	393
E.11. Configuration 2, model $A_2$ . . . . .	393
E.12. Configuration 3, model $AE_3$ . . . . .	394
E.13. Configuration 4, model $AE_3$ . . . . .	395
E.14. Configuration 5, model $AE_3$ , $1/2$ . . . . .	396
E.15. Configuration 5, model $AE_3$ , $2/2$ . . . . .	397
E.16. Configuration 6, model $AE_3$ . . . . .	397
E.17. SGR experiments (1 to 4). . . . .	398
E.18. SGR Experiment 5. . . . .	399
F.1. Experiment 1: configuration 1, model $A_2$ . . . . .	401
F.2. Experiment 2: configuration 1, model $A_2$ . . . . .	402
F.3. Experiment 3: configuration 1, model $A_2$ . . . . .	402
F.4. Experiment 4: configuration 1, model $A_2$ . . . . .	403
F.5. Experiment 5: configuration 1, model $A_2$ . . . . .	403
F.6. Experiment 6: configuration 2, model $A_2$ . . . . .	404
F.7. Experiment 7: configuration 2, model $A_2$ . . . . .	404
F.8. Experiment 8: configuration 2, model $A_2$ . . . . .	405
F.9. Experiment 9: configuration 3, model $AE_3$ . . . . .	405
F.10. Experiment 10: configuration 3, model $AE_3$ . . . . .	406
F.11. Experiment 11: configuration 3, model $AE_3$ . . . . .	406
F.12. Experiment 12: configuration 3, model $AE_3$ . . . . .	407
F.13. Experiment 13: configuration 4, model $AE_3$ . . . . .	407
F.14. Experiment 14: configuration 4, model $AE_3$ . . . . .	408
F.15. Experiment 15: configuration 4, model $AE_3$ . . . . .	408
F.16. Experiment 16: configuration 4, model $AE_3$ . . . . .	409
F.17. Experiment 17: configuration 5, model $AE_3$ . . . . .	409
F.18. Experiment 18: configuration 5, model $AE_3$ . . . . .	410
F.19. Experiment 19: configuration 5, model $AE_3$ . . . . .	410
F.20. Experiment 20: configuration 5, model $AE_3$ . . . . .	411
F.21. Experiment 21: configuration 5, model $AE_3$ . . . . .	411
F.22. Experiment 22: configuration 5, model $AE_3$ . . . . .	412
F.23. Experiment 23: configuration 5, model $AE_3$ . . . . .	412
F.24. Experiment 24: configuration 5, model $AE_3$ . . . . .	413
F.25. Experiment 25: configuration 6, model $AE_3$ . . . . .	413
F.26. Experiment 26: configuration 6, model $AE_3$ . . . . .	414
F.27. Experiment 27: configuration 6, model $AE_3$ . . . . .	414
F.28. Experiment 1, model $AIE_2$ . . . . .	415
F.29. Experiment 2, model $AIE_2$ . . . . .	416
F.30. Experiment 4, model $AIE_2$ . . . . .	417
F.31. Experiment 5, model $AIE_2$ . . . . .	418

# List of Tables

2.1.	Summary of literature review on thermal bridge assessment (N/A = Not Applicable, $U_{eq}$ equivalent $U$ -value of a wall with a thermal bridge, $k$ =thermal conductivity, $\varphi$ =heat flux density across a wall).	58
3.1.	Coefficients of NIST polynomial for T-type thermocouple between 0 and 400°C (error: $\pm 0.03$ K) [159].	82
3.2.	Summary of measured HFM offset for 7 identical sensors.	84
3.3.	Design values and uncertainties of input variables.	105
3.4.	Calculated quantities and propagated uncertainties.	106
3.5.	Summary of expected measurement uncertainties for the given sensors.	112
4.1.	Overview of the experimental campaigns.	115
4.2.	Summary of chapters in which each experimental campaign is used.	116
4.3.	List of sensors used in the experimental set-up.	118
4.4.	CEREMA: Summary of thickness and thermal properties of each setup layer.	125
4.5.	CEREMA: Summary of active tests configurations.	131
4.6.	SGR: Summary of thickness and thermal properties of each setup layer.	135
5.1.	Summary of steady-state $h$ -coefficient measurements.	165
5.2.	Summary of measured heat transfer coefficients ( $W.m^{-2}.K^{-1}$ ).	173
5.3.	Applicability of $h$ -measurement methods.	177
6.1.	Measured quantities and calculated thermal resistance (ISO 9869-1 [15]).	193
6.2.	Thermal conductivity and thickness of materials used in FE simulations.	194
6.3.	Detailed results on thermal bridge transmission coefficients estimation with the “ $I_{tb}$ method” and comparison of uncertainties between the present and “standard” approaches.	196
6.4.	Detailed results on thermal bridge transmission coefficients estimation with the “ $h$ method”.	197
6.5.	Measured quantities and calculated thermal resistance with ISO 9869-1 [15].	200
6.6.	Thermal conductivity and thickness of materials used in FE simulations.	203
6.7.	Estimated thermal bridge transmission coefficients.	203
6.8.	Thermal conductivity and thickness of materials used in FE simulations.	210
6.9.	Estimated $\psi$ values ( $mW.m^{-1}.K^{-1}$ ) for each steady-state experiment.	211
6.10.	Summary of mean features of steady-state methods.	215
6.11.	Summary of measurements needed for each method.	215

7.1.	Coefficients of the Gaver-Stehfest algorithm for $N = 10$ . . . . .	225
7.2.	Thermal properties used in the model (model parameters are in bold). . . . .	229
7.3.	Hybrid matrix $V_{\text{cor}}$ for the given test case ( $\sigma = 0.4 \text{ W.m}^{-2}$ ). . . . .	241
7.4.	Estimated parameters. . . . .	244
8.1.	Presentation of the most common types of thermal load for an active experiment. . . . .	264
8.2.	Hybrid $V_{\text{cor}}$ matrices for the Step and Square heating strategies ( $\sigma_{\varphi} = 0.4 \text{ W.m}^{-2}$ ). . . . .	267
8.3.	Summary of “white-box” direct models (The letter A stands for “active test”, I for “internal correction” and E for “external correction”). . . . .	276
8.4.	White-box direct model for the estimation of the properties of a heavyweight layer from outdoor measurements (The letter H stands for “heavyweight”). . . . .	277
8.5.	Summary of active tests configurations. . . . .	278
8.6.	Summary of “white-box” direct models. . . . .	282
8.7.	Hybrid matrix $V_{\text{cor}}$ for the given example ( $\sigma_{\varphi} = 0.4 \text{ W.m}^{-2}$ ). . . . .	282
8.8.	Estimated parameters $\hat{\beta}$ with reference values (model $A_2$ ). . . . .	283
8.9.	Presentation of ARX model. . . . .	285
8.10.	Thermal resistance estimations for a constant external temperature with two approaches: model $A_2 =$ “white-box”, model $A' =$ “black-box”. . . . .	288
8.11.	Estimations of thermal resistance for varying external temperature (cells are filled in gray when the estimated value is more than 10% away from the steady-state reference value). Depending on the experiment, $T_{\text{air,e}}$ is around a maximum: $\cap$ , or increasing: $\nearrow$ , or around a minimum: $\cup$ , or decreasing: $\searrow$ . . . . .	290
8.12.	Summary of models ( $\checkmark =$ yes, $x =$ no, $x\checkmark =$ not true in all configurations). . . . .	292
8.13.	Hybrid matrix $V_{\text{cor}}$ ( $\sigma = 0.4 \text{ W.m}^{-2}$ ). . . . .	296
8.14.	Estimated parameters $\hat{\beta}$ with reference values. . . . .	297
8.15.	Summary of estimated wall thermal resistances (cells are filled in light gray when the estimated value is more than 10% away from the steady-state reference value, and in dark gray for 20%). . . . .	298
8.16.	Summary of active homogeneous wall characterization method. . . . .	302
9.1.	Thermal properties used in the model. . . . .	310
9.2.	Hybrid $V_{\text{cor}}$ matrix for the Two-step approach ( $\sigma_{\varphi} = 0.4 \text{ W.m}^{-2}$ ). . . . .	312
9.3.	Hybrid $V_{\text{cor}}$ matrix for the Single-step approach ( $\sigma_{\varphi} = 0.4 \text{ W.m}^{-2}$ ). . . . .	313
9.4.	Summary of active test configurations of the CEREMA campaign. . . . .	315
9.5.	Summary of parameter estimation on sound area and thermal bridges (configurations 2, model $A_2$ ). . . . .	318
9.6.	Estimations of thermal resistances and thermal bridge transmission coefficients for every experiment. Depending on the experiment, $T_{\text{air,e}}$ is constant: $-$ , or around a maximum: $\cap$ , or increasing: $\nearrow$ , or around a minimum: $\cup$ , or decreasing: $\searrow$ . . . . .	320

9.7.	Summary of parameter estimation on the sound area and the thermal bridges (Experiment 1). The $\psi$ -value is calculated from the estimated thermal resistances. The parameter of interest ( $R_2$ ) is in bold. . . . .	327
9.8.	Summary of estimated $h$ and $\psi$ values for each studied thermal bridge and experiments 1, 2, 4 and 5. The reference values were obtained in steady-state (see Chap 8). . . . .	328
9.9.	Summary of active non-homogeneous wall characterization method. . . . .	331
A.1.	Coefficients of $\rho_\lambda^{\text{gold}}$ . . . . .	360
A.2.	Measured emissivity (7.7-9.2 $\mu\text{m}$ ). . . . .	362
C.1.	Input data for $\psi$ uncertainty calculation (metal rail). . . . .	378
E.1.	$V_{\text{cor}}$ matrix (for $\beta = \hat{\beta}$ and $\sigma = 8 \text{ W.m}^{-2}$ ). . . . .	386

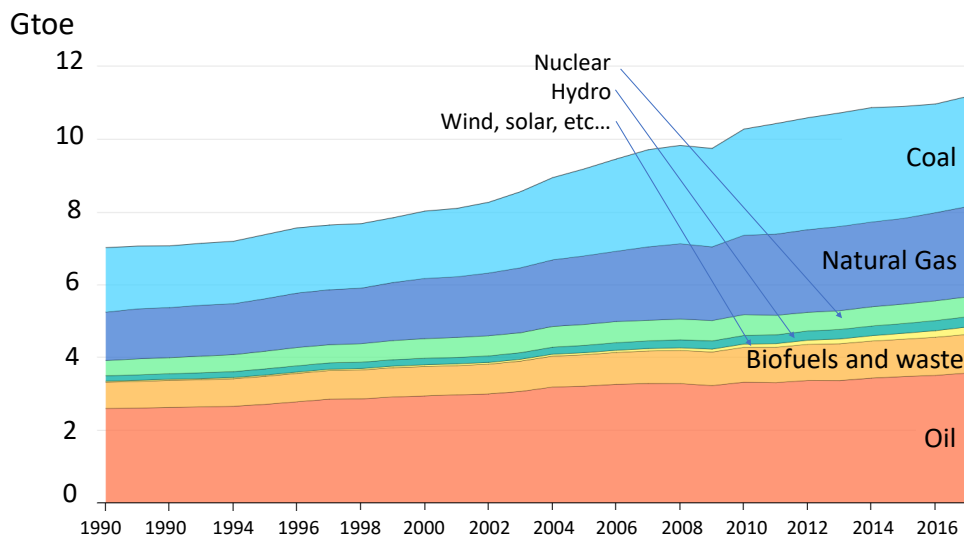


# 1. Introduction

## 1.1. General introduction

Among the greatest issues our society must face, today and tomorrow, are the effects of climate change and the reduction of accessible fossil fuel stocks. Indeed, the combustion of these fuels represents more than 80% of the ever-growing world supply of primary energy (see Fig 1.1) and is the leading cause of greenhouse gas (GHG) emissions. The world energy demand keeps growing because of population increase and improvement of living standards. The mitigation of GHG emissions relies on two parallel actions: the reduction of global energy consumption and the replacement of fossil fuels by renewable energies. In this context, the European Union (EU) 2030 climate & energy framework set three main targets:

- At least 40% cut in greenhouse gas emissions (from 1990 levels).
- At least 32% share for renewable energy.
- At least 32.5% improvement in energy efficiency.



**Figure 1.1.:** World primary energy supply by source (source: IEA, [www.iea.org](http://www.iea.org)). Gtoe = Giga tonne of oil equivalent.

Residential and non-residential buildings account for about 40% of total energy use in the EU [1]. The building sector has therefore a major role to play to reach these goals and minimize our environmental footprint. In addition, 82% of GHG emissions in the residential sector are imputable to heating (source: CEREN [2]).



Thus, thermal insulation of buildings is a domain with a great potential for energy savings.

In this context, it is important to assess the thermal performance of buildings, both for construction and renovation. The estimation of these performances usually relies on theoretical calculations. When *in situ* measurements are undertaken, the results often show some discrepancies with predictions: this is the so called “performance gap” (see [3, 4, 5, 6] and references therein). The mismatch between theory and practice can be due to several factors such as aging, moisture, quality of construction, and thermal bridging.

In order to correctly address issues related to the performance gap, knowledge of the overall building energy losses is not enough. Rather, the local thermal performance of each building element (walls, roof, windows, ...) is required. Thus, it is of interest to have accurate and easy to use *in situ* measurement methods. Several techniques were developed in the literature for the local or global characterization of building envelope on site. Yet, experimental campaigns conducted on building walls highlighted the discrepancies between the existing methods (see [7, 8] for instance). From this perspective, this thesis aims at enriching the pool of methods available for the estimation of the thermal performance of building elements, with a focus on thermal bridges.

The overall heat losses in a building are quantified by the Heat Loss Coefficient (HLC) and may be decomposed into several terms:

$$HLC = \underbrace{\sum_i U_i A_i}_{\text{1D losses}} + \underbrace{\sum_j \psi_j L_j + \sum_k \chi_k}_{\text{Thermal bridges}} + \underbrace{\rho c_p Q_V}_{\text{Air infiltrations}} \quad (1.1)$$

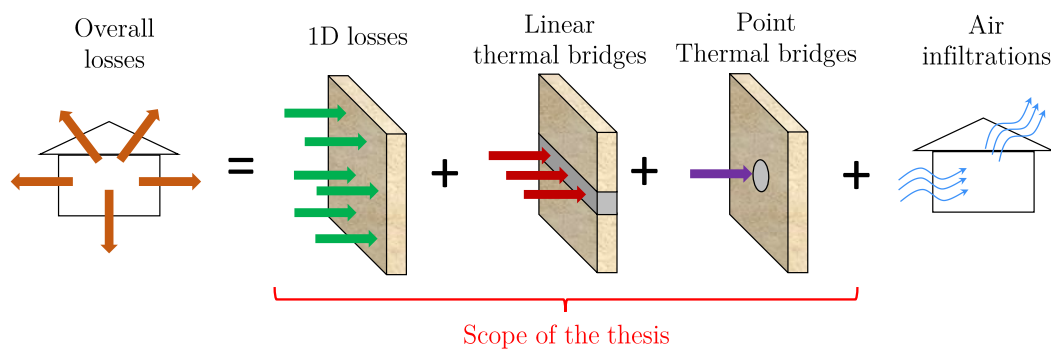
Heat losses through envelope

with:

- $HLC$  the overall Heat Loss Coefficient (in  $\text{W.K}^{-1}$ ).
- $U$  and  $A$  the thermal transmittance (in  $\text{W.m}^{-2}.\text{K}^{-1}$ ) and area of a wall without thermal bridge.
- $\psi$  and  $L$  the thermal transmittance (in  $\text{W.m}^{-1}.\text{K}^{-1}$ ) and length of a linear thermal bridge.
- $\chi$  the thermal transmittance (in  $\text{W.K}^{-1}$ ) of a point thermal bridge.
- $\rho$ ,  $c_p$  and  $Q_V$  the air density, heat capacity and flow rate, respectively.

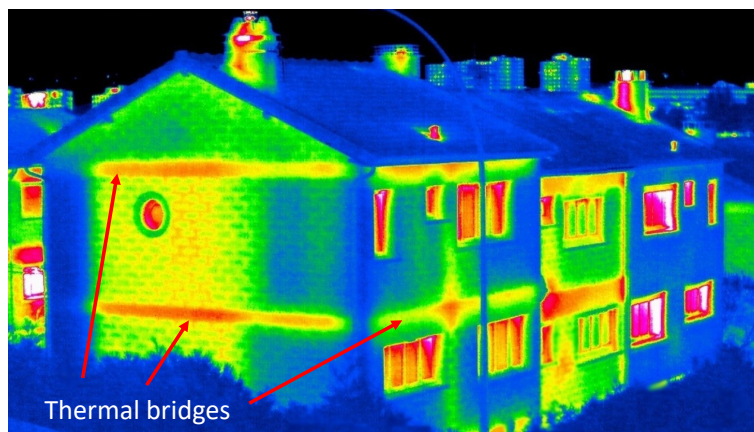
Equation 1.1 is illustrated in Fig 1.2. The present thesis focuses on the *in situ* measurement of heat losses through the building envelope. In other words, it aims at quantifying  $U$ ,  $\psi$  and  $\chi$  coefficients whereas air infiltrations are not addressed.

Thermal bridges (also called “cold bridges”) are irregularities and defects in the building envelope which locally increase heat losses. They may be of very different nature (wall/floor junction, openings, mechanical support of insulating materials,



**Figure 1.2.:** Illustration of heat losses in a building (Eq 1.1).

...). Figure 1.3 shows an example of a thermal image of a building where some thermal bridges are clearly visible.



**Figure 1.3.:** Example of thermal bridges (thermal image from [9]).

Thermal bridges can represent 10 % to 40 % of the energy final demand [10, 11], depending on the building geometry and insulation level. The use of low-conductivity materials tends to reduce the overall heat losses but also to increase the relative share of thermal irregularities. In addition, because of workmanship defects, thermal bridges may have more impact than expected. In cold climates, not only do thermal bridges impact the thermal comfort of occupants, they also increase the risk of condensation and mould growth [12, 13]. This may damage the building envelope and cause sanitary issues. For these reasons, it is important to quantify the influence of thermal bridges.

The chosen approach consists in developing active methods: an artificial thermal load is applied to the studied wall. This type of approach is common in Non Destructive Testing (NDT) for the detection and characterization of defects in materials (see [14] for instance). The transient response of the wall to this loading is then analyzed using an inverse technique to estimate the desired thermal properties (such as the wall thermal resistance). Active methods have two main advantages in the building domain when compared to steady-state (or “passive”) techniques. First, the experiment duration may be much shorter and only take a few hours (instead of

days [15]). Second, active methods are applicable in a much wider range of weather conditions. Indeed, they do not require a high and constant natural indoor/outdoor temperature gradient like steady-state methods. There are therefore not limited to winter-time measurements. In addition, quantitative infrared thermography (IRT) is a powerful tool for the characterization of thermal bridges (and more generally of non-homogeneous walls). Indeed, not only does thermal imaging enable to visualize surface temperature differences on an extended zone, it also does not disturb local heat transfers because it is contact-less.

This thesis was conducted in the context of a collaboration between the CERTES laboratory and Saint-Gobain Research Paris. Previous works conducted by this collaboration focused on the detection of thermal bridges in building walls. It set the frame of the work presented in this manuscript.

The next section presents thermal bridging in more details and section 1.3 introduces the plan of the manuscript.

## 1.2. Types of thermal bridges

There are several ways to categorize thermal bridges. According to Farkh [10], two main types of such irregularities can be found in a building:

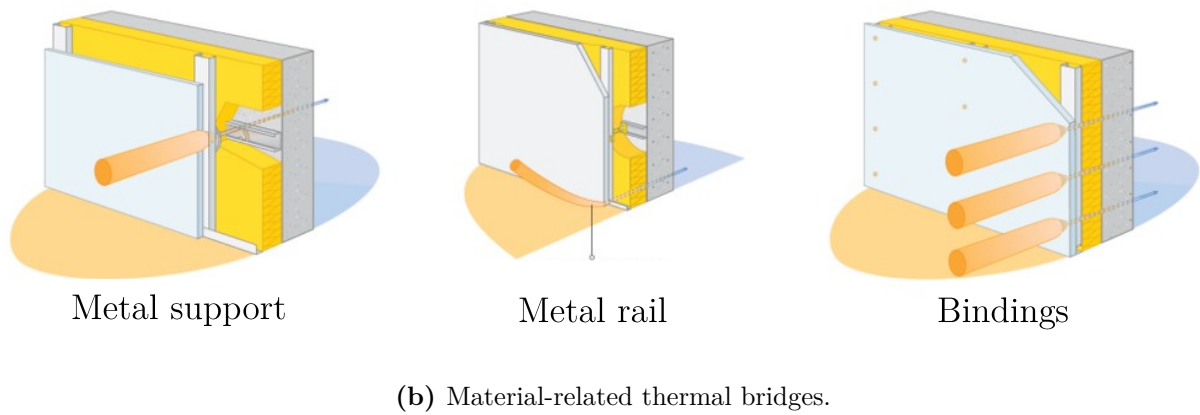
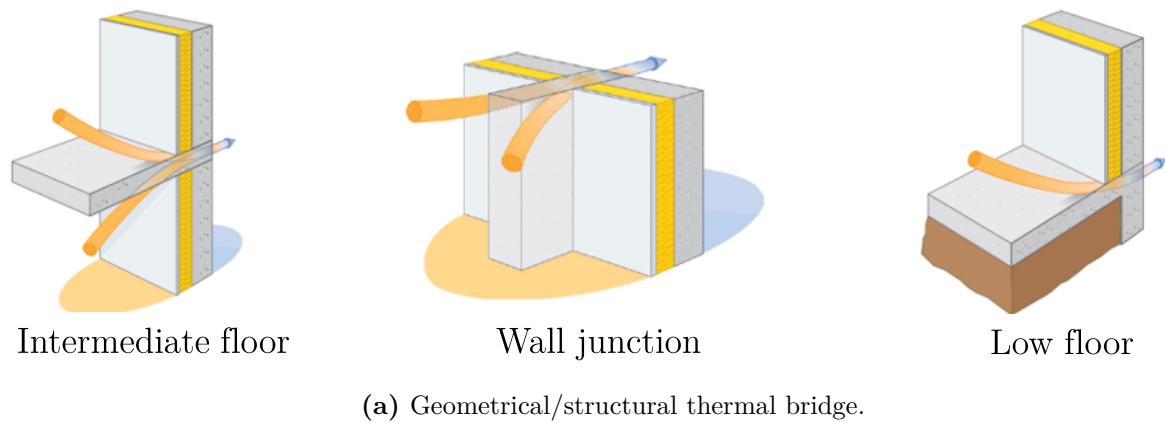
- “Geometrical” (or “structural”) thermal bridges are due to the overall shape of the building (e.g. wall/floor junctions, corners)
- “Material-related” thermal bridges are induced by irregularities in the insulation layers (e.g. mechanical supports of insulating materials).

Figure 1.4 proposes an illustration of some common thermal bridges for each category. This thesis focuses on material-related thermal bridges.

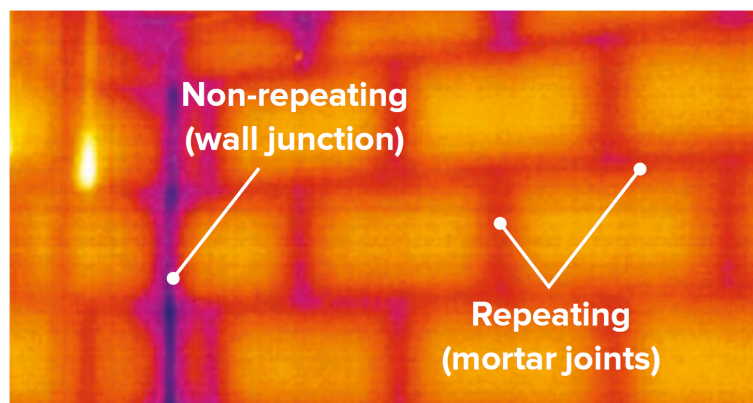
For the sake of completeness, let us mention that Whale [17] proposes another classification: “repeating” and “non-repeating” thermal bridges. Examples of repeating thermal bridges are mortar joints and wall-ties in masonry construction or timber or steel studs in framed construction. When their frequency is known and consistent, their effects can be accounted for directly in the U-value calculation for the building element itself. The remaining non-repeating thermal bridges are dealt with by  $\psi$ -values. Fig 1.5 proposes an illustration of repeating and non-repeating thermal bridges. This classification will not be used in the present thesis.

## 1.2. TYPES OF THERMAL BRIDGES

---



**Figure 1.4.:** Examples of thermal bridges in buildings, from [16, 10].



**Figure 1.5.:** Illustration of “repeating” and “non-repeating” thermal bridges, from [17].

### 1.3. Plan of the manuscript

The plan of the manuscript is organized by method: each chapter presents one or several method(s) and their application to one or several experimental campaigns conducted during this thesis. The dependencies between the methods are illustrated by the brick wall shown in Fig 1.6. Every chapter (each brick) is based on the methods and results presented in the chapters located below. For instance, the active characterization of a homogeneous wall (Chap 8) is based on contact measurements (Chap 3) and inverse methods (Chap 7) but does not require infrared thermography (Chap 3). Chapters 1, 2 and 4 form the base of the wall.

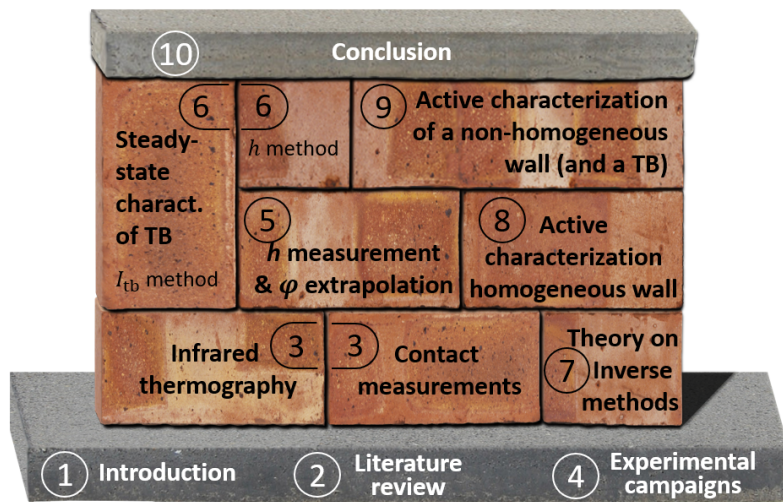


Figure 1.6.: Illustration of thesis plan.

Here is summarized the content of each chapter:

**Chapter 2** presents a literature review of existing methods for (i) the qualitative and quantitative assessment of thermal bridges and (ii) the measurement of a wall thermal transmittance.

**Chapter 3** deals with different experimental aspects of thermal metrology. The working principles of contact measurements as well as infrared thermography (IRT) are described.

**Chapter 4** introduces the four experimental campaigns conducted in the scope of the present thesis. The results obtained on these setups are exposed in the next chapters.

**Chapter 5** focuses on the *in situ* measurement of the heat transfer coefficient  $h$  on a building wall. Five methods are compared in steady and transient states. The quantification of the heat transfer coefficient enables to measure the surface heat flux  $\varphi$  on a non-homogeneous wall with IRT. This is useful for the characterization of non-homogeneous walls and thermal bridges (Chapters 6 and 9).

**Chapter 6** is about the quantification of a thermal bridge transmission coefficient from steady-state measurements. Two methods are presented: one inspired

from the literature ( $I_{tb}$  method) and one original ( $h$ -method). They are both based on IRT measurements. The values obtained are used as reference values in Chapters 8 and 9 to assess the relevance of active methods.

**Chapter 7** is fully theoretical. It presents the mathematical tools used in Chapters 8 and 9 in the active methods (thermal quadrupole formalism, inverse methods with a white-box model, and ARX black-box models).

**Chapter 8** introduces an active method for the estimation of a homogeneous wall thermal resistance. It is based on an inverse technique fed with contact measurements of surface heat fluxes and temperatures.

**Chapter 9** proposes a generalization of the above-mentioned active method in order to apply it to non-homogeneous walls and thermal bridges. It uses infrared thermography as well as a measurement of the heat transfer coefficient.

**Chapter 10** proposes a conclusion.



## 2. Literature review on *in situ* characterization of building walls and thermal bridge



**Figure 2.1.:** Illustration of thesis plan.

The objective of this first chapter is to review existing methods for the assessment of the thermal performances of thermal bridges and homogeneous walls. Section 2.1 first introduces the key performance indicators (KPI) commonly used for the thermal characterization of building envelope elements. Then, the literature review is divided in two parts:

- Section 2.2 presents a thorough review of methods developed for the assessment of thermal bridges in buildings. The detection of these irregularities (or defaults) as well as the quantification of their performances from measurements are addressed. Laboratory experiments and *in situ* measurements are distinguished. Studies combining measurements and numerical simulations are also presented, as well as full numerical works. The derivation of reduced models of thermal bridges (so-called “equivalent wall” models) is also addressed.
- Section 2.3 proposes a literature review of *in situ* measurement methods for the estimation of a building wall thermal transmittance ( $U$ -value). The methods are classified in three categories: steady-state, dynamic and active methods.

A conclusion is drawn in section 2.4.



## Nomenclature

### Acronyms

HLC	Heat Loss Coefficient
IRT	InfraRed Thermography
KPI	Key Performance Indicator
MRT	Mean Radiant Temperature
TB	Thermal Bridge

### Greek Symbols

$\alpha$	phase lag	rad
$\varepsilon$	surface emissivity	-
$\sigma$	Stefan-Boltzmann constant	$\text{W.m}^{-2}.\text{K}^{-4}$
$\phi$	heat flux	W
$\phi_{ii}, \phi_{ee}, \phi_{ie}$	structure factors	-
$\varphi$	heat flux density	$\text{W.m}^{-2}$
$\chi$	point thermal transmittance	$\text{W.K}^{-1}$
$\psi$	linear thermal transmittance	$\text{W.m}^{-1}.\text{K}^{-1}$

### Roman Symbols

$A$	area / amplitude	$\text{m}^2 / -$
$C$	heat capacity	$\text{J.K}^{-1}$
$ES$	Energy Saving factor	-
$f$	frequency	$\text{s}^{-1}$
$f_{\text{Rsi}}$	temperature factor	-
$h$	heat exchange coefficient	$\text{W.m}^{-2}.\text{K}^{-1}$
$I_{\text{tb}}$	thermal bridge incidence (or impact) factor	-
$k$	thermal conductivity	$\text{W.m}^{-1}.\text{K}^{-1}$
$L$	length	m
$L_{\text{tb}}$	thermal bridge width	m
$Nu$	Nusselt number	-
$Pr$	Prandtl number	-
$p$	Laplace variable	$\text{s}^{-1}$
$R$	thermal resistance	$\text{m}^2.\text{K}.\text{W}^{-1}$
$Ra$	Rayleigh number	-
$T$	temperature	K
$t$	time	s
$U$	wall thermal transmittance	$\text{W.m}^{-2}.\text{K}^{-1}$
$v$	wind speed	$\text{m.s}^{-2}$

### Superscripts

-	space average
c	convective
r	radiative

### Subscripts

1D	sound area (1D transfer)
e	exterior
env	environment
i	interior

---

op	operative
s	surface
tb	thermal bridge

## 2.1. Key Performance Indicators (KPI)

For a better understanding of the following sections, here are presented some quantities commonly used to quantify the thermal performance of walls and thermal bridges. Most of these key performance indicators will be used in this thesis.

### 2.1.1. Wall thermal transmittance $U$ and resistance $R$

A wall is thermally characterized either by its thermal resistance  $R$  ( $\text{m}^2 \cdot \text{K} \cdot \text{W}^{-1}$ ) or its thermal transmittance  $U$  ( $\text{W} \cdot \text{m}^{-2} \cdot \text{K}^{-1}$ ). The thermal problem is supposed one-dimensional. The wall thermal resistance is defined in steady-state as the ratio of the temperature difference  $\Delta T_s$  between the two surfaces of the wall over the heat flux density  $\varphi$  ( $\text{W} \cdot \text{m}^{-2}$ ) across the wall:

$$R_{\text{wall}} = \frac{\Delta T_s}{\varphi} \quad (2.1)$$

The  $U$ -value is the ratio of the heat flux density  $\varphi$  over the temperature difference  $\Delta T$  between the internal and external environments, in steady-state. It is also the inverse of the total thermal resistance which is the sum of  $R_{\text{wall}}$  and the superficial resistances  $R_{\text{si}}$  and  $R_{\text{se}}$  (thermal resistance between the wall surfaces and the internal and external environments). It comes:

$$U = \frac{\varphi}{\Delta T} = \frac{1}{R_{\text{si}} + R_{\text{wall}} + R_{\text{se}}} \quad (2.2)$$

Therefore, the heat flux across a wall is simply given by the following product:

$$\phi_{1D} = U \times A \times \Delta T \quad (2.3)$$

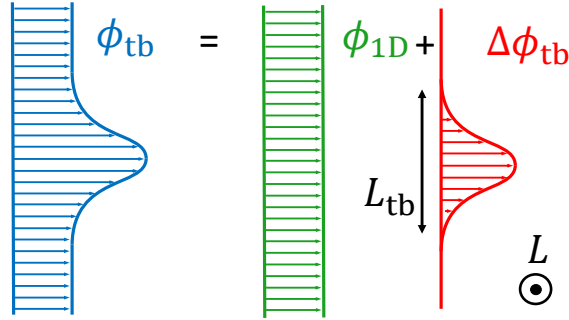
with  $A$  the wall area. The subscript “1D” means that heat transfers are supposed 1D in the wall (1D losses).

### 2.1.2. Thermal bridge transmittance $\psi$ or $\chi$

As explained above, a wall is thermally characterized by its thermal transmittance  $U$ . Similarly, thermal bridges are characterized by a transmission coefficient:  $\psi$  or  $\chi$  [18]. The latter are useful to work out the heat loss  $\Delta\phi_{\text{tb}}$  only due to the presence of the thermal bridge as illustrated in Fig 2.2):

$$\Delta\phi_{\text{tb}} = \phi_{\text{tb}} + \phi_{1D} \quad (2.4)$$

with  $\phi_{tb}$  the total heat flux including the thermal bridge.



**Figure 2.2.:** Illustration of heat losses in a building wall.

A linear thermal bridge (it is possible to identify an axis along which the orthogonal section of the thermal bridge does not change, such as wall/floor junctions) is characterized by a  $\psi$  coefficient ( $\text{W}\cdot\text{m}^{-1}\cdot\text{K}^{-1}$ ) defined such that (similarly to Eq 2.3):

$$\Delta\phi_{tb} = \psi \times L \times \Delta T \quad (2.5)$$

with  $L$  the length of the thermal bridge. Similarly, a point thermal bridge (such as corners, or pins used to hold insulation materials) are characterized by a  $\chi$  coefficient ( $\text{W}\cdot\text{K}^{-1}$ ):

$$\Delta\phi_{tb} = \chi \times \Delta T \quad (2.6)$$

As a consequence, the total heat flux  $\phi_{tot}$  through a building envelope is given by the summation of the different contributions:

$$\phi_{tot} = \left( \sum_i U_i \times A_i + \sum_j \psi_j \times L_j + \sum_k \chi_k \right) \times \Delta T \quad (2.7)$$

This equation only accounts for heat diffusion through the envelope materials: air infiltrations are not included.

### 2.1.3. Thermal bridge Incidence (or Impact) factor $I_{tb}$

The incidence (or impact) factor is a dimensionless number which quantifies the relative impact of the thermal bridge on the wall thermal transmittance [19, 20, 21, 22, 23]. It enables to perform a quantitative analysis of thermal bridges using infrared thermography without prior information on the structure of the wall. The

Impact factor is defined as the ratio between the total heat flux  $\phi_{\text{tb}}$  and the heat flux in absence of the thermal bridge  $\phi_{\text{1D}}$  [19]:

$$I_{\text{tb}} = \frac{\phi_{\text{tb}}}{\phi_{\text{1D}}} = \frac{h_{\text{tb}}A_{\text{tb}}(\overline{T}_{\text{tb}} - T_{\text{op}})}{h_{\text{1D}}A_{\text{1D}}(T_{\text{1D}} - T_{\text{op}})} \quad (2.8)$$

with  $h$  a total heat exchange coefficient,  $A$  an area,  $\overline{T}_{\text{tb}}$  the mean surface temperature on the thermal bridges,  $T_{\text{1D}}$  the surface temperature of the wall without thermal bridge and  $T_{\text{op}}$  the operative temperature. If the heat exchange coefficient is supposed uniform ( $h_{\text{tb}} = h_{\text{1D}}$ ) and the same areas are considered for the thermal bridge and sound areas ( $A_{\text{tb}} = A_{\text{1D}}$ ), the expression of the impact factor simplifies to:

$$I_{\text{tb}} = \frac{\overline{T}_{\text{tb}} - T_{\text{op}}}{T_{\text{1D}} - T_{\text{op}}} \quad (2.9)$$

The thermal transmittance  $U_{\text{tb}}$  of the wall including the thermal bridge can be derived as follows from the one-dimensional (sound area) transmittance  $U_{\text{1D}}$ :

$$U_{\text{tb}} = U_{\text{1D}} \times I_{\text{tb}} \quad (2.10)$$

A thermal bridge linear or point transmittance may also be calculated from  $I_{\text{tb}}$ :

$$\psi = L_{\text{tb}}U_{\text{1D}}(I_{\text{tb}} - 1) \quad (2.11)$$

$$\chi = A_{\text{tb}}U_{\text{1D}}(I_{\text{tb}} - 1) \quad (2.12)$$

with  $L_{\text{tb}}$  the impact width of a linear thermal bridge and  $A_{\text{tb}}$  the impact area of a point thermal bridge.

#### 2.1.4. The temperature factor $f_{\text{Rsi}}$

The temperature factor  $f_{\text{Rsi}}$  is also a dimensionless number used for thermal bridges impact assessments. It is useful to evaluate the risk of mould growth on thermal bridges [24]. Mould growth may damage the wall and has the potential to cause health problems. The temperature factor is given by:

$$f_{\text{Rsi}} = \frac{T_{\text{si}} - T_{\text{e}}}{T_{\text{i}} - T_{\text{e}}} \quad (2.13)$$

## 2.1. KEY PERFORMANCE INDICATORS (KPI)

---

with  $T_i$  and  $T_e$  the internal and external environment temperatures respectively, and  $T_{si}$  the internal surface temperature. To avoid mould growth, the surface temperature factor should be above a critical value. This threshold differs from one building type to another [25]. In the case of dwellings, a critical temperature factor of 0.75 is recommended. The temperature factor will not be used in this thesis.

## 2.2. Detection and quantification of thermal bridges

The existing studies on thermal bridges mainly concern theoretical and numerical works. Standardized approaches are based either on default/design values (e.g., ISO 14683 [18], or local regulations [26, 10]) or on simplified (or detailed) calculations: ISO 10211 [27]. These methods assume that the wall structure is perfectly known and rely on standard/default values for the thermal properties of the materials and both the external and internal environments (air temperature, relative humidity, wind, etc.). Therefore, standardized methods might lead to a preliminary assessment of the building envelope but they generally may not be in good agreement with the results of actual operating conditions.

This section presents a thorough literature review of methods developed for the detection and characterization of thermal bridges in buildings. First, studies dealing with the detection of these irregularities and defaults are presented (section 2.2.1). Infrared thermography (either “active” or “passive”) has been widely used in the past decades for this purpose. Then, the techniques developed for the quantification of thermal bridges performances from measurements are reported. Some studies were carried out in laboratory (section 2.2.2) whereas a few others involved *in situ* measurements (section 2.2.3). In addition, many studies combined measurements and numerical simulations either to improve the assessment of building thermal performance or to validate a thermal modeling (section 2.2.4). Finally, section 2.2.5 presents numerical studies. A focus is made on the derivation of an equivalent homogeneous wall model.

### 2.2.1. Detection of thermal bridges

Experimental methods used to detect the presence of thermal bridges in a building envelope are presented and discussed in this section. The use of infrared thermography for building applications and inspections was extensively documented in the past decades. A few thorough reviews were written on this topic, such as Balaras *et al.* [28], Kylili *et al.* [29], Lucchi [30] and Nardi *et al.* [31]. In addition, several studies aimed at determining the best conditions for the use of thermography in buildings. For instance, Lehmann *et al.* [32] showed that solar radiation impose strong restrictions in terms of infrared thermography. In addition, Datcu *et al.* [33] and Barreira *et al.* [34] showed that the wall surface emissivity is one of the parameters with the highest influence on thermographic measurements on buildings.

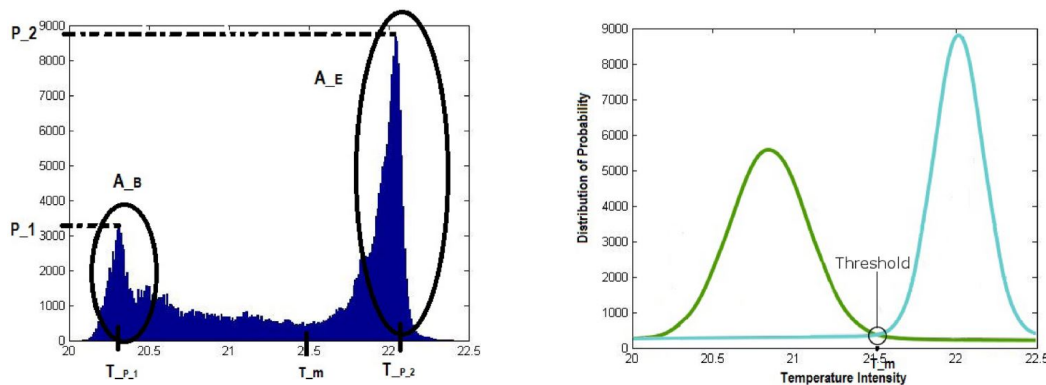
In this section, the distinction between “passive” and “active” infrared thermography (IRT) is made. In passive thermography, the thermal images of the building are recorded under natural conditions: the natural indoor/outdoor temperature gradient enables the visualization of the thermal irregularities and defaults. With active infrared thermography, an artificial load is applied to the building and the dynamic response of the envelope is analyzed.

### 2.2.1.1. Passive IRT

Passive IRT is a commonly used tool for qualitative assessments of building envelopes (see ISO 13187 [35]). It enables to detect irregularities and defaults on a building envelope (see for instance Ocaña *et al.* [36], Garcez *et al.* [37], Menezes *et al.* [38], Fox *et al.* [39, 40, 41] and Taylor *et al.* [24]).

ISO 6781 [42] specifies a qualitative method, by thermographic examination (infrared method), for detecting thermal irregularities in building envelopes. The method is used to identify wide variations in the thermal properties (including air tightness) of the components constituting the external envelopes of buildings.

Several recent studies deal with the automatic detection of thermal bridges from infrared images. Asdrubali *et al.* [43] introduced a methodology to detect the edges of thermal bridges on thermographic images. Two 2D thermal bridges are studied in a hot box facility: a pillar and a beam-pillar joint. The procedure consists in two steps. First, the thermal image contrast is enhanced thanks to an optimized version of the mathematical algorithm for digital image processing (DIP) based on the theory of sampling Kantorovich operators [44]. Second, a suitable thresholding is automatically chosen based on the analysis of the histogram of the enhanced thermal image (see Fig 2.3).

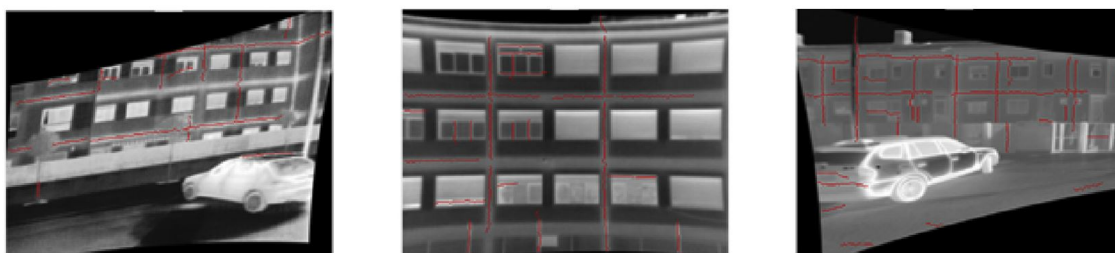


**Figure 2.3.:** Histogram of thermal image and threshold definition from Asdrubali *et al.* [43].

Garrido *et al.* [45] also proposed a method for an automatic detection of thermal bridges. It is an improvement of the procedure originally introduced by Cereijo *et al.* [46]. First, an image rectification is performed to correct geometrical distortion of the image. Then, a median filter is used to increase the signal to noise ratio. This allows detecting lines corresponding to thermal bridges. False detections are reduced using a thresholding method. Three criteria are used to improve the rate of automatic detection of thermal bridges up to 55 %, but 32 % of thermal bridges remain undetected. Figure 2.4 shows examples of thermal images on which thermal bridges are automatically detected.

Some authors also made some passive time-lapse IRT measurements. The “time-lapse” designation means that thermal images are continuously recorded during a period of time, up to several days. Traditional studies are only able to capture





**Figure 2.4.:** Automatic detection of thermal bridges from Garrido *et al.* [45].

particular defects at one moment in time and are limited by the interaction between transient weather conditions and materials. With passive time-lapse thermography, the evolution of heat losses can be better understood. Fox *et al.* [40] used this approach over several days for the detection of envelope defects on two different houses. Grinzato *et al.* [47] proposes a method for the detection of moisture in buildings.

Other studies used the sun as a heat source to generate the temperature gradient required to visualize the thermal bridges: this is called “solar thermography”. Bison *et al.* [48] demonstrated the interest of using solar thermography to detect delamination of plaster on the brick wall of a 700 years old building in Milan. Li *et al.* [49] used solar loading thermography for the detection of debonded ceramic tiles in building finish. The thermal properties of debonded areas (filled with air or water) are different from the rest of the façade. Similarly, Freitas *et al.* [50] used the sun-power to detect façade plaster detachment on building walls. The detachments are visible with higher temperature than the rest of the façade during the day (up to 2.5°C) and with lower temperatures after sunset. Laranjeira *et al.* [51] also applied solar IRT to detect bonding defects in adhered ceramic tiling on several building façades. They observed that bonding defects were detected with clear and cloudy sky conditions, particularly during or after the heating period depending on the building façade orientation. Ibarra-Castaneo *et al.* [52] performed thermography surveys over external walls of two buildings (in Canada and Italy) during summer. Signal processing techniques applied to data acquired during several days allowed the detection of surface features as well as large internal structures.

### 2.2.1.2. Active IRT

Active IRT is of common practice in the field of thermal non-destructive evaluation (TNDE) of materials. A material is stimulated (e.g., by a photothermal source) and the thermal response of the material (i.e., the thermogram) indicates whether or not a defect (or flaw) is present in the material.

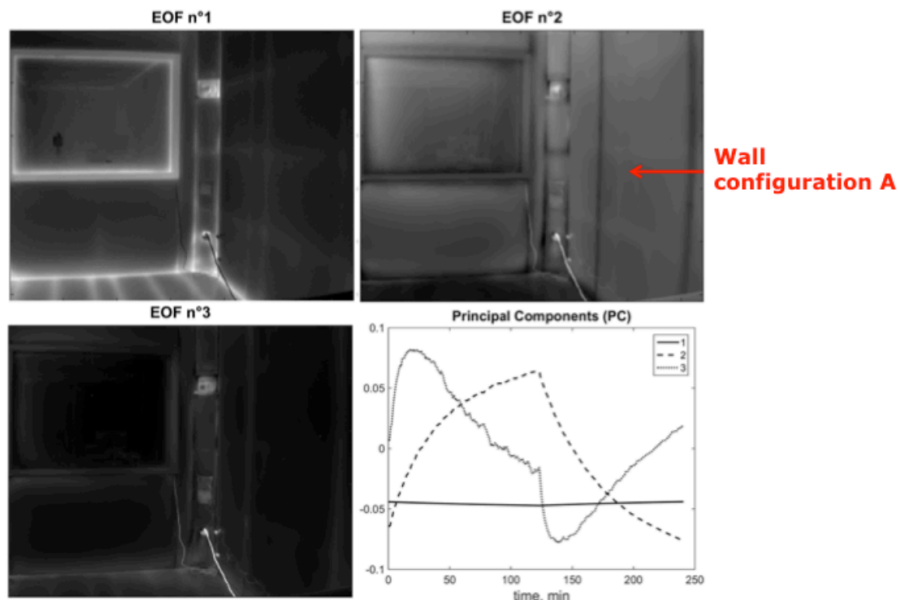
Applying an artificial thermal load to an object as large as a building is not straightforward. Active IRT in the building sector was first introduced by Grinzato *et al.* [53, 54]. The authors compared the potential of different experimental methods based on active IRT for the detection of defects in buildings. In their work, Grinzato *et al.* used both natural or artificial heat sources (i.e., the sun or controlled radiant

## 2.2. DETECTION AND QUANTIFICATION OF THERMAL BRIDGES

heat sources, respectively). The building envelope was monitored in transient regime and the thermal thermograms were analyzed to identify potential defects. The major drawback of the proposed methodology is the post-processing time needed for the analysis.

Other studies also used radiant heat sources. For instance, Kurita *et al.* [55] detected defects in elevated railway concrete structure. The surface was remotely heated with a 6 kW air-cooled xenon arc lamp coupled with a scanner system. In addition, Maierhofer *et al.* [56] made on site measurements on a concrete bridge for the detection of voids or delaminations inside or below the top asphalt layer. Infrared radiators were used to stimulate the surface. Taylor *et al.* [57] used radiant heaters to carry out active IRT measurements on sample walls in which insulation panels were removed or replaced by others to mimic the presence of thermal bridges.

Finally, Douguet *et al.* [58] proposed an active IRT method based on rapid heating of the room indoor air. This preliminary study, conducted by the CERTES lab and Saint-Gobain Research Paris, contributed to the definition of the present thesis. The method was applied *in situ* on a test cell for different wall configurations and moments of the year. Several thermal bridges are studied, including the mechanical supports used to hold the insulating materials. The application of Singular Value Decomposition (SVD) helps in the detection of thermal bridges. This study showed that active methods are advantageous for the detection of thermal bridges because they are applicable in most situation. In particular, they may be applied in summer whereas passive infrared thermography is limited to the cold season.



**Figure 2.5.:** Empirical orthogonal functions and their associated principal components after Singular Value Decomposition (SVD) of thermal images, from Douguet *et al.* [58].

## 2.2.2. Laboratory characterization

Several studies are based on the experimental characterization of thermal bridges in a controlled environment. Indeed, there are two main issues encountered in measurements made on building elements. First, the boundary conditions are not well defined. Second, outdoor conditions (temperature, humidity, wind speed) vary constantly: a steady-state is rarely achieved. Thus, some authors carried out experiments on samples of walls (that include thermal bridges) in a climate chamber. This section is divided into two paragraphs in order to distinguish studies that do not use IRT from studies that do. The main difference is that infrared methods can be applied *in situ* whereas non infrared ones cannot.

### 2.2.2.1. Tests in Hot box facilities without IRT

Asdrubali and Baldinelli [59] compared three different standards (the European EN ISO 8990 [60], the American ASTM C1363-05 [61] and the Russian GOST 26602.1-99 [62]) for the measurement of non-homogeneous building wall  $U$ -value with a hot box facility (shown in Fig 2.6). The comparison focuses on the differences of calibration, measurement procedures, and uncertainty evaluation. In the European and American standards, the power needed to maintain the chambers at constant temperature is measured whereas the Russian is based on heat flux measurements. The three standard are compared on measurements made on an aluminum framed window and the maximum difference in measured  $U$ -value is of 3%.



**Figure 2.6.:** General view of the hot box apparatus from Asdrubali and Baldinelli [59].

Martin *et al.* [63] studied the response of a thermal bridge in a guarded hot box testing facility. They performed steady-state measurements following standard ISO 8990 [60] and then modified the testing method in order to carry out dynamic experiments. Basically, the metering box (used to heat the sample) is removed and

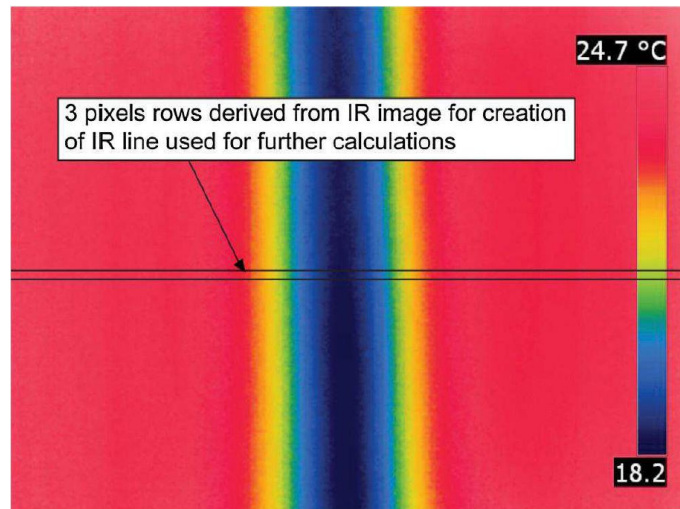
large heat flux meters (HFM) are implemented on the wall. Two similar walls are studied: one is homogeneous whereas the other one includes a thermal bridge (a pillar of reinforced concrete). A sinusoidal excitation is applied to the cold chamber air temperature. The measured thermal amplitudes and phase-lags of the heat fluxes are compared to those obtained from numerical simulations. The measured thermal bridge  $\psi$ -value is equal to  $0.20 \text{ W.m}^{-1}.\text{K}^{-1}$  which is close to the theoretical value of  $0.18 \text{ W.m}^{-1}.\text{K}^{-1}$  obtained from simulations (following ISO 11211 [27]). This method is used as a benchmark in O'Grady *et al.* [64] (see next paragraph).

### 2.2.2.2. Tests in Hot box facilities with IRT

O'Grady *et al.* [64] proposed a methodology for the characterization of thermal bridges using infrared thermography. From the surface energy balance in steady-state, the total heat flux for each pixel  $\phi_{\text{pixel}}$  is given by:

$$\phi_{\text{pixel}} = l_{\text{pixel}} \left[ h_{\text{pixel}}^c (T_i - T_{\text{s,pixel}}) + h_{\text{pixel}}^r (T_{\text{env}} - T_{\text{s,pixel}}) \right] \quad (2.14)$$

where  $l_{\text{pixel}}$  is the pixel length,  $T_i$  the indoor air temperature,  $T_{\text{s,pixel}}$  the measured temperature on the pixel and  $T_{\text{env}}$  the Mean Radiant Temperature (referred as the surrounding temperature in the paper). The convective heat exchange coefficients  $h_{\text{pixel}}^c$  is calculated from the Nusselt number by applying the Churchill-Chu empirical correlation [65]. The radiative heat exchange coefficient  $h_{\text{pixel}}^r$  is calculated from  $T_{\text{s,pixel}}$ ,  $T_{\text{env}}$  and the wall emissivity  $\varepsilon$ . Figure 2.7 presents an example of a thermal image of a wall with a linear thermal bridge.



**Figure 2.7.:** Sample IR image of a component with linear thermal bridge from O'Grady *et al.* [64].

Finally, the linear thermal transmittance is given by:

$$\psi = \frac{\sum_{\text{pixels}} \phi_{\text{pixel}} - \phi_{1D}}{T_i - T_e} \quad (2.15)$$

The methodology was validated in a calibrated hot box using a similar methodology as Martin *et al.* [63]. The three investigated specimens were made out of structural insulated panels (SIP) of different thickness with or without thermal bridge. The results show good agreement with steady-state results (the relative deviation on  $\psi$  ranges between 6 and 36 % for values between 0.016 and 0.253 W.m<sup>-1</sup>.K<sup>-1</sup>).

In another study [66], the same authors extended the method to outdoor conditions: the hot box facility was adapted to generate forced convection flows (wind speed between 0.5 and 4 m.s<sup>-1</sup>). They tested two specimens: a steel column used as structural member of a building external envelope and plain sample without thermal bridge. The Jürges equations were used instead of the Churchill-Chu correlation for the calculation of  $h_{\text{pixel}}^c$  given the forced convection nature of the flow. Unlike for indoor conditions, it was noticed that the spatial variation of  $h_{\text{pixel}}^c$  are negligible despite the 4 K temperature contrast on the thermal bridge. Also, the calculated  $\psi$ -value increases linearly with the wind speed.

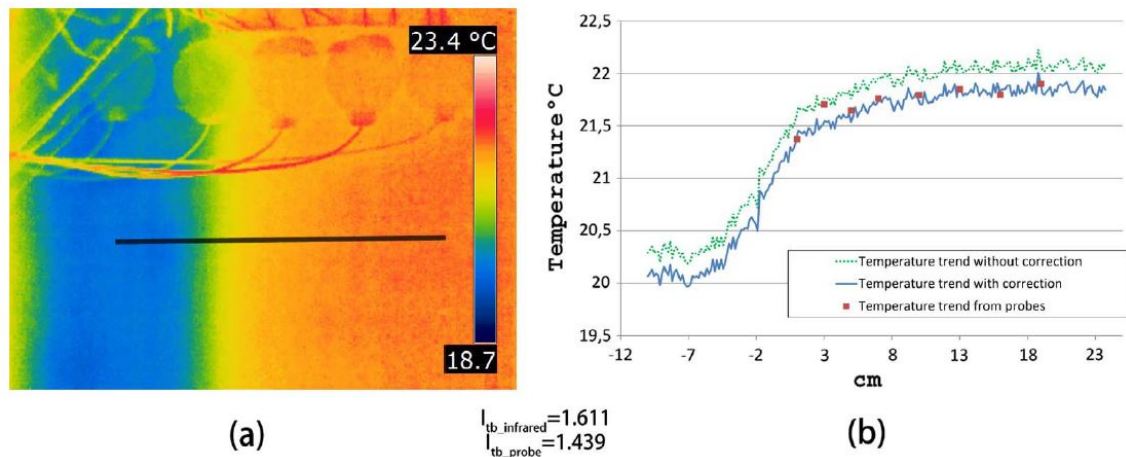
Baldinelli *et al.* [22] proposed a method in which the thermograms are corrected using data from the temperature probes (Ordinary Least Square minimization of the difference between them), as shown in Fig 2.8. The impact factor  $I_{\text{tb}}$  (see paragraph 2.2.3) is calculated in two ways: from infrared thermography and from contact measurements. Three thermal bridges were studied in a Hot-Box device: a pillar, a beam/pillar joint and a wall/wall joint. The same algorithm as in Asdrubali *et al.* [43] was used to enhance increase the resolution of the images (from 320 × 240 to 640 × 480 pixels). The application of this algorithm produced results closer to the experimental factor calculated by the probes. According to the authors, this mathematical approach could improve by 2% the accuracy on the experimental evaluation of the total building heat losses using IRT.

### 2.2.3. *In situ* characterization

The *in situ* characterization of thermal bridges is more complex because the environment is not controlled as it is inside a hot box test facility. Most authors working on the *in situ* quantification of thermal bridges measure the “Impact factor” (or “Incidence factor”) presented in section 2.1.

Benko [67] was one of the first to use infrared thermography for the quantitative assessment of thermal bridges. He introduced the dimensionless Energy Saving factor  $ES$  (energy saving possibility in case of correction of the thermal bridges) which is equal to the Impact factor. The author assumed that the heat transfer coefficient  $h$  is uniform over the considered areas and introduced the area factor

## 2.2. DETECTION AND QUANTIFICATION OF THERMAL BRIDGES

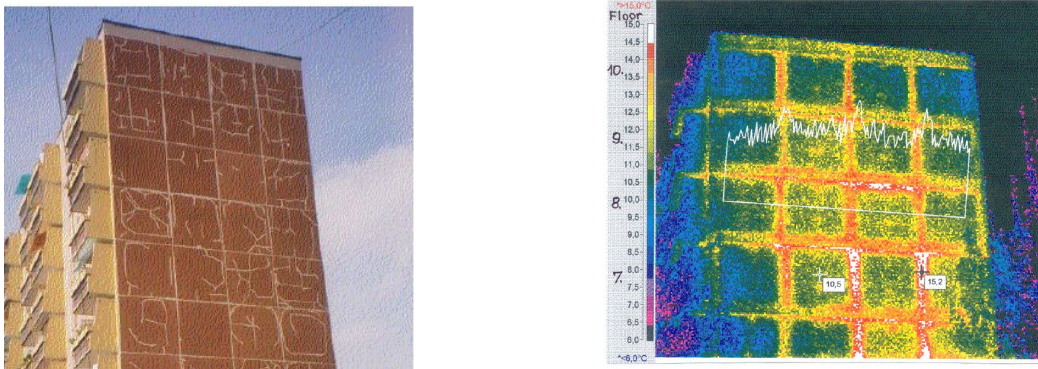


**Figure 2.8.:** Pillar thermal bridge (TB1): thermogram (a) and temperature trends (b) from Baldinelli *et al.* [22].

$a = A_{tb}/A_{1D}$ . Equation 2.8 becomes:

$$ES = a \frac{T_{avg} - T_{env}}{T_{min} - T_{env}} \quad (2.16)$$

with  $T_{avg}$  and  $T_{min}$  as the average and minimum temperatures on the thermogram and  $T_{env}$  the environment temperature (the author did not explain how this temperature was measured). Benko studied wall-joints on the façade of a multi-storey building (see Fig 2.9) and obtained  $ES$  factors between 0.38 and 0.46.



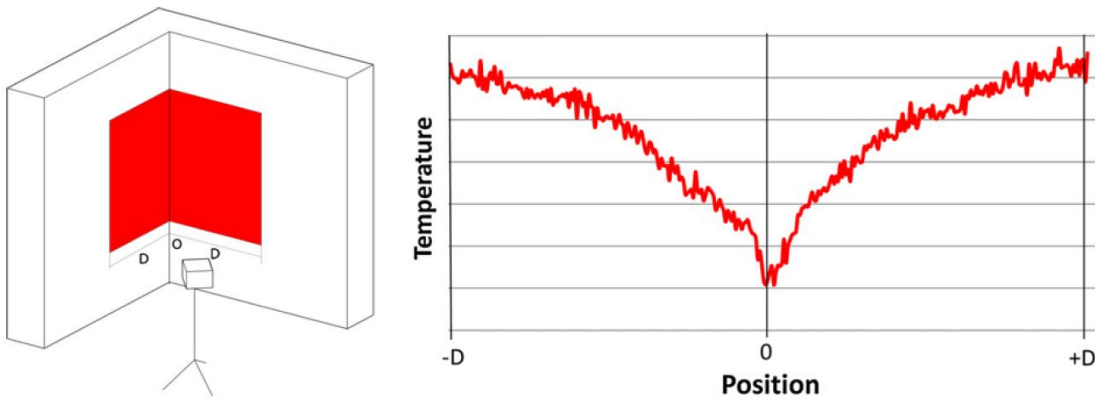
**Figure 2.9.:** Photo and thermal image of the slab joints of the building structure studied in Benko [67].

Asdrubali *et al.* [19] later proposed a methodology based on the same working principle and introduced the name “Incidence factor”. The authors calculated this factor from infrared measurements (such as the one shown in Fig 2.10) and measurements of the internal air temperature  $T_i$ . The latter is supposed equal to the mean radiant temperature and therefore to the operative temperature as well. The Impact factor

is therefore given by:

$$I_{tb} = \frac{\phi_{tb}}{\phi_{1D}} = \frac{\sum_{p=1}^N (T_i - T_{\text{pixel, is}})}{N (T_i - T_{1D, \text{is}})} = \frac{\overline{T_{tb}} - T_i}{T_{1D} - T_i} \quad (2.17)$$

where  $T_i$ ,  $T_{\text{pixel, is}}$ ,  $T_{1D, \text{is}}$  and  $N$  are respectively the internal air temperature, the internal surface temperature of a pixel, the sound wall surface temperature and the number of pixels used in the analysis. The temperature values in the two considered areas are given by a single thermogram which minimizes further sources of error. An crumpled aluminum sheet is used to estimate the mean radiant temperature and correct infrared measurements.

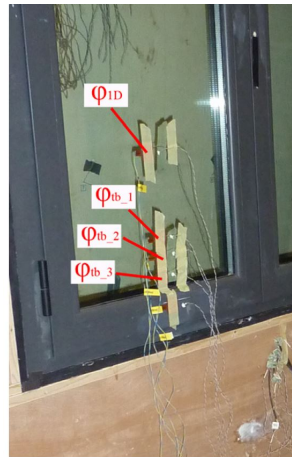


**Figure 2.10.:** Example of an angular thermal bridge and relative thermogram output from Asdrubali *et al.* [19].

The tests were undertaken in an experimental cell under quasi-steady-state conditions (a temperature difference of approximately 15 K was prescribed). The thermal bridge studied here was the window frame of a double glazed unit (see Fig 2.11). The validation of the proposed methodology was assessed with two different approaches: an instrumental heat flow analysis (where the heat losses are measured point by point through the window area) and a numerical analysis (with a two-dimensional model of the window). In order to improve the accuracy of the results, the same authors used some algorithms to enhance the thermographic images [43]. This reduced the absolute error of the studied thermal bridges.

In Bianchi *et al.* [20], the same authors carried-out measurements in test room (see Fig 2.12). The thermal bridges investigated are the junctions between wall, roof or floor as well as the corners. Their  $\psi$ -values were also calculated using the incidence factor methodology. The total thermal losses through the envelope was  $32.73 \text{ W.K}^{-1}$ , around 9% of which imputable to thermal bridges. The calculated  $I_{tb}$ -values range between 1.23 and 2.15. The results were compared to the evaluation of the energy consumption of the operating heat pump system in heating mode. The variation between these two approaches is lower than 1%.

Nardi *et al.* [21] studied three different types of thermal bridge in a house located in the University of Aquila (Italy) which underwent a refurbishment prior to the tests.



**Figure 2.11.:** Instrumented window (with heat flux meters) from Asdrubali *et al.* [19].



**Figure 2.12.:** Picture of the test-room facility used in Bianchi *et al.* [20].

The thermal bridges are an edge between two walls, an edge between a wall and the roof, and the junction between a girder (made out of reinforced concrete) and the perforated bricks masonry. The one-dimensional  $U$ -value,  $U_{1D}$ , was estimated with the methodology proposed by Albatici and Tonelli [68] based on passive IRT. The reference wall was chosen exposed north-north-east to reduce the influence of solar radiation. Experiments were carried out several times in different climatic conditions. The measured  $I_{tb}$  values were around 1.5 with a relative error of about 15% whereas the  $\psi$ -values are around  $0.22 \text{ W.m}^{-1}.\text{K}^{-1}$ . The comparison of the experimental results obtained with the use of infrared thermography and standard numerical calculations (finite elements) confirmed the validity of the experimental method proposed.

### 2.2.4. Methods combining measurements and calculations

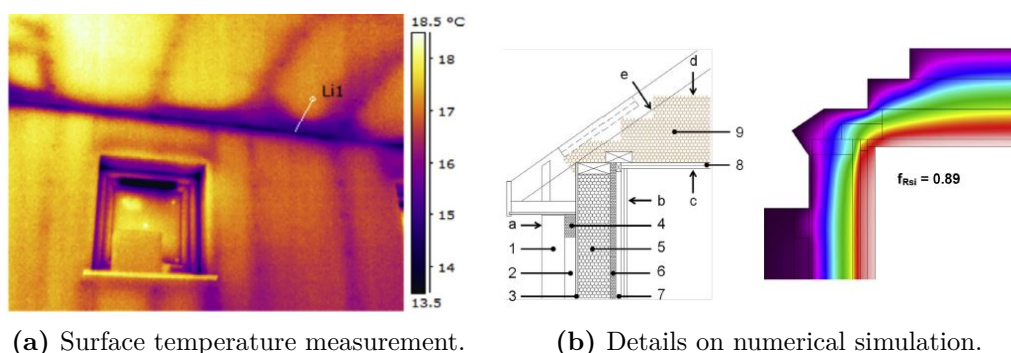
Many studies combine measurements (often *in situ*) with numerical simulations to assess the severity of a thermal bridge. ISO 10211 [27] details how numerical methods



should be built (geometry, boundary conditions, calculation rules, ...).

### 2.2.4.1. Combining measurement and simulations to assess thermal performance of building façades

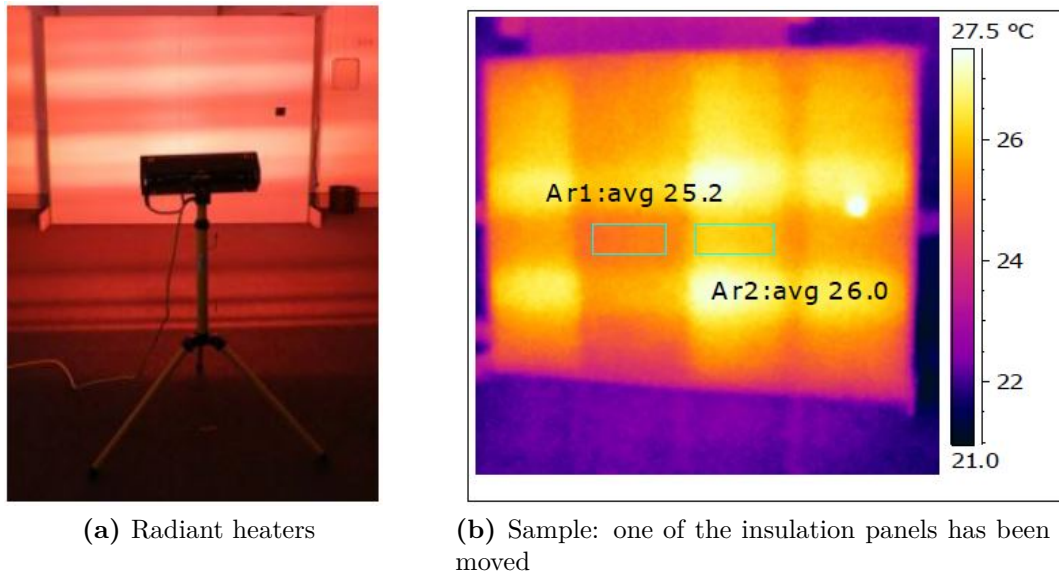
Taylor *et al.* [24] studied the possibility to combine thermography and computer simulations to support the thermal image interpretation (make it less subjective) for the investigation of insulation defects in buildings. In a first case study, modeling is used to investigate the surface temperature distribution resulting from missing perimeter insulation for an intermediate timber floor junction. The results show that it should be possible to detect the default with an internal thermographic survey, unlike with an external survey. The second case study is an eaves junction during the construction phase. The investigated bedroom has been heated by a 1.5 kW electrical fan heater during 4 h. Lower surface temperatures were observed at the junction between wall and ceiling (see Fig 2.13). The eaves detail was numerically simulated by assuming a correct insulation installation. The measured  $f_{Rsi}$  factor was lower than the simulated one. This confirms that the as-built detail is not performing as expected.



**Figure 2.13.:** Measurements and numerical simulations of eaves from Taylor *et al.* [24].

In a second similar paper ([57]), the authors investigated how thermal imaging can be used during the construction of new domestic buildings in order to identify problems at an early stage of construction. If an anomaly is identified in the building fabric, the cause of the defect and its severity must be addressed. The authors studied rigid insulation boards in partial-fill masonry cavity construction. Simulation results suggest that it may not be possible to establish the presence of the defect with infrared thermography. An external wall with two specific defect configurations was also tested: the replacement of one section of insulation with a section of different thermal performance and the removal of this section. Electrical radiant heaters were used (see Fig 2.14). Numerical simulations are in agreement with the thermographic survey: unlike a missing panel, a material with a different thermal conductivity within a wall is likely to be difficult to detect.

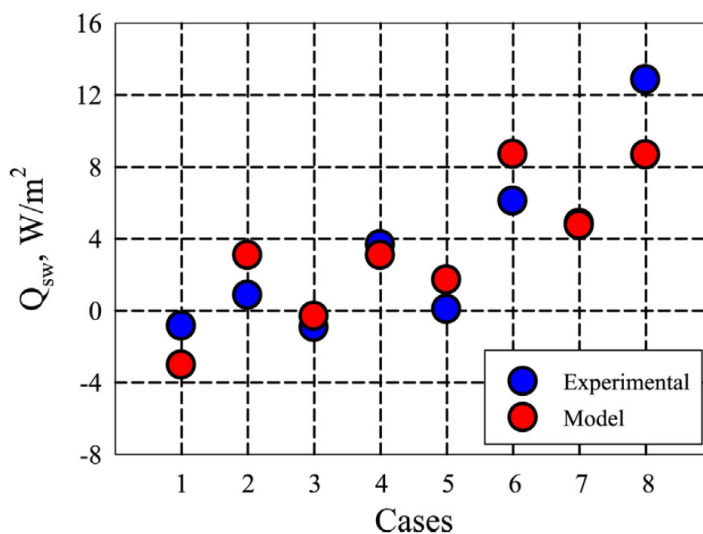
Cuce *et al.* [69] studied experimentally and theoretically the influence of an internal aerogel retrofitting on the thermal bridge effects in an actual residential UK



**Figure 2.14.:** Experimental setup to detect missing insulation panel from Taylor *et al.* [57].

building. The retrofitting consists in implementing a 20 mm aerogel blanket on internal walls of a test bedroom with a 12 mm of gypsum plasterboard. In this work, co-heating test is applied before and after the retrofit to assess the thermal performance of the aerogel. Temperature and heat flux measurements are made. The temperature difference between indoor and outdoor environment is measured every 2 min. The theoretical approach is based on a statistical analysis. A parametric model is developed to demonstrate the influence of the internal retrofitting on the heat loss through separating walls. The model is characterized by three independent parameters. A nonlinear regression analysis is applied to the experimental data to determine the optimum coefficients that give the heat loss from the separating wall as a function of the three independent parameters. The measurements are compared to the model in Fig 2.15. Results show an important increase of heat flux values after retrofit because of growing thermal bridges.

Aïssani *et al.* [70] investigated the impact of common workmanship errors on the thermal performance of insulation panels including defects. The experimental study was conducted under laboratory conditions, with the guarded hot plate method. Rear and front temperatures were measured with thermocouples and infrared thermography, respectively. Different types of defect are investigated (regular defects: groove and opening; irregular defects: crushes and sheath passages on flexible materials), as detailed in Fig 2.16. A coupling between experimental measurements and finite element modeling (inverse method) is carried out to estimate the effective thermal conductivity of the panels. Results show globally an increase of the thermal conductivity due to the presence of the studied defect. The measurement uncertainties are estimated by the “median rank method” (fit a cumulative distribution functions, CDF, to the measured points). Empirical correlations are built to express the effective thermal conductivity as function of the defect geometry.



**Figure 2.15.:** Comparison of heat flux values through measurements and the model from Cuce *et al.* [69].

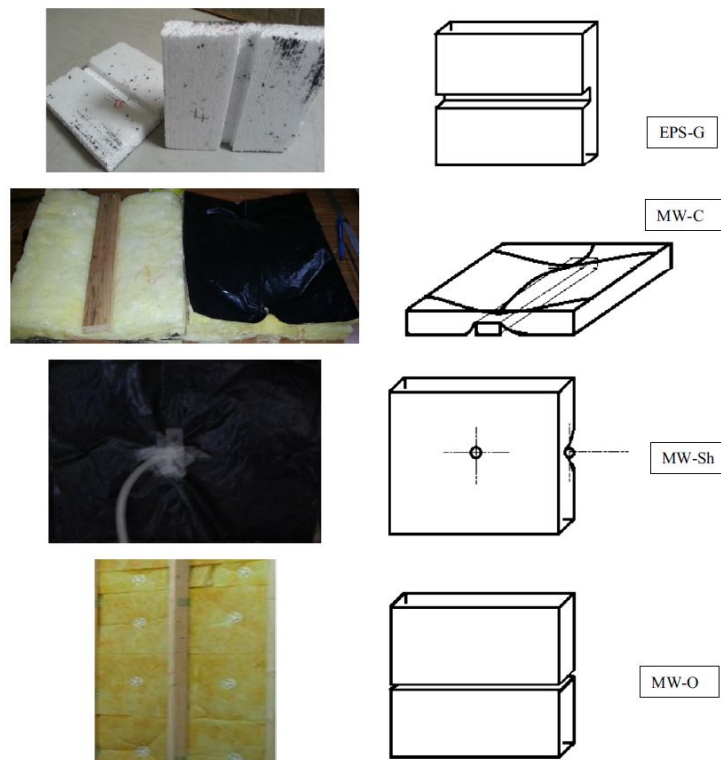
Authors consider that these correlations will provide more realistic predictions of energy needs of dwellings.

#### 2.2.4.2. Validation of a thermal modeling

Heinrich and Dahlem [71] compared the surface temperature distribution along a thermal bridge (I-beam in lightweight construction wall) collected using an IR image to that obtained using the finite element method (no precision is given about the method). They found that the zone of influence of the thermal bridge was smaller in the numerical model than the one measured using infrared thermography.

Zalewski *et al.* [72] focused on the characterization of thermal bridges in prefabricated building walls. Thanks to FE simulations, the authors computed the average U-value of the test wall with and without metallic frames and thus work-out the contribution of the thermal bridge (around 26% here). The numerical results were validated by measurements on an experimental wall. The tests were undertaken in an experimental cell under quasi-steady-state conditions (a temperature difference of approximately 20 K was prescribed). Passive IRT was used for the detection of TB. Two thermocouples measured the surface temperature. Heat flux were measured with tangential gradient flux-meters on three different locations of the test wall.

Ascione *et al.* [73] developed a numerical code that solves transient two-dimensional heat transfer in thermal bridges (the model is detailed in [74]). It is based on Conduction Transfer Functions (CTFs) and has a much lower computational time than classic methods such as Finite Difference [75]. The aim of this work was to compare the modeling results with measurements. The case study was an *in situ* L-shaped thermal bridge constituted by three homogeneous layers: an external plaster, a structural masonry made of tuff and an internal plaster. The experimental



**Figure 2.16.:** Different types of defects studied in Aïssani *et al.* [70].

setup was composed of an infrared camera (to localize the thermal bridge), several heat flux and temperature contact sensors, and a meteorological station to measure solar radiations. Results for the heat flux density showed good agreement between model and measurements for three different positions of the heat flux sensors: the percentage deviation varies between  $-12\%$  and  $+6\%$  with a mean value close to zero. Authors consider that the deviations were due to many aspects that are not taken into account by the model (e.g. actual conditions about wind, rain, effective solar radiation, thermal storage of the wall, not homogeneity of the materials).

Wróbel and Kisielewicz [76] developed a numerical model of several thermal bridges with THERM program. The thermal bridges studies were irregular concrete post and horizontal structural beam in 2-layer wall, meeting point of external wall and roof and external wall and floor connection. They could calibrate the model by using the infrared measurements. They could also compute the so-called dimensionless temperature coefficient  $f_{R_{si}}$ .

Serra *et al.* [77] presented an analytical solution to simulate heat diffusion in multi-layered media. It is based on phase-contrast calculation using 1D analytical expressions proposed in Tadeu and Simões [78] (Green's analytical functions). The phase-contrast induced by a specific layer was derived from simulation of a system including it, and of the same system without it. A numerical study introduced several test parameters: the result curves showed a peak in the frequency spectra at maximum phase-contrast which corresponds to the characteristic frequency used in defect detection. A laboratory active IRT experimental campaign based

on the pulse-phase thermography was also performed to confront model with measurements. A test specimen with a changeable inclusion/defect was developed (nine layers system). Active thermography measurements were performed in laboratory in reflection mode from two halogen lamps (2500 W each) with a rectangular heating curve (square pulse) followed by a cooling down process. Results showed that the increase of defect depth leads to a decrease of the characteristic frequency and blind frequency values, and to a decrease of the maximum phase-contrast value. It appeared that deeper defects require a higher frequency resolution and consequently longer testing periods. The generated curves predicted the range of frequencies for which the defect are visible as a function of its depth.

## 2.2.5. Numerical modeling

Several studies focused on the modeling of thermal bridges. Although they were developed to take thermal bridges into account in building energy simulation programs, these reduced models are of interest for the application of inverse methods (to estimate a thermal bridge properties).

### 2.2.5.1. Determination of an equivalent wall method

Several studies focused on the derivation of an equivalent wall model of a thermal bridge. The concept of the equivalent wall method is to replace the area disturbed by a thermal bridge, where the heat flux is 2D or 3D, by a simple 1D multilayer wall. This equivalent wall must have the same steady and dynamic thermal behaviors as the real wall [79]. Such reduced models are useful to account for thermal bridges effects in building energy simulation programs (BES) without significantly increasing computational time. This type of reduced model, however developed in a different context, is very interesting in the present thesis for the application of inverse methods. Thus, the existing methods for the determination of an equivalent wall are presented here.

The derivation of an equivalent wall model consists in estimating the thermal properties of each homogeneous layer (usually a resistance  $R$  and a heat capacity  $C$ ). Several methods to do so are presented below, following the classification proposed by Quinten and Feldheim [80].

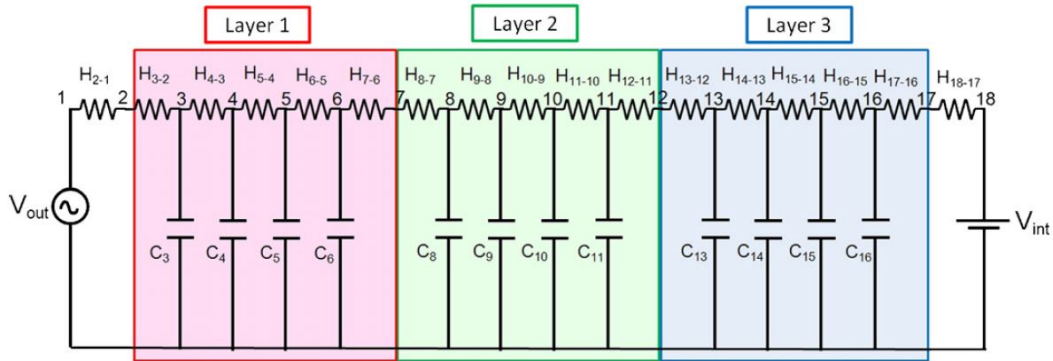
#### a. Identification method

The identification method, proposed by Martin *et al.* [81], is based on an equivalent electrical circuit (with  $RC$  structures) representing the thermal behavior of the thermal bridge. This allows representing the wall thermal resistance as well as its inertia. The estimation of the resistances and the capacities is performed by minimizing the difference between the outputs of the reduced model to those of dynamic simulation. The minimization was performed with the LORD algorithm [82] (methodology based on Nelder-Mead and Monte Carlo methods [83]).

Martin *et al.* [81] propose a criterion for the determination of the number  $N$  of capacities to be used for each layer:

$$N = \sqrt{\frac{2 \times R \times C \times f}{\pi}} \quad (2.18)$$

where  $R$  and  $C$  are the thermal resistance and capacity of the given layer, and  $f$  is the frequency considered (a period of 24 h for instance, for daily variations). From this criterion, the number of thermal capacities per layer was set to four. A three-layers equivalent structure is considered, with the same thickness for each layer. The method was tested for a junction floor-external wall. Numerical simulations of the thermal bridge were made with the FLUENT software. Typical temperature variations for the basque country were considered (for summer and winter conditions) for checking the validity of the method. Maximum absolute differences of 0.5 °C are noted for inner and outer temperatures as well as 0.4 W.m<sup>-2</sup> for heat flux. Then, the authors extended the method to ten other geometries of thermal bridges covering most of the current configurations existing in buildings. Increased differences between numerical simulations and equivalent wall method are noted. Nevertheless, the estimations of values (steady-state) obtained by the equivalent wall method remain close to the reference ones (maximum bias of 3.5%).



**Figure 2.17.:** Electric circuit model for three layers equivalent wall from Martin *et al.* [81].

### b. Structure factor method (or Transfer function method)

The structure factors method considers five parameters characteristics of a thermal bridge (overall resistance  $R$  and capacity  $C$ , as well as three structure factors:  $\phi_{ii}$ ,  $\phi_{ee}$  and  $\phi_{ie}$ ). The structure factors were introduced by Kossecka and Kosny [84], they are dimensionless and represent the fraction of heat stored in wall volume, in transition between two steady-states. They depend on the wall thermal structure. For instance,  $\phi_{ii}$  is large for wall in which most of the thermal mass is located near the indoor surface while most of the thermal insulation is located near the rear face of the wall [79]. They are calculated from the wall inner 3D temperature field  $T(x, y, z)$

obtained from steady-state numerical simulations taking  $\theta_{se} = 1$  K and  $\theta_{si} = 0$  K as boundary conditions (internal and external surface temperatures, respectively). The structure factors are given from integration over the considered volume  $V$ :

$$\phi_{ii} = \frac{1}{C} \int_V \rho c (1 - \theta(x, y, z))^2 dV \quad (2.19)$$

$$\phi_{ee} = \frac{1}{C} \int_V \rho c \theta^2(x, y, z) dV \quad (2.20)$$

$$\phi_{ie} = \frac{1}{C} \int_V \rho c \theta(x, y, z) (1 - \theta(x, y, z)) dV \quad (2.21)$$

They are also linked by the following relationship (they only have 2 degrees of freedom):

$$\phi_{ii} + 2\phi_{ie} + \phi_{ee} = 1 \quad (2.22)$$

The objective is to determine an equivalent 1D wall that has the same four independent parameters ( $R$ ,  $C$ ,  $\phi_{ii}$  and  $\phi_{ee}$ ) than the thermal bridge. According to Carpenter [85], an equivalent wall with 3-layers is a good optimum to mimic the behavior of a thermal bridge. This means that six quantities (three resistances and three capacities) have to be determined from only four equations (one for each independent parameter): the problem is under-determined.

Quinten and Feldheim [80] suggest a methodology consisting in settling down  $R_1$  and  $R_2$ , working out the other parameters from the four available equations, and iterate on  $R_1$  and  $R_2$  until physical results are obtained (positive capacities and resistances for instance). Aguilar *et al.* [86] used a similar trial and error method.

Quinten and Feldheim [80] also suggest an alternative method for an unequivocal determining of the equivalent wall. They closed the system with two additional equations:

$$R_1 = R \times (1 - \phi_{ii} + \phi_{ee}) \times 2\phi_{ie} \quad (2.23)$$

$$R_2 = R \times (1 + \phi_{ii} + \phi_{ee}) \times 2\phi_{ie} \quad (2.24)$$

This method is deterministic but it may not lead to accurate results. Indeed, the previous equations have no physical meaning.

Nagata [87] used a method that looks very different but that leads to the same system of equations. It is described as the “matrix of transfer functions method” in [80]. It is based on the knowledge of the transfer functions  $H_{Ai}(p)$ ,  $H_T(p)$ ,  $H_{Ae}(p)$

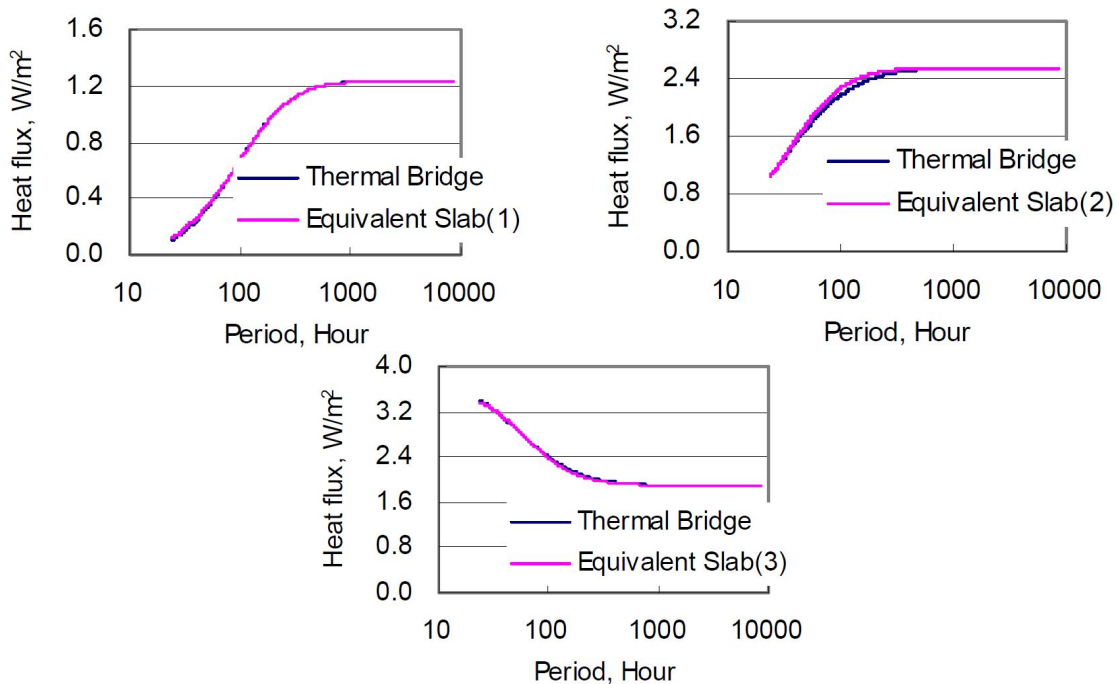
of the real structure in the Laplace domain:

$$\begin{bmatrix} \varphi_{si} \\ \varphi_{se} \end{bmatrix} = \begin{bmatrix} -H_{Ai}(p) & H_T(p) \\ H_T(p) & -H_{Ae}(s) \end{bmatrix} \times \begin{bmatrix} T_{si} \\ T_{se} \end{bmatrix} \quad (2.25)$$

It can be shown that the transfer functions can be calculated from the structure factors previously introduced. There is still an under-determined system of four equations for six unknowns to solve.

### c. The harmonic method

The harmonic method was introduced by Xianoa and Yi [88]. Here, harmonic variations of data (temperatures and fluxes) are considered. Modeling is performed using the thermal quadrupoles formalism. For specific periods (typically 24h), the amplitude  $A$  and the phase lag  $\alpha$  between the inside and outside temperatures are calculated. The aim is then to find an equivalent wall having similar amplitude  $A$  and phase lag  $\alpha$  for a few specific frequencies. Figure 2.18 shows results from [88]: the equivalent slab has a similar thermal behavior as the thermal bridge.



**Figure 2.18.:** Comparison of the heat flux between the Equivalent Slab and thermal bridge for 3 different configurations from Xianoa and Yi [88].

### d. Mixed methods

Quinten and Feldheim [80] proposed a new approach which they named “mixed method”. It is a mix between the harmonic and the structure factors approaches.



It enables to benefit from the strengths of each approach and lead to a unique solution. First, two parameters (such as  $R_1$  and  $R_2$ ) are discretized (this means that many values for each are tried). For every given couple, the four other parameters are calculated from the global quantities:  $R$  and  $C$  the impact factors  $\phi_{ii}$  and  $\phi_{ee}$ . Then, the couple of discretized parameters ( $R_1$  and  $R_2$ ) that minimizes the following quantity is retained:

$$F = \sum_f \frac{|A(f) - A'(f)|}{|A(f)|} + \frac{|\alpha(f) - \alpha'(f)|}{|\alpha(f)|} \quad (2.26)$$

with  $A(f)$  and  $\alpha(f)$  the real configuration amplitude and phase-lag for a given frequency  $f$ , and  $A'$  and  $\alpha'$  the same quantities for the equivalent wall. A few frequencies are chosen, such as the ones corresponding to periods of 10, 24 (1 day), 50, 100 and 8760 hours (1 year).

The validity of the method is checked on a four-layer structure (brick, air gap, insulating material, concrete wall). Finally, it is shown that in the case of the thermal bridge representing a junction floor - exterior wall, a maximum error of 0.9 % of the heat flux is obtained using the mixed method. A significant improvement is observed between a classic 1D estimation containing an additional term representing the thermal bridge ( $\psi$ -value) and the proposed mixed method. Thus, the equivalent wall method seems to lead to a 1-D structure having a behavior closer to reality than the classic consideration of a thermal bridge.

The authors recently improved their mixed method [89] by (i) using squared relative errors instead of relative errors the objective function (Eq 2.26) (ii) implementing Fourier boundary conditions instead of Dirichlet ones in numerical simulations, (iii) using real data in simulations for the indoor and outdoor temperatures. The methodology was validated on three different thermal bridges. The authors showed once again that the equivalent wall behaves significantly better than 1D classical approaches (using a  $\psi$ -value obtained in steady-state) as shown in Fig 2.19.

### 2.2.5.2. Other numerical studies on thermal bridges

Al-Sanea *et al.* [90] studied the influence of mortar joints between building blocks using finite volume 2D modeling. These authors used 1 year meteorological data for Riyadh climate. They considered variations of daily transmission loads through mortar joints for each month. The use of dynamic modeling allows defining and computing a daily dynamic thermal resistance  $R_d$ :

$$R_d = \frac{\int_0^{24h} |\Delta T| dt}{\int_0^{24h} |\varphi_i| dt} \quad (2.27)$$

A yearly-averaged dynamic  $R$ -value is also considered. This thermal resistance can be compared to the static nominal resistance  $R_n$  obtained considering 1D-transfers

in steady-state. The results showed a decrease of dynamic resistance of about 50 % and an increase of thermal loads of about 100 % for a surface of mortar joint of only 9 %. A strong increase of the amplitude of inner wall surface is also noted in that case.

Viot *et al.* [91] compared different methods for the calculation of thermal bridges heat losses in the case of a wood-frame construction. The COMSOL Multiphysics software was used for computations. In static regime, these authors considered the influence of the number of wood studs considered in the simulation. They have shown that the rounding of the value imposed by ISO 10211 [27] leads to a bad estimation (until 30 % in some situations) of heat losses through  $N$  similar consecutive thermal bridges. This indicates that steady-state values listed in catalogs are not satisfactory. Dynamic simulations were also performed to compare several models of existing simulation tools. The authors compared time shift and amplitude values. Significant differences are observed between results obtained using the models considered. Moreover, these differences depend on the number of wood studs considered for computation making impossible to choose a unique simplified model for any wall configuration.

### 2.2.6. Conclusion

To the best of the author knowledge, the influence of thermal bridges is usually not correctly taken into account in computation. This may contribute to an erroneous assessment of the losses due to thermal bridges and thus a source of discrepancy between the design and as built values (performance gap). This problem tends to be critical because multi-layer walls with high thermal resistance are now widely used in new dwellings and the relative contribution of thermal bridges in global heat losses becomes more and more important. This literature review, focused on the assessment of thermal bridges, is summarized in Tab 2.1.

The detection of thermal bridges on site is almost systematically performed by using passive infrared thermography. Provided the temperature difference between the internal and external environments is high enough, the presence of thermal bridges are revealed by surface temperature contrasts. However, a few studies showed that the use of an artificial thermal load (active approach) allows the detection of thermal bridges when desired, in most weather conditions.

The characterization of a thermal bridge in laboratory commonly involves the guarded hot box as a reference method. However, several references involve thermal thermography for *in situ* characterization. The process used usually consists in analyzing thermograms by comparing wall areas with and without any thermal bridge. Then, a quite simple analytical model is developed and is combined with infrared and air temperature measurements (incidence factor). Nevertheless, these *in situ* measurement methods still require stationary thermal conditions as well as a sufficient internal/external temperature gradient.

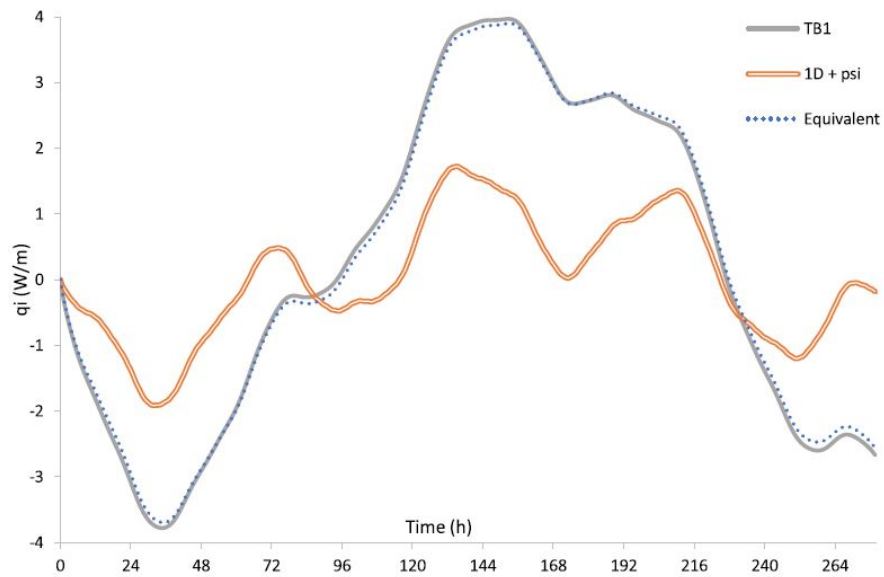
Computation results are frequently compared with measurements (infrared thermography, thermocouples, heat flux sensors) in order to validate or calibrate models, or

to confirm that actual performances of a dwelling are not in good agreement with theoretical predictions. Numerical simulations can also be associated with infrared measurements to make the interpretation of thermal images less subjective.

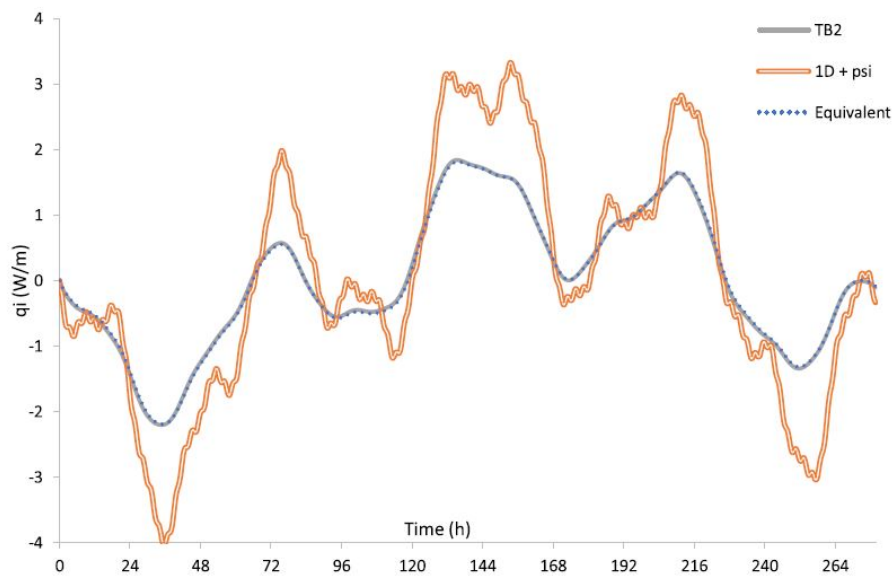
Theoretical studies are also conducted to analyze the influence of the properties of a thermal bridge. An interesting thermal bridge modeling method is the so-called “equivalent wall”. It has been shown that the steady-state and dynamic behaviors of a thermal bridge may be modeled by a three-layer homogeneous wall. This approach enables to obtain a reduced model, which is interesting for the application of an inverse method. Yet, the properties of the equivalent wall are estimated from fine numerical simulations of the considered wall. This fully numerical approach is not applicable in the current context of *in situ* measurements.

As said above, a few references involve a heating of the inside of the building for the detection of thermal bridges. Yet, no proper active approach to quantify the heat losses in a thermal bridge exists. Inverse methods are not used either: the measurement / simulation combination is only used in a direct comparison. Overall, developed *in situ* characterization methods seem to be dependent on stable weather conditions and on a sufficient thermal gradient in the wall. The association of measurements with a reduced model for a quantitative diagnosis of a thermal bridge is not realized in the literature. These methods have been common practice for many years in other infrared thermography domains both for defect detection and quantification [14]. Finally, the questions of uncertainty quantification are most of the time not addressed. At most, the difference between measurements numerical simulations is quantified. However, these simulations may be highly biased because of incorrect knowledge of materials properties and dimensions. Thus, this is not enough to define a confidence region around the measured quantities.

This thesis aims at addressing most of the limitations of existing methods. The chosen approach consists in developing an active method for the *in situ* quantification of heat losses in thermal bridges. The use of an inverse method would enable to estimate the intrinsic properties of a thermal bridge from dynamic measurements and allow quantifying the estimation uncertainties.



(a) Thermal bridge 1.



(b) Thermal bridge 2.

**Figure 2.19.:** Comparison of heat flux computed by the real model and the equivalent wall for two thermal bridges, from Quinten and Feldheim [89].

CHAPTER 2. LITERATURE REVIEW ON *IN SITU* CHARACTERIZATION  
OF BUILDING WALLS AND THERMAL BRIDGE

---

**Table 2.1.:** Summary of literature review on thermal bridge assessment (N/A = Not Applicable,  $U_{eq}$  equivalent  $U$ -value of a wall with a thermal bridge,  $k$ =thermal conductivity,  $\varphi$ =heat flux density across a wall).

Category	Study	Detection or Quantification	Type of study (measurements or simulations)	Thermal load	Uncertainty calculation (diff=difference)	
Detection	Passive IRT	ISO 6781 [42]	<i>In situ</i>	none	N/A	
		Asdrubali <i>et al.</i> [43]	<i>In situ</i>	none	N/A	
		Garrido <i>et al.</i> [45]	<i>In situ</i>	none	N/A	
		Fox <i>et al.</i> [40]	<i>In situ</i>	none	N/A	
		Grinzato <i>et al.</i> [47]	<i>In situ</i>	none	N/A	
		Bison <i>et al.</i> [48]	<i>In situ</i>	sun	N/A	
		Li <i>et al.</i> [49]	<i>In situ</i>	sun	N/A	
	Sun heating	Freitas <i>et al.</i> [50]	<i>In situ</i>	sun	N/A	
		Laranjeira <i>et al.</i> [51]	<i>In situ</i>	sun	N/A	
		Ibarra-Castaneo <i>et al.</i> [52]	<i>In situ</i>	sun	N/A	
		Grinzato <i>et al.</i> [53]	<i>In situ</i>	sun and radiant heating	N/A	
	Active IRT	Kurita <i>et al.</i> [55]	Detection	<i>In situ</i>	radiant heating	N/A
		Maierhofer <i>et al.</i> [56]	Detection	<i>In situ</i>	radiant heating	N/A
		Taylor <i>et al.</i> [57]	Detection	Lab	radiant heating	N/A
Douguet <i>et al.</i> [58]		Detection	<i>In situ</i>	air heating	N/A	
Measurements	in laboratory	Asdrubali <i>et al.</i> [59]	Lab	Hot Box	yes	
		Martin <i>et al.</i> [63]	Lab, Simu	Hot Box	diff to simu	
		O'Grady <i>et al.</i> [64]	Lab	Hot Box	diff to hotbox	
		O'Grady <i>et al.</i> [66]	Lab, Simu	Hot Box	diff to simu	
		Baldinelli <i>et al.</i> [22]	Lab	Hot Box	diff to contact measurements	
	In situ	Benko [67]	<i>In situ</i>	none	no	
		Asdrubali <i>et al.</i> [19]	<i>In situ</i> , Simu	none	yes	
		Bianchi <i>et al.</i> [20]	<i>In situ</i>	none	yes (energy consumption)	
		Nardi <i>et al.</i> [21]	<i>In situ</i> , Simu	none	yes	
		Taylor <i>et al.</i> [24]	<i>In situ</i> , Simu	none	no	
Expe/simu combination	Combination	ISO 10211 [27]	Simu	none	no	
		Cuce <i>et al.</i> [69]	<i>In situ</i> , Simu	none	no	
		Aissani <i>et al.</i> [70]	Lab, Simu	Guarded Hot Plate	no	
		Heinrich and Dahlem [71]	<i>In situ</i> , Simu	none	no	
	Validation	Zalewski <i>et al.</i> [72]	Lab, Simu	Climate chamber	no	
		Ascione <i>et al.</i> [73]	<i>In situ</i> , Simu	none	yes, on measured $\varphi$	
		Wróbel and Kisielewicz [76]	<i>In situ</i> , Simu	none	no	
		Serra <i>et al.</i> [77]	Lab, Simu	radiant heating	no	
		Quinten and Feldheim [80]	Simu	none	N/A	
		Quinten and Feldheim [89]	Simu	none	N/A	
Numerical modeling	Equivalent wall	Martin <i>et al.</i> [81]	Simu	none	N/A	
		Kossecka and Kosny [84]	Simu	none	N/A	
		Carpenter [85]	Simu	none	N/A	
		Nagata [87]	Simu	none	N/A	
	Others	Xiaona and Yi [88]	Simu	none	N/A	
		Al-Sanea <i>et al.</i> [90]	Simu	none	N/A	
		Viot <i>et al.</i> [91]	Simu	none	N/A	

## 2.3. Quantification of a wall thermal transmittance

This section presents a short literature review on the *in situ* quantification of a wall thermal transmittance. This topic was widely addressed in the literature in the past few years. Several very comprehensive reviews of  $U$ -value *in situ* measurement methods were recently published: see Bienvenido-Huertas *et al.* [92], Soares *et al.* [93] and Teni *et al.* [94] for instance. The existing methods may be classified in three categories: steady-state (section 2.3.1), dynamic (section 2.3.2) and active methods (section 2.3.3). In the last two categories, the dynamic behavior of the wall is analyzed, the difference is that active methods rely on an artificial thermal load.

### 2.3.1. Steady-state methods

Steady-state  $U$ -value *in situ* measurements are very simple in theory but show a lot of metrological and practical issues. These methods are more commonly used because they are rather simple to implement and to analyze.

The wall thermal transmittance is given by:

$$U = \frac{\varphi}{T_i - T_e} \quad (2.28)$$

with  $\varphi$  the heat flux across the wall and  $T_i$  and  $T_e$  the internal and external environment (or operative) temperatures, respectively. Different types of steady-state methods exist. They mainly differ in the way the heat flux  $\varphi$  is measured on the wall: with a heat flux meter (heat flux meter methods), with temperature sensors and knowledge of the heat transfer coefficient (thermometric methods) or with quantitative infrared thermography (IRT methods) [92]. These three types of methods are presented below.

#### 2.3.1.1. Heat flux meter methods (standard methods)

In the literature, many authors refer to the two following standards: ISO 8990 [60] and ISO 9869-1 [15]. The former details the experimental protocol to use in order to measure the thermal resistance  $R$  of a wall in steady-state with a hot box test facility. However, ISO 9869-1 [15] deals with *in situ* measurements. The method consists in implementing a heat flux meter (HFM) on the internal surface of a wall and temperature sensors on each side. This is the most used technique in the community. The wall  $R$  and  $U$  values are calculated from time-averages of the above mentioned measured quantities:

$$R = \frac{\sum_{j=1}^n (T_{si,j} - T_{se,j})}{\sum_{j=1}^n \varphi_j} \quad (2.29)$$

$$U = \frac{\sum_{j=1}^n \varphi_j}{\sum_{j=1}^n (T_{i,j} - T_{e,j})} \quad (2.30)$$

where the index  $j$  enumerates the individual measurements.  $T_{si}$  and  $T_{se}$  are the internal and external wall surface temperatures respectively.

This technique is based on stationary boundary conditions. Yet, proper steady-states are almost never encountered *in situ*. Thus, this average method relies on averaged data as an approximation for measurements under stationary conditions. A variation of this approach (also detailed in ISO 9869-1 [15]) adds a storage effect correction but in essence it remains a semi-stationary analysis method. For the measurement to be as reliable as possible, some conditions must be met which limits the applicability of the method:

- The wall must be homogeneous (which excludes ventilated walls).
- The wall must not include any thermal bridge (heat transfers must be 1D).
- The wall must face North because the sensor used must avoid direct sun radiations.
- The measurement duration depends on the wall and the weather conditions. Its minimum value is 72 h.

Several studies highlighted the limitations of ISO 9869-1 [15] methods. For instance, Ficco *et al.* [95] studied the experimental aspects of the application of this so-called “average method”. This study evaluated *in situ* the  $U$ -value of seven different building components under different measuring conditions using four commercial HFMs. The authors concluded that many operative conditions can considerably influence the results (e.g. high temperature gradient variations, heat flux inversions), whereas other factors seem to be less significant (e.g. sampling time, HFM dimensions).

In addition, Evangelisti *et al.* [96] studied the influence of some disturbing factors such as heating system-on and off on  $U$ -values measured according to ISO 9869-1 [15]. They carried out *in situ* measurements on three different walls. Thanks to numerical simulations fed with these measurements, the authors identified that heating system-on and off introduced a bias in the measured  $U$ -value up to 30%.

Gaspar *et al.* [97] investigated the minimum test duration for an accurate measurement of a wall  $U$ -value. The minimum duration was determined according to data quality criteria, variability of results criteria, and standardized criteria for different ranges of theoretical thermal transmittance. The results were obtained on three case studies (three façades typical of Spanish constructions). The authors found that durations recommended by ISO 9869-1 [15] are conservative and might be reduced. The dynamic method also lead to better results.

### 2.3.1.2. Thermometric methods

Some studies only used temperature sensors instead of a HFM to measure the heat flux on a wall. In this alternative approach, called the “thermometric method” [92]

or the “air-surface temperature ratio method” [98], the heat flux  $\varphi$  through the wall is calculated from the difference between the internal wall surface temperature  $T_{si}$ , the internal operative temperature  $T_i$ , and the internal total heat transfer coefficient  $h_i$ :

$$\varphi = h_i (T_i - T_{si}) \quad (2.31)$$

This method has the advantage of not suffering from the errors introduced by the use of a HFM. However, the internal heat transfer coefficient has to be estimated. Kim *et al.* [98] used the standard value  $h_i = 7.7 \text{ W.m}^{-2}.\text{K}^{-1}$  (from ISO 6946 [99] for instance). *In situ* measurements were made on four households. This method was compared to standard ISO 9869-1. According to the authors, the air-surface temperature ratio method enabled to perform shorter measurements than the standard method.

Bienvenido *et al.* [100] also used the standard value  $h_i = 7.7 \text{ W.m}^{-2}.\text{K}^{-1}$  in order to carry out measurements in eight case studies in the warm Mediterranean climate. This study aimed at identifying the best operating conditions and optimal data management. The authors concluded that the method leads to lower relative uncertainties in winter than in summer and that an indoor/outdoor temperature gradient of  $5^\circ\text{C}$  is sufficient. They also pointed out that measuring the heat transfer coefficient *in situ* could improve the method accuracy.

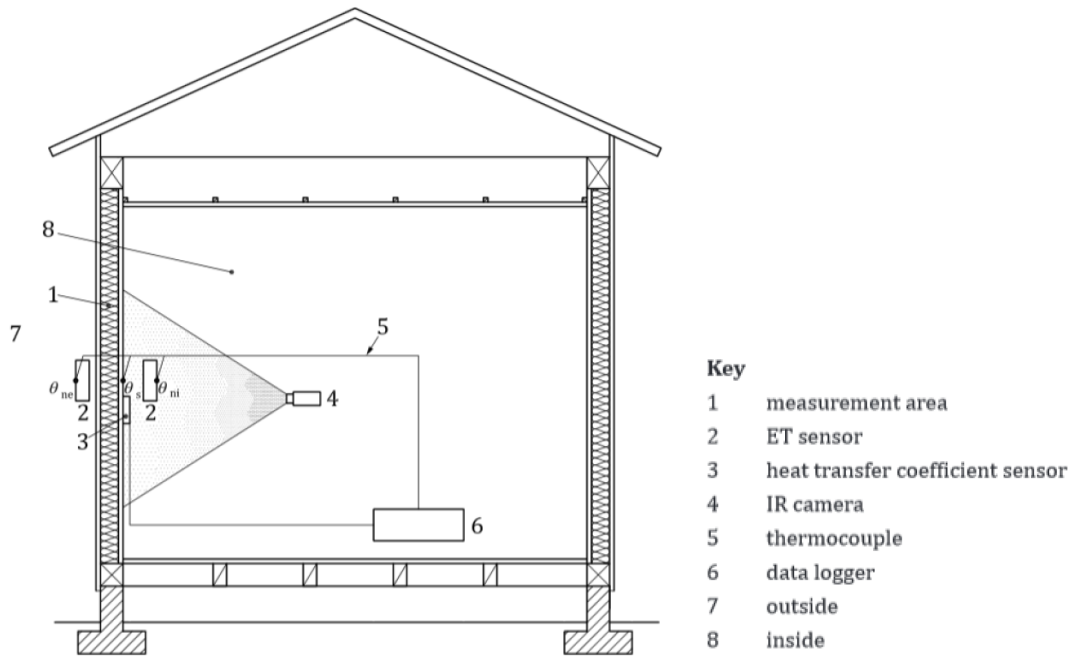
Finally, Andujar *et al.* [101] assigned to  $h_i$  a standard value of convective heat transfer coefficient ( $2.5 \text{ W.m}^{-2}.\text{K}^{-1}$ , from ISO 6946 [99] as well). They developed a device to apply this method easily (modular, scalable and fully wireless apparatus). The method was compared to the standard method from ISO 9869-1 [15] thanks to experiments carried out in a dwelling before and after energy retrofitting. The authors concluded that the thermometric method is a cheap, quick and reliable simple way to measure a wall  $U$ -value.

### 2.3.1.3. IRT methods

These methods measure the surface heat flux density  $\varphi$  from quantitative infrared thermography measurements.

Standard ISO 9869-2 [102] described a methodology to estimate a wall thermal transmittance from passive IRT and other sensors. The method was derived from Kato *et al.* [103]. As shown in Fig 2.20, it uses specific sensors to measure the operative temperature (referred as ET sensors, for “Environment Temperature”) on each side of the wall as well as the indoor total heat transfer coefficient (“total heat transfer coefficient sensor”). Infrared measurements enable to account for non-homogeneities in the wall surface temperature. In essence, it is a thermometric method given that the heat flux across the wall is worked out from the heat transfer coefficient and temperature measurements (see Eq 2.31).





**Figure 2.20.:** Experimental protocol for application of ISO 9869-2 [102].

Madding [104] was one of the first to propose a method to estimate a wall thermal transmittance from infrared measurements. He estimated the surface heat flux from its radiative and convective components:

$$\varphi = 4\varepsilon\sigma \left( \frac{T_{\text{si}} + T_{\text{env}}}{2} \right)^3 (T_{\text{si}} - T_{\text{env}}) + h^c (T_{\text{si}} - T_i) \quad (2.32)$$

with  $\varepsilon$  the wall surface emissivity,  $\sigma$  the Stefan-Boltzmann constant,  $h^c$  the convective heat transfer coefficient, and  $T_{\text{env}}$  the mean radiant temperature, respectively. The  $h^c$  coefficient was calculated using Holman [105] and Earle [106] empirical correlations (based on the air-to-wall temperature difference only). The value 0.95 (representative of most building materials) was assigned to the emissivity. The method was tested on a lab-scale experiment and a real wall.

Fokaides and Kalogirou [107] used a very similar method to perform measurements on five dwellings (insulated masonry and stone masonry) within two seasons. The wall heat flux density is given by:

$$\varphi = 4\varepsilon\sigma T_{\text{si}}^3 (T_{\text{si}} - T_{\text{env}}) + h^c (T_{\text{si}} - T_i) \quad (2.33)$$

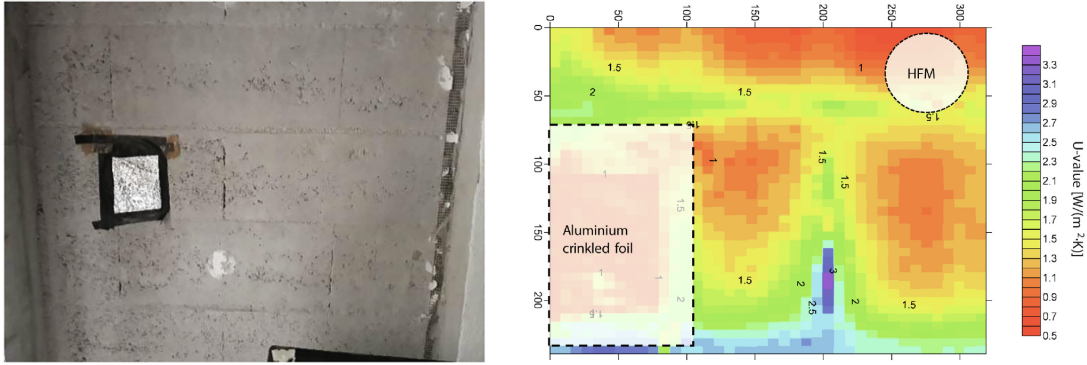
It may be seen that the calculation of the radiative component is slightly different. In addition, standard values from ISO 6946 [99] were assigned to the convective heat transfer coefficient  $h^c$  (instead of correlations). The emissivity was estimated from a table of standard values for building materials.

### 2.3. QUANTIFICATION OF A WALL THERMAL TRANSMITTANCE

Tejedor *et al.* [108, 109, 110] estimated the convective heat transfer coefficient from an empirical correlation based on dimensionless numbers:

$$\varphi = \varepsilon\sigma \left( T_{\text{env}}^4 - T_{\text{si}}^4 \right) + \left( 0.825 + \frac{0.387 \times Ra^{1/6}}{\left[ 1 + \left( \frac{0.492}{Pr} \right)^{9/16} \right]^{8/27}} \right) \times \frac{k}{L} (T_i - T_{\text{si}})^2 \quad (2.34)$$

with  $Ra$  and  $Pr$  the Rayleigh and Prandtl numbers, respectively,  $k$  the air thermal conductivity and  $L$  the height on the wall. The radiative heat transfer term is calculated thanks standard value of the wall emissivity (from ISO 6946 [99]). Two case studies are analyzed: a single-layer wall and a multi-layer one (external insulation). In [110], the authors used this method to work out 2D maps of  $U$ -values (see Fig 2.21) on non-homogenous walls. The methods was tested on three heavyweight walls inside a climate chamber.



**Figure 2.21.:** Picture (left) and 2D map of  $U$ -value (right) on a heavyweight wall, from Tejedor *et al.* [110].

Albatici *et al.* [68, 111] focused on outdoor measurements. The external convective heat transfer coefficient was estimated using a modified version of the Jürges equations [112]: the constant term, which estimates the radiative heat transfer coefficient, was removed from the equations. Instead, radiative heat losses are calculated from measured temperatures:

$$\varphi = \varepsilon\sigma \left( T_{\text{env}}^4 - T_{\text{se}}^4 \right) + 3.8054v (T_{\text{se}} - T_e) \quad (2.35)$$

with  $T_{\text{se}}$  and  $T_e$  the external surface and external environment temperatures, respectively, and  $v$  the wind velocity. The emissivity was measured with IRT by moving a hot element close to the wall surface and recording the apparent temperature of both the source and its reflected image on the wall. The authors studied *in situ* three buildings in [68] (two light structured buildings and one heavy structured building) as well as one experimental building in [111] where timber (light) and brick (heavy) structures were tested.

Dall'O *et al.* [113] used the full Jürges equations to estimate both convective and radiative heat transfer coefficients:

$$\varphi = (5.8 + 3.8054v) (T_{se} - T_c) \quad (2.36)$$

The authors studied 14 existing Italian buildings made in different construction periods. They concluded that the method is more reliable for solid-mass structures than externally insulated buildings.

Bienvenido *et al.* [114] thoroughly studied the influence of the correlation chosen for the internal heat transfer coefficient on results of quantitative IRT methods. A total of 25 correlations of temperature differences and 20 correlations of dimensionless numbers was tested. An experimental campaign was performed on three façades representative of most Spanish buildings (brick walls with or without insulation). The authors concluded that the use of correlations depending on dimensionless numbers gave better results (smaller bias on the measured thermal transmittance). Similarly, they studied in a second paper [115] the influence of the chosen correlation for the external heat transfer coefficient. In total, 46 correlations depending on the wind speed and 9 correlations depending on dimensionless numbers were compared. Given the difference in the results, it was not possible to establish a more adequate correlation for the external heat transfer coefficient.

Pajani [23, 116] proposed a method, which he named “Seid”, to measure a wall  $U$ -value only from infrared measurements (no temperature sensor is needed). This method consists in fixing onto the internal face of the wall an insulating material of known thermal resistance  $R_{ref}$  before starting the measurements. The thermal resistance should be close to the one of the wall and this reference material must be placed in the thermal scene monitored by the IR camera. The  $U$ -value is then given by:

$$U = \frac{1}{R_{ref}} \times \frac{T_{ref}^{app} - T_{si}^{app}}{T_{env} - T_{ref}^{app}} \quad (2.37)$$

with  $T_{si}^{app}$  and  $T_{ref}^{app}$  the apparent temperatures on the wall surface and the reference material, respectively. However, this ingenious method has not been experimentally tested by the author in the given papers.

Finally, Ibos *et al.* [8] implemented and compared three IRT methods (ISO 9869-2 [102], “Seid”, passive thermography) to ISO 9869-1 [15]. The measurement were performed *in situ* on a renovated residential building with two floors. The authors pointed out the high dispersion in the results obtained which highlights the fact that steady-state *in situ*  $U$ -value measurements are not straightforward.

### 2.3.2. Dynamic methods

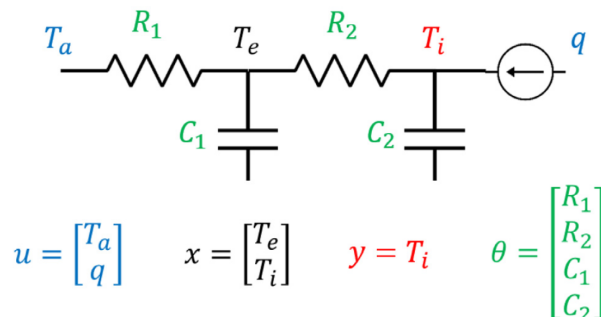
For steady-state methods to be accurate, several recommendations have to be followed, which limits their applicability. For instance, the weather conditions have to remain constant during several consecutive days to ensure a quasi-steady-state regime, and measurements may be very long (minimum 72 h according to ISO 9869-1 [15]).

Dynamic methods were developed to overcome these limitations. Basically, a more advanced dynamic data analysis can include the fluctuations in measured heat fluxes and temperatures instead of canceling them out. In addition, by using dynamic changes in temperature, dynamic methods usually do not require a consistently high internal/external temperature difference. In essence, they are models constructed from measurement data (inverse modeling).

#### 2.3.2.1. Gray-box approaches

Many studies used stochastic gray-box models to estimate a wall thermal transmittance from dynamic measurements. These models depend on parameters which have a physical meaning (usually thermal resistances and capacities: the so-called R-C models) so a physical interpretation of the results is possible. Grey-box models can describe complex phenomena and data structures. Heat transfers are described as a set of continuous differential equations formulated using the states considered. This approach was used in many studies. For instance, see Gutschker [117], Baker *et al.* [118], Jiménez *et al.* [119], Deconinck *et al.* [120, 121], Naveros *et al.* [122] and Bacher *et al.* [123].

Rouchier [124] proposed an overview of the main guidelines for a careful and optimal use of inverse techniques in buildings. It provides an introduction, along with useful references, to the topics of estimation error assessment, regularization, identifiability analysis, residual analysis, model selection and optimal experiment design. The methods are illustrated on the example of a simple R-C gray-box model (see Fig 2.22).



**Figure 2.22.:** Running example illustrating Rouchier [124] (R2C model).

Biddulph *et al.* [125] combined simple gray-box R-C model with Bayesian analysis to estimate a wall U-value and effective thermal mass. A total of 93 different sites

across England were monitored. Walls were expected to be solid (with no cavity or insulation). Measurements were collected in accordance with ISO 9869-1 [15]. According to the authors, the method needs only a few days of measurements, provides an estimate of the effective thermal mass, and could potentially be used in summer. This method was later improved by Gori *et al.* [126, 127]. The propagation of systematic measurement uncertainties on the thermophysical properties of building elements (e.g.  $R$ -value or  $U$ -value) was investigated using two case studies (a solid and a cavity wall) monitored long term.

De Simon *et al.* [128] proposed a Bayesian approach to sequentially infer thermophysical properties ( $U$ -value and thermal capacity) of a wall, given *in situ* measurements from the walls internal and external near-air temperatures and surface heat fluxes. The method was validated on both synthetic and real measurements. The authors concluded that this dynamic approach was shorter and more accurate than standards steady-state methods.

### 2.3.2.2. Black-box approaches

Black-box models are viewed in terms of their inputs and outputs. The internal structure of the models and the parameters involved have no physical meaning. Annex 58 of the International Energy Agency (IEA) [129] provided guidelines for the thermal performance characterization using time series data in buildings.

Several studies used black-box ARX models (“Auto Regressive with eXogenous inputs”). ARX models (and similar models such as ARMA, ARMAX, ...) belong to the System Identification area [130]. They have the advantage of being rather simple to use. The application of ARX methods for the thermal characterization of building walls was extensively discussed in Bauwens [131]. The parameters are involved in a linear relation between the inputs (usually temperatures) and the output (usually a heat flux), from measurements of these quantities. As an example:

$$\mathcal{A}(q)\varphi = \mathcal{B}(q)T_{si} + \mathcal{C}(q)T_{se} \quad (2.38)$$

with  $\mathcal{A}$ ,  $\mathcal{B}$  and  $\mathcal{C}$  polynomials in the backshift operator  $q$ . ARX models will be presented in further details in Chap 7.

Jiménez *et al.* [132, 133] was one of the first to use ARX models for the estimation of physical parameters in buildings. The authors showed that commonly used R-C networks may be re-written in the form of a parametric model such as ARX. The method was tested *in situ* on a simple homogeneous wall consisting of a sandwich of insulation between plywood. Naveros *et al.* [134] further developed this idea and presented the whole chain of transformation from thermal networks to ARX models. The authors carried out measurements on a lightweight opaque wall installed inside a test cell under outdoor weather.

Lambie *et al.* [119, 135] studied five exterior walls *in situ* before and after renovation. The authors compared several dynamic methods (linear regression, ARX,

Anderlinds' and grey-box methods). They concluded that only the linear regression model was not able to capture the dynamic duilbing behavior for a 1 h dataset.

Deconinck *et al.* [120] compared several semi-stationary and dynamic data analysis methods (regression modelling, ARX-modelling or stochastic grey-box modelling). The study was based on simulated and real measurements performed on a south-facing insulated cavity wall in a moderate European climate. The authors concluded that no real preference was shown for a particular method.

It may be noted that ARX models were also used for the *in situ* characterization of a building global heat loss coefficient (HLC): [136, 137, 138].

Recent studies used some tools from the artificial intelligence area. Bienvenido *et al.* [139] used the method with correction for storage effects from ISO 9869-1 to determine the  $U$ -value of walls. In order to simplify and fasten the postprocess analysis, the authors developed a multilayer perceptron (a type of artificial neural network, ANN). The dataset used to train and then test this network was composed of 69 subsets, each one corresponding to experiments carried out in different façades (multilayer walls with brick leaves, with or without insulation). The authors then optimized the method [140] (in terms of number of nodes and hidden layers) thanks to a dataset composed of 22,820 simulated tests. The authors showed that the  $U$ -value could be estimated without heat flux measurement. Finally, in a third study ([141]), they compared this multilayer perceptron to two other types of regression algorithm (“M5 Prime” and “random forest”). The models were trained on 11,579 simulated tests and then applied to two actual case studies. The M5 Prime algorithm with a time window of 2 days of observation made accurate estimations in the case studies.

### 2.3.2.3. Other approaches

Roulet *et al.* [142] proposed one of the first dynamic methods. It uses a linear model having a thermal conductivity and several time constants as unknowns. The system of equation is solved using Ordinary Least Squares (OLS) based on measurements data (heat fluxes and temperatures on both sides of the wall). Nine building elements (from very light to very heavy) were analyzed. Anderlind [143, 144] later proposed a simplification of this approach by expressing the heat flux as the sum of three terms: one for the steady-state behavior and the other two for dynamic variations. This way, the wall stationary behavior could be isolated. This approach was tested *in situ* on an insulated attic.

Larbi Youcef *et al.* [145] proposed an *in situ* measurement method of the thermal conductivity of an insulating material located inside a wall using an inverse method. The analysis was based on the indoor and outdoor wall surface temperatures. The measurements were made with infrared thermography and contact sensors. The heat transfer coefficients as well as weather data (air temperature and solar heat flux) were needed. Several days were required for the estimation to be accurate. The method was implemented *in situ* in a French building.

### 2.3.3. Active methods

The models used in dynamic methods usually require a significant amount of measurement data to be accurate (several days to several weeks). By using an artificial thermal load, active methods are a good alternative. Not only are they faster than other methods, they may also be less sensitive to weather conditions.

Ricciu *et al.* [146] estimated the dynamic thermal properties of walls using a harmonic thermal load, following recommendations from standard ISO 13786 [147]. The properties are estimated from an inverse technique based on the phase lag and amplitude ratio of temperature and heat flux either side of the wall. The model was applied to a real experiment on a full-size wall in a climate chamber. Lakatos *et al.* [148] applied the same method for the characterization of opaque aerogel insulation blankets. However, this method requires a sinusoidal excitation and is therefore not applicable *in situ*.

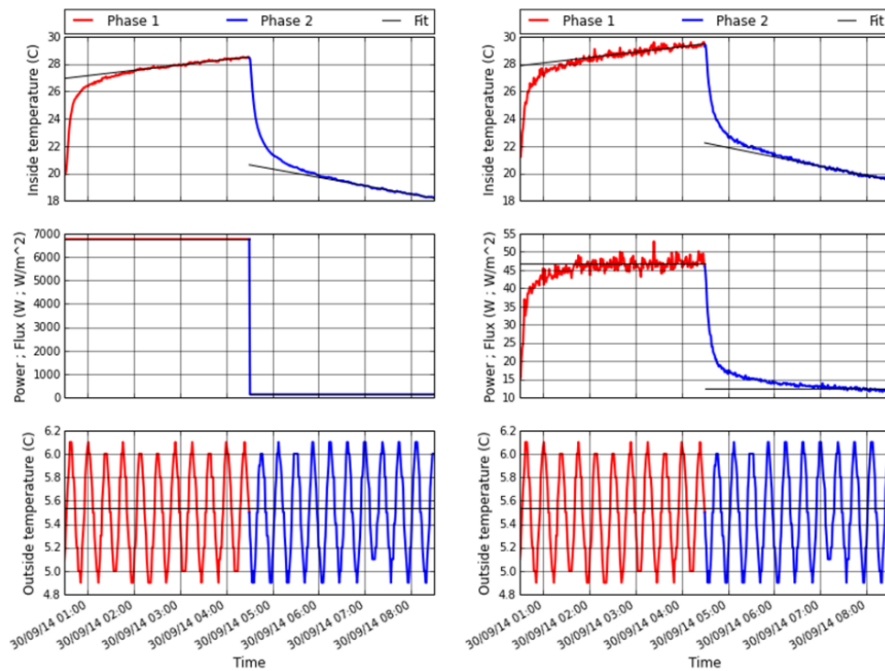
Meulemans *et al.* [149, 150] presented the “QUB/e” method. It consists in heating the interior of a building and fitting a simple two-parameter model to the measurement data in order to estimate the thermal transmittance of a building element. Both the heating and the free-cooling phases are analyzed and the  $U$ -value is given by:

$$U = \frac{a_2\varphi_1 - a_1\varphi_2}{a_2\Delta T_1 - a_1\Delta T_2} \quad (2.39)$$

where  $\varphi_i$ ,  $a_i$  and  $\Delta T_i$  are, respectively, the mean heat flux density, the slope of the internal air temperature and the internal/external air temperature difference at the end of the  $i^{\text{th}}$  phase (1 = heating phase, 2 = free cooling phase). The heating power, the air temperatures and the heat flux passing through a building element during a QUB/e test are plotted in Fig 2.23. The method was validated on several building walls, in a climate chamber as well as *in situ*. The main advantages of this technique are its rapidity (only a few hours are needed, typically one night) and simplicity. However, the heat fluxes are supposed constant during the active test.

Rasooli *et al.* [151] presented the Excitation Pulse Method (EPM). It is based on a triangular thermal load of the internal surface (see Fig 2.24). The wall thermal resistance (as well as the outer layers thermal conductivity and volumetric heat capacity) are determined from inverse modeling of the Response Factors [152]. From the a study of three walls (especially a 8.5-cm thick wall with unknown construction), the authors showed that the thermal resistance could be estimated in only a few hours (ISO 9869-1 method was also applied for validation). The authors then optimized the method thanks to study based on simulations and experiments in [153]. The experimental generation of a triangular pulse is complex: the distance between the radiant heat source and the wall is controlled and then the wall is cooled with a fan and an ice bag. In addition, the wall surface temperature rises by almost 60°C so the hypothesis of thermal properties independent of temperature might not hold true.

### 2.3. QUANTIFICATION OF A WALL THERMAL TRANSMITTANCE

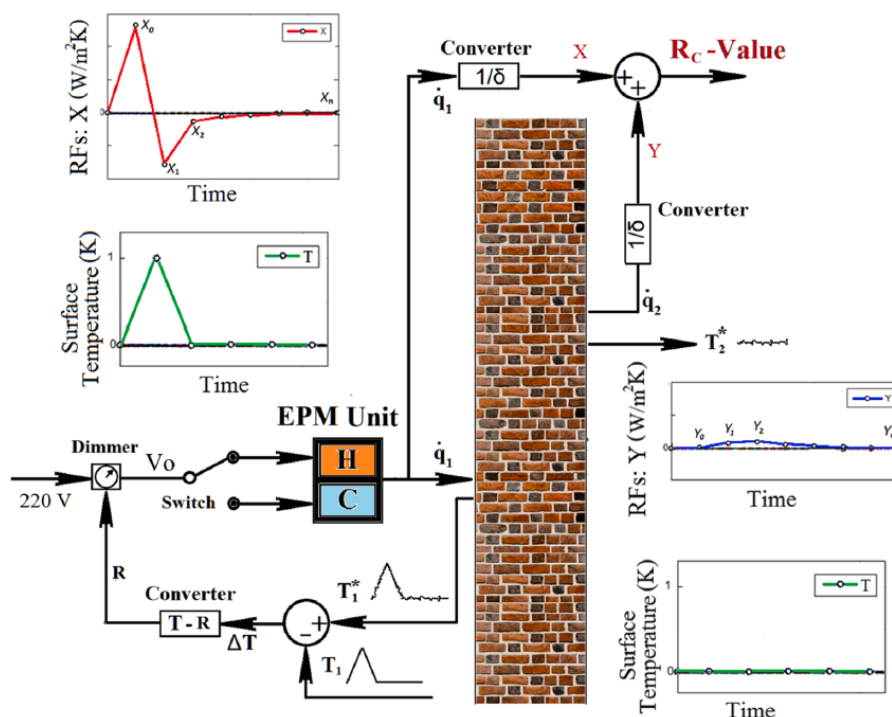


**Figure 2.23.:** Evolution of temperatures, heating power and heat flux density during a 4-hour QUB/e test. The red, blue and black solid lines correspond to the heating phase, the free cooling phase and the linear regressions used to derive the quantities used in the QUB formula, respectively. From Meulemans *et al.* [149].

Yang *et al.* [154] used a heat flux/temperature deconvolution method (Truncated Singular Value Decomposition, TSVD) to estimate a wall thermal resistance. The wall thermal properties were then estimated thanks to a model based on the thermal quadrupole formalism. From the measured surface temperatures and heat fluxes, the unit-pulse and unit-step responses at the front surface of the investigated wall were reconstructed through a deconvolution approach. Figure 2.25 shows results on one example. Two configurations were studied. Walls were made of mortar, concrete block, insulation material and plaster board. Experiments were carried out on two traditional multi-layer building walls using heating lamps. When the dense layer was heated firstly, its thermal effusivity could be estimated. However, when the insulation layer was heated firstly, its thermal resistance could be estimated. This method was therefore not validated for the measurement of the overall thermal resistance of a wall.

Larbi Youcef *et al.* [155] developed in laboratory a device to measure a wall thermal resistance from active IRT. The authors used halogen lamps inside a reflecting box on the internal side, as described in Fig 2.26. Specific heat transfer modeling based on the thermal quadrupole formalism and simplified asymptotic models were developed to identify parameters of interest by minimizing a functional that links measured and estimated temperatures (inverse method). The method was successfully applied to several commercial panels fixed onto a building wall. The authors highlighted that the sensitivity of the direct model to the heat transfer coefficients is one of the main limitations of the method.





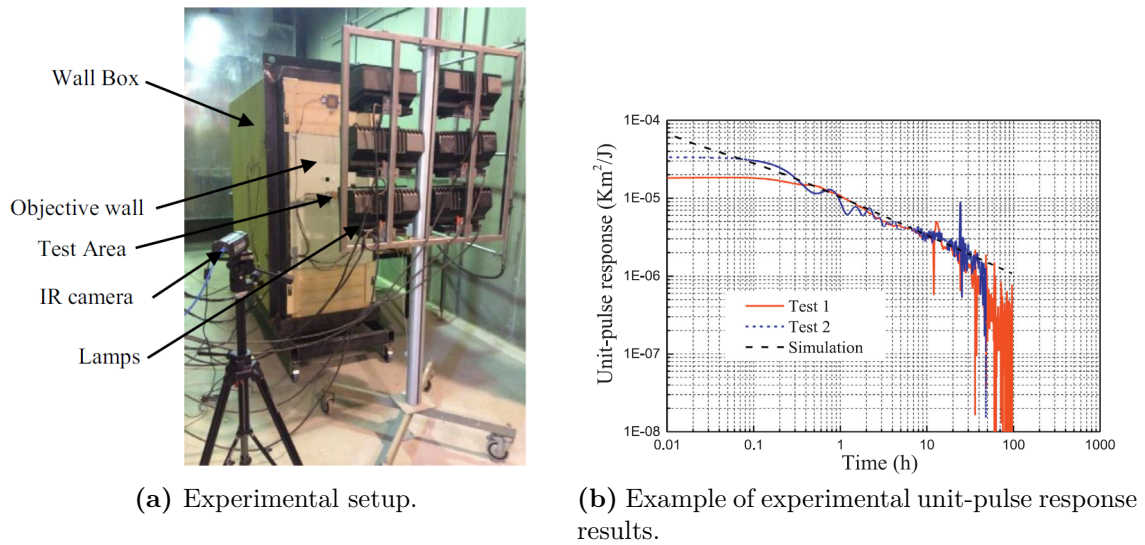
**Figure 2.24.:** Control system and working principles of the Excitation Pulse Method from Rasooli *et al.* [151].

Chaffar *et al.* [156] estimated the thermal properties (conductivity and volumetric heat) of a homogeneous wall by heating one face and recording the temperature of the other face using IRT. An inverse method based on a numerical model (finite difference) was used. The measurements are compared to the identified model in Fig 2.27. The method was first applied in laboratory on a homogenous gypsum plate and then *in situ* on a 15-mm thick homogeneous reinforced concrete shell. Similarly to Larbi Youcef *et al.* [155], this method is limited by the high sensitivity to the heat exchange coefficient. In addition, given that the thermal load is applied on one side of the wall whereas measurements are made on the other side, the signal to noise ratio will rapidly decrease as the thermal resistance and thermal mass of the wall increase.

### 2.3.4. Conclusion

Many measurement methods for the assessment of a wall thermal transmittance were developed in the literature. There is a high diversity in the proposed approaches both in terms of experimental protocol and postprocessing analysis. Each method offers advantages and limitations. The most widely used methods (especially the standardized ones) are based on steady-state assumptions. As a consequence, they usually require very long measurements, a high indoor/outdoor temperature gradient and are highly sensitive to outdoor conditions. From this perspective, dynamic methods are a good alternative. By analyzing the transient behavior of the wall, these methods are usually less demanding in terms of weather requirements: they do

### 2.3. QUANTIFICATION OF A WALL THERMAL TRANSMITTANCE



**Figure 2.25.:** Experimental setup and example of unit-pules response, from Yang *et al.* [154].

not require a consistently high temperature gradient. Many different models were developed in order to estimate the thermal resistance from measured temperature and heat flux (linear models, gray-box models, black-box models, ...).

Yet, most dynamic methods still rely on long measurements. Active methods were developed in order to overcome this limitation. By applying an artificial thermal load to the studied element, they are able to significantly reduce the measurement duration to a few hours. However, they suffer from some limitations. The main limitations to the use of these methods were identified as (i) a high sensitivity to the heat transfer coefficient, (ii) a complex and bulky apparatus, depending on the heating system, and (iii) the use of many contact sensors (intrusive as well ad resource and time consuming instrumentation).

The active method developed in this thesis aims at overcoming these constraints. An additional objective for the method was to be adaptable to non-homogeneous walls and thermal bridges.involve

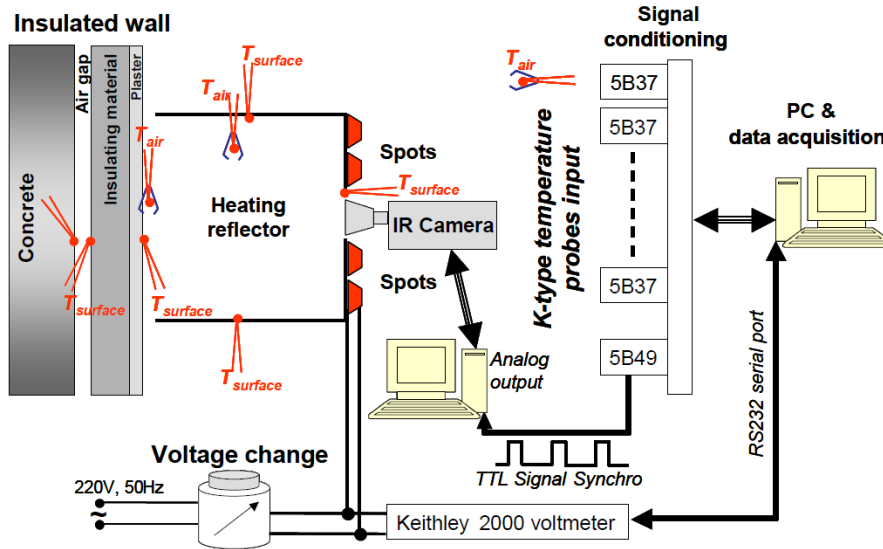


Figure 2.26.: Schematic view of the experimental setup of Larbi Youcef *et al.* [155].

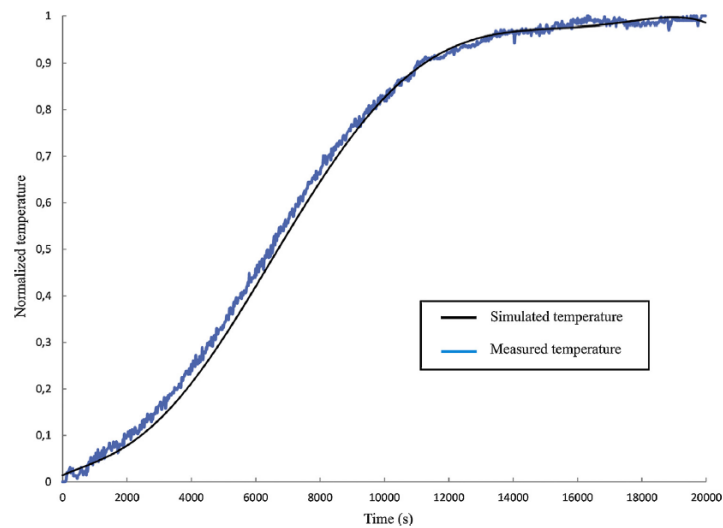


Figure 2.27.: Normalized measurements and simulated curves for an *in situ* concrete wall experiment, from Chaffar *et al.* [156].

### 2.4. Conclusion

This literature review showed that theoretical calculations or values from design predictions are not in good agreement with *in situ* measurements obtained in actual operating conditions. This contributes to the so-called “performance gap”. There is therefore a need for fast and reliable *in situ* measurement methods to quantify the thermal performance of building envelope elements.

Many different methods were developed in the past decades for the *in situ* characterization of a wall thermal transmittance. They method rely either on the analysis of the steady-state or the transient behavior of the wall and an artificial thermal load is sometimes used. The existing standards are based on steady-state assumptions. However, the characterization on site of a thermal bridge was a lot less addressed in the literature. Indeed, the only standards deal with numerical simulations and the few *in situ* measurements performed rely on a method based on steady-state assumptions.

For both  $U$ -value measurement and thermal bridge detection, it has been shown that active methods have the capability to overcome the main limitations of steady-state methods. Indeed, they do not require a high and constant indoor/outdoor temperature difference. This makes them applicable when desired, in most weather conditions. In addition, active methods usually require shorter measurements: they can estimate a wall  $U$ -value within a few hours whereas steady-state approaches usually require a few days (e.g. ISO 9869-1).

The literature review on  $U$ -value measurement methods also highlighted than one limitation of the some active methods is the high sensitivity to the heat transfer coefficient. In addition, in order to obtain a uniform heating of a wall, some active techniques require a bulky and cumbersome apparatus. Also, the implementation of many contact sensors might be intrusive as well as resource and time consuming. A few studies showed that heating the indoor air is an interesting alternative for its ease of implementation, capability to heat up the whole wall.

To overcome these limitations, this thesis proposes active methods for the *in situ* characterization of building walls and thermal bridges.



### 3. Experimental aspects



**Figure 3.1.:** Illustration of thesis plan.

This chapter presents several experimental aspects useful for a complete understanding of the following chapters. The first two sections are dedicated to thermal metrology. Section 3.1 focuses on contact measurements with thermocouples and heat flux meters whereas section 3.2 deals with infrared thermography (measurement without contact). Theoretical aspects as well as practical matters (such as sensor calibration) are described in details. Section 3.3 proposes a conclusion.

In addition, a few laboratory characterization methods used to measure material thermal properties (conductivity, diffusivity, emissivity and effusivity) are presented in Appendix A. These measurements are used as reference values to perform numerical simulations to compare with *in situ* characterization methods.

## Nomenclature

### Acronyms

BRDF	Bidirectional Reflectance Distribution Function
EPS	Expanded PolyStyrene
FOV	Field Of View
FPA	Focal Plane Array
HFM	Heat Flux Meter
IFOV	Instantaneous Field Of View
IRT	InfraRed Thermography
LWIR	Long Wave InfraRed domain
MRT	Mean Radiant Temperature
MWIR	Medium Wave InfraRed domain
NETD	Noise Equivalent Temperature Difference
NUC	Non-Uniformity Correction
QWIP	Quantum Well Infrared Photodetector
SNR	Signal to Noise Ratio
SWIR	Short Wave InfraRed domain
USB	Useful Spectral Band
XPS	eXtruded PolyStyrene

### Greek Symbols

$\alpha$	absorptance	-
$\beta$	fluid expansion coefficient	$K^{-1}$
$\gamma$	polar angle	rad
$\varepsilon$	emissivity	-
$\theta$	azimuthal angle	rad
$\lambda$	wavelength	m
$\rho$	reflectance	-
$\sigma$	Stefan-Boltzmann constant	$W.m^{-2}.K^{-4}$
$\tau$	transmittance	-
$\nu$	cinematic viscosity	$m^2.s^{-1}$
$\varphi$	heat flux density	$W.m^{-2}$
$\phi$	heat flux	W
$\Omega$	solid angle	sr

### Roman Symbols

$a$	thermal diffusivity	$m^2.s^{-1}$
$A$	area	$m^2$
$b$	thermal effusivity	$J.K^{-1}.m^{-2}.s^{-1/2}$
$c$	speed of light in vacuum	$m.s^{-1}$
$f_{r\lambda}$	BRDF	-
$g$	gravity acceleration	$m.s^{-2}$
$h$	Planck constant	J.s
$I$	radiant intensity	$W.m^{-2}.sr^{-1}.nm^{-1}$
$k$	thermal conductivity	$W.m^{-1}.K^{-1}$
$k_B$	Boltzmann constant	$J.K^{-1}$
$R$	infrared sensor sensitivity	-

---

<i>S</i>	HFM sensitivity coefficient	$\mu\text{V} \cdot (\text{W} \cdot \text{m}^{-2})^{-1}$
<i>t</i>	time	s
<i>T</i>	temperature	K
<i>u</i>	uncertainty	
<i>U</i>	voltage	V

**Superscripts**

<i>o</i>	Planck radiant intensity
'	directional quantity
<i>a</i>	absorbed
app	apparent
<i>c</i>	convective
<i>e</i>	emitted
<i>i</i>	incident
<i>r</i>	radiative
re	reflected

**Subscripts**

atm	atmosphere
corr	corrected
env	radiative environment
mea	measured
op	operative temperature
s	surface
<i>L</i>	linearized



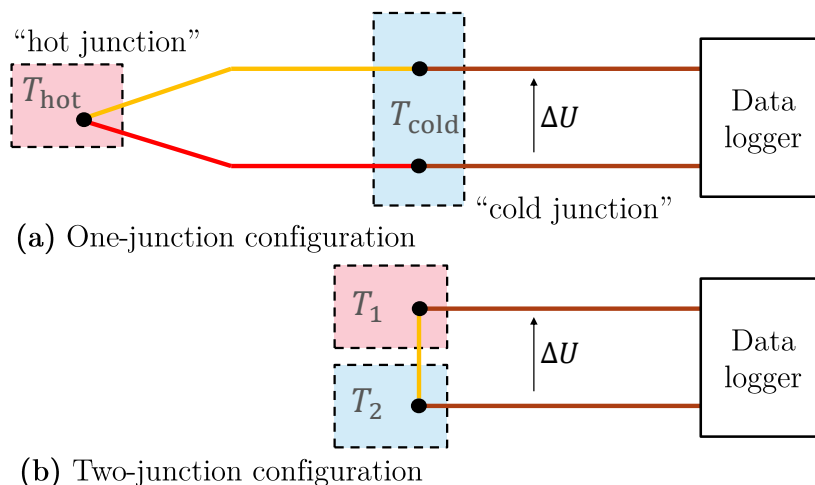
### 3.1. Contact thermal measurements

This section presents the contact sensors used in this thesis for temperature and heat flux metrology. Their working principles and calibration procedures are detailed.

#### 3.1.1. Thermocouples

##### 3.1.1.1. Presentation

A thermocouple is an electrical device made out of an electrical junction between two different conductive materials. Many different materials may constitute a thermocouple. The most common are K-type (chromel and alumel) and T-type (copper and constantan). K-type thermocouples may be used between approximately 0 and 1100°C whereas T-type ones work mainly around ambient temperature: between -180 and 300°C. As a result of the Seebeck effect, the thermocouple produces a temperature-dependent voltage which may be interpreted to measure temperature. Figure 3.2 presents the two possible configurations.



**Figure 3.2.:** Illustration of thermocouple working principle: One (a) and Two (b) junction configurations.

The one-junction case is the most common. It consists in placing one junction (called “hot junction”) where the temperature is to be measured. The other ones (referred as “cold junction”) are embedded inside the acquisition system. The thermocouple measures the temperature difference  $T_{\text{hot}} - T_{\text{cold}}$  between the junctions. Temperature  $T_{\text{cold}}$  is measured independently within the acquisition system which enables to determine  $T_{\text{hot}}$ . This so called “cold-junction compensation” is the main source of measurement uncertainty with a thermocouple.

The two-junction configuration is useful to directly measure a temperature difference between two objects, rather than one absolute temperature. There is no cold junction compensation. This reduces the measurement uncertainties.

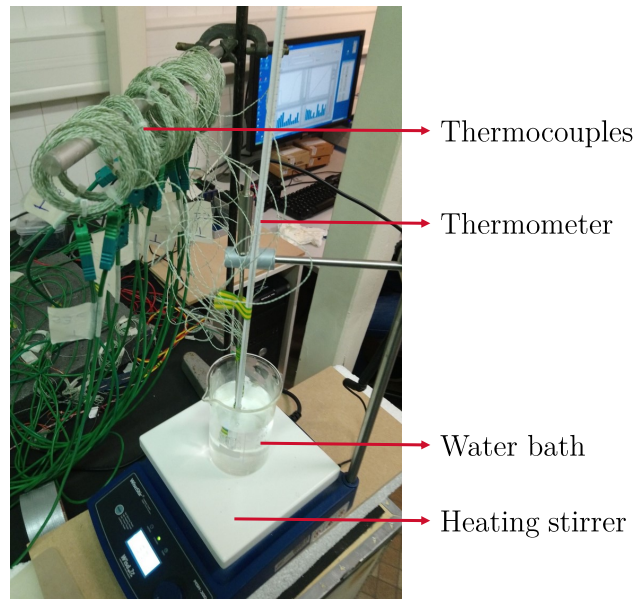
### 3.1. CONTACT THERMAL MEASUREMENTS

---

The thermocouples used in this thesis, either in the one-junction or two-junction configuration, are references 401-302 (K-type) and 401-305 (T-type) from TC Direct. The wires have a 0.2 mm diameter. The thermocouples are plugged on National Instruments<sup>®</sup> NI 9214 conditioning modules. These modules communicate with a computer via a 8-slot NI CompactDAQ USB chassis. The experimental setup is monitored by a LabView application. All thermocouples were first calibrated, as detailed below.

#### 3.1.1.2. Calibration: one-junction configuration

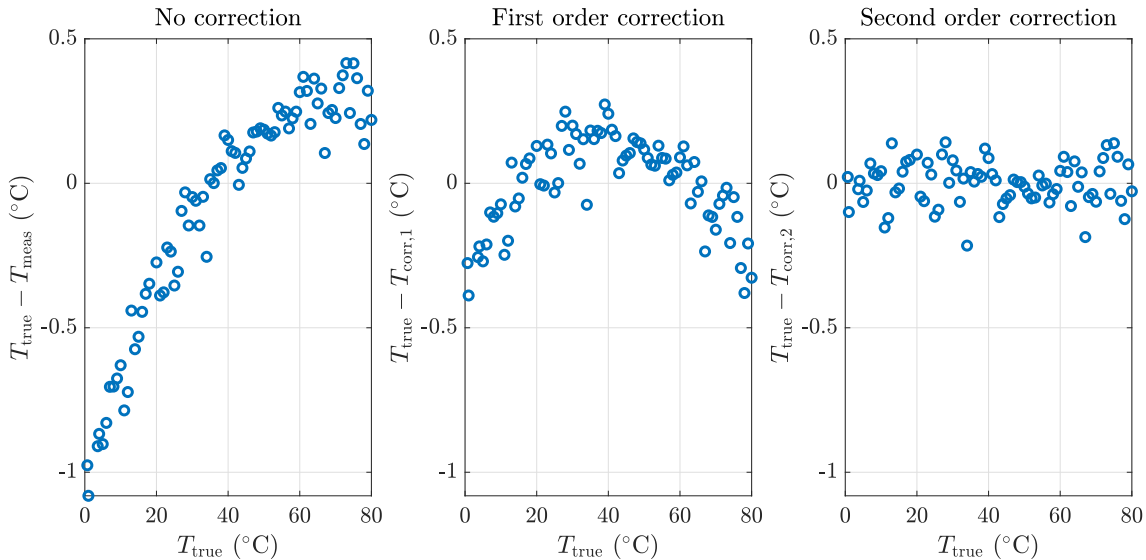
For the calibration, the hot junctions of the thermocouples were fixed together and immersed in water with a reference sensor. The water was cooled or heated to reach the desired temperature level for the calibration and stirred to avoid any temperature gradient within the liquid. The experiment setup is shown in Fig 3.3. A second order polynomial transformation is applied to each thermocouple signal to minimize the difference with the reference sensor. The latter was either a mercury thermometer, or a calibrated platinum sensor. The reference platinum sensor was used with an AOIP TM6612 temperature datalogger. The measurement uncertainty of this reference is of 0.2°C. An external calibration of these devices was performed by the manufacturer in order to ensure the metrological traceability to the ITS-90 [157].



**Figure 3.3.:** Example of thermocouple calibration in water.

The calibration process is illustrated on one example in Fig 3.4. On this example, the thermocouples are calibrated between 0 and 80°C (sampling every 1 K). Let  $T_{\text{true}}$  and  $T_{\text{meas}}$  be the temperature given by the reference sensor (mercury thermometer here) and measured by the thermocouple, respectively. It may be seen that these two temperatures are not equal and the difference between them depends on the temperature. If a first order polynomial is used to correct  $T_{\text{meas}}$ , there is still a non

negligible difference between  $T_{\text{true}}$  and the corrected temperature  $T_{\text{corr},1}$ . However, with a second order correction, the residuals  $T_{\text{true}} - T_{\text{corr},2}$  are unsigned (flat), which shows that the thermocouple calibration is successful.



**Figure 3.4.:** Example of difference between true temperature and measured temperature without and with correction (before and after thermocouple calibration).

The calibration uncertainty is given by:

$$u_{\text{calib}}(T) = \max(|T_{\text{true}} - T_{\text{corr}}|) \quad (3.1)$$

For the given example:  $u_{\text{calib}}(T) = 0.21$  K. The thermocouple measurement uncertainty is given from the calibration uncertainty and the reference sensor uncertainty  $u_{\text{calib}}(T)$  [158]:

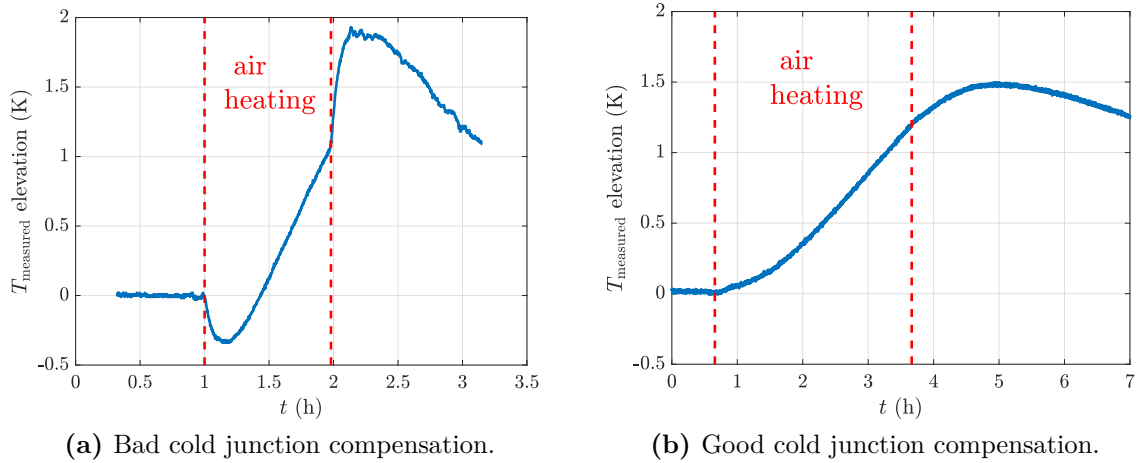
$$u(T) = \sqrt{u_{\text{calib}}^2(T) + u_{\text{ref}}^2(T)} \quad (3.2)$$

Uncertainty  $u_{\text{ref}}(T)$  is equal to 0.5 and 0.2 K for the mercury thermometer and the calibrated platinum sensor, respectively. This corresponds to a measurement uncertainty 0.29 or 0.54 K depending on the reference sensor used.

### 3.1.1.3. Bad cold junction compensation

To illustrate the complexity of temperature measurements, this paragraph presents an example of a bad cold junction compensation. The hot junction of a thermocouple is inserted between two thick boards of polystyrene. The sensor is plugged on a NI 9213 conditioning module and the air inside the room is heated thanks to electric fan heaters. The sampling period is of 5 s. The recorded hot junction temperature is plotted in Fig 3.5a.

### 3.1. CONTACT THERMAL MEASUREMENTS



**Figure 3.5.:** Example of measured hot junction temperatures with a bad (a) and a good (b) cold junction compensation.

The measured temperature suddenly decreases at the beginning of the heating phase and increases after the end of it. These results are obviously non physical as the temperature should rather increase and then decrease. This is due to a bad cold junction compensation. Indeed, this junction, located inside the NI 9213 conditioning module, is also heated by the air. Meanwhile, the hot junction is shielded from the air by polystyrene so its temperature variations are smaller and delayed in time. Consequently, the nonphysical decrease in measured temperature observed after  $t = 1$  h in Fig 3.5a is due to a badly compensated increase in cold junction temperature (and vice versa after  $t = 2$  h). This is a problem here because the error introduced by the cold junction is greater than the measurement uncertainty. Modules NI 9213 are not designed to be used in such conditions. However, modules NI 9214 are much more robust to varying room temperature because its cold junction is insulated (and therefore less sensitive to rapid temperature variations). For the same configuration, they are able to correctly measure the temperature, as shown in Fig 3.5b. The exact same thermocouple as in Fig 3.5a was used but this time is was plugged on a NI 9214 module. The experiment is similar: air heating and free cooling. The temperature inside the polystyrene keeps increasing after the end of the air heating phase because of the phase lag induced by the insulating material. As a consequence, NI 9214 modules is were used in this thesis.

#### 3.1.1.4. Calibration: two-junction configuration

In the two junction configuration, the measured voltage  $U$  (in  $\mu\text{V}$ ) is converted into Kelvin degrees thanks to the NIST polynomial [157] :

$$\Delta T = \sum_{k=0}^n a_k U^k \quad (3.3)$$

where coefficients  $a_k$  are given in Tab 3.1 for T-type thermocouples. The maximum error on this polynomial is  $u_{\text{NIST}} = 0.03$  K.

**Table 3.1.:** Coefficients of NIST polynomial for T-type thermocouple between 0 and 400°C (error:  $\pm 0.03$  K) [159].

coefficient	value	unit
$a_0$	0	K
$a_1$	$2.593 \times 10^{-2}$	K. $\mu$ V $^{-1}$
$a_2$	$-7.603 \times 10^{-7}$	K. $\mu$ V $^{-2}$
$a_3$	$4.638 \times 10^{-11}$	K. $\mu$ V $^{-3}$
$a_4$	$-2.165 \times 10^{-15}$	K. $\mu$ V $^{-4}$
$a_5$	$6.048 \times 10^{-20}$	K. $\mu$ V $^{-5}$
$a_6$	$-7.293 \times 10^{-25}$	K. $\mu$ V $^{-6}$

Because of the absence of cold junction compensation, no further calibration of the sensors was needed.

According to National Instrument documentation on NI 9214 module [160], the voltage is measured with an uncertainty  $u(U) = 0.03\%$ . The uncertainties are propagated [158] (parameters are assumed not correlated):

$$u(\Delta T) = \sqrt{u_{\text{NIST}}^2 + \left( \frac{d(\Delta T)}{dU} u(U) \right)^2} \quad (3.4)$$

with

$$\frac{d(\Delta T)}{dU} = \sum_{k=1}^n k a_k U^{k-1} \quad (3.5)$$

With the example of  $U = 100$   $\mu$ V, it comes  $\Delta T = 2.59 \pm 0.03$  K. The uncertainty on  $\Delta T$  is equal to the one of the NIST polynomial:  $u(\Delta T) = u_{\text{NIST}}$ . It means that the contribution of the measurement uncertainty on  $U$  to the overall uncertainty is negligible.

### 3.1.2. Heat flux meters

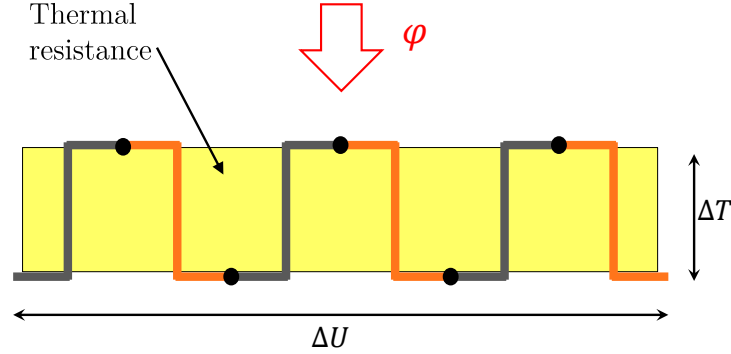
There are different types of heat flux meters (HFM) [161]. The ones used in this thesis are referred as “normal gradient” HFM because they measure a heat flux normal to the surface.

#### 3.1.2.1. Presentation

A heat flux meter is a thermopile sensor: it converts thermal energy into electrical energy. It consists of an array of thermocouple junctions arranged uniformly across

### 3.1. CONTACT THERMAL MEASUREMENTS

the surface of the sensor. The thermocouples can be connected in series of pairs with a junction located on either side of a thermal resistance layer, as illustrated in Fig 3.6.



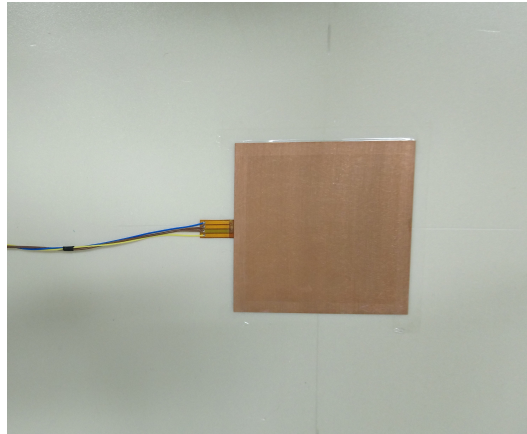
**Figure 3.6.:** Working principle of a heat flux meter.

The output voltage  $\Delta U$  of the device is directly proportional to the temperature difference  $\Delta T$  across the thermal resistance. At thermal equilibrium, it is therefore also proportional to the heat flux density  $\varphi$  going through the device. The output voltage is converted into heat flux thanks to the sensitivity coefficient  $S$ . In steady-state:

$$\varphi = \frac{\Delta U}{S} \quad (3.6)$$

Adding more thermocouples increases the voltage and therefore improves the signal to noise ratio. The heat flux meters used in this work are from Captec<sup>®</sup>. Their internal thermal resistance is made of Kapton. The sensors are  $100 \times 100 \text{ mm}^2$  large and have a sensitivity superior to  $60 \mu\text{V} \cdot (\text{W} \cdot \text{m}^{-2})^{-1}$  given with a 3 % uncertainty and have no thermal guard on the edges. One such sensor is presented in Fig 3.7. Also, a distinct thermocouple embedded inside the HFM measures the device temperature. Thanks to their small thickness (only 0.54 mm), these HFMs have a negligible thermal resistance and barely affect the air flow in the vicinity of the wall. Thus, the convective heat transfers are supposed not affected by their presence. In addition, the sensors were covered with some adhesive tape having the same infrared emissivity than the studied wall (see Section A.1) so that radiant heat transfers are not affected either.

It is important to point out that Eq 3.6 is based on a steady-state assumption whereas most measurements performed in this thesis are transient. Nevertheless, the characteristic time of the HFM used (a few minutes) is several orders of magnitude smaller than the characteristic time of temperature changes during the experiments (a few hours). Thus, the conditions are quasi-static and Eq 3.6.



**Figure 3.7.:** A  $100 \times 100 \text{ mm}^2$  heat flux meter from Captec<sup>®</sup> fixed on a wall.

### 3.1.2.2. Calibration

The sensitivities of the HFM are provided by the manufacturer. They are calibrated at ambient temperature thanks to a guarded hot box.[162]

Yet, a calibration of the data acquisition system was needed. Similarly to thermocouples, HFM are plugged on National Instruments NI9214 conditioning modules. However, it was noticed that heat fluxes were measured with a constant bias of a few  $\text{W.m}^{-2}$  (typically 3). Indeed, when the terminals of the HFM are swapped on the data logger inputs, the measured heat flux is not the exact opposite as it was before. Thus, this offset does not come from the sensor but rather from the acquisition system. A calibration procedure was carried out to remove the offset. Undertaking a measurement when the heat flux through the sensor is null would directly provide the offset. Nevertheless, this approach is not accurate because a perfectly null heat flux is complex to reach in practice.

An alternative approach is proposed. It consists in automatically switching the terminals of the HFM between each measurement point. This is done with a simple electrical assembly based on a relay, as shown in Fig 3.8.

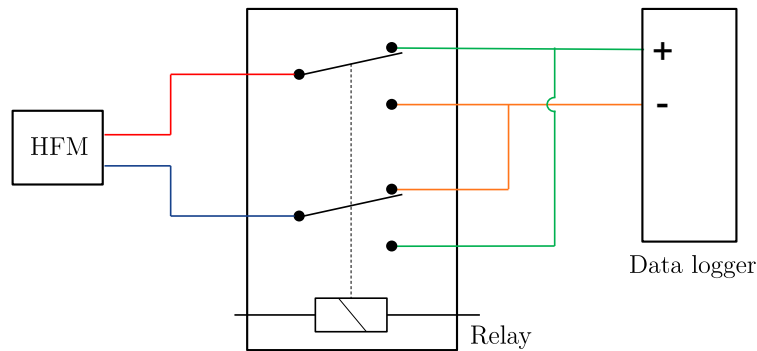
Then, even and odd points of the measured time series are separated to form two series. Each one corresponds to the heat flux measured as if the HFM had remained plugged in one way during the whole experiment. An example is shown in Fig 3.9. The indoor air was heated during 1 h to increase the measured heat flux. It may be noted that the average between the two series produces a constant signal (however noised). This confirms that the offset is not due to the HFM and demonstrates also that it does not depend on the heat flux magnitude. The mean value of the averaged signal is a good estimator of the offset. This calibration procedure was applied to each sensor, the results are gathered in Tab 3.2.

**Table 3.2.:** Summary of measured HFM offset for 7 identical sensors.

HFM	1	2	3	4	5	6	7
Offset ( $\text{W.m}^{-2}$ )	3.41	3.52	3.46	3.24	3.25	3.14	3.30

### 3.1. CONTACT THERMAL MEASUREMENTS

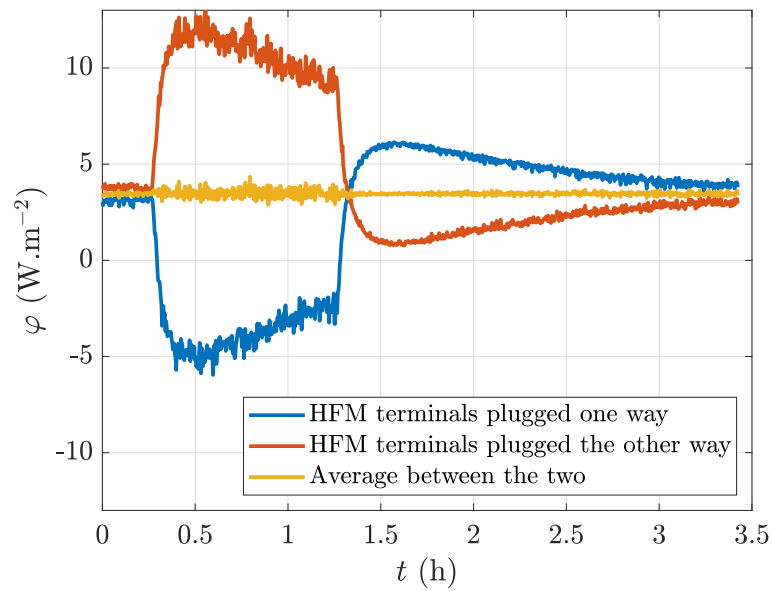
---



**Figure 3.8.:** Electrical assembly used to automatically switch the HFM terminals on the data logger inputs.

In average, the offset on the HFMs is of  $3.3 \text{ W}\cdot\text{m}^{-2}$ . This is absolutely not negligible. Indeed, this value is of the same order of magnitude as the heat flux through an insulated wall. For instance, the heat flux through a wall of thermal resistance  $4 \text{ m}^2\cdot\text{K}\cdot\text{W}^{-1}$  subject to a steady temperature gradient of  $15 \text{ K}$  is equal to  $3.75 \text{ W}\cdot\text{m}^{-2}$ . Thus, for the given data acquisition system, the present calibration is necessary for an accurate heat flux measurement on an insulated wall. The thermocouples embedded inside the HFMs were calibrated inside a regulating oven. The reference temperature was given by additional thermocouples previously calibrated.





**Figure 3.9.:** Measured heat flux during the offset-calibration procedure (sampling period: 7 s).

## 3.2. Infrared thermography

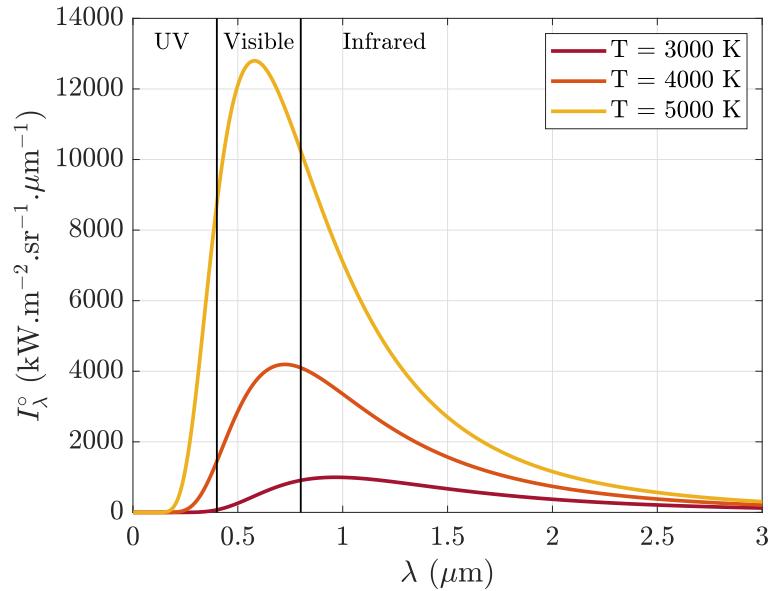
This section introduces to infrared thermography (IRT) measurements. Some basics about radiant intensities, radiative heat transfers and infrared thermography are first presented. Then, some metrological aspects about temperature and heat flux measurements with IRT are detailed.

### 3.2.1. Basics on radiant intensity

The Planck law describes the spectral density  $I_\lambda^\circ(T)$  of electromagnetic radiation emitted by a black body in thermal equilibrium at a given temperature  $T$  [163]:

$$I_\lambda^\circ(T) = \frac{2hc^2}{\lambda^5} \frac{1}{\exp\left(\frac{hc}{\lambda k_B T}\right) - 1} \quad (3.7)$$

with  $k_B = 1.38 \times 10^{-23} \text{ J.K}^{-1}$  the Boltzmann constant,  $h = 6.62 \times 10^{-34} \text{ J.s}$  the Planck constant,  $c = 3.00 \times 10^8 \text{ m.s}^{-1}$  the speed of light in vacuum and  $\lambda$  the wavelength in meter. The spectral radiance  $I_\lambda^\circ(T)$  is expressed in  $\text{W.m}^{-3}.\text{sr}^{-1}$ . In Fig 3.10, it is plotted as a function of  $\lambda$  for several temperatures.



**Figure 3.10.:** Planck law.

The wavelength  $\lambda_{\max}$  where the spectral radiance is maximum is given by the Wien law. Its simplify version gives:

$$\lambda_{\max}(T) = \frac{2898 \text{ [}\mu\text{m.K]}}{T} \quad (3.8)$$

with  $\lambda_{\max}$  in meter. It may be noted that the spectral radiance takes non-negligible values on a limited band of the electromagnetic spectrum. This useful spectral band (USB), depends on the temperature. In first approximation [164]:

$$\text{USB} = [\lambda_{\max}(T)/2 ; 8 \times \lambda_{\max}(T)] \quad (3.9)$$

The black body radiant intensity is related to its temperature by the Stefan law:

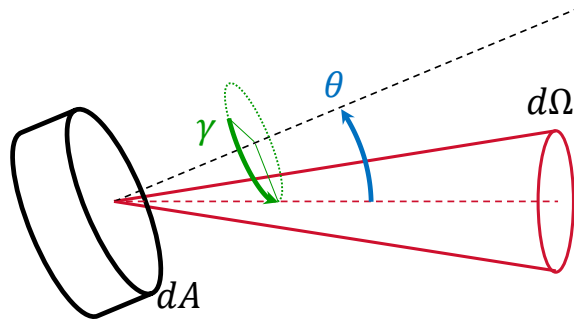
$$I^\circ(T) = \int_0^\infty I_\lambda^\circ(T) d\lambda = \frac{\sigma}{\pi} T^4 \quad (3.10)$$

with  $\sigma = 5.67 \times 10^{-8} \text{ W.m}^{-2}.\text{K}^{-4}$  the Stefan-Boltzmann constant.

## 3.2.2. Basics on radiative heat flux

### 3.2.2.1. Theory on radiative heat flux

We focus on radiative heat transfers between opaque bodies through a transparent medium. Let us consider an elementary surface of area  $dA$  exchanging radiation with another small element located inside the solid angle  $d\Omega$ . The azimuthal angle (angle between  $d\Omega$  and the normal of  $dA$ ) is noted  $\theta$  and the polar angle (quantifying the rotation around the normal) is noted  $\gamma$ . The configuration is illustrated in Fig 3.11.



**Figure 3.11.:** Illustration of elementary radiative heat flux.

The elementary spectral directional radiative heat flux is given by:

$$d\Phi_\lambda^{r'} = [I_\lambda^{e'} - I_\lambda^{a'}] dA \cos \theta d\Omega d\lambda \quad (3.11)$$

where  $I_\lambda^{e'}$  and  $I_\lambda^{a'}$  are spectral directional radiant intensities. The former is emitted by the surface whereas the later is absorbed by it. The quotation mark ' denotes

### 3.2. INFRARED THERMOGRAPHY

---

directional quantities (functions of angles  $\theta$  and  $\gamma$ ). We define the elementary radiant heat flux per surface area:

$$d\varphi_{\lambda}^{r'} = \frac{d\Phi_{\lambda}^{r'}}{dA} \quad (3.12)$$

The total heat flux per unit area  $\varphi$  is given from integration of  $d\varphi_{\lambda}^{r'}$  over the spectrum and the hemisphere:

$$\varphi^r = \int_{\lambda} \int_{\Omega} d\varphi_{\lambda}^{r'} d\Omega d\lambda \quad (3.13)$$

The absorbed intensity  $I_{\lambda}^{a'}$  is a fraction of the incident radiation  $I_{\lambda}^{i'}$ . This fraction is called the spectral directional absorptance and is noted  $\alpha'_{\lambda}$ :

$$I_{\lambda}^{a'} = \alpha'_{\lambda} I_{\lambda}^{i'} \quad (3.14)$$

Similarly, only a fraction of the black body radiation is emitted by the body. This fraction is the spectral directional emissivity  $\varepsilon'_{\lambda}$ :

$$I_{\lambda}^{e'} = \varepsilon'_{\lambda} I_{\lambda}^{\circ}(T_s) \quad (3.15)$$

with  $T_s$  the surface temperature of the body. According to the Kirchhoff law:

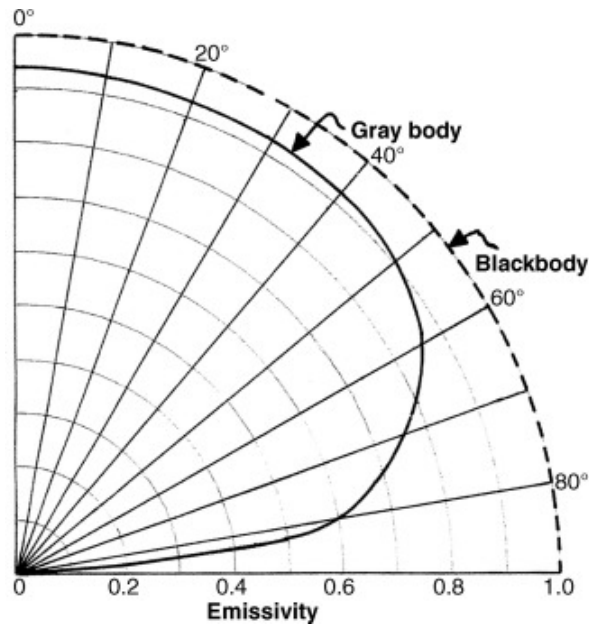
$$\alpha'_{\lambda} = \varepsilon'_{\lambda} \quad (3.16)$$

For a given material, the emissivity depends on the wavelength  $\lambda$ , the temperature  $T$ , and the direction. Simplified models are usually used, especially in the building sector:

- A black body is defined by  $\varepsilon = 1$ .
- A gray body has an emissivity that does not depend on the wavelength:  $\varepsilon'$ .
- A body with isotropic properties has an emissivity independent of the direction:  $\varepsilon_{\lambda}$ . For most materials, the emissivity is independent of the angle to the surface normal when this angle remains between  $-45^{\circ}$  and  $+45^{\circ}$  (see the example in Fig 3.12).

The body is supposed gray with isotropic properties (at least on the useful spectral band for the given temperature), and the incident radiant intensity is also supposed independent on the direction:

$$\varphi^r = \varepsilon \times \int_0^{\infty} [I_{\lambda}^{\circ}(T_s) - I_{\lambda}^i] d\lambda \times \int_{2\pi} \cos \theta d\Omega \quad (3.17)$$



**Figure 3.12.:** Example of different materials at ambient temperature, from [165].

An optimal solution to quantify the surrounding infrared radiation incident on the target surface must take into account the spatial distribution of the surrounding bodies, their temperature and their radiation properties. However, it is much simpler to find a solution in the assumption of surrounding bodies sufficiently far and randomly distributed around the target surface, in order to consider their emitted infrared radiation as uniform and isotropic. These assumptions allow defining an equivalent temperature of the surrounding, and then to estimate the infrared radiation incident on the target surface, using the Stefan–Boltzmann law [33]. This equivalent temperature is called the “Mean Radiant Temperature (MRT) and is noted  $T_{\text{env}}$ :

$$I_{\lambda}^i = I_{\lambda}^{\circ}(T_{\text{env}}) \quad (3.18)$$

Given the Stefan law (Eq 3.10) and the following result:

$$\int_{2\pi} \cos \theta d\Omega = \pi \quad (3.19)$$

it finally comes:

$$\varphi^r = \varepsilon \sigma (T_s^4 - T_{\text{env}}^4) \quad (3.20)$$

### 3.2.2.2. Radiative heat flux linearization

When the temperature difference  $T_s - T_{\text{env}}$  is small compared to  $T_s$  (typically a few Kelvin at ambient temperature), the radiative heat flux may be linearized:

$$\varphi^r = \varepsilon\sigma (T_s^4 - T_{\text{env}}^4) \quad (3.21)$$

$$= \varepsilon\sigma (T_s^2 + T_{\text{env}}^2) (T_s + T_{\text{env}}) (T_s - T_{\text{env}}) \quad (3.22)$$

$$= h^r (T_s - T_{\text{env}}) \quad (3.23)$$

with

$$h^r = \varepsilon\sigma (T_s^2 + T_{\text{env}}^2) (T_s + T_{\text{env}}) \quad (3.24)$$

$$\approx 4\varepsilon\sigma T_m^3 \quad (3.25)$$

where  $T_m$  is a mean temperature. In first approximation,  $T_m$  may be taken equal to  $(T_s + T_{\text{env}})/2$ ,  $T_s$  or  $T_{\text{env}}$ . This linearization is quite common in the building sector, given the small temperature differences involved.

For a better understanding of the impact of this simplification, Fig 3.13 plots the exact and linearized radiative heat fluxes ( $\varphi^r$  and  $\varphi_L^r$  respectively) calculated from two temperatures  $T_1$  and  $T_2$ . Temperature  $T_1$  is kept constant equal to 300 K whereas  $T_2$  varies between 300 and 400 K. As expected, the higher the temperature difference  $T_2 - T_1$ , the higher the difference between  $\varphi^r$  and  $\varphi_L^r$ . However, even for a 100 K temperature difference (which is unrealistically high in a building), the relative bias is only of 2 %. Therefore, in this thesis where temperatures differences are not smaller than a few Kelvin, radiative heat transfers may be linearized with almost not loss of accuracy.

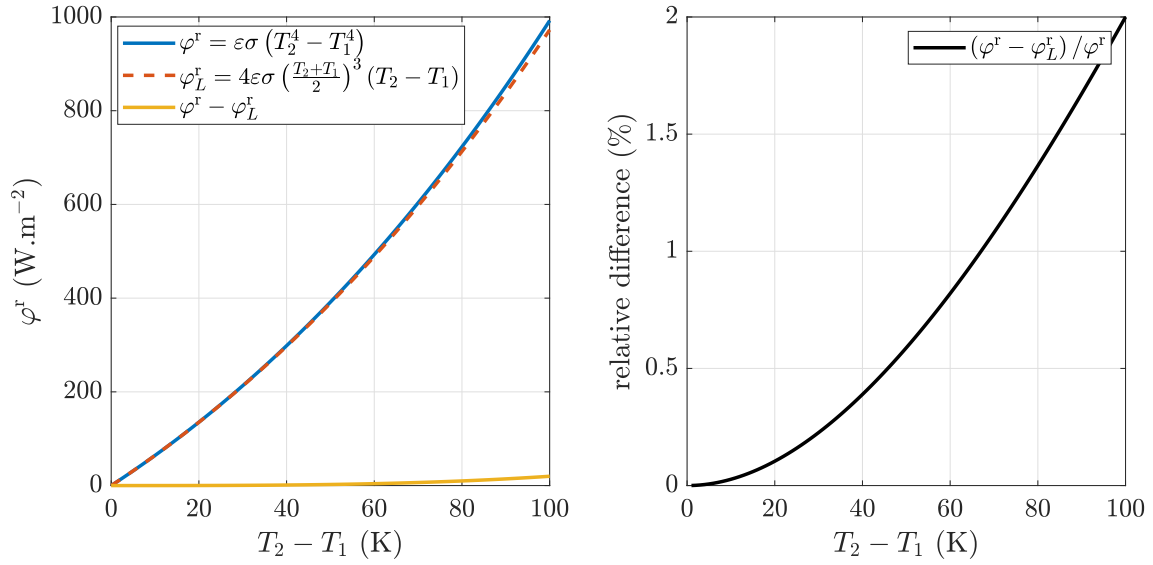
### 3.2.2.3. Total heat flux

The total heat flux  $\varphi$  on a wall is the sum of the radiative and convective heat fluxes:

$$\varphi = \varphi^r + \varphi^c \quad (3.26)$$

where

$$\varphi^c = h^c (T_s - T_{\text{air}}) \quad (3.27)$$



**Figure 3.13.:** Exact and linearized radiative heat flux as a function of the temperature difference for  $T_1 = 300$  K and  $T_2 \in [300; 400]$  K

with  $h^c$  the convective heat transfer coefficient. The total surface heat flux is therefore given by:

$$\varphi = \varepsilon\sigma (T_s^4 - T_{\text{env}}^4) + h^c (T_s - T_{\text{air}}) \quad (3.28)$$

If the radiative heat flux is linearized:

$$\varphi = h^r (T_s - T_{\text{env}}) + h^c (T_s - T_{\text{air}}) \quad (3.29)$$

It is sometimes convenient to work with the global heat transfer coefficient  $h$ :

$$h = h^r + h^c \quad (3.30)$$

We also define the operative temperature:

$$T_{\text{op}} = \frac{h^r T_{\text{env}} + h^c T_{\text{air}}}{h^r + h^c} \quad (3.31)$$

It is basically a weighted average of the air and mean radiant temperatures. Thus, without loss of generality, Eq 3.29 can be re-written as:

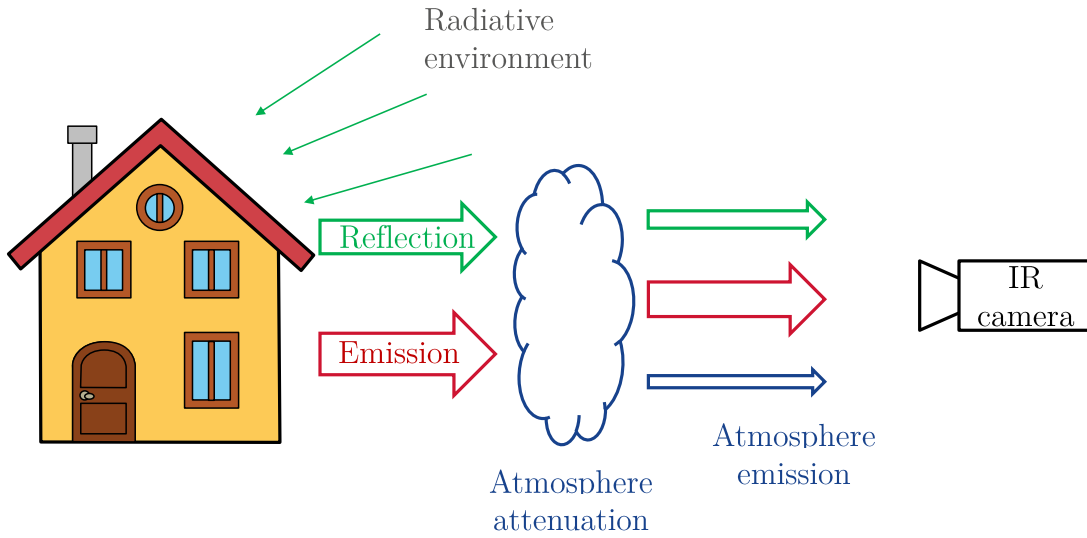
$$\varphi = h (T_s - T_{\text{op}}) \quad (3.32)$$

### 3.2.3. Thermography equation

An infrared camera measures radiant intensities. The spectral radiant intensity coming from the surface of an opaque body at temperature  $T_s$  through a non-scattering, homogenous and isothermal atmosphere at temperature  $T_{\text{atm}}$  is given by:

$$I_\lambda = \underbrace{\tau'_\lambda \varepsilon'_\lambda I_\lambda^\circ(T_s)}_{\text{emission}} + \underbrace{\tau'_\lambda \int_{\Omega} f_{r\lambda} I_\lambda^{i'} \cos(\theta') d\Omega'}_{\text{reflection}} + \underbrace{(1 - \tau'_\lambda) I_\lambda^\circ(T_{\text{atm}})}_{\text{atmosphere emission}} \quad (3.33)$$

with  $\tau'_\lambda$  the spectral atmosphere transmittance in the direction of the body,  $\varepsilon'_\lambda$  the spectral directional body surface emissivity and  $f_{r\lambda}$  the bidirectional reflectance distribution function (BRDF). Figure 3.14 illustrates the problem. The first term of this equation corresponds to the emission of the body surface. The emitted intensity is partly absorbed by the atmosphere, hence the  $\tau'_\lambda$  factor. The second term, which is noted  $\tau'_\lambda I_\lambda^{\text{re}}$ , quantifies the portion of the incident spectral radiant intensity  $I_\lambda^{i'}$  coming from the environment that is reflected on the body in the direction of the IR camera. It is also attenuated by the atmosphere. The third term is due to emission of the atmosphere.



**Figure 3.14.:** Illustration of infrared thermography.

In the general case, the reflection component cannot be analytically solved. Indeed, neither the BRDF  $f_{r\lambda}$  nor the spatial distribution of  $I_\lambda^{i'}$  are known (although it is possible to measure the BRDF). Some simplifying assumptions are therefore required. We use the MRT approximation presented in Eq 3.18 (we consider the surroundings as an isotropic medium at temperature  $T_{\text{env}}$ ):



$$I_{\lambda}^{\text{re}} = \int_{\Omega} f_{r\lambda} \cos(\theta') d\Omega' \times I_{\lambda}^i \quad (3.34)$$

$$= \rho_{\lambda}^{\Omega'} \times I_{\lambda}^{\circ}(T_{\text{env}}) \quad (3.35)$$

with  $\rho_{\lambda}^{\Omega'}$  the hemispherical directional reflectance of the body. From energy balance (Kirchhoff–Drapper law):

$$\rho_{\lambda}^{\Omega'} + \varepsilon'_{\lambda} = 1 \quad (3.36)$$

It comes:

$$I_{\lambda}^{\text{re}} = (1 - \varepsilon'_{\lambda}) I_{\lambda}^{\circ}(T_{\text{env}}) \quad (3.37)$$

In infrared thermography, the solid angle of a pixel is small and may be considered elementary. However, the spectral band  $\Delta\lambda$  of the sensor is large in order to improve the measurement signal to noise ratio (SNR). The sensor has a sensitivity  $R_{\lambda}$  that is not uniform over  $\Delta\lambda$ . It measures “effective” radiant intensities  $I_{\text{mea}}$ :

$$I_{\text{mea}} = \int_{\Delta\lambda} R_{\lambda} I_{\lambda} d\lambda \quad (3.38)$$

Combining it with equations 3.33 and 3.37 becomes:

$$I_{\text{mea}} = \int_{\Delta\lambda} \tau'_{\lambda} \varepsilon'_{\lambda} R_{\lambda} I_{\lambda}^{\circ}(T_s) d\lambda + \int_{\Delta\lambda} \tau'_{\lambda} (1 - \varepsilon'_{\lambda}) R_{\lambda} I_{\lambda}^{\circ}(T_{\text{env}}) d\lambda + \int_{\Delta\lambda} (1 - \tau'_{\lambda}) R_{\lambda} I_{\lambda}^{\circ}(T_{\text{atm}}) d\lambda \quad (3.39)$$

We now introduce the effective quantities:

$$\varepsilon = \frac{\int_{\Delta\lambda} \varepsilon'_{\lambda} R_{\lambda} I_{\lambda}^{\circ}(T) d\lambda}{\int_{\Delta\lambda} R_{\lambda} I_{\lambda}^{\circ}(T) d\lambda} \quad (3.40)$$

$$\tau = \frac{\int_{\Delta\lambda} \tau'_{\lambda} R_{\lambda} I_{\lambda}^{\circ}(T) d\lambda}{\int_{\Delta\lambda} R_{\lambda} I_{\lambda}^{\circ}(T) d\lambda} \quad (3.41)$$

$$(\varepsilon\tau) = \frac{\int_{\Delta\lambda} \varepsilon'_{\lambda} \tau'_{\lambda} R_{\lambda} I_{\lambda}^{\circ}(T) d\lambda}{\int_{\Delta\lambda} R_{\lambda} I_{\lambda}^{\circ}(T) d\lambda} \quad (3.42)$$

## 3.2. INFRARED THERMOGRAPHY

---

They are weighted averages over the spectral band  $\Delta\lambda$  where the weights are  $R_\lambda I_\lambda^\circ(T)$ . It may be noted that these effective quantities depend on the temperature. The temperature used to work them out will be noted with a subscript. From calibration of the camera:

$$\int_{\Delta\lambda} R_\lambda I_\lambda^\circ(T) d\lambda = I_\lambda^\circ(T) \quad (3.43)$$

It comes:

$$I_{\text{mea}} = (\varepsilon\tau)_s I_\lambda^\circ(T_s) + \tau_{\text{env}} I_\lambda^\circ(T_{\text{env}}) + (1 - \tau_{\text{atm}}) I_\lambda^\circ(T_{\text{atm}}) \quad (3.44)$$

Finally, building materials are usually supposed gray over  $\Delta\lambda$ , or alternatively averaged values are considered. This assumption removes correlations between  $\varepsilon$  and  $\tau$  and leads to the so-called thermography equation:

$$I_{\text{mea}} = \underbrace{\tau\varepsilon I^\circ(T_s)}_{\text{emission}} + \underbrace{\tau(1 - \varepsilon) I^\circ(T_{\text{env}})}_{\text{reflection}} + \underbrace{(1 - \tau) I^\circ(T_{\text{atm}})}_{\text{atmosphere emission}} \quad (3.45)$$

### 3.2.4. Infrared camera properties

This section presents the main technical properties of commonly used IR cameras. For more information in this topic, please refer to [166].

#### 3.2.4.1. Types of sensor

Historically, infrared cameras are sorted in two categories:

- Cameras using a unique infrared detector coupled to a mechanical scanning system to form an image of the thermal scene (IR scanning cameras).
- Cameras using an array of detectors. They are called Focal Plane Array (FPA) cameras. The thermal image is obtained from concatenation of the individual response of each elementary detector in a 2D matrix. Nowadays, this is the most frequently used type of camera.

The spectral response of a camera mainly depends on the materials used for the detector and the optics. Some detectors (such as InSb detectors) are sensitive in the wavelength domain comprised between 2 and 5  $\mu\text{m}$ . This is the so-called Band II domain, or Medium Wave InfraRed (MWIR) domain. Some other detectors are sensitive between 7 and 14  $\mu\text{m}$  which is the so-called Band III domain, or Long Wave InfraRed (LWIR) domain. This is the case of microbolometers and Quantum Well Infrared Photodetectors (QWIP) for instance. Microbolometers are thermal detectors, which means that the thermal response of each individual detector is due

to the variation of its temperature depending on the absorbed heat flux. These detectors are not cooled, but an internal system integrated to the camera allows compensating the temperature drift of the detector. QWIP detectors are quantum detectors, i.e. based on a conversion of absorbed photons in electrical carriers. These detectors have to be cooled to a low temperature (typically around the liquid nitrogen temperature, 77 K) to obtain a high SNR. In most cases, this cooling is performed by a Stirling engine.

LWIR and MWIR domains correspond to spectral bandwidths of high transparency of the atmosphere as seen in Fig 3.15. According to the Wien's law, LWIR detectors are well adapted to temperature measurements around ambient temperature (300 K), whereas MWIR detectors are better suited for higher temperature applications (see Fig 3.16). However, due to the higher sensitivity of MWIR detectors, some of them can be used also for ambient temperature measurements. Other wavelength domains can also be used for higher temperature applications: Short Wave InfraRed (SWIR) or visible domains.

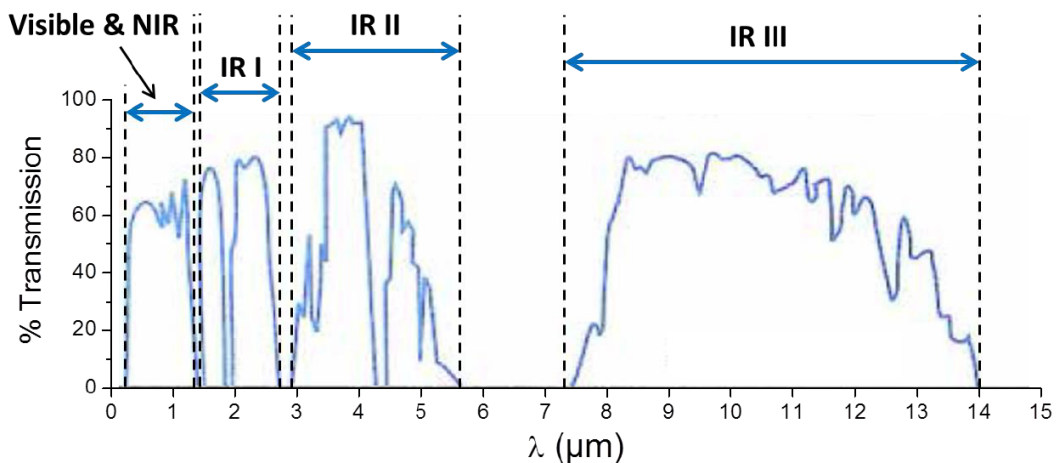


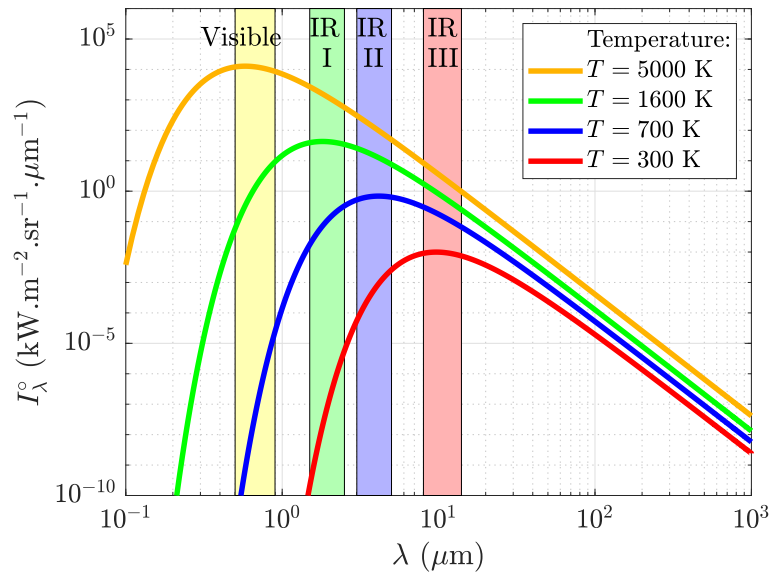
Figure 3.15.: Transmittance of the atmosphere, from [166].

### 3.2.4.2. Camera calibration

The calibration of the camera is performed by taking pictures of a black body at several temperatures. The commonly used relationship between the measured voltage  $V$  and the temperature  $T$  is derived from the Planck law:

$$T = \frac{B}{\ln\left(\frac{R}{V} + F\right)} \quad (3.46)$$

with  $B$ ,  $F$  and  $R$  three parameters to be determined from identification with black body measurements. This type of curve is valid for micro-bolometer cameras. Cooled cameras rather work with many calibration curves taking into account the



**Figure 3.16.:** Planck law and spectral bandwidths of infrared cameras.

integration time and the sensor internal temperature. An example of such calibration curves is presented in Fig 3.17 for a Jade III camera (from Rémy *et al.* [167]). This approach simplifies the use of the infrared camera but makes the calibration by the user more complex. The calibration process is generally performed by the camera manufacturer.

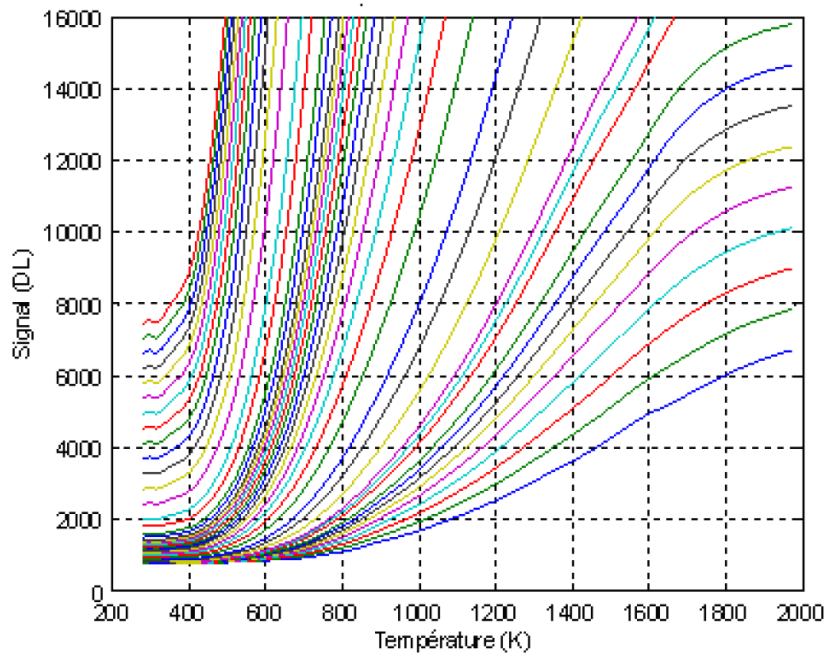
#### 3.2.4.3. Non-uniformity correction (NUC)

When the camera looks at a surface of uniform temperature, the pixels response is not uniform all over the sensor matrix. To limit the effects of this dispersion, a Non-Uniformity Correction (NUC) step is required. It consists in disposing a black body of uniform temperature in front of the camera. The software then makes the appropriate corrections for all the pixels to deliver the same signal. The remaining dispersion between pixels after the NUC is close to white noise. It may be noted that the NUC adds correlation between pixels.

To illustrate this, Fig 3.18 shows two infrared pictures of the same wall in steady-state taken one minute away. The left and right hand side pictures were recorder before and after the NUC respectively. It is clear that the Non-Uniformity Correction process removed the non-physical dispersion between pixels.

#### 3.2.4.4. Noise Equivalent Temperature Difference (NETD)

As seen above, non-uniformity correction enables to reduce differences between pixel responses. Nevertheless, some differences remain even when a uniform response is expected. These differences come from the camera electronics and may be treated as random noise. An example of the response histogram of the pixels of an IR camera is presented in Fig 3.19. The standard deviation of this distribution (plotted here



**Figure 3.17.:** Example of calibration curves for a Jade III camera with a 4  $\mu\text{m}$  monochromatic filter, from Rémy *et al.* [167].

in digital levels), can be converted in a temperature difference called the Noise Equivalent Temperature Difference (NETD). This parameter represents the spacial noise in a thermal image. Thus, a temperature difference lower than the NETD cannot be detected. The value of the NETD depends on the optic and detector used. The lowest NETD values are generally obtained with cameras equipped with cooled IR sensors.

### 3.2.4.5. Instantaneous Field of View (IFOV)

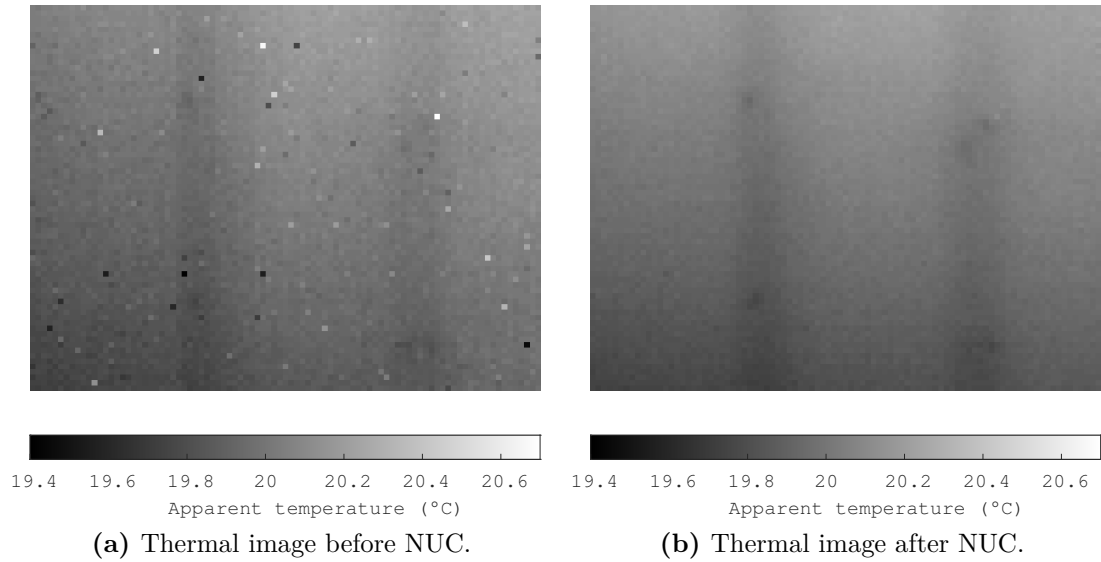
The Field Of View (FOV) of an infrared camera represents the Horizontal and Vertical angles, namely HFOV and VFOV respectively, which can be viewed through the IR lens used. The Instantaneous Field Of View (IFOV) represents the view angle corresponding to only one pixel. The IFOV is generally expressed in milliradians (mrad), and allows computing the size  $d$  of the smallest element that can be seen in a thermal scene, according to the simple following relationship:

$$d [\text{mm}] = \text{IFOV} [\text{mrad}] \times D [\text{m}] \quad (3.47)$$

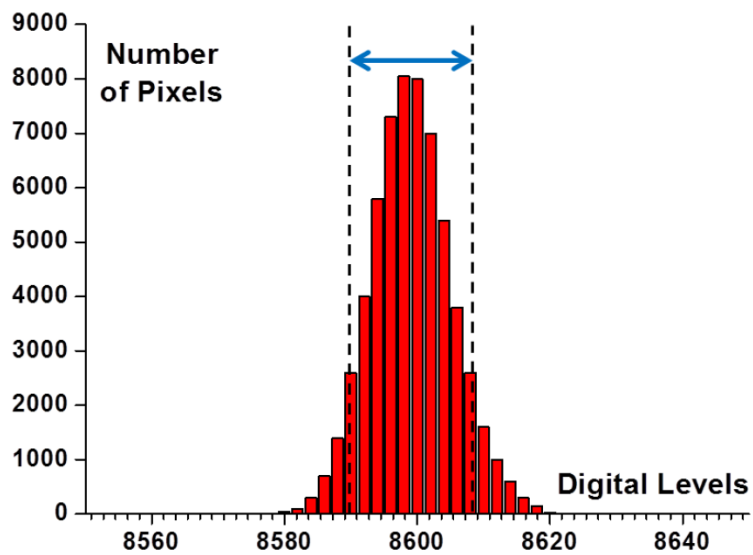
with  $D$  the distance between the thermal scene and the lens of the IR camera (see Fig 3.20).

### 3.2. INFRARED THERMOGRAPHY

---



**Figure 3.18.:** Impact of Non-Uniformity Correction (NUC) on recorded thermal images.



**Figure 3.19.:** Example of camera NETD computation from response histogram of pixels, from [166].

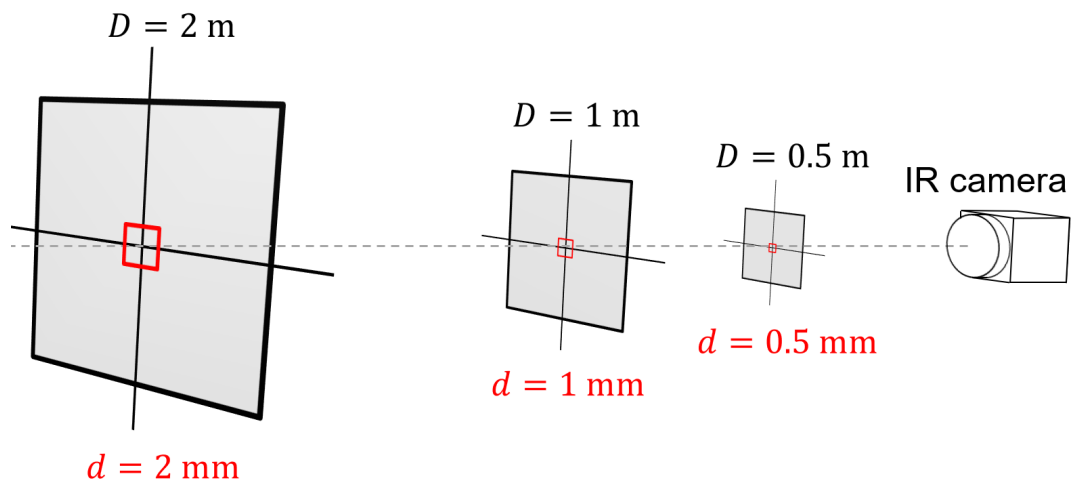


Figure 3.20.: Illustration of FOV and IFOV of a camera (IFOV = 1 mrad).

### 3.2.5. Temperature measurement with IRT

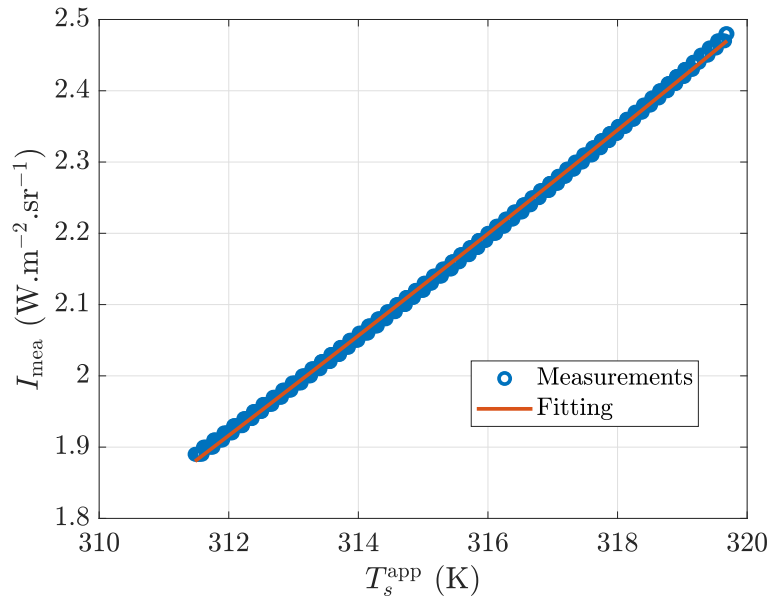
This section describes how IRT might be used to measure surface temperatures. Two different configurations are analyzed: the measurement of an absolute temperature and the measurement of a temperature difference between two objects of the same thermal image.

#### 3.2.5.1. Measurement of absolute temperatures

Even though the IR camera measures radiative intensity, the later is converted in a temperature: the apparent temperature (thanks to the calibration curve). The apparent temperature  $T_s^{\text{app}}$  of the observed surface is by definition the temperature of a black body which would emit the same radiant intensity as the one received by the camera:

$$I_{\text{mea}} = I^\circ(T_s^{\text{app}}) \quad (3.48)$$

The radiant intensity measured by the camera is considered to be proportional to  $T^4$  according to the Stefan-Boltzmann law (Eq 3.10) [168]. Figure 3.21 shows the relationship between the radiant intensity and the apparent temperature (calibration curve) provided by data extracted from a thermal image for an experience performed with a highly emissive sample and with  $\theta = 0^\circ$ , that is to say for the most important radiant intensity variations. One can observe that the chosen approximation is valid.



**Figure 3.21.:** Measured radiative intensity as a function of apparent temperature and fit with a power-four function.



From the fit, it comes from the following relationship:

$$I_{\text{mea}} = 5.71 \times 10^{-10} \times T_s^{\text{app},4} - 3.50 \quad (3.49)$$

Thus, it comes:

$$T_s^{\text{app},4} = \left[ \tau \varepsilon T_s^4 + \tau (1 - \varepsilon) T_{\text{env}}^4 + (1 - \tau) T_{\text{atm}}^4 \right] \quad (3.50)$$

hence

$$T_s = \left( \frac{T_s^{\text{app},4} - \tau (1 - \varepsilon) T_{\text{env}}^4 - (1 - \tau) T_{\text{atm}}^4}{\varepsilon \tau} \right)^{\frac{1}{4}} \quad (3.51)$$

This equation may be simplified if the atmosphere is supposed transparent ( $\tau = 1$ ) which is the case if the distance between the object and the camera does not exceed a few meters):

$$T_s = \left( \frac{T_s^{\text{app},4} - (1 - \varepsilon) T_{\text{env}}^4}{\varepsilon} \right)^{\frac{1}{4}} \quad (3.52)$$

The mean radiant temperature  $T_{\text{env}}$  is usually measured with a diffuse infrared mirror [169, 33]. If the latter is not perfect (its reflectance  $\rho$  is below unity), a correction is needed to estimate  $T_{\text{env}}$  from the mirror true temperature  $T_{\text{mirror}}$ :

$$T_{\text{env}} = \left( \frac{1}{\rho} T_{\text{mirror}}^{\text{app},4} + \left( 1 - \frac{1}{\rho} \right) T_{\text{mirror}}^4 \right)^{\frac{1}{4}} \quad (3.53)$$

It comes:

$$T_s = \left( \frac{1}{\varepsilon} T_s^{\text{app},4} + \left( 1 - \frac{1}{\varepsilon} \right) \left[ \frac{1}{\rho} T_{\text{mirror}}^{\text{app},4} + \left( 1 - \frac{1}{\rho} \right) T_{\text{mirror}}^4 \right] \right)^{\frac{1}{4}} \quad (3.54)$$

Consequently, the measurement of temperatures with IRT requires the measurement of many quantities:  $T_s^{\text{app}}$ ,  $T_{\text{mirror}}^{\text{app}}$ ,  $\varepsilon$ ,  $\rho$ , and  $T_{\text{mirror}}$ . This generates significant uncertainties (between 1 and 2 K [33]) which makes IRT unsuitable for accurate temperature measurements in most situations.

## 3.2. INFRARED THERMOGRAPHY

---

In addition, if the mirror is supposed perfect ( $\rho = 1$ ):

$$T_s = \left( \frac{1}{\varepsilon} T_s^{\text{app},4} + \left( 1 - \frac{1}{\varepsilon} \right) T_{\text{env}}^4 \right)^{\frac{1}{4}} \quad (3.55)$$

This simplification may only be made if the  $T_{\text{env}}$  and  $T_s^{\text{app}}$  are close. Indeed, because temperature are to the power four, the measurement may be significantly biased if the environment is notably hotter or cooler than the surface, even if  $\rho$  is very close to unity.

In addition, even with this simplified formulation, the accurate measurement of  $T_s$  with IRT requires  $\varepsilon$  and  $T_{\text{env}}$ .

### 3.2.5.2. Measurement of temperature differences

Despite infrared thermography not being very much adapted to absolute temperature measurements, it is more suitable for the measurement of temperature differences. Let us consider two objects referred as “1” and “2” located in the camera field of view. The radiative heat flux difference  $\varphi_1^r - \varphi_2^r$  may be derived from true temperatures with Eq 3.20 or from apparent temperatures with Eq 3.63 (see next section). By combining these two formulations, it comes:

$$\varphi_1^r - \varphi_2^r = \varepsilon \sigma (T_1^4 - T_2^4) = \sigma (T_1^{\text{app},4} - T_2^{\text{app},4}) \quad (3.56)$$

hence:

$$4\varepsilon \sigma T_m^3 (T_1 - T_2) = 4\sigma T_m^{\text{app},3} (T_1^{\text{app}} - T_2^{\text{app}}) \quad (3.57)$$

with  $T_m^3 = (T_1^2 + T_2^2)(T_1 + T_2)$  and  $T_m^{\text{app},3} = (T_1^{\text{app},2} + T_2^{\text{app},2})(T_1^{\text{app}} + T_2^{\text{app}})$ . Therefore:

$$T_1 - T_2 = \frac{T_m^{\text{app},3}}{T_m^3} \frac{T_1^{\text{app}} - T_2^{\text{app}}}{\varepsilon} \quad (3.58)$$

If temperature differences are small, the ratio  $T_m^{\text{app},3}/T_m^3$  is very close to unity:

$$T_1 - T_2 \approx \frac{T_1^{\text{app}} - T_2^{\text{app}}}{\varepsilon} \quad (3.59)$$

Therefore, when temperature contrasts are small, the true temperature difference is directly derived from the apparent temperature difference and the surface emissivity.

The MRT  $T_{\text{env}}$  is not required. Thus, the measurement uncertainties are much smaller than for absolute temperature measurements. In addition, most building materials have a high emissivity in the infrared spectrum (around 0.95) so the error made on the temperature difference due to incorrect knowledge of  $\varepsilon$  is small.

### 3.2.6. Heat flux measurement with IRT

The measurement of the total heat flux on a surface with infrared thermography is not straightforward. This section shows how apparent temperatures may be used advantageously instead of true temperatures to reduce measurement uncertainties.

#### 3.2.6.1. Method

The common approach with IRT consists in first measuring the surface temperature  $T_s$  (using either Eq 3.54 or 3.55) and then using this value to work out the heat flux with Eq 3.28. Yet, as detailed above, an infrared camera does not directly measure temperatures, but radiative intensities. These intensities may be easily converted to radiative heat fluxes without knowledge of either  $\varepsilon$  nor  $T_s$ . In other words, the classical approach performs an unnecessary return trip from radiative heat flux to temperature (with  $\varepsilon$  among others) and then back to radiative heat flux (with  $\varepsilon$  again).

A more sensible approach consists in deriving  $\varphi^r$  directly from radiative intensities (expressed in apparent temperatures). Indeed, Eq 3.50 with  $\tau = 1$  gives:

$$\frac{\sigma}{\pi} T_s^{\text{app},4} = \frac{\sigma}{\pi} [\varepsilon T_s^4 + (1 - \varepsilon) T_{\text{env}}^4] \quad (3.60)$$

$$\sigma T_s^{\text{app},4} = \varepsilon \sigma (T_s^4 - T_{\text{env}}^4) + \sigma T_{\text{env}}^4 \quad (3.61)$$

$$= \varphi^r + \sigma T_{\text{env}}^4 \quad (3.62)$$

Hence:

$$\varphi^r = \sigma (T_s^{\text{app},4} - T_{\text{env}}^4) \quad (3.63)$$

The total heat flux becomes:

$$\varphi = \sigma (T_s^{\text{app},4} - T_{\text{env}}^4) + h^c (T_s - T_{\text{air}}) \quad (3.64)$$

The surface emissivity is therefore not required to measure  $\varphi^r$  with IRT when the apparent temperature is directly used. This reduces the measurement uncertainties. The convective term however remains unchanged and still requires quantification of the true temperature  $T_s$ .

### 3.2.6.2. Numerical application

To quantitatively compare the two approaches, the measurement uncertainties are calculated on an example. The design values and uncertainties of  $T_s^{\text{app}}$ ,  $T_{\text{env}}$ ,  $T_{\text{air}}$ ,  $\varepsilon$  and  $h^c$  chosen for this example are summarized in Tab 3.3. The atmosphere is supposed transparent and the mirror is supposed perfect.

**Table 3.3.:** Design values and uncertainties of input variables.

Variable	Unit	Design value
$T_s^{\text{app}}$	K	$305.00 \pm 0.02$
$T_{\text{env}}$	K	$300.00 \pm 0.02$
$T_{\text{air}}$	K	$300.00 \pm 0.30$
$\varepsilon$	-	$0.95 \pm 0.05$
$h^c$	$\text{W.m}^{-2}.\text{K}^{-1}$	$2.00 \pm 0.20$

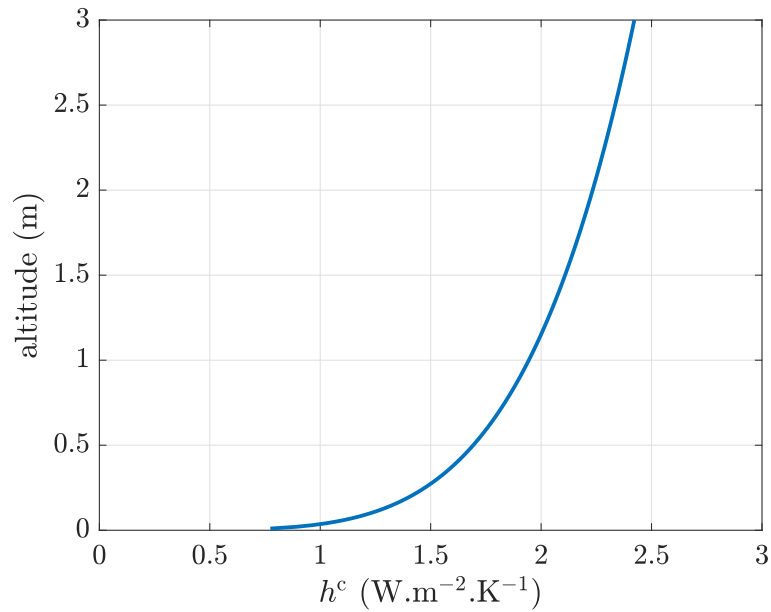
The measurement uncertainty of the apparent temperatures is set to the infrared camera NETD (equals to 0.02 K for the cooled camera used). The air temperature is supposed measured with a thermocouple, hence its 0.3 K measurement uncertainty. The emissivity is seldomly measured with a high accuracy on the field. Therefore, its uncertainty is set to 0.05. Most building materials have an emissivity includes in the range  $0.95 \pm 0.05$ .

The convective heat transfer coefficient is estimated using the Eckert and Jackson empirical correlation (natural convection on a vertical plate) [170]:

$$Nu_x = 0.0295 \frac{Pr^{1/15}}{(1 + 0.494Pr^{2/3})^{2/5}} Ra_x^{2/5} \quad (3.65)$$

with  $Nu_x = \frac{h^c \cdot x}{k}$ ,  $Pr = \frac{\nu}{a}$ ,  $Ra = \frac{g \cdot \beta \cdot \Delta T \cdot x^3}{\nu^2} Pr$ , respectively the Nusselt, The Prandtl and the Rayleigh numbers. Length  $x$  the characteristic dimension of the problem (here the altitude),  $\nu$ ,  $a$  and  $k$  are the fluid (air here) cinematic viscosity, thermal diffusivity and thermal conductivity respectively,  $g$  the gravity acceleration,  $\beta$  the expansion coefficient of the fluid ( $\beta = 1/T_{\text{gas}}$  for an ideal gas) and  $\Delta T$  the difference between the wall and the fluid temperatures. The convective heat transfer coefficient calculated with this empirical correlation is plotted as a function of the altitude  $x$  in Fig 3.22. The averaged value over a 3 m high wall is equal to  $2.0 \text{ W.m}^{-2}.\text{K}^{-1}$ . For the given example, the radiative heat transfer coefficient (see Eq 3.25) is estimated to  $h^r = 5.6 \text{ W.m}^{-2}.\text{K}^{-1}$  which leads to an overall coefficient  $h = h^r + h^c = 7.6 \text{ W.m}^{-2}.\text{K}^{-1}$ . This result is in good agreement with the standard value of the global heat transfer coefficient  $h = 7.69 \text{ W.m}^{-2}.\text{K}^{-1}$  commonly used in buildings (see ISO 14683 [18] and ISO 6946 [99] for instance). The uncertainty on the  $h^c$  is supposed equal to 10% ( $0.2 \text{ W.m}^{-2}.\text{K}^{-1}$ ).

From the values given in Tab 3.3, the surface temperature  $T_s$  as well as the various heat fluxes are calculated and their uncertainties are propagated. Let  $Y$  be a function



**Figure 3.22.:** Convective heat transfer coefficient  $h^c$  calculated with Eckert and Jackson empirical correlation [170] as a function of the altitude.

of  $n$  variables named  $x_1, x_2, \dots, x_n$ . The uncertainty on  $Y$  may be derived from the uncertainty on each variable  $x_i$  [158]:

$$u(Y) = \sqrt{\sum_{i=1}^n \left( \frac{\partial Y}{\partial x_i} \times u(x_i) \right)^2} \quad (3.66)$$

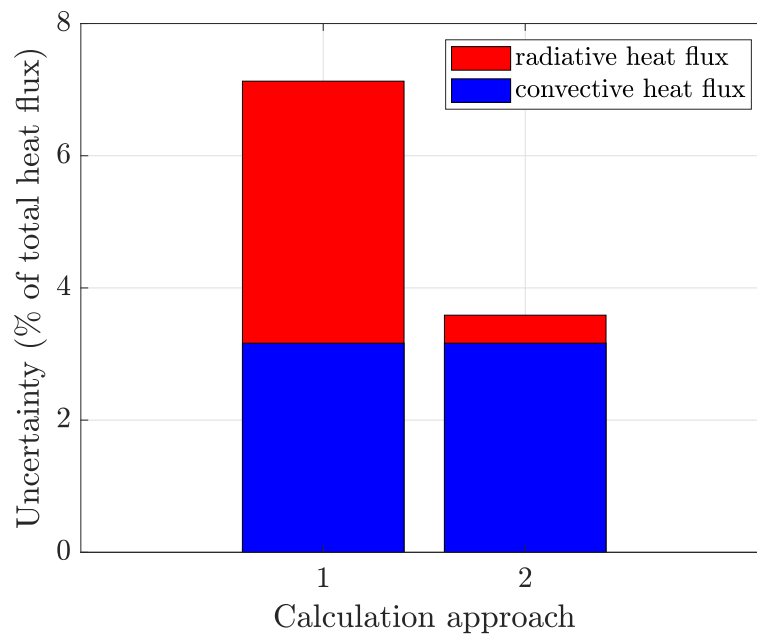
The values and uncertainties of the calculated temperature and heat fluxes are gathered in Tab 3.4.

**Table 3.4.:** Calculated quantities and propagated uncertainties.

Variable	Unit	Calculated value
$T_s$ (Eq 3.55)	K	$305.25 \pm 0.27$
$\varphi^c$ (Eq 3.27)	$\text{W.m}^{-2}$	$10.51 \pm 1.33$
$\varphi^r$ (from $T_s$ : Eq 3.20)	$\text{W.m}^{-2}$	$31.39 \pm 1.66$
$\varphi^r$ (from $T_s^{\text{app}}$ : Eq 3.63)	$\text{W.m}^{-2}$	$31.39 \pm 0.18$

Figure 3.23 plots the calculated heat flux uncertainties. The values are given as percentages of the total heat flux  $\varphi^r + \varphi^c$ .

As expected, the measurement uncertainty on  $\varphi^r$  is significantly reduced (divided by 9) by working directly with apparent temperatures delivered by the camera instead of calculating the true temperature. The uncertainty on  $\varphi^c$  however still requires  $T_s$  and cannot be reduced. In the end, by changing the method to estimate the heat flux, the measurement uncertainty is halved. Most of the remaining uncertainty comes from  $\varphi^c$ .



**Figure 3.23.:** Uncertainties on the measured surface heat flux: Approach 1= true temperature-based. Approach 2= apparent temperature-based.

### 3.2.7. Geometrical corrections

The images recorded by an IR camera sometimes suffer from geometrical distortions. For the scale to be uniform across the images, these distortions were corrected in two steps: fisheye correction and camera angle correction. The effects of vignetting are not treated here. In optics, vignetting is a reduction of an image's brightness or saturation toward the periphery compared to the image center. This may cause an underestimation of the radiant intensity measured on side pixels [14]. The vignetting effects may be corrected by measuring the camera modulation transfer function pixel per pixel [171]. This correction was not deemed necessary for the camera used given that no vignetting effect was noticed on the thermal images.

#### 3.2.7.1. Fisheye correction

The wide-angle lenses of the camera slightly distorts the lines of perspective in the image. This so-called “fisheye” distortion was corrected using the model proposed by Scaramuzza *et al.* [172] already implemented in MATLAB<sup>®</sup> (computer vision toolbox). Figure 3.24 shows the example of a thermal image before and after Fisheye correction. It may be seen that the straight elements on the borders of the image were initially curved. After correction, they appear straight on the image.

#### 3.2.7.2. Camera angle correction

When the camera looks at a wall with an angle, the recorded image is distorted. Let  $\alpha$  be this angle between the normal to the wall and the camera and  $\theta$  the camera field of view, as illustrated in Fig 3.25.

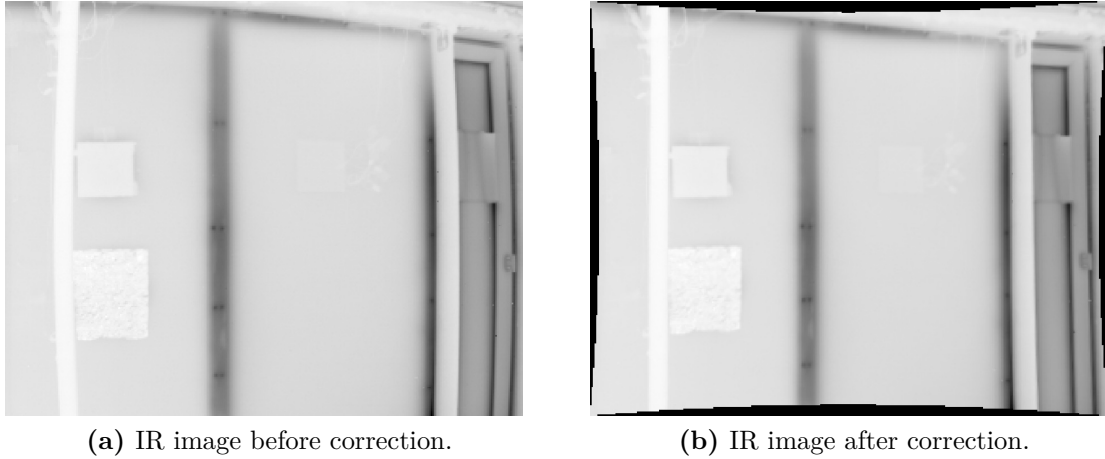


Figure 3.24.: Example of fisheye correction.

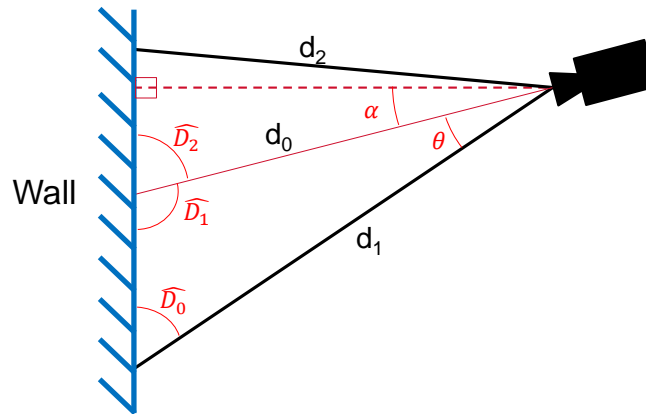


Figure 3.25.: Scheme of the situation.

From the sine theorem:

$$\frac{\sin(\widehat{D}_1)}{d_1} = \frac{\sin(\widehat{D}_0)}{d_0} \quad (3.67)$$

It comes:

$$\frac{d_1}{d_0} = \frac{\sin(\widehat{D}_1)}{\sin(\widehat{D}_0)} = \frac{\sin\left(\frac{\pi}{2} + \alpha\right)}{\sin\left(\pi - \left(\frac{\pi}{2} + \alpha\right) - \theta\right)} = \frac{\cos(\alpha)}{\cos(\alpha + \theta)} \quad (3.68)$$

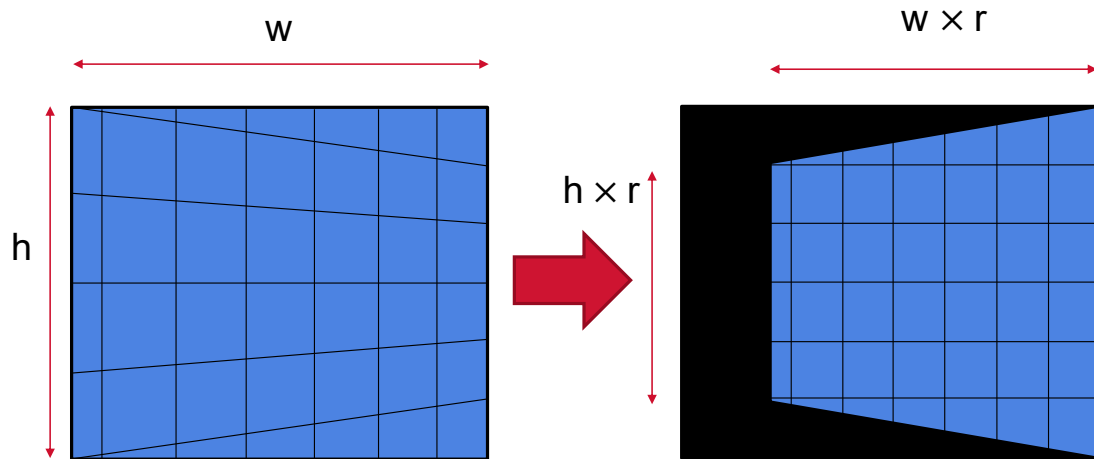
Similarly:

$$\frac{d_2}{d_0} = \frac{\sin\left(\frac{\pi}{2} - \alpha\right)}{\sin\left(\pi - \left(\frac{\pi}{2} - \alpha\right) - \theta\right)} = \frac{\cos(\alpha)}{\cos(\alpha - \theta)} \quad (3.69)$$

We introduce the distance ratio  $r$  as follows:

$$r = \frac{d_2}{d_1} = \frac{\cos(\alpha + \theta)}{\cos(\alpha - \theta)} < 1$$

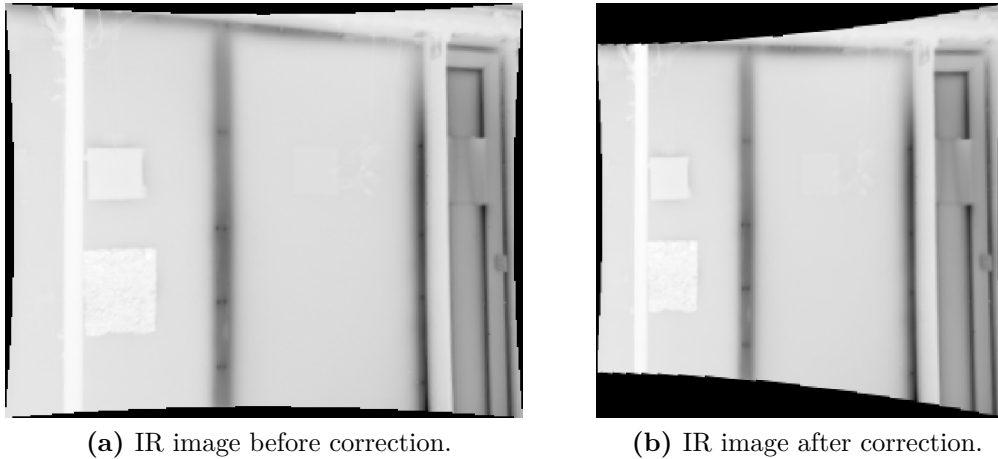
This ratio is also equal to the ratio of the length of the image before and after correction, as detailed in Fig 3.26.



**Figure 3.26.:** Illustration of camera angle correction.

Figure 3.27 presents an infrared image before and after correction of the angle. On this example:  $\alpha = 15^\circ$  and  $\theta = 22.5^\circ$  so  $r = 0.8$ . It is important to point out that the angle to the wall normal should be kept below  $45^\circ$ , so that the directional emissivity does not vary significantly.





**Figure 3.27.:** Example of camera angle correction.

### 3.2.8. IR Camera used

The IR camera used in this thesis is the reference SC7000 from FLIR<sup>®</sup> (see Fig 3.28). It has a cooled matrix sensor of  $320 \times 256$  pixels working in the  $7.7 - 9.2 \mu\text{m}$  spectral band and has a 20 mK NETD. A wide angle lens (12 mm F2,  $44^\circ \times 36^\circ$ ) was used. Images were recorded typically every 15 s, each frame being an average of 200 frames taken within 2 s.



**Figure 3.28.:** Photography of the infrared camera (SC7000 from FLIR<sup>®</sup>).

The spectral band of the sensor is rather narrow. The advantage is that the emissivity of most common building materials is rather constant on this interval. As an example, Fig 3.29 plots the spectral emissivity of a few materials, measured with an IR spectrometer. Inside the  $7.7 - 9.2 \mu\text{m}$  band, the curves are rather flat. More information about these measurements can be found in Appendix A.

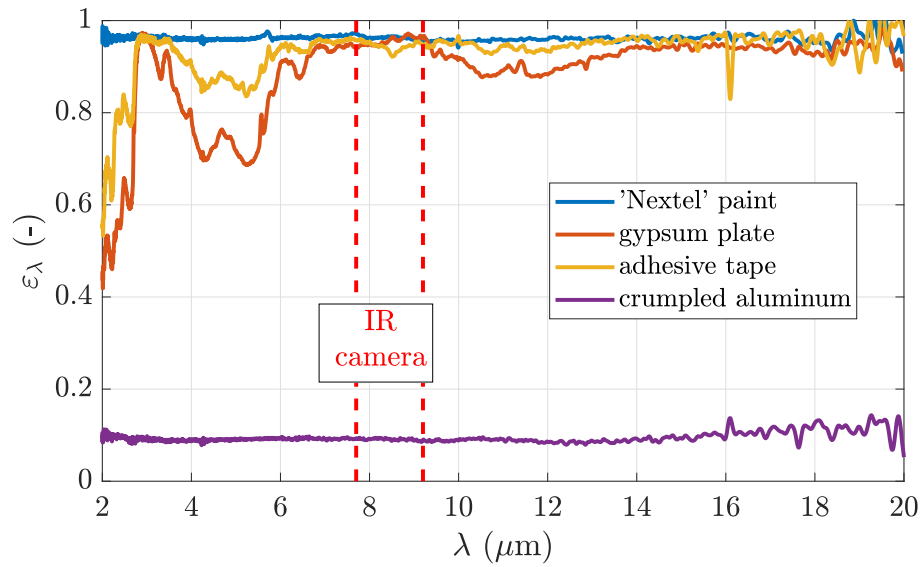


Figure 3.29.: Example of measured spectral emissivities.

### 3.3. Conclusion

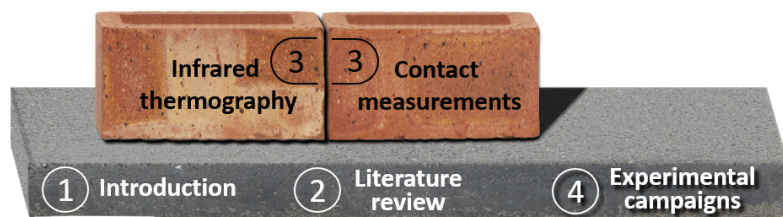
On the one hand, this section presented three contact measurement methods as well as their calibration procedures. They involve the measurement of an absolute temperature  $T$  with a one-junction thermocouple, a temperature difference with a two-junction thermocouple, and a heat flux density with a heat flux meter. The magnitude of the measurement uncertainties (for the sensors used) in this thesis are summarized in Tab 3.5. The given thermocouple measurement uncertainty implies the use of a platinum sensor as reference sensor. In addition, the uncertainty for the HFM does not include the correction of the bias introduced by the acquisition system.

**Table 3.5.:** Summary of expected measurement uncertainties for the given sensors.

Quantity	Sensor	Uncertainty
$T$	Thermocouple (one-junction configuration)	0.3 K
$\Delta T$	Thermocouple (two-junction configuration)	0.03 K
$\varphi$	Heat flux meter	3 %

On the other hand, many aspects of infrared thermography were presented. The infrared camera measures radiant intensities and converts them into apparent temperatures thanks to one or many calibration curves. Basically, this is a very powerful tool for the qualitative visualization of an object's surface temperature. However, from a metrological point of view, the measurement of an absolute true temperature is rather complex and suffers from high uncertainties. Indeed, many quantities have to be measured to correct for reflection on the object as well as attenuation and emission of the atmosphere. Mainly, the surface temperature of the surroundings and the object emissivity have to be known. Nevertheless, the measurement of a temperature difference between two objects of the same thermal image is much more accurate because only the value of the emissivity is required. In addition, given that most building materials are highly emissive, the error made on the measured temperature difference due to poor knowledge of the emissivity is rather small.

## 4. Presentation of experimental campaigns



**Figure 4.1.:** Illustration of thesis plan.

This chapter introduces the four experimental campaigns undertaken during this thesis. The results obtained on these campaigns will be presented in the following chapters.

Section 4.1 proposes an overview of the setups in order to present their main features and purpose. Sections 4.2 to 4.5 present in details of each experimental campaign. Finally, a conclusion is drawn in section 4.6.

## Nomenclature

### Acronyms

HFM	Heat Flux Meter
SGR	Saint-Gobain Research Paris
TB	Thermal Bridge

### Greek Symbols

$\omega$	pulsation	$\text{rad.s}^{-1}$
----------	-----------	---------------------

### Roman Symbols

$e$	thickness	m
$h$	heat transfer coefficient	$\text{W.m}^{-2}.\text{K}^{-1}$
$k$	thermal conductivity	$\text{W.m}^{-1}.\text{K}^{-1}$
$R$	thermal resistance	$\text{m}^2.\text{K.W}^{-1}$
$T$	temperature	K

### Subscripts

e	external
i	internal
in	internal interface
s	surface

## 4.1. Overview

Some experimental campaigns are based on a wall built in laboratory whereas others deal with *in situ* measurements. Because some setups are used in several chapters of this manuscript, they are all presented in this section. Their main purpose are summarized in Tab 4.1. The setups are named after their location.

**Table 4.1.:** Overview of the experimental campaigns.

Name	Wall type	Environment	Objective
CERTES 1	lab scale	Laboratory	Validate steady-state thermal bridge characterization methodologies
CERTES 2	lab scale	Laboratory	Test $h$ -coefficient measurement methods and validate heat flux extrapolation technique
CEREMA	full scale	Climate Chamber	Validate active characterization methodologies (homogeneous wall and thermal bridge)
SGR	full scale	Field	Perform <i>in situ</i> measurements

Basically, the use of these setups was sequential. The CERTES 1 setup was built to understand the problem better and to identify the main difficulties of *in situ* thermal bridge characterization. A method for the steady-state measurement of a thermal bridge transmission coefficient was successfully validated with this experimental wall. For the application of active methods, this setup was useful to identify one main hurdle: the measurement of a heat flux on a thermal bridge.

The second experimental campaign was conducted in order to break through this barrier. It was found that the heat transfer coefficient was needed. Therefore, the main goal of this second setup was to test several methods to measure this coefficient *in situ*. Then, the setup was used to validate the extrapolation process that enables to measure the heat flux field over a wall surface (thanks to the heat transfer coefficient, among other).

Based on the knowledge obtained with the first two setups, active methods for the characterization of a wall (either homogeneous or not) were designed. The CEREMA experimental campaign was carried out in order to validate these methods in a controlled environment and to assess their robustness.

Finally, the SGR (for Saint-Gobain Research Paris) test cell was used to test the active methods *in situ* on lightweight walls.

As presented in Tab 4.2, some chapters present results obtained on one or several setups.

**Table 4.2.:** Summary of chapters in which each experimental campaign is used.

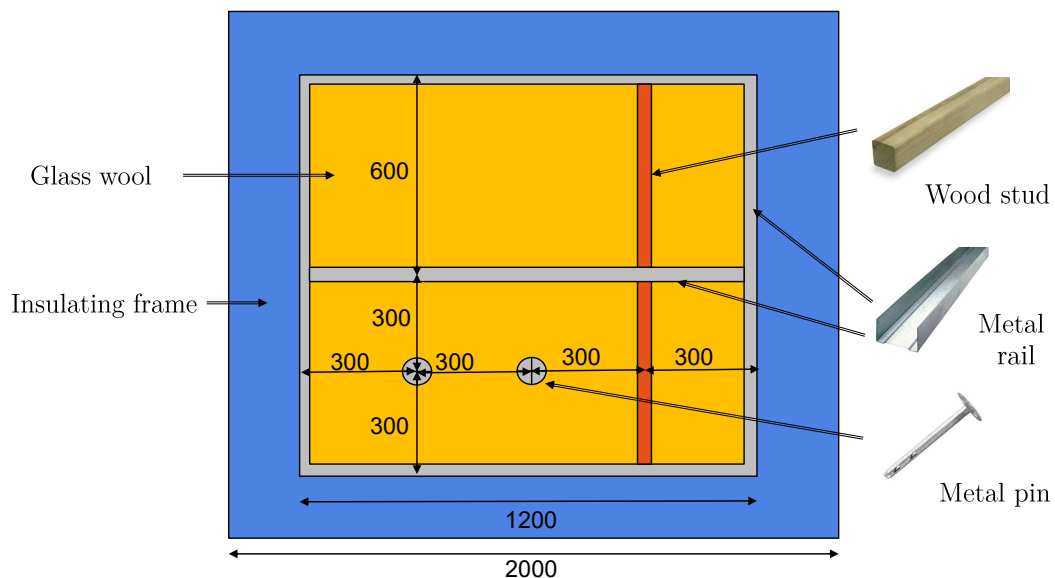
Setup	Chapter			
	5	6	8	9
CERTES 1	x	✓	x	x
CERTES 2	✓	x	x	x
CEREMA	x	✓	✓	✓
SGR	x	✓	✓	✓

## 4.2. CERTES 1 setup

### 4.2.1. Presentation

In order to test the thermal bridge characterization methodology, a  $1.2 \times 1.2 \text{ m}^2$  experimental wall was built in laboratory. As shown in Fig 4.3, it has three layers. From the inside to the outside, they are made out of gypsum, glass wool and extruded polystyrene. A flat heating resistance from Captec<sup>®</sup> (see Fig 4.4) is placed on the rear side. It is used to generate a temperature gradient inside the setup. The wall global thermal resistance is  $2.9 \text{ m}^2 \cdot \text{K} \cdot \text{W}^{-1}$  (between the internal surface and the heating resistance). Within the glass wool layer, more conductive materials are inserted to create thermal bridges: a metal rail, a wood stud and two metal pins. These materials are commonly used in internal insulation systems. Figure 4.5 shows a picture of the setup without the gypsum layer. Several thermocouples and heat flux meters are positioned inside the setup. Finally, the assembly is placed inside the polystyrene frame shown in Fig 4.6 to minimize lateral and back heat losses. Numerical simulations of the whole setup were performed on COMSOL for the design of the setup. The dimensions of the insulating frame were set such that two-thirds of the heat generated by the heating resistance cross the setup. The remaining third diffuses through the rear and lateral sides with approximately equal proportions (one sixth each).

The front face is observed with an infrared camera. A thermal image of the setup taken in steady-state is displayed in Fig 4.7.



**Figure 4.2.:** CERTES 1: Front view of the setup without the gypsum board (dimensions in mm).



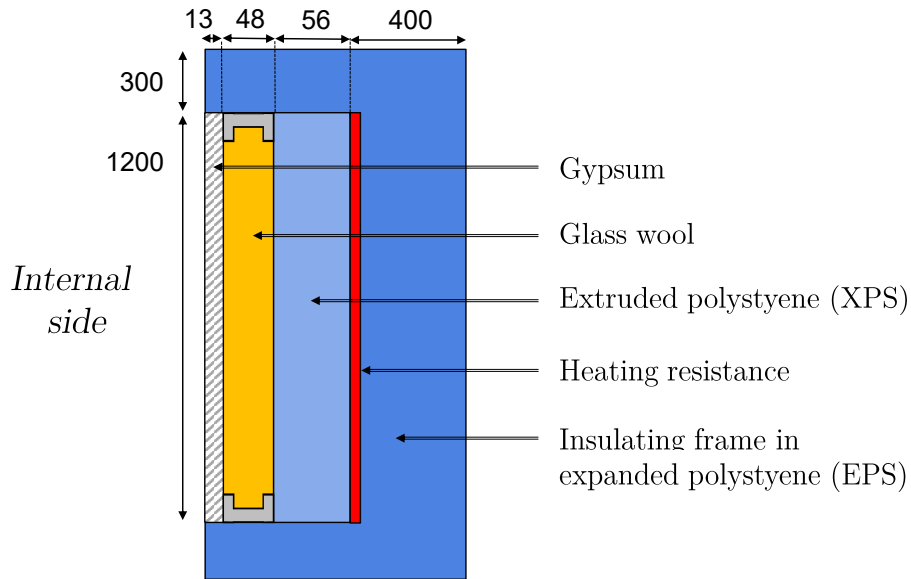


Figure 4.3.: CERTES 1: Cut out of the setup (dimensions in mm).

#### 4.2.2. Sensor instrumentation

The sensors used in the set-up as summarized in Tab 4.3. Heat flux meters are of three different geometries in order to match the geometry of the thermal bridges. These sensors are shown in Fig 4.8.

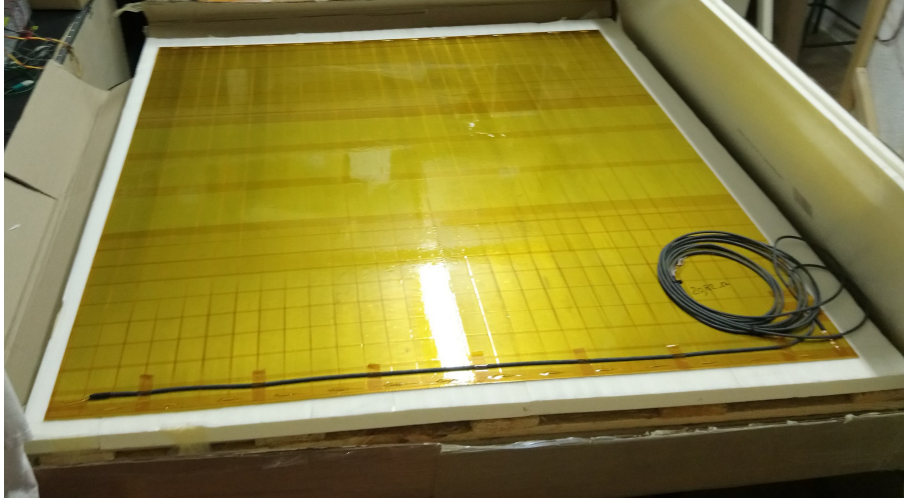
Table 4.3.: List of sensors used in the experimental set-up.

Sensor type	Dimension	Quantity	Description
K-type thermocouple	$\varnothing$ 0.54 mm	13	-
Square HFM	100×100 mm <sup>2</sup>	6	sound area
Rectangular HFM	10×150 mm <sup>2</sup>	2	linear thermal bridges
Circular HFM	$\varnothing$ 30 mm	1	metal pins

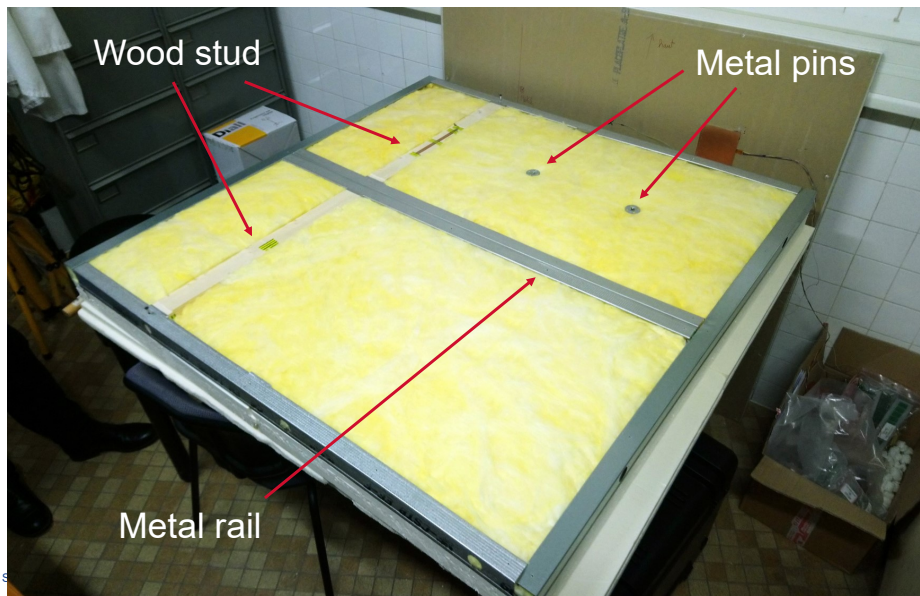
A detailed map of the sensors location on the set up is displayed in Fig 4.9. Many are located inside the setup. Indeed, even though the parameter estimation is supposed to be based on infrared and surface measurement measurements, internal contact sensors are useful to better understand the thermal behavior of the setup. Basically, four zones are studied: the sound area, and the three types of thermal bridge (wood stud, metal rail & metal pin). On each one of them, either a thermocouple or a heat flux meter is instrumented at every interface (labeled from 0 to 3). In addition, for each one of the four zones, a thermocouple is placed in a similar zone (the second pin, another part of the wood stud...) to assess the influence of instrumentation on the thermal response. One heat flux meter is also added behind the heating film (interface 4) on the sound area. Finally thermocouples measure the air temperature 20 cm away from the setup.

## 4.2. CERTES 1 SETUP

---



**Figure 4.4.:** CERTES 1: Heating resistance.



**Figure 4.5.:** CERTES 1: Picture of the setup without the gypsum board.

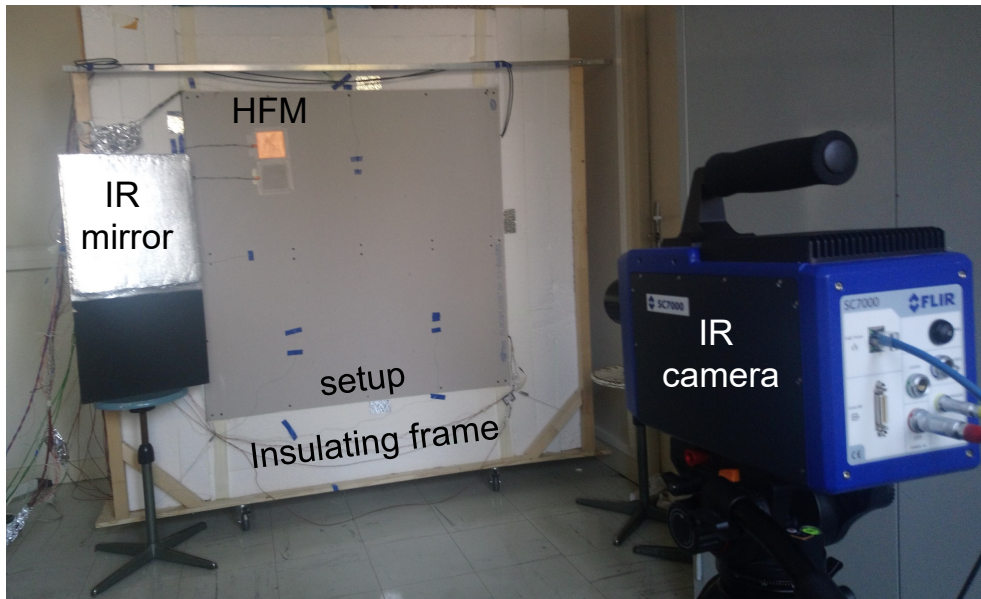


Figure 4.6.: CERTES 1: Picture of the setup in working conditions.

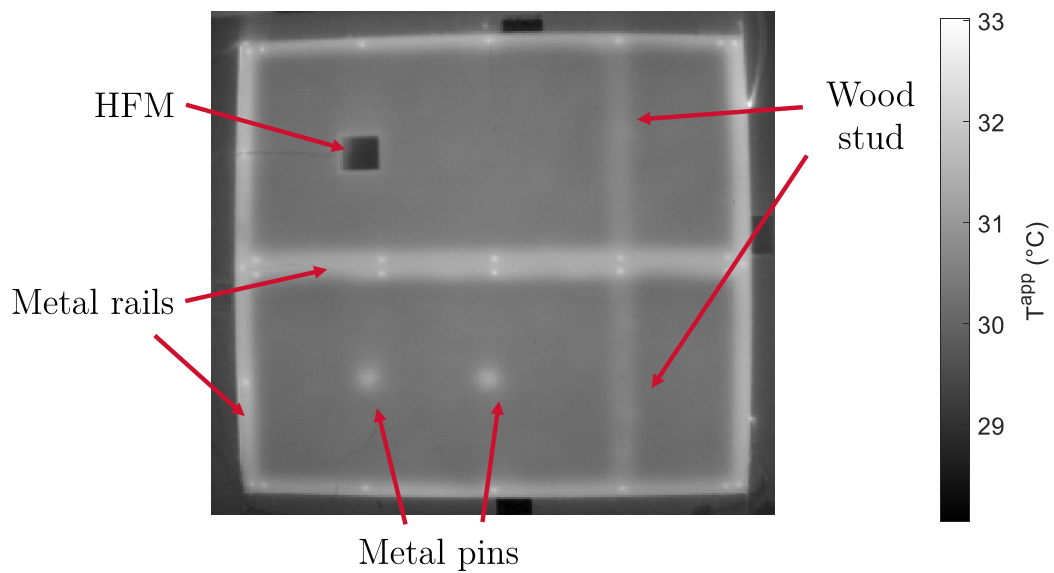
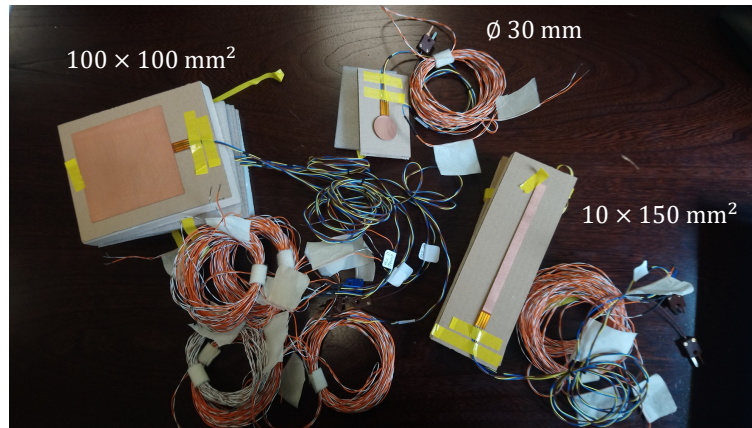
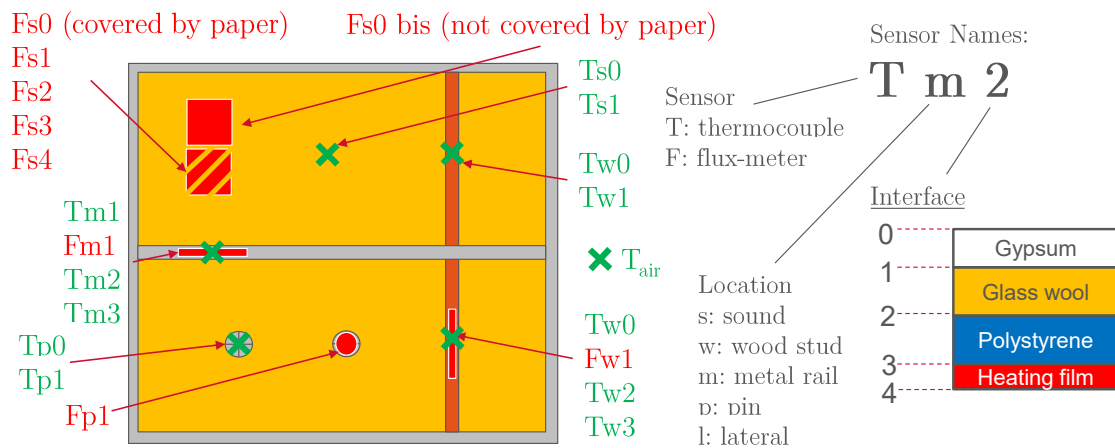


Figure 4.7.: CERTES 1: Infrared image in steady-state.

## 4.2. CERTES 1 SETUP



**Figure 4.8.:** CERTES 1: Picture of heat flux meters with their prolongation cables.

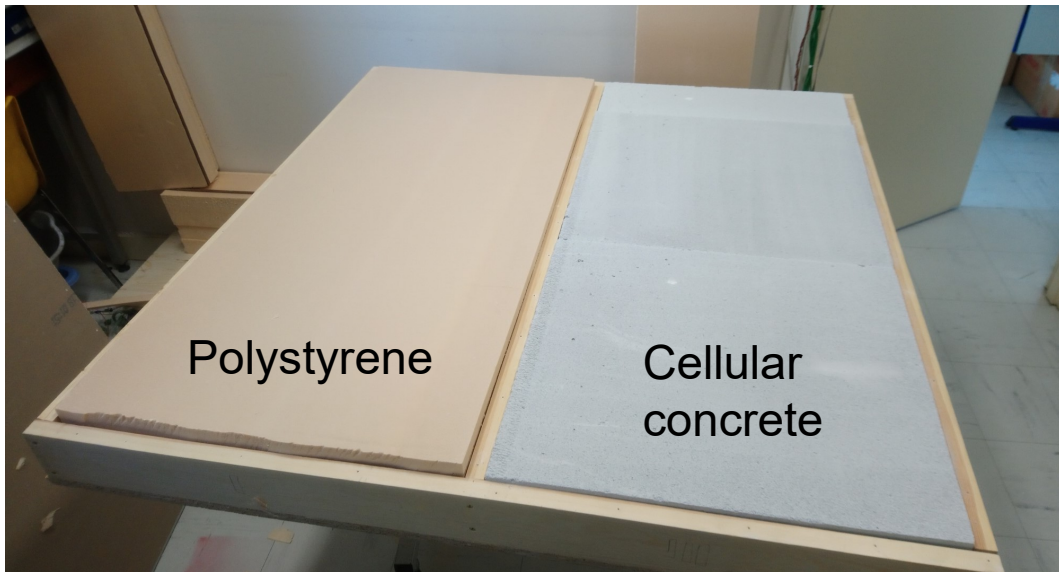


**Figure 4.9.:** CERTES 1: Location of the thermocouples and HFMs instrumented inside and on the experimental set-up.

### 4.3. CERTES 2 setup

This setup was built for two purposes. First, it was used to test simultaneously all the  $h$  coefficient measurement methods developed in this thesis. Second, it was useful to validate the heat flux extrapolation methodology once the  $h$  coefficient is known. This is detailed in chapter 5.

It is an experimental  $1.2 \times 1.2 \text{ m}^2$  wall built in laboratory. It consists of a first 13 mm-thick gypsum layer behind which two different 90 mm-thick materials are disposed: expanded polystyrene on one side and cellular concrete on the other side. A picture of the open setup (without the gypsum layer) is presented in Fig 4.10. These materials were chosen because they have rather different thermal effusivities. The latter, calculated from measurements with the “Hot Disk” method, were estimated to 43 and  $277 \text{ J.m}^{-2}.\text{K}^{-1}.\text{s}^{-1/2}$  for the polystyrene and the cellular concrete respectively. These exact values are of little importance as they will not be used later. The only requirement is that the effusivities are different enough for the two parts of the setup of have a notably different thermal response to a heating of the internal air.



**Figure 4.10.:** CERTES 2: Picture of the setup without the gypsum layer.

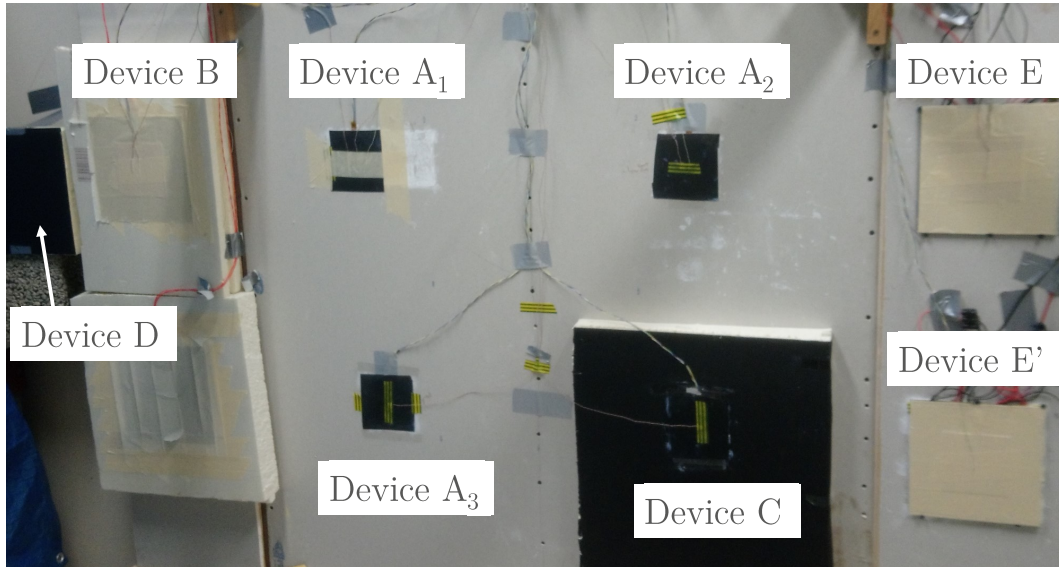
Therefore, this setup is composed of two different zones where heat transfers can be considered 1D. The objective is to extrapolate the heat flux measured by contact on the first zone to the second zone thanks to the heat transfer coefficient. Because the second zone is also 1D, a contact measurement (HFM) on it enables to validate the extrapolation methodology.

The setup is fixed on an internal wall of a  $4 \times 5 \times 3 \text{ m}^3$  room. An insulating frame (made of 30 cm of extruded polystyrene) installed around the setup limits lateral losses. Several sensors and devices were implemented to measure the overall heat transfer coefficient. They are detailed in Chapter 5. Figure 4.11 presents a picture of the instrumented setup. The sensors are referred by a letter, the significance of

### 4.3. CERTES 2 SETUP

---

which is detailed in Chap 5. Finally, four 500 W electric fan heaters inside the room are used to generate off-equilibrium conditions by heating the air in order to test the  $h$ -measurement methods in transient conditions.



**Figure 4.11.:** CERTES 2: Picture of the instrumented setup (see Chap 5 for a description of each device).

## 4.4. CEREMA

### 4.4.1. Presentation of the wall

This third experimental campaign aims at validating the active methods for the characterization of both a homogenous wall and a thermal bridge. The measurements are performed on a real wall built inside a climate chamber at CEREMA (Centre d'Etude et d'Expertise sur les Risques, l'Environnement, la Mobilité et l'Aménagement) in Nancy, France. The chamber is  $4 \times 4 \times 3 \text{ m}^3$  and contains two independent modules (see Fig 4.12) able to control the temperature between  $-30$  and  $30^\circ\text{C}$ . The wall is built between these two modules so that a different temperature can be set on each side.



**Figure 4.12.:** CEREMA: Climate chamber modules at CEREMA, Nancy.

The wall is 3.2 m wide and 2 m high, and is made of concrete building blocks (see Fig 4.13) on which a standard internal insulation system is fixed. The latter consists in 100 mm of glass wool, gypsum boards, and some metal rails to hold them. This is a very common configuration encountered in french buildings. The wall was designed to have a thermal resistance of about  $3.5 \text{ m}^2 \cdot \text{K} \cdot \text{W}^{-1}$ . The material thickness and thermal properties are given in Tab 4.4. Figure 4.14 shows a picture of the wall before installation of the last two gypsum layers. There is a narrow door on the right hand side of the wall.

Metal rails of different geometries are used in order to generate several types of thermal bridge. A cut-out of the wall is presented in Fig 4.15. The first two thermal bridges (noted TB 1 and TB 2) are made of 48 mm-thick metal rails. The difference between them is that TB 1 is located in the middle of a gypsum board whereas TB 2 falls at the junction between two boards. The rail therefore crosses half of the insulation layer. However, the metals rails used for the third thermal bridge (TB 3) are 100 mm-thick which means they go through the entire thickness of glass wool. Figure 4.16 shows pictures of the metal rails for each thermal bridges. In addition, there is a zone (referred as the “sound area”) without thermal bridge in the middle of the wall.

#### 4.4. CEREMA



**Figure 4.13.:** CEREMA: Wall before installation of the glass wool and gypsum boards.

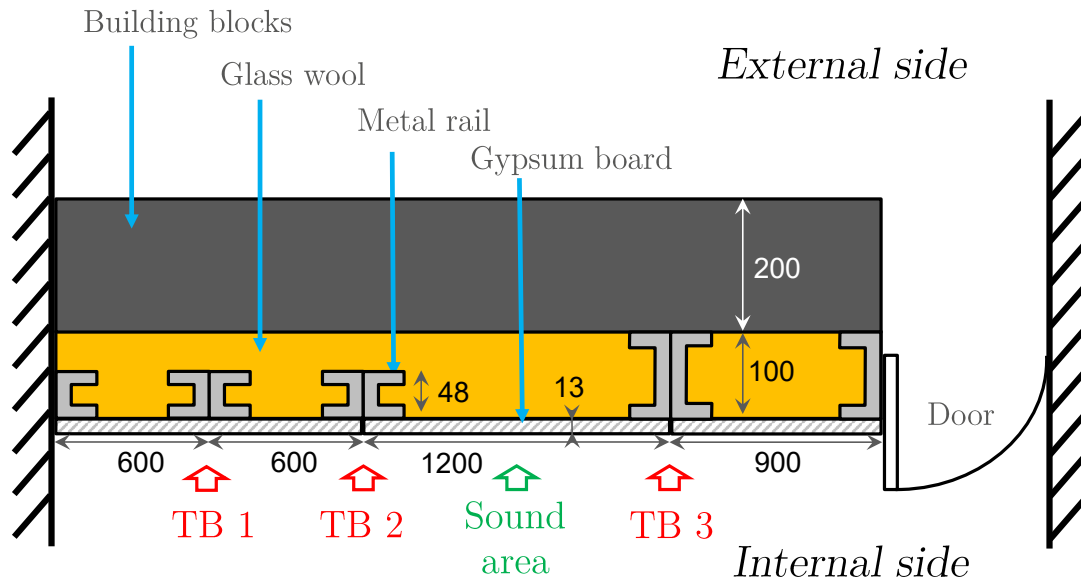
**Table 4.4.:** CEREMA: Summary of thickness and thermal properties of each setup layer.

Layer	$e$ (m)	$k$ (W.m <sup>-1</sup> .K <sup>-1</sup> )	$R$ (m <sup>2</sup> .K.W <sup>-1</sup> )
gypsum board	0.013	0.23	0.06
		(Hot Disk measurements)	
glass wool	0.10	0.034	3.12
		(manufacturer)	
building blocks	0.20	≈ 0.7	≈ 0.3
		(raw estimation)	
		Total	≈ 3.5



**Figure 4.14.:** CEREMA: Wall before the installation of the gypsum boards.





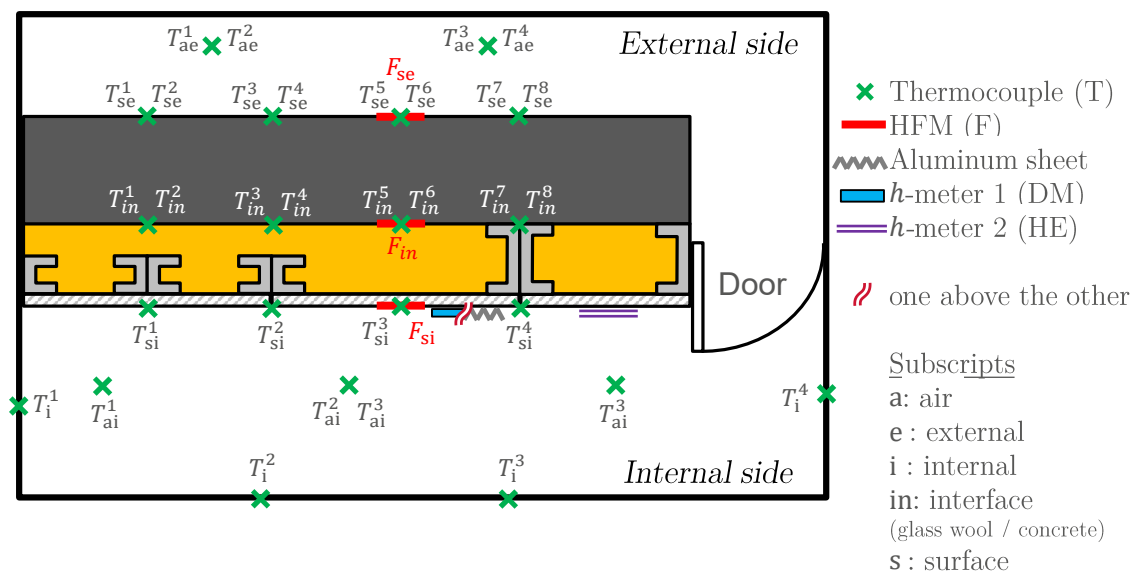
**Figure 4.15.:** CEREMA: Illustration of wall layout and position of thermal bridges (dimensions in mm).



**Figure 4.16.:** CEREMA: Pictures of metal rails used to hold the insulation system (thermal bridges).

### 4.4.2. Sensor instrumentation

Heat flux meters and thermocouples are implemented on surfaces as well as inside the wall. Their locations are detailed in Fig 4.17. Some thermocouple symbols have two references because two sensors are located in this location, but at a different altitude (1 m and 1.5 m high). This is useful to check that there is no vertical temperature gradient in the setup. On each region of interest (thermal bridges and sound area), thermocouples are instrumented on the external surface (“se”), on the interface between the load bearing wall and the insulation system (“in”), and on the internal surface (“si”). The latter has fewer thermocouples because surface temperature differences are also measured by the infrared camera. On the sound area, HFMs are also instrumented on each surface. Some thermocouples are used to measure the air temperature. A crumpled aluminum sheet (useful to estimate the mean radiant temperature with the infrared camera) is fixed on the sound area. Finally, two “*h*-meters” are instrumented on the wall in order to measure the global surface heat transfer coefficient (see Chap 5). The first one, referred as “*h*-meter 1”, is based on the double measurement (DM) method: it is a piece of extruded polystyrene with HFM fixed on it. The sensor named “*h*-meter 2” is the assembly used in the Harmonic Excitation (HE) method. These methods are presented in Chap 5.



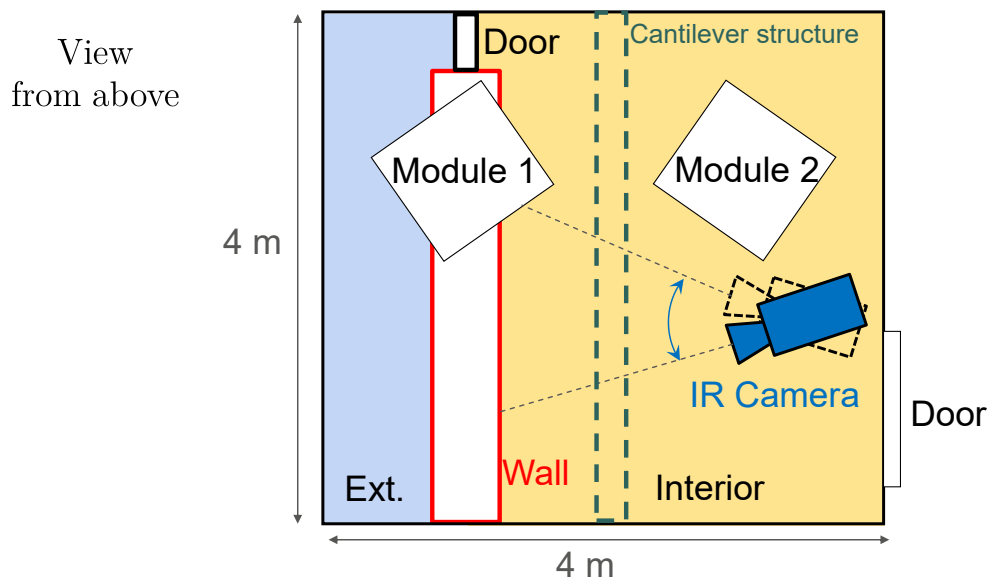
**Figure 4.17.:** CEREMA: Detail of sensor instrumentation: double referenced thermocouple symbols means that there are two sensors on the given location at a different altitude.

### 4.4.3. About infrared measurements

On the internal side of the wall, an infrared camera is used to capture the surface temperature. However, given the dimensions of the room, the distance between the

wall and the camera is too short for the wall to fit entirely within the camera field of view. Two solutions are implemented to fix this issue.

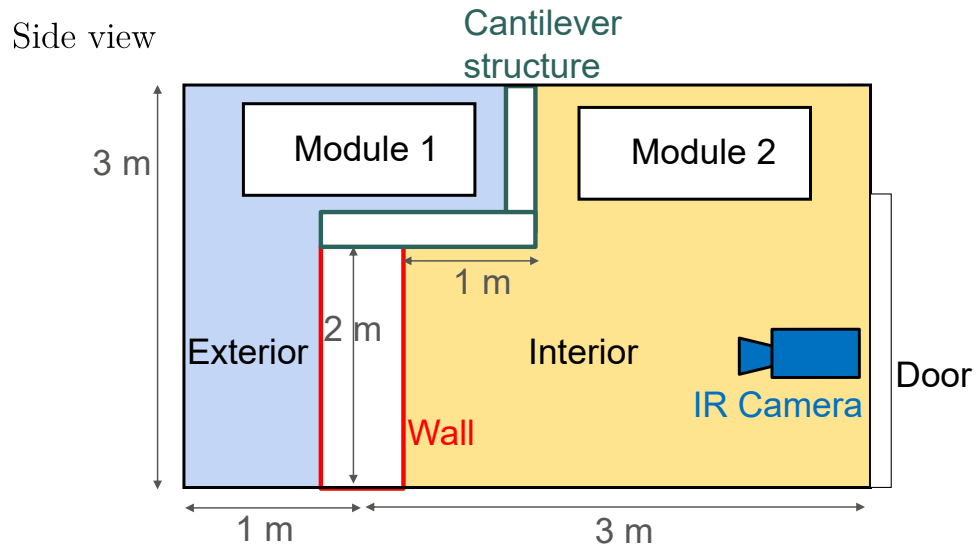
First, the wall is not built in the center of the chamber (between the two modules) because the camera would be less than 2 m away from the wall. As illustrated in Fig 4.18, the wall was rather built below one of the module, leaving about 3 m on the internal side (where the infrared camera is) and 1 m on the external side. A cantilever structure above the wall allows generating two volumes so that each module regulates the temperature on each side of the wall (see Fig 4.19). The cantilever structure is supported by one pole on each side as well as one in the middle, as seen in Fig 4.20.



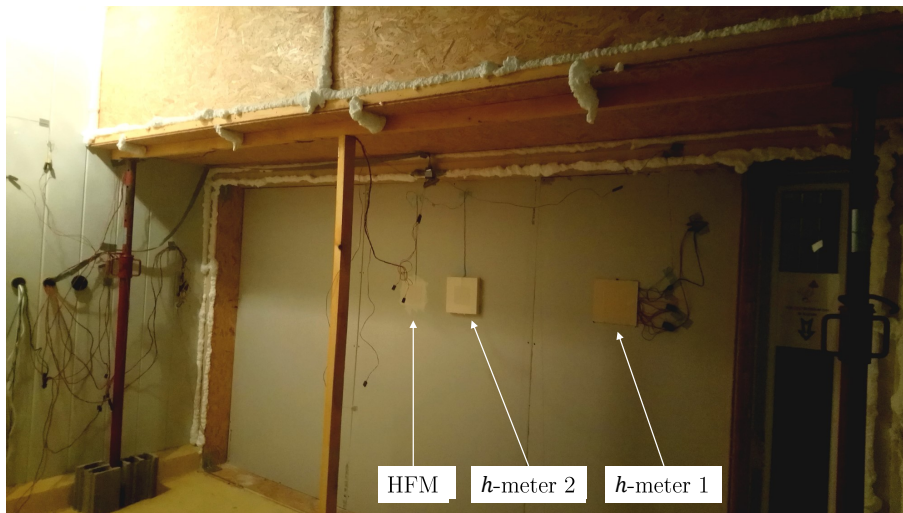
**Figure 4.18.:** CEREMA: Scheme of the climate chamber: view from above.

Second, the camera was mounted on a rotating plateau. By rotating the camera back and forth between every image, it was possible to record two parallel movies of the scene: even frames focus on the left-hand-side of the wall whereas odd frames focus on the right-and-side. There is a small time lag between the two movie but this is not a problem as it is perfectly known and small when compared to the experiment duration. The camera alternated between positions  $-15^\circ$  and  $+15^\circ$  ( $0^\circ$  corresponding to the normal to the wall). Because the camera is always looking at the wall with an angle, images are corrected to compensate for the geometrical distortion. Figure 4.21 displays two consecutive thermal images captured in steady-state. The first one shows the left-hand side of the wall whereas the second image shows the right-hand side. Figure 4.22 presents the reconstructed thermogram from these two images. The central pole supporting the cantilever structure is visible.

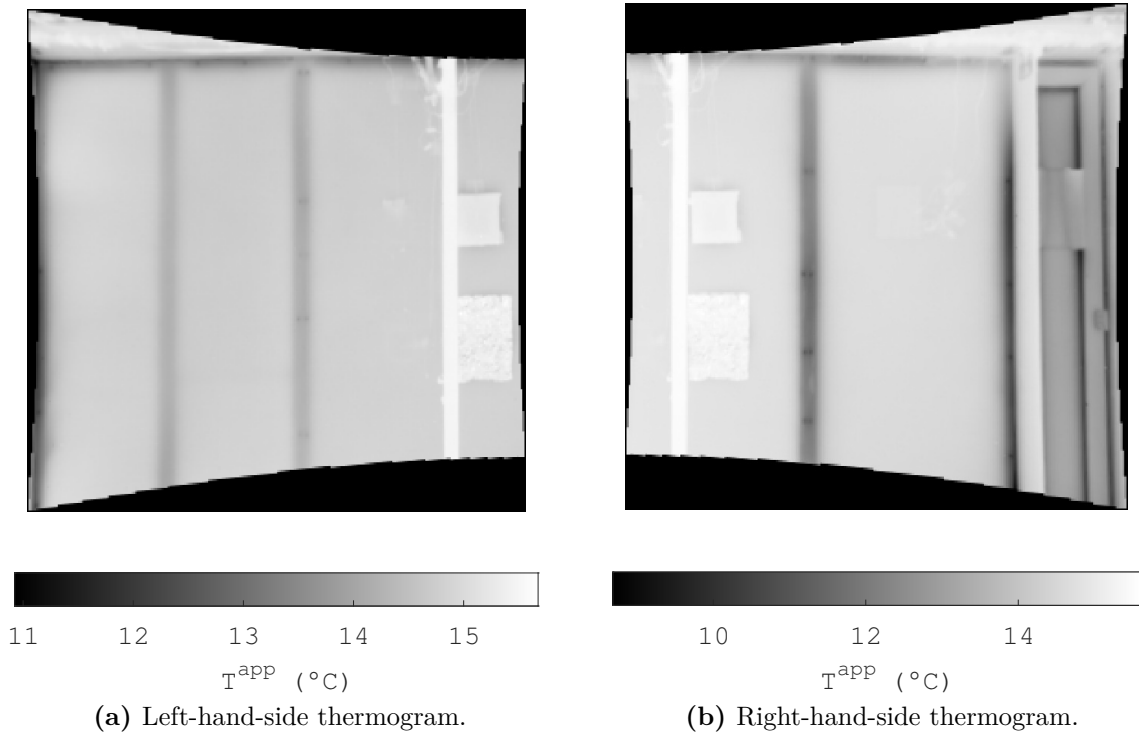
For steady-state measurements, the regulation modules of the climate chamber are used on both sides of the wall. For active test however, the module in the internal side is switched off and is replaced by two 500 W electric fan heaters.



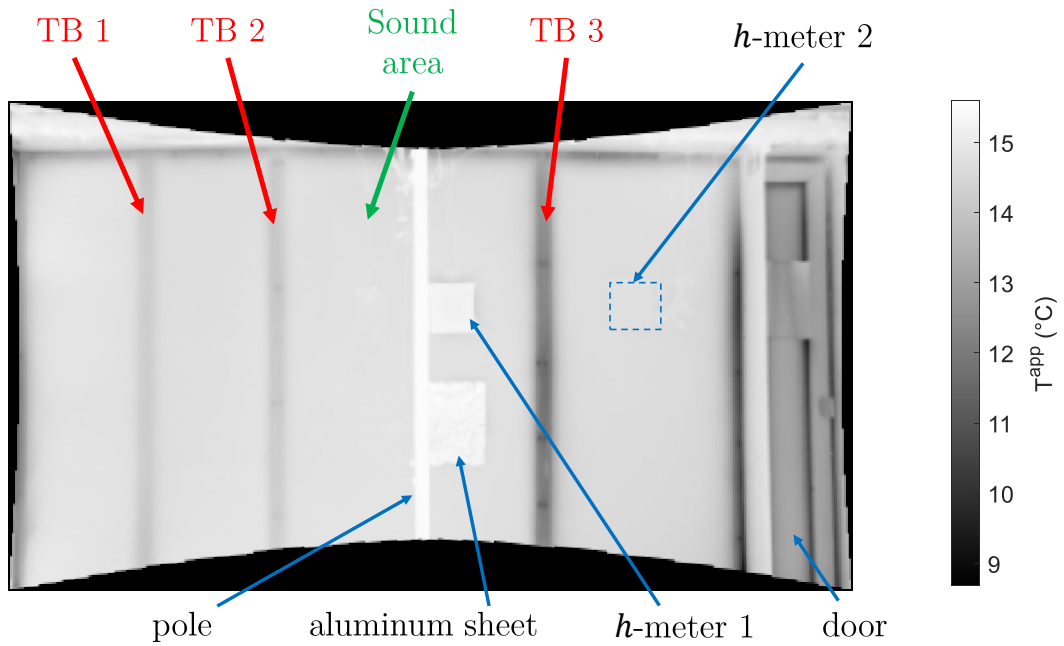
**Figure 4.19.:** CEREMA: Schemes of the climate chamber: side view.



**Figure 4.20.:** CEREMA: Picture of the finished wall with the cantilever structure above.



**Figure 4.21.:** CEREMA: Example of two consecutive thermograms captured during a steady-state experiment.



**Figure 4.22.:** CEREMA: Thermogram of the wall in steady-state with geometrical correction.

#### 4.4.4. Detail of experimental campaign

In order to perform steady-state measurements, the temperature on each side of the wall is kept constant for several days thanks to the climate chamber regulation system. The internal and external air temperatures are set to 15 and  $-5^{\circ}\text{C}$ , respectively.

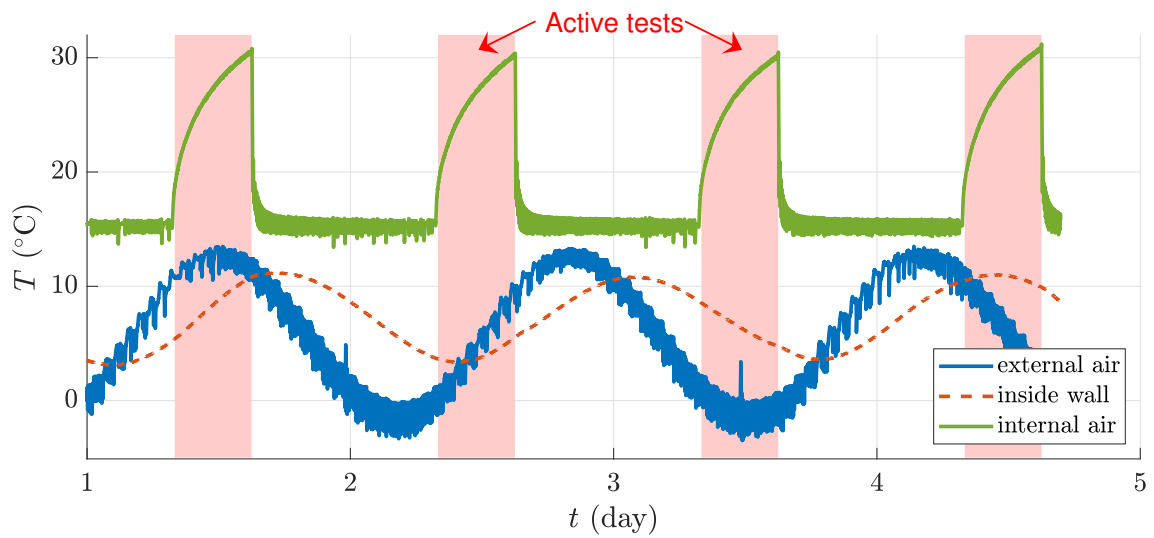
Then, to assess the repeatability and robustness of the active methods, several configurations were tested during the experimental campaign. They are summarized in Tab 4.5. During the whole campaign, the internal air temperature  $T_{\text{air},i}$  remains equal to  $15^{\circ}\text{C}$  (except of course during the active tests). The differences come from the external air temperature  $T_{\text{air},e}$ . In configurations 1 and 2, the external air temperature  $T_{\text{air},e}$  is constant and equal to 5 and  $15^{\circ}\text{C}$  respectively. In these configurations, the wall is at thermal equilibrium before the test.

In the other configurations,  $T_{\text{air},e}$  is no longer constant: it has a sinusoidal evolution which simulates day/night cycles. The mean value of these oscillations is  $5^{\circ}\text{C}$  except for configuration 6 ( $15^{\circ}\text{C}$ ). Three amplitudes were tested: 5, 10 and 15 K (peak-to-peak amplitudes) for configurations 3, 4 and 5-6 respectively.

**Table 4.5.:** CEREMA: Summary of active tests configurations.

Configuration	$T_{\text{air},i}$ ( $^{\circ}\text{C}$ )	$T_{\text{air},e}$ ( $^{\circ}\text{C}$ )	number of tests
1	15	5	5
2	15	15	3
3	15	$5 + 2.5 \cos(\omega t)$	4
4	15	$5 + 5.0 \cos(\omega t)$	4
5	15	$5 + 7.5 \cos(\omega t)$	8
6	15	$15 + 7.5 \cos(\omega t)$	3

Even though the oscillations simulate day/night cycles, their period was set to 32 h instead of 24 h. This setting has a practical motivation: it enables to perform an active test every day at the same hour with different  $T_{\text{air},e}$ . This is illustrated in Fig 4.23 where the temperatures are plotted for several consecutive days ( $T_{\text{in}}$  is the temperature of the interface between the glass wool and the concrete blocks). This simulates *in situ* experiments undertaken at different moments of the day. Given that low frequencies thermal waves penetrate deeper a wall than high frequencies ones, the chosen period of 32 h is a conservative choice.



**Figure 4.23.:** CEREMA: Example of internal and external temperatures for consecutive active tests (configuration 5).

## 4.5. SGR

### 4.5.1. Presentation

This measurement campaign is performed inside an outdoor  $2 \times 5 \times 2.5$  m<sup>3</sup> lightweight test cell at Saint-Gobain Research Paris. The aim is to test *in situ* the steady-state and active characterization methods developed in the thesis. The test cell, referred as “SGR”, is shown in Fig 4.24. It the one used in Douguet *et al.*[58]. The walls are made of about 3 cm of polyurethane. A standard internal insulation system is installed on them, as shown in figures 4.25 and 4.26.



**Figure 4.24.:** SGR: Picture of the test cell.

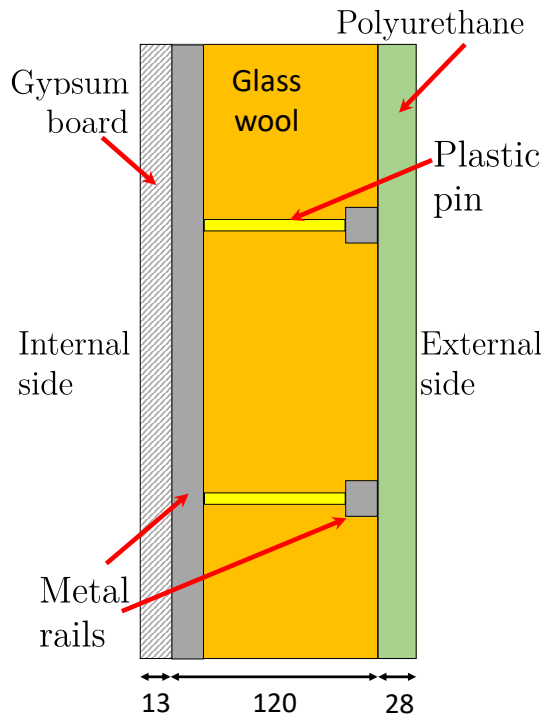
The dimensions and thermal properties of each layer are gathered in Tab 4.6. The overall wall thermal resistance is around  $5.2 \text{ m}^2 \cdot \text{K} \cdot \text{W}^{-1}$ . The 13 mm-thick gypsum boards and the 120 mm-thick glass wool layer are held by metal supports. Horizontal supports are placed on the polyurethane wall whereas the gypsum boards are screwed to vertical ones. The supports are linked by plastic pins. The vertical rails are positioned 60 mm away from each other (standard configuration) except on the East wall where there are only 30 mm away. This later configuration was implemented on purpose, to study the impact of the distance between the rails.

### 4.5.2. Sensor instrumentation

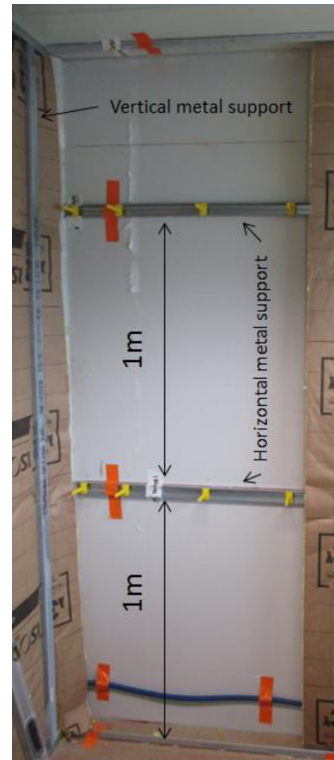
Figure 4.27 presents a scheme of the SGR.

The North and East walls are studied. Not only are their orientation ideal to minimize solar radiation, they are also free from openings. On the contrary, there is a window on the west wall and a door as well as a window on the south wall. Like in the CEREMA experimental campaign, the infrared camera is mounted on a





(a) Vertical cut-out of the wall (dimensions in mm).



(b) Picture of the open wall.

**Figure 4.25.:** SGR: Scheme and picture of the wall layout.

rotation system so that thermal images of both North and East walls are captured during each experiment.

The test room was built before our experimental campaign so no sensor could be installed inside the walls. However, one heat flux meter and one thermocouple are fixed on each side of the two studied walls. Attention were paid to instrument these sensors on sound areas (away from thermal bridges). Crumpled sheets of aluminum are implemented on both walls as well as a “*h*-meter” on the North wall. Two thermocouples are used to measure the indoor air temperature.

The thermal bridges which will be studied are illustrated in Fig 4.28. Two of them are located on the North wall: they are referred are “TB N1” and “TB N2”. Similarly, the three thermal bridges studied on the East wall are named “TB E1”, “TB E2”, “TB E3”.

### 4.5.3. Infrared measurements

Fig 4.29 presents two consecutive thermograms captured during a steady-state experiment. The two images show the North and East was and do not have the same spatial resolution because the distance to the camera is different. The images were corrected for geometrical distortions. The aluminum sheets and the *h*-meter are visible. The thermal bridges are visible as well, despite small temperature contrasts.



Figure 4.26.: SGR: Picture of the North wall insulation system.

Table 4.6.: SGR: Summary of thickness and thermal properties of each setup layer.

Layer	$e$ (m)	$k$ (W.m <sup>-1</sup> .K <sup>-1</sup> )	$R$ (m <sup>2</sup> .K.W <sup>-1</sup> )
gypsum board	0.013	0.23	0.06
glass wool	0.12	(Hot Disk measurements) 0.032	3.75
polyurethane	≈ 0.035 (manufacturer)	≈ 0.025 (manufacturer)	≈ 1.4
Total			≈ 5.15

#### 4.5.4. Detail of experimental campaign

For pseudo-steady-state tests, the indoor air temperature  $T_{\text{air},i}$  is kept constant for several days thanks to two controlled 500 W electric fan heaters. The setpoint temperature is 35°C. The measurements were carried out in late february, 2020. As shown in Fig 4.30, this induces about 30 K temperature difference between the internal and external wall surfaces. Data measured on the North wall are shown here.

For active tests, three heaters of the same type are simultaneously turned on for several hours. Figure 4.31 plots the evolution of the internal air temperature during the active tests. These experiments were performed in march 2020.

Between active tests, the internal air temperature is controlled to make it as constant as possible. The setpoint temperature between the active tests was gradually

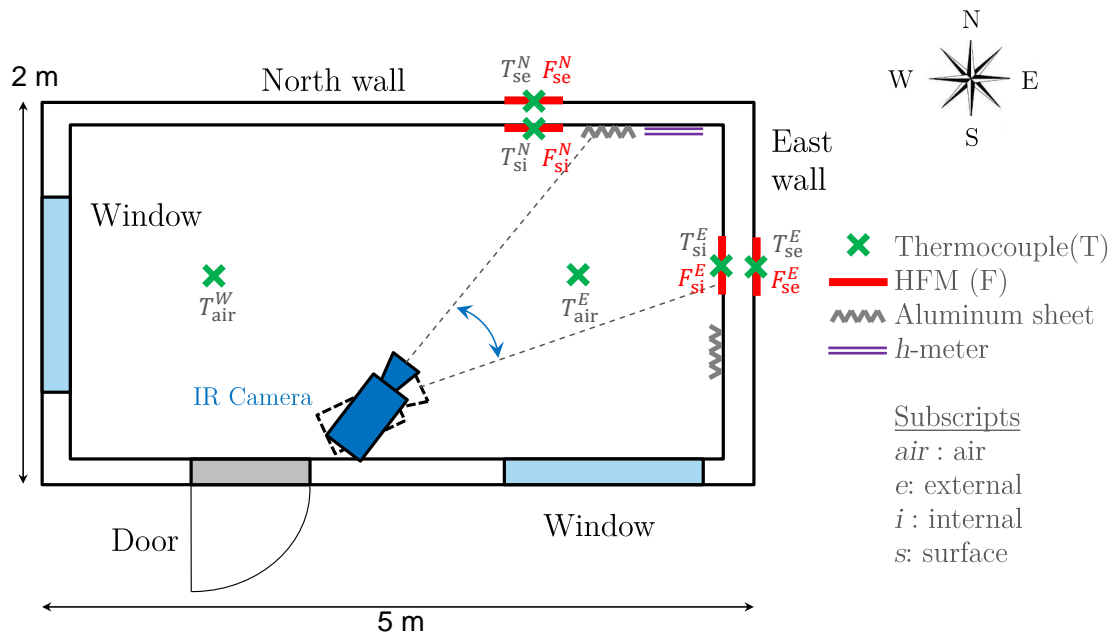


Figure 4.27.: SGR: Scheme of the test cell (top view).

increased from 17 to 25°C in an attempt to improve the regulation (the higher the indoor/outdoor temperature gradient, the easier the regulation).

During the active tests, the internal air temperature rise by 15 to 20 K, depending on the experiment.

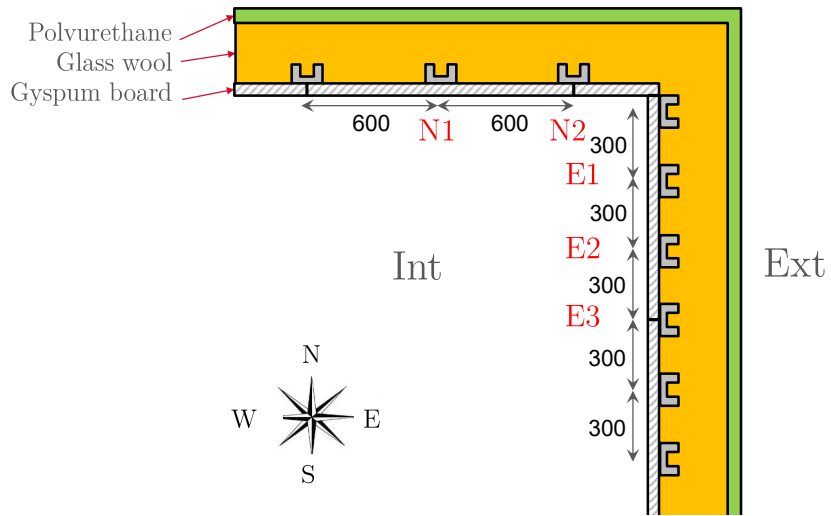


Figure 4.28.: SGR: Scheme of thermal bridges (focus on North-East corner).

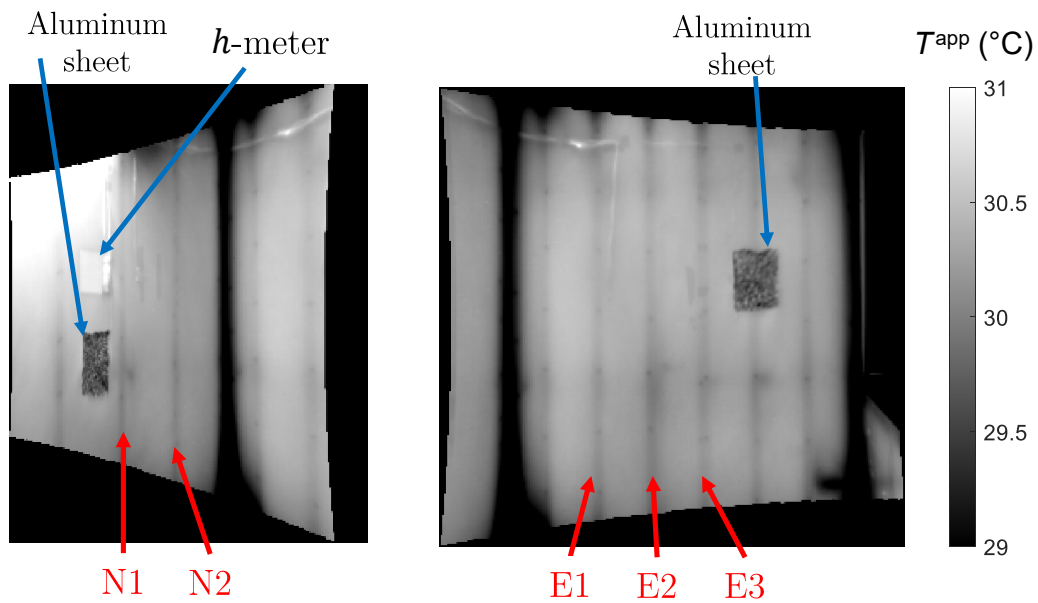
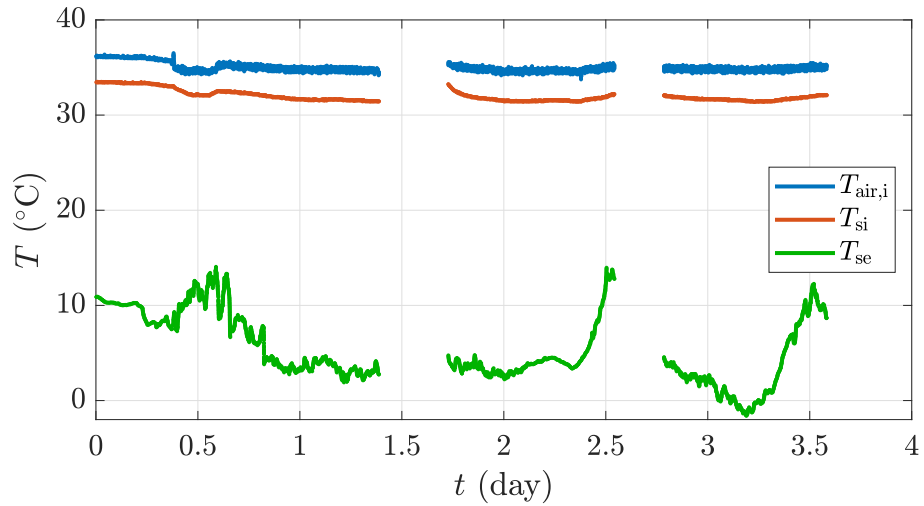
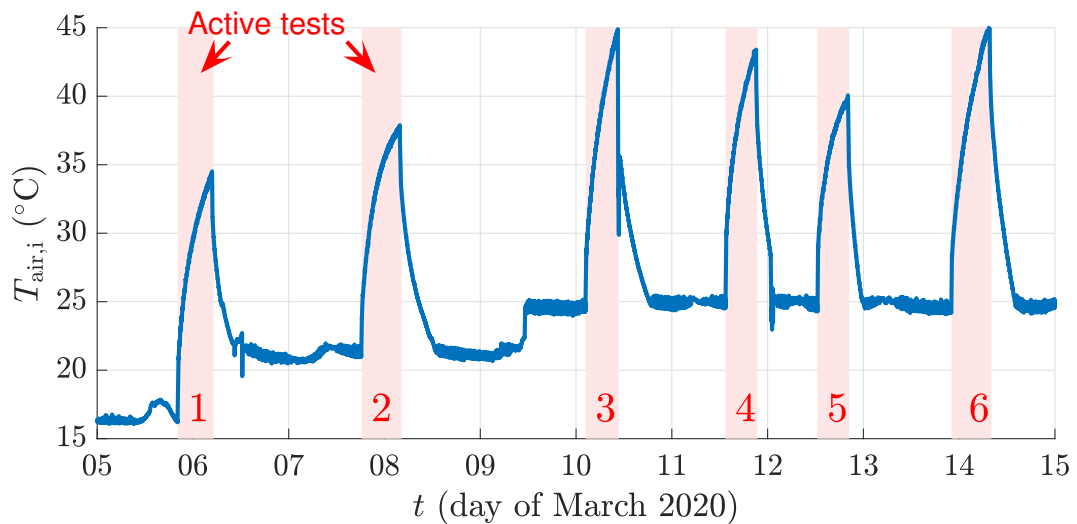


Figure 4.29.: SGR: Example of two consecutive thermograms captured during a steady-state experiment (Left = North wall, Right = East wall).



**Figure 4.30.:** SGR: Measured air and surface (North wall) temperatures during pseudo-steady-state measurements.



**Figure 4.31.:** SGR: Internal room air temperature during and between the six active tests.

### 4.6. Conclusion

Several experimental campaigns were developed in this thesis. They were used sequentially. The CERTES 1 setup was design to obtain a better understanding of measurements on thermal bridges. Thanks to its embedded heating resistance, this lab-scale setup was mainly used to validate steady-state methods for the quantification of a thermal bridge transmission coefficient  $\psi$  or  $\chi$ . Then, is was identified that the overall heat transfer coefficient  $h$  on a building wall was required for the dynamic measurement of the surface heat flux on a thermal bridge. The CERTES 2 setup was built to implement and validate several *in situ*  $h$  measurement methods. Then, the CEREMA experimental campaign was conducted in order to validate active measurement methodologies on a full-scale insulated load-bearing wall in a controlled environment. Thanks to the climate chamber regulation system, many weather configurations could be simulated. Finally, measurements were carried out inside the SGR test cell to test the active methods in situ and on a different type of wall: a lightweight wall.



# 5. Measurement of wall heat transfer coefficient

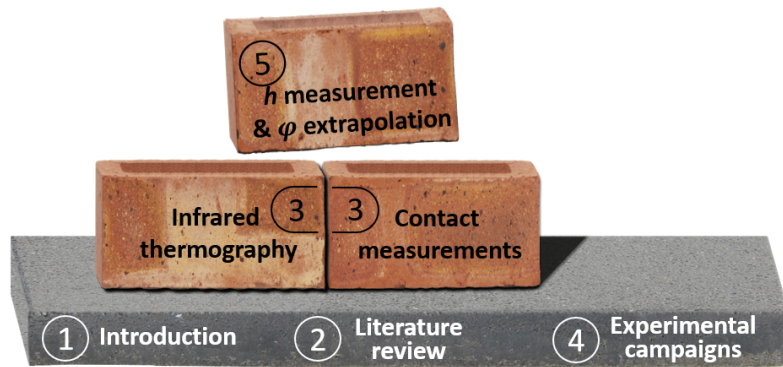


Figure 5.1.: Illustration of thesis plan.

This chapter deals with the *in situ* measurement of the total heat transfer coefficient  $h$  on a building wall in unsteady conditions. The knowledge of this quantity may be valuable in several contexts. As an example, it may be useful to reduce uncertainties in building energy simulations. In the scope of this thesis, the measurement of  $h$ , when combined with thermal images, enables to quantify the heat flux field all over a wall surface. This is done by extrapolating one local contact measurement to the rest of the wall. This procedure may be used for the *in situ* estimation of the equivalent thermal resistance of a non-homogeneous wall, for instance by coupling it with the active method presented in Chap 8. It may also be useful for the characterization of a thermal bridge (e.g. estimation of a  $\psi$  transmission coefficient). This is the scope of Chap 9. Thus, the  $h$ -measurement methods presented in this chapter were tested in the context of active tests: the internal air was heated for several hours.

The results presented in the present chapter were published in [173], [174] and [175].

Section 5.1 introduces the methodology and the heat flux extrapolation procedure. Section 5.2 summarizes the existing methods for  $h$ -coefficient evaluation in buildings and their limitations. Section 5.3 presents the five  $h$  measurement methodologies tested. One of them (the “Harmonic Excitation” method) is presented in further details in section 5.4. Section 5.5 focuses on the calculation of the measurement uncertainties. Section 5.6 presents results obtained in steady and transient states



respectively. These results were obtained in laboratory. It may be noted that measurements of the heat transfer coefficients were also performed in a climate chamber (see CEREMA experimental campaign). Finally, these results are discussed in section 5.7 and a conclusion is drawn in section 5.8.

---

## Nomenclature

### Acronyms

DM	Double measurement
HE	Harmonic Excitation
HFM	Heat Flux Meter
MRT	Mean Radiant Temperature
OT	Operative Temperature
TEC	ThermoElectric Cooler (Peltier modules)

### Greek Symbols

$\zeta$	phase lag	rad
$\lambda$	thermal conductivity	$\text{W.m}^{-1}.\text{K}^{-1}$
$\nu$	kinematic viscosity	$\text{m}^2.\text{s}^{-1}$
$\sigma$	Stefan-Boltzmann constant	$\text{W.m}^{-2}.\text{K}^{-4}$
$\varphi$	heat flux density	$\text{W.m}^{-2}$

### Roman Symbols

$A$	amplitude	
$a$	thermal diffusivity	$\text{m}^2.\text{s}^{-1}$
$C$	heat capacity per unit surface	$\text{J.m}^{-2}.\text{K}^{-1}$
$f$	frequency	$\text{s}^{-1}$
$FT$	Fourier Transform	
$Gr$	Grashof number	-
$h$	global heat transfer coefficient	$\text{W.m}^{-2}.\text{K}^{-1}$
$j$	imaginary number such that $j^2 = -1$	-
$L_c$	characteristic length	m
$N$	number of points	-
$Nu$	Nusselt number	-
$P$	period	s
$Pr$	Prandtl number	-
$Ra$	Rayleigh number	-
$T$	Temperature	K
$u$	uncertainty	
$U$	voltage	V
$Y$	thermal admittance	$\text{W.m}^{-2}.\text{K}^{-1}$

### Superscripts

$\sim$	complex harmonic notation
$-$	mean value
app	apparent
c	convective
r	radiative

### Subscripts

$A, B, C, D, E$	device name
op	operative

## 5.1. Motivation

As shown in section 3.2.2.3 of Chap 3, under the assumption of linearizable radiative heat fluxes, the heat flux  $\varphi$  on a wall surface is given by:

$$\varphi = h(T - T_{\text{op}}) \quad (5.1)$$

where the total heat exchange coefficient  $h$  and the operative temperature  $T_{\text{op}}$  are given by [102]:

$$h = h^c + h^r \quad (5.2)$$

$$T_{\text{op}} = (h^c T_{\text{air}} + h^r T_{\text{env}}) / h \quad (5.3)$$

with  $h^c$  and  $h^r$  the convective and radiative heat exchange coefficients,  $T_{\text{env}}$  the mean radiant temperature and  $T_{\text{air}}$  the air temperature outside the near-wall boundary layer. It is important to point out that both  $h$  and  $T_{\text{op}}$  are local quantities and might not be uniform all over the considered wall. The radiative heat transfer coefficient is given by:

$$h^r = 4\varepsilon\sigma T_m \quad (5.4)$$

with  $\varepsilon$  the wall emissivity,  $\sigma$  the Stefan-Boltzmann constant and  $T_m$  a mean temperature. In first approximation,  $T_m$  may be taken equal to  $(T + T_{\text{env}}) / 2$ ,  $T$  or  $T_{\text{env}}$ .

Five methods for the *in situ* measurement of the overall heat transfer coefficient on a wall surface are studied and compared in this chapter. Two of them are inspired from techniques found in the literature whereas the remaining three are novel and were developed during this thesis. For each method, the measurement uncertainties are thoroughly quantified. The methods must take into account both convective and radiative heat exchanges. Also, measurement devices must be as non-intrusive as possible: they should not modify convective and radiative exchanges. Some methods are able to monitor the evolutions of the heat transfer coefficient with time. Their applicability for measurements in both steady and transient regimes (during active tests) is investigated.

One of the main difficulty is that the operative temperature  $T_{\text{op}}$  is not known. It is usually assumed equal to the air temperature. This assumption is deemed acceptable in steady-state indoor conditions in well insulated buildings: the air and the surrounding objects have approximately the same temperature. However, it does not hold true in old buildings where cold surfaces due to the lack of insulation

generate thermal imbalance. Moreover, this assumption is also false in transient regimes when radiation and convection have a very different behavior. The following paragraphs present several  $h$ -measurement methods developed and experimented here.

Heat flux meters (HFMs) are commonly used to measure the heat flux across a plain wall where the transfers are one-dimensional. However, in the presence of thermal bridges, the heat transfers are 2D or 3D and HFM cannot be used anymore. More generally, heat losses on a building wall are seldomly uniform: a local heat flux measurement is usually not representative of the whole wall. Therefore, an accurate quantification of the losses would require the use of many sensors which might be expensive, time consuming, as well as intrusive. As said above, the proposed solution consists in extrapolating the heat flux measured on a sound area 1 to a nearby area 2. Indeed, if the two areas have the same emissivity, are close to each other and at a similar altitude,  $h$  and  $T_{op}$  may be considered equal on them. It comes:

$$\varphi_2 = \varphi_1 + h(T_2 - T_1) \tag{5.5}$$

Then, by measuring  $\varphi_1$  with a HFM,  $T_2 - T_1$  with thermocouples or infrared thermography, and  $h$  with a specific device, the second heat flux  $\varphi_2$  can be derived.

## 5.2. Literature review on total $h$ -coefficient evaluation

A first approach is to use a standard value. Standard ISO 6946 [99] defines default  $h$ -values to use in building numerical simulations: 7.7 and 25  $\text{W}\cdot\text{m}^{-2}\cdot\text{K}^{-1}$  for indoor and outdoor vertical surfaces, respectively. This provides an order of magnitude of the heat exchange coefficient but does not take into account the configuration specificity (ventilation rate, surface temperature differences, geometry, etc).

A second approach consists in using one of the many empirical correlations developed in the literature to estimate the convective heat transfer coefficient  $h^c$  [170]. The radiative component  $h^r$  is then estimated from surface temperature and emissivity measurements. However, most commonly used correlations are based upon experiments using small free edged heated plates under natural convection [176]. This is usually not representative of *in situ* conditions in buildings. Even when the conditions are similar, there is an important discrepancy between correlations. For instance, Dascalaki [177] compared fifty-eight  $h^c$  correlations (see [170] for instance). Only ten of them were for enclosures, with a variability of almost 50% in Nusselt numbers. The latter is the dimensionless ratio of convective to conductive heat transfer across a boundary:

$$Nu = \frac{h^c L_c}{\lambda} \quad (5.6)$$

with  $L_c$  the characteristic dimension of the problem,  $\lambda$  the air thermal conductivity. Most natural convection correlations link the Nusselt number with the Prandtl number  $Pr$  as well as either the Grashof  $Gr$  or the Rayleigh  $Ra$  number:

$$Pr = \frac{\nu}{a} \quad (5.7)$$

with  $\nu$  and  $a$  the air kinematic viscosity and thermal diffusivity, respectively.

$$Gr = \frac{g\beta\Delta T L_c^3}{\nu^2} \quad (5.8)$$

with  $g$  the gravitational acceleration,  $\beta$  the air thermal expansion coefficient and  $\Delta T$  the air-to-wall temperature difference.

$$Ra = Gr \times Pr \quad (5.9)$$

In building applications the calculation of  $Gr$  (or similarly  $Ra$ ) is not straightforward at all. Indeed, because the temperature is usually not uniform in a room, the choice

of the location where the air temperature is measured has a major impact on  $\Delta T$  and therefore on  $Gr$ . Consequently, an empirical correlation may not be able to provide an accurate estimation of the local heat transfer coefficient.

Third, one of the best ways to have a proper estimation of the  $h$ -coefficient is probably to measure it. Almost every measurement method found in the literature focuses on the convective component  $h^c$ . In some cases, substituting low emissivity surfaces with high emissivity ones would enable to include the radiative exchanges in the measured quantity.

On the one hand, for outdoor applications, the measurement methods are based on the use of heated plates. In Jayamaha *et al.* work [178], a measuring device is placed in a cut out of a plate. It is made out of a HFM of low emissivity mounted on a film heater itself fixed on an insulating material. The film is fed so that the plate temperature is kept constant. The  $h^c$  coefficient is derived from a thermal balance including the surface heat flux, surface-to-air temperature difference and radiative exchanges. The temperature difference spans from 12 to 20 K. Many other authors similarly performed outdoor  $h^c$  measurements. Their device is not always fixed in a cut out of a plate but is also based on a heating component and a heat flux measurement. Using the same method, Hagishima and Tanimoto [179] generated  $h^c$  maps on building canopy surfaces whereas Loveday and Taki [180] focused on small buildings. Ito [181] proposed a slightly different method as he used two distinct plates heated at different temperatures. By working with the heat flux and temperature differences between them, the measurement of the air temperature is no longer needed. Ohlsson *et al.* [182] made a thorough uncertainty estimation of the methods developed by Ito and Loveday. This work is based on lab-scale measurements of small plate under forced convection. In another study [183], the same authors investigated the impact of response time of usual outdoor  $h$ -measurement devices. They suggest modifications to reduce this response time in order to be able to capture faster variations of  $h$ .

On the other hand, in indoor applications, every measurement method was implemented in steady-state and most of them in a controlled environment. Khalifa and Marshall [184] made  $h^c$  measurements in a  $3 \times 2.4 \times 2$  m<sup>3</sup> test-cell. The study covers most widely used heating configurations in buildings. Radiative heat transfers are neglected. Awbi and Hatton [176] used a similar protocol in a  $4 \times 3 \times 2.5$  m<sup>3</sup> chamber. The main difference is that heating plates were used to provide surface heating on each wall. Wallenten [185] measured the  $h^c$  in an environment more realistic of building situations: a  $3 \times 3.6 \times 2.4$  m<sup>3</sup> room equipped with radiator and ventilation systems. The  $h^r$  value is calculated from temperature measurements and view factors (as well as the emissivity). These methods are not applicable *in situ*. Indeed, the heat fluxes were derived from temperature measurements on each side of thin and non-insulated walls of perfectly known conductivity: the wall forms a HFM itself. In addition, the  $h$ -coefficient was calculated taking a space average of the air temperature as reference temperature. According to Wallenten [185], this reference temperature may be arbitrary chosen for numerical simulation purposes. In our applications however, the reference temperature has to be the operative temperature. These methods may be extended to the measurement of the total  $h$ -coefficient by

swapping low emissivity surfaces by high emissivity ones.

An alternative for indoor  $h^c$  measurement is the so-called “Mayer ladder”. This concept can be traced back to Mayer [186] and has the advantage of being applicable *in situ*. It is based on the measurement of the air boundary layer thickness close to the studied surface. The Mayer ladder was not originally developed for building applications, and was designed for an air/surface temperature difference  $\Delta T$  of 22 K. Delaforce *et al.* [187] extended the method to the building sector, with  $\Delta T$  around 2 K. Works of Irving *et al.* [188], Griffith *et al.* [189] and Davis *et al.* [190] also involved the use of a Mayer ladder in buildings. Nevertheless, unlike previously presented methods, the Mayer ladder cannot be modified to include radiative heat transfers for the direct measurement of the total  $h$ -coefficient. The radiative component would have to be estimated from temperature and emissivity measurements of the surrounding environment.

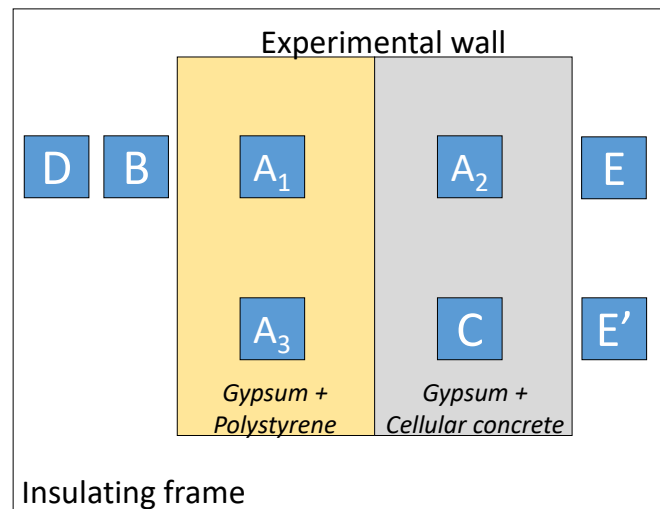
The only reference found that deals with a direct measurement of the total  $h$ -coefficient is the ISO 9869-2 standard [102]. It is derived from Kato *et al.* [103] and proposes a measurement device. It is made out of a HFM sandwiched between a copper plate (with a high emissivity coating) on the front side and a heating resistance on the rear side. The latter is insulated with a piece of polystyrene and the complete device placed in front of the wall. Thanks to the heating resistance, the device-to-air temperature difference is kept between 3 and 10 K. The operative temperature is measured by another device using a thermocouple inserted between a copper plate (also with a high emissivity coating) and some polystyrene. This device is referred as “ET sensor”, for Environment Temperature sensor. It is said that the device should be placed near the wall but should not touch it either. The initial method proposed by Kato *et al.* [103] used a black globe sensor, but the exchanges around a sphere are not representative of those on a wall surface. This method is unfortunately only applicable in steady-state. In addition, because of the high temperature elevation on the  $h$ -measurement device, the natural convection conditions on its surface must be different from the ones on the wall surface. This probably introduces a measurement bias.

Consequently, the literature review showed very few *in situ* measurement methods of the global heat exchange coefficient  $h$  on a building wall. This chapter presents five different measurement methods of indoor  $h$ -coefficient. As said above, three of them are original methods. The other two are derived from Ito [181] and the ISO 9869-2 standard [102] respectively. No difficulty is foreseen to apply them outdoor, even though this was not tested in the scope of this thesis.

## 5.3. Measurement setup and methods

### 5.3.1. Experimental setup

In this chapter, measurements are undertaken on the CERTES 2 setup, presented in section 4.3. Several  $h$  measurement devices are fixed on this wall. They are presented in details in the next section. Fig 5.2 illustrates the layout of the experimental wall and shows the location of the  $h$  measurement devices. All the devices are based on contact measurements and are labeled by letters, the significance of which are detailed below. Fig 5.3 shows a picture of the instrumented wall.

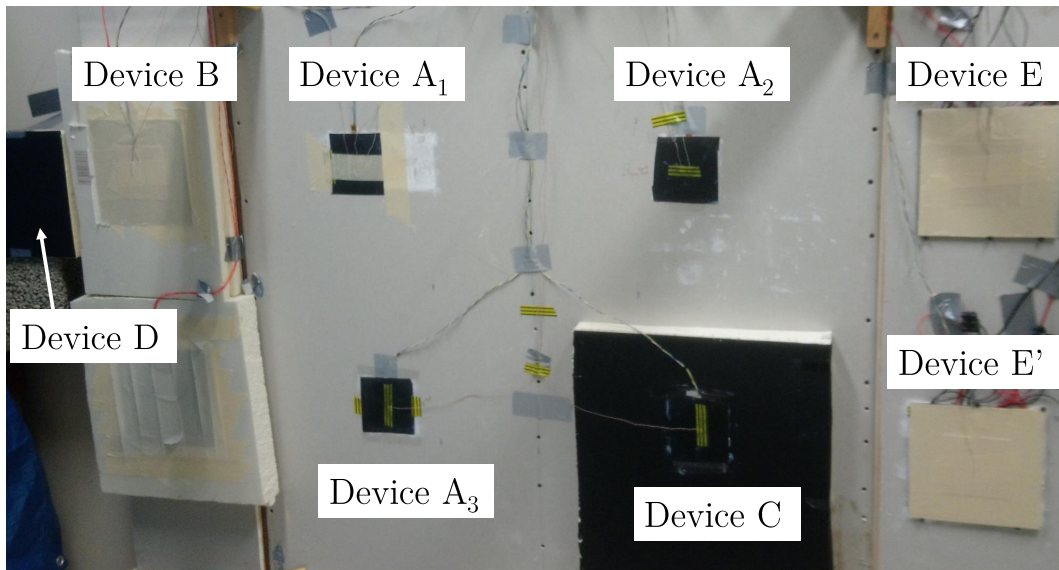


**Figure 5.2.:** Schematic front view of the studied experimental wall within its insulating frame and location of all the devices used (labeled by letters: devices having the same letter are identical).

In most configurations, only temperature differences between two areas are required rather than absolute temperatures. Therefore, each temperature difference is directly measured by fixing one junction of a thermocouple on the first area, and the second junction on the other area (two-junction configuration, see Fig 3.2 in Chap 3). There is therefore no cold junction compensation and the measured quantity is directly the temperature difference between the two junctions. This reduces the measurement uncertainties (see Chap 3). In addition, the air temperature is measured 15 cm from the wall by a thermocouple shielded from radiation with aluminum tape. It may be noted that the different sensors used (thermocouples and HFMs covered with paper) are supposed non-intrusive. This hypothesis is sensible given the negligible thickness (0.5 mm) and thermal resistance of the HFM when compared to the ones of the wall.

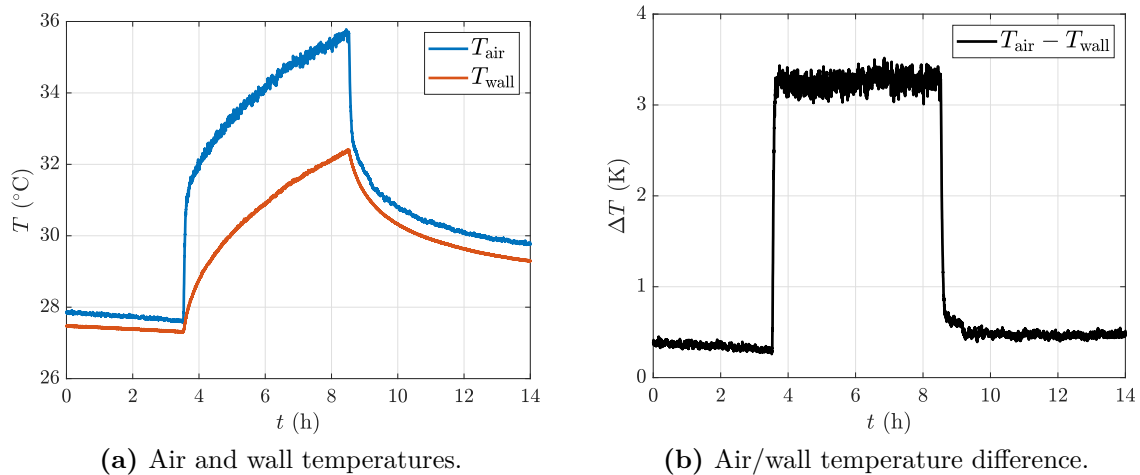
In order to generate off-equilibrium conditions (and to simulate an active test), the four electrical heaters were switched on for five hours and then switched off. Before the application of this thermal load, the room remained at thermal equilibrium for at least two days. Fig 5.4 plots the wall and air temperatures measured during such an experiment. The mean radiant temperature  $T_{\text{env}}$  is supposed to be close to  $T_{\text{wall}}$ .





**Figure 5.3.:** Picture of the instrumented setup.

These plots confirms that the usual assumption  $T_{op} = T_{air}$  is not valid in this type of off-equilibrium situation. For this reason and also because of the air stratification, the definition and use of  $T_{op}$  is complex, hence the advantage of our method that does not require  $T_{op}$ .



**Figure 5.4.:** Measured air and wall temperature during an experiment.

### 5.3.2. Double measurement method 1 (DM1)

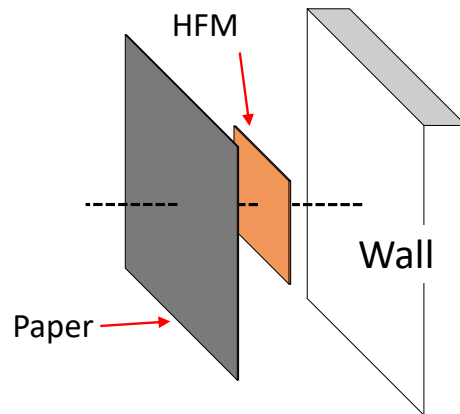
This method and the following one rely on measurements on two different surfaces (noted  $A_1$  and B in figures 5.2 and 5.3). It is based on the same principle as developed by Ito [181]. First, a HFM is placed on the wall. Some paper is fixed on this sensor for it to have the same emissivity as the wall. This is the device A shown

in Fig 5.5. Let  $\varphi_A$  and  $T_A$  be the heat flux and temperature measured on its surface. A heating resistance is placed next to it and another HFM on top of it measures  $\varphi_B$  and  $T_B$  (see device B in Fig 5.6). The resistance is fed with a constant power to ensure that  $T_B$  is always about  $1^\circ\text{C}$  higher than  $T_A$ . A lower value would reduce the signal to noise ratio while a too high temperature difference would significantly alter the convection pattern near the wall. The measured value would then not be representative of normal conditions on a building wall.

The heat flux on each surface is given by Eq 5.1. Both  $h$  and  $T_{\text{op}}$  are then supposed equal on the two surfaces. The heat transfer coefficient is therefore expressed as:

$$h = \frac{\varphi_B - \varphi_A}{T_B - T_A} \quad (5.10)$$

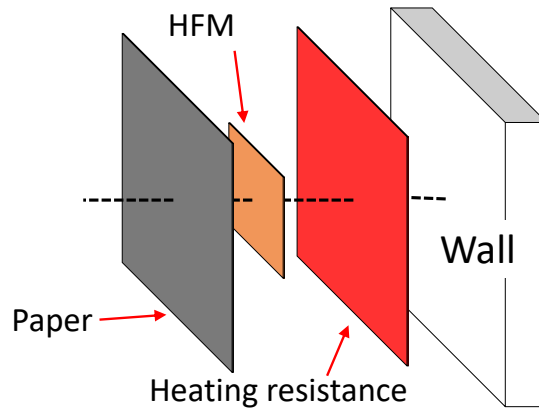
This way,  $h$  can be determined without knowledge of  $T_{\text{op}}$ . This method has the advantage of being applicable in steady state as well as in transient regimes. The heating resistance ensures that  $T_B - T_A > 0$ .



**Figure 5.5.:** Device A: simple HFM directly fixed on the wall (used in DM1 and DM2 methods).

#### 5.3.3. Double measurement method 2 (DM2)

This method, developed during this thesis, is a variation of the previous one. It uses devices  $A_3$  and C of Fig 5.2 ( $A_3$  is preferred to  $A_1$  because it is closer to C and at the same altitude). The installation is similar to the previous one, except that the heating resistance is replaced by a piece of material. Device C is illustrated in Fig 5.7. The thermal effusivity of this material should be different from that of the wall. A 50 mm-thick piece of extruded polystyrene is used here. Basically, a change in the internal temperature of the room induces a temperature difference between surfaces A and C because they are mounted on different materials. Similarly to



**Figure 5.6.:** Device B: a HFM mounted on a heating resistance fixed on the wall (used in the DM1, OT1 and OT2 methods).

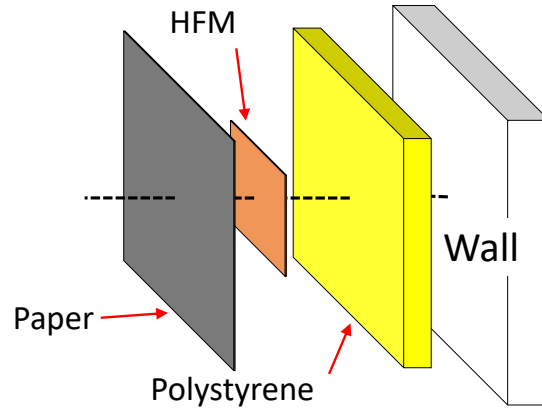
Eq. 5.10, it comes:

$$\varphi_C - \varphi_A = h(T_C - T_A) \quad (5.11)$$

with  $\varphi_C$  and  $T_C$  the heat flux and the temperature measured on the added material, respectively. The calculation of  $h$  is not as straightforward as in the previous method because there may be moments when the temperature difference  $T_C - T_A$  is null. However, plotting  $\varphi_C - \varphi_A$  as a function of  $T_C - T_A$  gives a straight line of slope  $h$ . This method has the advantage of being very simple to implement since it only requires a piece of polystyrene and two HFMs. However, a temperature difference is required between the wall and the sensor. It must be enforced by an external heat source. In the present study, the room air temperature is heated with electric fan heaters. Steady-state measurements would be possible if the internal/external temperature gradient is high enough to generate the desired temperature difference. This is not the case here. For outdoor applications, the thermal load could come from solar radiation or from daily variations in the air temperature.

### 5.3.4. Operative temperature measurement method 1 (OT1)

This method, as well as the next one, relies on the measurement of the operative temperature  $T_{op}$  on the wall surface. It is based on the ISO 9869-2 standard [102]. The operative temperature is measured thanks to a thermocouple sandwiched between a copper plate and a piece of polystyrene, as presented in Fig 5.8 (Device D). According to [102], the device should be placed near the wall but should not touch it. The copper plate ensures the surface temperature uniformity. Thanks to the insulating material on the rear side, the copper plate mainly exchanges with the surrounding environment both by convection and radiation. At equilibrium, by



**Figure 5.7.:** Device C: a HFM mounted on a piece of extruded polystyrene fixed on the wall (used in the DM2 method).

definition of  $T_{\text{op}}$ :

$$T_D = T_{\text{op}} \quad (5.12)$$

Then, Eq. 5.1 is used to derive  $h$  from the heat flux on the heated surface (Device B):

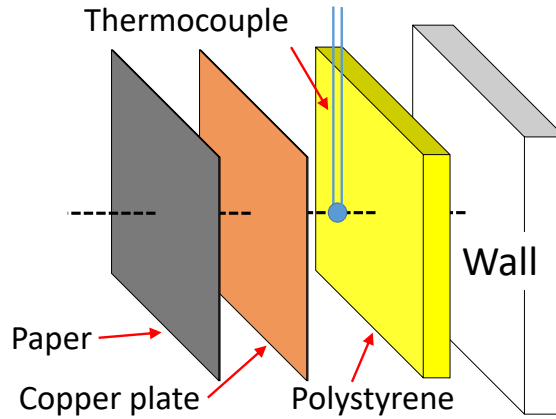
$$h = \frac{\varphi_B}{T_B - T_{\text{op}}} \quad (5.13)$$

Similarly to the DM2 method, the main advantage of this method is its simplicity. Unfortunately, it requires that the copper plate be at thermal equilibrium with the surrounding environment. This assumption is usually valid in steady-state. It is however less valid when the environment temperature conditions change by a few degrees in one hour, such as in our experiment in which the air is heated.

In addition, there is no guarantee in transient regimes that  $T_B - T_{\text{op}} \neq 0$  during the total duration of the experiment. Therefore, a linear regression is sometimes preferable than the division of Eq. 5.13.

### 5.3.5. Operative temperature measurement method 2 (OT2)

This method is a variation of the OT1 method and was developed in the scope of this thesis. The working principle is similar, but the way  $T_{\text{op}}$  is measured is different: Device E (see Fig 5.9) is used instead of Device D. Essentially, an active system allows compensating non equilibrium conditions when the environment temperature varies rapidly. As illustrated in Fig 5.9, a matrix of nine “Thermoelectric Coolers” (TEC, also referred as “Peltier modules”) is sandwiched between two  $200 \times 200 \text{ mm}^2$  aluminum plates of 1 mm thickness. The later are implemented to



**Figure 5.8.:** Device D: a thermocouple sandwiched between a copper plate and extruded polystyrene (used in the OT1 method).

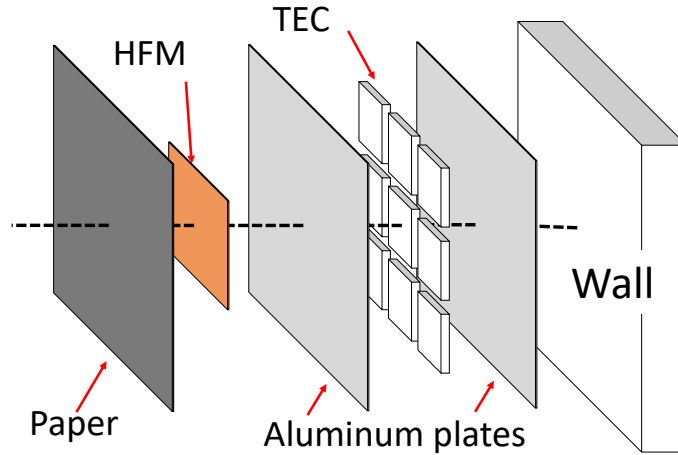
make the temperature uniform on either side of the device. This assembly, which is around 5 mm-thick, is fixed on the wall. A  $100 \times 100 \text{ mm}^2$  heat flux meter is placed on the front side. In practice, the feeding of the Peltier modules is live-controlled so that the surface heat flux  $\varphi_E$  is always null. If there is no heat flux on the surface of the device, it means that its temperature  $T_E$  is equal to the operative temperature  $T_{\text{op}}$ :

$$T_E = T_{\text{op}} \quad (5.14)$$

Therefore,  $T_{\text{op}}$  is directly given by the measurement of the device surface temperature. From this, Eq. 5.13 is used to obtain the  $h$  coefficient.

The voltage command  $U$  of the TECs is updated at every time step so that  $\varphi_E$  remains close to zero. The use of a PID controller was first considered. Unfortunately, the considered system taking  $U$  as input and  $\varphi_E$  as output is not invariant in time. Indeed, depending on the history of the system, its response will differ: if the temperature of the rear side changes, the required voltage to maintain  $\varphi_E = 0$  changes as well. Consequently, classical control systems are not applicable. Therefore, a simple iterative approach was retained. At every time step  $t_i$ ,  $\varphi_E$  is measured. If it is too high or too low (a threshold value  $\varphi_{\text{lim}} = 0.01 \text{ W.m}^{-2}$  is defined), the command  $U$  is incremented or decremented by a step  $\delta U$ :

$$\begin{cases} \varphi_E(t_i) < -\varphi_{\text{lim}} & : U(t_i) = U(t_{i-1}) + \delta U \\ -\varphi_{\text{lim}} < \varphi_E(t_i) < \varphi_{\text{lim}} & : U(t_i) = U(t_{i-1}) \\ \varphi_E(t_i) > \varphi_{\text{lim}} & : U(t_i) = U(t_{i-1}) - \delta U \end{cases} \quad (5.15)$$



**Figure 5.9.:** Device E: a HFM mounted on an array of Thermoelectric coolers fixed on the wall (used in the OT2 and HE methods).

### 5.3.6. Harmonic excitation measurement method (HE)

This last novel method was also developed during this thesis. A sinusoidal thermal load is applied to a surface. It uses another Device E (shown in Fig 5.9 and referred as device E' in Fig 5.2): a HFM mounted on TECs. This time, the thermoelectric coolers are fed with a sinusoidal electric signal so that they deliver a harmonic thermal power.

The operative temperature  $T_{op}$  is supposed to be constant for several oscillation periods. The temperature and heat flux are supposed measured exactly at the surface of the device. In the frequency domain (superscript  $\sim$  refers to complex harmonic notation), Eq 5.1 becomes:

$$\tilde{\varphi} = h\tilde{T} \quad (5.16)$$

where  $\tilde{\varphi} = \varphi - \bar{\varphi}$  with  $\bar{\varphi}$  the mean value during the few periods considered, similarly for  $\tilde{T}$ . The estimated heat transfer coefficient  $\hat{h}$  is simply given by:

$$\hat{h} = \Re \left( \frac{\tilde{\varphi}}{\tilde{T}} \right) = \frac{A_\varphi}{A_T} \cos(\zeta) \quad (5.17)$$

with  $\Re$  the real part operator,  $A_\varphi$  and  $A_T$  the heat flux and temperature amplitudes and  $\zeta$  the phase lag between the two signals. The  $h$  value is derived from the discrete Fourier transforms  $FT_T$  and  $FT_\varphi$  of the signals:

$$\hat{h} = \Re \left( \frac{FT_\varphi(k_f)}{FT_T(k_f)} \right) \quad (5.18)$$

## CHAPTER 5. MEASUREMENT OF WALL HEAT TRANSFER COEFFICIENT

---

with  $k_f$  the index of the harmonic corresponding to the excitation frequency  $f$ .

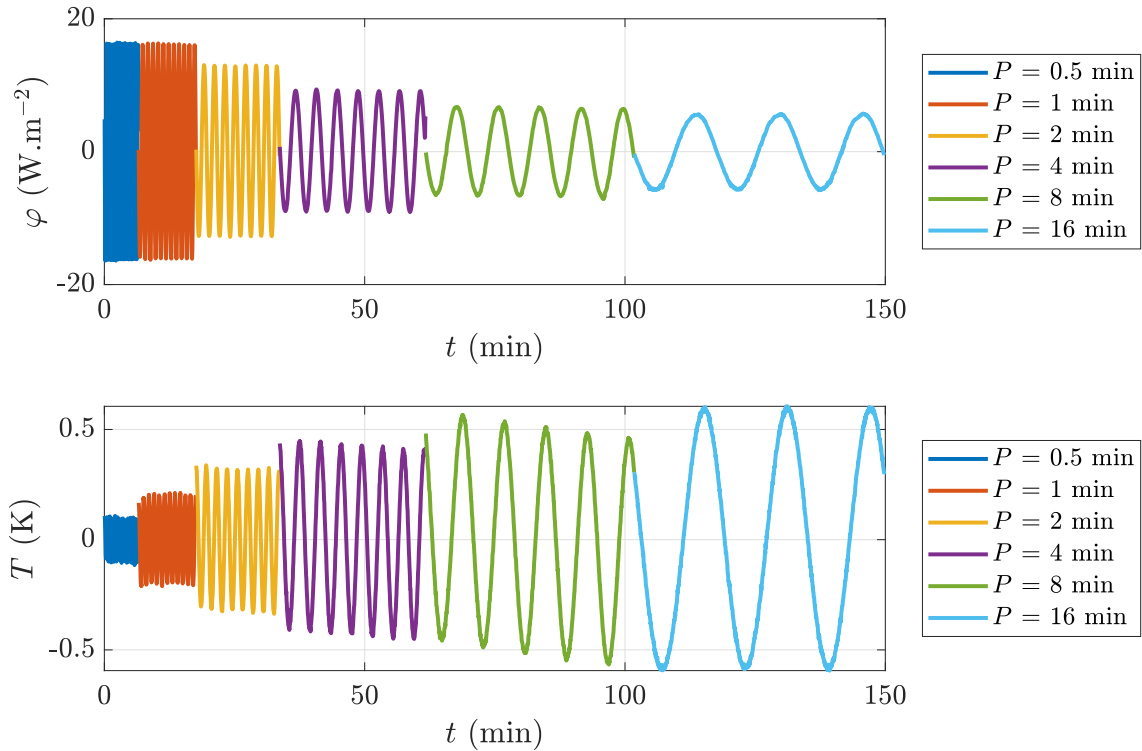
The best operating conditions for the use of this “ $h$ -meter” are determined from a dedicated study presented in the next section.

## 5.4. Focus on Harmonic Excitation method (HE)

For the harmonic method, the best working conditions were to be determined. This section focuses on the optimization of this specific method. Two parameters have to be adjusted: the period and the amplitude of the oscillations. In addition, a simple analytical model of the device is developed in order to better understand its behavior and the bias of the method. This study was presented in [174, 175].

### 5.4.1. Influence of the oscillation period

The oscillation period  $P$  is varied between 0.5 and 16 min during an indoor steady-state experiment. The applied voltage and the operating conditions are kept constant. The measured heat flux and temperature are plotted in Fig 5.10.

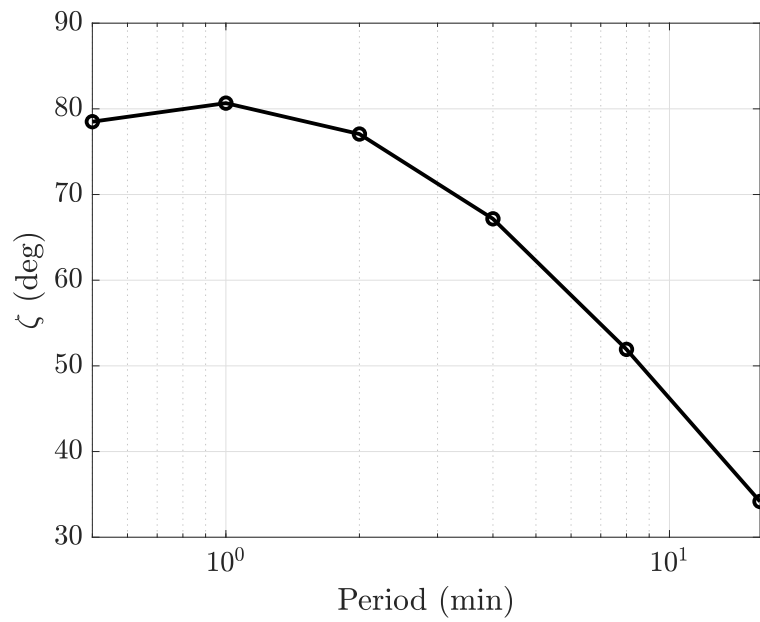


**Figure 5.10.:** Measured heat flux (up) and temperature (down) on  $h$ -meter surface for several oscillation periods (variations around mean value).

It may be noted that the higher  $P$ , the higher  $A_T$  and the smaller  $A_\varphi$ . In addition, as shown in Fig 5.11 the phase lag  $\zeta$  between  $\varphi$  and  $T$  increases as  $P$  decreases. At high frequencies,  $\zeta$  is even close to  $90^\circ$ . These observations are explained in more details in section 5.4.3. Finally, the impact of the period on the estimated heat transfer coefficient  $\hat{h}$  is presented in Fig 5.12.

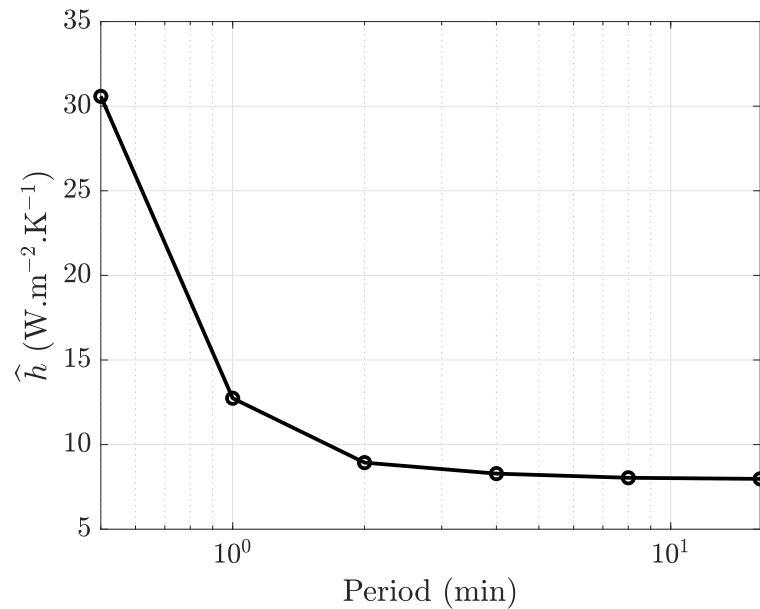
Thus, a too short period leads to significant over-prediction of the  $h$ -value (a value around  $7.7 \text{ W.m}^{-2}.\text{K}^{-1}$  is expected [99]). This is mainly due to the thermal inertias of the HFM and the aluminum plate which are neglected in the model. At high





**Figure 5.11.:** Influence of oscillation period on phase lag between  $\varphi$  and  $T$ .

frequency, these inertias have a strong impact on the phenomenon. On the other side, increasing the oscillation period above 5 min has almost no influence on the measured value. Therefore, the period of 5 min was retained.

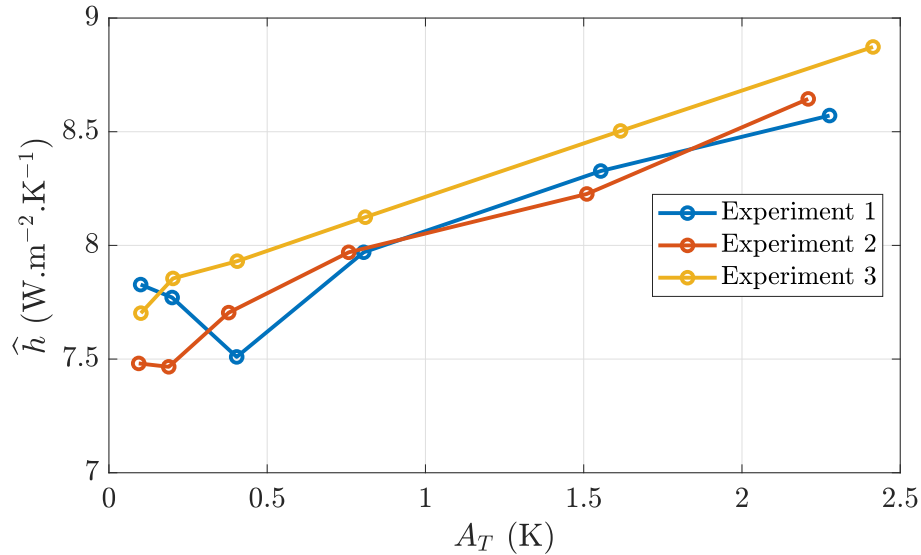


**Figure 5.12.:** Influence of oscillation period on estimated  $h$ -value.

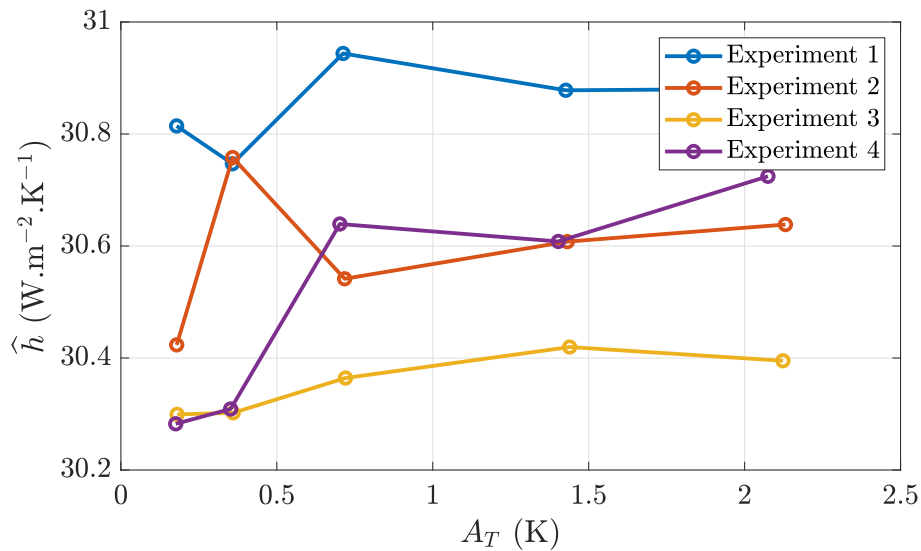
#### 5.4.2. Influence of the oscillation amplitude

To optimize the oscillation amplitude, the magnitude of the voltage supplied to the TEC was varied. Two configurations were tested: natural convection and forced

convection. For the second one, a fan was used. The impact of the amplitude of temperature oscillations on the estimated heat transfer coefficient is visible in figures 5.13 and 5.14. The experiments were repeated several times to assess the repeatability of the measurements.



**Figure 5.13.:** Measured  $h$ -coefficient according to the amplitude of temperature oscillations  $A_T$  in natural convection.



**Figure 5.14.:** Measured  $h$ -coefficient according to the amplitude of temperature oscillations  $A_T$  in forced convection.

A good reproducibility is noted in both configurations: the difference between the experiments are around 5 and 2% for the natural and forced convection cases respectively. In natural convection, the higher the temperature amplitude, the higher  $\hat{h}$ . This result is physical as in natural convection,  $h^c$  strongly depends on the temperature difference between the surface and the fluid. Nevertheless, for the “ $h$ -meter” to be less intrusive as possible (does not locally change  $h$ ),  $A_T$  should be small. It

may be noted that  $\hat{h}$  is almost constant (between  $7.5$  and  $8 \text{ W}\cdot\text{m}^{-2}\cdot\text{K}^{-1}$ , depending on the experiment) when  $A_T$  is below  $0.5 \text{ K}$ . In forced convection however,  $\hat{h}$  does not depend on the amplitude, which is also physical. The estimated value is much higher: around  $30.5 \text{ W}\cdot\text{m}^{-2}\cdot\text{K}^{-1}$ . Therefore, for the measurement to be accurate in any situation, the oscillations of the temperature should remain below  $0.5 \text{ K}$ . As a consequence, the power supplied to the TECs was set such that the temperature amplitude was close to  $0.3 \text{ K}$ .

### 5.4.3. Theoretical model

In order to justify some of the tendencies observed, a simple analytical model of the  $h$ -meter was developed. Basically, the measured temperature and heat flux are not exactly the one on the surface of the device. Indeed, the HFM is located below some adhesive tape (useful to increase its emissivity) and the HFM itself is covered with a copper sheet. These layers introduce a bias in the measurement of surface quantities despite their very small thicknesses. As shown in Fig 5.15, they are modeled here as a unique layer of thermal resistance  $R$  and capacity  $C$ .

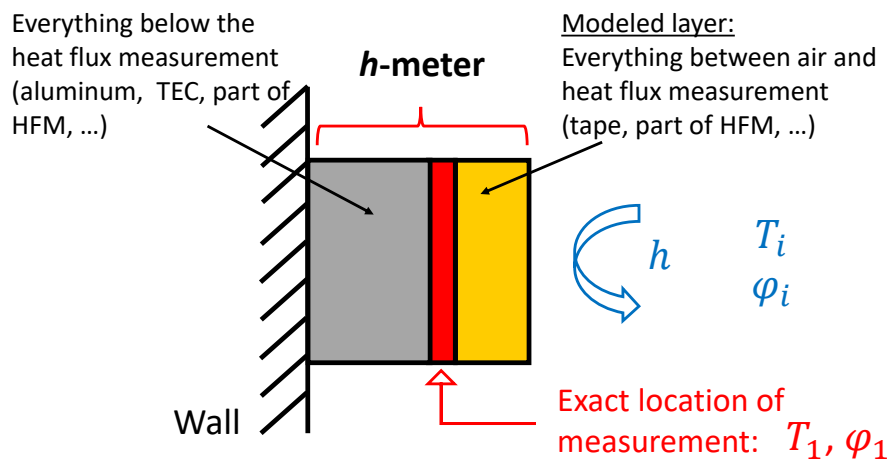


Figure 5.15.: Simplified scheme of the  $h$ -meter.

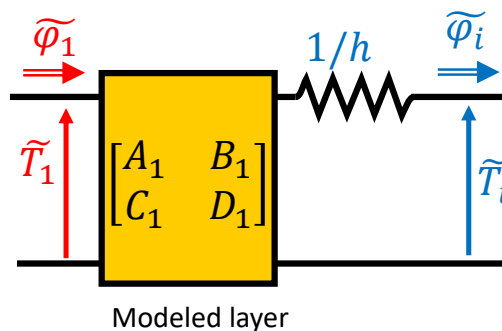


Figure 5.16.: Electrical analogy of the modeled layer.

The problem is modeled in the frequency domain with the thermal quadrupole formalism [191] (see electrical analogy in Fig 5.16):

$$\begin{bmatrix} \widetilde{T}_1 \\ \widetilde{\varphi}_1 \end{bmatrix} = \begin{bmatrix} A_1 & B_1 \\ C_1 & D_1 \end{bmatrix} \times \begin{bmatrix} 1 & 1/h \\ 0 & 1 \end{bmatrix} \times \begin{bmatrix} \widetilde{T}_i \\ \widetilde{\varphi}_i \end{bmatrix} \quad (5.19)$$

with

$$\begin{bmatrix} A_1 & B_1 \\ C_1 & D_1 \end{bmatrix} = \begin{bmatrix} \cosh(\sqrt{j2\pi fRC}) & \sinh(\sqrt{j2\pi fRC}) / \sqrt{j2\pi fC/R} \\ \sinh(\sqrt{j2\pi fRC}) \times \sqrt{j2\pi fC/R} & \cosh(\sqrt{j2\pi fRC}) \end{bmatrix} \quad (5.20)$$

with  $j$  the imaginary number such that  $j^2 = -1$ . The cut-off frequency  $1/(2\pi RC)$  was roughly estimated to 0.5 Hz (for 0.2 mm of adhesive tape of thermal conductivity  $0.1 \text{ W}\cdot\text{m}^{-1}\cdot\text{K}^{-1}$  and diffusivity  $0.13 \times 10^{-6} \text{ m}^2\cdot\text{s}^{-1}$ ) which is two orders of magnitude above the oscillation frequency. Then, Eq 5.20 is simplified to:

$$\begin{bmatrix} A_1 & B_1 \\ C_1 & D_1 \end{bmatrix} \xrightarrow{f \rightarrow 0} \begin{bmatrix} 1 & R \\ j2\pi fC & 1 \end{bmatrix} \quad (5.21)$$

The indoor air temperature is supposed constant:  $\widetilde{T}_i = 0$ . It comes the admittance:

$$Y = \frac{\widetilde{\varphi}_1}{\widetilde{T}_1} = \frac{D_1 h + C_1}{A_1 + hB_1} \xrightarrow{f \rightarrow 0} \frac{h + j2\pi fC}{1 + hR} \quad (5.22)$$

Hence

$$\|Y\| \simeq \frac{\sqrt{h^2 + 4\pi^2 f^2 C^2}}{1 + hR} \quad (5.23)$$

$$\zeta \simeq \text{atan}\left(\frac{2\pi fC}{h}\right) \quad (5.24)$$

and, given that  $hR \ll 1$ :

$$\hat{h} = \Re(Y) \simeq \frac{h}{1 + hR} \simeq h - h^2 R \quad (5.25)$$

Eq 5.24 proves that the phase lag  $\zeta$  between the measured quantities  $T_1$  and  $\varphi_1$  increases with the oscillation frequency, and therefore decreases with the period, as noted in Fig 5.11. As seen in Eq 5.25, the thermal resistance  $R$  of the small layer between the measurement location and the air introduces a negative bias on  $\hat{h}$  that increases linearly with  $R$  and quadratically with  $h$ . Eq 5.23 shows that the higher thermal capacity  $C$  of the layer, the higher  $\|Y\| = A_\varphi/A_T$  which increases the measurement uncertainties (see Eq 5.29 in the next section).

## 5.5. Uncertainty calculations

For each method described in section 5.3, the measurement uncertainties are calculated. According to the GUM (Guide to the expression of uncertainty in measurements, [192]), measurement uncertainty components should be grouped into two categories: type-A and type-B. Type-A uncertainties are evaluated by statistical methods whereas type-B ones are evaluated otherwise. For each measurement method, both types of uncertainties are estimated in order to work out the combined uncertainty:

$$u = \sqrt{u_{\text{type-A}}^2 + u_{\text{type-B}}^2} \quad (5.26)$$

### 5.5.1. Type-A uncertainty

The type-A uncertainty is founded on statistical distribution.

First, the DM2 and OT2 methods are based on a linear regression  $Y = h \times X + b$  in which the slope is the desired  $h$ -value.  $X$  is a temperature difference while  $Y$  is either a heat flux (OT2 method) or a heat flux difference (DM2 method). The statistical uncertainty on the slope obtained by linear regression is commonly given by [193]:

$$u(h) = \frac{1}{\sqrt{N}} \frac{u(Y)}{\text{Var}(X)} \quad (5.27)$$

with  $N$  the number of points,  $u(Y)$  the standard deviation of the noise on the  $Y$  vector and  $\text{Var}(X)$  the statistical variance of the  $X$  vector. Yet, this common equation supposes that  $X$  is perfectly known which is not the case in our application. Indeed, both  $Y$  and  $X$  are measured quantities. Equation 5.27 may be modified to include the standard deviation  $u(X)$  of the noise on  $X$  [193]:

$$u(h) = \frac{1}{\sqrt{N}} \frac{\sqrt{u^2(Y) + h^2 u^2(X)}}{\text{Var}(X)} \quad (5.28)$$

Second, the HE method is based on Fourier transforms of signals. The calculation of the uncertainty on  $h$  in this situation is detailed in Appendix B.1. Calculations lead to:

$$u(h) = \frac{1}{A_T} \sqrt{u^2(A_\varphi) + \left(\frac{A_\varphi}{A_T}\right)^2 u^2(A_T)} \quad (5.29)$$

with  $A_T$  and  $A_\varphi$  the temperature and heat flux amplitudes,  $u(A_T)$  and  $u(A_\varphi)$  their corresponding uncertainties. The amplitudes are worked out from the Fourier transform harmonic corresponding to the excitation frequency:

$$A_T = |FT_T(k_j)| \quad (5.30)$$

The uncertainties are given by the noise on the other harmonics:

$$u^2(A_T) = \text{Var}(FT_T(k_j))|_{k \neq k_j} \quad (5.31)$$

Similarly with  $\varphi$ .

### 5.5.2. Type-B uncertainty

In this case, type-B uncertainties correspond to systematic errors. Let  $\alpha$  be the desired quantity, function of  $m$  parameters  $\beta_1, \dots, \beta_m$ . The propagation law [192] relates the uncertainty over  $\alpha$  to the ones of the  $\beta_i$ :

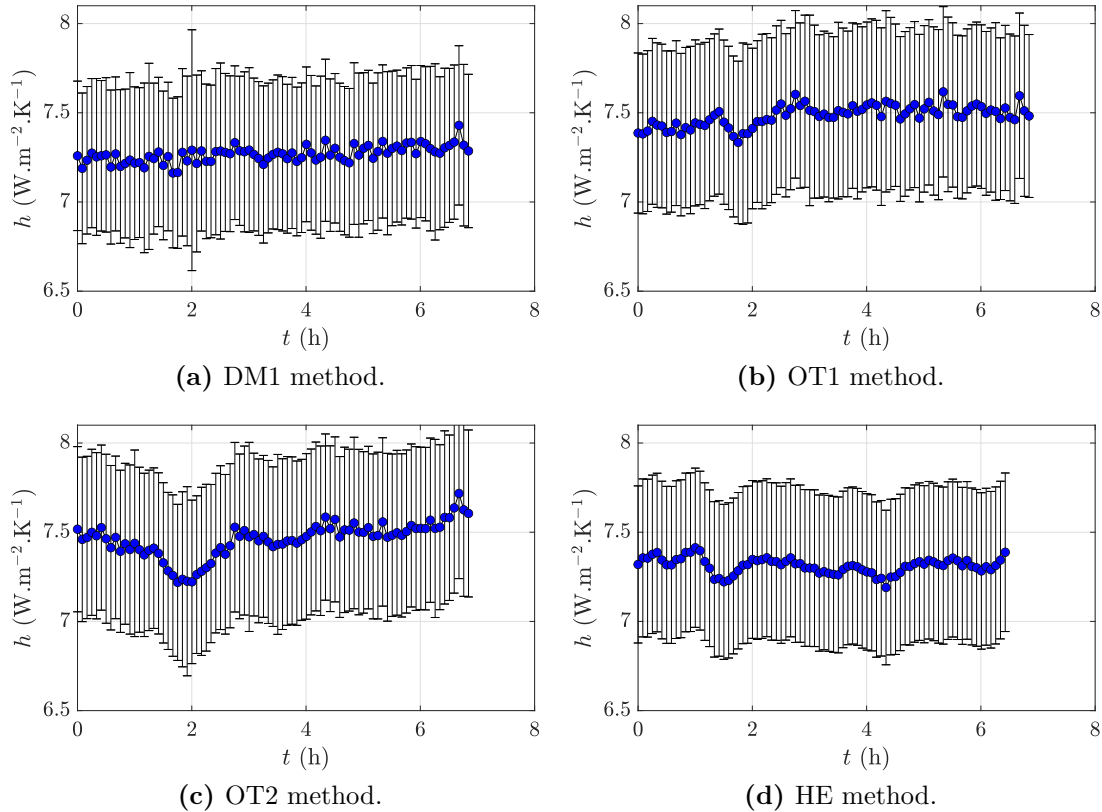
$$u(\alpha) = \sqrt{\sum_{i=1}^m \left( \frac{\partial \alpha}{\partial \beta_i} u(\beta_i) \right)^2} \quad (5.32)$$

According to the HFM manufacturer, heat fluxes are measured with an uncertainty of 3%. In addition, the measured temperature differences are given with an accuracy of 0.03 K (see Chap 3). This value originates in the Seebeck coefficients used to convert voltage in temperature.

## 5.6. Results

### 5.6.1. Steady-state results

First, results obtained in pseudo-steady-states are given here (the air heaters are not used). The measurements presented were made indoor during an afternoon of July 2018 in Créteil, France. The internal air temperature measured close to the wall was constant around  $28.1^{\circ}\text{C}$  during the whole duration of the experiment. All  $h$ -measurement devices are implemented simultaneously on the experimental wall. The DM2 method is not used here as the temperature gradient between the two sides of the wall is not high enough in steady-state to generate a sufficient temperature difference between the wall and device C. A representative sample of the results are given in Figures 5.17a to 5.17d. The evolution of the measured  $h$ -value for 7 hours is plotted with uncertainty bars. The mean values are summarized in Tab 5.1.



**Figure 5.17.:** Steady-state  $h$  measurements.

Basically, every method predicts a similar  $h$ -coefficient, close to the  $7.7 \text{ W.m}^{-2}.\text{K}^{-1}$  standard value from standards ISO 14683 [18] and ISO 6946 [99]. The maximum discrepancy between the methods is around  $0.2 \text{ W.m}^{-2}.\text{K}^{-1}$ , which is lower than the uncertainty of each method separately. This calculated uncertainty is almost independent of the method used. This is because the type-A uncertainty is here almost negligible with respect to the type-B uncertainty (measurements are issued from averages over a large amount of points).

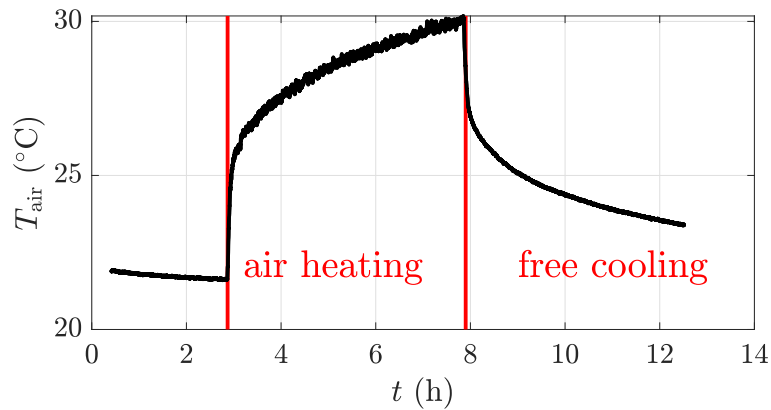
**Table 5.1.:** Summary of steady-state  $h$ -coefficient measurements.

Method	$h$ ( $\text{W}\cdot\text{m}^{-2}\cdot\text{K}^{-1}$ )
DM1	$7.27 \pm 0.41$
DM2	not applicable
OT1	$7.48 \pm 0.45$
OT2	$7.46 \pm 0.45$
HE	$7.31 \pm 0.44$

It may be observed that the OT1 and OT2 methods lead to very close estimates of  $h$ . This confirms that the two ways of measuring the operative temperature  $T_{\text{op}}$  are equivalent in steady-state conditions. Indeed, the voltage applied to the thermoelectric coolers in the OT2 methods was almost null throughout the experiment. Therefore, the active compensation was not needed to maintain the surface heat flux equal to zero and the environment temperature sensor from ISO 9869-2 standard [102] is sufficient.

### 5.6.2. Transient results

The electrical heaters are here turned on for 5 h and then turned off. Figure 5.18 plots the air temperature evolution. The air temperature rises by about 8 K. It is important to point out at this stage that the measurement noise is much more important when the heaters are turned on, especially for heat flux measurements. This noise is less due to the acquisition hardware than the air turbulence induced by the electric fan heaters. The following paragraphs present results for each  $h$ -measurement method.

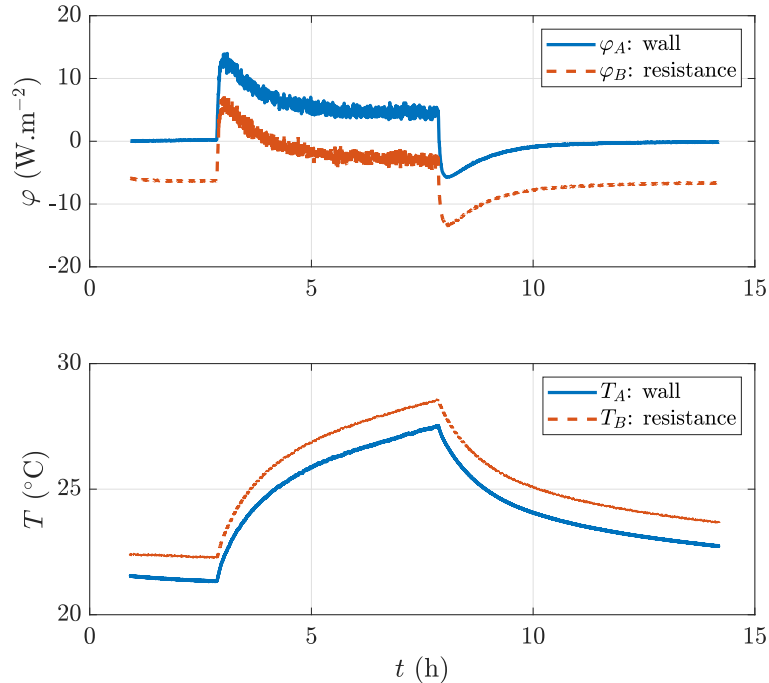
**Figure 5.18.:** Evolution of the air temperature, measured 15 cm away from the wall.

#### 5.6.2.1. DM1 method

The heat fluxes and temperatures measured on surfaces A and B are shown in Fig 5.19. Thanks to the heating resistance, temperature  $T_B$  is always greater than



$T_A$ . In addition,  $\varphi_A > \varphi_B$  given the chosen convention (a positive heat flux enters the wall). The air heating and free-cooling phases are clearly visible in the measurements (between hour 3 and hour 8 and after hour 8, respectively).



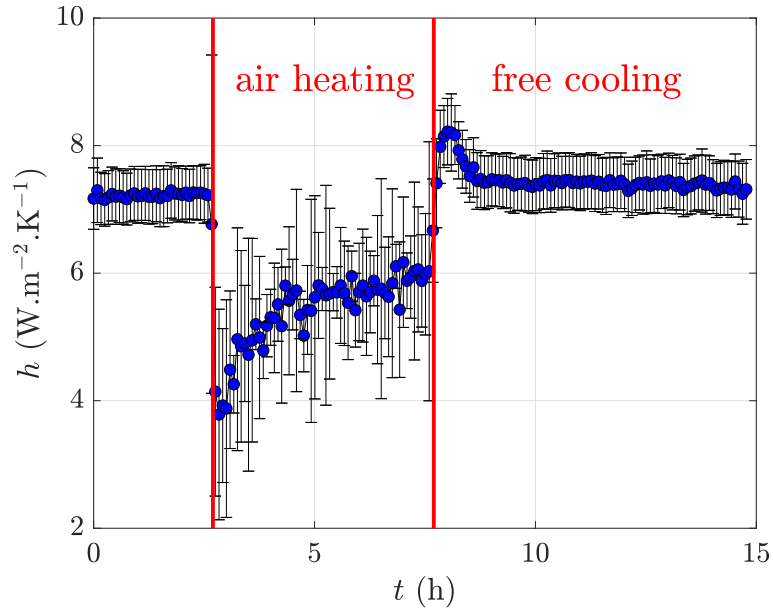
**Figure 5.19.:** DM1 method: surface heat flux and temperature measurements.

Figure 5.20 plots the calculated  $h$ -values (see Eq 5.10) as a function of time. Each point is obtained from temperatures and heat fluxes averaged over 5 min. Because of the very high noise level on heat fluxes during the heating period, the uncertainties are larger than during the free-cooling phase. Surprisingly, the measured  $h$ -value is also smaller, especially just after the heaters are turned on. This observation might be explained by the sign of heat flux  $\varphi_B$ : it is negative before the heating phase, becomes positive at the beginning of it and comes back negative about an hour later. These heat flux inversions could alter the results as convective heat transfers may be different when the surface is either heated or cooled by the air.

### 5.6.2.2. DM2 method

Similarly, measured heat fluxes and temperatures on surfaces A and C are given in Fig 5.21. Because the wall and the piece of polystyrene have a different effusivity, they also have a different thermal response when heated by the air. Indeed, the insulated material heats up and cools down faster than the wall. The heat flux that enters it is consequently smaller.

As shown in Figures 5.22a and 5.22b, plotting the heat flux difference  $\Delta\varphi$  against the temperature difference  $\Delta T$  during each phase gives a straight line of slope  $h$ . This confirms that  $h$  may be considered constant during each period. It is also greater during the first one, unlike predictions from the DM1 method. As already



**Figure 5.20.:** DM1 method: measured  $h$ -coefficient against time.

pointed out, there is much more noise when the heaters are on than off. It may also be observed that the density of points is not uniform: the smaller the  $\Delta T$ , the higher the density. Therefore, a classic linear regression would favor low  $\Delta T$  measurements and would not necessarily be aligned with the few high  $\Delta T$  points. This issue was fixed by applying weights to the points. These weights are inversely proportional to the point density (estimated by evenly discretizing the  $\Delta T$  axis and counting the number of points present in each section).

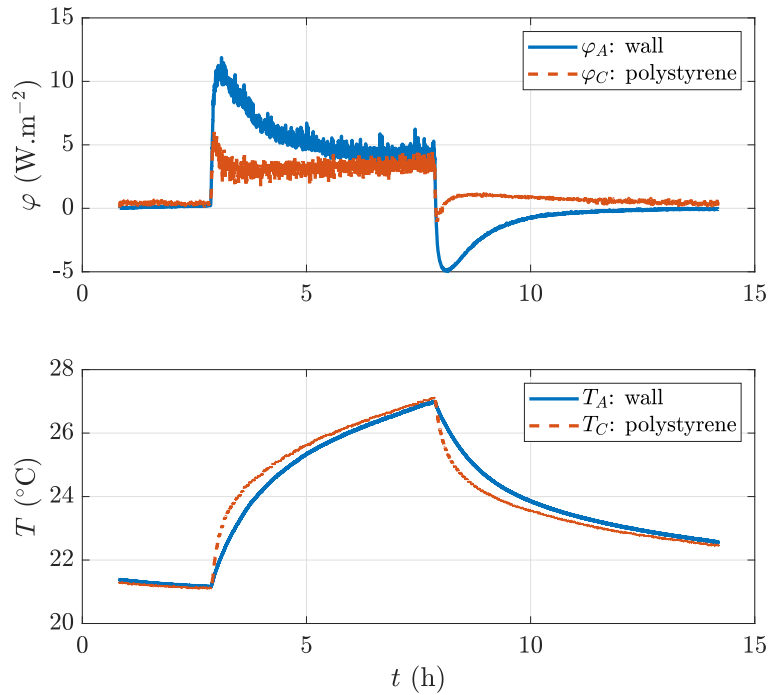
### 5.6.2.3. OT1 method

This method was not able to measure the  $h$ -coefficient in transient regime. Indeed, device C needs to be at thermal equilibrium to perform a proper measurement of the operative temperature  $T_{\text{op}}$ . With a biased measurement of  $T_{\text{op}}$ , the application of Eq. 5.13 leads to highly non-physical results. The different measured  $T_{\text{op}}$  are presented in more details in the following paragraph (see Fig 5.24).

### 5.6.2.4. OT2 method

The first graph in Fig 5.23 plots the heat fluxes  $\varphi_A$  and  $\varphi_E$  measured on the wall and on the device E.

As desired,  $\varphi_E$  remains null during the experiment even though the room air is heated. The second graph displays the evolution of the voltage  $U$  applied to the thermoelectric coolers enclosed inside the device. In the chosen convention, a negative voltage corresponds to a heating of the front surface. At the beginning of the experiment, the room is globally at thermal equilibrium (pseudo steady-state), hence  $U \approx 0\text{V}$ . When the air temperature suddenly increases, the surface temperature of the zero-flux device has to increase as well in order to ensure  $\varphi_E = 0$ ,



**Figure 5.21.:** DM2 method: surface heat flux and temperature measurements.

the TECs feeding voltage is negative. During the free-cooling period, the opposite trend is observed: the device front surface has to be cooled down to follow the decrease in the air temperature so  $U > 0$ . The rear face of the device is therefore heated. Unfortunately, because it is directly fixed on the wall, the heat generated by the TECs cannot be rapidly dissipated. The system then diverges as  $U$  has to be constantly increased to compensate for the rear face temperature elevation. As shown in Fig 5.23, between the 9<sup>th</sup> and 10<sup>th</sup> hours of experiment, the voltage sharply increases until it reaches the safety limit set to 3 V. Consequently, the design of the zero-flux device should be modified in order to dissipate the heat generated on its rear side and enable longer measurements of  $T_{\text{op}}$  during the free-cooling phase.

Figure 5.24 displays the measured temperatures. The air temperature  $T_{\text{air}}$  measured with a thermocouple near the device is also plotted. These results are shown to illustrate the fact that the usual assumption  $T_{\text{op}} = T_{\text{air}}$  in indoor building conditions does not hold true in highly transient conditions like the present one. For instance, during the heating period,  $T_{\text{env}}$  is significantly lower than  $T_{\text{air}}$  because the surface temperature of the surrounding objects is smaller thanks to their inertia which reduces  $T_{\text{op}}$ .

Similarly to the DM2 method, the wall heat flux  $\varphi_A$  is plotted against the temperature difference  $\Delta T = T_A - T_E$  (see Figures 5.25a and 5.25b). Despite the measurement noise (especially during the heating period), a straight line can again be fitted on the experiment to retrieve the  $h$ -coefficient value. Again, according to this method,  $h$  is slightly greater during the first phase.

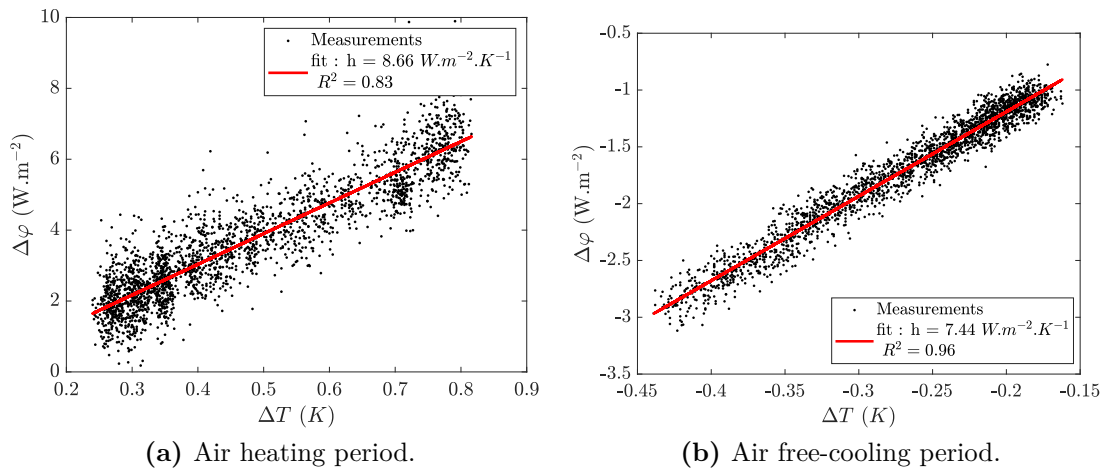
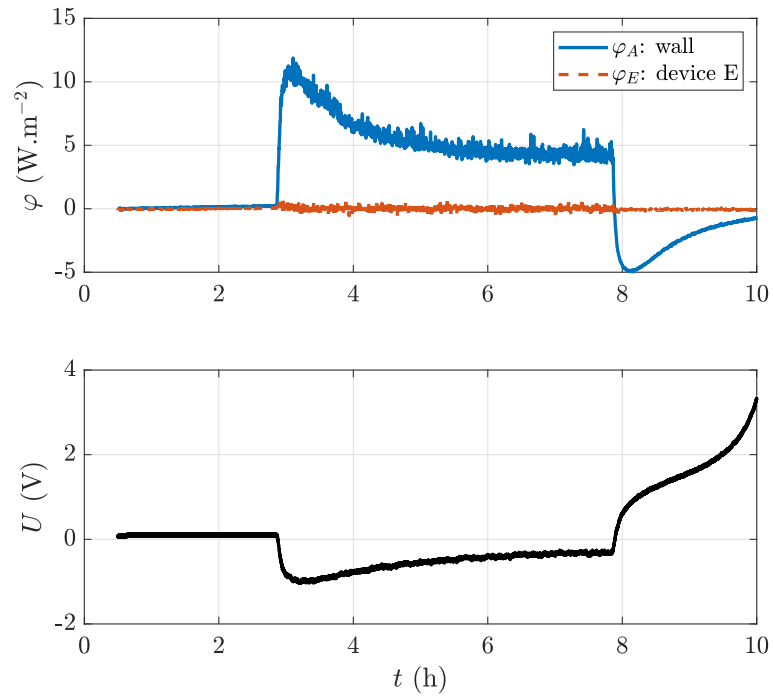


Figure 5.22.: DM2 method: linear regressions.

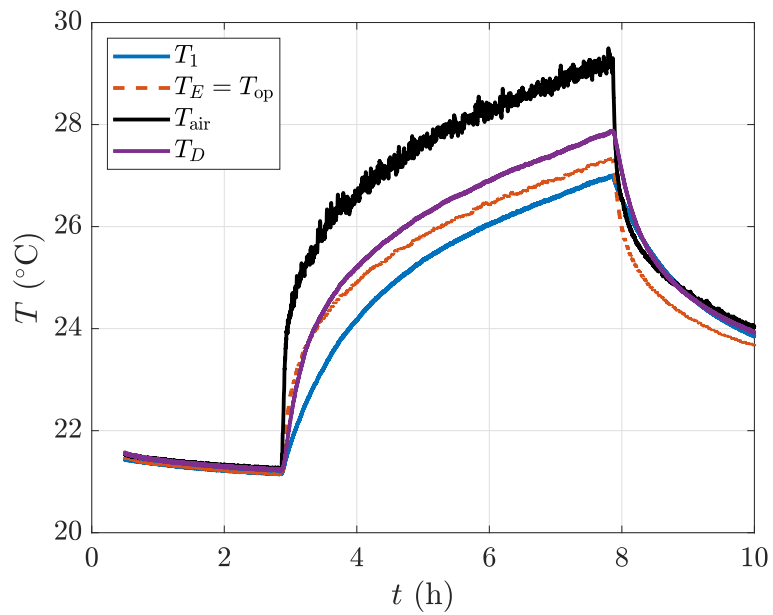
### 5.6.2.5. HE method

The heat flux and temperature measured on the Harmonic device (Device E) are plotted over a few oscillation periods of the heating phase in Fig 5.26, and of the cooling phase in Fig 5.27. As expected, the signal to noise ratio is better on signals in Fig 5.27, especially for the heat flux.

The measured  $h$  coefficients are plotted in Fig 5.28 along with error bars. Each point corresponds to an analysis over 6 consecutive periods. With this method, the measured  $h$  coefficient is higher during the heating period than during the free-cooling one. At the very beginning of each phase, there is a sharp increase or decrease of the calculated  $h$ -value. This result is not physical. It is due to a fast modification of the operative temperature: among the 6 consecutive periods used for the analysis, the first ones belong to a regime different from the last ones. Thus, for the measurement to be accurate, one should pay attention to avoid fast varying conditions.



**Figure 5.23.:** OT2 method: measured surface heat fluxes and TEC voltage command.



**Figure 5.24.:** OT2 method: comparison of measured temperatures.

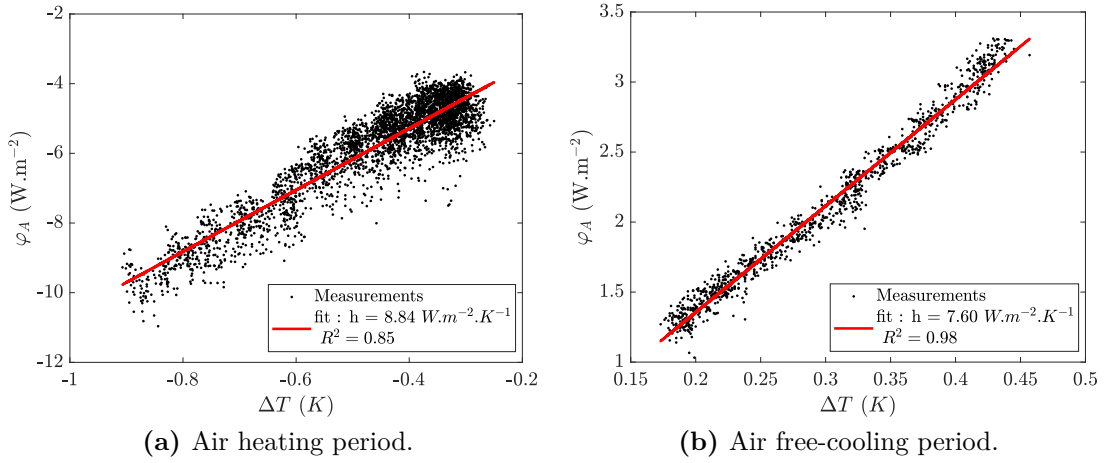


Figure 5.25.: OT2 method: linear regressions.

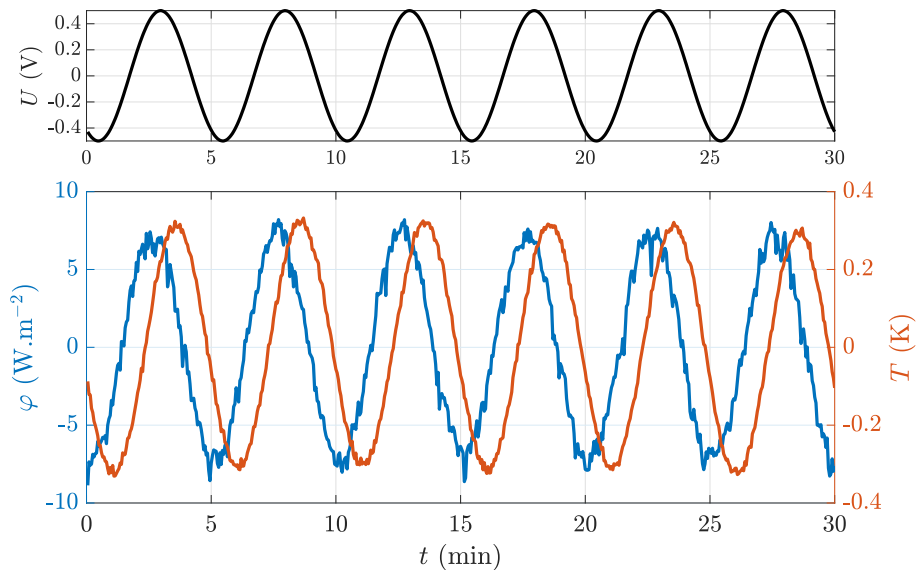


Figure 5.26.: HE method: air heating phase.

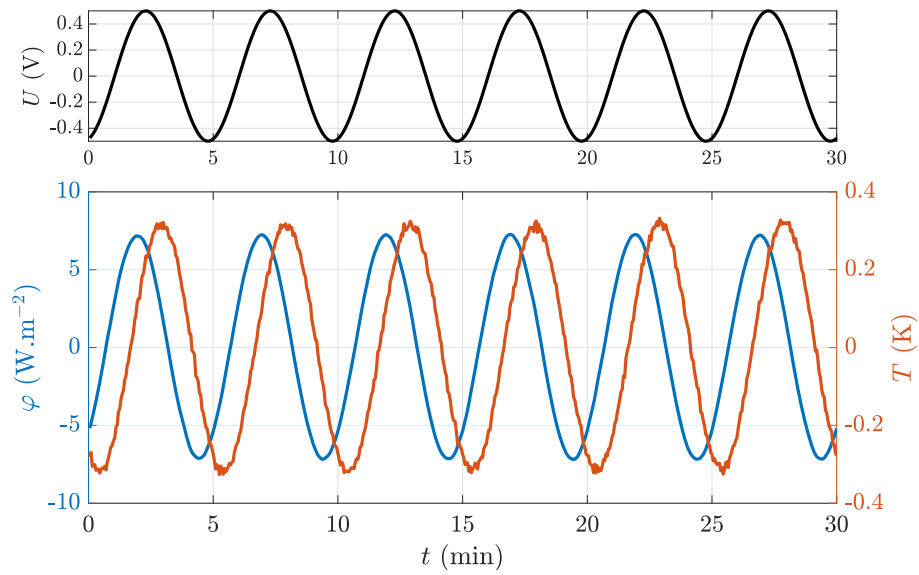


Figure 5.27.: HE method: air free-cooling phase.

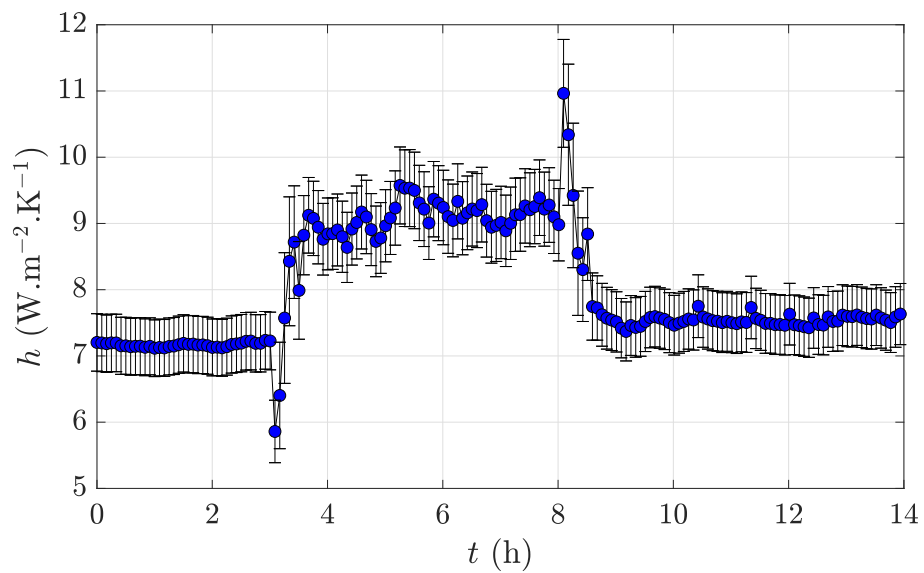
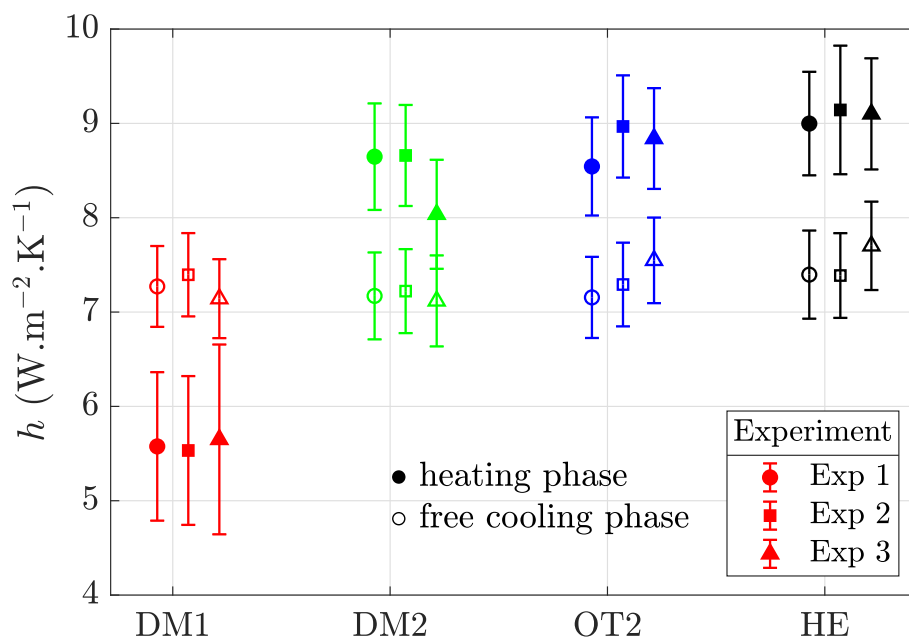


Figure 5.28.: HE method: measured  $h$ -coefficient value against time.

## 5.7. Discussion

### 5.7.1. Comparison of methods

To test the methods repeatability, the same experiment was repeated three times. The electrical heaters were turned on for 5 hours. The resulting measured  $h$ -coefficients are plotted in Figure 5.29 for both the heating and the cooling periods. For the sake of brevity, only one  $h$  value per period is retained for each method (the mean value over the period). No result from the OT1 method is provided since it proved to be only applicable in steady-state. The results are also summarized in Tab 5.2.



**Figure 5.29.:** Comparison of  $h$  measurement methods: heating period (full markers) and free-cooling period (empty markers). The colors correspond to the methods.

**Table 5.2.:** Summary of measured heat transfer coefficients ( $\text{W}\cdot\text{m}^{-2}\cdot\text{K}^{-1}$ ).

		DM 1	DM 2	OT 2	HE
Heating period	Exp 1	$5.6 \pm 0.8$	$8.6 \pm 0.6$	$8.5 \pm 0.5$	$9.0 \pm 0.5$
	Exp 2	$5.5 \pm 0.8$	$8.6 \pm 0.5$	$9.0 \pm 0.5$	$9.1 \pm 0.7$
	Exp 3	$5.6 \pm 1.0$	$8.6 \pm 0.6$	$8.8 \pm 0.5$	$9.1 \pm 0.6$
Free cooling period	Exp 1	$7.3 \pm 0.4$	$7.2 \pm 0.5$	$7.2 \pm 0.4$	$7.4 \pm 0.5$
	Exp 2	$7.4 \pm 0.4$	$7.2 \pm 0.4$	$7.3 \pm 0.4$	$7.4 \pm 0.4$
	Exp 3	$7.1 \pm 0.42$	$7.1 \pm 0.5$	$7.5 \pm 0.5$	$7.7 \pm 0.5$

First, the measurement spread is globally more important during the heating phase. This is because of the higher noise on the heat flux measurements. Moreover, the uncertainties for the DM1 method are noticeably higher (about twice as big) when



the heaters are on. The uncertainties given by the other methods are not significantly affected by the noise level. This is explained by the fact that, in the current configuration, the type-A uncertainty is very small (typically  $0.2 \text{ W.m}^{-2}.\text{K}^{-1}$ ) compared to the type-B one (typically  $0.45 \text{ W.m}^{-2}.\text{K}^{-1}$ ) while only type-A uncertainty takes the noise into account. The linear fits of the DM2 and OT2 methods are based on a high number of points (around 2000 in general) which reduces the statistical uncertainty given by Eq 5.28. In addition, with the HE method, the amplitude of the modulated heat flux is higher than other heat fluxes measured. The signal to noise ratio is therefore much higher, even during the heating period.

As seen in Fig 5.29, all methods lead to similar results during the free-cooling period. Interestingly, the measured  $h$ -coefficients are close to the  $7.7 \text{ W.m}^{-2}.\text{K}^{-1}$  default value given by ISO standard 14683 [18] for indoor conditions. This result was to be expected because the free-cooling phase is close to standard heat exchange conditions encountered in buildings. In this particular configuration, using the standard value or the result of a measurement makes little difference. However, the proposed approach has the advantage of quantifying the uncertainty, while the standard value is given without any confidence interval.

The average measured  $h$ -coefficient of the heating period is higher, around  $8.5 \text{ W.m}^{-2}.\text{K}^{-1}$  for the DM2 and OT2 methods and even higher with the HE one: around  $9 \text{ W.m}^{-2}.\text{K}^{-1}$ . The DM1 method differs from the other ones as it surprisingly predicts a lower  $h$ -value: around  $5.5 \text{ W.m}^{-2}.\text{K}^{-1}$ . Given that the other methods gave satisfactory results, no further investigation was conducted to understand the reasons of this apparently non-physical result.

As a conclusion, the DM1 and OT1 methods are not able to measure the  $h$ -coefficient in transient regimes in which the air is heated. The HE methods leads to a small over-estimation during the heating period.

### 5.7.2. Comparison to empirical correlations

The measurements are compared to predictions from two empirical correlations of  $h^c$  for vertical natural convection problems from the literature. The convective heat transfer coefficient may be derived from the dimensionless Nusselt number  $Nu_x$ :

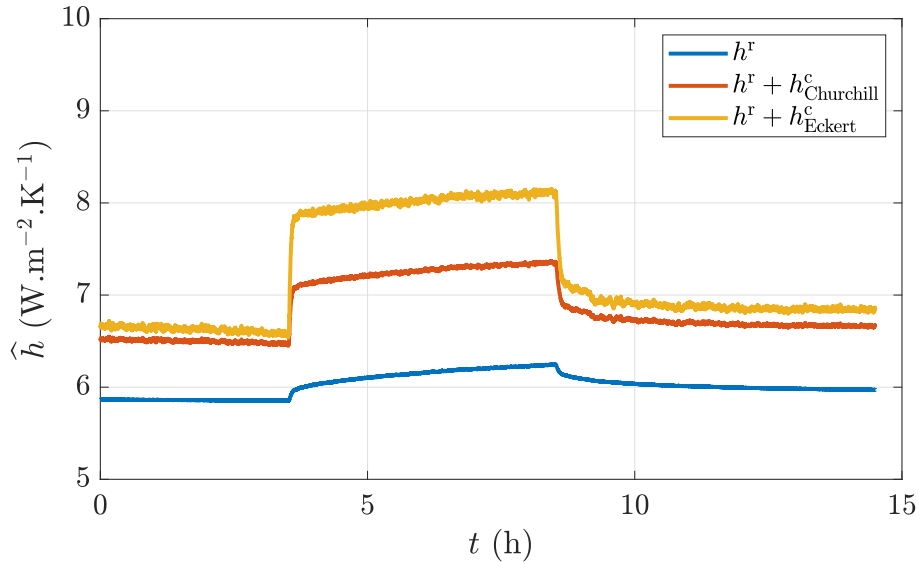
$$h^c = Nu_x \times \frac{\lambda}{x} \quad (5.33)$$

with  $x$  the characteristic dimension of the problem (here the altitude) and  $\lambda$  the air thermal conductivity. The empirical correlations are given as follows:

$$Nu_x = 0.0295 \frac{Pr^{1/15}}{(1 + 0.494Pr^{2/3})^{2/5}} Ra_x^{2/5} \quad (\text{Eckert [170]}) \quad (5.34)$$

$$Nu_x = 0.68 + \frac{3}{4} \times 0.515 \times Ra_x^{1/4} \quad (\text{Churchill [164]}) \quad (5.35)$$

with  $Pr = \frac{\nu}{a}$ ,  $Ra = \frac{g \cdot \beta \cdot \Delta T \cdot x^3}{\nu^2} Pr$ , respectively the Prandtl and Rayleigh numbers,  $\nu$ ,  $a$  the kinematic viscosity and thermal diffusivity respectively,  $g$  the gravity acceleration,  $\beta = 1/T_{\text{air}}$  the air expansion coefficient (modeled as an ideal gas) and  $\Delta T = T_{\text{air}} - T_{\text{wall}}$ . The combination of measured temperatures (see Fig 5.4), equations 5.34, 5.35 (for  $h^c$ ) and 5.4 (for  $h^r$ ) lead to the estimated  $\hat{h}$ -value plotted in Fig 5.30.



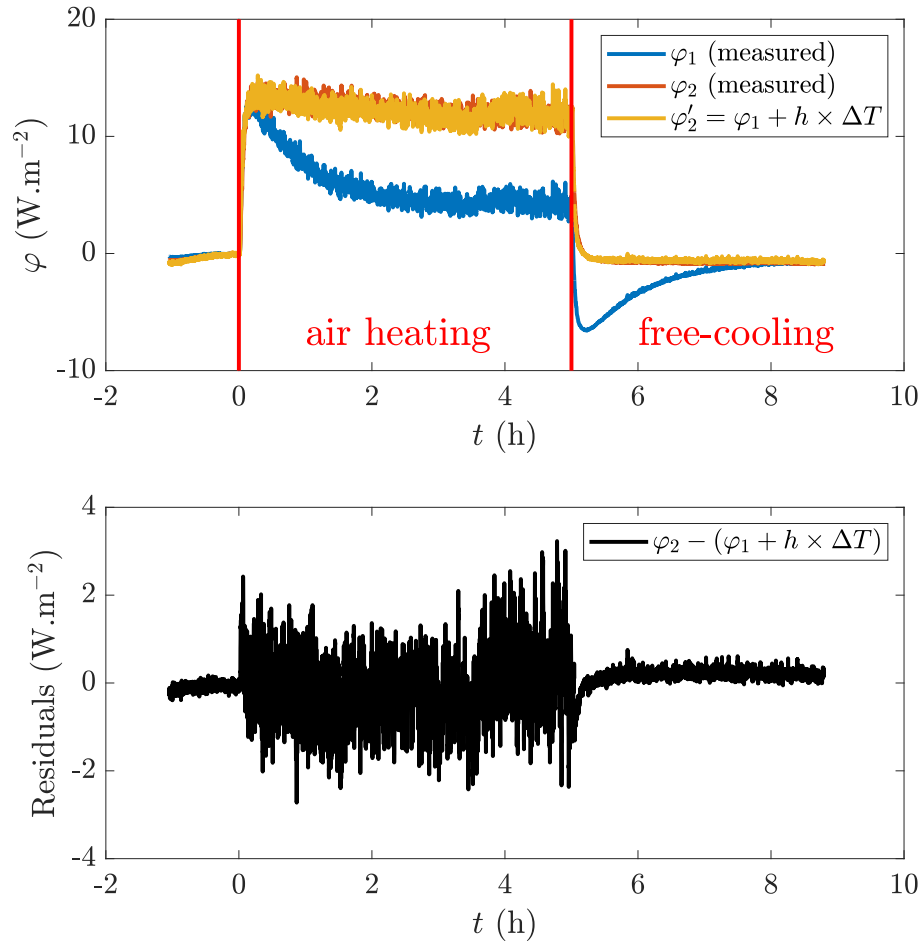
**Figure 5.30.:** Estimated  $h$ -value from empirical correlations.

It may be noticed that the two tested correlations both under-predict  $h$  but also give results that are very different from each other, especially during the heating phase. This is an illustration of the limitations of empirical correlations: they were developed in laboratory conditions that are not always representative of *in situ* conditions. For instance, they were developed for a uniform temperature or heat flux. In particular, the air movements induced by the heaters probably turns the natural convection into mixed convection.

### 5.7.3. Heat flux reconstruction

As explained in the introduction, the measurement of the global  $h$  coefficient enables to extrapolate the heat flux measured on a zone 1 to a nearby zone (see Eq 5.5). An example of a heat flux reconstruction is shown in Fig 5.31. In this example, the  $h$  value measured by the DM2 method was used. The  $h$  coefficient is considered constant within each period (air heating and free cooling). The measured and reconstructed heat fluxes  $\varphi_2$  and  $\varphi'_2$  are rather well superimposed. The residuals, that is to say the difference  $\varphi_2 - \varphi'_2$ , are plotted in the second graph of Fig 5.31. They are rather well centered around zero and almost not signed. In addition, their magnitude is equal to the noise level (which is significantly higher during the heating phase). A little bias is observed at the beginning of the free-cooling period. This is induced by the simplified approach of considering  $h$  constant.

As a consequence, it is possible to reconstruct the measured heat flux on a zone 2 from contact measurements on a zone 1,  $h$ -coefficient value and temperature difference between zones 1 and 2. In practice, this is very interesting as it means that the heat flux field over a non-homogeneous wall may be measured from a single contact measurements and infrared thermography. This method is therefore almost non-intrusive.



**Figure 5.31.:** Heat flux extrapolation using measured  $h$ -coefficient.

## 5.8. Conclusion

The measurement of heat losses on building walls is not trivial. First, heat flux meters cannot be used on thermal bridges because of the 2D or 3D nature of the heat transfers encountered. Second, the heat losses are rarely uniform over a wall and it is usually not convenient to cover the wall with contact sensors. At this time, there is no universal measurement method allowing this quantification in all situations. Therefore, we proposed a new method consisting in extrapolating the local heat flux measured by a HFM on one location to the rest of the wall, even in the presence of thermal bridges. This requires the knowledge of the total heat exchange coefficient  $h$ . It is usually supposed known or estimated by empirical correlations from the literature. The accuracy of this approach is limited, especially because it cannot take into account the specificity of the encountered *in situ* configuration. In addition, in the context of a building, the choice of the reference temperatures to use in the correlations is not straightforward. This chapter focuses on the indoor *in situ* measurement of  $h$  in unsteady conditions. To this end, five  $h$ -measurement techniques were implemented: three of them are original whereas the other two are inspired from the published literature. The DM1 method relies on the measurements of both the temperature and the heat flux on two nearby surfaces: the bare wall and a heating resistance fixed on it. The DM2 approach is very similar, only the resistance is swapped with a piece of extruded polystyrene. The OT1 and OT2 methods are based on the measurement of the operative temperature, coupled with a heat flux measurement on the wall. While the OT1 method uses a passive device to measure  $T_{op}$ , the OT2 one is based on an active compensation of surface heat losses thanks to thermoelectric coolers. Finally, in the HE approach, the temperature of a surface is modulated (using thermoelectric coolers as well) and a Fourier analysis is performed. These five techniques are not all applicable both in steady and transient states. Table 5.3 summarizes their applicability.

**Table 5.3.:** Applicability of  $h$ -measurement methods.

Method	Applicable in:		Reference
	Steady-state	Transient state	
DM1	<b>Yes</b>	<b>Yes</b> but under-estimation	inspired from [181]
DM2	Not always	<b>Yes</b>	present study
OT1	<b>Yes</b>	No	ISO 9869-2 [102]
OT2	<b>Yes</b>	<b>Yes</b>	present study
HE	<b>Yes</b>	<b>Yes</b>	present study

In steady-state, the different methods measured a very similar  $h$  coefficient that proved to be close to the  $7.7 \text{ W.m}^{-2}.\text{K}^{-1}$  standard value from ISO 6946 [99]. To

complete these results, an unsteady regime was artificially generated by heating the air of the room thanks to electric fan heaters. The unsteady results spread was more important than steady-state ones but most of the implemented methods measured higher  $h$ -coefficient during the heating phase (between  $8.5$  and  $9 \text{ W.m}^{-2}.\text{K}^{-1}$ ) than during the free-cooling one (around  $7.5 \text{ W.m}^{-2}.\text{K}^{-1}$ , very close to the steady-state values).

Finally, it was demonstrated that it is possible to estimate heat losses onto a wall surface if the heat flux is measured locally in a given “reference” zone and if the global heat exchange coefficient is measured using one of the proposed methods. The third information required is the temperature difference between the reference zone and the rest of the wall surface. We have tested successfully this approach by measuring the temperature difference between two distinct zones with a thermocouple. The use of an infrared camera should allow obtaining accurately a map of temperature differences on the wall surface and thus to obtain a map of heat losses.

## 6. Steady-state characterization of a wall and a thermal bridge

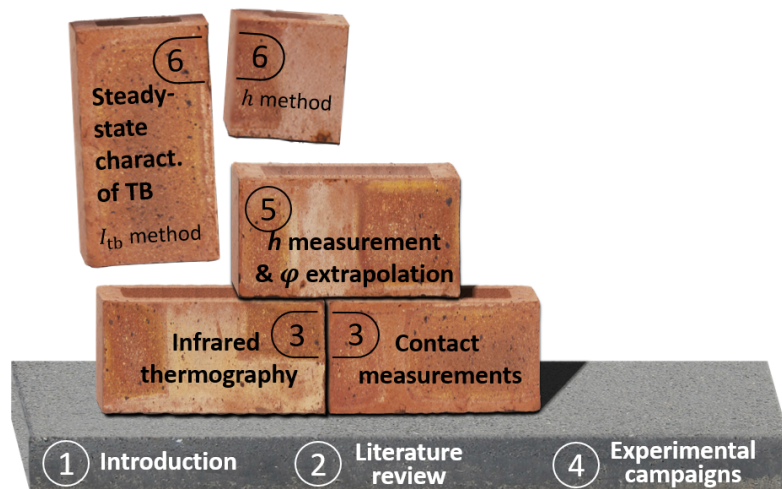


Figure 6.1.: Illustration of thesis plan.

This chapter presents three steady-state measurement methods. The first one aims at characterizing the thermal resistance  $R$  (or thermal transmittance  $U$ ) of a homogenous wall: it is the average method of ISO 9869-1 [15]. The other two focus on the estimation of a thermal bridge transmission coefficient  $\psi$  or  $\chi$ . The “ $I_{\text{tb}}$  method” is inspired from the literature. It consists in estimating the so-called “impact factor” with infrared thermography and to combine it with the wall thermal resistance  $R$  measured according to ISO 9869-1. Two different approaches for the calculation of  $I_{\text{tb}}$  are compared. Finally, the “ $h$  method” does not require the prior estimation of  $R$  but is based on the knowledge of the overall heat transfer coefficient  $h$  and the wall emissivity  $\varepsilon$ .

These three methods are mainly used to obtain reference values for  $R$ ,  $\psi$  and  $\chi$ . Indeed, they are accurate in a controlled environment when a steady-state can be achieved, but they are not well adapted to *in situ* measurements. The reference values will be useful to assess the relevance of results of the active methods presented in later chapters. All three steady-state methods are tested on the CERTES 1, the CEREMA, and the SGR experimental campaigns. As a reminder, the first two setups are inside a controlled environment (in laboratory and in a climate chamber) whereas the third one is located outside (field tests). These results were presented in [194] and [195] for the CERTES 1 setup and in [196] for the CEREMA setup.

Section 6.1 describes the three methodologies. The results are presented in sections 6.2 to 6.4 whereas section 6.5 draws a conclusion.

---

## Nomenclature

### Acronyms

BC	Boundary Conditions
HFM	Heat Flux Meter
FE	Finite Element
IRT	InfraRed Thermography
IFOV	Instantaneous Field Of View
MRT	Mean Radiant Temperature
ROI	Region Of Interest
SA	Sound Area
SNR	Signal to Noise Ratio
TB	Thermal Bridge

### Greek Symbols

$\varepsilon$	surface emissivity	-
$\phi$	heat flux	W
$\varphi$	heat flux density	W.m <sup>-2</sup>
$\chi$	point thermal transmittance	W.K <sup>-1</sup>
$\psi$	linear thermal transmittance	W.m <sup>-1</sup> .K <sup>-1</sup>

### Roman Symbols

$A_{tb}$	point thermal bridge influence area	m <sup>2</sup>
$e$	thickness	m
$h$	heat transfer coefficient	W.m <sup>-2</sup> .K <sup>-1</sup>
$I_{tb}$	incidence (or impact) factor	-
$k$	thermal conductivity	W.m <sup>-1</sup> .K <sup>-1</sup>
$L$	length of linear thermal bridge	m
$L_{tb}$	width of linear thermal bridge	m
$N$	number of pixels	-
$R$	thermal resistance	m <sup>2</sup> .K.W <sup>-1</sup>
$T$	temperature	K
$u$	uncertainty	
$U$	thermal transmittance	W.m <sup>-2</sup> .K <sup>-1</sup>
$x$	horizontal axis	m
$z$	altitude (distance from the floor)	m

### Superscripts

$\wedge$	estimated
$-$	mean quantity (space average)
app	apparent
c	convective
r	radiative

### Subscripts

1D	one dimensional (sound area)
e	external
env	environment
i	internal
insul	insulation system



op	operative
ref	reference
s	surface of the wall
tb	thermal bridge

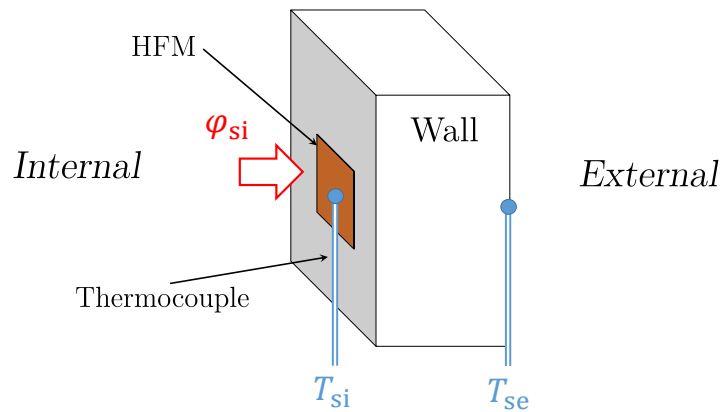
## 6.1. Methodologies

### 6.1.1. Characterization of a homogenous wall: $R$ and $U$ values

This method aims at measuring the thermal resistance  $R$  or transmittance  $U$  of a homogeneous wall. It is also useful to measure the thermal transmittance  $U_{1D}$  of a homogeneous section of a wall with thermal bridges. Indeed, as introduced in Chap 2 and detailed in the next section, this quantity is required in the calculation of the thermal bridges transmission coefficients with the “ $I_{tb}$  method”. The heat transfers have to be 1D on the studied section of the wall. In practice, one must check that the surface temperature is uniform, with an infrared camera for instance.

#### 6.1.1.1. Method presentation

The  $U$ -value is measured in steady-state from contact measurements, with a method inspired from ISO 9869-1 [15] (presented in Chap 2). Although this standard has limitations *in situ*, it is well suited for measurements in a controlled environment. The internal and external wall surface temperatures,  $T_{si}$  and  $T_{se}$  respectively, are measured with thermocouples. The heat flux  $\varphi_{si}$  through the wall is measured with a heat flux meter (HFM) fixed on the internal surface. The situation is illustrated in Fig 6.2.



**Figure 6.2.:** Illustration of wall instrumentation for steady-state measurements.

In steady-state, the wall thermal resistance is given by:

$$R_{\text{wall}} = \frac{T_{si} - T_{se}}{\varphi_{si}} = \frac{\Delta T_{\text{sie}}}{\varphi_{si}} \quad (6.1)$$

and the wall thermal transmittance by:

$$U = \frac{1}{R_{si} + R_{\text{wall}} + R_{se}} \quad (6.2)$$

with  $R_{\text{si}} = 0.13$  and  $R_{\text{se}} = 0.04 \text{ m}^2 \cdot \text{K} \cdot \text{W}^{-1}$  the internal and external superficial resistances. These are standard values used in the building sector (see ISO 14683 [18], ISO 6946 [99] or RT2012 [197] for instance).

In practice, the measured quantities are averaged over a period of time. In a controlled environment (e.g. CERTES 1 setup, CEREMA setup), the averaging mainly increases the Signal to Noise Ratio (SNR) and one or two hours of measurements are enough (once thermal equilibrium is reached). *In situ*, the averaging also enables to filter out temperature variations due to unsteady weather conditions. The minimum experiment duration is much higher: at least three days of continuous measurements according to ISO 9869-1 [15]. This duration depends on the type of wall and the weather variations. The recommendations for *in situ* measurements will be further discussed in section 6.4.

### 6.1.1.2. Measurement uncertainties

The measurement uncertainties on  $R$  are propagated from measurement uncertainties on  $\Delta T_{\text{sie}}$  and  $\varphi_{\text{si}}$  [158]:

$$u(R) = R \times \sqrt{\left(\frac{u(\Delta T_{\text{sie}})}{\Delta T_{\text{sie}}}\right)^2 + \left(\frac{u(\varphi_{\text{si}})}{\varphi_{\text{si}}}\right)^2} \quad (6.3)$$

It may be noted that the temperature difference  $\Delta T_{\text{sie}}$  is measured directly: its uncertainty is not the composed uncertainty of  $T_{\text{si}}$  and  $T_{\text{se}}$  (see Chap 3).

## 6.1.2. Characterization of a thermal bridge: “ $I_{\text{tb}}$ method”

### 6.1.2.1. Method presentation

As its name implies, the method is based on the so-called “incidence factor” (or “impact factor”)  $I_{\text{tb}}$ , as presented in Chap 2. This quantity was initially introduced by Asdrubali *et al.* [19]. It is the ratio of the global thermal transmittance  $U_{\text{tb}}$  of a wall with thermal bridges over the transmittance  $U_{1\text{D}}$  of the same wall without thermal bridge (in practice, a nearby “sound area”). In steady-state,  $I_{\text{tb}}$  is also a heat flux density ratio:

$$I_{\text{tb}} = \frac{U_{\text{tb}} \text{ steady-state}}{U_{1\text{D}}} \frac{\overline{\varphi_{\text{tb}}}}{\varphi_{1\text{D}}} \quad (6.4)$$

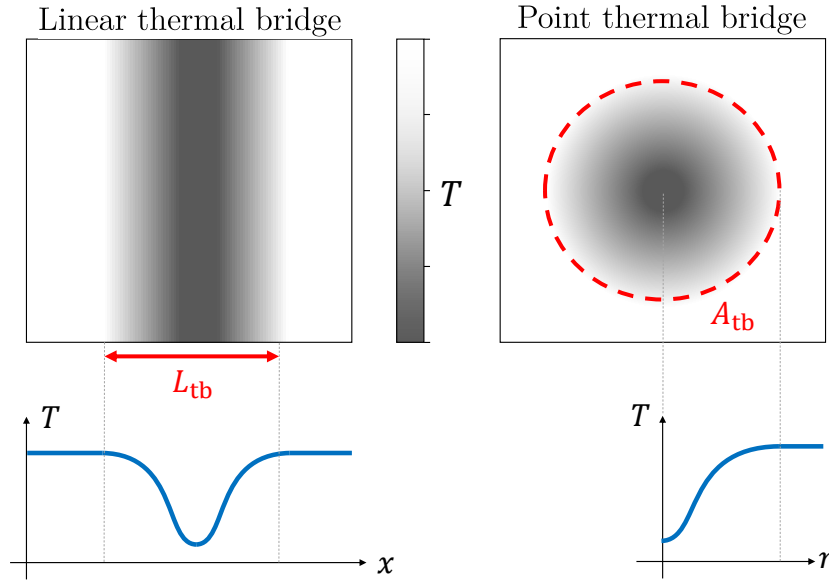
with  $\overline{\varphi_{\text{tb}}}$  the mean heat flux density on the thermal bridges and  $\varphi_{1\text{D}}$  the sound area heat flux density. The expression of the linear and point thermal bridge transmit-

tances may be written as a function of the incidence factor:

$$\psi = L_{tb}U_{1D}(I_{tb} - 1) \quad (6.5)$$

$$\chi = A_{tb}U_{1D}(I_{tb} - 1) \quad (6.6)$$

with  $L_{tb}$  the width of a linear thermal bridge and  $A_{tb}$  the area of a point thermal bridge. These dimensions correspond to the influence zone of the thermal bridge as shown in Fig 6.3 where simulated thermal images are presented. Outside these zones, the thermal bridge has a negligible impact on the surface temperature field. The threshold is typically the measurement noise). The choice of  $L_{tb}$  and  $A_{tb}$  will be studied in more details on the example of the CEREMA setup in section 6.3.



**Figure 6.3.:** Illustration of thermal bridge dimensions (simulated thermal images).

Two approaches for the measurement of  $I_{tb}$  are compared. The so-called “standard approach” was proposed by Asdrubali *et al.* [19] and we propose another approach.

#### 6.1.2.2. “Standard approach” for $I_{tb}$ measurement

In the approach proposed by Asdrubali *et al.* [19] (which we will call the “standard approach”), the incidence factor is calculated from true temperatures. Under the assumption of linearized radiative heat fluxes, Eq 6.4 becomes:

$$I_{tb} = \frac{\overline{\varphi}_{tb}}{\varphi_{1D}} = \frac{h_{tb}(\overline{T}_{tb} - T_{op})}{h_{1D}(T_{1D} - T_{op})} \quad (6.7)$$

with  $h$  a total heat transfer coefficient,  $T_{\text{op}}$  the operative temperature,  $\overline{T_{\text{tb}}}$  the thermal bridge mean surface temperature and  $T_{1\text{D}}$  the sound area (1D zone) surface temperature. In theory,  $T_{1\text{D}}$  is uniform around the thermal bridge. In practice however, the temperature on each side of the thermal bridge may be slightly different. If so,  $T_{1\text{D}}$  becomes the average of the surface temperatures measured on each side of the thermal bridge (see section 6.2 for instance).

Two simplifying assumptions are made. First, the air temperature  $T_{\text{air}}$  and mean radiant temperature  $T_{\text{env}}$  are supposed equal (and therefore also equal to  $T_{\text{op}}$ ). This is a realistic hypothesis indoor, in steady-state, inside a well insulated room: the air and the surface of the surrounding objects have approximately the same temperature. Second, the overall heat transfer coefficient is supposed uniform over the studied area:  $h_{1\text{D}} = h_{\text{tb}}$ . This means that the surface emissivity as well as the convective heat transfer coefficient have to be uniform. This is also realistic given the small temperature contrasts usually at stake in buildings. It comes the expression of the incidence factor proposed by Asdrubali *et al.* [19]:

$$I_{\text{tb}} = \frac{\overline{T_{\text{tb}}} - T_{\text{air}}}{T_{1\text{D}} - T_{\text{air}}} \quad (6.8)$$

Thus, the value of the heat transfer coefficient is not needed. However, in this formulation,  $T_{\text{air}}$  is measured with thermocouples whereas temperatures  $\overline{T_{\text{tb}}}$  and  $T_{1\text{D}}$  are measured by infrared thermography (which requires knowledge of the surface emissivity  $\varepsilon$ ). As detailed in Chap 3, the measurement of a true absolute temperature with an infrared camera is not straightforward and is subjected to high uncertainties (between 1 and 2 K [33]). The true surface temperature  $T_{\text{s}}$  is given by:

$$T_{\text{s}} = \left[ \frac{1}{\varepsilon} T_{\text{s}}^{\text{app},4} + \left( 1 - \frac{1}{\varepsilon} \right) T_{\text{env}}^4 \right]^{\frac{1}{4}} \quad (6.9)$$

with  $T_{\text{s}}^{\text{app}}$  the surface apparent temperature. The mean radiant temperature may be measured with an infrared mirror. From this perspective, it is interesting to work directly with apparent temperatures instead of true temperatures.

### 6.1.2.3. Proposed approach for $I_{\text{tb}}$ measurement

In order to reduce the measurement uncertainties, another approach is proposed here. By detailing the expression of the radiative and convective components of the surface heat fluxes, it comes:

$$\frac{\varphi_{\text{tb}}}{\varphi_{1\text{D}}} = \frac{h_{\text{tb}}^{\text{r}} (\overline{T_{\text{tb}}} - T_{\text{env}}) + h_{\text{tb}}^{\text{c}} (\overline{T_{\text{tb}}} - T_{\text{air}})}{h_{1\text{D}}^{\text{r}} (T_{1\text{D}} - T_{\text{env}}) + h_{1\text{D}}^{\text{c}} (T_{1\text{D}} - T_{\text{air}})} \quad (6.10)$$

Under the same assumptions as before ( $T_{\text{air}} \approx T_{\text{env}} \approx T_{\text{op}}$ , uniform  $h^{\text{c}}$  and  $h^{\text{r}}$ ), it may be shown that the heat flux ratio is equal to the radiative heat flux ratio:

$$\frac{\varphi_{\text{tb}}}{\varphi_{\text{1D}}} = \frac{(h^r + h^c) (\overline{T_{\text{tb}}} - T_{\text{env}})}{(h^r + h^c) (T_{\text{1D}} - T_{\text{env}})} \quad (6.11)$$

$$= \frac{\overline{T_{\text{tb}}} - T_{\text{env}}}{T_{\text{1D}} - T_{\text{env}}} \quad (6.12)$$

Temperature  $T_{\text{env}}$  was chosen in these equations instead of  $T_{\text{air}}$  or  $T_{\text{op}}$  simply because it is the one that will be measured (with an infrared mirror). By multiplying the numerator and the denominator by  $h^r$ , it comes the expressions of the radiative heat fluxes (see Chap 3):

$$\frac{\varphi_{\text{tb}}}{\varphi_{\text{1D}}} = \frac{h^r (\overline{T_{\text{tb}}} - T_{\text{env}})}{h^r (T_{\text{1D}} - T_{\text{env}})} \quad (6.13)$$

$$= \frac{\varphi_{\text{tb}}^r}{\varphi_{\text{1D}}^r} \quad (6.14)$$

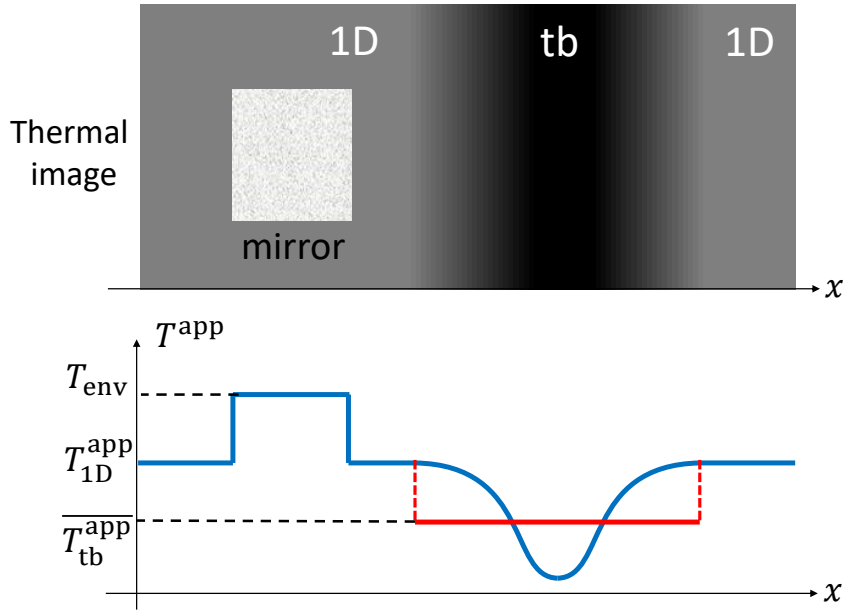
This new formulation is of interest because radiative heat flux measurements with an infrared camera are easier and more accurate than total heat flux measurements (see section 3.2). By expressing radiative heat fluxes as a function of apparent temperatures, the incidence factor becomes:

$$I_{\text{tb}} = \frac{\varphi_{\text{tb}}^r}{\varphi_{\text{1D}}^r} = \frac{\overline{T_{\text{tb}}^{\text{app}}} - T_{\text{env}}}{T_{\text{1D}}^{\text{app}} - T_{\text{env}}} = \frac{\Delta T_{\text{tb}}^{\text{app}}}{\Delta T_{\text{1D}}^{\text{app}}} \quad (6.15)$$

Figure 6.4 proposes an illustration of the apparent temperatures used in this formula. This approach has the main advantage of not requiring the value of the wall emissivity  $\varepsilon$ . In addition, every temperature involved is obtained from the same thermal image. This removes the bias induced by comparing measurements from different sensors (camera and thermocouple). Although the camera itself is made of an array of different sensors, the NUC procedure tends to remove the dispersion of their response (see Chap 3). For these two reasons, the measurement uncertainties of this approach are smaller than that of the “standard” approach (see section 6.2 for a numerical application on the example of the CERTES 1 setup). Therefore, the present approach will be used instead of the “standard” one.

#### 6.1.2.4. Measurement uncertainties

Once the impact factor is known, the  $\psi$  and  $\chi$  coefficients are calculated using equations 6.5 and 6.6 respectively. Measurement uncertainty  $u(\psi)$  on  $\psi$  (similarly



**Figure 6.4.:** Scheme of apparent temperatures used in  $I_{\text{tb}}$  calculation.

for  $\chi$ ) is obtained from uncertainty propagation [158]:

$$u(\psi) = \sqrt{\left(\frac{\partial\psi}{\partial L_{\text{tb}}}\text{u}(L_{\text{tb}})\right)^2 + \left(\frac{\partial\psi}{\partial U_{1\text{D}}}\text{u}(U_{1\text{D}})\right)^2 + \left(\frac{\partial\psi}{\partial I_{\text{tb}}}\text{u}(I_{\text{tb}})\right)^2} \quad (6.16)$$

where

$$L_{\text{tb}} = N_{\text{p}} \times \frac{L_{\text{ref}}}{N_{\text{ref}}} \quad (6.17)$$

with  $N_{\text{p}}$  the number of pixels corresponding to  $L_{\text{tb}}$  on the thermal image. A ruler of known length  $L_{\text{ref}}$  is introduced in the camera field of view and  $N_{\text{ref}}$  is its corresponding number of pixels on the image ( $L_{\text{ref}}/N_{\text{ref}}$  is the scale of the image, or the size of one pixel). Alternatively, the scale of the image can also be determined from the camera to wall distance and the camera IFOV (Instantaneous Field of View).

The uncertainty calculation is presented in further details in Appendix C.1.

To demonstrate the advantage of the proposed method which uses apparent temperatures, the measurement uncertainties are calculated and compared with those obtained if true temperatures are used (see section 6.2).

### 6.1.3. Characterization of a thermal bridge: “ $h$ method”

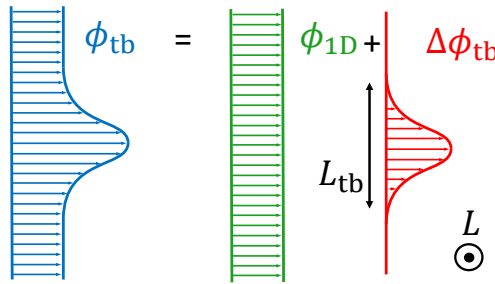
This alternative method requires the quantification of the surface overall heat exchange coefficient  $h$  as well as the wall emissivity  $\varepsilon$  but relies on fewer assumptions.

#### 6.1.3.1. Method presentation

As presented in Chap 3, the transmission coefficient of a linear thermal bridge is given by:

$$\psi = \frac{\Delta\phi_{\text{tb}}}{L \times \Delta T_{\text{ie}}} \quad (6.18)$$

with  $\Delta\phi_{\text{tb}}$  the additional heat flux due to the thermal bridge,  $\Delta T_{\text{ie}}$  the internal/external temperature difference and  $L$  the length of the thermal bridge, as illustrated in Fig 6.5.



**Figure 6.5.:** Illustration of a linear thermal bridge contribution to the overall surface heat flux.

We define the thermal bridge additional heat flux density:

$$\Delta\varphi_{\text{tb}} = \frac{\Delta\phi_{\text{tb}}}{L \times L_{\text{tb}}} \quad (6.19)$$

It comes:

$$\psi = L_{\text{tb}} \frac{\Delta\varphi_{\text{tb}}}{\Delta T_{\text{ie}}} \quad (6.20)$$

The additional heat flux density  $\Delta\varphi_{\text{tb}}$  is obtained from the total heat transfer coefficient  $h$  and the mean surface temperatures on the thermal bridge and the nearby sound area:

$$\Delta\varphi_{\text{tb}} = h (\overline{T}_{\text{tb}} - T_{1D}) \quad (6.21)$$



The temperature difference is derived from the apparent temperature difference measured with IRT and the wall emissivity (see Chap 3):

$$\overline{T}_{\text{tb}} - T_{\text{1D}} = \frac{\overline{T}_{\text{tb}}^{\text{app}} - T_{\text{1D}}^{\text{app}}}{\varepsilon} \quad (6.22)$$

Finally:

$$\psi = L_{\text{tb}} \frac{h}{\Delta T_{\text{ie}}} \frac{\Delta T_{\text{tb-1D}}^{\text{app}}}{\varepsilon} \quad (6.23)$$

with  $\Delta T_{\text{tb-1D}}^{\text{app}} = \overline{T}_{\text{tb}}^{\text{app}} - T_{\text{1D}}^{\text{app}}$ . Similarly, the transmission coefficient of a point thermal bridge is given by:

$$\chi = A_{\text{tb}} \frac{h}{\Delta T_{\text{ie}}} \frac{\Delta T_{\text{tb-1D}}^{\text{app}}}{\varepsilon} \quad (6.24)$$

Thus, this method for the quantification of a thermal bridge  $\psi$  or  $\chi$  value is based on knowledge of the wall overall heat transfer coefficient  $h$  and emissivity  $\varepsilon$ . The mean radiant temperature and the air temperature are not required. The  $h$  coefficient may be estimated from (i) a standard value, (ii) an empirical correlation from the literature, (iii) an *in situ* measurement (see Chap 5). A standard value may be assigned to the wall emissivity  $\varepsilon$ . It depends on the surface wall material. Most building materials have an emissivity close to 0.95. In this thesis, the emissivities were measured in laboratory, with an infrared spectrometer (see Appendix A).

In practice, the surface temperature difference  $\Delta T_{\text{sie}}$  on the sound area is measured instead of  $\Delta T_{\text{ie}}$ . These two quantities are related by:

$$\Delta T_{\text{ie}} = \Delta T_{\text{sie}} + \varphi_{\text{1D}} (R_{\text{si}} + R_{\text{se}}) \quad (6.25)$$

### 6.1.3.2. Measurement uncertainties

The calculation a  $\psi$  (or  $\chi$ ) coefficient is obtained from the combination five physical quantities:  $L_{\text{tb}}$  (or  $A_{\text{tb}}$  for a point thermal bridge),  $\Delta T_{\text{ie}}$ ,  $h$ ,  $\varepsilon$  and  $\Delta T_{\text{tb-1D}}^{\text{app}}$ . The measurement uncertainty on  $\psi$  (or  $\chi$ ) is obtained from propagation of the uncertainties [158] of each one of these components (noted  $\beta_k$ ):

$$u(\psi) = \sqrt{\sum_{k=1}^5 \left( \frac{\partial \psi}{\partial \beta_k} u(\beta_k) \right)^2} \quad (6.26)$$

The detailed calculations are presented in Appendix C.1.

In addition, thanks to a thorough uncertainty analysis (see Appendix C.3), the infrared measurements was identified as the main source of error.

### 6.1.4. Conclusion

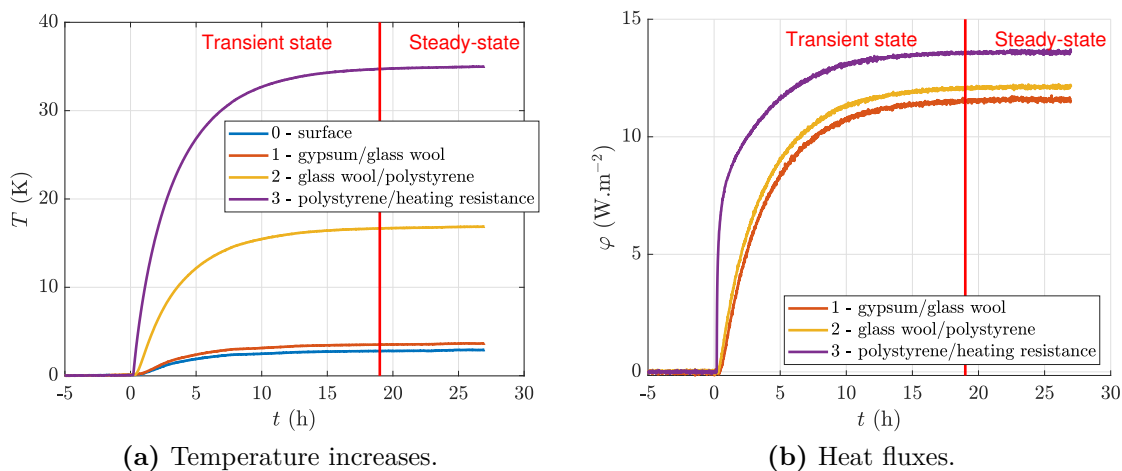
The average method from ISO 9869-1 enables to measure the thermal resistance of a homogeneous section of a wall from contact measurements. Then, two methods for the quantification of a thermal bridges transmission coefficient were presented. The “ $I_{tb}$  method” is inspired from the literature. An improvement of it consists in calculating the impact factor with apparent temperatures instead of true temperatures as in the “standard approach”. This removes the dependency to the surface emissivity and tends to reduce the measurement uncertainties. However, this method is based on many assumptions. In particular, the air and mean radiant temperatures must be equals. This assumption is not valid if the building is not well insulated. In addition, the presence of openings may generate cold surfaces and bias the measurement of the mean radiant temperature. Alternatively, the “ $h$ -method” enables to work out a  $\psi$  or  $\chi$  coefficient without this hypothesis. Nevertheless, both the heat transfer coefficient and the emissivity have to be known. The application of these methods to the CERTES 1 setup, the CEREMA, and the SGR setups is presented in the following sections.

## 6.2. Results on the CERTES 1 setup

Here are presented results of these steady-state characterization method applied to the CERTES 1 setup. The values obtained will be used as references for the active methods presented in later chapters. The setup is presented in section 4.2. It is heated by a flat heating resistance fixed on its rear side. As a consequence, unlike what is usually observed, the temperature on the thermal bridges is higher than that on the sound area. A curtain was fixed in front of the windows to ensure that the air temperature is close to the mean radiant temperature.

### 6.2.1. Contact measurements and $R$ estimation

A steady-state is supposed reached when temperatures and heat fluxes are less than 1% way from their final value. This 1% threshold is inspired from ISO 8990 [60]. As shown in Fig 6.6, this occurs after about 19 h of uniform heating of the flat resistance. On this example, the heating power is 20 W which corresponds to a surface heat flux density to about  $12 \text{ W.m}^{-2}$ .



**Figure 6.6.:** Measured temperature elevations and heat fluxes inside the setup during transient state and steady-state (reached when temperature and heat fluxes are less than 1% away from their final value).

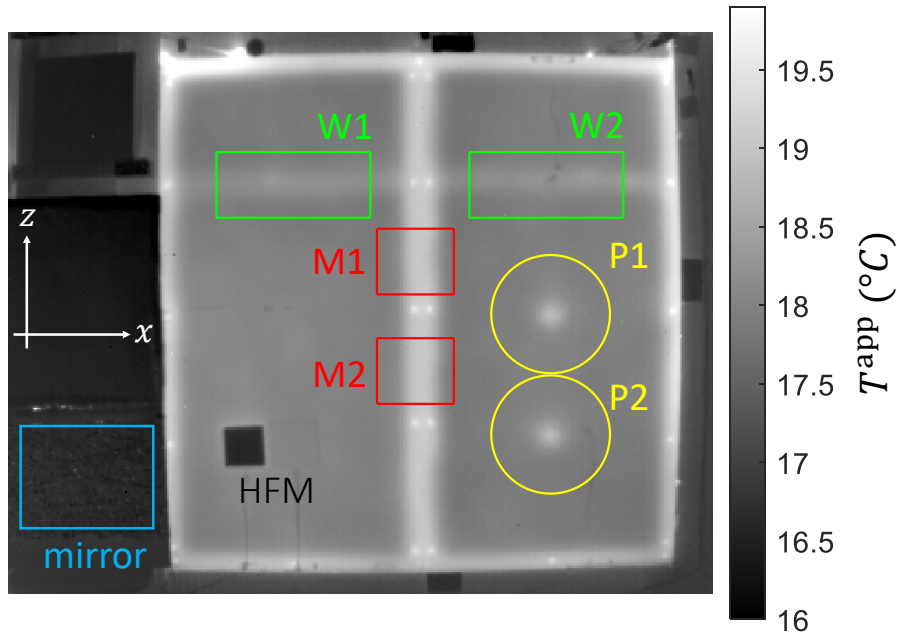
In practice, the heat flux and front face temperature are measured with a HFM located below the gypsum layer (between the gypsum and glass wool layers) because surface measurements were significantly noisier. The thermal resistance of the gypsum layer (derived from thermal conductivity measurements with the Hot Disk method) is then added to the measured thermal resistance in order to estimate the wall resistance. The results are gathered in Tab 6.1. The wall thermal resistance and transmittance are estimated to  $2.75 \pm 0.08 \text{ m}^2.\text{K.W}^{-1}$  and  $0.34 \pm 0.01 \text{ W.m}^{-2}.\text{K}^{-1}$ , respectively. The gypsum thermal resistance is  $0.05 \text{ m}^2.\text{K.W}^{-1}$  which represents less than 2% of the overall setup resistance.

**Table 6.1.:** Measured quantities and calculated thermal resistance (ISO 9869-1 [15]).

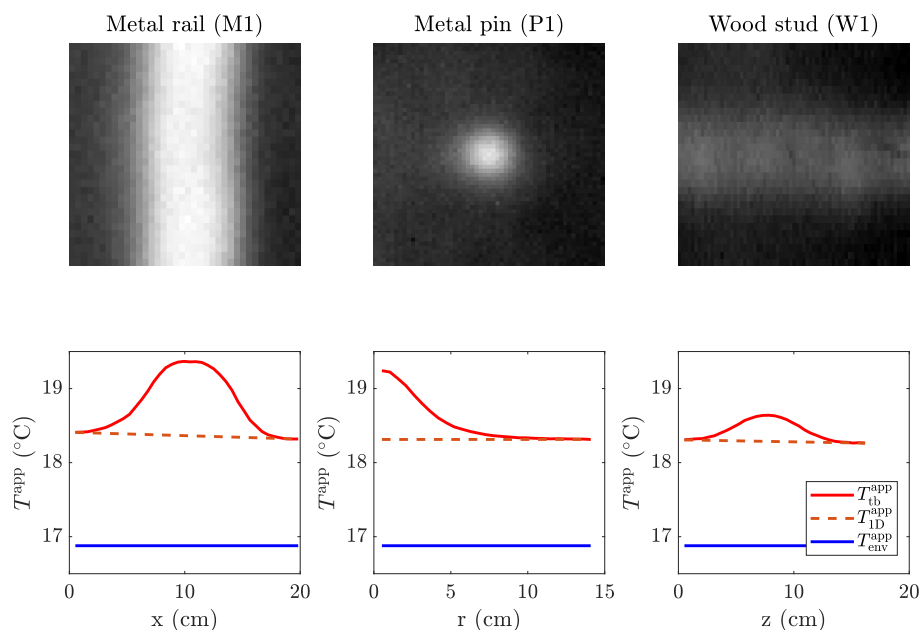
	Unit	Measured value
$\Delta T_{\text{sie}}$	K	$31.4 \pm 0.1$
$\varphi_{\text{si}}$	$\text{W}\cdot\text{m}^{-2}$	$11.7 \pm 3\%$
$R_{1\text{D}}$	$\text{m}^2\cdot\text{K}\cdot\text{W}^{-1}$	$2.75 \pm 0.08$
$U_{1\text{D}}$	$\text{W}\cdot\text{m}^{-2}\cdot\text{K}^{-1}$	$0.34 \pm 0.01$

### 6.2.2. Infrared measurements

Figure 6.7 shows a thermal image of the setup. It is the average of 120 frames captured in steady-state during 1 h. The thermal bridges appear hotter than the sound area because the wall is heated from behind. The Regions Of Interest (ROIs) used for the quantification of the  $\psi$  and  $\chi$  coefficients are shown. Each thermal bridge is referenced by a letter: “M” for a metal rail, “W” for a wood stud, and “P” for a metal pin. The apparent temperature profiles  $T^{\text{app}}$  in the vicinity of each thermal bridge are extracted from these ROIs and shown in Fig 6.8. The mean radiant temperature measured on the aluminum sheet is also plotted.

**Figure 6.7.:** Thermal image of the CERTES 1 setup in steady-state, with ROIs (two per thermal bridge, “M”=metal rail, “P”=metal pin, and “W”=wood stud).

It may be seen that the magnitude of the temperature contrast due to the thermal bridge is smaller for the wood stud (about 0.4 K) than for the metal rail and the metal pins (about 1 K). However, the impacted area is much smaller for the metal pin than for the other thermal bridges so the additional heat flux will be smaller as



**Figure 6.8.:** Time averaged apparent temperature profiles on thermal bridges in steady-state ( $T_{\text{tb}}^{\text{app}} > T_{\text{1D}}^{\text{app}}$  because the setup is heated from behind).

well. Also, the curve of  $T_{\text{1D}}^{\text{app}}$  is not quite flat for the linear thermal bridges. This is due to edge effects induced by the small dimension of the setup: heat transfers are not quite 1D between the thermal bridges. This non-homogeneity is however very small when compared to temperature contrasts on thermal bridges.

### 6.2.3. Numerical simulations

Heat transfers inside the setup are numerically simulated with the Finite Element (FE) method using COMSOL Multiphysics<sup>®</sup> [198]. The results of these simulations are useful to obtain a value to compare with measurement results. The simulations are briefly described here. Please refer to Appendix C.2 for more details.

Material thicknesses and thermal properties implemented in the simulations are given in Tab 6.2. The thermal conductivities come from measurements with the Hot Disk method, except for the insulating materials for which manufacturer's data are used.

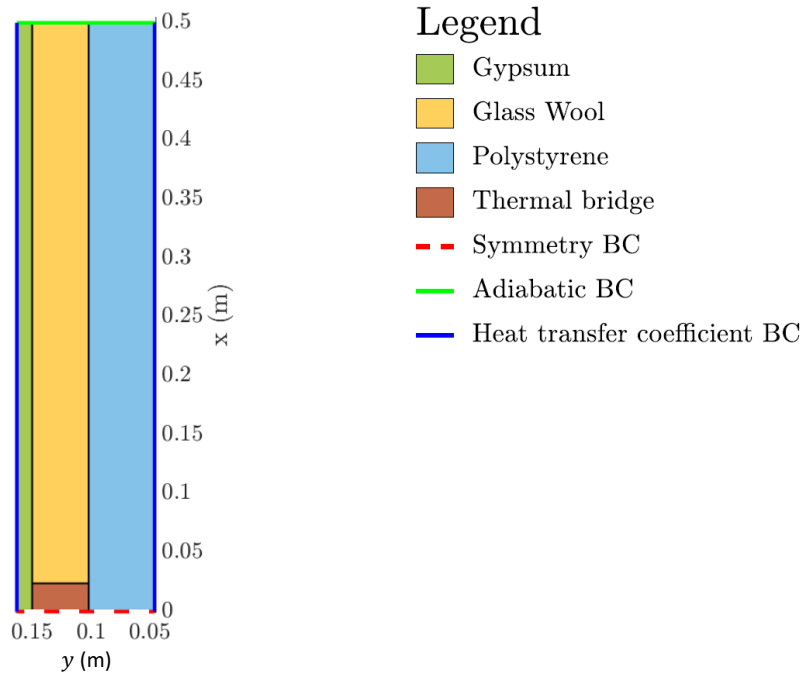
**Table 6.2.:** Thermal conductivity and thickness of materials used in FE simulations.

	$k$ ( $\text{W}\cdot\text{m}^{-1}\cdot\text{K}^{-1}$ )	$e$ (mm)
Gypsum	0.23 (Hot Disk)	13
Glass wool	0.043 (Manufacturer)	48
Polystyrene	0.035 (Manufacturer)	56
Metal	70.2 (Hot Disk)	48
Wood	0.11 (Hot Disk)	48

Each thermal bridge is simulated with a specific 2D model. Thanks to symmetries,

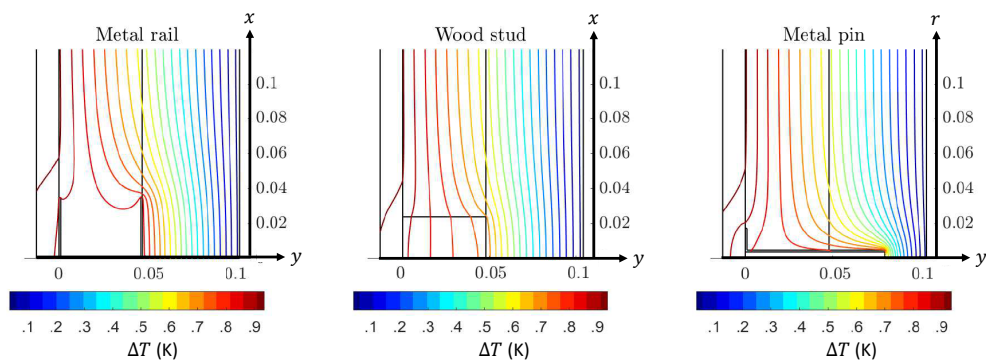
## 6.2. RESULTS ON THE CERTES 1 SETUP

only one half of each thermal bridge is modeled. On the front and rear surfaces, a heat exchange coefficient and a uniform operative temperature are defined. The domain is made large enough (50 cm) for the heat transfers to be 1D away from the thermal bridge. Fig 6.9 presents the FE model of the wood stud with the boundary conditions (BC). Mesh convergence was checked.



**Figure 6.9.:** Domain and Boundary Conditions (BC) used in FE simulations (wood stud example).

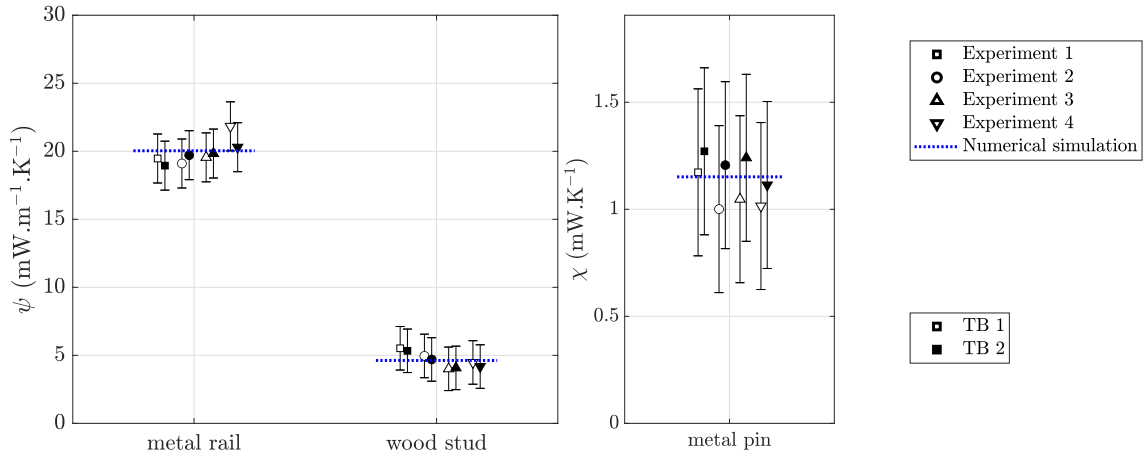
In order to have a first visualization of the impact of thermal bridges, Fig 6.10 plots the temperature iso-contours in steady-state. The internal/external temperature difference is arbitrarily set to 1 K. It may be seen that most of the impact of the thermal bridges on the temperature field is localized a few centimeters away from the center (symmetry BC). The  $\psi$  and  $\chi$  values are worked out from these temperature fields.



**Figure 6.10.:** Isothermal lines in the vicinity of each thermal bridge in steady-state for a unit temperature difference.

### 6.2.4. Results for the “ $I_{tb}$ method”

Several experiments were carried out on the setup to assess the method reproducibility. They were made in two different rooms, two setup orientations, and several heating powers. The results are gathered in Fig 6.11 and summarized in Tab 6.3. Each coefficient is calculated at two distinct locations (see ROIs in Fig 6.7).



**Figure 6.11.:** Results of thermal bridge transmission coefficient estimations, “ $I_{tb}$  method”.

**Table 6.3.:** Detailed results on thermal bridge transmission coefficients estimation with the “ $I_{tb}$  method” and comparison of uncertainties between the present and “standard” approaches.

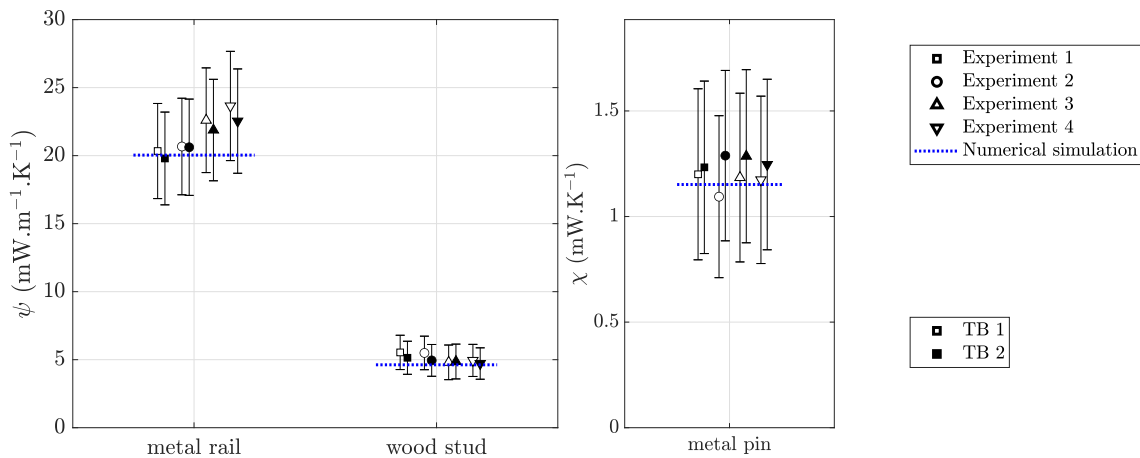
Thermal bridge	Coefficient	Unit	Mean	Standard deviation	Uncertainty	
					present approach	standard approach
metal rail	$\psi$	$\text{mW}\cdot\text{m}^{-1}\cdot\text{K}^{-1}$	19.8	0.8	1.8	4.0
wood stud	$\psi$	$\text{mW}\cdot\text{m}^{-1}\cdot\text{K}^{-1}$	4.5	0.6	1.6	3.8
meal pin	$\chi$	$\text{mW}\cdot\text{K}^{-1}$	1.1	0.1	0.4	0.9

There is a good agreement with numerical simulations: the differences are not significant and are below the measurement uncertainties. In addition, the method shows a rather good reproducibility: results spread is of 4% for the metal rail and between 10 and 15% for the other thermal bridges. Measurements on the metal rail are more accurate because this thermal bridge has a higher surface temperature contrast than others (better SNR on the thermal image). It may also be noted that the spread between measurements is smaller than the uncertainty. The measurement uncertainties in the “standard approach ( $I_{tb}$  calculated from true temperatures)” are significantly higher (about twice) than in the proposed approach ( $I_{tb}$  calculated from apparent temperatures). This confirms the interest of the proposed approach.

### 6.2.5. Results for the “ $h$ method”

This setup was built and used before the development of *in situ* methods for the measurement of the overall heat transfer coefficient  $h$  on the surface of a building wall (see Chap 5). Therefore, the  $h$ -coefficient was not measured. Yet, the study on the CERTES 2 setup presented in Chap 5 showed that, in steady-state, the indoor  $h$ -value is very close to the standard value  $7.7 \text{ W.m}^{-2}.\text{K}^{-1}$  (ISO 6946 [99] and ISO 14683 [18]). Given that the CERTES 1 and CERTES 2 setups are rather similar (gypsum plate with an internal insulation material beneath), and were used in the same room, the previous conclusion is supposed valid here as well. Therefore, the thermal bridges  $\psi$  and  $\chi$  coefficients are estimated taking  $h = 7.7 \text{ W.m}^{-2}.\text{K}^{-1}$ . In addition, the emissivity of the setup surface was measured in laboratory with an infrared spectrometer (see Chap 3).

The results are shown in Fig 6.12 and Tab 6.4. It may be seen that they are in agreement with the results of the “ $I_{\text{tb}}$  method” presented in Fig 6.11 (the difference is lower than the measurement uncertainties), despite the fact that a standard value was used for  $h$ . The measurement uncertainties are higher in average (except for the wood stud).



**Figure 6.12.:** Results of thermal bridge transmission coefficient estimations, “ $h$  method”.

**Table 6.4.:** Detailed results on thermal bridge transmission coefficients estimation with the “ $h$  method”.

Thermal bridge	Coefficient	Unit	Mean	Standard deviation	Uncertainty
metal rail	$\psi$	$\text{mW.m}^{-1}.\text{K}^{-1}$	21.5	1.4	3.7
wood stud	$\psi$	$\text{mW.m}^{-1}.\text{K}^{-1}$	5.1	0.3	1.2
meal pin	$\chi$	$\text{mW.K}^{-1}$	1.2	0.1	0.4



### 6.2.6. Conclusion

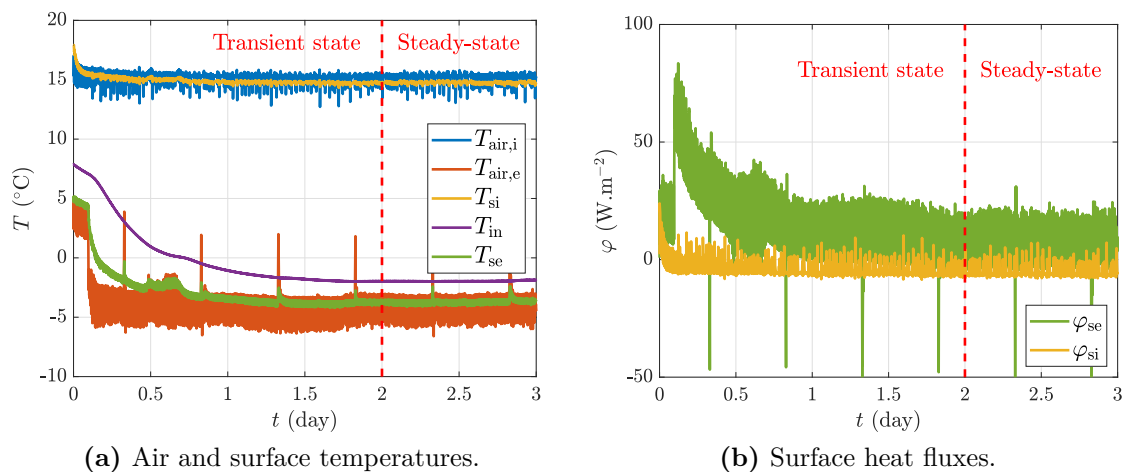
The steady-state characterization methods were successfully applied to the CERTES 1 setup. The thermal resistance of the sound area could be estimated:  $2.75 \pm 0.08 \text{ m}^2 \cdot \text{K} \cdot \text{W}^{-1}$ . The two methods for the measurement of thermal bridges  $\psi$  and  $\chi$  coefficients were compared. A very good agreement is noted between as well as with the numerical simulations. The measurement uncertainty of the “ $I_{\text{tb}}$  method” could be halved by calculating the impact factor with apparent temperatures (proposed approach) rather than with true temperatures (standard approach). Thus, the proposed approach will be preferred in other experimental campaigns. The heat transfer coefficient was not measured on this setup. Instead, the standard value for indoor building wall surfaces was used in the “ $h$  method”. The estimated  $\psi$ -values for the metal rail, the wood stud, and the metal pins are  $19.8 \pm 1.8$ ,  $4.5 \pm 1.6$  and  $1.1 \pm 0.4 \text{ W} \cdot \text{m}^{-1} \cdot \text{K}^{-1}$ , respectively.

## 6.3. Results on CEREMA experiments

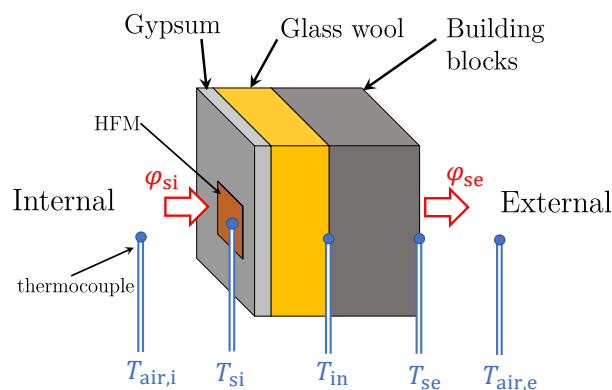
The CEREMA experimental campaign was presented in section 4.4. It is a full-size internally insulated load-bearing wall built inside a climate chamber.

### 6.3.1. Contact measurements and $R$ estimation

The two modules of the climate chamber are used to keep the internal and external air temperatures equal to 15 and  $-5^{\circ}\text{C}$  respectively. This 20 K temperature difference is set for three days before performing the measurements to ensure that a steady-state is reached. Figure 6.13 plots the evolution of some temperatures and heat fluxes measured just after activation of the modules. The names of the plotted quantities are described in Fig 6.14. It may be seen that after only two days, the wall reached a steady-state.



**Figure 6.13.:** Measured temperatures heat fluxes during transient and steady states (see Fig 6.14 for nomenclature).



**Figure 6.14.:** Scheme of main contact sensors for thermal resistance measurements.

Surface measurements are significantly noised because the climate chamber regulation system induces small air temperature oscillations. Therefore, measured quantities are averaged over two hours to filter out these oscillations and to improve the SNR. The sampling time is 30 s. From measurements on the sound area, the wall thermal resistance is estimated to  $R_{\text{wall}} = 3.49 \pm 0.11 \text{ m}^2.\text{K}.\text{W}^{-1}$ . This corresponds to a thermal transmittance  $U_{1\text{D}} = 0.27 \pm 0.01 \text{ W}.\text{m}^{-2}.\text{K}^{-1}$ . In addition, the thermal resistance of the insulation system (gypsum + glass wool) is estimated to  $R_{\text{insul}} = 3.15 \pm 0.10 \text{ m}^2.\text{K}.\text{W}^{-1}$ . This latter value could be obtained from a thermocouple measurement inside the wall ( $T_{\text{in}}$ ). The results are summarized in Tab 6.5.

**Table 6.5.:** Measured quantities and calculated thermal resistance with ISO 9869-1 [15].

	Whole wall	Insulation system (gypsum+glass wool)
$\Delta T_{\text{sie}}$ (K)	$18.9 \pm 0.1$	$16.9 \pm 0.1$
$\varphi_{\text{si}}$ ( $\text{W}.\text{m}^{-2}$ )	$5.35 \pm 3\%$	$5.35 \pm 3\%$
$R$ ( $\text{m}^2.\text{K}.\text{W}^{-1}$ )	$3.49 \pm 0.11$	$3.15 \pm 0.10$
$U$ ( $\text{W}.\text{m}^{-2}.\text{K}^{-1}$ )	$0.27 \pm 0.01$	-

### 6.3.2. Measurement of $h$

The setup is equipped with two devices (see Fig 4.20 of Chap 4) for the measurement of the overall heat transfer coefficient: “ $h$ -meter 1” is based on the Double Measurement (DM) method whereas “ $h$ -meter 2” relies on the Harmonic Excitation (HE) method. They correspond to devices “B” and “E” in Chap 5.

On this setup, the HE method could not be used for steady-state experiments. Indeed, the climate chamber regulation system induces small air temperature oscillations whereas the harmonic method requires the operative temperature to remain constant for a few periods. Moreover, the climate chamber and the harmonic device have a similar characteristic time (oscillation period).

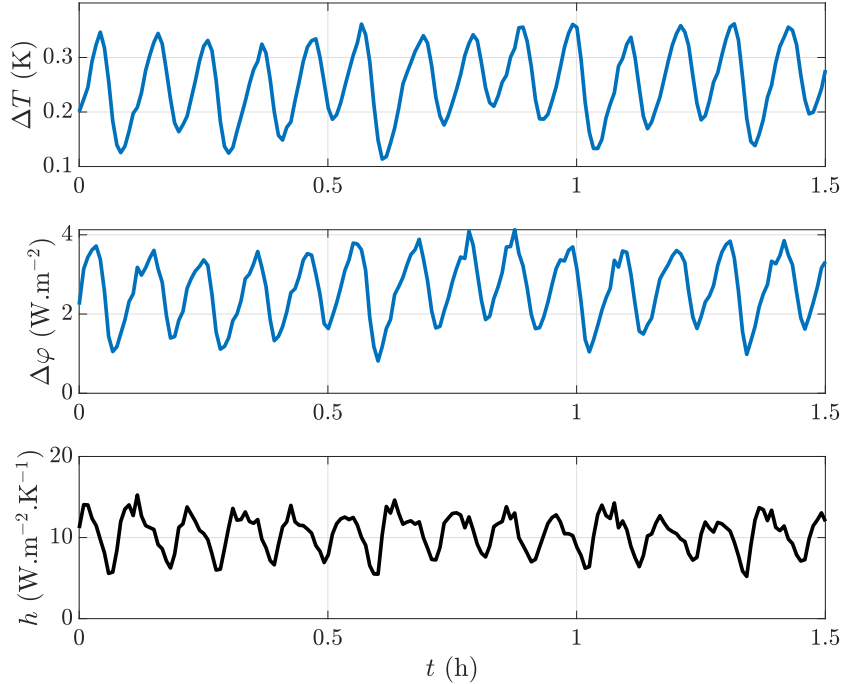
Thus, for steady-state measurements, the DM method is used with “ $h$ -meter 1”. Basically, heat flux is measured on two nearby locations: directly on the wall, and on the piece of polystyrene forming “ $h$ -meter 1”. The temperature difference between these areas is directly measured with a thermocouple in the “two-junction” configuration (see Chap 3). Thanks to the 20 K temperature difference enforced between the internal and external environments, the temperature on the polystyrene is higher than that on the wall. An estimation of the heat transfer coefficient is directly obtained from the temperature and heat flux differences between these two areas:

$$h = \frac{\Delta\varphi}{\Delta T} \tag{6.27}$$

where  $\Delta\varphi$  and  $\Delta T$  are the time averaged quantities. The measurement uncertainty is given by:

$$u(h) = h \sqrt{\left(\frac{u(\Delta\varphi)}{\Delta\varphi}\right)^2 + \left(\frac{u(\Delta T)}{\Delta T}\right)^2} \quad (6.28)$$

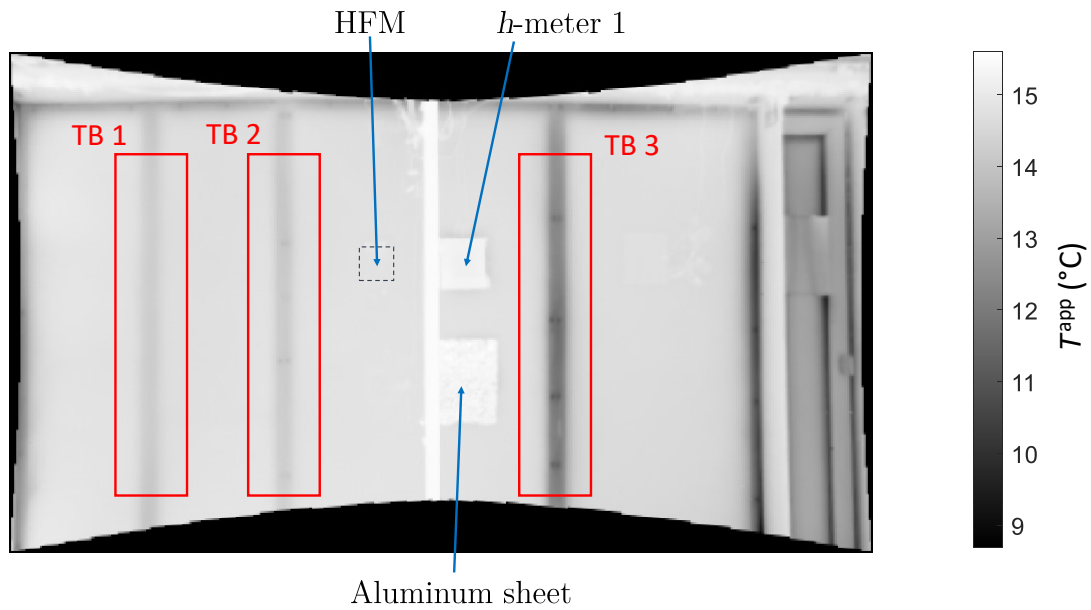
Figure 6.15 plots the evolution of  $\Delta T$ ,  $\Delta\varphi$  and  $h$  during a steady-state experiment. The oscillations due to the chamber regulation system are clearly visible. Yet, by averaging the measurements over a high number of periods (at least 10), these oscillations may be filtered out. On this example, the  $h$ -coefficient is estimated to  $10.2 \pm 1.4 \text{ W.m}^{-2}.\text{K}^{-1}$ . This value, which is higher than the standard of  $7.7 \text{ W.m}^{-2}.\text{K}^{-1}$ , is explained by the fan of the climate chamber module which increases convective heat losses. This value is also close to the one measured during active tests when the electric fan heaters are turned on.



**Figure 6.15.:** Measured temperature and heat flux difference between the wall surface and the surface of a piece of polystyrene fixed on the wall (“ $h$ -meter 1”).

### 6.3.3. Infrared measurements

Fig 6.16 presents a reconstructed thermogram of the setup, obtained in steady-state. It is the average of 120 thermograms captured every minute during two hours of steady-state. The ROIs around each thermal bridge are also displayed. In addition, Fig 6.17 plots the apparent temperature profiles obtained from a vertical average of the apparent temperature inside these regions. The temperature of the mirror (crumpled aluminum sheet) is also plotted.



**Figure 6.16.:** Reconstructed thermogram of the setup in steady-state, with ROIs.

As expected, the temperature contrast is much higher on TB 3 than on the other thermal bridges. In addition, the temperature is almost invariant with the altitude: the regulation modules of the climate chamber prevents air stratification. The small black dots on TB 2 and TB 3 are the screws holding the gypsum plate to the metal frame. It may also be noticed that the measurement noise is very small. Indeed, not only has the cooled sensor of the camera a small sensitivity (20 mK), the profiles are also obtained from space and time averages of 120 thermograms.

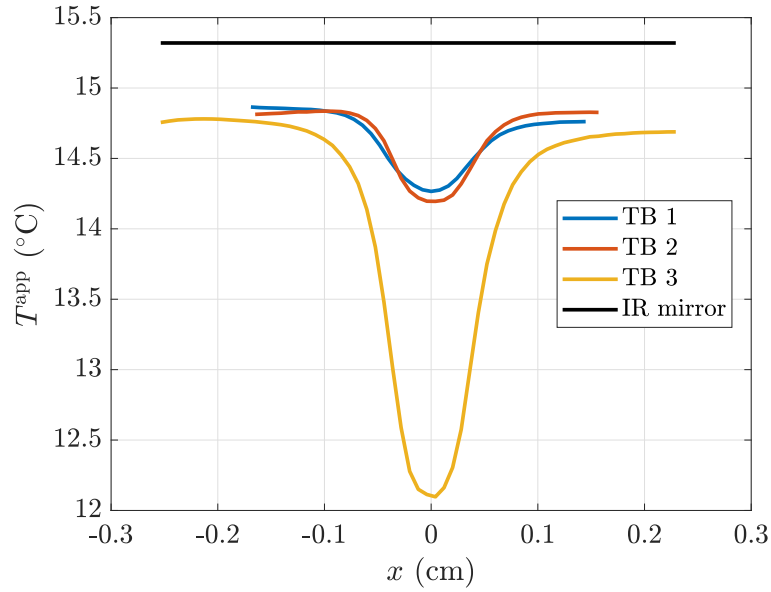
### 6.3.4. Numerical simulations

Similarly to the CERTES 1 setup, numerical simulations of the CEREMA wall were run. They are built in the same way as presented in section 6.2.3. The materials thickness and thermal conductivity used are presented in Tab 6.6. The equivalent thermal conductivity of the concrete building blocks was estimated from measurement of their thermal resistance in steady-state.

Figure 6.18 plots the results of the simulations: iso-thermal lines in steady-state with a unit temperature difference between the internal and external environments. It is clear that TB 3 has a much higher impact on the temperature field than TB 1 and TB 2.

### 6.3.5. Results of $\psi$ -value calculation

The apparent temperature profiles shown in Fig 6.17 are used to work out the thermal bridges incidence factor  $I_{tb}$  which is required in the estimation of the  $\psi$  coefficient.



**Figure 6.17.:** Measured apparent temperature profiles on thermal bridges in steady-state.

**Table 6.6.:** Thermal conductivity and thickness of materials used in FE simulations.

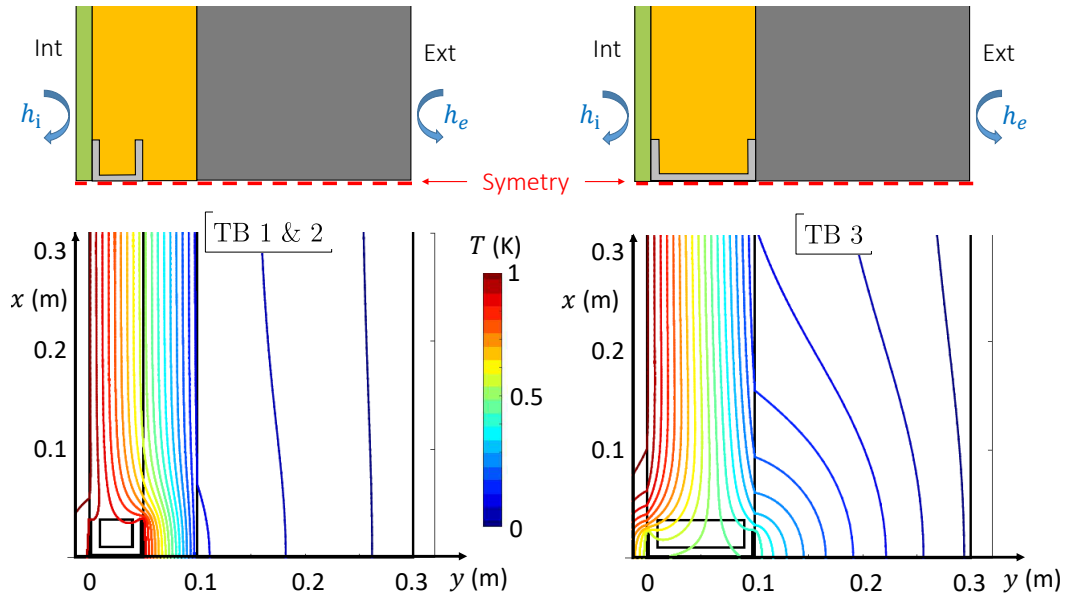
	$k$ (W.m <sup>-1</sup> .K <sup>-1</sup> )	$e$ (mm)
Gypsum	0.23 (Hot Disk)	13
Glass wool	0.032 (Manufacturer)	100
Metal	70.2 (Hot Disk)	1
Concrete blocks	0.71 (from $R$ measurement)	200

The measured thermal bridge transmission coefficients and their uncertainties are summarized in Tab 6.7. These values are obtained from average over the whole height of the thermal bridges. Additional heat losses due to TB 3 are about four times superior than those due to TB 1 and TB 2. In addition, TB 2 has slightly a higher  $\psi$ -value than TB 1. This small difference is explained by the presence of a joint between two gypsum boards and screws on TB 2.

**Table 6.7.:** Estimated thermal bridge transmission coefficients.

		TB 1	TB 2	TB 3
“ $I_{tb}$ method”	$I_{tb}$ (-)	$1.31 \pm 0.06$	$1.34 \pm 0.07$	$1.90 \pm 0.07$
	$\hat{\psi}$ (mW.m <sup>-1</sup> .K <sup>-1</sup> )	<b><math>26 \pm 5</math></b>	<b><math>30 \pm 5</math></b>	<b><math>117 \pm 8</math></b>
“ $h$ ” method”	$\hat{h}$ (W.m <sup>-2</sup> .K <sup>-1</sup> )	$10.2 \pm 1.4$	$10.2 \pm 1.4$	$10.2 \pm 1.4$
	$\hat{\psi}$ (mW.m <sup>-1</sup> .K <sup>-1</sup> )	<b><math>27 \pm 7</math></b>	<b><math>30 \pm 7</math></b>	<b><math>135 \pm 10</math></b>
simulations	$\psi$ (mW.m <sup>-1</sup> .K <sup>-1</sup> )	<b>24</b>	<b>24</b>	<b>172</b>

It may be seen that the two methods lead to very similar results, especially for TB 1 and TB 2. The estimated transmission coefficient of TB 3 is slightly higher with the “ $h$  method” than the “ $I_{tb}$  method”. The later also has lower measurement un-



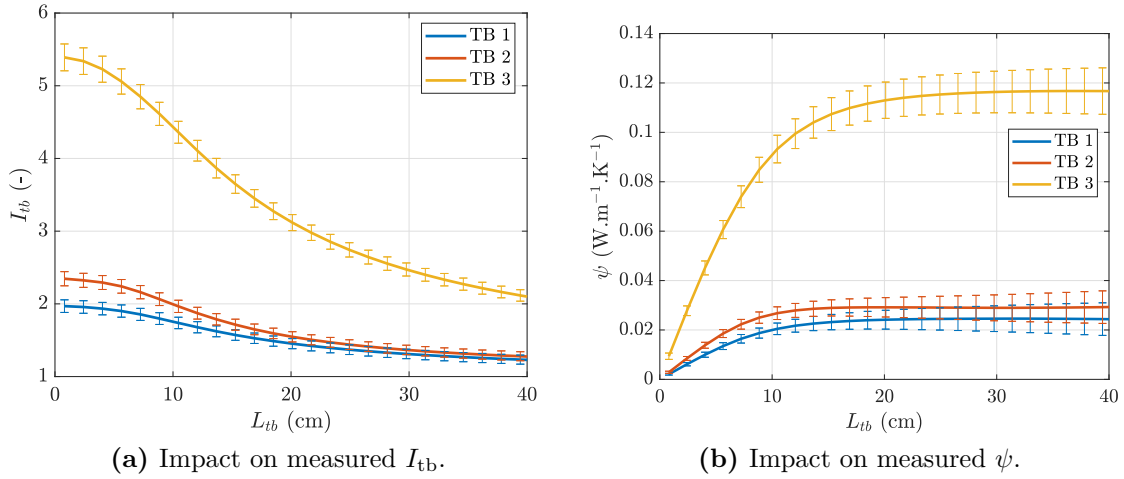
**Figure 6.18.:** Isothermal lines in the vicinity of the thermal bridges in steady-state for a unit temperature difference.

certainties. For this reason, the results of the “ $I_{tb}$  method” will be used as reference values for active methods.

The  $\psi$  values predicted by the numerical simulations are close to the measurement results for TB 1 (8% difference). The same model is used for these two thermal bridges. In other words, the joint between the gypsum boards and the screws are not taken into account, which explains the higher difference between measurements and simulations for TB 2: 25%. In addition, simulations overestimate the transmission coefficient of TB 3 (32%). It is thought that the discrepancy comes from a bad thermal contact between the metal rail and the building blocks. Indeed, the rail is not screwed on the blocks but only held on its top and bottom ends. For TB 1 and TB 2, there is an insulation layer between the rail and the concrete layer so contact thermal resistances have a much smaller impact.

### 6.3.6. Robustness assessment

This section presents the impact of  $L_{tb}$  and the altitude  $z$  on the measured  $\psi$  values. This analysis is presented for this setup only because of its large dimensions. An interesting result is that the measured  $\psi$ -value is rather robust to the choice of  $L_{tb}$ . As this length increases, the incidence factor  $I_{tb}$  decreases as shown in Fig 6.19a. This result is physical because when  $L_{tb}$  is large,  $\varphi_{tb}$  in Eq 6.4 is obtained from average over a larger zone mainly containing the sound area. However,  $\psi$  rapidly reaches a plateau as  $L_{tb}$  increases (see Fig 6.19b): the increase in  $L_{tb}$  compensates for a decrease in  $I_{tb}$ . This property is also predicted by the theory. However, the uncertainty on  $\psi$  keeps increasing with  $L_{tb}$  because the magnitude of  $I_{tb}$  tends to zero. For the wall considered, the temperature profile to select for the analysis needs to have a width  $L_{tb}$  approximately above 20 cm for TB 1 and TB 2 and above 30 cm for TB 3. Thus,  $L_{tb} = 30$  cm was set for each thermal bridge.



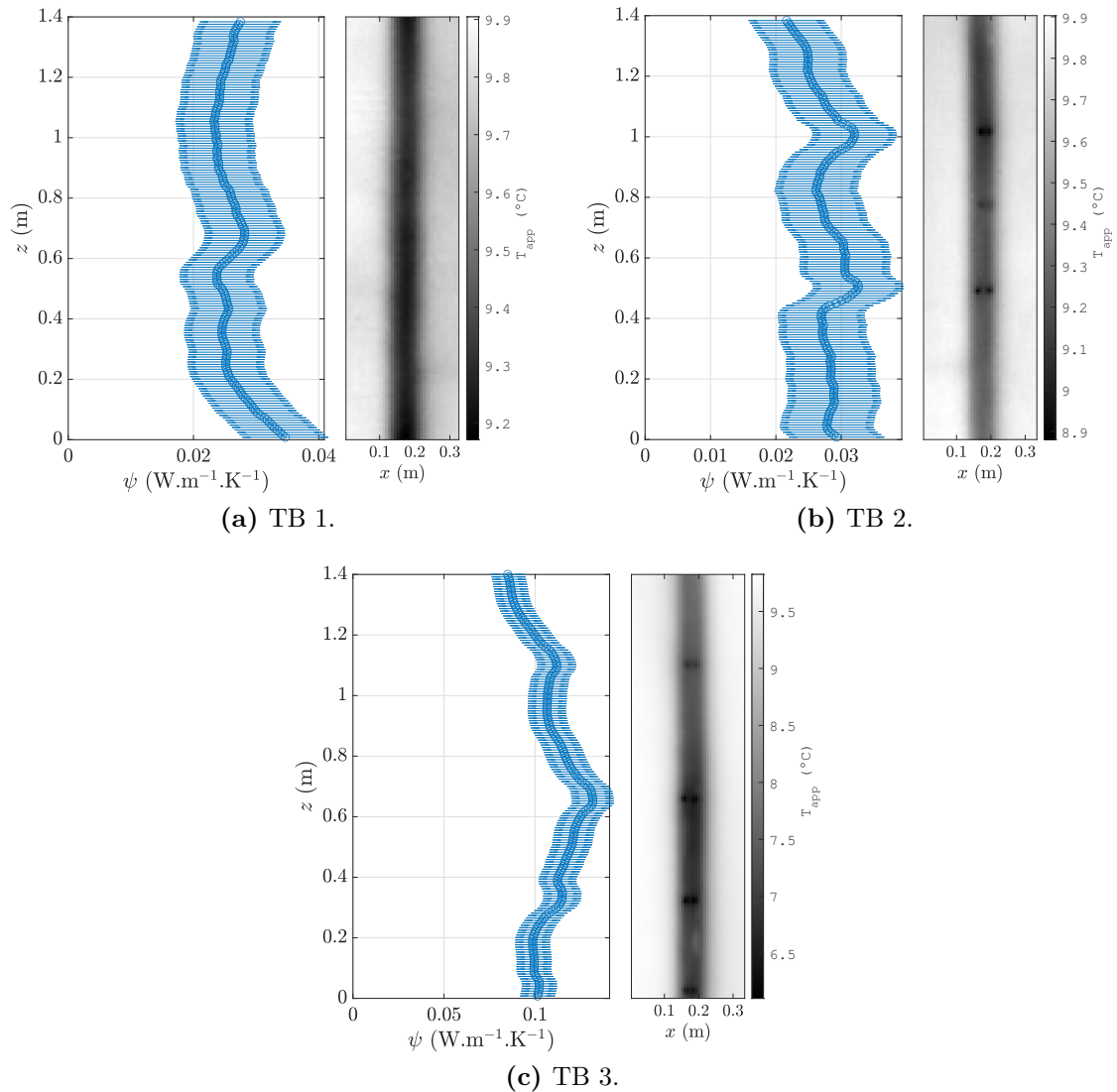
**Figure 6.19.:** Impact of  $L_{tb}$  on measured  $I_{tb}$  and  $\psi$  for each thermal bridge.

In addition, the  $\psi$ -value is rather independent on the altitude  $z$  of the ROIs used to derive the extract temperature profiles, as shown in figures 6.20a, 6.20b and 6.20c. The standard deviation of these profiles are equal to 2.2, 2.3 and 11.9  $\text{mW}\cdot\text{m}^{-1}\cdot\text{K}^{-1}$  which is about 10% of the mean  $\psi$ -value. The screws are clearly visible on  $\psi$  profiles for TB 2 and TB 3. In addition, there is a small edge effect on the bottom of TB 1: the estimated transmission coefficient slightly increases.

### 6.3.7. Conclusion

The thermal resistance of the sound area was measured from contact measurements in steady-state. A 20 K temperature gradient is enforced between the two sides of the wall. A steady-state is reached after about three days. The thermal resistance of the whole wall and the insulation system are estimated to  $3.49 \pm 0.11$  and  $3.15 \pm 0.10$   $\text{m}^2\cdot\text{K}\cdot\text{W}^{-1}$ , respectively. Like with the CERTES 1 setup, the “ $I_{tb}$ ” and “ $h$ ” methods lead to very similar results. The heat transfer coefficient was measured thanks to two HFM: one fixed on the wall, and the other one fixed nearby on





**Figure 6.20.:** Impact of altitude  $z$  on measured  $\psi$  coefficient and thermal image.

a piece of polystyrene (double measurement method). The  $\psi$  coefficient of TB 3 ( $120 \text{ W.m}^{-1}.\text{K}^{-1}$ ) is about four time higher than that of TB 1 and TB 2 ( $26$  and  $30 \text{ W.m}^{-1}.\text{K}^{-1}$ ). In addition, because TB 1 is not located on a joint between gypsum boards and has no screw, its has a smaller thermal transmittance than TB 2. A small discrepancy with the numerical simulations in noted on TB 3. This difference is thought to be due to a contact thermal resistance between the metal rail and the concrete building blocks. Finally, it was showed that the measured  $\psi$  coefficient is rather independent from the altitude and the chosen width  $L_{\text{tb}}$ , provided the latter is above 20 cm (30 cm for TB 3).

## 6.4. Results on SGR experiments

The SGR experimental campaign deals with *in situ* measurements. Here, the reference values for the thermal bridge transmission coefficients will be estimated with the “*h* method”. The “*I<sub>tb</sub>* method” could not be used because the measurement of the mean radiant temperature was biased by the presence of windows and other cold surfaces. A curtain should have been implemented to avoid such issue but it was not anticipated.

### 6.4.1. Contact measurements and *R* estimation

The average method from standard ISO 9869-1 [15] was used to measure the thermal resistance of the north and east walls. For light elements (i.e. specific heat capacity per unit area of less than 20 kJ.m<sup>-2</sup>.K<sup>-1</sup>), the standard provides some specific recommendations:

- The analysis is carried out only on data acquired at night (from one hour after sunset until sunrise), to avoid the effects of solar radiation.
- The test may be stopped when the result after three subsequent nights do not differ more than ±5%. Otherwise, it shall be continued.

Figure 6.21 plots the internal/external surface temperature difference  $\Delta T_{\text{sie}}$  and the internal surface heat flux  $\varphi_{\text{si}}$  measured on the north and east wall of the SGR test cell for three consecutive nights (the same nights as in Fig 4.30 in Chap 4). The internal temperature is controlled in order to remain constant around 35°C. Given the rather low external temperatures measured during the experiments, there is almost a 30 K temperature difference between the two sides of the walls.

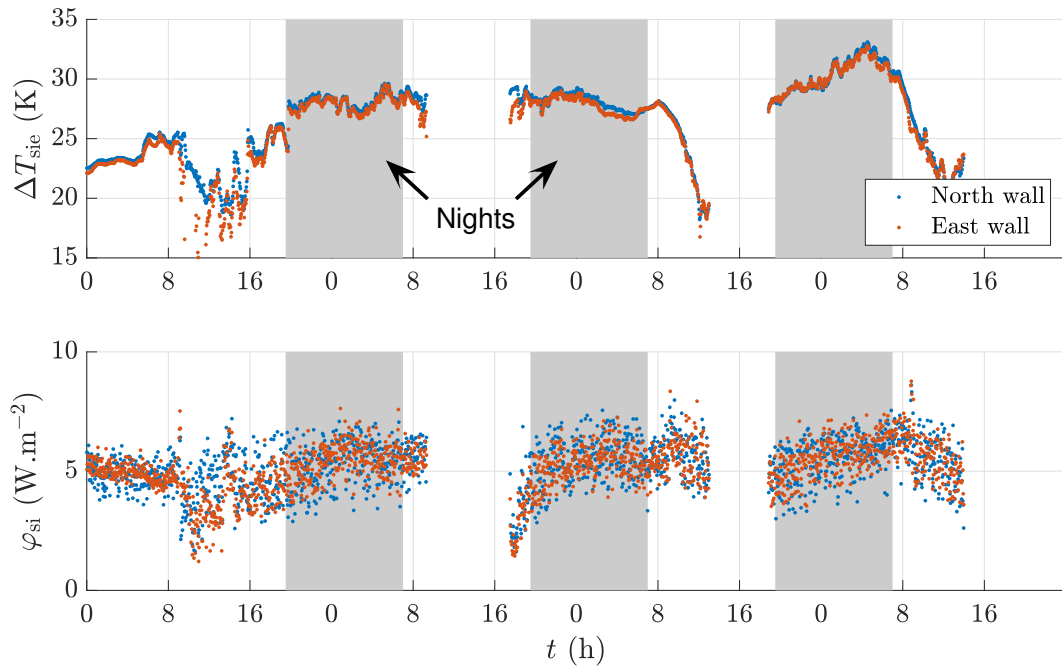
It may be noted that the heat flux and temperature difference are both rather constant during the three nights (shaded area) and the two walls have a very similar behavior. The weather conditions were close to optimal for an building energy diagnostic: the sky was cloudy for several consecutive days and there was very little wind.

The data collected during the nights is extracted and concatenated, as shown in Fig 6.22. Then, the temperature difference and the heat flux are averaged between the first measurement point and an upper limit *n*:

$$\overline{\Delta T_n} = \frac{1}{n} \sum_{k=1}^n \Delta T_{\text{sie}}(k) \quad (6.29)$$

and

$$\overline{\varphi_n} = \frac{1}{n} \sum_{k=1}^n \varphi_{\text{si}}(k) \quad (6.30)$$



**Figure 6.21.:** Internal/external surface temperature difference  $\Delta T_{\text{sie}}$  and internal surface heat flux  $\varphi_{\text{si}}$  measured during three consecutive cloudy nights of a pseudo-steady-state experiment.

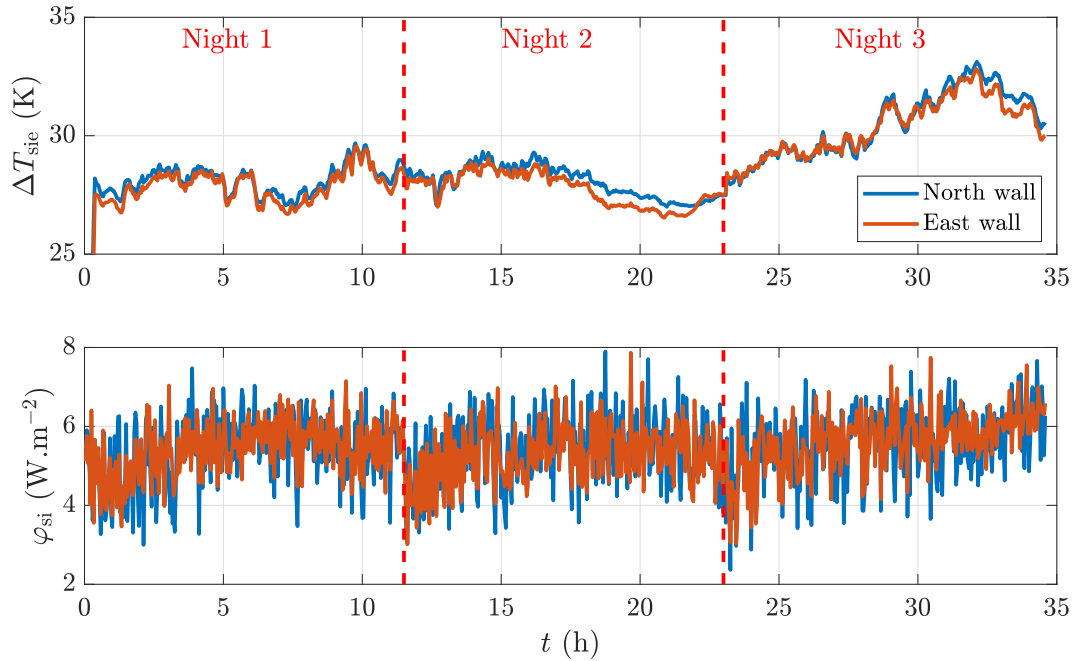
Thus, the upper bar here refers to time-averaged quantities. The estimated thermal resistance for a given  $n$  is simply given by:

$$\hat{R}_n = \frac{\overline{\Delta T_n}}{\overline{\varphi_n}} \quad (6.31)$$

The evolution of  $\hat{R}$  with  $n$  is plotted in Fig 6.23 for each wall. It may be seen that the estimated thermal resistance after three subsequent nights do not differ more that  $\pm 5\%$  (except at the very beginning). Thus, the estimation of  $R$  is deemed satisfying. The mean value over the last two nights for both walls is  $5.25 \pm 0.16 \text{ m}^2 \cdot \text{K} \cdot \text{W}^{-1}$  which is close to the theoretical value  $5.2 \text{ m}^2 \cdot \text{K} \cdot \text{W}^{-1}$  (calculated from manufacturer data, see Tab 4.6 in section 4.5).

#### 6.4.2. Measurement of $h$

The heat transfer coefficient is needed in the “ $h$  method” for the quantification of a thermal bridge  $\psi$ -value. It is measured with the  $h$ -meter fixed on the north wall. It uses the Harmonic Excitation (HE) method. The  $h$ -value estimated during four consecutive hours are plotted in Fig 6.24 as example. The estimation is not quite constant with time because of air movements induced by the temperature regulation system. However, the averaged value over several hours is very reproducible. Indeed, the averaged  $h$ -value measured during the three nights presented above are



**Figure 6.22.:** Concatenated night-time measurement data.

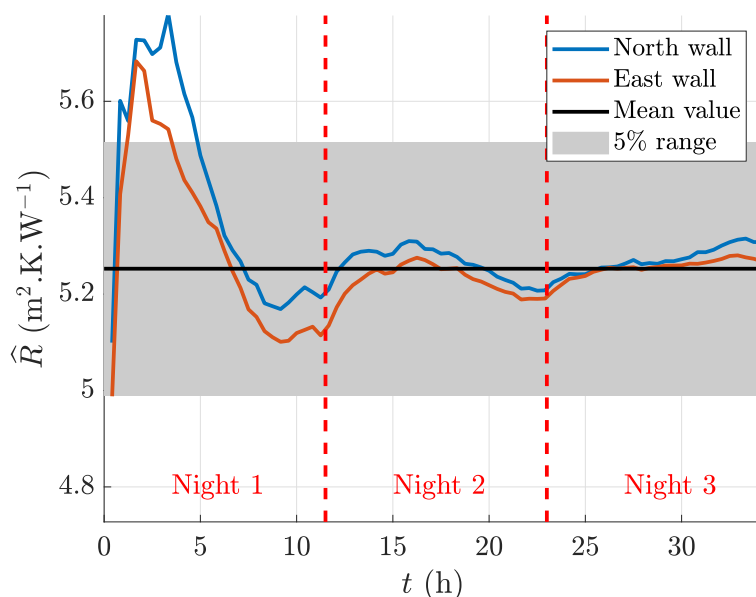
$9.94 \pm 0.78$ ,  $9.79 \pm 0.82$ ,  $9.88 \pm 0.76$   $\text{W}\cdot\text{m}^{-2}\cdot\text{K}^{-1}$ . Similarly to the CEREMA experiments, the measured heat transfer coefficient is higher than the standard value  $7.7$   $\text{W}\cdot\text{m}^{-2}\cdot\text{K}^{-1}$  because of the air movements induced by the temperature regulation system (electric fan heaters here).

### 6.4.3. Infrared measurements

An example of thermograms obtained in pseudo-steady-state are presented in Fig 6.25. The images are the average of 120 frames captured during 2 h. The two images do not have the length same scale because the east and north wall were filmed with a different angle. The aluminum sheet on each wall as well as the “ $h$ -meter” on the north wall may be noted. The metal rails inside the walls are visible, despite the small surface temperature contrasts (about  $0.2$  K). In comparison, the temperature contrast on the corners of the SGR are much higher. The ROIs of the five studied thermal bridges ( $N_1$  and  $N_2$  on the north wall;  $E_1$ ,  $E_2$  and  $E_3$  on the east wall) are shown on the thermal images. Figure 6.26 plots the apparent temperature profiles extracted from these ROIs. The temperature on each side of the thermal bridges is not always equal because of edge effects. Apart from this, the five temperature profiles are rather similar.

### 6.4.4. Numerical simulation

Similarly to the other setups, 2D numerical simulations were run to estimate the theoretical  $\psi$  value of the thermal bridges. The thickness and the thermal conductivity of the materials are given in Tab 6.8. The computational domain, as well as



**Figure 6.23.:** Estimation of walls thermal resistance from cumulated data as a function of dataset upper limit.

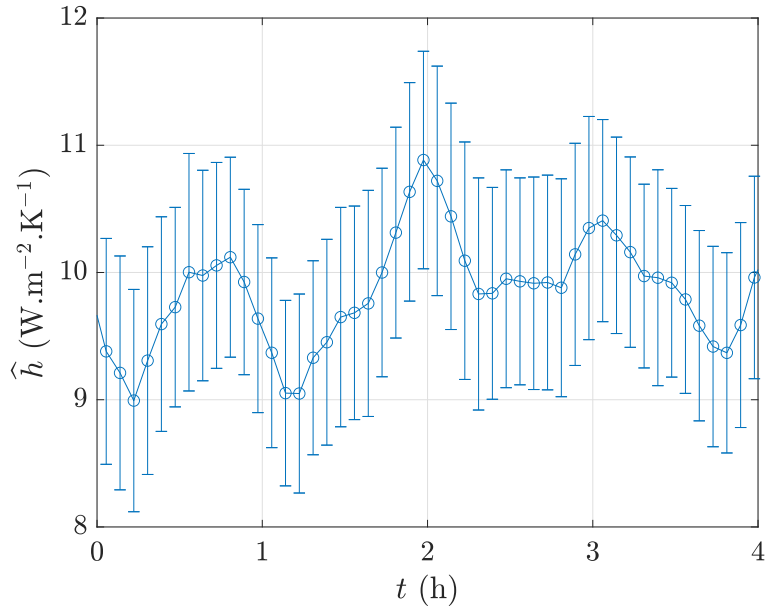
the results obtained for a unit internal/external temperature difference, are plotted in Fig 6.27. Given than all the thermal bridges studied on this setup are identical, a single numerical model was generated. In addition, only the vertical metal rails are modeled. The horizontal ones and the plastic pins between then are not taken into account. The corresponding transmission coefficient is equal to  $3.8 \text{ mW}\cdot\text{m}^{-1}\cdot\text{K}^{-1}$ .

**Table 6.8.:** Thermal conductivity and thickness of materials used in FE simulations.

	$k$ ( $\text{W}\cdot\text{m}^{-1}\cdot\text{K}^{-1}$ )	$e$ (mm)
Gypsum	0.23 (Hot Disk)	13
Glass wool	0.032 (Manufacturer)	120
Metal	70.2 (Hot Disk)	1
Polyurethane	0.025 (Manufacturer)	35

#### 6.4.5. Results of $\psi$ -values calculation

To assess the method reproducibility, the thermal bridge transmission coefficients are measured each one of the three nights presented above. The results are gathered in Tab 6.9. The measured heat transfer coefficients are reminded. All the thermal bridges studied have a similar  $\psi$ -value. The latter have a very small magnitude: around  $4.5 \text{ mW}\cdot\text{m}^{-1}\cdot\text{K}^{-1}$ . This is due to the small thickness of the metal rails (about 3 cm) when compared to the thickness of the insulation layers (about 15 cm). The numerical simulations predicted a slightly smaller linear transmittance. The measurement uncertainty is around 20%. Most of it comes from the very small temperature contrasts measured on the wall surface. The standard deviation between the three experiments is smaller than the individual uncertainties: below



**Figure 6.24.:** Sample of surface heat transfer coefficient measured on the north wall during the first night.

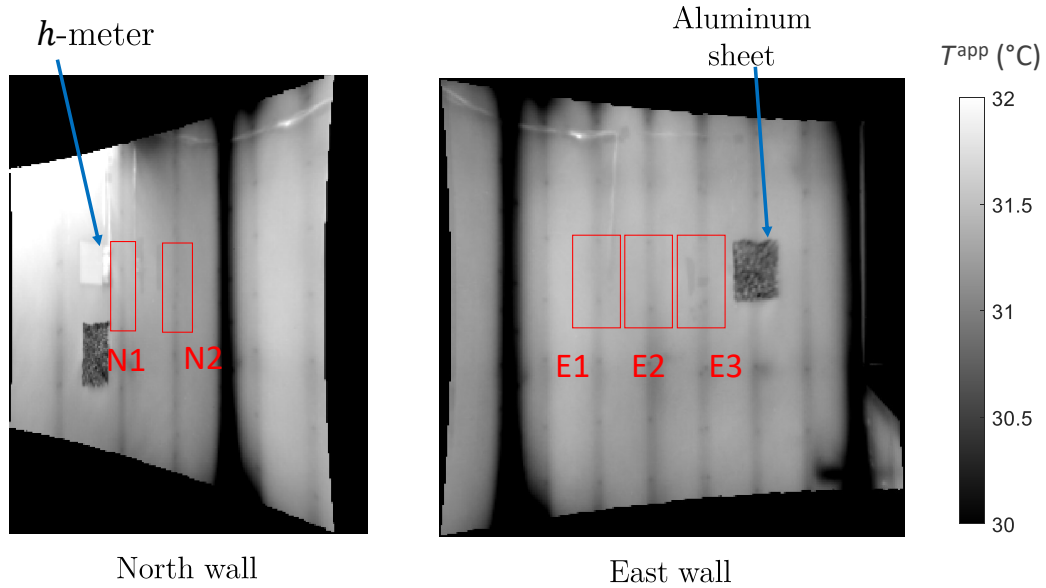
10%.

**Table 6.9.:** Estimated  $\psi$  values ( $\text{mW}\cdot\text{m}^{-1}\cdot\text{K}^{-1}$ ) for each steady-state experiment.

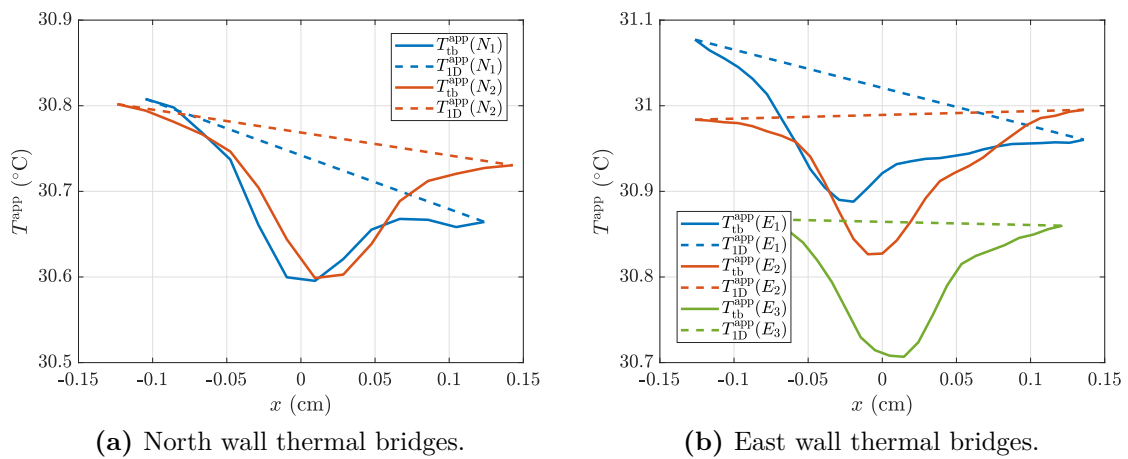
	TB	Night 1	Night 2	Night 3	Average	SD	Simu
$\hat{h}$ ( $\text{W}\cdot\text{m}^{-2}\cdot\text{K}^{-1}$ )	-	$9.94 \pm 0.78$ ,	$9.79 \pm 0.82$	$9.88 \pm 0.76$	9.87	0.07	-
$\hat{\psi}$ ( $\text{mW}\cdot\text{m}^{-1}\cdot\text{K}^{-1}$ )	N1	$4.0 \pm 1.0$	$4.0 \pm 1.0$	$4.4 \pm 1.0$	4.1	0.2	3.8
	N2	$4.8 \pm 1.2$	$4.7 \pm 1.2$	$5.5 \pm 1.1$	5.0	0.4	3.8
	E1	$6.2 \pm 1.1$	$5.6 \pm 1.1$	$5.3 \pm 1.0$	5.7	0.5	3.8
	E2	$4.1 \pm 1.1$	$4.6 \pm 1.1$	$5.1 \pm 1.0$	4.3	0.5	3.8
	E3	$5.1 \pm 1.0$	$4.5 \pm 1.0$	$4.6 \pm 0.9$	4.7	0.3	3.8

### 6.4.6. Conclusion

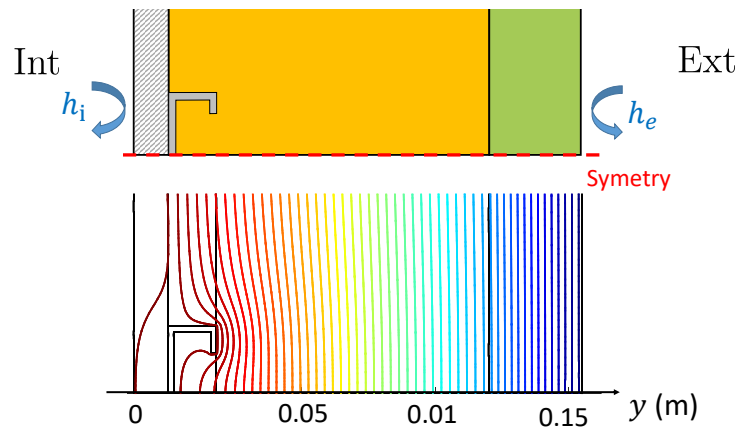
The thermal resistance of the north and east walls of the SGR test cell were measured in situ according to ISO 9869-1. The specific recommendations given for lightweight structures were followed. The estimated thermal resistance:  $5.25 \pm 0.16 \text{ m}^2\cdot\text{K}\cdot\text{W}^{-1}$ , is in good agreement with manufacturer data. In addition, the thermal bridges in the walls were estimated using the “ $h$  method”. Indeed, the “ $I_{\text{tb}}$  method” could not be used because the measurement of the mean radiant temperature with an infrared mirror was biased by the presence of cold surfaces (windows and door). The thermal bridges transmission coefficients are around  $5 \text{ mW}\cdot\text{m}^{-1}\cdot\text{K}^{-1}$ . These low values are explained by the small thickness of the metal rails.



**Figure 6.25.:** Thermograms of thermal bridges in steady-state with ROIs (average of 120 frame capture during 2 h of pseudo-steady-state).



**Figure 6.26.:** Measured apparent temperature profiles on thermal bridges in steady-state.



**Figure 6.27.:** Section of the computational domain and temperature iso-contours in the vicinity of the thermal bridge.



## 6.5. Conclusion

This chapter presented three steady-state measurement methods. The first method focuses on the quantification of a homogeneous wall thermal resistance  $R$ . It is the average method from ISO 9869-1. The other two aim at measuring a thermal bridge transmission coefficient  $\psi$  or  $\chi$ . The “ $I_{\text{tb}}$  method” is a variation of an existing method whereas the “ $h$  method” was developed during this thesis. Their main features are summarized in Tables 6.10a to 6.10c. The hypotheses to be made, the equipment required, as well as the pros and cons of the techniques are described. In addition, Table 6.11 summarizes the physical quantities which must be measured for each method.

The so-called “ $I_{\text{tb}}$  method” is an improvement of a method from the literature. It is based on the prior quantification of a thermal bridge incidence factor  $I_{\text{tb}}$  with infrared thermography. The main improvement consists in reducing the measurement uncertainties on  $I_{\text{tb}}$  by estimating it from apparent temperatures instead of true temperatures. This alternative approach is based on the same hypotheses as the “standard approach” but enables to halve the measurement uncertainties on  $\psi$  and  $\chi$  coefficients. The “ $I_{\text{tb}}$  method” is attractive for its simplicity. Indeed, there is not much equipment required apart from an infrared camera. In addition, the values of the global heat transfer coefficient  $h$  and the wall emissivity  $\varepsilon$  are not required for the quantification of  $I_{\text{tb}}$ . However, the method is based on many assumptions which make it only applicable indoor, in steady-state, and inside a well insulated room. One of most limiting hypothesis (*i.e.* hard to achieve *in situ*) is the equality between the air and the mean radiant temperatures. The operator must pay attention to cover cold surfaces (with a curtain for instance) for an accurate measurement of the mean radiant temperature (MRT).

The “ $h$  method” is an interesting alternative as it does not need the air and mean radiant temperatures to be equal, and the measurement of the latter is not needed. However, it requires the knowledge of both the heat transfer coefficient  $h$  and the wall emissivity  $\varepsilon$  which might increase the uncertainties. The  $h$ -value may be measured *in situ* or estimated with an empirical correlation or a default value if the conditions are met (typically, if no heating system is used).

All three methods were validated on the CERTES 1, CEREMA, and SGR setups (except for the “ $I_{\text{tb}}$  method” which was not applicable on the SGR experiments). When they are compared, the “ $I_{\text{tb}}$ ” and “ $h$ ” method lead to very similar results. In addition, a good agreement with predictions from numerical simulations was noted.

These methods are based on steady-state assumptions so they require long measurements (several days) and might be rather sensitive to weather conditions. Nevertheless, when the conditions are met (such as in laboratory or inside a climate chamber), these methods are accurate. This is the reason why it has been used in this thesis to obtain reference values for thermal bridge transmission coefficients. For *in situ* applications, the active methods presented in later chapters are more relevant. The present methods could also be valuable for a characterization of thermal bridges inside a guarded hot box.

6.5. CONCLUSION

**Table 6.10.:** Summary of mean features of steady-state methods.

(a) Measurement of a homogeneous wall thermal resistance  $R$ .

Hypotheses	Equipment	Comments
<ul style="list-style-type: none"> <li>• steady-state</li> </ul>	<ul style="list-style-type: none"> <li>• one HFM</li> <li>• temperature sensors</li> </ul>	Pros <ul style="list-style-type: none"> <li>• easy to implement</li> </ul> Cons <ul style="list-style-type: none"> <li>• local measurement</li> <li>• only works in steady-state</li> </ul>

(b) Measurement of a thermal bridge impact factor  $I_{tb}$  (combine with Tab 6.10a for quantification of  $\psi$  or  $\chi$  coefficient with “ $I_{tb}$ ” method).

Hypotheses	Equipment	Comments
<ul style="list-style-type: none"> <li>• steady-state</li> <li>• small <math>\Delta T</math></li> <li>• uniform <math>h^r</math> and <math>h^c</math></li> <li>• uniform <math>\varepsilon</math></li> <li>• <math>T_{air} = T_{env}</math></li> </ul>	<ul style="list-style-type: none"> <li>• infrared camera</li> <li>• aluminum sheet</li> <li>• ruler for scale</li> </ul>	Pros <ul style="list-style-type: none"> <li>• easy to implement</li> <li>• no need of <math>h</math> or <math>\varepsilon</math></li> </ul> Cons <ul style="list-style-type: none"> <li>• only works indoor, in steady-state and inside a well insulated building</li> </ul>

(c) Measurement of a thermal bridge  $\psi$  or  $\chi$  coefficient (“ $h$  method”).

Hypotheses	Equipment	Comments
<ul style="list-style-type: none"> <li>• steady-state</li> <li>• small <math>\Delta T</math></li> <li>• uniform <math>h</math></li> <li>• uniform <math>\varepsilon</math></li> </ul>	<ul style="list-style-type: none"> <li>• temperature sensors</li> <li>• infrared camera</li> <li>• <math>h</math>-meter</li> <li>• ruler for scale</li> </ul>	Pros <ul style="list-style-type: none"> <li>• no need of <math>T_{air} = T_{env}</math></li> <li>• applicable outdoor (in theory)</li> </ul> Cons <ul style="list-style-type: none"> <li>• need of <math>h</math> and <math>\varepsilon</math></li> <li>• only works in steady-state</li> </ul>

**Table 6.11.:** Summary of measurements needed for each method.

Quantity	Sensor	“ $I_{tb}$ method”			
		ISO 9869-1	standard approach	present approach	“ $h$ -method”
$\varphi_{si}$	HFM	✓	✓	✓	x
$\Delta T_{sie}$ or $\Delta T_{ie}$	Thermocouples	✓	✓	✓	✓
$\Delta T^{app}$	IRT	x	✓	✓	✓
$\varepsilon$	standard value	x	✓	x	✓
$h$	$h$ -meter/ standard value	x	x	x	✓



## 7. Theory on Inverse methods

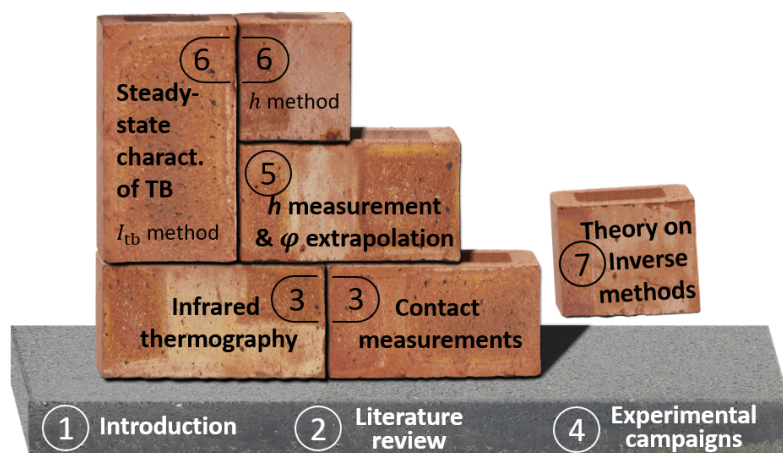


Figure 7.1.: Illustration of thesis plan.

This theoretical chapter introduces the main mathematical tools used in the thesis. They will be applied in Chap 8 and 9 to estimate a wall thermal resistance (or equivalent resistance) from active measurements.

Section 7.1 presents the construction of a direct model of a wall with the thermal quadrupole formalism. Section 7.2 deals with inverse methods for non-linear parameter estimation problems using a white-box direct model. Section 7.3 is about ARX (Auto-Regressive with eXogenous inputs) black-box models. They are an alternative to previous white-box based approaches. Section 7.4 presents a conclusion.

## Nomenclature

### Acronyms

ACF	AutoCorrelation Function
ARMA	Auto-Regressive with Moving Average
ARX	Auto-Regressive with eXogenous inputs
CCF	Cross-Correlation Function
OLS	Ordinary Least Squares
SISO	Single Input Single Output
SVD	Singular Value Decomposition

### Greek Symbols

$\beta$	vector of model unknown parameters	
$\epsilon$	measurement noise	
$\theta$	temperature difference $T - T_{\text{ref}}$	K
$\mu$	damping factor	
$\rho$	correlation coefficient	
$\sigma$	noise standard deviation	
$\tau$	thermal characteristic time	s
$\tau_T$	thermal load time constant	s
$\varphi$	heat flux density	W.m <sup>-2</sup>

### Roman Symbols

$A, B, C, D$	thermal quadrupole coefficients	
$\mathcal{A}, \mathcal{B}, \mathcal{C}$	ARX polynomials	
$a, b, c$	ARX polynomial parameters	
$a$	thermal diffusivity	m <sup>2</sup> .s <sup>-1</sup>
$A_T$	thermal load amplitude	K
$b$	thermal effusivity	J.K <sup>-1</sup> .m <sup>-2</sup> .s <sup>-1/2</sup>
$C$	thermal capacity per unit surface	J.K <sup>-1</sup> .m <sup>-2</sup>
cov	covariance	
cor	correlation matrix	
$e$	layer thickness / error	m / -
E	expectancy operator	
$f$	function / frequency	- / s <sup>-1</sup>
$f_s$	sampling frequency	s <sup>-1</sup>
$h$	heat transfer coefficient / system impulse response	W.m <sup>-2</sup> .K <sup>-1</sup> / -
$G$	deconvolution matrix	
$H$	ARX matrix	
$I$	identity matrix	
$j$	complex number such that $j^2 = -1$	
$J$	cost function	
$k$	thermal conductivity	W.m <sup>-1</sup> .K <sup>-1</sup>
$m$	number of measurement points	-
$n$	number of parameters of the model	-
$n_a, n_b, n_k$	ARX number of parameters	-
$N$	Gaver-Stehfest algorithm order	-
$p$	probability density function / Laplace variable	- / s <sup>-1</sup>

---

$P$	period	s
$q$	backshift operator	
$\mathbf{r}$	residuals	
$R$	thermal resistance	$\text{m}^2 \cdot \text{K} \cdot \text{W}^{-1}$
$t$	time	s
$tol$	De Hoog algorithm tolerance	
$T$	temperature	K
$\mathbf{u}$	model input	
var	variance	
$V_{\text{cor}}$	hybrid matrix	
$x$	abscissa	
$\mathbf{x}$	state vector	
$\mathbf{x}_0$	initial conditions	
$X$	sensitivity	
$X^*$	reduced sensitivity	
$\mathbf{y}$	model output	
$Z$	estimated thermal impedance (ARX)	$\text{m}^2 \cdot \text{K} \cdot \text{W}^{-1}$
$Z$	theoretical thermal impedance	$\text{m}^2 \cdot \text{K} \cdot \text{W}^{-1}$
<b>Superscripts</b>		
$\wedge$	estimated	
$\sim$	quantity in the Laplace domain	
T	matrix transpose operator	
<b>Subscripts</b>		
e	external surface	
i	internal surface	
max	maximum	
mo	model	
op	operative	
ref	reference	
s	surface	

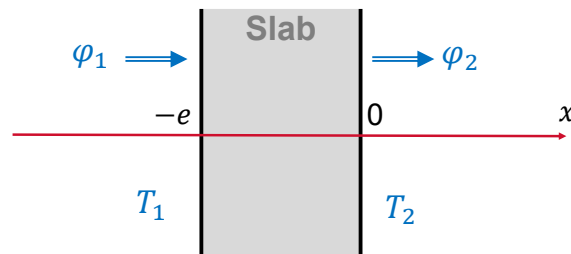
## 7.1. Direct model definition with thermal quadrupole formalism

In order to apply an inverse method, a model of the physical phenomenon at stake is required (“direct model”, see section 7.2).

The thermal quadrupole formalism [191] is very convenient to model one-dimensional multi-layer heat conduction problems. This approach uses the Laplace transform of the heat equation. In the Laplace domain, relations between surface temperatures and heat fluxes are simply given by a  $2 \times 2$  matrix multiplication. Models derived with the thermal quadrupoles belong to the “semi-analytical” category because a numerical Laplace inversion algorithm is required to obtain data in the time domain. However, if the data is analyzed directly in the frequency domain, the model is fully analytical. The models are implemented in MATLAB.

### 7.1.1. Thermal quadrupole formalism from 1D slab equations

Let us consider a 1D slab of thickness  $e$  located between abscissa  $x = -e$  and  $x = 0$  and subjected to Dirichlet boundary conditions, as illustrated in Fig 7.2. The slab is supposed initially at thermal equilibrium.



**Figure 7.2.:** Scheme of a simple slab (1D problem).

The heat conduction problem is defined by the heat equation:

$$\frac{\partial^2 T(x, t)}{\partial x^2} = \frac{1}{a} \frac{\partial T(x, t)}{\partial t} \quad (7.1)$$

the following Dirichlet boundary conditions:

$$\forall t > 0 : \begin{cases} T(x = -e, t) = T_1 \\ T(x = 0, t) = T_2 \end{cases} \quad (7.2)$$

and the initial condition:

$$\forall x \in \llbracket -e, 0 \rrbracket : T(x, t = 0) = T_{\text{ref}} \quad (7.3)$$

with  $a$  the thermal diffusivity of the material. In practice, the absolute temperature  $T$  is not directly calculated: the relative temperature  $\theta = T - T_{\text{ref}}$  is rather used. Temperature  $T$  may then be substituted by  $\theta$  in the previous equations ( $\theta(x, t = 0) = \theta_{\text{ref}} = 0$ ).

The Laplace transform  $\tilde{f}$  of a function  $f$  is given by:

$$\tilde{f} : p \mapsto \int_0^\infty f(\tau) \exp(-\tau p) d\tau \quad (7.4)$$

In the Laplace domain, equations 7.1 and 7.2 become (the initial condition is null):

$$\frac{\partial^2 \tilde{\theta}(x, p)}{\partial x^2} = \frac{p}{a} \tilde{\theta}(x, p) \quad (7.5)$$

$$\begin{cases} \tilde{\theta}(x = -e, p) &= \tilde{\theta}_1(p) \\ \tilde{\theta}(x = 0, p) &= \tilde{\theta}_2(p) \end{cases} \quad (7.6)$$

with  $p$  the Laplace variable. The 1D heat flux density  $\varphi$  is derived from the temperature gradient with the Fourier's law:

$$\varphi = -k \frac{\partial T}{\partial x} \quad (7.7)$$

with  $k$  the medium thermal conductivity. The solutions of Eq 7.5 are:

$$\begin{cases} \tilde{\theta}(x, p) &= K_1 \times \cosh(\alpha x) + K_2 \times \sinh(\alpha x) \\ \tilde{\varphi}(x, p) &= -k\alpha K_1 \times \sinh(\alpha x) - k\alpha K_2 \times \cosh(\alpha x) \end{cases} \quad (7.8)$$

with  $\alpha = \sqrt{\frac{p}{a}}$ , and  $K_1$  and  $K_2$  two constants determined from the boundary conditions:

$$\begin{cases} \tilde{\theta}(x = 0, p) &= K_1 \\ \tilde{\varphi}(x = 0, p) &= -kK_2 \sqrt{\frac{p}{a}} \end{cases} \quad (7.9)$$



hence

$$\begin{cases} \widetilde{\theta}_1 &= \cosh(\alpha e) \times \widetilde{\theta}_2 + \sinh(\alpha e) / (k\alpha) \times \widetilde{\varphi}_2 \\ \widetilde{\varphi}_1 &= k\alpha \sinh(\alpha e) \times \widetilde{\theta}_2 + \cosh(\alpha e) \times \widetilde{\varphi}_2 \end{cases} \quad (7.10)$$

Finally, the thermal quadrupole formulation of the 1D slab equation is obtained from the matrix form of Eq 7.10:

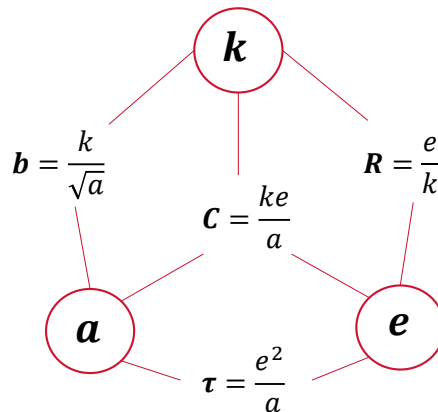
$$\begin{bmatrix} \widetilde{\theta}_1 \\ \widetilde{\varphi}_1 \end{bmatrix} = \begin{bmatrix} A & B \\ C & D \end{bmatrix} \begin{bmatrix} \widetilde{\theta}_2 \\ \widetilde{\varphi}_2 \end{bmatrix} \quad (7.11)$$

with  $A$ ,  $B$ ,  $C$  and  $D$  the quadrupole coefficients:

$$\begin{bmatrix} A & B \\ C & D \end{bmatrix} = \begin{bmatrix} \cosh\left(e\sqrt{\frac{p}{a}}\right) & \sinh\left(\sqrt{\frac{p}{a}}e\right) / \left(k\sqrt{\frac{p}{a}}\right) \\ \sinh\left(\sqrt{\frac{p}{a}}e\right) \times k\sqrt{\frac{p}{a}} & \cosh\left(e\sqrt{\frac{p}{a}}\right) \end{bmatrix} \quad (7.12)$$

### 7.1.2. Parameterization

A single-layer 1D slab has two degrees of freedom. In other words, two parameters are sufficient to define its thermal behavior. Basically, from the slab three “basic” characteristics used so far (thickness  $e$ , thermal conductivity  $k$ , and thermal diffusivity  $a$ ), four physical parameters may be derived, as illustrated in Fig 7.3. They are: a thermal resistance  $R = e/k$ , a thermal capacity  $C = ke/a$ , a thermal characteristic time  $\tau = e^2/a$ , and a thermal effusivity  $b = k/\sqrt{a}$ .



**Figure 7.3.:** A 1D uniform wall is thermally characterized by any two of the four parameters  $R$ ,  $C$ ,  $\tau$  and  $b$  which are derived from  $e$ ,  $k$  and  $a$ .

Any couple of parameters among  $R$ ,  $C$ ,  $\tau$  and  $b$  may be used to characterize the slab. The quadrupole coefficients of the different parameterizations are given as follows:

- Parameterization  $(R, C)$ :

$$\begin{bmatrix} A & B \\ C & D \end{bmatrix} = \begin{bmatrix} \cosh(\sqrt{pRC}) & \sinh(\sqrt{pRC}) / (\sqrt{p\frac{C}{R}}) \\ \sinh(\sqrt{pRC}) \times \sqrt{p\frac{C}{R}} & \cosh(\sqrt{pRC}) \end{bmatrix} \quad (7.13)$$

- Parameterization  $(R, b)$ :

$$\begin{bmatrix} A & B \\ C & D \end{bmatrix} = \begin{bmatrix} \cosh(Rb\sqrt{p}) & \sinh(Rb\sqrt{p}) / (b\sqrt{p}) \\ \sinh(Rb\sqrt{p}) \times b\sqrt{p} & \cosh(Rb\sqrt{p}) \end{bmatrix} \quad (7.14)$$

- Parameterization  $(R, \tau)$ :

$$\begin{bmatrix} A & B \\ C & D \end{bmatrix} = \begin{bmatrix} \cosh(\sqrt{p\tau}) & \sinh(\sqrt{p\tau}) / (\frac{\tau}{R}\sqrt{p}) \\ \sinh(\sqrt{p\tau}) \times \frac{\tau}{R}\sqrt{p} & \cosh(\sqrt{p\tau}) \end{bmatrix} \quad (7.15)$$

- Parameterization  $(\tau, b)$ :

$$\begin{bmatrix} A & B \\ C & D \end{bmatrix} = \begin{bmatrix} \cosh(\sqrt{p\tau}) & \sinh(p\tau) / (b\sqrt{p}) \\ \sinh(p\tau) \times b\sqrt{p} & \cosh(p\tau) \end{bmatrix} \quad (7.16)$$

- Parameterization  $(\tau, C)$ :

$$\begin{bmatrix} A & B \\ C & D \end{bmatrix} = \begin{bmatrix} \cosh(\sqrt{p\tau}) & \sinh(p\tau) / (C\sqrt{\frac{p}{\tau}}) \\ \sinh(p\tau) \times C\sqrt{\frac{p}{\tau}} & \cosh(p\tau) \end{bmatrix} \quad (7.17)$$

- Parameterization  $(C, b)$ :

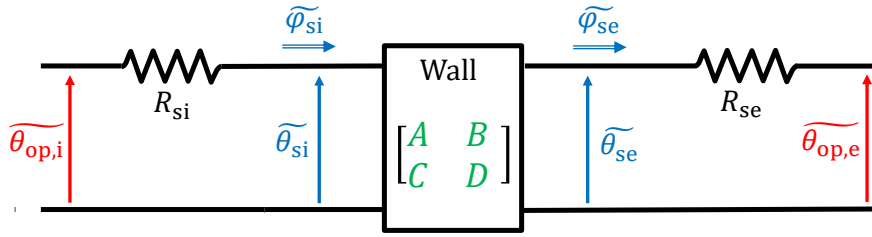
$$\begin{bmatrix} A & B \\ C & D \end{bmatrix} = \begin{bmatrix} \cosh(\frac{C}{b}\sqrt{p}) & \sinh(\frac{C}{b}\sqrt{p}) / (b\sqrt{p}) \\ \sinh(\frac{C}{b}\sqrt{p}) \times b\sqrt{p} & \cosh(\frac{C}{b}\sqrt{p}) \end{bmatrix} \quad (7.18)$$

In this thesis, the couple  $(R, b)$  was chosen to parameterize the quadrupole matrix. Indeed,  $R$  is the parameter we want to estimate whereas  $b$  has the advantage of being independent of the layer thickness. It is also the parameter characterizing a semi-infinite layer. This choice will have no impact on the well-posedness of the problem (see section 7.2). Indeed,  $R$  will be estimated with the same uncertainty regardless of the second parameter chosen (either  $b$ ,  $C$  or  $\tau$ ).

### 7.1.3. Application to a multilayer building wall

Here is detailed the derivation of the model of a multi-layer 1D wall exchanging heat with the surrounding environments of operative temperatures  $\theta_{\text{op},i}$  and  $\theta_{\text{op},e}$  with heat transfer coefficients  $h_i$  and  $h_e$  (or superficial resistances  $R_{\text{si}}$  and  $R_{\text{se}}$ ). A representation of the problem is shown in Fig 7.4 (electrical analogy).

The  $2 \times 2$  matrix which characterizes a multi-layer wall is given by multiplication of the matrices of each individual layer:



**Figure 7.4.:** Electrical analogy of a 1D wall exchanging heat with the surrounding environments.

$$\begin{bmatrix} \widetilde{\theta}_{si} \\ \widetilde{\varphi}_{si} \end{bmatrix} = \prod_{k=1}^N \begin{bmatrix} A_k & B_k \\ C_k & D_k \end{bmatrix} \begin{bmatrix} \widetilde{\theta}_{se} \\ \widetilde{\varphi}_{se} \end{bmatrix} \quad (7.19)$$

$$= \begin{bmatrix} A & B \\ C & D \end{bmatrix} \begin{bmatrix} \widetilde{\theta}_{se} \\ \widetilde{\varphi}_{se} \end{bmatrix} \quad (7.20)$$

with  $N$  the number of layers. Thus, the internal surface heat flux may be expressed as a function of the wall surface temperatures:

$$\widetilde{\varphi}_{si} = \frac{D}{B} \widetilde{\theta}_{si} - \frac{1}{B} \widetilde{\theta}_{se} \quad (7.21)$$

This formulation will be used in later chapters for the application of inverse methods. The complete model (i.e. including heat transfer coefficients) is given by:

$$\begin{bmatrix} \widetilde{\theta}_{op,i} \\ \widetilde{\varphi}_{si} \end{bmatrix} = \begin{bmatrix} 1 & 1/h_e \\ 0 & 1 \end{bmatrix} \prod_{k=1}^N \begin{bmatrix} A_k & B_k \\ C_k & D_k \end{bmatrix} \begin{bmatrix} 1 & 1/h_e \\ 0 & 1 \end{bmatrix} \begin{bmatrix} \widetilde{\theta}_{op,e} \\ \widetilde{\varphi}_{se} \end{bmatrix} \quad (7.22)$$

$$= \begin{bmatrix} A' & B' \\ C' & D' \end{bmatrix} \begin{bmatrix} \widetilde{\theta}_{op,e} \\ \widetilde{\varphi}_{se} \end{bmatrix} \quad (7.23)$$

The internal surface heat flux is here given by:

$$\widetilde{\varphi}_{si} = \frac{D'}{B'} \widetilde{\theta}_{op,i} - \frac{1}{B'} \widetilde{\theta}_{op,e} \quad (7.24)$$

#### 7.1.4. Numerical Laplace inversion

Equations 7.21 and 7.24 relates quantities in the Laplace domain. In order to derive from them a model in the time domain, a numerical Laplace inversion algorithm is

required. Two such algorithms are commonly used and presented here: the Gaver-Stehfest and De Hoog algorithms.

#### 7.1.4.1. Gaver-Stehfest algorithm

The Gaver-Stehfest algorithm [199] has been popular due to its simplicity and adequacy for exponentially decaying functions. With this algorithm, the inverse Laplace transform  $f$  of a function  $\tilde{f}$  is given by the following sum:

$$f(t) = \frac{\ln(2)}{t} \sum_{i=1}^N c_i(N) \tilde{f}\left(\frac{i \ln(2)}{t}\right), \quad n \geq 1, t > 0 \quad (7.25)$$

where  $N$  is the order of the algorithm. Coefficients  $c_i(N)$  are defined by:

$$c_i(N) = (-1)^{\frac{N}{2}+i} \sum_{k=\lfloor \frac{i+1}{2} \rfloor}^{\min(i, \frac{N}{2})} \frac{k^{\frac{N}{2}} (2k)!}{\left(\frac{N}{2} - k\right)! k! (k-1)! (i-k)! (2k-i)!}, \quad N \geq 1, 1 \leq k \leq N \quad (7.26)$$

with  $\lfloor \cdot \rfloor$  the integer part operator. The method is quite easy to program since the coefficients can be computed once and saved as constants. For most cases, the algorithm with  $N = 10$  is well adapted to simple precision calculations. The corresponding coefficients are given in Tab 7.1.

**Table 7.1.:** Coefficients of the Gaver-Stehfest algorithm for  $N = 10$ .

$c_1$	$c_2$	$c_3$	$c_4$	$c_5$	$c_6$	$c_7$	$c_8$	$c_9$	$c_{10}$
$\frac{1}{12}$	$-\frac{385}{12}$	1279	$-\frac{46871}{3}$	$\frac{505465}{6}$	$-\frac{473915}{2}$	$\frac{1127735}{3}$	$-\frac{1020215}{3}$	$\frac{328125}{2}$	$-\frac{65625}{2}$

However, depending on the studied function, the value of the hyperparameter  $N$  might have to be increased for the algorithm to converge. For instance, polynomial functions of high order require a higher value of  $N$ . Let us take the example of the following function on a given interval  $[0, t_{\max}]$ :

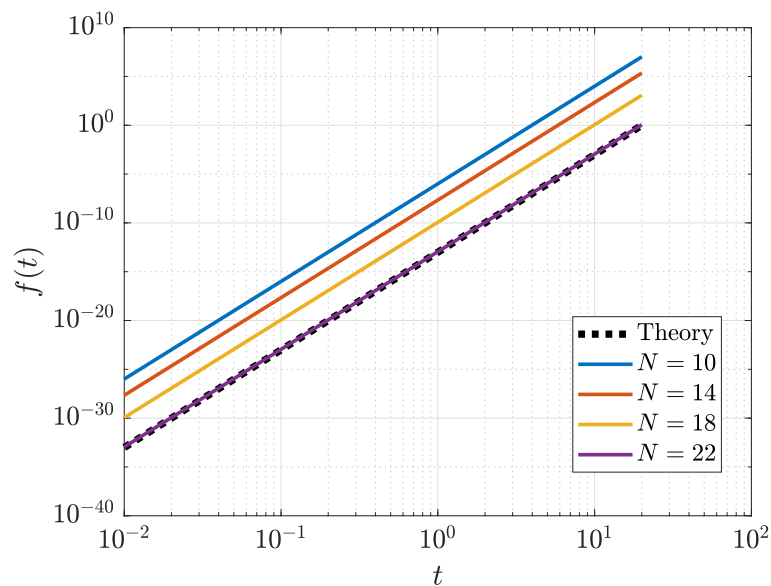
$$f : t \mapsto Kt^{10} \quad (7.27)$$

with  $K$  the normalizing constant such that  $f(t_{\max}) = 1$ . The Laplace transform of

this function is:

$$\tilde{f} : p \mapsto K \frac{10!}{p^{11}} \quad (7.28)$$

Figure 7.5 shows the impact of  $N$  on the results of the Gaver-Stehfest algorithm applied to this function with  $t_{\max} = 100$ . It may be seen that inversions with  $N < 22$  lead to a biased function in the time domain. As a consequence, the order of the Gaver-Stehfest algorithm has to be adapted to the function (note that a too high order can lead to the divergence of the algorithm).



**Figure 7.5.:** Time-domain functions obtained from application of the Gaver-Stehfest algorithm on function in Eq 7.28 for several orders  $N$ .

#### 7.1.4.2. De Hoog algorithm

The more recent De Hoog algorithm [200] is more robust. This is the algorithm used in the present thesis. It is implemented in the “invlap” MATLAB function [201]. The algorithm is based on an accelerated form of the Fourier series numerical inverse Laplace transform algorithm. The un-accelerated approach is:

$$f(t) = \frac{\exp(\gamma t)}{T} \left( \frac{\tilde{f}(\gamma)}{2} + \sum_{k=1}^{2M} \Re \left[ \tilde{f} \left( \gamma + \frac{j\pi k}{T} \right) \exp \left( \frac{j\pi k t}{T} \right) \right] \right) \quad (7.29)$$

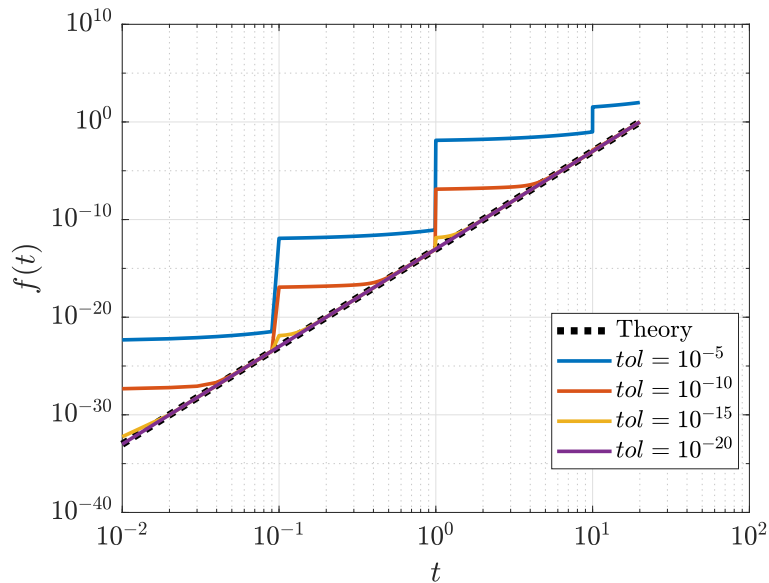
with

$$\gamma = \alpha - \frac{\log(tol)}{2T} \quad (7.30)$$

where  $T = 2t_{\max}$  is a scaled time,  $M$  defines the length of the Fourier series expansion (there are  $2M + 1$  terms),  $\alpha$  is the largest pole of  $\tilde{f}$ , and  $tol$  is the numerical tolerance of approaching pole. However, this approach requires so many function evaluations that it is not practical. Hence the use of a non-linear acceleration (see [200] for further details).

In the “invlap” MATLAB function, hyperparameters  $\alpha$  and  $tol$  are taken as inputs and  $M$  is set to 20. The tolerance  $tol$  proposes a trade-off between accuracy and speed, its default value is  $10^{-9}$ . In addition, the algorithm splits up the time vector in pieces of same order of magnitude and inverts one piece at a time. Indeed, simultaneous inversion for times covering several orders of magnitudes gives inaccurate results for small times.

Similarly with the Gaver-Stehfest algorithm, the choice of the tolerance value  $tol$  depends on the function to invert. As an example, Figure 7.6 plots the results obtained from application of the De Hoog algorithm to the polynomial function given in Eq 7.28. The tolerance is varied whereas  $\alpha = 0$  (default value). For such high order polynomial function, the tolerance has to be decreased to  $10^{-20}$  for the Laplace inversion to be accurate. The discontinuities observed for higher tolerance values are due to the split of the time vector in pieces of same order of magnitude.



**Figure 7.6.:** Time-domain functions obtained from application of the Gaver-Stehfest algorithm on function in Eq 7.28 for several tolerances  $tol$  and  $\alpha = 0$ .

### 7.1.4.3. Limitation of numerical Laplace inversion algorithms

Numerical inverse Laplace transform algorithms are reliable for some type of functions, such as decaying signals. However, they may behave poorly for other type of functions. Typically, the inversion in the Laplace domain of oscillating functions is

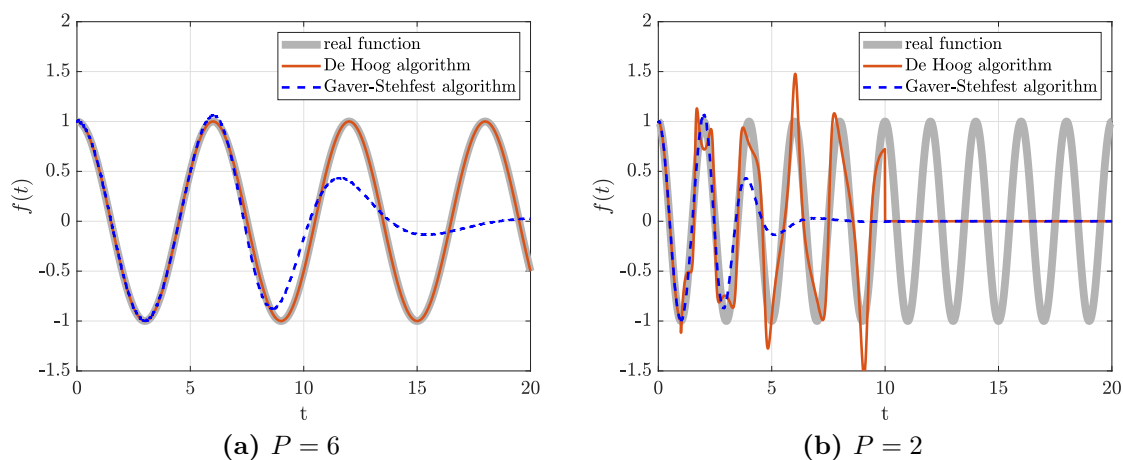
usually not possible. Let us consider the example of a simple cosine function:

$$f : t \mapsto \cos\left(2\pi\frac{t}{P}\right) \quad (7.31)$$

with  $P$  the period. The Laplace transform of this function is:

$$\tilde{f} : t \mapsto \frac{p}{p^2 + P^2} \quad (7.32)$$

Figure 7.7 plots the estimated functions in the time domain after application of the Gaver-Stehfest and De Hoog algorithms to  $\tilde{f}$ . The inversions are performed on the interval  $[0; 20]$  for two different periods:  $P = 2$  and  $P = 6$ . It is clear that the Gaver-Stehfest is not able to inverse this function. While the signal is correctly reconstructed at short times, its amplitude decreases and becomes null after a few periods. The De Hoog algorithm is more robust as it is able to reconstruct the cosine function for a signal with a small number of periods (about three here in the  $P = 6$  case). Yet, when the number of periods increases (see  $P = 2$  case), the algorithm diverges. Increasing  $N$  or decreasing  $tol$  does not improve the inversions.



**Figure 7.7.:** Numerical Laplace inversions of a cosine function ( $N = 20$  for Gaver-Stehfest algorithm,  $tol = 10^{-20}$  and  $\alpha = 0$  for De Hoog algorithm).

As a consequence, the numerical Laplace inversion of a function is not straightforward. One must pay attention to the choice of the algorithm hyperparameters and avoid periodic functions.

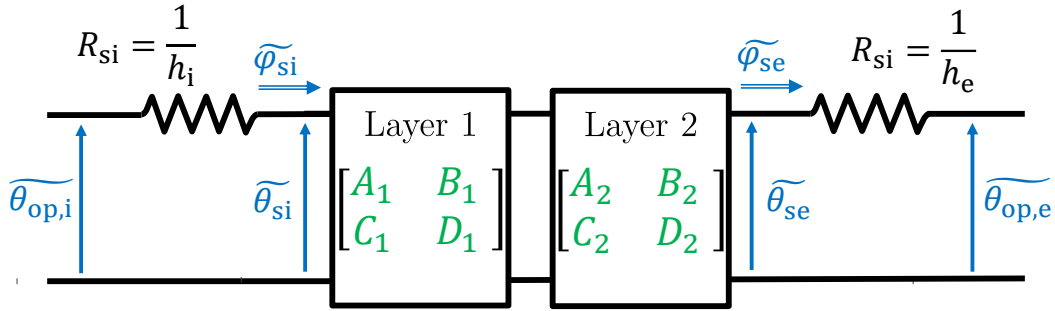
### 7.1.5. Test case: a two-layer wall subjected to internal air heating

The analyses presented in the following sections will be illustrated on synthetic data representative of measurements performed in this thesis. The test case is an

## 7.1. DIRECT MODEL DEFINITION WITH THERMAL QUADRUPOLE FORMALISM

insulated two-layer wall subjected to air heating on the internal side. The model is illustrated in Fig 7.8. Surface heat flux  $\varphi_{si}$  is treated as the model output whereas temperature  $\theta_{si}$  is the model input. This choice will be justified in Chap 8. The wall is initially at thermal equilibrium and the external operative temperature is kept constant:  $T_{\text{ref}} = T_{\text{op,e}}$  so  $\theta_{\text{ref}} = 0$ .

The wall is similar to the one of the Bungalow experimental campaign (see section 4.5). It is made of a 13 mm thick gypsum layer on the internal side with an insulating layer behind it. The insulation layer is supposed made of 120 mm of glass wool. The thermal properties assigned to the layers are detailed in Tab 7.2. These values have different origins: measurements in laboratory with the Hot Disk method (for  $k_1$  and  $a_1$ ), manufacturer data (for  $k_2$ ) and standard values from the literature (for  $b_2$  [202]). A standard value is also assigned to  $h_i$  and  $h_e$  (see ISO 14683 [18] for instance).



**Figure 7.8.:** Model used for the generation of synthetic measurements.

**Table 7.2.:** Thermal properties used in the model (model parameters are in bold).

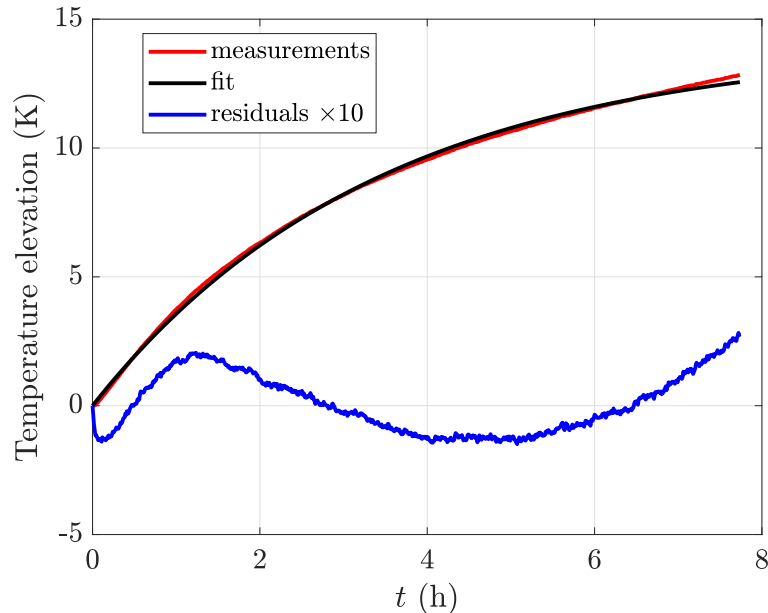
	Parameter	Value	Unit	Origin of value
	$h_i$	<b>7.7</b>	$\text{W}\cdot\text{m}^{-2}\cdot\text{K}^{-1}$	<b>Standard value</b> [18]
Layer 1	$e_1$	0.013	m	Measurement
	$k_1$	0.23	$\text{W}\cdot\text{m}^{-1}\cdot\text{K}^{-1}$	Hot Disk measurements
	$a_1$	0.30	$\text{m}^2\cdot\text{s}^{-1}$	Hot Disk measurements
	$R_1$	<b>0.06</b>	$\text{m}^2\cdot\text{K}\cdot\text{W}^{-1}$	<b>from <math>e_1</math> and <math>k_1</math></b>
	$b_1$	<b>420</b>	$\text{J}\cdot\text{K}^{-1}\cdot\text{m}^{-2}\cdot\text{s}^{-1/2}$	<b>from <math>k_1</math> and <math>a_1</math></b>
Layer 2	$e_2$	0.12	m	Measurement
	$k_2$	0.032	$\text{W}\cdot\text{m}^{-1}\cdot\text{K}^{-1}$	Manufacturer data
	$R_2$	<b>3.75</b>	$\text{m}^2\cdot\text{K}\cdot\text{W}^{-1}$	<b>from <math>e_2</math> and <math>k_2</math></b>
	$b_2$	<b>21</b>	$\text{J}\cdot\text{K}^{-1}\cdot\text{m}^{-2}\cdot\text{s}^{-1/2}$	<b>Literature</b> [202]
	$h_e$	<b>25</b>	$\text{W}\cdot\text{m}^{-2}\cdot\text{K}^{-1}$	<b>Standard value</b> [18]

A temperature profile is assigned to the internal operative temperature  $\theta_{\text{op,i}}$ . For the sake of simplicity, the profile is exponential:

$$\theta_{\text{op,i}}(t) = A_T \left( 1 - \exp\left(-\frac{t}{\tau_T}\right) \right) \quad (7.33)$$



with  $A_T = 14$  K and  $\tau_T = 3.4$  h. These two values were obtained from a fit on measurement data, as seen in Fig 7.9. The fit is not perfect and would not be suitable for the accurate estimation of the thermal resistance from these measurements: a more complex function should be used. However, for the purpose of the current theoretical study, this simple exponential fit is suitable.



**Figure 7.9.:** Exponential function fitted on measurement data (operative temperature).

The problem is modeled with the thermal quadrupole formalism. In the Laplace domain, it comes (see Eq 7.24):

$$\widetilde{\varphi}_{\text{si}}(p) = \frac{D'(\boldsymbol{\beta}, p)}{B'(\boldsymbol{\beta}, p)} \times \widetilde{\theta}_{\text{op},i}(p) \quad (7.34)$$

with  $p$  the Laplace variable, and  $B'$  and  $D'$  the coefficients of the thermal quadrupole matrix:

$$\begin{bmatrix} A' & B' \\ C' & D' \end{bmatrix} = \begin{bmatrix} 1 & 1/h_i \\ 0 & 1 \end{bmatrix} \begin{bmatrix} A_1 & B_1 \\ C_1 & D_1 \end{bmatrix} \begin{bmatrix} A_2 & B_2 \\ C_2 & D_2 \end{bmatrix} \begin{bmatrix} 1 & 1/h_e \\ 0 & 1 \end{bmatrix} \quad (7.35)$$

and  $\boldsymbol{\beta}$  the unknown parameter vector:

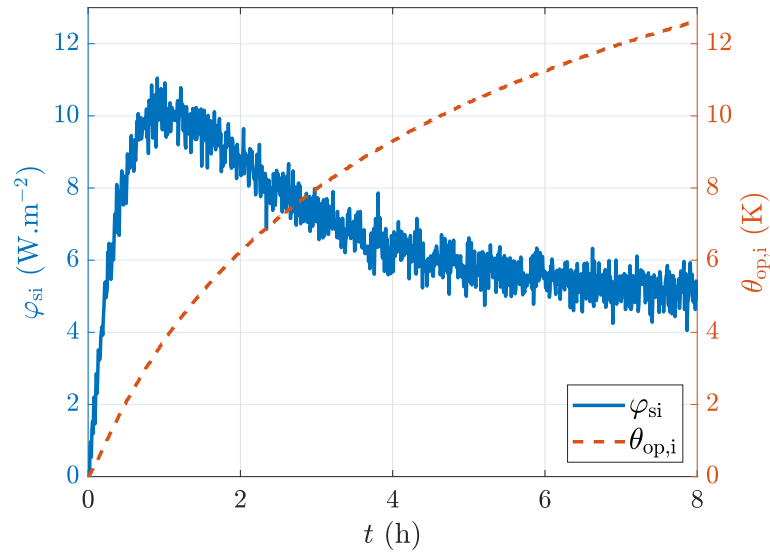
$$\boldsymbol{\beta} = [h_i \ R_1 \ b_1 \ R_2 \ b_2 \ h_e] \quad (7.36)$$

The obtained synthetic measurements are presented in Fig 7.10. The experiment duration is set to 8 h. White noises of standard deviation 0.01 K and  $0.4 \text{ W}\cdot\text{m}^{-2}$  are

## 7.1. DIRECT MODEL DEFINITION WITH THERMAL QUADRUPOLE FORMALISM

---

added to  $\theta_{op,i}$  and  $\varphi_{si}$ , respectively. These values were estimated from measurements. The sampling time is 30 s (similar to measurements performed on the experimental setups).



**Figure 7.10.:** Synthetic data generated from the model of a two-layer wall subjected to internal air heating.

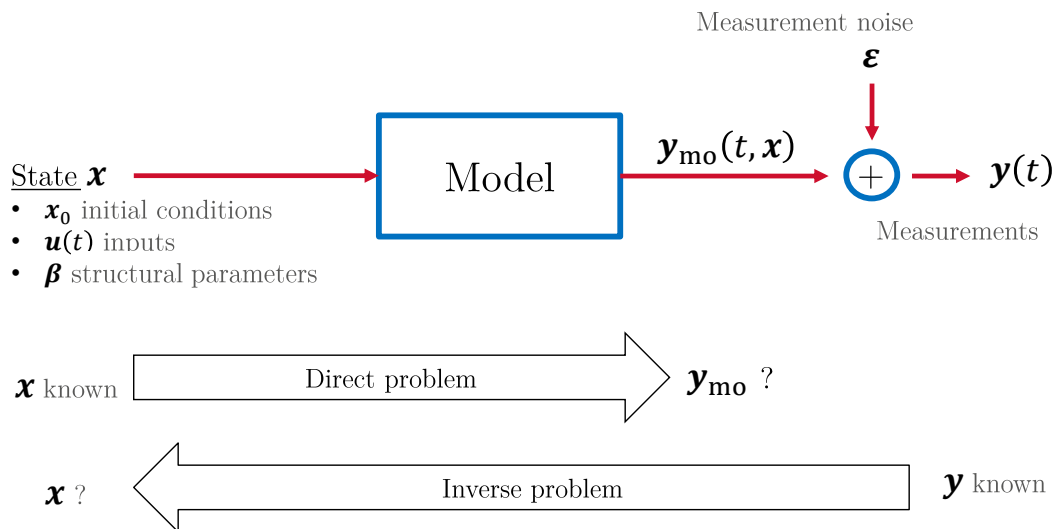
## 7.2. Inverse method with “white-box” models

This section quickly presents inverse methods for non-linear parameter estimation problems and the mathematical tools involved. For further information on the topic, the reader may refer to [203, 204, 205, 206, 207, 208, 209, 210, 211, 212]. The material thermal properties are supposed independent of the temperature. Moisture issues are not taken into account either.

### 7.2.1. Presentation

The measurement of a physical property from an experiment is possible if the outcomes of this experiment are enough sensitive to this property. Let us consider a model that links the so-called “independent” variables (time usually) to the state vector  $\mathbf{x}$  (composed of “dependent variables”) and the outputs variables  $\mathbf{y}_{\text{mo}}$ , as illustrated in Figure 7.11. The state vector  $\mathbf{x}$  contains one or several of the following dependent variables:

- Initial conditions  $\mathbf{x}_0$
- Input variables  $\mathbf{u}(t)$
- System structural parameters  $\beta$



**Figure 7.11.:** Illustration of inverse problems.

The function that models the physical phenomenon is called the “direct model” (as a reference to the direct problem). If the initial state  $\mathbf{x}_0$ , the inputs  $\mathbf{u}(t)$  and the structural parameters  $\beta$  are known, the output  $\mathbf{y}_{\text{mo}}$  may be calculated. Direct models may be of various origins and are usually sorted in three categories:

- When the structure of the model is determined from physical equations (usually derived from conservation principles, such as the heat equation), the model is a “white-box”. The model is referred as “knowledge model”.

- A “black-box” model is determined heuristically: it involves mathematical relations and the parameters may not have any physical meaning.
- Between these two categories, “gray-box” models have a structure determined from first principles and the parameters have a physical meaning.

In this section, we focus on the white-box approach. The inverse problem consists in estimating some components of the state vector  $\mathbf{x}$  from observations  $\mathbf{y}$  (measurements) of the model output  $\mathbf{y}_{\text{mo}}$ . To be more specific, the current problem is a parameter estimation problem: the objective is to estimate parameters  $\boldsymbol{\beta}$  from  $\mathbf{y}$  for given input  $\mathbf{u}(t)$  and initial  $\mathbf{x}_0$  conditions. This process is called “identification”.

The estimation procedure consists in finding the optimum parameter vector  $\hat{\boldsymbol{\beta}}$  that minimizes the distance between the model  $\mathbf{y}_{\text{mo}}$  and the measurements  $\mathbf{y}$ . This distance is quantified by the quadratic cost function (or objective function):

$$J(\boldsymbol{\beta}) = \sum_{i=1}^m (y(t_i) - y_{\text{mo}}(t_i, \boldsymbol{\beta}))^2 \quad (7.37)$$

$$= (\mathbf{y} - \mathbf{y}_{\text{mo}}(t, \boldsymbol{\beta}))^T (\mathbf{y} - \mathbf{y}_{\text{mo}}(t, \boldsymbol{\beta})) \quad (7.38)$$

$$= \mathbf{r}(t, \boldsymbol{\beta})^T \mathbf{r}(t, \boldsymbol{\beta}) \quad (7.39)$$

with  $m$  the number of observations (number of measurement points). The difference  $\mathbf{r}(t, \boldsymbol{\beta}) = \mathbf{y} - \mathbf{y}_{\text{mo}}(t, \boldsymbol{\beta})$  between the model and the measurements is called the “residuals”. For the sake of clarity, the dependency of  $\mathbf{y}_{\text{mo}}$  on the inputs and the initial condition are omitted in the notations.

As detailed in Fig 7.12, there are six sources of estimation error [205]. They are due to: the direct calculation ( $e_1$ ), the model hypothesis ( $e_2$ ), the noise ( $e_3$ ), the sensor calibration and digitization ( $e_4$ ), the supposed known parameters ( $e_5$ ), and the inverse problem ill-posedness ( $e_6$ ). Thus, the estimation error  $e_\beta$  of a parameter  $\beta$  may be written as:

$$e_\beta \approx e_1 + e_2 + (e_3 \text{ or } e_6) + e_4 + e_5 \quad (7.40)$$

The errors are presented as additive. This is a simplifying assumption: couplings between errors are not taken into account.

Inverse methods are not straightforward to use because inverse problems are usually ill-posed. In the sense of Hadamard [213], a mathematical problem is said ill-posed if it fails to fulfill the three following requirements:

- A solution exists.
- The solution is unique.
- The solution behavior changes continuously with the initial conditions.

The difficulty in inverse problems mainly comes from the second and third requirements. Indeed, the solution may not be unique if strong correlations between parameters exist. In addition, the third requirement means that a tiny change in the

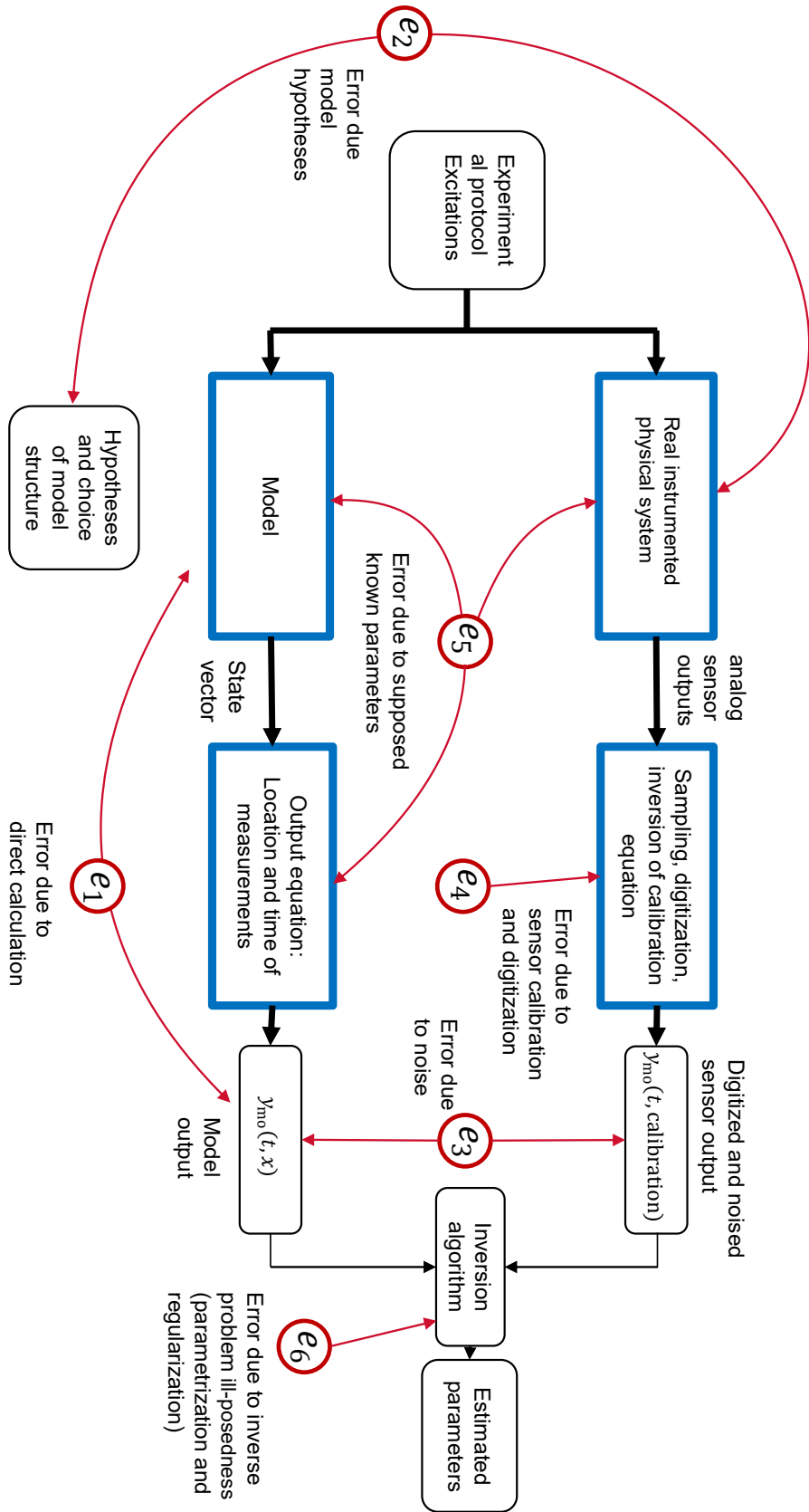


Figure 7.12.: Components of the estimation error, inspired from [205].

output  $\mathbf{y}$  (due to noise for instance) will induce a massive change in  $\hat{\boldsymbol{\beta}}$ . In this situation, the parameters cannot be estimated, or the estimation uncertainties are very high.

The identification may be done using the ordinary least squares (OLS) method. The latter is either linear or non-linear, depending on the structure of the direct model.

The analysis of parameter estimation problems aims at quantifying uncertainties on the estimated parameters. This analysis is useful to determine the ideal experiment and direct model to use for a given objective. A model with too few parameters will not be able to capture the physical phenomenon at stake whereas with a model with too many parameters, the latter could not be estimated. The model must have about as many parameters as degrees of freedom of the problem (parsimony concept). The tools useful to determine this number are presented in section 7.2.3. Let us first present the procedure to estimate the parameters assuming the problem is not too ill-posed.

## 7.2.2. Solving

### 7.2.2.1. Cost function minimization

The estimation process consists in minimizing the cost function  $J$  defined in Eq 7.37. Mathematically, we seek the parameter vector  $\boldsymbol{\beta}$  for which all the partial derivatives of  $J$  are null:

$$\forall t \geq 0, \forall j \in \llbracket 1, n \rrbracket : \left. \frac{\partial J(t, \boldsymbol{\beta})}{\partial \beta_j} \right|_{t, \beta_k \text{ for } k \neq j} = 0 \quad (7.41)$$

$$-2 \sum_{i=1}^m X_{ij}(t, \boldsymbol{\beta}) \times (y_i - y_{\text{mo}}(t_i, \boldsymbol{\beta})) = 0 \quad (7.42)$$

with  $n$  the number of parameters and  $X_{ij}$  the sensitivity coefficients:

$$\forall i \in \llbracket 1, m \rrbracket, \forall j \in \llbracket 1, n \rrbracket : X_{ij}(t, \boldsymbol{\beta}) = \left. \frac{\partial y_{\text{mo}}(t_i, \boldsymbol{\beta})}{\partial \beta_j} \right|_{\beta_k \text{ for } k \neq j} \quad (7.43)$$

We define the sensitivity matrix  $X$ . In this  $m \times n$  matrix, the  $j^{\text{th}}$  column corresponds to the sensitivity coefficient vector  $\mathbf{X}_j$  according to the  $j^{\text{th}}$  parameter:

$$X = \underbrace{\begin{bmatrix} \vdots & & \vdots & & \vdots \\ \mathbf{X}_1 & \cdots & \mathbf{X}_j & \cdots & \mathbf{X}_n \\ \vdots & & \vdots & & \vdots \end{bmatrix}}_{n \text{ parameters}} \left. \vphantom{\begin{bmatrix} \vdots & & \vdots & & \vdots \\ \mathbf{X}_1 & \cdots & \mathbf{X}_j & \cdots & \mathbf{X}_n \\ \vdots & & \vdots & & \vdots \end{bmatrix}} \right|_{m \text{ data points}} \quad (7.44)$$

In matrix form, Eq 7.42 becomes:

$$-2X^T(\boldsymbol{\beta})(\mathbf{y} - \mathbf{y}_{\text{mo}}(t, \boldsymbol{\beta})) = \mathbf{0} \quad (7.45)$$

For linear models,  $X$  is independent of  $\boldsymbol{\beta}$  and  $\mathbf{y}_{\text{mo}}(t, \boldsymbol{\beta}) = X\boldsymbol{\beta}$ . The previous equation leads to the OLS estimator which is explicitly defined:

$$\hat{\boldsymbol{\beta}} = (X^T X)^{-1} X^T \mathbf{y} \quad (7.46)$$

When the model is not linear with respect to  $\boldsymbol{\beta}$ , the sensitivity matrix is defined locally (i.e. around a nominal parameter vector  $\boldsymbol{\beta}^{\text{nom}}$ ). The resolution of Eq 7.45 requires an iterative method based on a 1<sup>st</sup> order development in Taylor series:

$$\mathbf{y}_{\text{mo}}(\hat{\boldsymbol{\beta}}^{(k+1)}) \approx \mathbf{y}_{\text{mo}}(\hat{\boldsymbol{\beta}}^{(k)}) + X^{(k)}(\boldsymbol{\beta} - \hat{\boldsymbol{\beta}}^{(k)}) \quad (7.47)$$

where  $\hat{\boldsymbol{\beta}}^{(k)}$  and  $X^{(k)}$  are the parameters and the sensitivity matrix estimated in the  $k^{\text{th}}$  iteration.

Combining Eq 7.45 with Eq 7.47, the estimator at iteration  $k + 1$  is given by:

$$\hat{\boldsymbol{\beta}}^{(k+1)} = \hat{\boldsymbol{\beta}}^{(k)} + (X^{(k)T} X^{(k)})^{-1} X^{(k)T} (\mathbf{y} - \mathbf{y}_{\text{mo}}(\hat{\boldsymbol{\beta}}^{(k)})) \quad (7.48)$$

This iterative procedure is the Gauss-Newton method. The matrix  $X^{(k)T} X^{(k)}$  is called the “information matrix”. It needs to be invertible:

$$\det(X^{(k)T} X^{(k)}) \neq 0 \quad (7.49)$$

In other words, the sensitivity coefficients have to be non-null and linearly independent. If the problem is ill-posed, the determinant of the information matrix tends to zero. The estimability of the parameters depends on the conditioning of the information matrix.

The choice of the initial parameter vector is important. Indeed, if the initial parameters are far from the optimum ones, the minimization algorithm might get stuck in a local minimum (biased estimation). To avoid this, several sets of initial parameters should be tested. If they do not all lead to the same result, it means that local minima exist.

Finally, the iterative method converges when the residuals are of the same order of magnitude as the measurement noise  $\sigma$ :

$$J\left(\hat{\boldsymbol{\beta}}^{(k)}\right) \approx m\sigma^2 \quad (7.50)$$

### 7.2.2.2. Levenberg-Marquardt algorithm

In this thesis, the Levenberg-Marquardt algorithm [214, 215, 216] was used to perform the cost function minimization. It was chosen for its robustness and stability. The algorithm is briefly introduced here and is presented in more details in Appendix D.1. It uses a regularization process based on Tikhonov penalization [217]. Basically, Eq 7.48 is changed to:

$$\hat{\boldsymbol{\beta}}^{(k+1)} = \hat{\boldsymbol{\beta}}^{(k)} + \left(X^{(k)\text{T}} X^{(k)} + \mu^{(k)} D^{(k)}\right)^{-1} X^{(k)\text{T}} \left(\mathbf{y} - \mathbf{y}_{mo}\left(\hat{\boldsymbol{\beta}}^{(k)}\right)\right) \quad (7.51)$$

where  $\mu$  is a damping factor and  $D$  a positive definite diagonal matrix (usually,  $D = I$ ). This regularization enables the algorithm to converge even when the problem is rather ill-posed (when the determinant of the information matrix is close to zero).

As the algorithm converges, the value of the damping factor decreases. When the damping factor is large, the algorithm is equivalent to the gradient method which converges slowly but is more stable to initial conditions far away from the optimum. However, when the damping factor  $\mu$  is very small, the Levenberg-Marquardt algorithm becomes equivalent to the Gauss-Newton method: convergence is rather fast but it requires to have initial values close to the optimum. Thus, the Levenberg-Marquardt algorithm combines the advantages of the Gauss-Newton and the gradient methods. This algorithm is used thanks to the “lsqnonlin” function in MATLAB “Optimization Toolbox”.

### 7.2.2.3. Expectancy of the estimator

The model is supposed unbiased and data points are corrupted by an additive noise  $\boldsymbol{\varepsilon}$ :

$$\mathbf{y}(t) = \mathbf{y}_{mo}(t, \boldsymbol{\beta}) + \boldsymbol{\varepsilon}(t) \quad (7.52)$$

This noise is treated as a stochastic variable of zero mean, constant standard deviation  $\sigma$  and uncorrelated with time (white noise):

$$E(\boldsymbol{\varepsilon}) = 0; \text{cov}(\boldsymbol{\varepsilon}) = \sigma^2 I \quad (7.53)$$



with  $I$  the identity matrix,  $E$  and  $\text{cov}$  the expectancy and variance-covariance operators, respectively.

Given the expression of the estimator:

$$\hat{\beta} = \beta + (X^T X)^{-1} X^T (\mathbf{y} - \mathbf{y}_{\text{mo}}(\beta)) \quad (7.54)$$

Its expectancy is:

$$E(\hat{\beta}) = E\left[\beta + (X^T X)^{-1} X^T \boldsymbol{\varepsilon}\right] \quad (7.55)$$

$$= \beta + (X^T X)^{-1} X^T E[\boldsymbol{\varepsilon}] \quad (7.56)$$

because the noise is of zero mean, it comes:

$$E(\hat{\beta}) = \beta \quad (7.57)$$

The estimator is therefore unbiased: in average (over a high number of estimations), the estimated parameters are equal to the true parameters.

### 7.2.3. Tools to estimate parameters estimability

Here are presented the tools useful to determine whether the parameters of the model can be estimated for the given experiment and to quantify the estimation uncertainties.

#### 7.2.3.1. Reduced sensitivity coefficients and sensitivity matrix

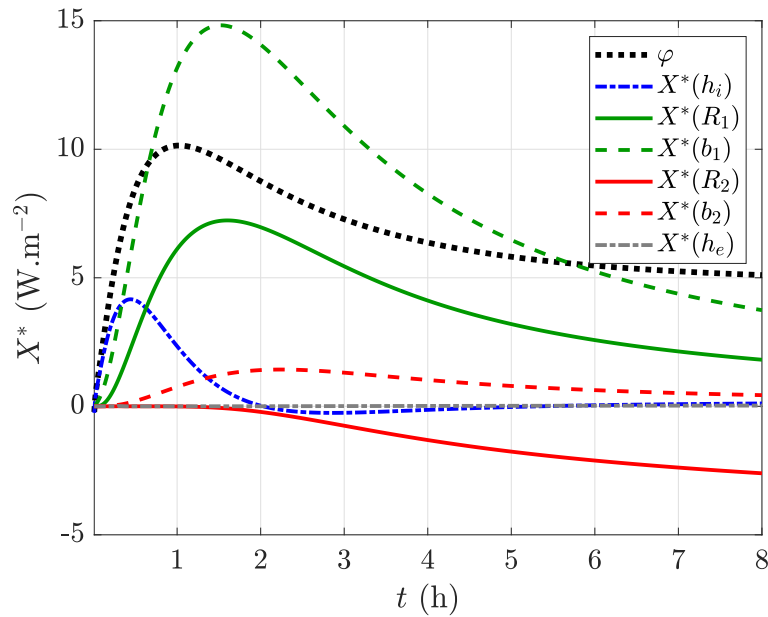
As seen above, the minimization of the cost function is based on the sensitivity matrix  $X$ . Usually, the different parameters of the model are expressed in different units which prevents a direct comparison of the sensitivity coefficients. Therefore, the reduced sensitivity coefficients  $\mathbf{X}_j^*$  are rather used. They all have the same unit as  $\mathbf{y}_{\text{mo}}$  and are given by:

$$\forall j \in \llbracket 1, n \rrbracket : \mathbf{X}_j^* = \beta_j \mathbf{X}_j = \beta_j \left. \frac{\partial \mathbf{y}_{\text{mo}}(t, \boldsymbol{\beta}^{\text{nom}})}{\partial \beta_j} \right|_{\beta_k \text{ for } k \neq j} \quad (7.58)$$

The analysis of reduced sensitivity coefficients  $\mathbf{X}_j^*$  is useful to help determining whether the problem is ill-posed. Indeed, it was shown above that the information

matrix  $X^T X$  needs to be invertible. The sensitivity analysis enables a first qualitative assessment of each parameter influence. Parameters with a null or nearly-null reduced sensitivity have a negligible impact on the model output and cannot be estimated. These parameters may be referred as “irrelevant” [218]. On the contrary, parameters with a non-null sensitivity are “relevant”. In addition, if some sensitivity coefficients have a similar behavior (when plotted as a function of time, their curves have a similar shape), it means that the corresponding parameters are correlated and their simultaneous estimation will be inaccurate. In other words it means that the information contained in the sensitivity matrix is redundant.

As an example, Fig 7.13 plots the reduced sensitivity coefficients of the test case introduced in section 7.1.5. The estimated heat flux is also plotted. It may be seen that  $h_e$  has a negligible sensitivity for the whole duration of the experiment. It is an irrelevant parameter and it cannot be estimated with the given experiment. Thus, this parameter will be supposed known. In addition, the sensitivity curves of  $R_1$  and  $b_1$  have a similar shape: these two parameters are correlated. This will increase the estimation uncertainty of these parameters. Finally, the magnitude of the reduced sensitivity coefficients of  $R_2$  and  $b_2$  is smaller than that of  $R_1$  and  $b_1$ : the internal surface heat flux is more sensitive to the properties of the first layer.



**Figure 7.13.:** Reduced sensitivity coefficients for the test case (section 7.1.5).

### 7.2.3.2. Variance of the estimator

The standard deviation of estimation error of the parameters may be evaluated from the variance-covariance matrix  $\text{cov}(\hat{\beta})$ . This is useful to estimate the accuracy of the estimation process from the statistical hypotheses made on the measurements.

By definition:

$$\text{cov}(\widehat{\boldsymbol{\beta}}) = \text{E} \left[ (\widehat{\boldsymbol{\beta}} - \text{E}(\widehat{\boldsymbol{\beta}})) (\widehat{\boldsymbol{\beta}} - \text{E}(\widehat{\boldsymbol{\beta}}))^{\text{T}} \right] \quad (7.59)$$

$$= \text{E} \left[ (\widehat{\boldsymbol{\beta}} - \boldsymbol{\beta}) (\widehat{\boldsymbol{\beta}} - \boldsymbol{\beta})^{\text{T}} \right] \quad (7.60)$$

substituting  $\widehat{\boldsymbol{\beta}}$  by its expression:

$$\text{cov}(\widehat{\boldsymbol{\beta}}) = \text{E} \left[ (X^{\text{T}}X)^{-1} X^{\text{T}} \boldsymbol{\varepsilon} \boldsymbol{\varepsilon}^{\text{T}} X (X^{\text{T}}X)^{-1} \right] \quad (7.61)$$

$$= (X^{\text{T}}X)^{-1} X^{\text{T}} \text{E}(\boldsymbol{\varepsilon} \boldsymbol{\varepsilon}^{\text{T}}) X (X^{\text{T}}X)^{-1} \quad (7.62)$$

The noise is supposed uncorrelated of constant standard deviation:

$$\text{E}(\boldsymbol{\varepsilon} \boldsymbol{\varepsilon}^{\text{T}}) = \sigma^2 I \quad (7.63)$$

finally:

$$\text{cov}(\widehat{\boldsymbol{\beta}}) = \sigma^2 (X^{\text{T}}X)^{-1} \quad (7.64)$$

also written as

$$\text{cov}(\widehat{\boldsymbol{\beta}}) \approx \begin{bmatrix} \text{var}(\widehat{\beta}_i) & \text{cov}(\widehat{\beta}_i, \widehat{\beta}_j) & \cdots \\ & \text{var}(\widehat{\beta}_j) & \cdots \\ \text{sym} & & \ddots \end{bmatrix} \quad (7.65)$$

Therefore, the variance-covariance matrix depends on the measurement noise and the inverse of the information matrix  $X^{\text{T}}X$ . The diagonal terms are the variances related to the estimation of each parameter whereas each off diagonal term is the covariance between two parameters. These variances are relevant for an unbiased model and measurements corrupted with a white noise.

We also define the correlation matrix:

$$\text{cor}(\widehat{\boldsymbol{\beta}}) \approx \begin{bmatrix} 1 & \rho_{ij} & \cdots \\ \rho_{ij} & 1 & \cdots \\ \vdots & \vdots & \ddots \end{bmatrix} \quad \text{with} \quad \rho_{ij} = \frac{\text{cov}(\widehat{\beta}_i, \widehat{\beta}_j)}{\sqrt{\text{var}(\widehat{\beta}_i) \text{var}(\widehat{\beta}_j)}} \quad (7.66)$$

The correlation coefficient  $\rho_{ij}$  quantifies the correlation between parameters  $\beta_i$  and  $\beta_j$ . If the correlation coefficient is close to zero, it means that the two parameters

are not correlated. However, the closer  $\rho_{ij}$  is to -1 or 1, the stronger the correlation. These coefficients quantify the correlations between parameters over the whole time horizon and therefore do not provide as much information as the reduced sensitivity curves. As an example, parameters may become correlated only at the end of the experiment.

A hybrid matrix  $V_{\text{cor}}$  may be built from the covariance and correlation matrices and is a very useful tool to assess the ill-posedness of the considered problem:

$$V_{\text{cor}}(\hat{\beta}) \approx \begin{bmatrix} \sqrt{\text{var}(\hat{\beta}_i)/\hat{\beta}_i} & \rho_{ij} & \cdots \\ & \sqrt{\text{var}(\hat{\beta}_j)/\hat{\beta}_j} & \cdots \\ \text{sym} & & \ddots \end{bmatrix} \quad (7.67)$$

As an example, the  $V_{\text{cor}}$  matrix for the present test case is given in Tab 7.3. The noise level is set to  $\sigma = 0.4 \text{ W.m}^{-2}$ . The matrix exhibits strong correlations between parameters  $h_i$ ,  $R_1$  and  $b_1$  whereas only the correlation between  $R_1$  and  $b_1$  was noticeable on the reduced sensitivity curves in Fig 7.13. Because of these correlations, the relative estimation uncertainties of these three parameters are higher than those of  $R_2$  and  $b_2$  despite the higher magnitude of their reduced sensitivities. Here parameter  $R_2$  is estimated with a 2.5% uncertainty. The correlation between parameters are further studied below.

	$h_i$	$R_1$	$b_1$	$R_2$	$b_2$
$h_i$	0.237	0.995	-0.996	-0.817	-0.715
$R_1$		1.616	1.000	-0.841	-0.772
$b_1$			0.784	0.836	0.761
$R_2$				0.025	0.858
$b_2$					0.206
	sym				

**Table 7.3.:** Hybrid matrix  $V_{\text{cor}}$  for the given test case ( $\sigma = 0.4 \text{ W.m}^{-2}$ ).

### 7.2.3.3. Rank of the sensitivity matrix and number of degrees of freedom

Correlations between parameters contribute to the ill-posedness of the inverse problem and increase the estimation uncertainty of the parameters. The real number of degrees of freedom of the problem depends on the rank of the reduced sensitivity matrix  $X^*$ . As seen above, the reduced sensitivity curves and the  $V_{\text{cor}}$  matrix are very useful tools to detect correlations between two parameters. However, there might be correlations between three or more parameters. If so, there is a linear relationship between the reduced sensitivity coefficients of these parameters.

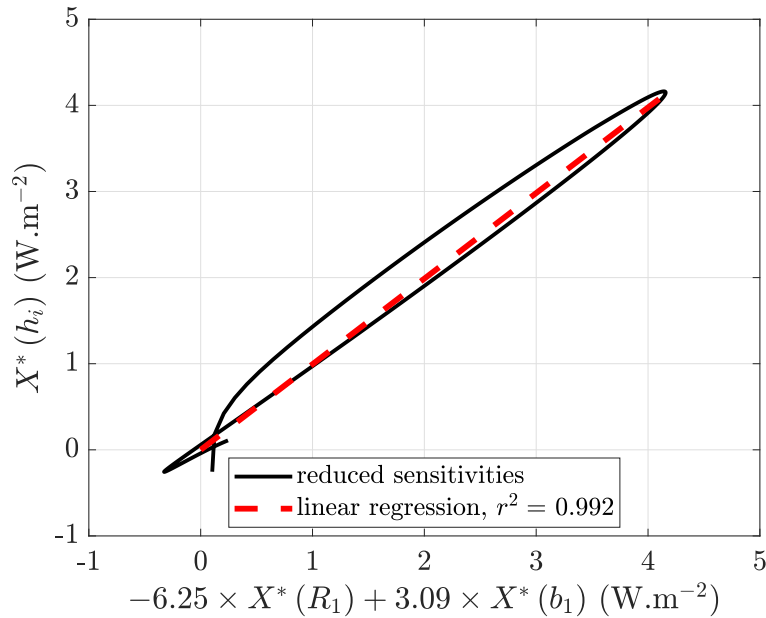
The Singular Value Decomposition (SVD) of the reduced sensitivity matrix may be useful to estimate the real number of degrees of freedom of the problem. The rank of  $X^*$  is equal to its number of non-null singular values.

The SVD of an  $m \times n$  matrix is a linear algebraic factorization which can be calculated as follows:

$$X^* = USV^T \tag{7.68}$$

where  $U$  is a  $m \times m$  orthogonal matrix,  $S$  is a  $m \times n$  diagonal matrix (with the singular values of  $X^*$  in the diagonal sorted in descending order) and  $V$  is a  $n \times n$  orthogonal matrix.

For the present test case, no correlation between  $h_i$  and  $R_1$  nor between  $h_i$  and  $b_1$  was noticed on the reduced sensitivity curves (Fig 7.13) whereas the corresponding correlation coefficients in the  $V_{\text{cor}}$  matrix are very close to unity (Tab 7.3). This is because these three parameters are correlated all together. As shown in Fig 7.14, there is a linear relationship between their reduced sensitivity coefficients.



**Figure 7.14.:** Example of linear combination between three reduced sensitivity coefficients.

In addition, the singular values of  $X^*$  are:

$$s = [311 \ 42 \ 29 \ 3.0 \ 0.2] \tag{7.69}$$

It may be noticed that the last singular value is much smaller than the other ones, and the second to last is also rather small. This indicates that the problem number of degrees of freedom is 3 or 4 (there is not universal quantitative criterion to conclude on the exact number of degrees of freedom).

Therefore, parameter  $h_i$  will now be supposed perfectly known and the model has four remaining unknown parameters:  $R_1$ ,  $b_1$ ,  $R_2$ , and  $b_2$ . As presented in Chap 8, in

practice model input is the internal surface temperature  $\theta_{si}$  instead of the operative temperature  $\theta_{op,i}$  so that  $h_i$  is by construction not included in the model.

#### 7.2.3.4. Residual analysis

The expectancy of the residuals is given by:

$$E(\mathbf{r}(t, \hat{\boldsymbol{\beta}})) = E(\mathbf{y} - \mathbf{y}_{mo}(t, \hat{\boldsymbol{\beta}})) \quad (7.70)$$

$$= E(X(\boldsymbol{\beta} - \hat{\boldsymbol{\beta}})) \quad (7.71)$$

$$= E\left(-X(X^T X)^{-1} X^T \boldsymbol{\varepsilon}(t, \hat{\boldsymbol{\beta}})\right) \quad (7.72)$$

$$= -X(X^T X)^{-1} X^T E(\boldsymbol{\varepsilon}(t, \hat{\boldsymbol{\beta}})) \quad (7.73)$$

$$= 0 \quad (7.74)$$

Thus, if the model is unbiased, the expectancy of the residuals is null. It is important to check that this is the case: residuals must be “unsigned” (flat with the shape of a white noise). If they are “signed”, this indicates that the estimation is biased. The bias may come from the values of the supposed known parameters or from the direct model itself if it does not depict correctly the physical phenomenon.

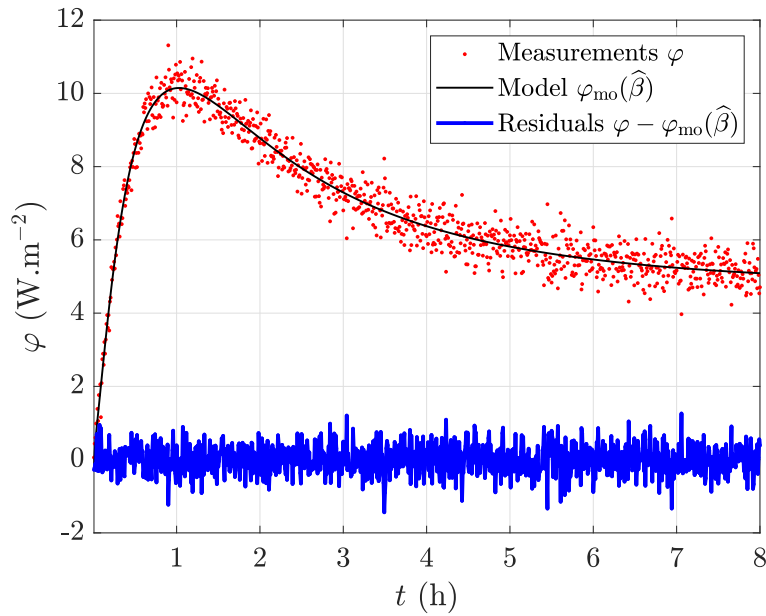
Unsigned residuals is not a guarantee of a correct parameter estimation. Indeed, an inverse method applied to an over-determined problem (more parameters than degrees of freedom) may lead to flat residuals. It also depends on the noise magnitude: a small bias might be hard to detect on a very noisy signal.

Figure 7.15 plots the residuals for the current test case. The noised synthetic measurements as well as the model after parameter estimation are also plotted. The initial values were obtained from a random sampling 10% away from the nominal values. The residuals are unsigned and their standard deviation is close to the noise level. The estimated parameters and their estimation uncertainty are presented in Tab 7.4a.

If a quadratic bias is deliberately added to the measurements, the residuals are signed (see Fig 7.16) and the estimation is significantly biased (see Tab 7.4b).

#### 7.2.4. Conclusion

Inverse methods consist in estimating the parameters of a model (the so-called “direct” model) from minimization of the difference between the model output and



**Figure 7.15.:** Example of unbiased estimation from noised synthetic data (unsigned residuals).

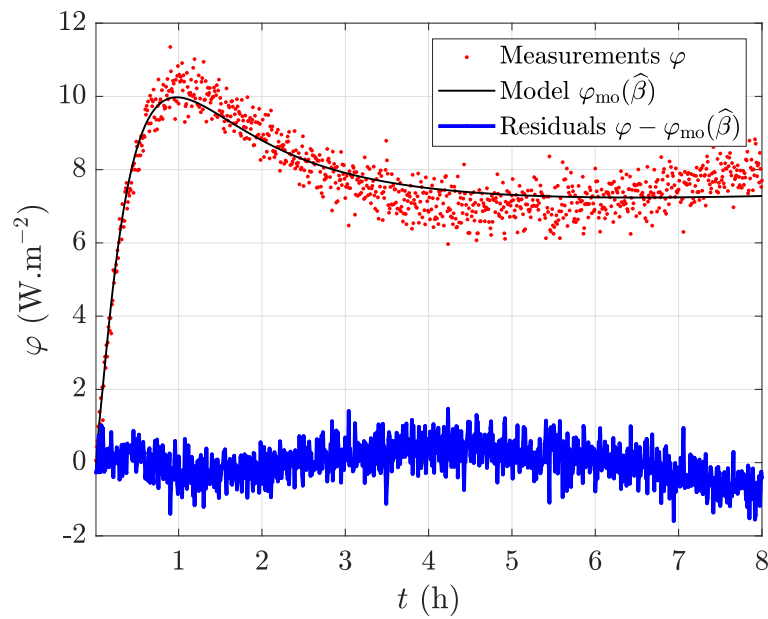
**Table 7.4.:** Estimated parameters.

	(a) Unbiased estimation.			(b) Biased estimation.		
	$\hat{\beta}$	$\sigma_{\hat{\beta}}$	$\beta_{\text{nom}}$	$\hat{\beta}$	$\sigma_{\hat{\beta}}$	$\beta_{\text{nom}}$
$R_1$	0.061	0.008	0.060	$R_1$	0.037	0.050
$b_1$	415	23	420	$b_1$	529	210
$R_2$	3.78	0.05	3.75	$R_2$	2.02	0.06
$b_2$	31.2	3.4	30.0	$b_2$	19.0	218

measurements. When the model is not linear according to its parameters, the minimization is based on an iterative procedure (e.g. the Levenberg-Marquardt algorithm).

Because of the ill-posed nature of inverse problems, the application of an inverse method is not straightforward. The experiment protocol, the direct model to use and the parameters to estimate have to be chosen according to the desired objective (estimation of a wall thermal resistance for instance). Several tools exist to assist the use of an inverse method:

- The observation of the reduced sensitivity coefficients enables a qualitative assessment of the influence of each parameter on the model output. Parameters with a null sensitivity are irrelevant and cannot be estimated whereas parameters with a high sensitivity are more likely to be estimable with a decent uncertainty. Correlations between two parameters may also be detected from the shape of the reduced sensitivity curves.
- The  $V_{\text{cor}}$  matrix provides quantitative information about parameters estimability. The diagonal terms contain the relative estimation uncertainty of each



**Figure 7.16.:** Example of biased estimation from noised synthetic data (signed residuals).

unknown parameter. This value is the minimum estimation uncertainty one could expect from application of the inverse method: it does not take into account the presence of a bias in the model for instance. The off-diagonal terms quantify the correlation between two parameters.

- The real degree of freedom of the problem may be estimated from the rank of the sensitivity matrix. The model should not have more parameters than the problem number of degrees of freedom.
- The residuals must be carefully analyzed to check the absence of a bias. They should be unsigned (flat), have the shape of white noise and a standard deviation close to the measurement noise level.

The tools were illustrated on synthetic data obtained from the modeling of a two-layer wall subjected to air heating which is representative of the experiments performed in this thesis.



### 7.3. System identification: “black-box” ARX models

This section aims at presenting ARX models for the estimation of physical properties. This type of black-box model belongs to the System Identification framework. It is an interesting alternative to inverse methods based on a white-box model presented in the previous section. The basics of system identification are presented here with a focus on ARX models. For further information, please refer to [130].

#### 7.3.1. Presentation

The system identification framework is a well known domain that has applications in automatic (for control purpose mainly) and in signal processing [130]. System identification techniques may be an efficient tool to formulate a reliable model. This model may be used as a direct model to solve an inverse problem. Such a low order model is interesting since it requires less computational time for simulation than high order models (such as white-box ones). In some cases, the structure of the identified model may be sufficient to obtain the desired characterization of the system. Even though the parameters of the model have no physical meaning, they may be combined in order to estimate a physical property such as a thermal resistance. This is the approach chosen here. Let us first introduce the main system identification methods.

##### 7.3.1.1. The deconvolution problem

For the sake of conciseness, system identification tools are presented for the Single Input Single Output (SISO) case. Let us consider a wall subjected to a thermal load (or input)  $u(t)$ . A sensor monitors the evolution of the output  $y(t)$ . This output may be either a temperature or a heat flux. The evolution of the output in response to the thermal load is a convolution problem (Duhamel’s theorem):

$$\forall t > 0 \quad : \quad y(t) = y(0) + u(t) \otimes h(t) \quad (7.75)$$

$$y(t) = y(0) + \int_0^{\infty} u(t - \tau) \times h(\tau) d\tau \quad (7.76)$$

with  $\otimes$  the convolution product and  $h$  the impulse response of the system. For mono-variable linear systems (thermal properties are independent of the temperature), the impulse response fully characterizes the system. One could imagine measuring directly the impulse response from an experiment. It would consist in replacing the input on the real problem by a known pulse, and to measure the output. However, this approach is not reliable since the impulse response magnitude is very low, especially when one wants to preserve the linear behavior of the system. Therefore,

the objective is to estimate  $h$  from measurements of both the input  $u$  and the output  $y$ : it is a deconvolution problem.

Several powerful techniques were developed in the system identification and signal processing domains that lead to more accurate estimations of the impulse response of the system. These techniques are classified in two sets of methods, namely “non-parametric” and “parametric”.

### 7.3.1.2. Non-parametric methods

Several non-parametric methods exist. The most common are the “deconvolution”, the “correlation” and the “spectral” techniques. The deconvolution method is detailed here to illustrate the non-parametric approach.

An easy technique for the deconvolution of Eq 7.76 is to consider the discrete form of this relation:

$$y_{\text{mo}}(k\Delta t) = \sum_{i=0}^k u(k\Delta t) \times h((k-i)\Delta t) \quad (7.77)$$

with  $y_{\text{mo}}$  predictions of the output. The initial condition is supposed null:  $y_{\text{mo}}(0) = 0$ . Assuming the duration of the experiment is  $t_f = m\Delta t$  where  $\Delta t$  is the sampling time interval, this relation can be expressed in matrix form:

$$\underbrace{\begin{bmatrix} y_{\text{mo},0} \\ y_{\text{mo},1} \\ \vdots \\ y_{\text{mo},m} \end{bmatrix}}_{\mathbf{y}_{\text{mo}}} = \underbrace{\begin{bmatrix} u_0 & & & 0 \\ u_1 & u_0 & & \\ \vdots & \ddots & \ddots & \\ u_m & \cdots & u_1 & u_0 \end{bmatrix}}_G \underbrace{\begin{bmatrix} h_0 \\ h_1 \\ \vdots \\ h_m \end{bmatrix}}_h \quad (7.78)$$

with  $y_{\text{mo},k} = y_{\text{mo}}(k\Delta t)$  and  $u_k = u(k\Delta t)$  for  $k \in \llbracket 0, m \rrbracket$ . Given that  $\lim_{k \rightarrow \infty} h_k = 0$ , it is reasonable to truncate the series. Assuming an additive measurement error  $\varepsilon$  of normal distribution (zero mean and constant standard deviation):

$$\mathbf{y} = \mathbf{y}_{\text{mo}} + \varepsilon = G\mathbf{h} + \varepsilon \quad (7.79)$$

Vector  $\mathbf{h}$  can thus be estimated in the least square sense, in order to minimize  $\varepsilon^T \varepsilon = (\mathbf{y} - G\mathbf{h})^T (\mathbf{y} - G\mathbf{h})$ . It comes:

$$\hat{\mathbf{h}} = (GG^T)^{-1} G^T \mathbf{y} \quad (7.80)$$

However, this procedure is quite sensitive to measurement errors. This is the main reason why parametric methods were preferred in this thesis.

### 7.3.1.3. Parametric methods

This approach consists in identifying the parameters involved in a linear relation between the input  $u(t)$  and output  $y(t)$ , from measurements of these two quantities. Without any kind of physical consideration of the heat transfer process, it is assumed a general relationship of the following form:

$$y_{\text{mo}}(t) + \sum_{i=1}^{n_a} \alpha_i \frac{d^i y_{\text{mo}}(t)}{dt^i} = \sum_{i=0}^{n_b-1} \beta_i \frac{d^i u(t)}{dt^i} \quad (7.81)$$

This kind of model is consistent with the behavior of thermal systems since the heat diffusion equation relies on the first order derivative of the temperature for all the points of the system. It is thus reasonable to admit that temperatures and heat fluxes at time  $t$  must depend on their values at previous times. The series are truncated so that they define a low order model.

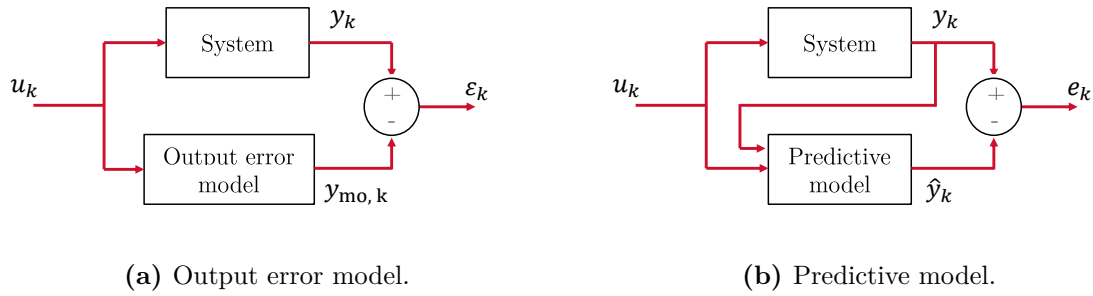
Using the discrete form of the derivatives, an equivalent form of Eq 7.81 expresses the output at time  $k\Delta t$  from the input and output at previous times:

$$y_{\text{mo},k} = \sum_{i=1}^{n_a} a_i y_{\text{mo},k-i} + \sum_{i=0}^{n_b-1} b_i u_{k-i} \quad (7.82)$$

with  $y_{\text{mo},k} = y_{\text{mo}}(k\Delta t)$  and  $u_k = u(k\Delta t)$ . This is the so-called “output error model”. Replacing the model output at previous times with the measurement leads to the “predictive model”:

$$\hat{y}_k = - \sum_{i=1}^{n_a} a_i y_{k-i} + \sum_{i=0}^{n_b-1} b_i u_{k-i} \quad (7.83)$$

with  $\hat{y}_k$  the estimator of  $y$ . Identification of parameters  $a_i$  and  $b_i$  significantly differs according to the choice of the model (see Fig 7.17). In the case of the predictive model, the parameters are estimated with a linear minimization process. With the output error model, the sensitivity functions depend on the parameters and a non linear minimization procedure is required. The covariance matrix for the parameter estimates is often very difficult to calculate using the output error method. Furthermore, the most common validation techniques cannot be applied, e.g. test for white noise and normally distributed residuals. Therefore, the output error method should only be used under special conditions [132] and predictive models were preferred in this thesis.



**Figure 7.17.:** Illustration of parameter identification according to the model representation.

#### 7.3.1.4. Presentation of ARX models

Among predictive models, the ARX formulation (Auto-Regressive with eXogenous inputs) is one of the most widespread. In the SISO case, the problem is written as:

$$\mathcal{A}(\boldsymbol{\beta}, q) \mathbf{y} = \mathcal{B}(\boldsymbol{\beta}, q) \mathbf{u} \quad (7.84)$$

where  $q$  is the delay (or back-shift) operator defined such that  $q^{-1}z_k = z_{k-1}$  with  $z$  either  $u$  or  $y$ .  $\mathcal{A}$  and  $\mathcal{B}$  are polynomials in  $q$ . Their orders are  $n_a$  and  $n_b - 1$  respectively:

$$\mathcal{A}(\boldsymbol{\beta}, q) = 1 + a_1 q^{-1} + \dots + a_{n_a} q^{-n_a} \quad (7.85)$$

$$\mathcal{B}(\boldsymbol{\beta}, q) = b_0 + b_1 q^{-1} + \dots + b_{n_b-1} q^{-n_b+1} \quad (7.86)$$

with  $\boldsymbol{\beta}$  the parameter vector which contains the  $a_i$  and  $b_i$  coefficients:

$$\boldsymbol{\beta} = [a_1, \dots, a_{n_a}, b_0, \dots, b_{n_b-1}]^T \quad (7.87)$$

Parameters  $a_i$  and  $b_i$  have no physical meaning: it is a “black-box” model. Equations 7.85 and 7.86 define a so-called ARMA model (Auto-Regressive with Moving Average). The ARX formulation is similar except that polynomial  $\mathcal{B}$  is multiplied by a time shift operator  $q^{-n_k}$  where  $n_k$  is the number of input samples that occur before the input affects the output (also called the “dead time” in the system).

For any instant  $k$ , an estimator  $\hat{y}_k$  of the output is given by:

$$\hat{y}_k = - \sum_{i=1}^{n_a} a_i y_{k-i} + \sum_{i=0}^{n_b-1} b_i u_{k-i-n_k} \quad (7.88)$$

Numbers  $n_a$ ,  $n_b$  and  $n_k$  are hyperparameters of the model. Their choice is the object

of section 7.3.3.3. The Multi-Input, Single Output case is presented and discussed in Appendix D.2

## 7.3.2. Solving

### 7.3.2.1. Estimation of model parameters

The problem is linear and may be written in matrix form:

$$\mathbf{y}_{\text{mo}}(\boldsymbol{\beta}) = H\boldsymbol{\beta} \quad (7.89)$$

where matrix  $H$  contains the measured input and output:

$$H = \begin{bmatrix} y_{n-1} & y_{n-2} & \cdots & y_{n-n_a} & u_{n-n_k} & u_{n-1-n_k} & \cdots & u_{n-n_b+1-n_k} \\ y_n & y_{n-1} & \ddots & \vdots & u_{n+1-n_k} & u_{n-n_k} & \ddots & \vdots \\ \vdots & \ddots & \ddots & y_{n-2} & \vdots & \ddots & \ddots & u_{n-1-n_k} \\ y_{n+n_a-1} & \cdots & y_n & y_{n-1} & u_{n+n_b+1-n_k} & \cdots & u_{n+1-n_k} & u_{n-n_k} \\ \vdots & \vdots & \ddots & \vdots & \vdots & \vdots & \ddots & \vdots \\ y_{m-1} & y_{m-2} & \cdots & y_{m-n_a} & u_{m-n_k} & u_{m-1-n_k} & \cdots & u_{m-n_b+1-n_k} \end{bmatrix} \quad (7.90)$$

For matrix  $H$  to be full, the first  $n - 1$  of the  $m$  measurements points are removed:

$$\mathbf{y} = [y_n, y_{n+1}, \dots, y_m]^T \quad (7.91)$$

with  $n = \max(n_a + 1, n_b + n_k)$ . The output  $\mathbf{y}$  is supposed corrupted with an additive white noise  $\boldsymbol{\varepsilon}$  of standard deviation  $\sigma_y$ :

$$\mathbf{y} = \mathbf{y}_{\text{mo}}(\boldsymbol{\beta}) + \boldsymbol{\varepsilon} = H\boldsymbol{\beta} + \boldsymbol{\varepsilon} \quad (7.92)$$

Because the model is linear in  $\boldsymbol{\beta}$ , no iterative procedure is required. The Ordinary Least Square (OLS) estimator  $\hat{\boldsymbol{\beta}}$  of this linear problem is directly given by:

$$\hat{\boldsymbol{\beta}} = (H^T H)^{-1} H^T \mathbf{y} \quad (7.93)$$

Eq 7.84 may be re-written into the form of a transfer function. Here, we decide to work with the inverse of the transfer function (this will simplify the estimation of

the thermal resistance, see next below):

$$\hat{Z}(\hat{\beta}, q) = \frac{u}{y} = \frac{\mathcal{A}(\hat{\beta}, q)}{\mathcal{B}(\hat{\beta}, q)} \quad (7.94)$$

This expression may be written as a function of the frequency  $f$  taking  $q = 2j\pi\frac{f}{f_s}$ , with  $j^2 = -1$  and  $f_s$  the sampling frequency. It comes:

$$\hat{Z}(\beta, f) = \frac{\sum_{i=0}^{n_a} a_i \exp\left(-2j\pi\frac{f}{f_s}i\right)}{\sum_{i=0}^{n_b-1} b_i \exp\left(-2j\pi\frac{f}{f_s}i\right)} \quad (7.95)$$

with  $a_0 = 1$ . A model in the frequency domain may be fitted on the estimated transfer function in order to estimate some of the system physical properties [219]. However, as detailed below, this is not necessary to estimate a wall thermal resistance (the latter may be expressed explicitly from the parameters).

### 7.3.2.2. Thermal impedance and estimate of a wall thermal resistance

Even though the individual parameters included in  $\beta$  have no physical meaning, it is possible to derived physical quantities from them. For instance, a wall thermal resistance may be estimated taking  $u = \theta_{si}$  and  $y = \varphi_{si}$ , the internal surface temperature and heat flux. With this pair of input / output, the inverse of the ARX model transfer function is an impedance.

The estimator of the wall thermal resistance is the value of the impedance for a null frequency:

$$\hat{R} = \mathcal{Z}(\beta, 0) \quad (7.96)$$

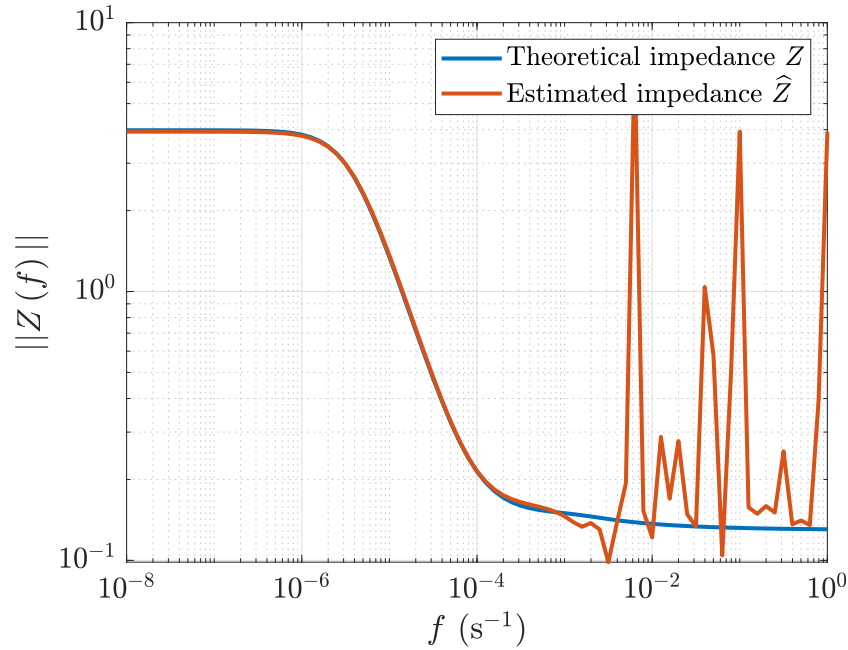
$$= \frac{\mathcal{A}(\beta, 1)}{\mathcal{B}(\beta, 1)} \quad (7.97)$$

$$= \frac{\sum_{i=0}^{n_a} a_i}{\sum_{i=0}^{n_b-1} b_i} \quad (7.98)$$

In order to be consistent with previous sections, let us consider again the test case presented in section 7.1.5 (two-layer wall subjected to air heating). On this example, the input is not the surface temperature but the internal operative temperature:  $u = \theta_{op,i}$ . The only difference is that the thermal resistance which will be estimated by the model includes the surface resistance  $R_{si} = 1/h_i$ . The parameter vector  $\hat{\beta}$  is estimated from the synthetic measurements presented in Fig 7.10 with  $n_a = n_b = 20$  and  $n_k = 0$ . Figure 7.18 plots the module of the estimated impedance  $\hat{Z}$  as a function of  $f$ . As a reminder, the sampling frequency is  $f_s = 1/30 = 0.033 \text{ s}^{-1}$ .

The results are compared to the theoretical impedance  $Z$  which is derived from the thermal quadrupole formalism taking  $p = j2\pi f$ :

$$Z(f) = \frac{\widetilde{\theta}_{\text{op,i}}(j2\pi f)}{\widetilde{\varphi}_{\text{si}}(j2\pi f)} = \frac{D'(j2\pi f)}{B'(j2\pi f)} \quad (7.99)$$



**Figure 7.18.:** Theoretical and estimated impedances (inverse of transfer function) from ARX model applied to the test case with  $n_a = n_b = 20$  and  $n_k = 0$ .

In this example, it may be seen that the impedance (inverse of the transfer function) is rather well estimated at low frequencies. Yet, above  $f = 10^{-4} \text{ s}^{-1}$ , the estimated impedance diverges because the input and output data are not rich enough in high frequency information. This is not an issue here because we are interested in the wall thermal resistance, which is a steady-state quantity.

On the current example:  $\widehat{R} = 3.91 \text{ m}^2 \cdot \text{K} \cdot \text{W}^{-1}$ , which is close to the theoretical value:  $3.94 \text{ m}^2 \cdot \text{K} \cdot \text{W}^{-1}$ .

### 7.3.3. Tools to assess the quality of estimation

The estimation of the parameters of an ARX model is linear which means that there is always a solution. Thus, attention must be paid to check the relevance of this solution.

### 7.3.3.1. Variance of the estimator

The variance-covariance matrix of the estimated parameter vector  $\hat{\beta}$  is derived in the same way as in the white-box case (see Sec 7.2.3.2):

$$\text{cov}(\hat{\beta}) = \sigma_y^2 (H^T H)^{-1} \quad (7.100)$$

This expression explicitly depends on the noise  $\sigma_y$  on the output signal. The noise  $\sigma_u$  on the input signal is somehow included in the  $H$  matrix. The uncertainty on  $\hat{R}$  is obtained from propagation of the elements of this variance-covariance matrix:

$$\sigma_R^2 = X_R \cdot \text{cov}(\hat{\beta}) \cdot X_R^T \quad (7.101)$$

with  $X_R$  the sensitivity matrix (horizontal vector here):

$$X_R = \left[ \frac{\partial R}{\partial a_1}, \dots, \frac{\partial R}{\partial a_{n_a}}, \frac{\partial R}{\partial b_0}, \dots, \frac{\partial R}{\partial b_{n_b-1}} \right] \quad (7.102)$$

where the partial derivatives of  $R$  are:

$$\forall i \in \llbracket 1, n_a \rrbracket : \frac{\partial R}{\partial a_i} = -\frac{\mathcal{A}(\beta, 1)}{\mathcal{B}(\beta, 1)^2} \quad (7.103)$$

$$\forall i \in \llbracket 0, n_b - 1 \rrbracket : \frac{\partial R}{\partial b_i} = \frac{1}{\mathcal{B}(\beta, 1)} \quad (7.104)$$

### 7.3.3.2. Residuals analysis

The ARX model simplifies the actual wall behavior. The difference between the model response  $\mathbf{y}_{\text{mo}}$  and the real wall response  $\mathbf{y}$  is quantified by the residuals:

$$\varepsilon = \mathbf{y} - \mathbf{y}_{\text{mo}}(\hat{\beta}) \quad (7.105)$$

Some models are better than others and the analysis of the residuals enables to argue which one performs best. The output predicted by the model is derived from the following recurrence relationship:

$$y_{\text{mo},k}(\hat{\beta}) = y_k \text{ for } k \leq \max(n_a, n_b) \quad (7.106)$$

$$y_{\text{mo},k}(\hat{\beta}) = -\sum_{i=1}^{n_a} a_i y_{\text{mo},k-i}(\hat{\beta}) + \sum_{i=0}^{n_b-1} b_i u_{k-i} \text{ for } k > \max(n_a, n_b) \quad (7.107)$$



If the model completely describes the wall response, it leaves none of its variability undescribed. The residuals then constitute a white noise. There are several tools to test for white noise, such as autocorrelation and cross-correlation functions (in the time domain) and cumulated periodogram (in the frequency domain, not presented here) [129].

A necessary condition for white noise is that there is no autocorrelation in the residuals nor cross-correlation between the residuals and the input variable(s). Auto-Correlation Functions (ACF) plot the value for a signal autocorrelation, as a function of the number of lags [131]. A signal autocorrelation, for lag  $j$ , indicates how similar the signal is with a version of itself, lagged  $j$  time steps. The residuals ACF are given by:

$$Q_{\varepsilon}(j) = \frac{1}{m} \sum_{k=j}^m \varepsilon_k \varepsilon_{k-j} \quad \text{for } j \geq 0 \quad (7.108)$$

Similarly, Cross-Correlation Functions (CCFs) plot the values for a signal cross-correlation with another signal, as a function of the number of lags. The CCFs of the residuals and the input is given by:

$$Q_{\varepsilon u}(j) = \frac{1}{m} \sum_{k=j}^m \varepsilon_k u_{k-j} \quad \text{for } j \geq 0 \quad (7.109)$$

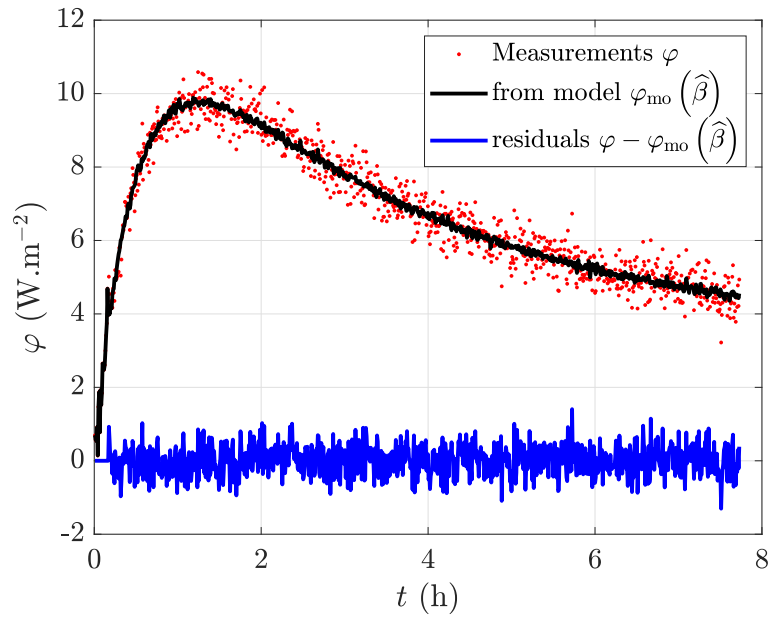
Negative lags may be defined by swapping  $u$  and  $\varepsilon$  in this expression. We define the normalized autocorrelation and cross-correlation functions as:

$$Q_{\varepsilon}^*(j) = \frac{Q_{\varepsilon}(j)}{Q_{\varepsilon}(0)} \quad (7.110)$$

$$Q_{\varepsilon u}^*(j) = \frac{Q_{\varepsilon u}(j)}{Q_{\varepsilon u}(0)} \quad (7.111)$$

One must check that the autocorrelation and cross-correlation functions are of small magnitude in order to confirm that the residuals are close to white-noise.

Figure 7.19 plots the residuals for the test case after parameter estimation on synthetic measurement. The model response and measurements are also compared. By construction, the residuals are null for the first points (see Eq 7.106). The normalized autocorrelation and cross-correlation functions are plotted in Fig 7.20. The 99% confidence region marking statistically insignificant correlations displays as a shaded region along the Y-axis. As a conclusion, the residuals pass the validation tests on this example.



**Figure 7.19.:** Residuals of ARX estimation (test case), with  $n_a = n_b = 20$  and  $n_k = 0$ .

### 7.3.3.3. Choice of number of parameters

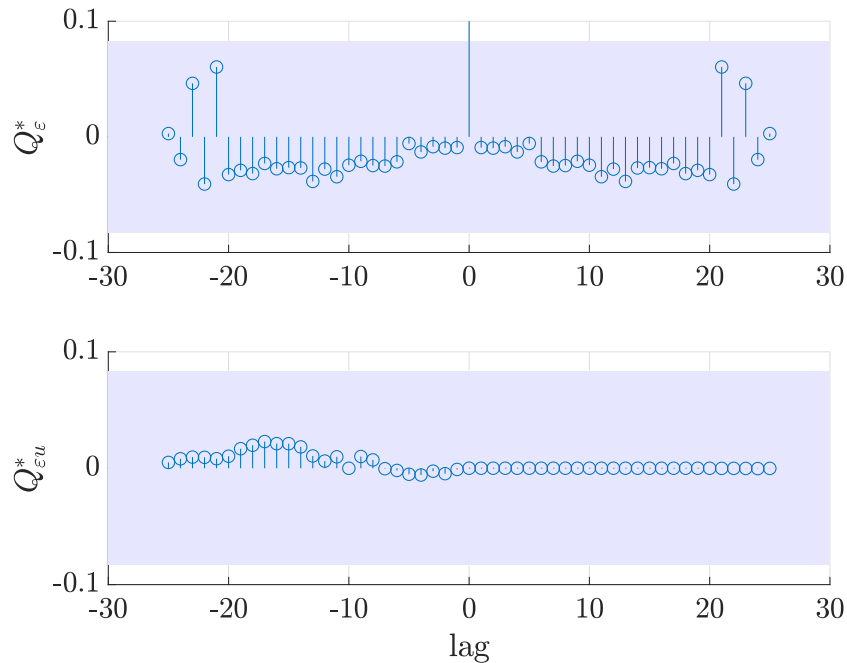
Hyperparameters  $n_a$ ,  $n_b$  and  $n_k$  have to be set. In the current context, parameter  $n_k$  may be set to zero. Indeed, there is no physical justification here to support the existence of a dead time between the internal temperature and heat flux.

However, the polynomial orders  $n_a$  and  $n_b$  have to be set by a trial-and-error procedure. There is no standard rule to define these numbers. In practice, they may be increased until the estimated quantity becomes independent on their value.

The thermal resistance estimated on the current test case is plotted in Fig 7.21 as a function of  $n_a$  with  $n_a = n_b$ . This latter equality was only set to simplify the analysis. It may be observed that the fewer the orders, the higher the bias on the estimated value and the higher the estimation uncertainty. As the orders increase, the bias tends to zero and the uncertainty keeps decreasing slowly. On this example,  $n_a$  and  $n_b$  should be greater than 20 for the estimation to be accurate.

### 7.3.4. Conclusion

Some tools from the System Identification framework may be used to estimate physical quantities from experiments. ARX models are studied here. These black-box models consist in identifying the parameters involved in a linear relation between the input and output, from measurements of these two quantities. Although the estimated parameters have no physical meaning, they may be combined to form an estimate of a wall thermal resistance if the model input and output are the internal surface temperature and heat flux, respectively.

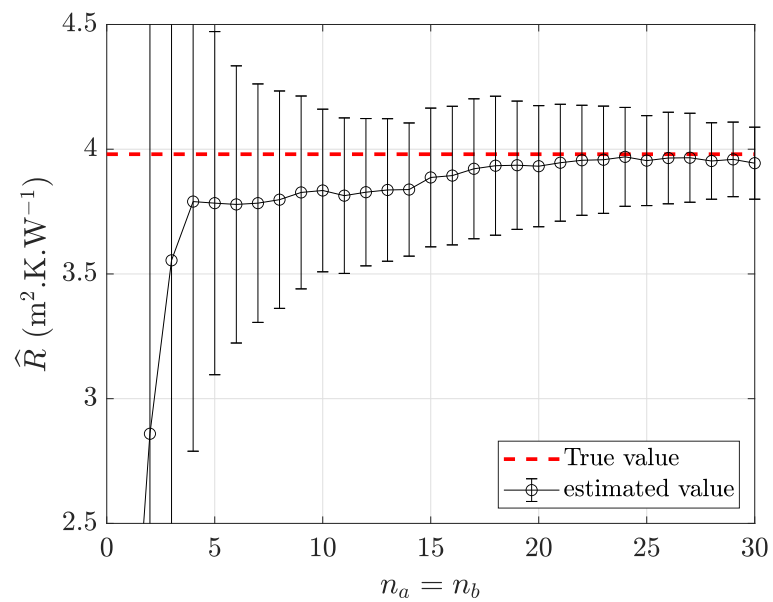


**Figure 7.20.:** Normalized autocorrelation and correlation coefficients for the test case. They are of small magnitude.

By construction, ARX models are linear in the parameters, which means that the estimation is direct and does not require any iterative procedure. It also means that the estimation will always deliver a result even if the problem is very ill-posed. Thus, several tools must be used to assess the quality of the estimation:

- The estimation uncertainty over the desired quantity (thermal resistance here) may be derived from the variance-covariance matrix of the estimated parameters of the ARX model. The value of this uncertainty is a good indicator of the quality of the estimation.
- Similarly to the white-box approach, the residuals (difference between measurements and model outputs) must be close to white noise. If not, it means that the model is not able to capture the physical phenomenon. Analysis of the residuals autocorrelation and cross-correlation functions enables to assess their “whiteness”.
- The estimation must not be dependent to the structure of the model (polynomial orders). The values of the hyperparameters must be chosen according to the desired quantity.

Similarly to section 7.2, the methods were illustrated on the example of a two-layer wall subjected to air heating on the internal side.



**Figure 7.21.:** Estimated thermal resistance as a function of hyperparameters  $n_a$  and  $n_b$  (test case).

## 7.4. Conclusion

This chapter presented several mathematical tools useful for the estimation of physical properties of a system from measurements. To be more specific, these methods will be used in later chapters for the estimation of a wall thermal resistance (or equivalent thermal resistance) from active measurements.

The derivation of a direct model of a wall with the thermal quadrupole formalism was presented. These white-box semi-analytical methods are very convenient to model dynamic 1D heat transfer problems. They may be used as direct model for the application of an inverse technique. Alternatively, black-box ARX models may be used.

For both approaches, several tools exist to assess the quality of the parameter estimation. The experiment, the direct model to use and the unknown parameters to estimate must be defined according to these validation tools.

The methods were presented on synthetic data. Chapters 8 and 9 will apply them to real measurements for the estimation of a homogeneous wall thermal resistance and a non-homogeneous wall equivalent thermal resistance, respectively.

## 8. Active characterization of a homogeneous wall

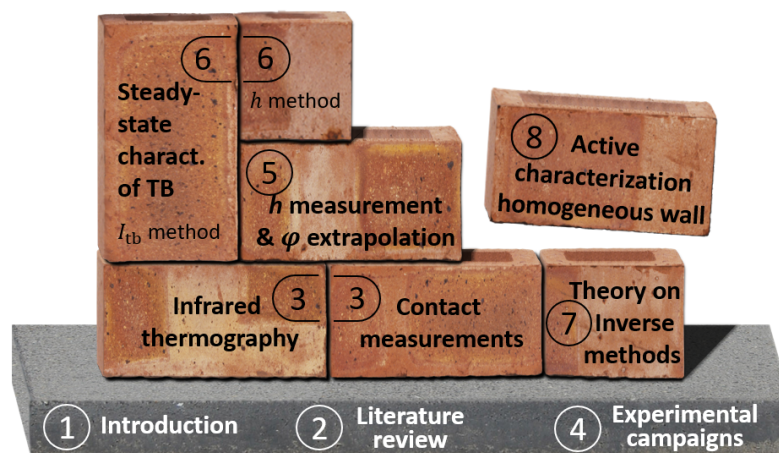


Figure 8.1.: Illustration of thesis plan.

Existing standardized methods for the *in situ* measurement of a wall thermal resistance  $R$  (or transmittance  $U$ ) are based on steady-state assumptions. They usually require very long measurements and are highly sensitive to outdoor conditions. Several dynamic and active methods were also developed in academia. They are often robust to outdoor conditions but also present some limitations which should be addressed for a wider uptake of *in situ* measurements by the construction industry. The duration required for the measurement is often recognized as the main challenge.

This chapter proposes an active method for the measurement of a homogeneous wall thermal resistance. It mainly consists in heating the indoor air and using inverse methods to estimate the wall thermal resistance from heat flux and temperature measurements. Unlike dynamic temperature-temperature common approaches, this heat flux-temperature alternative enables to bypass the surface heat transfer coefficient and therefore to reduce a major source of uncertainty. In addition, only a few hours of measurements (typically 6 to 8) are required. Two types of approaches are proposed for the inverse procedure: non-linear inversion with a “white-box” model and linear inversion with a “black-box” ARX model. The methods are validated on the CEREMA setup (full-scale internal insulated load-bearing wall built inside a climate chamber) and SGR setup (lightweight insulated wall *in situ*). The results of this chapter were presented in [220] and [221].

Section 8.1 of this chapter presents the active methodology (choice of thermal load, experimental protocol...) whereas section 8.2 focuses on the white-box approach (mainly the definition of the direct model). Sections 8.3 and 8.4 present the results obtained from application of the active method on the CEREMA and SGR experimental campaigns, respectively. Finally, section 8.5 draws a conclusion.

---

## Nomenclature

### Acronyms

ARMA	Auto-Regressive with Moving Average
ARX	Auto-Regressive with eXogenous inputs
HFM	Heat Flux Meter
HLC	Heat Loss Coefficient
IRT	InfraRed Thermography
MISO	Multiple Inputs, Single Output
NDT	Non Destructive Testing
OLS	Ordinary Least Squares
PRBS	PseudoRandom Binary Sequence
SISO	Single Input, Single Output
SNR	Signal to Noise Ratio

### Symbols

$\nearrow$	temperature increasing
$\searrow$	temperature decreasing
$\cap$	temperature around a maximum
$\cup$	temperature around a minimum

### Greek Symbols

$\alpha$	polynomial coefficients	
$\beta$	parameter vector	
$\Gamma$	gamma function	
$\varepsilon$	noise	
$\sigma$	noise standard deviation	
$\lambda$	Lagrange weighting factor	-
$\tau$	thermal load characteristic time	s
$\omega$	pulsation	
$\varphi$	heat flux density	W.m <sup>-2</sup>

### Roman Symbols

$A, B, C, D$	thermal quadrupole matrix coefficients	
$\mathcal{A}, \mathcal{B}, \mathcal{C}$	ARX polynomials	
$a, b, c$	ARX polynomial parameters	
$A_T$	thermal load amplitude	K
$b$	thermal effusivity	J.K <sup>-1</sup> .m <sup>-2</sup> .s <sup>-1/2</sup>
cov	variance-covariance matrix	
Covar	covariance operator	
$f$	frequency	s <sup>-1</sup>
$f_e$	excitation frequency	s <sup>-1</sup>
$f_s$	sampling frequency	s <sup>-1</sup>
$h$	total heat transfer coefficient	W.m <sup>-2</sup> .K <sup>-1</sup>
$j$	complex number such that $j^2 = -1$	
$k$	layer index	
$M$	thermal quadrupole matrix	
$N$	number of model layers	
$n$	polynomial order	



$p$	Laplace variable	$s^{-1}$
$P$	power density	$W.m^{-2}$
$q$	backshift operator	
$Q$	energy density	$J.m^{-2}$
$R$	thermal resistance	$m^2.K.W^{-1}$
$T$	temperature	$K$
$t$	time	$s$
$u$	uncertainty	
$U$	thermal transmittance	$W.m^{-2}.K^{-1}$
Var	variance operator	
$V_{cor}$	hybrid matrix	
$X$	sensitivity matrix	
$X^*$	reduced sensitivity matrix	
$Y$	thermal admittance	$W.m^{-2}.K^{-1}$
$Z$	thermal impedance	$m^2.K.W^{-1}$
$\hat{Z}$	estimated thermal impedance from ARX	$m^2.K.W^{-1}$
<b>Superscripts</b>		
$\sim$	Laplace transform	
$\wedge$	estimated value	
–	relative evolution before active test	
+	relative evolution during active test	
0	initial conditions (beginning of active test)	
1 – 2	label of layers included in the model	
<b>Subscripts</b>		
e	external	
i	external	
in	wall internal interface	
mo	model	
op	operative	
s	surface	

## 8.1. Presentation of the active methodology

### 8.1.1. Definition of model inputs and output

To perform active measurements, it was chosen to heat up the room internal air thanks to electric fan heaters. This thermal load is similar to the one used in the QUB/e method [149] and has the advantage of being easy to implement *in situ*. In addition, it provides a rather uniform heating of the wall (although not perfect because of air stratification). In contrast, the use of a radiant heating source would only heat up a limited area of the wall.

Surface temperatures  $T_{si}$  and  $T_{se}$  are chosen as the excitations of the thermal problem (thermal load), as illustrated in Fig 8.2. The way in which these surfaces were heated in the first place (air heating, radiant heat source, ...) does not matter in the analysis. The only requirement is that the heating must be uniform enough for the heat transfers to be supposed 1D in the studied section of the wall.

The internal surface heat flux  $\varphi_{si}$  is the model output. The other way around ( $\varphi_{si}$  as input and  $T_{si}$  as output) could have been used but, as detailed below, only the noise on the output is taken into account in the uncertainty calculation whereas the noise on the inputs has to be neglected. As shown in section 8.3 for instance, the Signal to Noise Ratio (SNR) is much worse on  $\varphi_{si}$  than  $T_{si}$ .

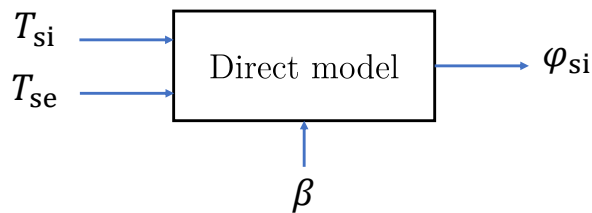


Figure 8.2.: Definition of model inputs and output.

### 8.1.2. Theoretical study: justification of thermal load


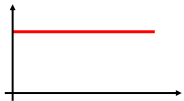
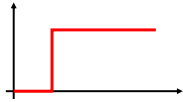
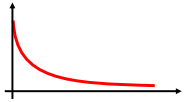
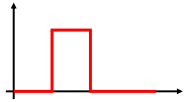
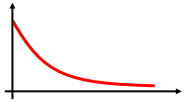
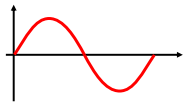

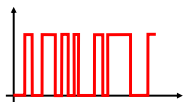
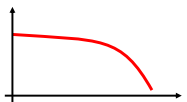
Here is presented a theoretical study based on synthetic data. Its aims at determining the main features of the thermal load to apply in order to perform active measurements (e.g. type of heating, duration, ...). As a complement, Appendix E.1 proposes another theoretical study showing that it is not interesting to work with normalized signals (whereas signals are usually normalized with the flash method for instance [14]).

#### 8.1.2.1. Common thermal loads

There are many different types of thermal loads than can be applied to a material to perform an active experiment. The most common are: “Pulse-heating”, “Step-heating”, “Square-heating”, “Lock-in” (sinusoidal-heating) and “Random-heating”

[14]. They are presented in Tab 8.1. The shape of their temporal evolution, their frequency spectrum, and the parameters which define them are given.

**Table 8.1.:** Presentation of the most common types of thermal load for an active experiment.

Temporal evolution	Frequency spectrum	Thermal load parameters
Flash 		<ul style="list-style-type: none"> <li>• <math>Q</math>: energy density (<math>\text{J.m}^{-2}</math>)</li> <li>• <math>t_R</math>: relaxation phase duration (s)</li> </ul>
Step 		<ul style="list-style-type: none"> <li>• <math>P</math>: power density (<math>\text{W.m}^{-2}</math>)</li> <li>• <math>t_H</math>: thermal load total duration (s)</li> </ul>
Square 		<ul style="list-style-type: none"> <li>• <math>P</math>: power density (<math>\text{W.m}^{-2}</math>)</li> <li>• <math>t_H</math>: thermal load total duration (s)</li> <li>• <math>t_R</math>: relaxation phase duration (s)</li> </ul>
Sinus 		<ul style="list-style-type: none"> <li>• <math>P</math>: maximum power density (<math>\text{W.m}^{-2}</math>)</li> <li>• <math>f</math>: excitation frequency (s)</li> <li>• <math>t_H</math>: thermal load total duration (s)</li> </ul>
Random 		<ul style="list-style-type: none"> <li>• <math>P</math>: power density (<math>\text{W.m}^{-2}</math>)</li> <li>• <math>t_H</math>: thermal load total duration (s)</li> <li>• random sequence (PRBS for instance)</li> </ul>

A pulse (or a flash) is a signal very rich in frequencies since the Fourier transform of Dirac distribution is a constant. However, this type of thermal load requires a high energy density which generates a very high and fast temperature increase on the sample surface. This may be incompatible with the material standard conditions of use. Pulse-heating is limited to the analysis of highly conductive or thin samples and therefore do not apply to building walls. In addition, it is in practice complicated to obtain a uniform heating over an extended area with a flash.

Step and Square thermal loads are probably the easiest ones to implement. Indeed, they imply heating the material with a constant power density for a given duration. With Step-heating, only measurements recorded during the heating phase are taken into account, whereas with Square-heating, the cooling phase is also analyzed. The main drawback of these thermal loads is that their frequency spectrum is rather poor and mainly contains low frequency information. However, this is not a problem for the estimation of a wall thermal resistance. Indeed, a thermal resistance is a steady-state characteristic so its estimation mainly requires low frequency information.

A Sinusoidal thermal load (Lock-in) is useful to detect very small temperature vari-

ations while limiting the required power density. It also enables to quantify the phase-lag between the thermal excitation and the measured thermal response. However, this type of loading only provides information at the given excitation frequency. Distinct measurements may be carried out for each desired frequency but this entails very long experimental campaigns.

Finally, Random-heating consists in generating a sequence of heating and free-cooling phases of random durations. One common type of such sequence is the so-called PseudoRandom Binary Sequence (PRBS). A Random thermal load is an interesting trade-off between Pulse-heating and Lock-in. Indeed, the signal is richer in frequency than a sinusoidal signal but does not require a energy density as large as with Pulse heating. However, in the current context the thermal load comes from heating of the air. Because of the air thermal inertia, the wall surface temperature would not follow a real PRBS sequence but a much smoother filtered sequence.

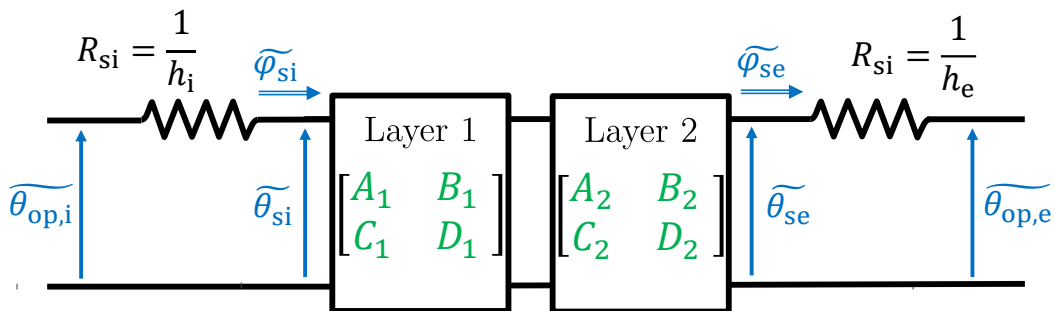
For the present study, Step and Square heatings were chosen for their ease of use and their ability to provide low frequency information in a reasonable amount of time.

### 8.1.2.2. Step-heating vs Square-heating

The electric fan heaters are turned on for several hours and then turn off. From this perspective, the thermal load may be categorized as either Step-heating or Square-heating even though the model inputs ( $T_{si}$  and  $T_{se}$ ) have a smoother shape. This section compares the two alternatives in order to identify the most suited one for the estimation of a wall thermal resistance.

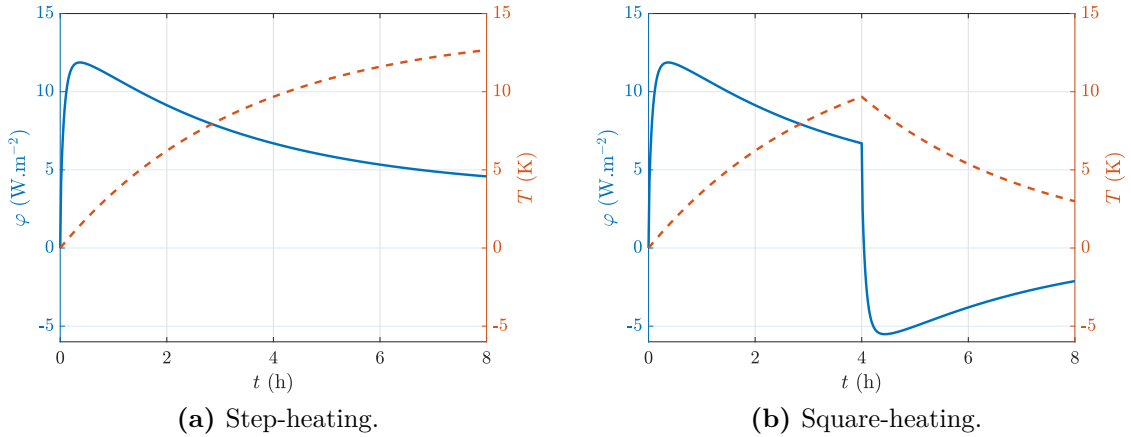
The analysis is based on the same test case used in Chap 7 for the illustration of inverse methods: a two-layer thermally insulated wall (gypsum + glass wool) subjected to internal air heating (modeled with an exponential function). The test case is thoroughly presented in section 7.1.5 and its layout is reminded in Fig 8.3.

The heat transfer coefficients  $h_i$  and  $h_e$  are supposed perfectly known. As developed in section 8.2.3.1, in practice the surface temperatures  $T_{si}$  and  $T_{se}$  would be measured and treated as inputs instead of  $T_{op,i}$  and  $T_{op,e}$ , so parameters  $h_i$  and  $h_e$  would not be included in the model.



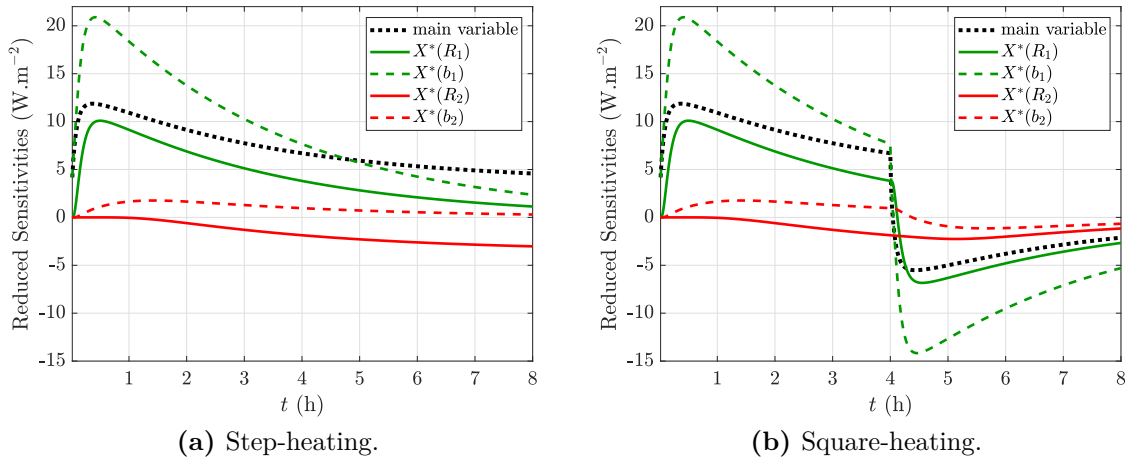
**Figure 8.3.:** Model used for the generation of synthetic measurements.

The experiment duration is set to 8 h. The Step-heating and Square-heating strategies are compared. For the latter, the heaters are supposed turned off at mid-experiment (4 h). The internal surface temperature and heat flux for each approach are plotted in Fig 8.4.



**Figure 8.4.:** Internal surface temperature and heat flux for the Step and Square heating strategies (test case).

Figure 8.5 plots the model reduced sensitivity coefficients for both heating strategies and Tab 8.2 presents the corresponding hybrid matrices  $V_{cor}$ . They were calculated from nominal parameter values given in section 7.1.5 and  $\sigma_\varphi = 0.4 \text{ W.m}^{-2}$  (noise standard deviation).



**Figure 8.5.:** Reduced sensitivity coefficients for the Step and Square heating strategies (test case).

Parameters  $R_1$  and  $b_1$  have a high sensitivity but are correlated with each other (correlation coefficient equal to -0.96). Parameter  $b_2$  has a much smaller reduced sensitivity. The main parameter of interest is  $R_2$  as it is the thermal resistance of the insulation layer which represents the major part of the wall overall resistance. It may be seen that during the heating phase, its reduced sensitivity keeps increasing

**Table 8.2.:** Hybrid  $V_{\text{cor}}$  matrices for the Step and Square heating strategies ( $\sigma_\varphi = 0.4 \text{ W.m}^{-2}$ ).

(a) Step-heating.					(b) Square-heating.				
	$R_1$	$b_1$	$R_2$	$b_2$		$R_1$	$b_1$	$R_2$	$b_2$
$R_1$	0.05	-0.96	-0.25	-0.64	$R_1$	0.035	-0.96	-0.10	-0.65
$b_1$		0.021	0.18	0.45	$b_1$		0.015	0.01	0.47
$R_2$			0.012	0.49	$R_2$			0.013	0.28
$b_2$	sym			0.07	$b_2$	sym			0.049

with time. It then decreases during the free-cooling phase. In addition, the relative estimation uncertainty of  $R_2$  (diagonal term in  $V_{\text{cor}}$  matrix) is slightly higher for the Square-heating case than for the Step-heating case. The relative uncertainty for the other parameters is smaller on Square-heating.

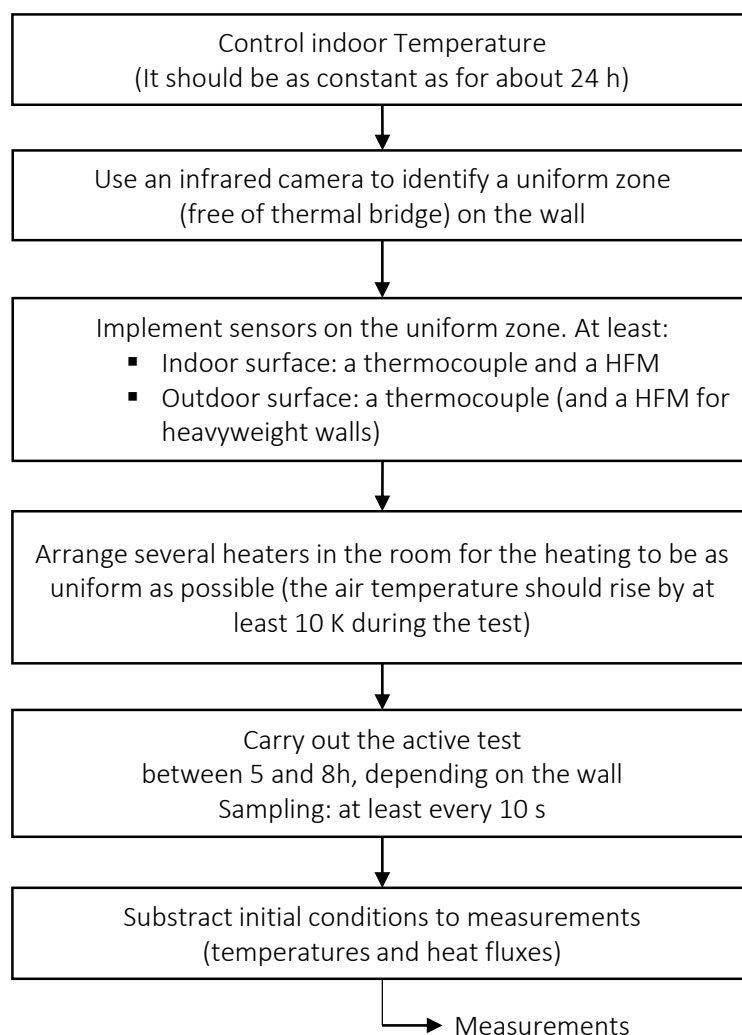
Square-heating is slightly richer in frequencies than Step-heating, which explains the smaller relative uncertainties noted on most parameters. However, the thermal resistance of the wall is a steady-state characteristic so there is no need for an excitation rich in high frequencies. Low frequency signals can probe the wall deeper than high frequency ones. From this perspective, Step-heating is more adapted because it is richer in low-frequency information. In addition, dealing with Square-heating measurements is a little bit more complex. Indeed, sharp variations in  $\varphi_{\text{si}}$  (such as the one that occurs when the heaters are turned off) are complex to measure accurately. The time response of the HFM used may not be negligible in such moments. Also, as presented in Tab 8.1, Square-heating is characterized by one more parameter than Step-heating: the heating phase duration. If the wall constitution is not known, choosing *a priori* a relevant value for this parameter might be complicated. For Step-heating, only the heating power has to be set *a priori*. Indeed, the total experimental duration may be set arbitrarily large, and the best time horizon to use for the analysis may be defined *a posteriori*.

As a consequence, not only is Step-heating simpler to implement and to post-process than Square-heating, it also minimizes the estimated uncertainty of  $R_2$ . It was therefore chosen for the active measurements.

### 8.1.3. Experimental protocol

Before presenting the inverse methods, let us present in more details the experimental protocol as well as the required instrumentation. The points described below are summarized in the flow chart in Fig 8.6. The numerical values given are indicative. They are relevant for the types of wall tested but might slightly differ in other situations.

Before the active test, the indoor temperature should be as constant as possible (for a duration of about 24 h, depending on the wall). The best is to control this temperature if a regulation system is present in the building or if one can be installed. As detailed in the next section, it is possible to correct the effects of a non-constant



**Figure 8.6.:** Flow chart of experimental aspects for active measurements.

internal surface temperature before the test. However, this makes the model more complex and might increase the estimation uncertainty of the wall thermal resistance. Given this recommendation to have a rather constant internal temperature, one could argue that, instead of using an active method, a simple steady-state technique could estimate the wall thermal resistance. It is important to point out that the conditions required for the current active method are less restrictive than for a steady-state one. First, the wall does not need to be quite at steady-state before the active test: variations of a few degrees in the internal temperature (and even higher for the external temperature) is not an issue. In other words, the active method is less sensitive to unsteady initial conditions than steady-state approaches. Second, the active method is applicable even if the initial internal/external temperature gradient is null. In comparison, a steady-state approach needs a high temperature difference to have a decent SNR.

Some thermocouples and heat flux meters have to be implemented on the wall. The operator should pay attention to fix these sensors on areas of the wall where heat

transfers may be considered 1D (away from thermal bridges). Such areas can be detected using an infrared camera: the surface temperature must be uniform. At least 3 sensors must be implemented and a fourth is recommended in some cases:

- A HFM on the internal surface of the wall to measure  $\varphi_{si}$ . It must have the same emissivity than the wall (in the infrared spectrum). The sensor may be covered with some adhesive tape for instance.
- A thermocouple on the same location as the heat flux meter to measure  $T_{si}$ . Ideally, this thermocouple is embedded inside the HFM.
- A thermocouple on the external surface of the wall to measure  $T_{se}$ .
- If the wall is heavyweight, it might be necessary to implement another HFM at the same location as the previous thermocouple to measure  $\varphi_{se}$ .

Some heaters also have to be installed inside the room. They should be located on the floor and arranged such that the heating is as uniform as possible. The heating power depends on the building Heat Loss Coefficient (HLC) and mainly affects the signal to noise ratio. From previous measurements, we recommend that the indoor air temperature rises by at least 10 K during the active test.

The duration of the test also depends on the considered wall. A duration of around 6 h proved to work well for the walls tested in the scope of this thesis. However, the experiment should be carried out longer if possible: the ideal duration for the analysis may be set *a posteriori*, simply by truncating the measurements. The experiment should be made by night. Although daytime measurements are possible (see internal and external corrections in next section), the measurement uncertainties are generally higher than night-time measurements.

Finally, the initial conditions (values of the measured quantities just before the heating phase) must be subtracted from the measurements. This enables to consider only the variations of heat fluxes and temperatures induced by the artificial thermal load. Constant temperature gradients inside the wall are removed by this subtraction (superimposition theorem).

### 8.1.4. Conclusion

The ideal experimental protocol for the estimation of wall thermal resistance from active measurements was defined. As thermal load, the internal air temperature is heated. It was shown that analyzing a free cooling period after the heating phase does not reduce the estimation uncertainty of the thermal resistance: Step-heating is more suitable than Square-heating. As a consequence, only the amplitude of the thermal load has to be set *a priori*: the ideal experiment duration may be tuned during the post-processing step.

The next section presents the application of an inverse method with a white-box model. The ARX approach for the estimation of a wall thermal resistance was described in Chap 7 and is not presented in the current chapter.



## 8.2. Presentation of the white-box approach

The “white-box” approach is based on a non-linear parameter estimation procedure applied to a white-box direct model. The latter is derived from the heat equation using the thermal quadrupole formalism. The application of the white-box approach for the estimation of a wall thermal resistance is presented here with a focus on the definition of the direct model. The mathematical tools involved were presented in Chap 7.

### 8.2.1. Overview of the method

The method is composed of three main steps:

1. Find an analytical expression of the model inputs
2. Define the direct model
3. Perform parameter estimation

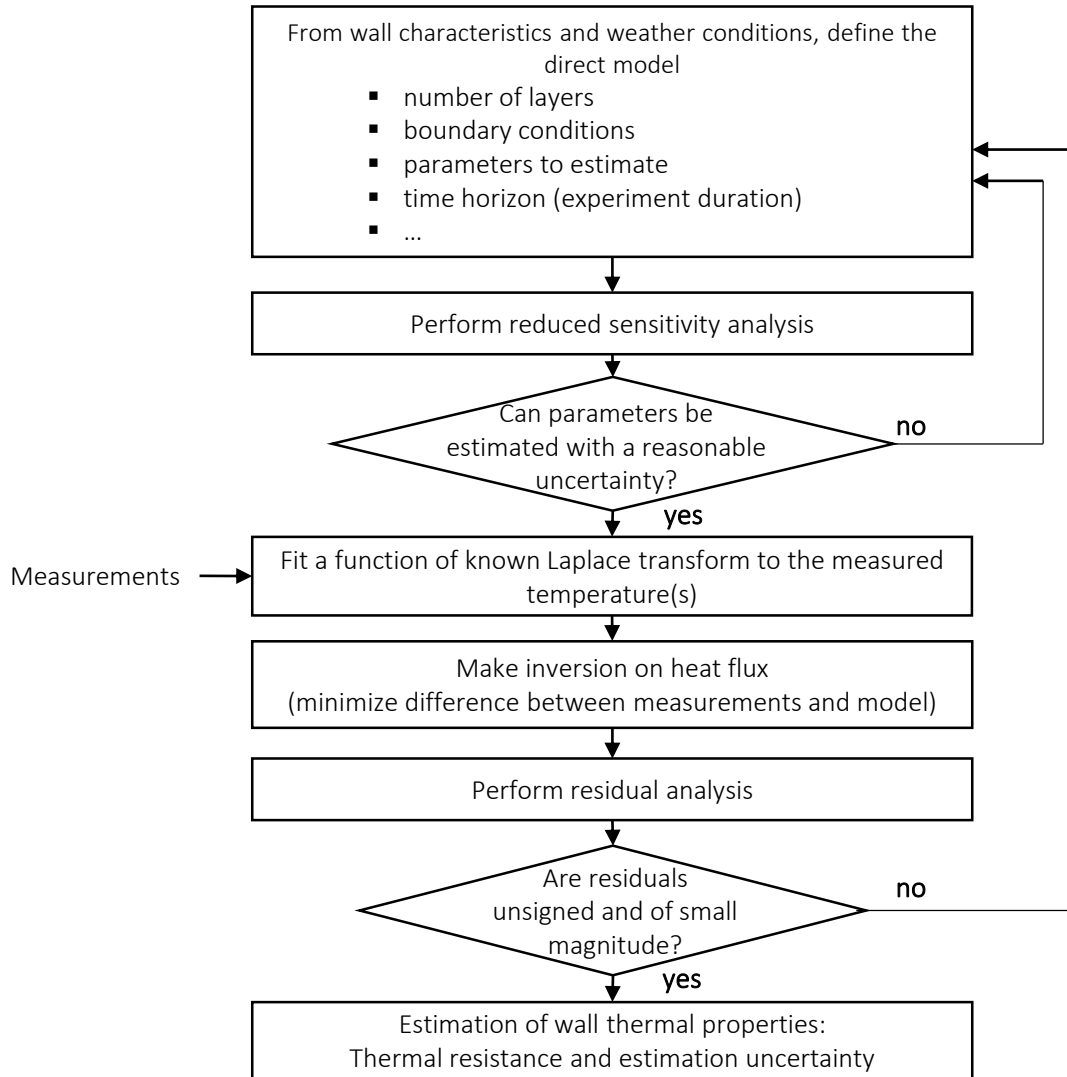
First, the direct model depends on the parameter vector  $\beta$  (thermal properties of the wall layers) but also on one or two inputs (surface temperatures). The thermal quadrupole formalism requires to have an analytical expression of the Laplace transform of these temperatures. In Non-Destructive Testing (NDT) [14], thermal loads are usually a pulse or a step, so that their Laplace transform are simple and only depends on one constant. Here, the evolutions of  $T_{si}$  and  $T_{se}$  are more complex (see Fig 8.4a for instance). Therefore, the chosen approach is to fit a function of known Laplace transform to the input curves. This function does not need to have any physical meaning, but it must be as close as possible to the measured data. Depending on the shape of the curve, the function may be a polynomial or an exponential for instance. It is important to point out that this fit removes the measurement noise on the temperatures. Thus, this noise is supposed null in the evaluation of the estimation uncertainties of the wall thermal resistance. Only the noise on the output  $\varphi_{si}$  is taken into account. Yet, given that the SNR is a significantly higher on the temperatures than on the heat fluxes, this hypothesis has a limited impact on the calculated uncertainty. This confirms the choice of  $\varphi_{si}$  as model output.

Second, the output of the direct model of the wall must be defined parsimoniously. It has to be complex enough to be able to model the physical phenomenon but simple enough for its parameters to be estimable. Several models may be defined depending on the situation. Some model reduction steps may be required. This is the topic of the next section.

Third, the optimum parameter vector  $\hat{\beta}$  that minimizes the difference between the model output and the measurements is estimated with the Levenberg-Marquardt algorithm (see Chap 7). The time horizon chosen for the minimization may be tuned for the estimation to be as accurate as possible.

The whole process is summarized in Fig 8.7. This flow chart includes the three previous points as well as some checks. Given the ill-posed nature of inverse problems,

the parameter estimation might not be straightforward. A thorough analysis of the reduced sensitivities, variance-covariance matrix, and the residuals is necessary to assess the relevance of the results (see Chap 7). The direct model and time horizon might have to be changed according to these analyses (iterative process).



**Figure 8.7.:** Flow chart of inverse technique for application of the white-box approach.

### 8.2.2. Analytical expressions of the inputs

A function of known Laplace transform must be fitted to the measured temperatures. Several functions were tested. It was found that a polynomial function in  $1/k$  fitted well  $\theta_{si}^+$ :

$$f(\alpha, t) = \sum_{i=k}^n \alpha_k t^{1/k} \tag{8.1}$$

whereas a polynomial function was well adapted to other temperatures ( $\theta_{si}^-$  and  $\theta_{se}$ ):

$$g(\boldsymbol{\alpha}, t) = \sum_{i=k}^n \alpha_k t^k \quad (8.2)$$

with  $\boldsymbol{\alpha}$  the vector of parameters that is adjusted during the fitting process. The later is done with the Levenberg-Marquardt algorithm. The Laplace transform of the previous functions are given by:

$$\tilde{f}(\boldsymbol{\alpha}, p) = \sum_{k=1}^n \alpha_k \frac{\Gamma\left(\frac{1}{k} + 1\right)}{p^{\frac{1}{k}+1}} \quad (8.3)$$

$$\tilde{g}(\boldsymbol{\alpha}, p) = \sum_{k=1}^n \alpha_k \frac{k!}{p^{k+1}} \quad (8.4)$$

with  $\Gamma$  the gamma function. The degree  $n$  of each function is set high enough to make the residuals as low as possible. A high degree will not affect the well-posedness of the problem, it only lightly slows down the calculations. This is not an issue given that the estimation is almost instantaneous. The components of each vector  $\boldsymbol{\alpha}$  (one per model input) are set before estimation of the thermal resistance and are not included in the vector of unknown parameters  $\boldsymbol{\beta}$ .

### 8.2.3. Direct model definition

#### 8.2.3.1. Model reduction

As detailed in section 7.2, the complexity of the model must be adapted to the needs. A few model reduction steps are required for the number of unknown parameters of the direct model to match the problem number of degrees of freedom.

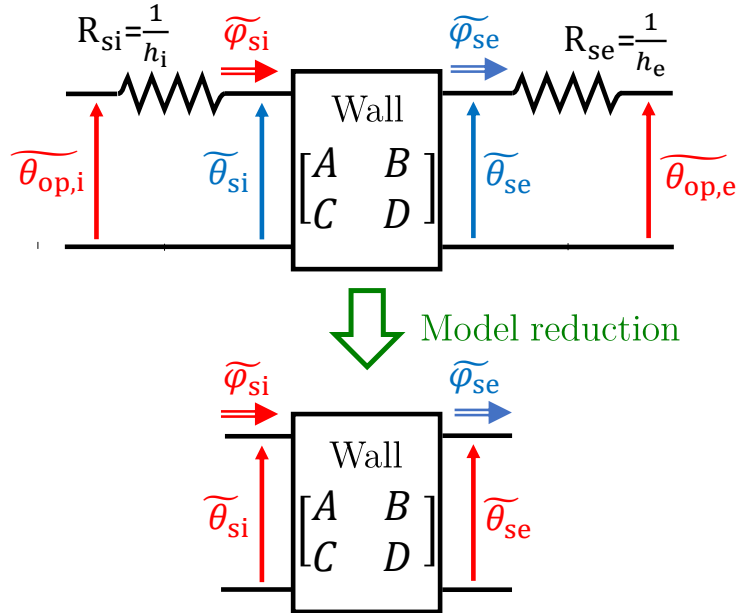
The first model reduction step is the hypothesis of 1D heat transfers. Then, the test case thoroughly studied in Chap 7 enabled to draw two important conclusions for the type of active tests studied in this thesis:

- The external overall heat transfer coefficient  $h_e$  is an irrelevant parameter as its reduced sensitivity has a negligible magnitude.
- The internal overall heat transfer coefficient  $h_i$  is highly correlated with the thermal properties of the first layer of the wall:  $R_1$  and  $b_1$ .

Thus, it was chosen not to model the heat exchanges with the surroundings, as illustrated in Fig 8.8. The surface temperatures and heat flux densities are directly measured on the wall with contact sensors (thermocouples and heat flux meters). By doing so, the knowledge of the operative temperatures  $\theta_{op,i}$  and  $\theta_{op,e}$  and the overall

## 8.2. PRESENTATION OF THE WHITE-BOX APPROACH

heat transfer coefficients  $h_i$  and  $h_e$  is not required to resolve the heat transfers inside the wall.



**Figure 8.8.:** Illustration the real (top) and reduced (bottom) thermal problems: surface resistances and operative temperatures are excluded from the model. Measured quantities are written in red.

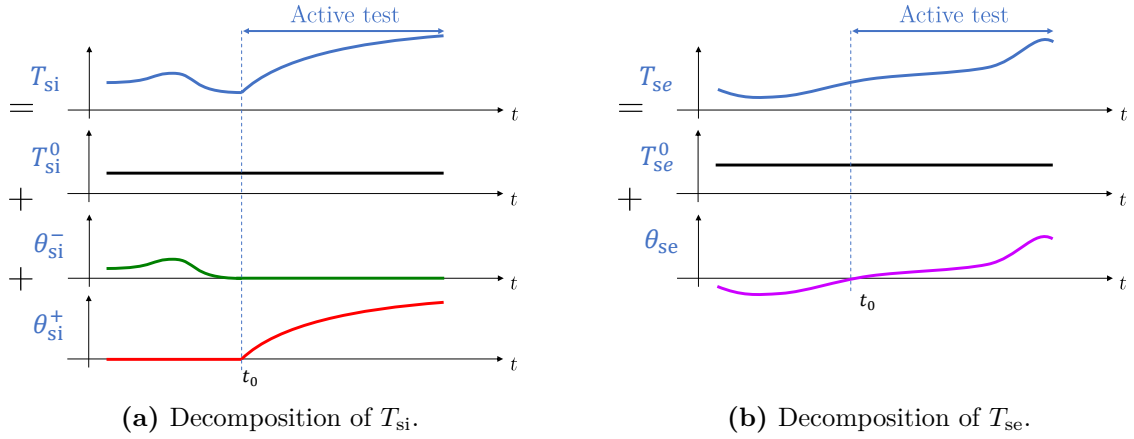
This approach is interesting for four reasons:

- It removes two unknown parameters which makes the inverse problem less ill-posed.
- Coefficients  $h_i$  and  $h_e$  are supposed constant in the model which might not be the case during the whole duration of the experiment. This could introduce a bias in the model and reduce the accuracy of the parameter estimation.
- It enables to bypass the operative temperatures  $T_{op,i}$  and  $T_{op,e}$ . The latter are very complex to measure as they account for both radiative and convective heat transfers. In the building sector, the operative temperature is usually supposed equal to the air temperature. This assumption might be relevant inside a well-insulated building and in quasi-steady state: the indoor environment is close to thermal equilibrium. However, it is no longer valid here in active tests: because the internal air is rapidly heated, its temperature becomes very different from the mean radiant temperature (see Chap 5).
- No measurement of the solar heat flux is required so no weather station is required as in [145].

Consequently, using surface temperatures and heat fluxes as inputs and output of the model allows overcoming these difficulties.

### 8.2.3.2. Decomposition of inputs and model nomenclature

Thanks to the superimposition theorem, the model inputs ( $T_{si}$  and  $T_{se}$ ) may be decomposed into several terms. The situation is illustrated in Fig 8.9. The active test starts at time  $t = t_0$ .



**Figure 8.9.:** Decomposition of internal and external surface temperatures (superimposition theorem).

We introduce the following notations:

$$T_{si}(t) = T_{si}^0 + \theta_{si}^-(t) + \theta_{si}^+(t) \quad (8.5)$$

$$T_{se}(t) = T_{se}^0 + \theta_{se}(t) \quad (8.6)$$

where:

- $T_{si}^0 = T_{si}(t_0)$  is the value of  $T_{si}$  at the beginning of the active test.
- $\theta_{si}^-$  is the relative evolution of  $T_{si}$  before the active test:

$$\theta_{si}^-(t) = \begin{cases} T_{si}(t) - T_{si}^0 & \text{for } t \leq t_0 \\ 0 & \text{for } t > t_0 \end{cases} \quad (8.7)$$

- $\theta_{si}^+$  is the relative evolution of  $T_{si}$  during the active test:

$$\theta_{si}^+(t) = \begin{cases} 0 & \text{for } t \leq t_0 \\ T_{si}(t) - T_{si}^0 & \text{for } t > t_0 \end{cases} \quad (8.8)$$

- $T_{se}^0 = T_{se}(t_0)$  is the value of  $T_{se}$  at the beginning of the active test.
- $\theta_{se}$  is the relative evolution of  $T_{se}$  during the whole experiment (before and during the active test):

$$\theta_{se}(t) = T_{se}(t) - T_{se}^0 \quad (8.9)$$

## 8.2. PRESENTATION OF THE WHITE-BOX APPROACH

---

As described in section 8.1.3, the values at  $t = t_0$  are subtracted so that only variations of temperatures and heat fluxes are taken into account in the analysis. Furthermore, the decomposition of  $T_{\text{si}}$  in  $\theta_{\text{si}}^-$  and  $\theta_{\text{si}}^+$  is useful to distinguish the contribution of the active test (heaters turned on) from the disturbance due to non-stable initial conditions.

Similarly, we introduce  $\varphi_{\text{si}}^+$ :

$$\varphi_{\text{si}}^+(t) = \varphi_{\text{si}}(t) - \varphi_{\text{si}}^0 \quad \text{for } t > t_0 \quad (8.10)$$

with  $\varphi_{\text{si}}^0 = \varphi_{\text{si}}(t_0)$ . In the Laplace domain, the evolution of  $\varphi_{\text{si}}^+$  is obtained from simple multiplication of the inputs by the wall thermal admittances  $Y_{\text{si}}$  and  $Y_{\text{se}}$ :

$$\widetilde{\varphi}_{\text{si}}^+ = \underbrace{Y_{\text{si}}(\boldsymbol{\beta}) \times \widetilde{\theta}_{\text{si}}^+}_{\text{active test}} + \underbrace{Y_{\text{si}}(\boldsymbol{\beta}) \times \widetilde{\theta}_{\text{si}}^-}_{\text{internal correction}} + \underbrace{Y_{\text{e}}(\boldsymbol{\beta}) \times \widetilde{\theta}_{\text{se}}}_{\text{external correction}} \quad (8.11)$$

with  $\boldsymbol{\beta}$  the parameter vector:

$$\boldsymbol{\beta} = [R_1 \ b_1 \ \dots \ R_N \ b_N] \quad (8.12)$$

where  $N$  is the number of layers of the modeled wall. For sake of conciseness, the dependency of each quantity to the Laplace variable  $p$  was removed in Eq 8.11. The thermal admittances are defined from the coefficients of the wall quadrupole matrix:

$$Y_{\text{si}}(\boldsymbol{\beta}, p) = \frac{D(\boldsymbol{\beta}, p)}{B(\boldsymbol{\beta}, p)} \quad (8.13)$$

and

$$Y_{\text{se}}(\boldsymbol{\beta}, p) = \frac{1}{B(\boldsymbol{\beta}, p)} \quad (8.14)$$

It may be noted that the initial values  $T_{\text{si}}^0$ ,  $T_{\text{se}}^0$  and  $\varphi_{\text{si}}^0$  cancel out in Eq 8.11. The first term of this equation is the most important one as it quantifies the thermal response of the wall to the active test. In an ideal case, that is to say if (i) the internal temperature is constant before the active test and (ii) the external temperature is constant during the whole experiment, the two other terms are null. The second term (referred as ‘‘internal correction’’) corrects the effect of a non-constant initial surface temperature. The third term (called ‘‘external correction’’) enables to take into account variations in the external temperature, that is to say unsteady weather conditions. Including or not the correction terms does not change the number of

parameters ( $Y_{si}$  and  $Y_{se}$  depend on the same parameter vector  $\beta$ ). However, this increases the model complexity and the amount of information available for the parameter estimation.

To conclude, the definition of the direct model is driven by the choice of:

1. The number of modeled layers  $N$  (usually 2 or 3).
2. The inclusion of the “internal correction” if  $\theta_{si}^-$  is not null.
3. The inclusion of the “external correction” if  $\theta_{se}$  is not null.

Table 8.3 summarizes the different direct models which can be built and proposed a nomenclature. The letter A stands for “active test”, I for “internal correction” and E for “external correction”.

**Table 8.3.:** Summary of “white-box” direct models (The letter A stands for “active test”, I for “internal correction” and E for “external correction”).

Name	Illustration	Equation
$A_N$		$\widetilde{\varphi}_{si}^+ = Y_{si}(\beta) \times \widetilde{\theta}_{si}^+$
$AI_N$		$\widetilde{\varphi}_{si}^+ = Y_{si}(\beta) \times \widetilde{\theta}_{si}^+ + Y_{si}(\beta) \times \widetilde{\theta}_{si}^-$
$AE_N$		$\widetilde{\varphi}_{si}^+ = Y_{si}(\beta) \times \widetilde{\theta}_{si}^+ + Y_{se}(\beta) \times \widetilde{\theta}_{se}$
$AIE_N$		$\widetilde{\varphi}_{si}^+ = Y_{si}(\beta) \times \widetilde{\theta}_{si}^+ + Y_{si}(\beta) \times \widetilde{\theta}_{si}^- + Y_{se}(\beta) \times \widetilde{\theta}_{se}$

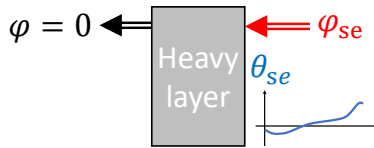
### 8.2.3.3. The heavyweight wall case

This section focuses on the case of a heavyweight wall internally insulated (such as the CEREMA wall). In this configuration, the simultaneous estimation of the thermal properties of all the layers with an inverse method might not be possible. Indeed, the problem might be ill-posed because of a too high number of parameters. One solution is to supposed perfectly known the properties of the heavy layer. These properties may be estimated using a different model based on external measurements.

## 8.2. PRESENTATION OF THE WHITE-BOX APPROACH

This model differs from the others as it takes as output the external surface heat flux  $\varphi_{se}$ . As shown in Tab 8.4, the input is the external surface temperature  $\theta_{se}$ . As boundary condition, the heat flux on the other side of the heavy layer (between it and the insulation layers) is supposed null. This simplifying assumption is deemed reasonable given the presence of thermal insulation.

**Table 8.4.:** White-box direct model for the estimation of the properties of a heavy-weight layer from outdoor measurements (The letter H stands for “heavyweight”).

Model	Illustration	Equation
$H_N$		$\widetilde{\varphi}_{se} = \frac{C(\beta,p)}{A(\beta,p)} \times \widetilde{\theta}_{se}$

It is important to highlight that this model is only applicable if the external temperature  $\theta_{se}$  varies (it is the thermal load). If the latter is constant, the heavy layer is not probed and its thermal properties cannot be estimated. However, this is not an issue given that in this situation, models  $A_N$  or  $AI_N$  may be applied: the temperature between the insulating layers and the heavy layers is constant (only the insulating layers are modeled, see CEREMA experiments as an example). As a conclusion,  $H_N$  model is only applicable when needed.

### 8.2.4. Conclusion

The application of the white-box approach for the estimation of a homogeneous wall thermal resistance was presented. First, a function of known Laplace transform is fitted to the model inputs (surface temperatures). Then, a reduced direct model is defined. The following model reduction steps are considered:

- Suppose heat transfers are 1D.
- Measure  $T_{si}$  and  $\varphi_{si}$  to exclude  $h_i$  from the model.
- Measure  $T_{se}$  (end  $\varphi_{se}$  is model  $H_N$  is used) to exclude  $h_e$  from the model.

The direct model is defined by the number of modeled layers and the number of inputs: correction terms may be added to take into account variations in the internal surface temperature before the active test and in the external temperature. In the case of a heavyweight wall, a model based on external measurements might be necessary. Finally, the unknown parameters are estimated with the Levenberg-Marquardt algorithm.



### 8.3. Application to CEREMA experimental campaign

The active method is validated on measurements performed in the CEREMA experimental campaign (presented in section 4.4 of Chap 4). The experimental campaign includes 27 active tests divided among 6 configurations, as reminded in Tab 8.5. The external air temperature  $T_{\text{air,e}}$  is either constant (configurations 1 and 2) or variable (configurations 3 to 6).

**Table 8.5.:** Summary of active tests configurations.

Configuration	$T_{\text{air,i}}$ (°C)	$T_{\text{air,e}}$ (°C)	test IDs	number of tests
1	15	5	1-5	5
2	15	15	6-8	3
3	15	$5 + 2.5 \cos(\omega t)$	9-13	4
4	15	$5 + 5.0 \cos(\omega t)$	14-17	4
5	15	$5 + 7.5 \cos(\omega t)$	18-25	8
6	15	$15 + 7.5 \cos(\omega t)$	25-27	3

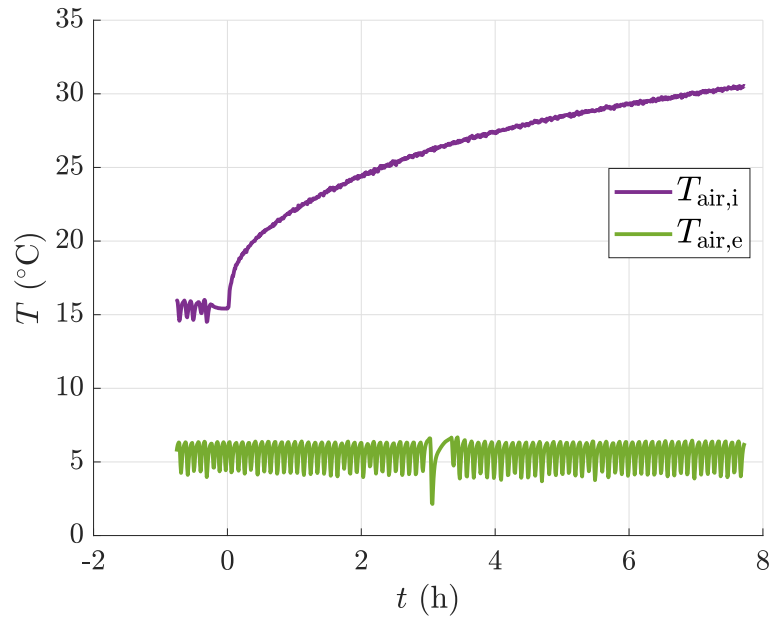
The “white-box” and “black-box” ARX approaches (see Chap 7) are compared. The objective here is to estimate the thermal resistance of the insulation system. Indeed, the load-bearing layer only represents a small part of the overall thermal resistance (10% here). Besides, in the context of the energy performance assessment of a new building, the main objective is to assess the performance of the insulating materials. Finally, the method could be applied before and after energy retrofitting work to quantify the increment in thermal resistance.

A typical active test of configuration 1 will be used in the following sections to illustrate the inverse methods.

#### 8.3.1. Measurements on one example

The air temperatures measured during the chosen active test are plotted in Fig 8.10. The initial internal and external temperatures were set to 15 and 5°C respectively for two days so that a steady-state was achieved. To perform the active test, two electric fan heaters are turned on and the regulation system on the same side of the wall is simultaneously turned off. The external temperature remains controlled to 5°C during the whole experiment. After 8 hours of constant heating, the internal air temperature rises by 15 K up to 30°C. The small temperature oscillations observed on  $T_{\text{air,e}}$  are due to the regulation system of the climate chamber.

Figure 8.11 plots the evolution of the wall internal surface temperature  $T_{\text{si}}$  and heat flux  $\varphi_{\text{si}}$ , measured on the sound area (i.e. away from the thermal bridges) during the same experiment. The temperature  $T_{\text{in}}$  of the interface between the glass wool and the concrete blocks is also plotted. The surface temperature increases up to 28°C. Meanwhile, the heat flux rapidly reaches a maximum, then decreases and tends to stabilize. Temperature  $T_{\text{in}}$  remains almost constant during the experiment.



**Figure 8.10.:** Internal and external air temperatures during an active test (the heaters are turned on at  $t = 0$ ).

Sections 8.3.2 and 8.3.3 present the two analysis methods (white-box and black-box) taking these measurements as example.

### 8.3.2. White-box method

Inverse methods based on a white-box model were presented in section 7.2 of Chap 7. Their application to the estimation of a wall thermal resistance was introduced in section 8.2.

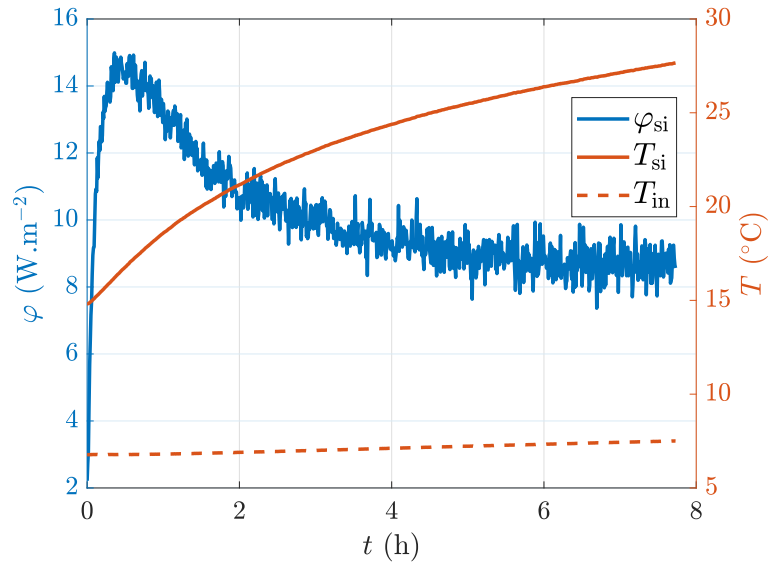
#### 8.3.2.1. Analytical expression of the input

A polynomial function in  $1/k$  (Eq ) of order  $n = 7$  is fitted to the measured internal surface temperature  $\theta_{si}^+$ . It may be seen on Fig 8.12 that the chosen function fits well the measurement data. Increasing the polynomial order does not reduce the residuals.

#### 8.3.2.2. Direct model definition

Several models of different complexity were tested. They are derived from tables 8.3 and 8.4, and are summarized in Tab 8.6. Thanks to the regulation system of the climate chamber,  $T_{si}$  is constant before the active tests so no “internal correction” was required. The models differ in the number of modeled layers and the “external correction” term. They are defined as follows:

**Model  $A_2$**  is the simplest one as it includes no correction term. It has been observed that during the duration of an active experiment (typically 8 h), the

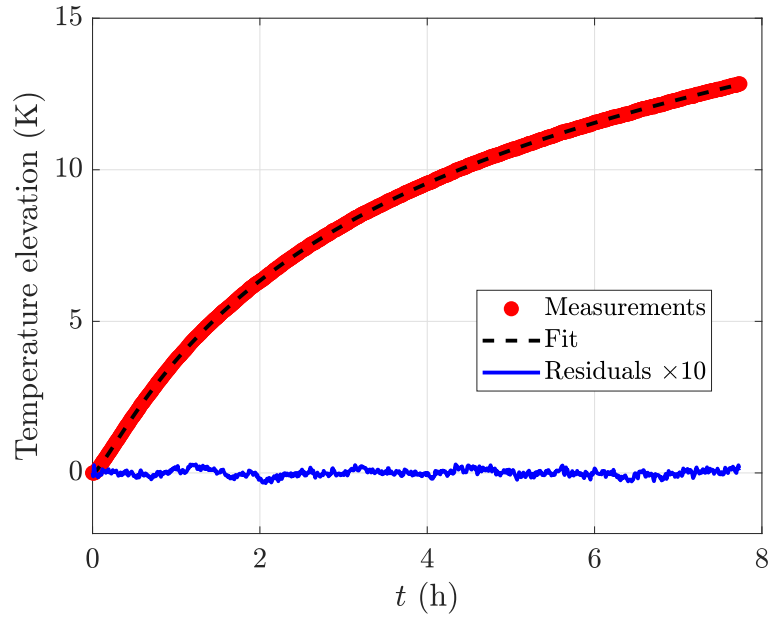


**Figure 8.11.:** Surface heat flux and temperature measured on the internal wall surface during an active test, as well as wall internal temperature.

temperature  $T_{in}$  of the interface between the glass wool and the concrete blocks barely increases (see Fig 8.11). Indeed, not only are the blocks located behind an insulating material (the thermal wave needs time to reach them), they also have a very high thermal inertia. Thus, model  $A_2$  excludes the third layer and replaces it by the boundary condition  $T_{in} = \text{constant}$ . Since initial values are removed, this is equivalent to  $\tilde{\theta}_{in} = 0$ . This model only takes into account the first two layers (gypsum and glass wool) hence the “1-2” superscripts in Tab 8.6. This simplified model has four unknown parameters (two per modeled layer) and is useful to estimate the thermal resistance of the insulation system.

**Model  $AE_{in,2}$**  is similar to model  $A_2$  in the sense that it excludes the concrete blocks layer and has the same four unknown parameters. However, temperature  $T_{in}$  is no longer supposed constant. It is measured and is the second input of the model. It plays the role of  $T_{se}$  and is included in the model through an “external correction” term. Yet, the “external” designation is not suitable here given that  $T_{in}$  is not the external surface temperature. This justifies the name “ $AE_{in,2}$ ” instead of “ $AE_2$ ”. This configuration is not applicable *in situ* since no thermocouple can be installed inside the wall. Nevertheless, it is useful to gain valuable insight on the current experiments.

**Model  $AE_3$**  is more complete than the previous ones as it includes all three layers (see the “1-3” superscripts in Tab 8.6). Thus, model  $AE_3$  has six parameters. The rear surface temperature  $T_{se}$  is measured and is an input of the model (external correction). However, all six parameters cannot be estimated simultaneously because of strong correlations (the inverse problem is too ill-posed). Thus, the thermal properties of the third layer ( $R_3$  and  $b_3$ ) are supposed perfectly known in the estimation. In practice, one could use standard values for this type of material. For more accuracy, it is proposed here to estimate them



**Figure 8.12.:** Function fit on model input  $\theta_{si}^+$  (from CEREMA experiment,  $n = 7$ ).

by using model  $H_1$  (see section 8.2.3.3). This is therefore a two-step procedure.

**Model  $H_1$**  differs from the others as it is not meant to estimate the thermal resistance of the insulation system. It aims at providing values of  $R_3$  and  $b_3$  to feed model  $AE_3$  and only models the building blocks (“3” superscript). It takes as output the surface heat flux  $\varphi_{se}$  measured with a HFM on the external side of the wall. The input is the external surface temperature  $T_{se}$ . As boundary condition, the heat flux between layers 2 and 3 is supposed null. This simplifying assumption is deemed reasonable given the presence of thermal insulation. This model is not applicable if the external temperature is constant. It can therefore only be used in configurations 3 to 6.

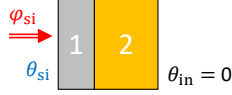
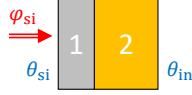
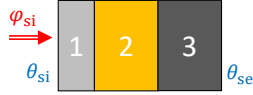
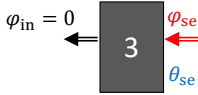
### 8.3.2.3. Sensitivity analysis and estimation of uncertainties

For the sake of conciseness, only the sensitivity analysis of model  $A_2$  is detailed here. Figure 8.13 plots the evolution of the reduced sensitivities with  $\beta = \hat{\beta}$  the optimum parameter vector after parameter estimation (see Tab 8.8 in next section).

First, it may be noted that the sensitivities to the parameters of the first layer,  $R_1$  and  $b_1$ , have a larger amplitude than those of the second layer ( $R_2$  and  $b_2$ ). This is because the model is more sensitive to parameters of the closest layer to the measurement location of  $\varphi_{si}$ . The curves of  $X^*(R_1)$  and  $X^*(b_1)$  also have a similar shape:  $R_1$  and  $b_1$  are correlated. It might be complex to estimate them both accurately: many different combinations of them might lead to the same heat flux  $\varphi_{mo}$ . In addition,  $b_2$  has a low reduced sensitivity when compared to the other ones so its estimation uncertainty will be greater. Finally, the sensitivity to  $R_2$  has a non negligible amplitude and a unique shape.

The sensitivity to  $R_2$  keeps increasing with time (in absolute values). This suggests

**Table 8.6.:** Summary of “white-box” direct models.

Model	Illustration	Equation	Parameters
$A_2$		$\widetilde{\varphi}_{si}^+ = Y_{si}^{1-2}(\boldsymbol{\beta}) \times \widetilde{\theta}_{si}^+$	$\boldsymbol{\beta} = [R_1 \ b_1 \ R_2 \ b_2]$
$AE_{in,2}$		$\widetilde{\varphi}_{si}^+ = Y_{si}^{1-2}(\boldsymbol{\beta}) \times \widetilde{\theta}_{si}^+ + Y_{se}^{1-2}(\boldsymbol{\beta}) \times \widetilde{\theta}_{in}$	$\boldsymbol{\beta} = [R_1 \ b_1 \ R_2 \ b_2]$
$AE_3$		$\widetilde{\varphi}_{si}^+ = Y_{si}^{1-3}(\boldsymbol{\beta}) \times \widetilde{\theta}_{si}^+ + Y_{se}^{1-3}(\boldsymbol{\beta}) \times \widetilde{\theta}_{se}$	$\boldsymbol{\beta} = [R_1 \ b_1 \ R_2 \ b_2 \ R_3 \ b_3]$ ( $R_3$ and $b_3$ supposed known)
$H_1$		$\widetilde{\varphi}_{se} = \frac{C_3(\boldsymbol{\beta})}{A_3(\boldsymbol{\beta})} \times \widetilde{\theta}_{se}$	$\boldsymbol{\beta} = [R_3 \ b_3]$

that there is a minimum experiment duration for the estimation of  $R_2$  to be accurate. In addition, because the sensitivity to  $R_2$  is small at the beginning of the experiment, the first instants are not taken into account in the estimation procedure (the first 10 min).

For the given example, the  $V_{cor}$  matrix is shown in Tab 8.7 ( $\sigma_\varphi = 0.4 \text{ W.m}^{-2}$ ).

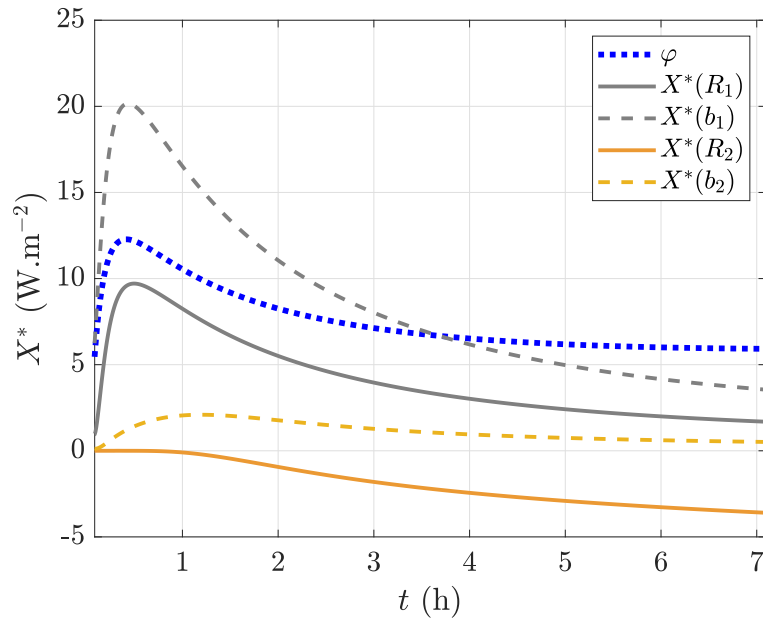
**Table 8.7.:** Hybrid matrix  $V_{cor}$  for the given example ( $\sigma_\varphi = 0.4 \text{ W.m}^{-2}$ ).

	$R_1$	$b_1$	$R_2$	$b_2$
$R_1$	0.13	0.98	-0.31	-0.67
$b_1$		0.06	0.26	0.53
$R_2$			0.02	0.52
$b_2$	sym			0.10

The comments previously made from Fig 8.13 are confirmed by this matrix. Indeed, the correlation coefficient between  $R_1$  and  $b_1$  is close to 1 (0.98) which proves that these two parameters are correlated. Also, parameter  $b_2$  is estimated with a relative uncertainty of 10% whereas it is not very much correlated to any other parameter. This is due to its low reduced sensitivity. The estimation of  $R_2$  is rather accurate given that its relative uncertainty is only 2%.

#### 8.3.2.4. Parameter estimation

Figure 8.14 plots the measurement data  $\varphi$  alongside the model  $\varphi_{mo}$  after estimation of the optimum parameters  $\widehat{\boldsymbol{\beta}}$  (with model  $A_2$ ). The latter are given in Tab 8.8. The



**Figure 8.13.:** Reduced sensitivities of white-box model  $A_2$  for the given example.

reference values given in this table have different origins: measurements in laboratory with the Hot Disk method (for  $R_1$  and  $b_1$ ), manufacturer data (for  $R_2$ ) and standard value from the literature (for  $b_2$ : [202]). The residuals are unsigned (flat) and of rather small magnitude, which is a prerequisite for the parameter estimation to be accurate.

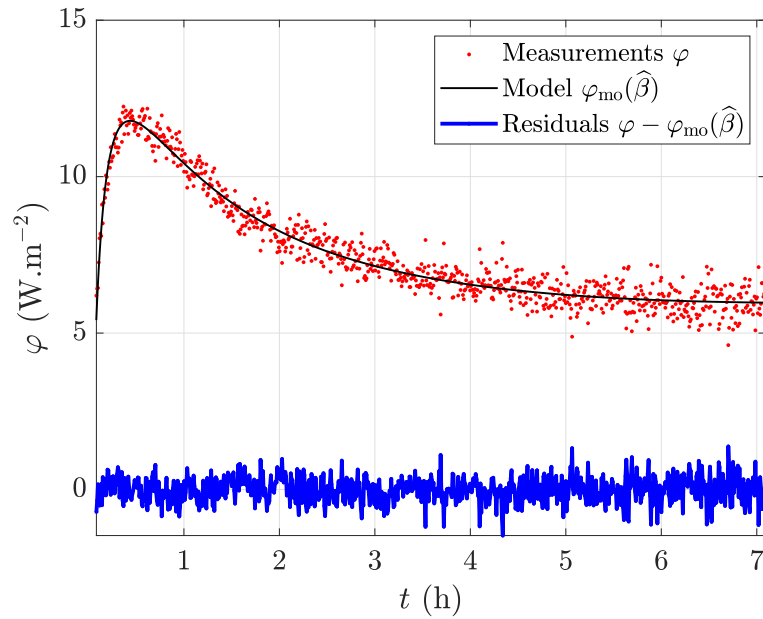
**Table 8.8.:** Estimated parameters  $\hat{\beta}$  with reference values (model  $A_2$ ).

$\hat{\beta}$	Unit	Estimation	Reference	Origin of reference
$R_1$	$\text{m}^2.\text{K}.\text{W}^{-1}$	$0.05 \pm 0.01$	0.06	Hot Disk measurements
$b_1$	$\text{J}.\text{K}^{-1}.\text{m}^{-2}.\text{s}^{-1/2}$	$421 \pm 24$	420	Hot Disk measurements
$R_2$	$\text{m}^2.\text{K}.\text{W}^{-1}$	$3.04 \pm 0.05$	3.12	Manufacturer data
$b_2$	$\text{J}.\text{K}^{-1}.\text{m}^{-2}.\text{s}^{-1/2}$	$35.9 \pm 3.5$	21	Literature

Thus, the proposed inverse method successfully estimated the thermal properties of the insulation system, especially  $R_1$ ,  $b_1$  and  $R_2$ . On this example, the thermal resistance  $R_2$  is only about 5% away from its reference value. In addition, the thermal resistance of the insulation system is estimated at  $3.09 \pm 0.06 \text{ m}^2.\text{K}.\text{W}^{-1}$  which is close to the value measured in steady-state:  $3.15 \text{ m}^2.\text{K}.\text{W}^{-1}$  (see Chap 6). The estimation uncertainties are small but they only take into account the random component of the error.

### 8.3.2.5. Robustness of the method

On the one hand, since the minimization procedure is iterative, the initial parameter vector chosen might have an impact on the estimated values if local minima of the cost function exist. It was checked here that changing the initial conditions (random sampling 10% away from the reference values) do not affect the estimation.



**Figure 8.14.:** Comparison between measurements and model after parameter estimation (model  $A_2$ ).

On the other hand, the duration of the active tests was set to about 8 h. This choice is justified because a longer experiment would not improve the estimation of the thermal resistance. Indeed, Fig 8.15 plots  $\widehat{R}_1 + \widehat{R}_2$  and its uncertainty for several durations of the same experiment (still for model  $A_2$ ). Only the upper limit of the time horizon is modified: the lower one is kept constant equal to 10 min. Indeed, the first points were to be removed because HFM measurements are not accurate at the beginning of the experiment (the heat flux increase is too fast). It was noted that increasing further the lower bound of the time horizon has a little impact on the results.

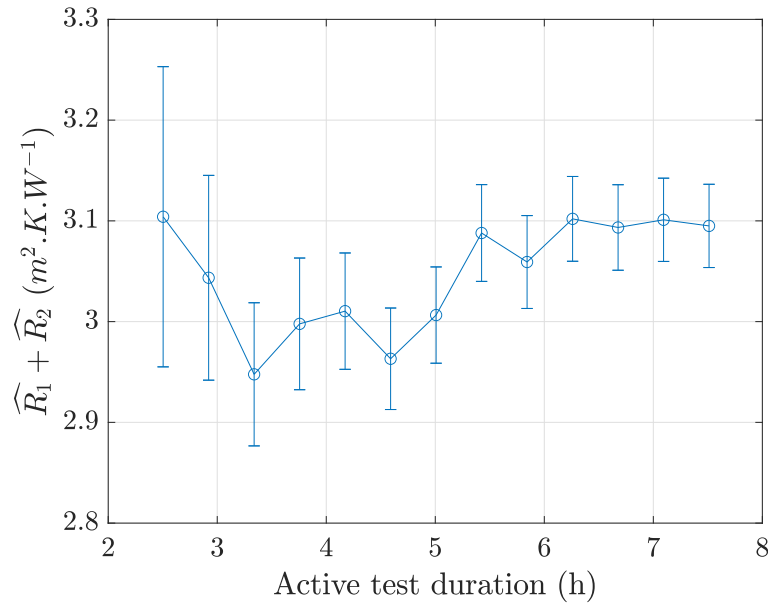
It may be observed on Fig 8.15 that after about 6 h, the estimated thermal resistance is no longer dependent on the duration of the experiment. Also, the estimation uncertainty decreases during the first six hours and then stabilizes. Thus, for this wall, longer experiments are not required.

### 8.3.3. Black-box ARX method

The application of ARX models for the estimation of a wall thermal resistance was presented in section 7.3 of Chap 7.

#### 8.3.3.1. Presentation of the model

By analogy to white-box model  $A_2$  presented in Tab 8.6, we define the ARX model  $A'$ . It uses the same data as its white-box" counterpart and is presented in Tab 8.9. This Single Input Single Output (SISO) model is not able to take into account variations



**Figure 8.15.:** Impact of experiment duration (upper limit of time horizon) on thermal resistance estimation (model A<sub>2</sub>).

in the external surface temperature. As explained in Appendix D.2, MISO models could not estimate the wall thermal resistance for the given experiment.

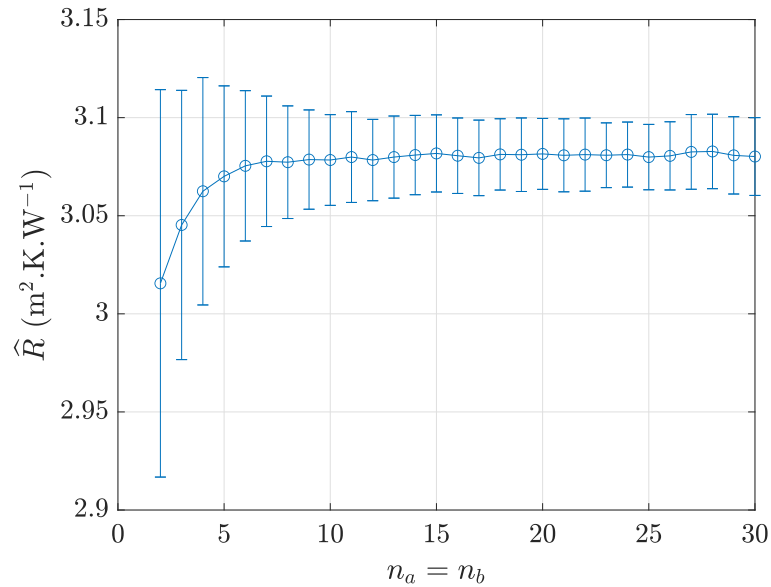
**Table 8.9.:** Presentation of ARX model.

Model	Illustration	Equation	Parameters
A'		$\mathcal{A}(q) \varphi_{si} = \mathcal{B}(q) T_{si}$	$\beta = [a_1 \dots a_{n_a} \ b_0 \dots b_{n_b-1}]$

### 8.3.3.2. Choice of number of parameters

The number of parameters  $n_a$ ,  $n_b$  have to be defined. Fig 8.16 plots the estimated thermal resistance  $\widehat{R}$  as a function of  $n_a$  with  $n_b = n_a$  for model A' and configuration 1. It may be observed that the fewer the parameters, the higher the bias on the estimated value and the higher the estimation uncertainty. To be more specific, above about  $n_a = n_b = 10$ , the estimated resistance and its uncertainty are both independent on the number of parameters. Thus, given that the calculations are almost instantaneous (even for a high number of parameters), setting high values for  $n_a$  and  $n_b$  is a relevant conservative choice. The  $n_a = n_b$  condition was taken to simplify the analysis. It was observed that setting different values for  $n_a$  and  $n_b$  does not reduce the minimum number of parameters required for the estimation to be accurate. Consequently,  $n_a = n_b = 25$  is set for the estimations. The sampling period is 30 s.

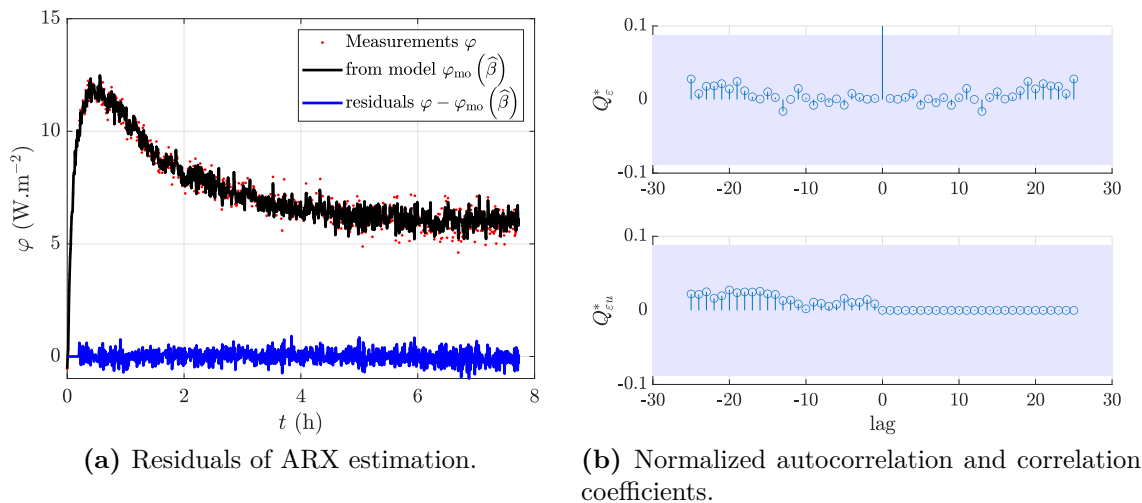




**Figure 8.16.:** Impact of ARX model number of parameters on the estimated thermal resistance (model A'). The sampling period is 30 s.

### 8.3.3.3. Residuals analysis

Figure 8.17a plots the residuals for the present experiment. The model response and measurements are also compared. In addition, the normalized autocorrelation and cross-correlation functions are plotted in Fig 7.20. The 99% confidence region marking statistically insignificant correlations displays as a shaded region along the Y-axis. It may be seen that the residuals pass the validation tests of whiteness.



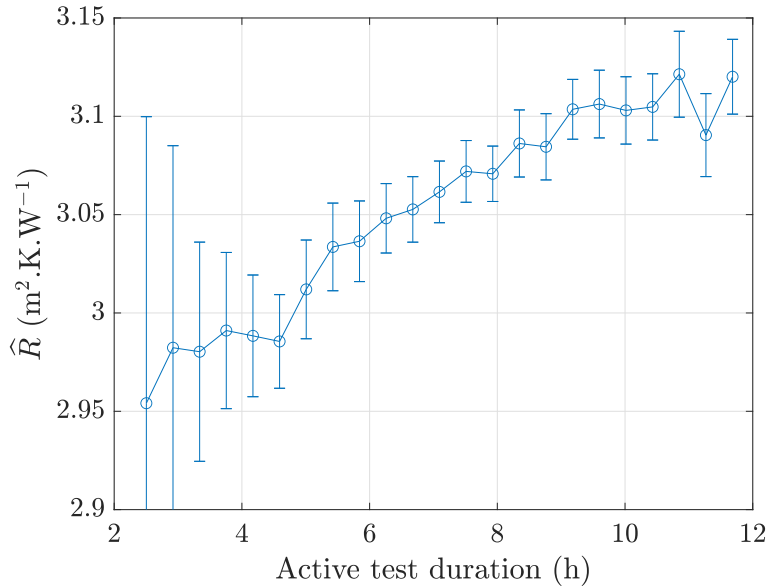
(a) Residuals of ARX estimation.

(b) Normalized autocorrelation and correlation coefficients.

**Figure 8.17.:** Residual analysis with  $n_a = n_b = 25$  and  $n_k = 0$ .

### 8.3.3.4. Impact of time horizon

Figure 8.18 plots the estimated thermal resistance for several durations of the active test. Similarly to Fig 8.15, the upper bound of the time horizon is changed whereas its lower bound is kept constant (10 min). This analysis was performed on a longer active test (about 12 h).



**Figure 8.18.:** Impact of experiment duration on thermal resistance estimation (ARX approach, with model A’).

It is clear that the uncertainty increases as the experiment duration decreases below 5 h. However, unlike with the “white-box” model (Fig 8.15), the estimated resistance keeps increasing slightly with time above 5 h (although the slope flattens so much that  $\hat{R}$  seems to converge after about 10 h). This is because the thermal resistance  $\hat{R}$  estimated by the ARX approach is supposed to be the total resistance of the wall:  $R_1 + R_2 + R_3$ . In theory,  $\hat{R}$  asymptotically reaches this overall resistance after a very long time. This was checked on synthetic data modeling a much longer active test. As mentioned above, a test duration of a few hours (even 12 h) is not enough to probe the load-bearing layer effectively and to estimate its thermal resistance with the proposed active methodology. Therefore,  $\hat{R}$  corresponds here to the resistance of the insulation system.

Finally, it is interesting to point out that for short measurements, the ARX approach gives better results (closer to the real value) than the “white-box” approach. Indeed, after only 2 h, it is able to estimate a thermal resistance rather close to the one of the insulation system, and with a decent uncertainty.

### 8.3.4. Test of the methods on different configurations

To assess the robustness of the white-box and black-box methodologies on the current type of wall, they were tested on the 27 experiments presented in Tab 8.5.

### 8.3.4.1. Constant external conditions

This section presents the results obtained on experiments with a constant external temperature (configurations 1 and 2). The thermal resistance of the insulation system (gypsum + glass wool) was determined using models  $A_2$  (the simplest white-box model) and  $A'$ . The results of the estimations are summarized in Tab 8.10. They are compared to reference values obtained in steady-state (see section 6.3 of Chap 6). The average and standard deviation of the estimated quantities are also given. The measurements, the identified model outputs and the residuals and model  $A_2$  for each test are given in Appendix E.4.

**Table 8.10.:** Thermal resistance estimations for a constant external temperature with two approaches: model  $A_2$  = “white-box”, model  $A'$  = “black-box”.

Config	Exp	Model $A_2$ ( $R_1 + R_2$ )	Model $A'$ ( $R_1 + R_2 + R_3$ )
Reference	Steady -state	$3.15 \pm 0.10$	$3.49 \pm 0.11$
1	1	$3.09 \pm 0.04$	$3.01 \pm 0.03$
	2	$3.05 \pm 0.03$	$3.01 \pm 0.02$
	3	$3.16 \pm 0.03$	$3.07 \pm 0.02$
	4	$3.14 \pm 0.06$	$2.96 \pm 0.03$
	5	$3.07 \pm 0.02$	$3.01 \pm 0.01$
2	6	$3.06 \pm 0.04$	$2.93 \pm 0.02$
	7	$3.16 \pm 0.02$	$3.10 \pm 0.01$
	8	$3.09 \pm 0.02$	$3.04 \pm 0.02$
average		3.10	3.01
standard deviation		0.04	0.06

Several conclusions may be drawn. First, the “white-box” and “black-box” approaches give very similar results. For both of them, the thermal resistance is slightly underestimated but the distance to the reference value of  $R_1 + R_2$  is almost always below 5%. The “white-box” model seems to predict a slightly higher thermal resistance than the ARX model. Thus, both approaches estimate rather well the thermal resistance of the insulation system, although the ARX model was supposed to estimate the global thermal resistance of the wall:  $R_1 + R_2 + R_3$ . As explained above, this is due to the high thermal inertia of the building blocks.

Also, configurations 1 and 2 lead to the same results whereas they have a different initial temperature gradient: 10 and 0 K respectively. This reflects the superimposition theorem: constant temperature differences are canceled out when initial conditions are subtracted. This is one of the main advantages of this active method: only temperature and heat flux relative variations are analyzed. This would allow performing measurements all year long (as long as the external temperature is close to be constant), instead of only in winter like with steady-state methods.

Finally, the methods are repeatable as the dispersion of the results for the eight experiments undertaken is rather small (around 5%). It is also of the same order of magnitude as the estimation uncertainty.

Consequently, in the favorable case when the external temperature is constant, there is no need to use more complex models to estimate the performance of the thermal insulation. Only two measured quantities are required: the internal surface heat flux  $\varphi_{\text{si}}$  and temperature  $T_{\text{si}}$ .

It is not possible to determine the thermal resistance of the concrete layer in this configuration. Indeed, as explained above, during the 8 hours of the experiment, the temperature of the concrete blocks barely increases so this layer cannot be probed efficiently. A very much longer experiment would be required which would not be representative of *in situ* active measurements. This is not considered as an issue in this study: the majority of the wall thermal resistance comes from the insulation system and a characterization of the latter is enough for the assessment of an energy retrofit.

#### 8.3.4.2. Varying external conditions

This section analyzes the impact of variations in the external temperature on the parameter estimation. As mentioned above, ARX MISO models were not able to accurately predict the thermal resistance, so only results obtained with the white-box approach are presented.

Table 8.11 summarizes the estimations of  $R_1 + R_2$  (thermal resistance of the insulation system) in configurations 3 to 6 using models  $A_2$ ,  $AE_{\text{in},2}$  and  $AE_3$ . The measurements, the identified model outputs and the residuals for each experiment and model  $AE_3$  are plotted in Appendix E.4.

First, it may be observed that in configuration 3, estimations with model  $A_2$  have a small bias (maximum 15%). Consequently, for this type of wall, model  $A_2$  is suitable when the external temperature varies with an amplitude up to about 5 K.

Then, it appears that results from model  $A_2$  are significantly biased for some experiments but rather accurate for others. This entirely depends on the behavior of  $T_{\text{air},e}$  before and during the experiment. In every configuration (except number 6), at least four active tests are performed following the pattern reminded in Fig 8.19.

For the first test,  $T_{\text{air},e}$  is around the maximum of its sinusoid. It increases during the second test, is around its minimum during the third one and decreases for the fourth test. These four regimes correspond to the four symbols  $\cap$ ,  $\nearrow$ ,  $\cup$  and  $\searrow$  used in Tab 8.11. For every configuration, model  $A_2$  always over-predicts the resistance when  $T_{\text{air},e}$  is around its maximum, under-predicts it when  $T_{\text{air},e}$  is around its minimum and paradoxically predicts it well when  $T_{\text{air},e}$  varies significantly. These observations are explained by the evolution of the temperature  $T_{\text{in}}$  between the insulation system and the concrete blocks (see Fig 8.19). Indeed, material inertia induce a phase lag of about 6 h between  $T_{\text{air},e}$  and  $T_{\text{in}}$ . Consequently, when  $T_{\text{air},e}$  is rather stable around an extremum,  $T_{\text{in}}$  varies a lot, and vice versa. Thus, inaccurate estimations correspond to situations for which  $T_{\text{in}}$  varies significantly. Model  $A_2$  was indeed based on the assumption of a constant  $T_{\text{in}}$ . For *in situ* applications on this type of wall, it is therefore recommended to start the active test at sunset (when the temperature starts decreasing). This is in accordance with usual guidelines for *in situ*

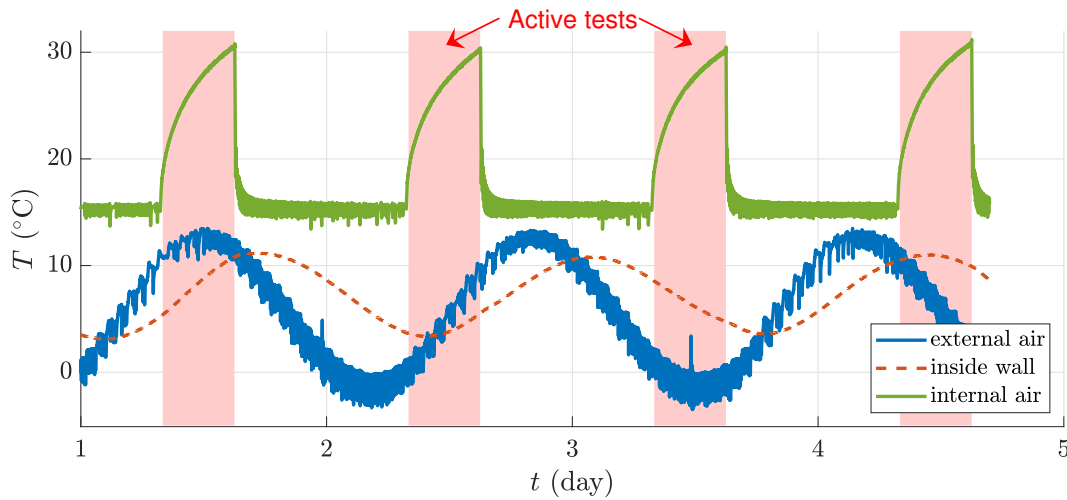
**Table 8.11.:** Estimations of thermal resistance for varying external temperature (cells are filled in gray when the estimated value is more than 10% away from the steady-state reference value). Depending on the experiment,  $T_{\text{air,e}}$  is around a maximum:  $\cap$ , or increasing:  $\nearrow$ , or around a minimum:  $\cup$ , or decreasing:  $\searrow$ .

Config	Exp	$T_{\text{air,e}}$	Model A <sub>2</sub> ( $R_1 + R_2$ )	Model AE <sub>in,2</sub> ( $R_1 + R_2$ )	Model AE <sub>3</sub> ( $R_1 + R_2$ )
Reference	Steady -state	-	$3.15 \pm 0.10$	$3.15 \pm 0.10$	$3.15 \pm 0.10$
3	9	$\cap$	$3.62 \pm 0.07$	$3.01 \pm 0.06$	$2.98 \pm 0.06$
	10	$\nearrow$	$3.20 \pm 0.06$	$3.05 \pm 0.07$	$3.02 \pm 0.07$
	11	$\cup$	$2.81 \pm 0.06$	$2.99 \pm 0.07$	$3.01 \pm 0.07$
	12	$\searrow$	$3.11 \pm 0.05$	$3.02 \pm 0.05$	$3.05 \pm 0.05$
4	13	$\cap$	$4.19 \pm 0.12$	$2.96 \pm 0.07$	$2.90 \pm 0.08$
	14	$\nearrow$	$3.25 \pm 0.07$	$3.05 \pm 0.09$	$3.01 \pm 0.83$
	15	$\cup$	$2.64 \pm 0.04$	$3.16 \pm 0.05$	$3.20 \pm 0.06$
	16	$\searrow$	$3.01 \pm 0.05$	$2.93 \pm 0.04$	$2.95 \pm 0.04$
5	17	$\cap$	$5.84 \pm 0.33$	$3.42 \pm 0.15$	$3.33 \pm 0.15$
	18	$\cap$	$6.09 \pm 0.32$	$3.40 \pm 0.13$	$3.36 \pm 0.13$
	19	$\nearrow$	$3.20 \pm 0.08$	$3.08 \pm 0.10$	$3.06 \pm 0.13$
	20	$\nearrow$	$3.10 \pm 0.07$	$2.96 \pm 0.09$	$2.93 \pm 0.13$
	21	$\cup$	$2.23 \pm 0.04$	$2.95 \pm 0.06$	$2.99 \pm 0.06$
	22	$\cup$	$2.23 \pm 0.04$	$2.95 \pm 0.12$	$2.99 \pm 0.05$
	23	$\searrow$	$3.07 \pm 0.06$	$3.07 \pm 0.05$	$3.08 \pm 0.05$
	24	$\searrow$	$3.08 \pm 0.06$	$3.00 \pm 0.05$	$3.01 \pm 0.05$
6	25	$\cap$	$5.15 \pm 0.24$	$3.02 \pm 0.08$	$2.96 \pm 0.10$
	26	$\nearrow$	$3.40 \pm 0.08$	$2.99 \pm 0.12$	$2.97 \pm 0.14$
	27	$\searrow$	$2.92 \pm 0.08$	$2.95 \pm 0.05$	$2.94 \pm 0.05$
average			$3.48$	3.05	3.04
standard deviation			$1.09$	0.14	0.13

thermal diagnoses of buildings which recommend measurements to be performed by night. The estimation uncertainties are smaller than the spread (standard deviation) between measurements, which confirms that a single experiment might lead to an accurate estimation of the thermal resistance.

Model AE<sub>in,2</sub> was developed to overcome this limitation: instead of considering  $T_{\text{in}}$  constant, this temperature is measured and taken as an input of the model. As shown in Tab 8.11, the thermal resistance is now well estimated for every experiment: results are within the 10% band (relative difference to the reference value obtained in steady-state) and even within the 5% band most of the time. Hence, model AE<sub>in,2</sub> is not limited by variations of the external temperature. However, it requires the implementation of a temperature sensor inside the wall, which is not possible *in situ*.

Model AE<sub>3</sub> is more applicable as it only relies on surface measurements. Nevertheless, it requires a two-step procedure. First,  $R_3$  and  $b_3$  are estimated with an inverse method based on model H<sub>1</sub> and fed with measurements of  $\varphi_{\text{se}}$  and  $T_{\text{se}}$ . The



**Figure 8.19.:** Example of internal and external temperatures for consecutive active tests (configuration 5).

estimated values are  $\widehat{R}_3 = 0.28 \pm 0.01 \text{ m}^2 \cdot \text{K} \cdot \text{W}^{-1}$  and  $\widehat{b}_3 = 706 \pm 8 \text{ J} \cdot \text{K}^{-1} \cdot \text{m}^{-2} \cdot \text{s}^{-1/2}$ . Please refer to Appendix E.2 for more details. In addition, Appendix E.3 shows the impact a bias on  $R_3$  and  $b_3$  has on the estimation of the insulation system thermal resistance. Second, these obtained values are supposed known in model  $\text{AE}_3$  for the estimation of the thermal properties of the insulation system. The results, shown in Tab 8.11, are as good as with model  $\text{AE}_{\text{in},2}$ : the thermal resistance may be estimated regardless of the evolution of  $T_{\text{air},e}$ . The estimated uncertainties are of the same magnitude as the spread between experiments. Finally, it may be noted that model  $\text{AE}_3$  supposes  $R_3$  and  $b_3$  perfectly known. This means that their uncertainty do not contribute to the uncertainty of  $\widehat{R}_1 + \widehat{R}_2$  which is therefore underestimated.

### 8.3.5. Conclusion

The active method for the estimation of a wall thermal resistance was tested on experiments undertaken on the CEREMA setup. The white-box and black-box approaches are compared. When the external temperature is constant, both approaches are able to estimate the thermal resistance of the insulation system. They are based on models  $A_2$  and  $A'$ . These “simple” models do not include any correction term and only need measurements of the internal surface heat flux and temperature for about 6 h. The methods show a good repeatability (5%) and the relative difference to the reference value, obtained from ISO 9869-1 [15], is below 5%. These models cannot estimate the overall thermal resistance of the wall. However, this limitation is not deemed major because the insulation system represents most of the overall thermal resistance (90% here). In addition, in the case of a building retrofit, the application of the method before and after refurbishment could quantify the increase in thermal resistance (because the heavyweight layer is unchanged).

The robustness of the method on this type of wall is assessed by undertaking experiment with unsteady external temperature. Estimations with simple models  $A_2$

and  $A'$  are still rather accurate if the amplitude of the external temperature variations is smaller than 5 K. Above this limit, the simple models (both “white” and “black” boxes) only deliver good results if the active test is performed at moments of the day when the temperature inside the wall is rather constant. Because of material thermal inertia, this corresponds to moment when the variation of the external temperature is maximum.

More complex “white-box” models ( $AE_{in,2}$  and  $AE_3$ ) are developed to overcome the limitations due to a varying external temperature. Indeed, they include an “external correction” term. They lead to accurate estimations of the wall thermal resistance (below 10% difference to the reference value) in every tested configuration. However, model  $AE_{in,2}$  requires a temperature measurement inside the wall, which is hardly applicable *in situ*. It is presented here for a better understanding of the problem. Model  $AE_3$  only relies on surface measurements but requires some *a priori* knowledge about the thermal properties of the load-bearing layer. Though, the later may be derived from external surface measurements with a distinct model (model  $H_1$ ). It may be noted that for lightweight walls (low thermal inertia), this two step procedure might not be required (see results in section 8.4 with SGR experiments for instance).

However, more complex ARX models with several inputs are not able to correctly estimate the thermal resistance with the proposed active procedure when the external temperature is not constant. This is due to the short measurement duration: the studies from the literature which successfully used similar MISO ARX models are all based on much longer datasets (from 6 to 35 consecutive days of measurement).

As a conclusion, for the studied wall, white-box models deliver more accurate and robust estimates than the black-box (ARX) models tested, except for very short measurements (around 2 h) for which the ARX approach is more stable. The models implemented and their applicability are summarized in Tab 8.12.

**Table 8.12.:** Summary of models ( $\checkmark$  = yes,  $x$  = no,  $x\checkmark$  = not true in all configurations).

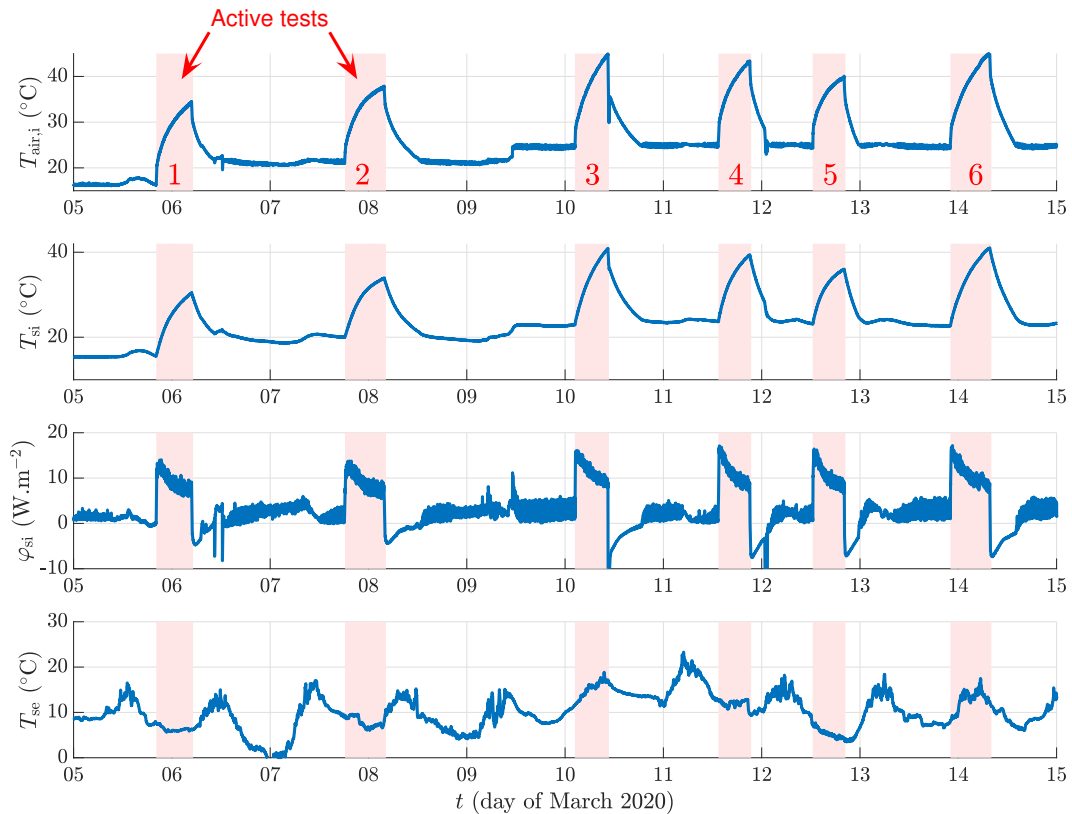
Model	$A_2$	$AE_{in,2}$	$AE_3+H_1$	$A'$
White-box (W) or Black-box (B)	W	W	W	B
only surface measurements	$\checkmark$	$x$	$\checkmark$	$\checkmark$
only indoor measurements	$\checkmark$	$x$	$x$	$\checkmark$
robust to $T_e$ variations in $[0, 5]$ K	$\checkmark$	$\checkmark$	$\checkmark$	$\checkmark$
robust to $T_e$ variations in $[5, 15]$ K	$x\checkmark$	$\checkmark$	$\checkmark$	$x\checkmark$
minimum experiment duration (h)	$\approx 6$	$\approx 6$	$\approx 6$	$\approx 2$

## 8.4. Application to SGR experiments

For a further validation of the active method developed, *in situ* measurements were performed in the SGR test cell (presented in section 4.5 of Chap 4). The results obtained on the CEREMA experimental campaign showed that the ARX approach is only able to estimate a wall thermal resistance if the external temperature is constant or close to constant. This is not the case for the SGR experiments for which the external temperature is subjected to natural variations, so only the white-box approach is used in this section.

### 8.4.1. All active measurements

Figure 8.20 plots the evolution of north wall surface temperatures and heat flux during the six active tests carried out. Indeed, the internal air temperature is kept constant between the active tests. The high noise magnitude on the heat flux between each test is due to the temperature regulation system.



**Figure 8.20.:** Presentation of active measurements for the SGR experimental campaign. The active tests are highlighted in red.

The internal surface temperature rises by 14 to 18 K depending on the active test. It is not quite constant between the tests. It is clear that the external surface temperature  $T_{se}$  is not constant during the measurement campaign. Experiments 3 and 6 were performed during the day (the active test started at 8 a.m) whereas

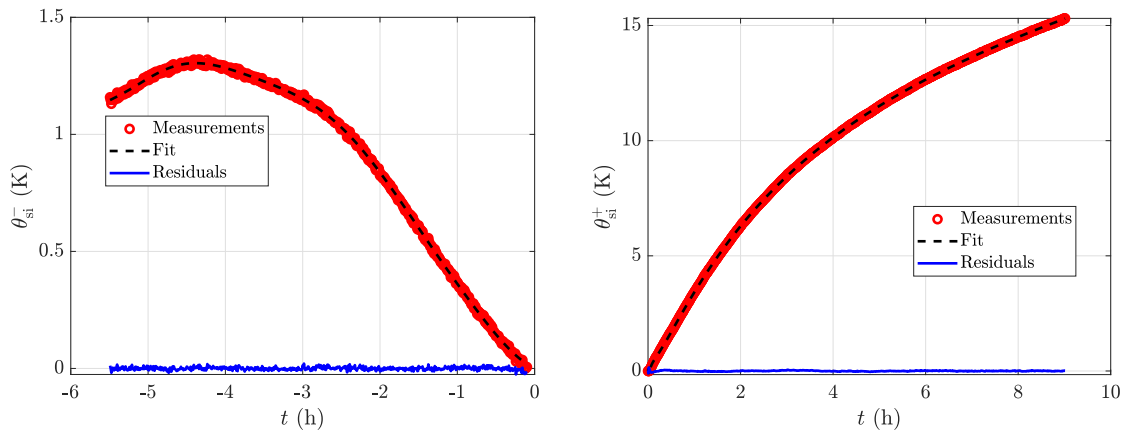


the other four were performed by night: the heating started between 9 and 10 p.m. (after the sunset).

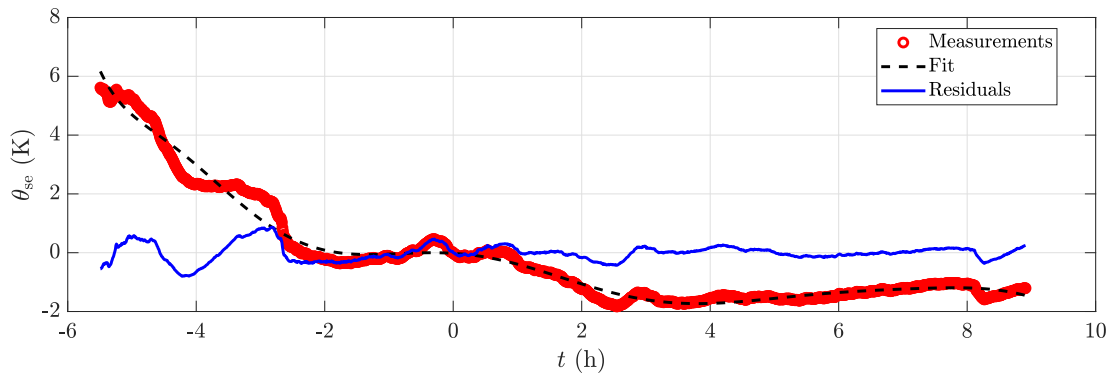
## 8.4.2. White-box method

### 8.4.2.1. Analytical expressions of the inputs

A function of known Laplace transform is fitted on each model input:  $\theta_{si}^-$ ,  $\theta_{si}^+$  and  $\theta_{se}$ . The measurements and the fitted functions are compared in Fig 8.21 (a polynomial function in  $1/k$  for  $\theta_{si}^+$  and a polynomial function for the other two). The active test starts at  $t = 0$ . It may be seen that the residuals on  $\theta_{si}^-$  and  $\theta_{si}^+$  are small. However, the fit on  $\theta_{se}$  is less accurate given that the curve is much less “smooth”. Increasing too much the polynomial order would make the De Hoog algorithm diverge. However, because this temperature is located on the external side of the wall whereas the heat flux is measured on the internal side, the small variations in  $\theta_{se}$  are filtered out by the wall and do not impact  $\varphi_{si}$ . As a consequence, it is not a problem if the function fitted on  $\theta_{se}$  does not reproduced the exact variations of the measurements as long as the global tendency is correct (decreasing temperature on this example).



(a) Function fit on  $\theta_{si}^-$  (polynomial of order 10). (b) Function fit on  $\theta_{si}^+$  (polynomial in  $1/k$  of order 7).

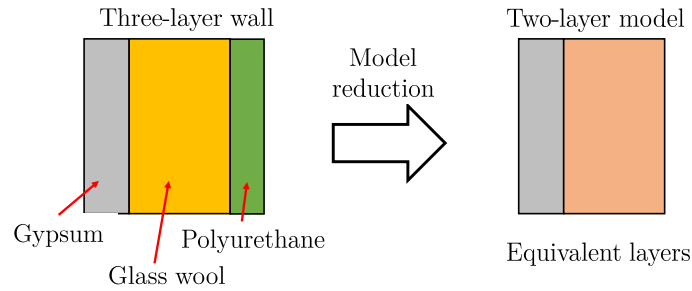


(c) Function fit on  $\theta_{se}$  (polynomial of order 10).

**Figure 8.21.:** Function fitted on model inputs.

### 8.4.2.2. Direct model definition

Several models were compared to assess the impact of internal and external correction terms on the parameter estimation. They all have two layers: the first one models the gypsum board whereas the second one models the glass wool and the polyurethane layers. Given that these two insulating materials have rather similar thermal properties, they are modeled as a single layer which reduced the number of unknown parameters. This model reduction step is illustrated in Fig 8.22.



**Figure 8.22.:** Illustration of model reduction: the three-layer wall is modeled with a two-layer model.

The models tested follow the nomenclature proposed in Tab 8.3:

**Model  $A_2$**  has no correction term.

**Model  $AI_2$**  has an internal correction only.

**Model  $AE_2$**  has an external correction only.

**Model  $AIE_2$**  has both internal and external corrections.

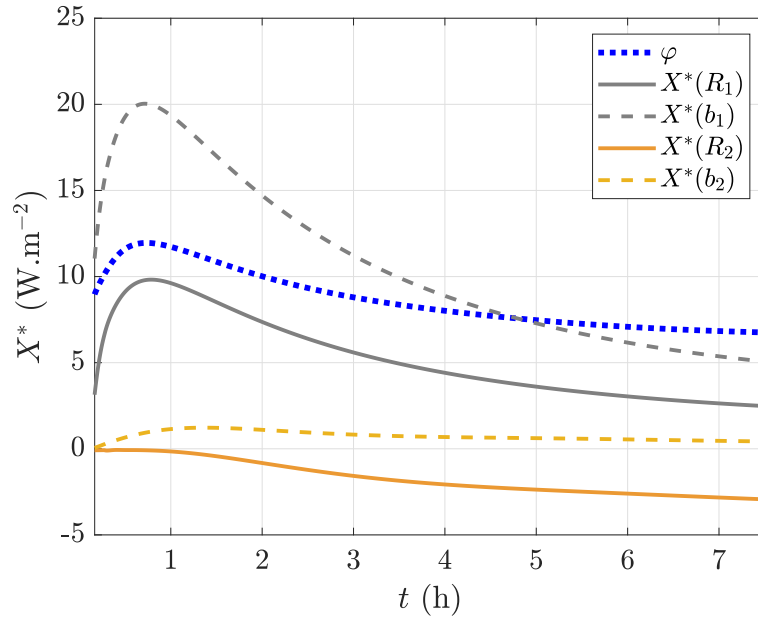
There is no need for a two-step procedure on this type of lightweight wall (models only have two layers). In later sections, the example of Experiment 1 (see Fig 8.20) with model  $AIE_2$  is used to illustrate the white-box method.

### 8.4.2.3. Sensitivity analysis and estimation of uncertainties

The parameters reduced sensitivity coefficients for the example of the first experiment are plotted in Fig 8.23. The sensitivity matrix is calculated with  $\beta = \hat{\beta}$  the optimum vector after parameter estimation (see Tab 8.14 in next section). The corresponding  $V_{\text{cor}}$  matrix is given in Tab 8.13. It was calculated with  $\sigma = 0.4 \text{ W.m}^{-2}$ . The conclusions drawn from these information are identical to the ones presented in section 8.3.2.3 for the CEREMA measurements:

- Parameters  $R_1$  and  $b_1$  have a high reduced sensitivity but are correlated.
- Parameter  $b_2$  has a small sensitivity.
- Parameter  $R_2$  has a non-negligible reduced sensitivity and is not correlated to any other parameter.

The parameter of interest,  $R_2$ , is estimated with a 2% uncertainty according to the  $V_{\text{cor}}$  matrix. It may be reminded that this uncertainty is the minimum value one could expect as it does not take into account a possible bias in the model.



**Figure 8.23.:** Reduced sensitivities of model  $A_2$  (Experiment 1).

**Table 8.13.:** Hybrid matrix  $V_{\text{cor}}$  ( $\sigma = 0.4 \text{ W.m}^{-2}$ ).

	$R_1$	$b_1$	$R_2$	$b_2$
$R_1$	0.15	-0.99	-0.59	-0.84
$b_1$		0.07	0.55	0.77
$R_2$			0.02	0.77
$b_2$				0.23

#### 8.4.2.4. Parameter estimation

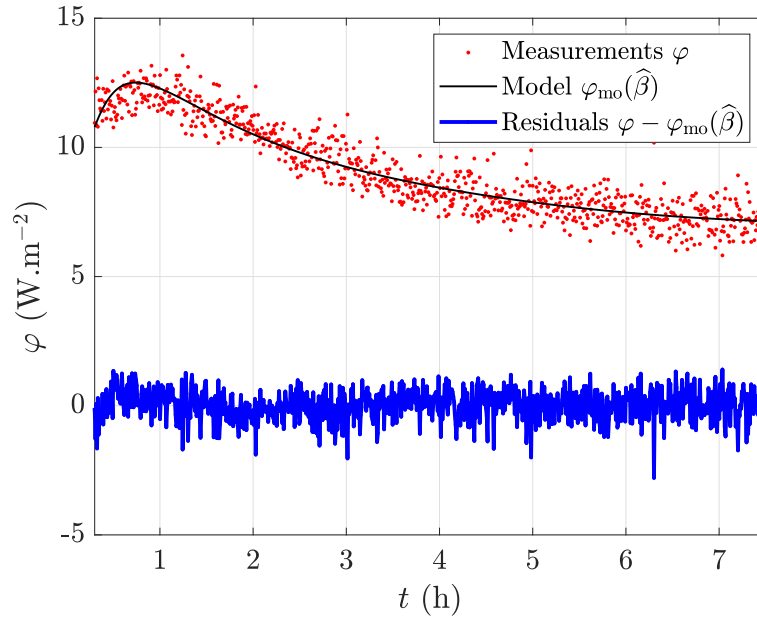
The measurements of Experiment 1 are compared to the model after estimation of the parameters in Fig 8.24. The estimated parameters are gathered in Tab 8.14. The estimated parameters are close to the references values. The latter comes from: measurements in laboratory with the Hot Disk method (for  $R_1$  and  $b_1$ ), manufacturer data (for  $R_2$ ) and standard value from the literature (for  $b_2$ : [202]). The insulation layer thermal resistance is slightly underestimated: 4.67 instead of 5.15  $\text{m}^2.\text{K.W}^{-1}$  (9% relative difference).

The overall thermal resistance  $R = R_1 + R_2$  is estimated at  $4.82 \pm 0.11 \text{ m}^2.\text{K.W}^{-1}$  which is close to the result of steady-state measurements ( $5.25 \text{ m}^2.\text{K.W}^{-1}$ , see Chap 6).

#### 8.4.2.5. Robustness of the method

To assess the relevance of the estimated parameters, it was checked that:

- The estimation is independent from the initial parameter vector. The initial parameters were randomly sampled 10% away from their reference values.



**Figure 8.24.:** Comparison between measurements and model after parameter estimation.

**Table 8.14.:** Estimated parameters  $\hat{\beta}$  with reference values.

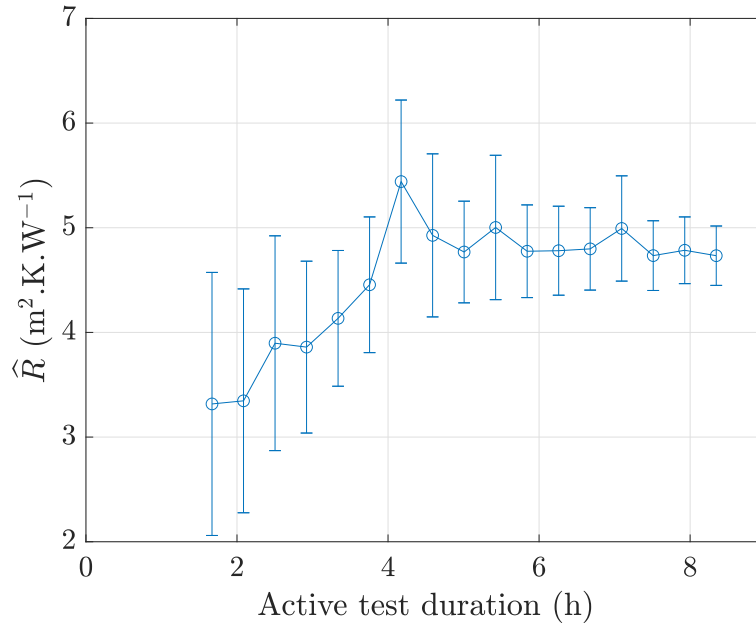
$\hat{\beta}$	Unit	Estimation	Reference	Origin of reference
$R_1$	$\text{m}^2.\text{K}.\text{W}^{-1}$	$0.05 \pm 0.01$	0.06	Hot Disk measurements
$b_1$	$\text{J}.\text{K}^{-1}.\text{m}^{-2}.\text{s}^{-1/2}$	$448 \pm 28$	420	Hot Disk measurements
$R_2$	$\text{m}^2.\text{K}.\text{W}^{-1}$	$4.77 \pm 0.10$	5.15	Manufacturer data
$b_2$	$\text{J}.\text{K}^{-1}.\text{m}^{-2}.\text{s}^{-1/2}$	$25.1 \pm 5.1$	21	Literature

- The estimation is independent of the time horizon. The upper bound of the horizon used in the inversion was varied from 2 to 8 h. The lower bound was kept constant equal to 20 min. As seen in Fig 8.25, the estimated thermal resistance  $\hat{R} = \hat{R}_1 + \hat{R}_2$  becomes independent of the time horizon after about 5 h of heating.

### 8.4.3. Test of the method on different configurations

The estimated wall thermal resistance for each experiment and each model are summarized in Fig 8.26 and Tab 8.15. The measurements, the model output and the residuals for each experiment are presented in Appendix E.5. Without correction, the estimation is highly biased: night-time measurements under-predict  $R$  whereas day-time measurements over-predict it. With the implementation of the corrections terms, and especially the external one, this bias is significantly reduced: the estimations are less than 10% away from the results of steady-state measurements.

Figure 8.27 plots the contribution of each term (A, I and E) in the calculation of the output of model AIE<sub>2</sub>. Experiments 1 and 3 are taken as examples.



**Figure 8.25.:** Impact of experiment duration (upper limit of time horizon) on thermal resistance estimation.

**Table 8.15.:** Summary of estimated wall thermal resistances (cells are filled in light gray when the estimated value is more than 10% away from the steady-state reference value, and in dark gray for 20%).

Expe	A <sub>2</sub>	AI <sub>2</sub>	AE <sub>2</sub>	AIE <sub>2</sub>
Ref	5.25 ± 0.15	5.25 ± 0.15	5.25 ± 0.15	5.25 ± 0.15
1	3.37 ± 0.08	4.38 ± 0.15	3.61 ± 0.10	4.82 ± 0.27
2	3.83 ± 0.09	4.04 ± 0.27	4.72 ± 0.20	5.26 ± 0.26
3	8.95 ± 0.62	7.66 ± 0.42	5.53 ± 0.26	4.70 ± 0.23
4	4.26 ± 0.14	4.72 ± 0.26	4.71 ± 0.37	4.68 ± 0.36
5	2.91 ± 0.07	3.40 ± 0.15	4.48 ± 0.28	4.76 ± 0.30
6	8.28 ± 0.56	7.60 ± 0.34	4.83 ± 0.26	5.02 ± 0.39

For Experiment 1,  $T_{\text{si}}^-$  increases and decreases (see Fig 8.20) which results in a positive internal correction term. In addition,  $T_{\text{se}}$  decreases before the test and is rather constant during it: the external correction term is positive of small magnitude. In the end, the heat flux predicted with corrections is higher than without any correction.

It is the other way around for Experiment 3:  $T_{\text{si}}^-$  slightly decreases and increases whereas  $T_{\text{se}}$  increases significantly. As a consequence, the internal correction term is negative of small amplitude and the external one is negative as well but with a rather high amplitude. The corrected heat flux is smaller than the non-corrected one.

Thus, depending on the experiment, the internal and external correction terms might be either useless or necessary for the model to be unbiased. It may be reminded that the smaller the correction terms, the smaller the estimation uncertainties. The

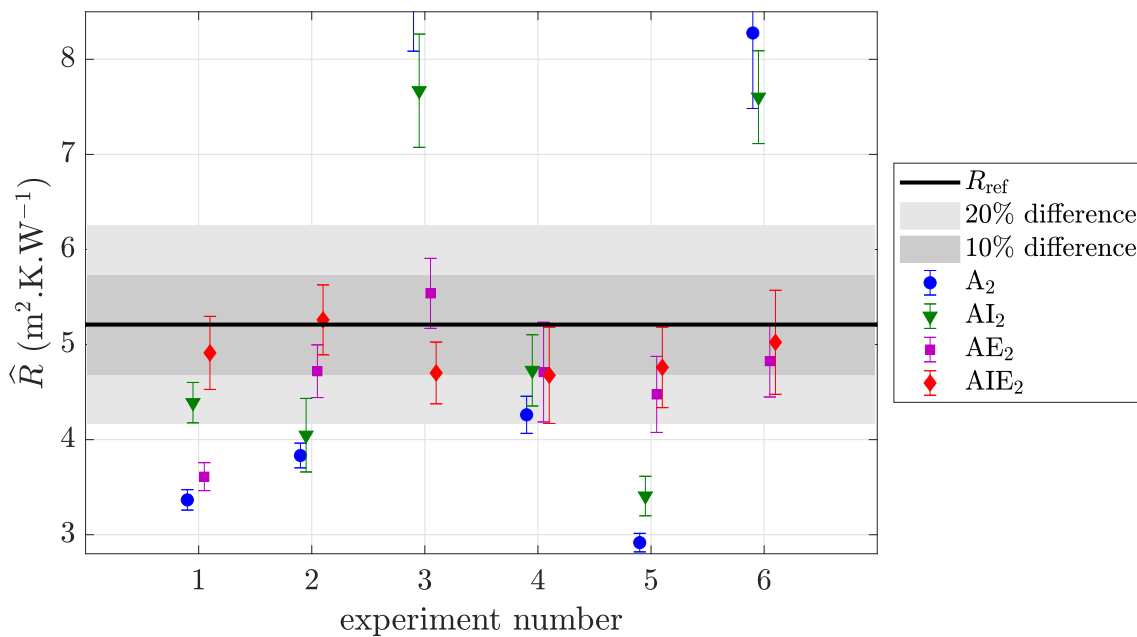


Figure 8.26.: Summary of wall thermal resistance estimations for every model.

operator should therefore try to ensure that the internal temperature before the active test and the external temperature before and during the test are as constant as possible.

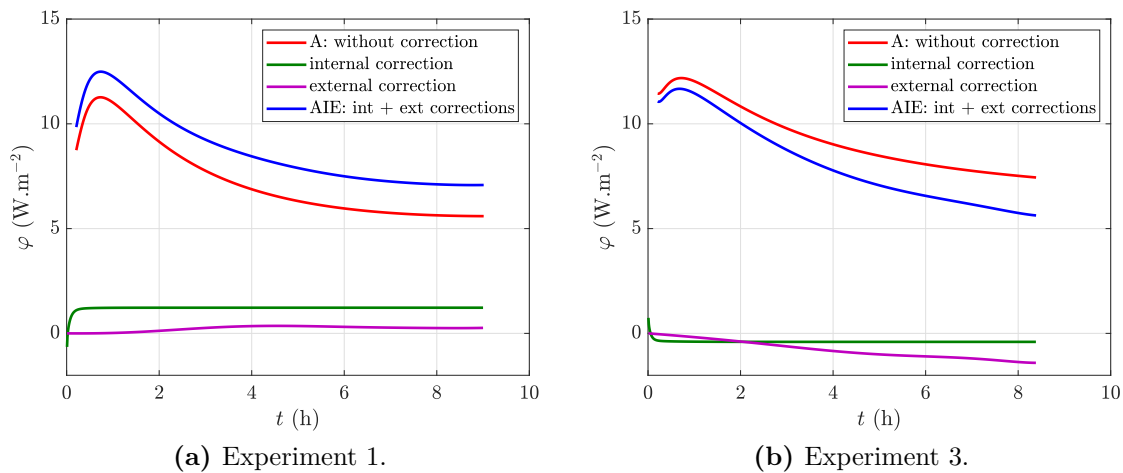


Figure 8.27.: Contribution of each term in the calculation of  $\varphi_{m0}$ .

#### 8.4.4. Conclusion

The inverse method with a white-box model successfully estimated the thermal resistance of the lightweight wall of the SGR experiment. Six *in situ* active tests were carried out: two during the day and the other four during the night. Two-layer direct models are used: the glass wool and the polyurethane layers are modeled as a single equivalent slab (they have similar thermal properties).

The simple model  $A_2$ , which only uses measurements on the internal surface, was not able to estimate the wall thermal resistance. Indeed, because this model supposes that the external surface temperature remains constant before and during the active test, it is biased when this condition is not met. Unlike the CEREMA wall, there is no heavyweight layer to dampen the weather variations. Day-time measurements overestimate the thermal resistance by about 75% whereas night-time measurements underestimate it by up to 40%. The inclusion of an external correction term (model  $AE_2$ ) gives much better results. However, the estimation is still biased if the internal surface temperature is not constant before the active test, as in Experiment 1. If so, the internal correction term is required. In the end, the estimations with model  $AIE_2$  are no more than 10% away from the reference value measured in steady-state. This proves the robustness of the method to unsteady weather conditions and validate its applicability *in situ* on lightweight highly insulated walls (thermal resistance above  $5 \text{ m}^2 \cdot \text{K} \cdot \text{W}^{-1}$ ).

## 8.5. Conclusion

This chapter proposed a rapid active method for the *in situ* measurement of the thermal resistance of a homogeneous building wall. It consists in heating the indoor air for a few hours and to apply inverse methods to measured surface heat fluxes and temperatures. This thermal load was chosen for its ease of implementation and its capability to perform a rather uniform heating of the wall. Thanks to a thorough sensitivity analysis based on synthetic measurements, it was found that Step-heating was more suitable than Square-heating to estimate a wall thermal resistance. Only the heating power has to be set *a priori*: the time horizon to use for the analysis may be set *a posteriori*.

Two different types of modeling are compared: “white-box” models and ARX “black-box” models. The white-box approach is based on a 1D direct model derived from the thermal quadrupole formalism. The derivation of a reduced model is necessary for the thermal resistance of the wall to be estimable. The most important model reduction step consists in measuring both the internal surface temperature and heat flux: this removes the heat transfer coefficient from the model parameters. The internal surface heat flux is the model output whereas the surface temperature are the inputs. The direct model may include two correction terms. The “internal correction” compensates for the disturbance due to a non-constant internal surface temperature before the active test. The “external correction” is necessary when the variations in the external surface temperature are not negligible, which corresponds to most *in situ* situations. There is not one single model that is better than any other in all configurations. The most suited one depends on the studied wall as well as the weather conditions. If no prior information on the internal wall structure is available, one could also imagine testing several predefined models until one works well (assessed by an analysis of sensitivities and residuals). ARX methods are an interesting alternative as they are simpler to use and more robust than white-box methods in some cases (especially for short measurements). However, they cannot include correction terms.

The active method was tested on the CEREMA and SGR experimental campaigns. The first one studies a heavy wall with an internal insulation system (representative of about 70% of French buildings) inside a climate chamber whereas the second one studies a lightweight wall *in situ*. The active tests typically last 8 hours (but 5 h is usually enough to obtain good results) during which the indoor air temperature rises by about 15 K.

A heavy wall has the advantage of dampening the external temperature variations. Therefore, a model without correction term (white-box or ARX) might be sufficient to estimate the thermal resistance of the internal insulation system if the external temperature does not vary too much (less than about 5 K). However, if it does vary significantly, a two step procedure is necessary because a direct estimation of all the layers is not possible (the problem is too ill-posed). First, the thermal properties of the heavy layer are estimated with a specific model from external surface heat flux and temperature measurements. Second, the thermal resistance of the insulation system is estimated thanks to a model with external correction



where the properties of the heavy layer are supposed known. On the contrary, the properties of a lightweight wall may be estimated in a single inversion using a model with correction terms. However, a model without correction terms is not applicable because the sensitivity to weather variations is higher than for a heavy-weight wall.

Table 8.16 summarizes the active method (hypotheses, equipment needed, pros and cons). The main limitation of this method is that it is local. Indeed, it is based on contact measurements made on one specific location of the wall. In addition, it is more complex than steady-state methods which reduces its applicability at large scales. Chapter 9 presents a generalization of this method to non-homogeneous walls and thermal bridges.

**Table 8.16.:** Summary of active homogeneous wall characterization method.

Hypotheses	Equipment	Comments
<ul style="list-style-type: none"> <li>• 1D heat transfers</li> <li>• material properties independent of temperature</li> </ul>	<ul style="list-style-type: none"> <li>• temperature sensors</li> <li>• heat flux meters</li> <li>• acquisition system</li> <li>• heaters</li> </ul>	<p>Pros</p> <ul style="list-style-type: none"> <li>• fast (4 to 6 hours)</li> <li>• <math>h</math> and <math>T_{op}</math> are not required</li> <li>• robust to varying external conditions (but influence of solar heat flux not investigated)</li> </ul> <p>Cons</p> <ul style="list-style-type: none"> <li>• only local measurements</li> <li>• more complex post-processing than steady-state methods</li> </ul>

# 9. Active characterization of a non-homogeneous wall

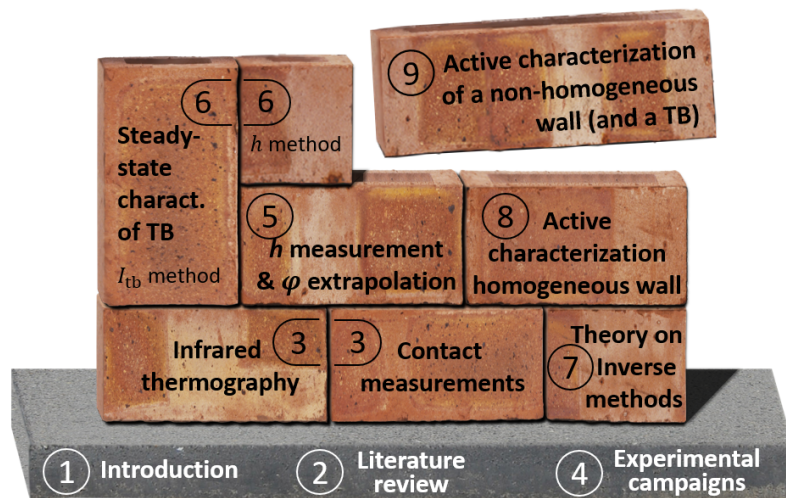


Figure 9.1.: Illustration of thesis plan.

This chapter presents a generalization of the active method for the characterization of a homogeneous wall presented in Chapter 8. Thanks to the quantification of the total heat transfer coefficient combined with infrared thermography, the temperature and heat flux fields on the surface of a non-homogeneous wall may be measured. These measurements are fed to an inverse method to estimate the wall equivalent thermal resistance. By calculating the local equivalent resistance of a thermal bridge, this method also enables to estimate its transmission coefficient  $\psi$  or  $\chi$ . The content of this chapter are presented in [196].

Section 9.1 introduces the methodology and its optimization thanks to a theoretical study. Sections 9.2 and 9.3 present the results obtained during the CEREMA and SGR experimental campaigns, respectively. A conclusion is drawn in section 9.4.

## Nomenclature

### Acronyms

HFM	Heat Flux Meter
IRT	InfraRed Thermography
ROI	Region Of Interest
SA	Sound Area
TB	Thermal bridge

### Greek Symbols

$\beta$	parameter vector	
$\varepsilon$	emissivity	-
$\omega$	pulsation	rad.s <sup>-1</sup>
$\sigma$	noise standard deviation	
$\tau$	thermal load characteristic time	s
$\varphi$	heat flux density	W.m <sup>-2</sup>
$\chi$	point thermal transmittance	W.K <sup>-1</sup>
$\psi$	linear thermal transmittance	W.m <sup>-1</sup> .K <sup>-1</sup>

### Roman Symbols

$A_T$	thermal load amplitude	K
$b$	thermal effusivity	J.K <sup>-1</sup> .m <sup>-2</sup> .s <sup>-1/2</sup>
$h$	total heat transfer coefficient	W.m <sup>-2</sup> .K <sup>-1</sup>
$L_{tb}$	linear thermal bridge width	m
$R$	thermal resistance	m <sup>2</sup> .K.W <sup>-1</sup>
$T$	temperature	K
$t$	time	s
$u$	uncertainty	
$U$	thermal transmittance	W.m <sup>-2</sup> .K <sup>-1</sup>
$V_{cor}$	hybrid matrix	

### Superscripts

$\wedge$	estimated value
-	space average
1D	sound area
tb	thermal bridge

### Subscripts

1D	sound area
e	external
i	external
in	wall internal interface
mo	model
s	surface
tb	thermal bridge

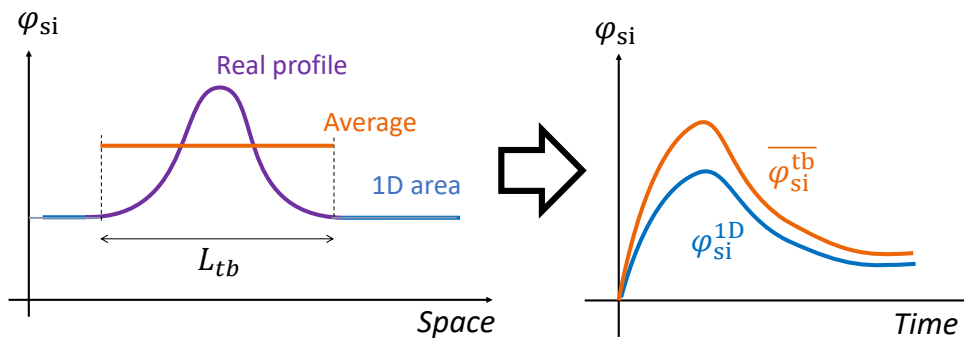
## 9.1. Presentation of the method

The method is presented here on the example of a wall with a linear thermal bridge. Yet, it is also applicable to a point thermal bridge and more generally to any non-homogeneous wall having at least one sound area (where heat transfers are 1D).

### 9.1.1. General method

#### 9.1.1.1. Homogenization for model reduction

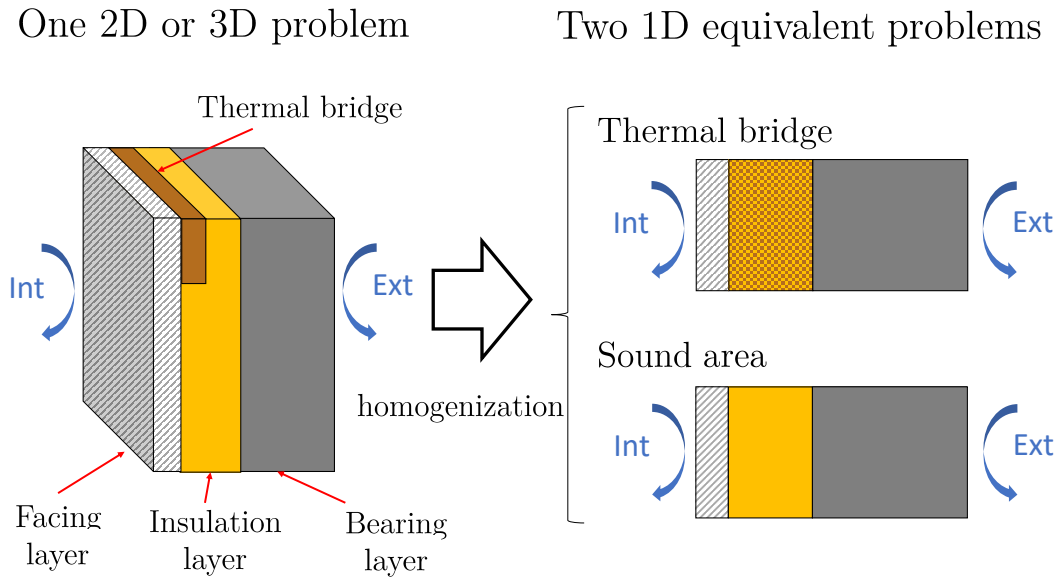
As seen in previous chapters, inverse methods require the direct model to be adapted to the problem and the parameter(s) of interest. There is a balance between accuracy and complexity to be found. In the case of a non-homogeneous wall, some assumptions have to be made to reduce the complexity of the modeling. Basically, instead of working with a detailed 2D map of the wall surface heat losses, the proposed methodology only uses the averaged temperature and heat flux over the surface. As shown in Fig 9.2, the heat flux profile on a thermal bridge is averaged over its influence area ( $L_{tb}$  for a linear thermal bridge) so that only two distinct regions are treated: thermal bridge area (TB), and sound area (1D). The same approach is applied to the surface temperature.



**Figure 9.2.:** Illustration of homogenization of surface heat flux.

This space-averaging allows turning one 2D or 3D thermal problem into two 1D problems (see Fig 9.3). The region influenced by the thermal bridge is then treated exactly like a 1D multi-layer wall with equivalent thermal properties. Indeed, as seen in Chap 2, several authors proved that a thermal bridge can be modeled by an equivalent homogeneous multi-layer wall having the same thermal behavior (see Martin *et al.* [81] and Quinten *et al.* [89] for instance).

First, this homogenization has the advantage of considerably reducing the modeling complexity: 1D problems can easily be implemented (with the thermal quadrupole



**Figure 9.3.:** Illustration of the homogenization procedure on a three-layer wall: it turns one 2D or 3D thermal problem into two 1D problems.

formalism for instance). No complex finite element or volume modeling is required. Second, this reduces the number of unknown parameters in the model and therefore makes the inverse problem less ill-posed. Third, the method can be applied to many different thermal bridge geometries. No *a priori* knowledge of the wall internal design is required (thermal bridge size, depth, shape...).

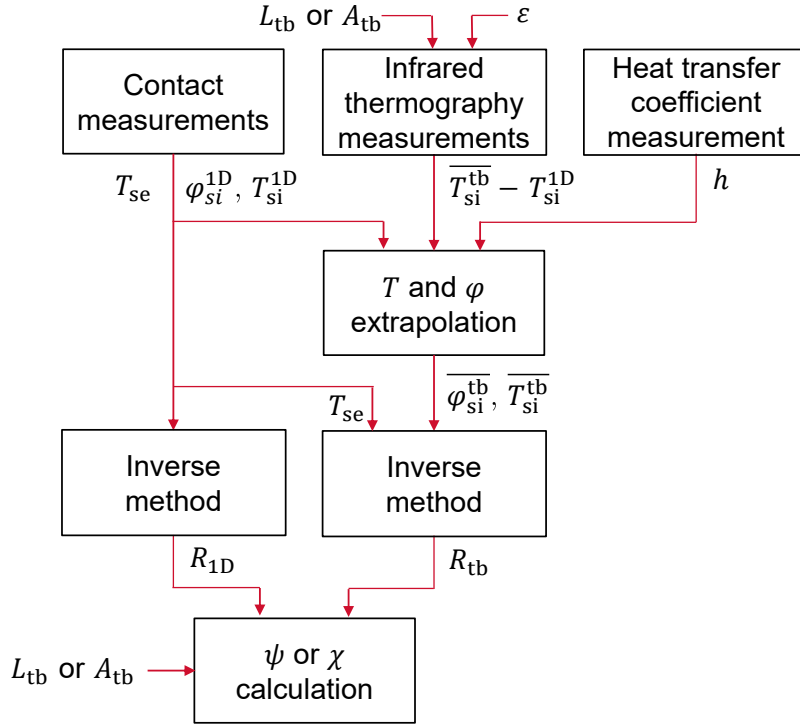
The choice of the thermal bridge influence area is important. If it is too small, only a fraction of the additional heat losses is taken into account. If it is too large, the additional losses become negligible in front of the 1D-losses and the thermal bridge area cannot be distinguished from the sound area.

### 9.1.1.2. General active method for the estimation of $\psi$ and $\chi$ coefficients

The active method presented here is a generalization of the active method based on an inverse technique presented in Chap 8. The white-box approach was chosen for its robustness and adaptability. It relies on simultaneous measurements of the wall surface temperatures  $T_{si}$ , and potentially  $T_{se}$ , as well as the heat flux  $\varphi_{si}$  using contact sensors (thermocouples and heat flux meter). Thanks to the homogenization procedure mentioned above, this technique which was originally designed for the characterization of a homogeneous wall, may be applied to a non-homogeneous wall.

The complete methodology to estimate a thermal bridge transmission coefficient is summarized in Fig 9.4.

As a first step, the temperature and heat flux fields on the surface of the thermal bridge must be measured. Contact sensors are not applicable here since heat transfers are not 1D. In addition, using an array of many sensors to measure the surface temperature and heat flux fields would be very intrusive as well as time consuming.



**Figure 9.4.:** Flow chart of the active method for the characterization of a thermal bridge.

Instead,  $\overline{T_{si}^{tb}}$  and  $\overline{\varphi_{si}^{tb}}$  are extrapolated from their counterparts  $T_{si}^{1D}$  and  $\varphi_{si}^{1D}$  measured with contact sensors on a nearby sound area (see Chap 5):

$$\overline{\varphi_{si}^{tb}} = \varphi_{si}^{1D} + h \times (\overline{T_{si}^{tb}} - T_{si}^{1D}) \quad (9.1)$$

with  $\overline{\varphi_{si}^{tb}}$  and  $\overline{T_{si}^{tb}}$  the mean (space average) heat flux and temperature on the surface of the considered thermal bridge. The extrapolation is performed thanks to infrared thermography measurements (from the temperature difference  $\overline{T_{si}^{tb}} - T_{si}^{1D}$ ) and quantification of the total heat transfer coefficient  $h$  using a “ $h$ -meter”.

As presented in details in Chap 3), the wall emissivity  $\varepsilon$  is needed to convert apparent temperature differences  $\Delta T^{\text{app}}$  to true temperature differences  $\Delta T$ . Assuming temperature differences are small:

$$\Delta T = \frac{\Delta T^{\text{app}}}{\varepsilon} \quad (9.2)$$

In this thesis, the wall surface emissivity was measured in laboratory (see AppendixA.1). Let us remind that with IRT measurements, an error on the emissivity might lead to a significant error on the absolute true temperature. Yet, temperatures differences are less sensitive to the emissivity value. Given that most building

materials have a high emissivity in the infrared spectrum (between 0.9 and 0.95), the error made on the measurement of true temperature differences due to incorrect knowledge of  $\varepsilon$  is small. Thus, the value of the emissivity may be obtained from tabulated default values.

The thermal bridge surface temperature and heat flux are averaged over its area of influence. Then, the sound area thermal resistance  $R_{1D}$  and the thermal bridge equivalent resistance  $R_{tb}$  are estimated with an inverse method. Finally, the thermal bridge transmittance  $\psi$  is worked out from these two resistances through the corresponding transmittances ( $U_{tb}$  and  $U_{1D}$ ):

$$\psi = L_{tb}(U_{tb} - U_{1D}) \quad (9.3)$$

where

$$U_{tb} = \frac{1}{R_{si} + R_{tb} + R_{se}} \quad (9.4)$$

$$U_{1D} = \frac{1}{R_{si} + R_{1D} + R_{se}} \quad (9.5)$$

with  $R_{si} = 0.13$  and  $R_{se} = 25 \text{ m}^2 \cdot \text{K} \cdot \text{W}^{-1}$  from standards such as ISO 6946 [99]. The estimation uncertainty  $u(\varphi)$  of the thermal bridge transmission coefficient is propagated from estimation uncertainties on  $R_{tb}$  and  $R_{1D}$  [158]:

$$u(\varphi) = \sqrt{\left(\frac{\partial \psi}{\partial L_{tb}} u(L_{tb})\right)^2 + \left(\frac{\partial \psi}{\partial R_{tb}} u(R_{tb})\right)^2 + \left(\frac{\partial \psi}{\partial R_{1D}} u(R_{1D})\right)^2} \quad (9.6)$$

The next section presents a theoretical study useful to determine the best way to estimate the wall thermal properties.

## 9.1.2. Theoretical study: Two-step and Single-step approaches

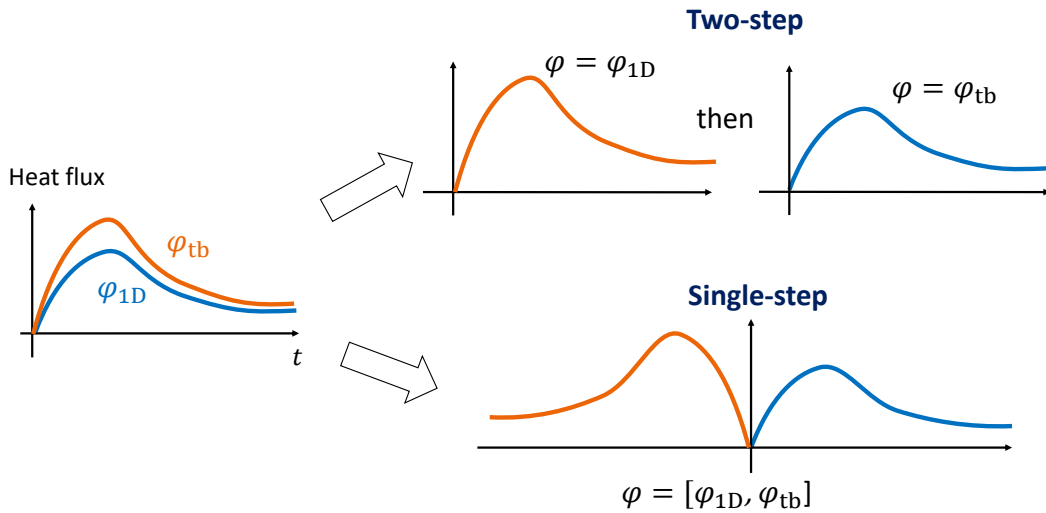
There are several ways here to apply the inverse method. The thermal bridge and sound areas may be treated sequentially (Two-step approach) or simultaneously (Single-step approach). This section compares the two approaches on an example.

### 9.1.2.1. Presentation

For the characterization of a thermal bridge, two measurement data vectors are used:  $\varphi_{1D}$  and  $\varphi_{tb}$ . For each of them, a direct model is defined in order to apply an inverse technique:  $\varphi_{mo}^{1D}$  and  $\varphi_{mo}^{tb}$ . These two direct models are usually identical but may be different (e.g. different number of modeled layers). In some cases, one

or several parameters are common to both models. For instance, in the type of wall illustrated in Fig 9.3 where the thermal irregularity is located inside the second layer, the first and third layers are identical on the thermal bridge and sound areas. Therefore, it might be advantageous to take this into account in the inverse method. For this reason, two different approaches are compared.

With the “Two-step” approach, no parameter is shared between the two direct models. This is the most general situation. A distinct inverse method is applied independently to each data vector  $\varphi_{1D}$  and  $\varphi_{tb}$ . If some layers of the wall are common to both areas, each inversion gives a different estimation of their thermal properties. On the contrary, the “Single-step” approach only provides one estimate per shared parameter. Basically, the inverse method is applied to the concatenated vector  $\varphi = [\varphi_{1D}; \varphi_{tb}]$ . The direct model is built similarly:  $\varphi_{mo}(\beta) = [\varphi_{mo}^{1D}(\beta); \varphi_{mo}^{tb}(\beta)]$ . This approach enables  $\varphi_{mo}^{1D}$  and  $\varphi_{mo}^{tb}$  to share some parameters. The two approaches are illustrated in Fig 9.5. The first half of the concatenated vector is flipped for aesthetics purposes.



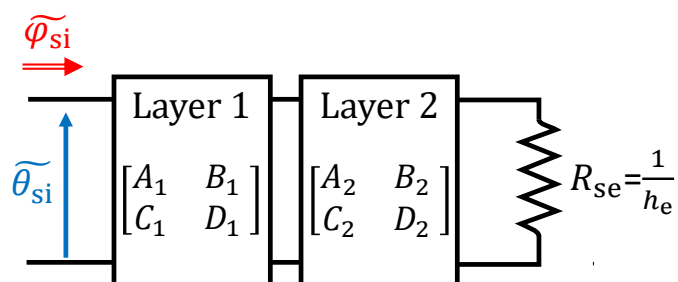
**Figure 9.5.:** Illustration of Two-step and Single-step approaches for the characterization of a thermal bridge.

These two approaches are compared on synthetic data generated by the two-layer model presented in Sec 7.1.5 of Chap 7 and already used several times in previous chapters. It is illustrated in Fig 9.6. Layer 1 and layer 2 are supposed made of gypsum (13 mm) and glass wool (120 mm), respectively. This wall is similar to the walls of the SGR setup. The wall is initially at thermal equilibrium and the external environment temperature remains constant. Heat flux  $\varphi_{si}$  is the model output, as usual, and temperature  $T_{si}$  is the model single input, given by an exponential function:

$$T_{si}(t) = A_T \left( 1 - \exp\left(-\frac{t}{\tau}\right) \right) \quad (9.7)$$



with  $A_T = 14$  K and  $\tau = 3.4$  h.



**Figure 9.6.:** Two-layer model used for the comparison of the Two-step and Single-step approaches.

For sake of simplicity, the same input  $T_{si}$  is applied to both areas even though it should be slightly different in practice when the wall is heated by the air. The model has five parameters: the first layer thermal properties  $R_1$  and  $b_1$ , the second layer ones  $R_2$  and  $b_2$ , and the external heat exchange coefficient  $h_e$ . The latter will be supposed perfectly known for the parameter estimation. In practice, the external surface temperature  $T_{se}$  would be measured and treated as a second input of the model (external correction, see Chap 8), so parameter  $h_e$  would not be included in the model. The thermal properties assigned to the sound area and the thermal bridge (modeled as a homogeneous wall with equivalent thermal properties) are summarized in Tab 9.1. Both areas have the same facing layer in gypsum, hence the same values for  $R_1$  and  $b_1$ . The thermal bridge is located inside the second layer. The corresponding equivalent layer has a lower thermal resistance and higher thermal effusivity than the sound area.

**Table 9.1.:** Thermal properties used in the model.

Sound area		Thermal bridge		Unit
Parameter	Value	Parameter	Value	
$R_1$	0.06	$R_1$	0.06	$\text{m}^2 \cdot \text{K} \cdot \text{W}^{-1}$
$b_1$	420	$b_1$	420	$\text{J} \cdot \text{K}^{-1} \cdot \text{m}^{-2} \cdot \text{s}^{-1/2}$
$R_2^{\text{ID}}$	3.75	$R_2^{\text{tb}}$	2.50	$\text{m}^2 \cdot \text{K} \cdot \text{W}^{-1}$
$b_2^{\text{ID}}$	30	$b_2^{\text{tb}}$	60	$\text{J} \cdot \text{K}^{-1} \cdot \text{m}^{-2} \cdot \text{s}^{-1/2}$
$h_e$	25	$h_e$	25	$\text{W} \cdot \text{m}^{-2} \cdot \text{K}^{-1}$

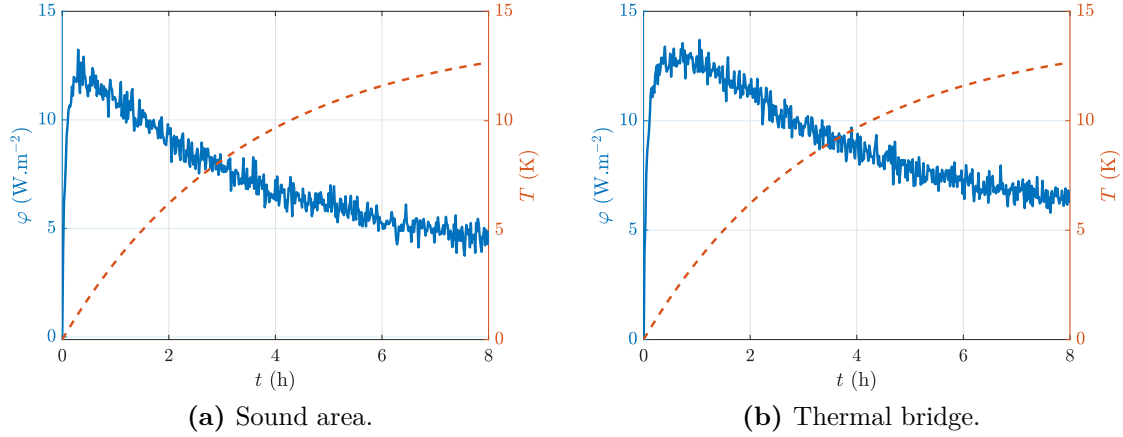
The values assigned to  $R_2^{\text{tb}}$  and  $b_2^{\text{tb}}$  are inspired from measurements performed on thermal bridges of the CEREMA experiments.

### 9.1.2.2. Two-step approach

Figure 9.7 plots the synthetic measurements (obtained from the model presented above) for the sound and thermal bridge areas. The input  $T_{si}$  of the model is also

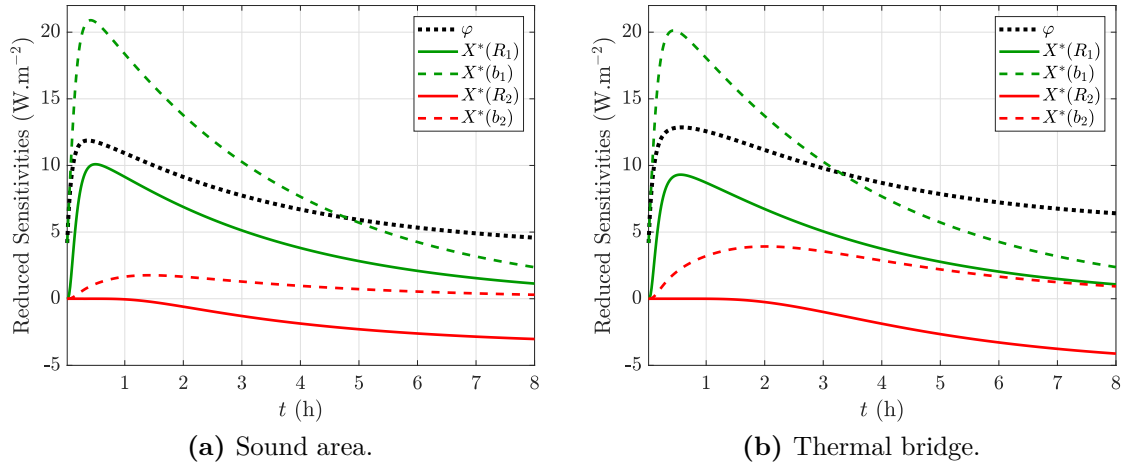
## 9.1. PRESENTATION OF THE METHOD

plotted. A random noise is added to the heat flux signals. Its standard deviation is  $\sigma = 0.4 \text{ W.m}^{-2}$  which is representative of measurements. The sampling period is 30 s. As expected, the heat flux on the thermal bridge is higher than that on the sound area.



**Figure 9.7.:** Synthetic measurements for the Two-step approach.

The reduced sensitivity coefficients are shown in Fig 9.8. Their shapes are slightly different between the two cases, especially for parameters  $R_2$  and  $b_2$  (the sensitivities depend on the reference values because the model is non-linear). The hybrid matrices  $V_{\text{cor}}$  are presented in Tab 9.2. They are very similar. Only the relative uncertainty on  $b_2$  is significantly different because there is a factor two between  $b_2^{\text{tb}}$  and  $b_2^{\text{1D}}$ .



**Figure 9.8.:** Reduced sensitivity coefficients for the Two-step approach.

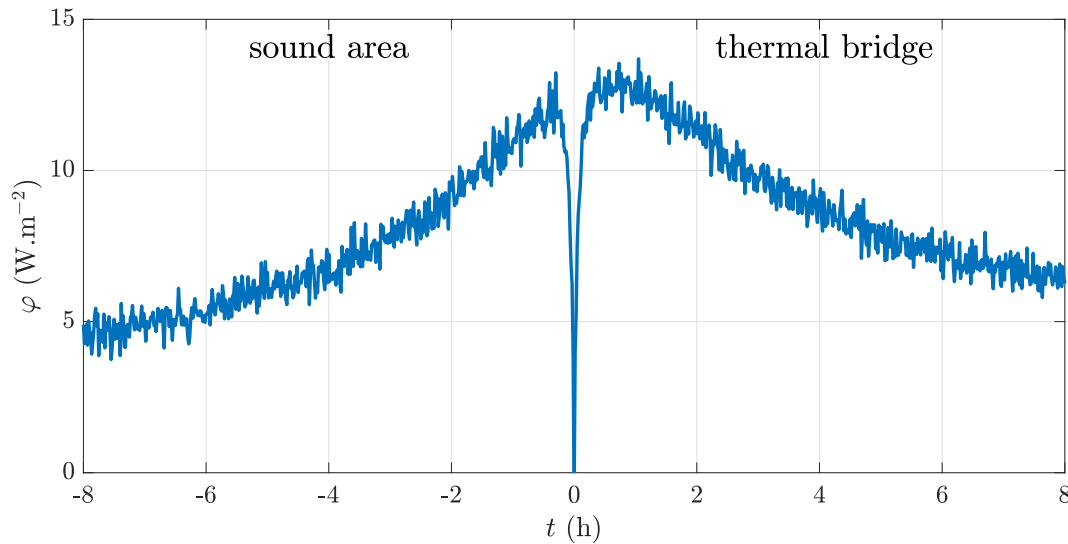
The estimation uncertainty of the thermal resistances  $R_2^{\text{1D}}$  and  $R_2^{\text{tb}}$  of the insulation layer is around 1.2%. This apparently low value comes from the high number of measurements points. As said in Chap 8, in this formulation, the only source of uncertainty is the random measurement noise. The presence of possible bias in the model for instance is not considered. Therefore, the present calculated uncertainty is probably lower than the uncertainty one could expect from *in situ* measurements.

**Table 9.2.:** Hybrid  $V_{\text{cor}}$  matrix for the Two-step approach ( $\sigma_\varphi = 0.4 \text{ W.m}^{-2}$ ).

(a) Sound area.				(b) Thermal bridge.					
	$R_1$	$b_1$	$R_2^{1D}$	$b_2^{1D}$		$R_1$	$b_1$	$R_2^{\text{tb}}$	$b_2^{\text{tb}}$
$R_1$	0.050	-0.97	-0.25	-0.64	$R_1$	0.047	-0.97	-0.34	-0.63
$b_1$		0.021	0.18	0.45	$b_1$		0.019	0.25	0.46
$R_2^{1D}$			0.012	0.50	$R_2^{\text{tb}}$			0.011	0.61
$b_2^{1D}$	sym			0.073	$b_2^{\text{tb}}$	sym			0.025

### 9.1.2.3. Single-step approach

In the Single-step approach, the measurement data vector  $\varphi$  is obtained from concatenation of  $\varphi_{1D}$  and  $\varphi_{\text{tb}}$ , as shown in Fig 9.9. Vector  $\varphi_{1D}$  is flipped and is assigned to negative time values. This convention is only useful to ease the visual comparison of  $\varphi_{1D}$  and  $\varphi_{\text{tb}}$  on the graphs and has no effect on the results.

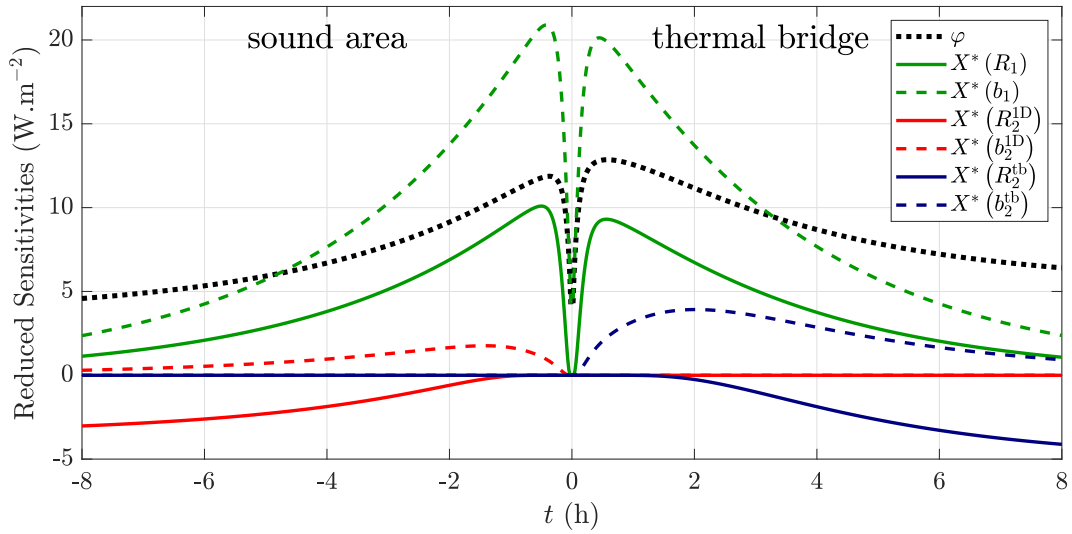


**Figure 9.9.:** Example of concatenated measurement vector  $\varphi = [\varphi_{1D}, \varphi_{\text{tb}}]$  for the Single-step approach (synthetic measurements).

The parameter vector is composed of six elements:

$$\beta = [R_1, b_1, R_2^{1D}, b_2^{1D}, R_2^{\text{tb}}, b_2^{\text{tb}}] \quad (9.8)$$

The reduced sensitivity coefficients are given in Fig 9.10. The shared parameters ( $R_1$  and  $b_1$ ) have a non-null sensitivity on both sides of the graph (sound area and thermal bridge). On the contrary, parameters which are specific to one area are null on one side. The corresponding  $V_{\text{cor}}$  matrix is given in Tab 9.3 .



**Figure 9.10.:** Reduced sensitivity coefficients for the Single-step approach.

**Table 9.3.:** Hybrid  $V_{\text{cor}}$  matrix for the Single-step approach ( $\sigma_\varphi = 0.4 \text{ W.m}^{-2}$ ).

	$R_1$	$b_1$	$R_2^{1D}$	$b_2^{1D}$	$R_2^{tb}$	$b_2^{tb}$
$R_1$	0.032	-0.97	-0.17	-0.64	-0.26	-0.58
$b_1$		0.013	0.13	0.47	0.19	0.41
$R_2^{1D}$			0.011	0.45	0.09	0.23
$b_2^{1D}$				0.048	0.34	0.82
$R_2^{tb}$					0.010	0.56
$b_2^{tb}$						0.018
	sym					

#### 9.1.2.4. Comparison and choice of approach

From a theoretical point of view, it turns out that the Single-step approach is slightly better than the Two-step one. Indeed, the relative estimation uncertainty of every parameter is smaller with Single-step. To be more specific, on the current example the uncertainties of  $R_1$  and  $b_1$  are around 5.0 and 2.1% respectively with Two-step whereas these values are 3.2 and 1.3% with Single-step. The uncertainty of  $b_2$  is also reduced. However, the improvement is negligible for the thermal resistance  $R_2$  of the second layer. Indeed, the relative estimation uncertainties of  $R_2^{1D}$  and  $R_2^{tb}$  are 1.2 and 1.1% with the Two-step procedure whereas they are 1.1 and 1.0% with the Single-step one. Thus, given that the parameter of interest is  $R_2$ , the very small differences in its estimation uncertainty obtained in this theoretical study are not sufficient to conclude that Single-step is more suitable than Two-step.

From an experimental point of view, the Single-step approach is less attractive. When applied to real measurements, it was noticed that the residuals are sometimes signed with Single-step while unsigned with Two-step. This is because the former approach has less degrees of freedom than the latter. By sharing parameters between both areas, it is assumed that some layers are identical on the thermal bridge and sound areas. This might not be quite the case in practice for many reasons, such as the presence of a contact resistance between layers, screws in the facing layer, or a

joint between two gypsum boards (e.g. thermal bridges in CEREMA wall). Because the models used are reduced models, such small features are not explicitly modeled but are taken into account in the values of the equivalent thermal properties of the modeled layers. In addition, the thermal bridge is modeled as a homogeneous wall despite its 2D or 3D nature. Even though the thermal bridge and sound areas are made of the same facing layer, the corresponding thermal properties of the equivalent model might be different. By construction, the Single-step approach cannot take into account these differences and is therefore more likely to lead to signed residuals and biased parameter estimation.

As a conclusion, the Two-step approach is more suitable than the Single-step one. Not only is it more general (no need to identify common layers between the sound area and the thermal bridge), it also leads to a better parameter estimation. Single-step removes some degrees of freedom which slightly reduces the estimation uncertainties (yet not much for the parameter of interest). However, it might introduce a bias in the model. This is an illustration of the bias/variance trade-off of inverse methods.

### 9.1.3. Conclusion

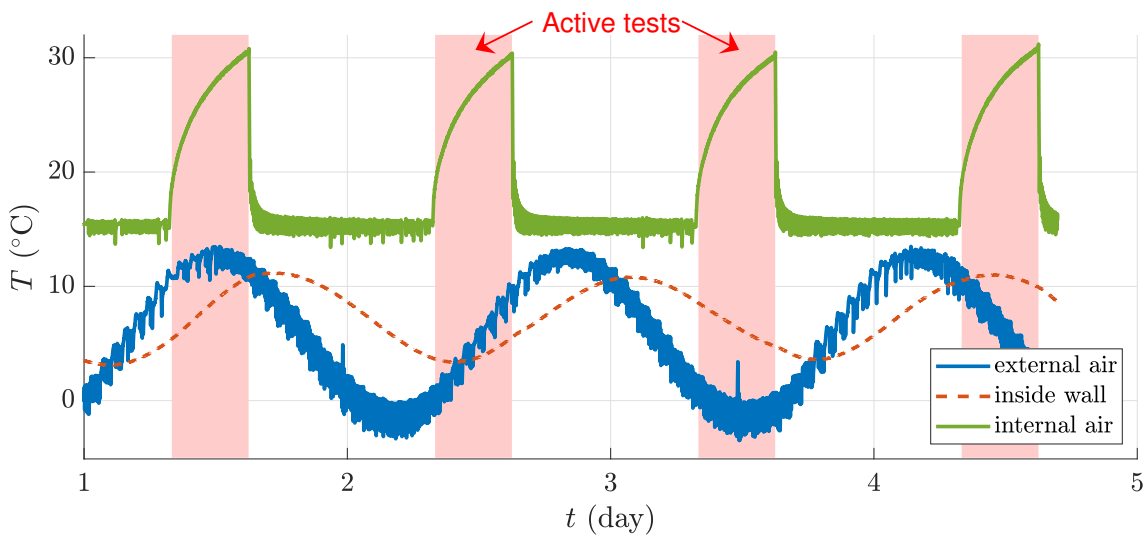
The active method presented in Chap 8 was designed for the estimation of the thermal resistance of a homogeneous wall. Yet, it may also be applied to non-homogeneous walls: the parameters of the direct model becomes the properties of an equivalent 1D wall having the same thermal behavior as the real wall. The surface temperature and heat flux fields are measured by extrapolating the measurements made with contact sensors on a nearby sound area. This requires the knowledge of the heat transfer coefficient  $h$  (measured with a specific device) and the wall emissivity  $\varepsilon$  (a tabulated value may be used). Finally, a theoretical study based on synthetic data showed that it is better to estimate the parameters of the thermal bridge and sound areas sequentially (Two-step approach) rather than simultaneously (Single-step approach). The following sections present the application of the method to the CEREMA and SGR experimental campaigns.

## 9.2. Results on CEREMA experiments

The method is tested on measurements performed during the CEREMA experimental campaign. This setup built inside a climate chamber was presented in Chap 4 and used in Chap 8 for the estimation of the sound area thermal resistance. The configurations tested are reminded in Tab 9.4. Figure 9.11 also reminds the type of active tests performed (the external temperature is either constant or sinusoidal).

**Table 9.4.:** Summary of active test configurations of the CEREMA campaign.

Configuration	$T_{\text{air},i}$ (°C)	$T_{\text{air},e}$ (°C)	test IDs	number of tests
1	15	5	1-5	5
2	15	15	6-8	3
3	15	$5 + 2.5 \cos(\omega t)$	9-13	4
4	15	$5 + 5.0 \cos(\omega t)$	14-17	4
5	15	$5 + 7.5 \cos(\omega t)$	18-25	8
6	15	$15 + 7.5 \cos(\omega t)$	25-27	3



**Figure 9.11.:** Example of internal and external temperatures for consecutive active tests (configuration 5).

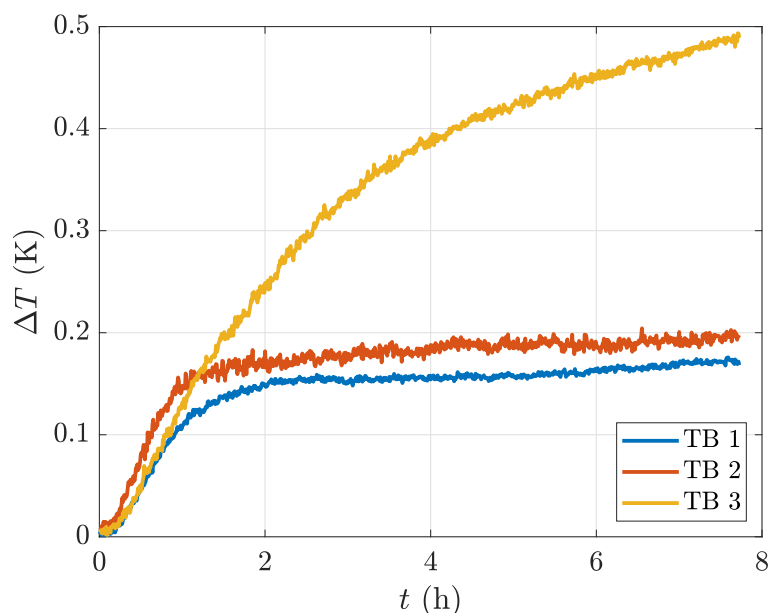
### 9.2.1. Detailed results on one example

The results are detailed on the example of an active test of configuration 2.

#### 9.2.1.1. Temperature and heat flux extrapolation

The mean measured temperature differences  $\Delta T = T_{\text{si}}^{1D} - \overline{T_{\text{si}}^{\text{tb}}}$  between the sound area and the three thermal bridges are plotted in Fig 9.12. These temperatures,

obtained from InfraRed Thermography (IRT), are space averages over the Regions Of Interest (ROIs) shown in Fig 9.13. This figure shows a thermal image captured after 4 h of heating. The ROIs were placed at the same altitude as the  $h$ -meter (harmonic excitation method) and the HFM. Indeed, because of air stratification, the heat transfer coefficient may not be quite uniform all over the wall height whereas the extrapolation process is based on a uniformity assumption. As with steady-state calculations (see section 6.3), the width  $L_{tb}$  of the ROIs is set to 30 cm.

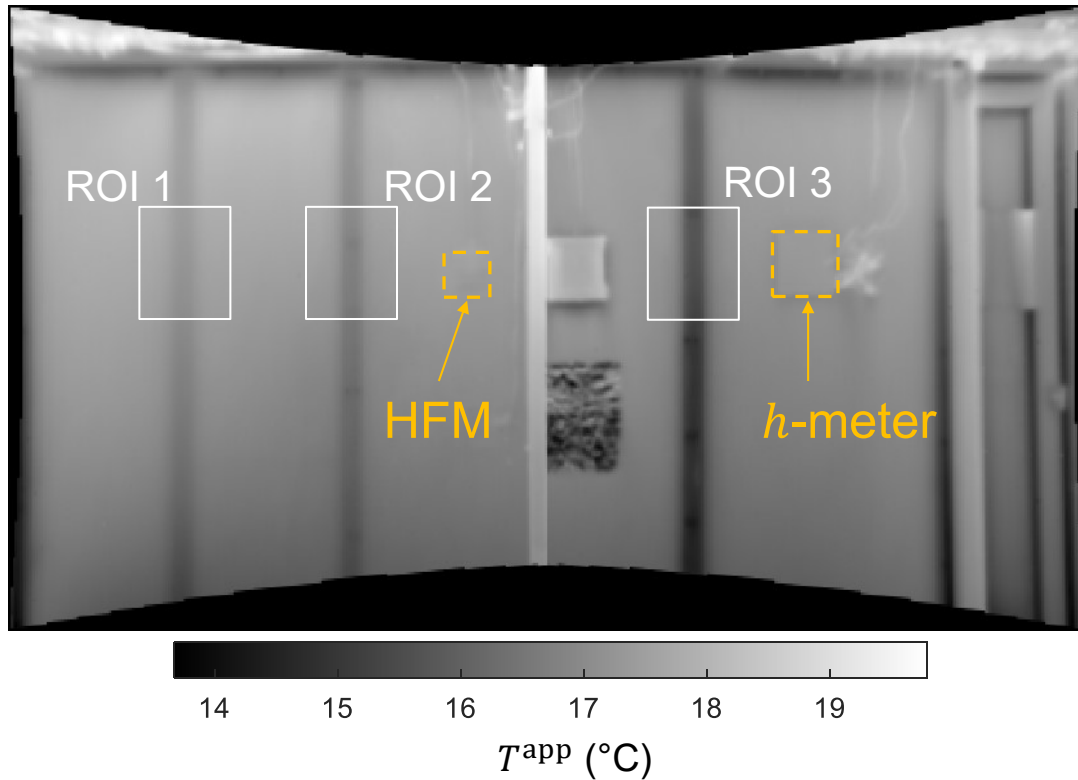


**Figure 9.12.:** Evolution of temperature differences between thermal bridges and sound area (from IRT) during an active test (configuration 2).

At the beginning of the experiment, the temperature differences are null because initial conditions are subtracted. Then, they are positive because the temperature on thermal bridges is lower than that on the sound area. The heat transfer coefficient is estimated to  $9.6 \pm 0.5 \text{ W.m}^{-2}.\text{K}^{-1}$ . This is above the standard value of  $7.7 \text{ W.m}^{-2}.\text{K}^{-1}$  for indoor building walls [99]. The difference is due to the heaters which generate air movements and therefore increase convective heat losses. The measured  $h$ -value of 9.6 is in good agreement with the measurements undertaken in similar conditions with other methods, presented in Chap 5.

Surface temperatures and heat fluxes are then extrapolated from the sound area to each thermal bridge. These quantities are plotted in Fig 9.14. Temperature contrasts are small (about 0.2 K) when compared to temperature temporal evolutions (about 15 K). Thus, the different curves are hardly distinguishable. Nevertheless, these small temperature contrasts lead to much more noticeable heat flux density contrasts. As expected, the lowest heat flux is measured on the sound area and the highest one on TB 3. The heat flux on TB 3 slightly increases at the end of the experiment whereas it keeps decreasing on the other zones. This result looks odd but it is physical, as proved by the parameter estimation below.

It may be noticed that heat flux curves in Fig 9.14 have a highly correlated noise. This is because the noise on the heat flux increment  $h \times \Delta T$  is much smaller (about



**Figure 9.13.:** Thermal image captured during an active test (configuration 2, after 4 h of heating) and ROIs used for temperature and heat flux extrapolation. The HFM is on the sound area.

0.03 W.m<sup>-2</sup>) that the noise on  $\varphi_{1D}$  measured with a HFM (about 0.4 W.m<sup>-2</sup>).

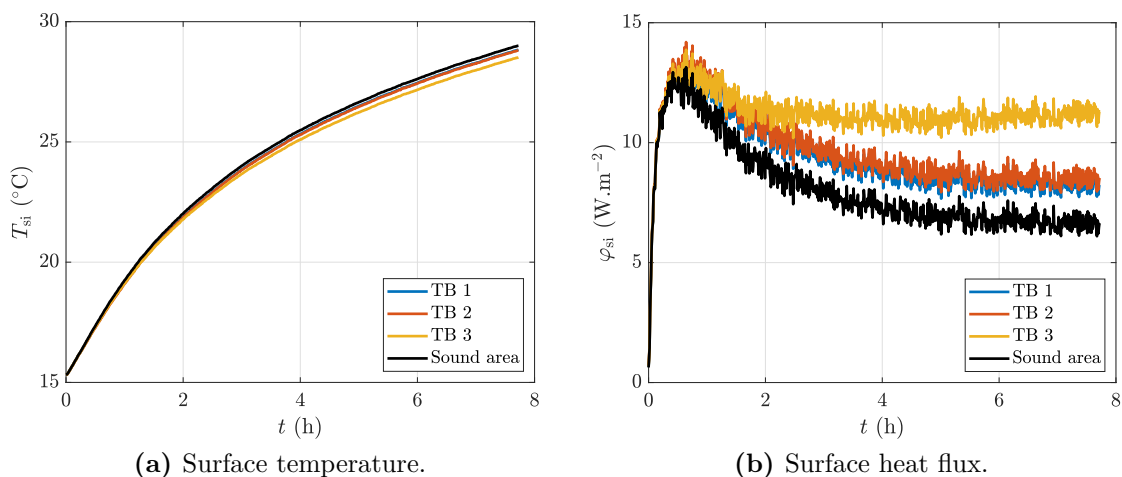
The extrapolated surface temperatures and heat fluxes are then used to estimate the wall equivalent thermal properties by inverse method.

### 9.2.1.2. Parameter estimation

Figure 9.15a compares the measured surface heat flux  $\varphi$  on the sound area to the model prediction  $\varphi_{\text{mo}}(\hat{\beta})$  after estimation of the parameter vector  $\hat{\beta}$ . Figures 9.15b, 9.15c and 9.15d present the same quantities for TB 1, TB 2 and TB 3, respectively. The residuals are not signed: they have the shape of a white noise. In addition, their standard deviation is equivalent to the noise level:  $\sigma_{\varphi} = 0.4 \text{ W.m}^{-2}$ . It proves that the model can fit the measurement data and the only remaining difference is the measurement noise. Note that the first 10 minutes of the experiment were removed from the analysis because HFM measurements are inaccurate at the beginning of the heating phase ( $\varphi_{\text{si}}$  increases too fast). It was shown in Chap 8 that an active test of about 6 h is enough here for the parameter estimation to be accurate.

The estimated parameters and their associated uncertainties are gathered in Tab 9.5. The reference values for the sound area (presented in Chap 8) are included in the





**Figure 9.14.:** Evolution of wall surface temperature and heat flux extrapolated from the sound area to the thermal bridges (configuration 2).

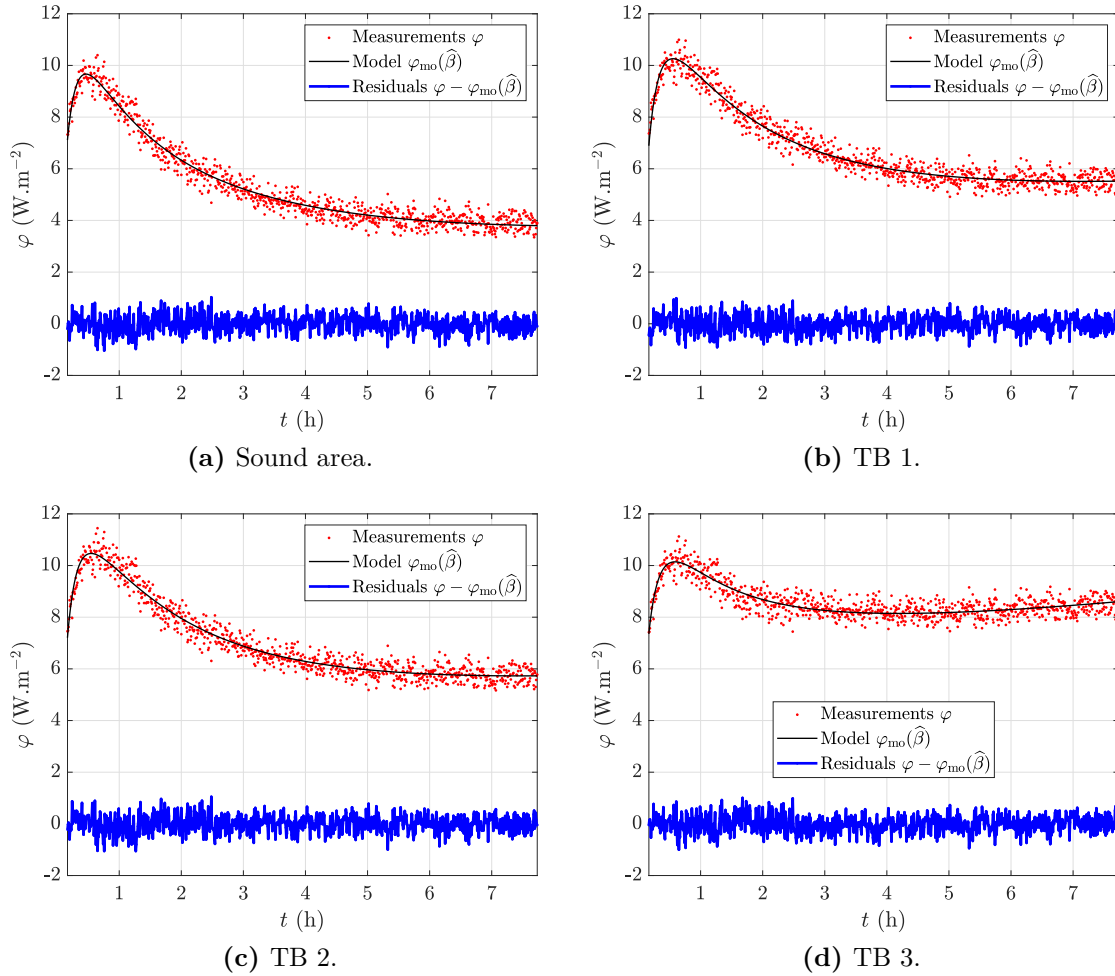
table. They have different origins: measurements in laboratory with the Hot Disk method (for  $R_1$  and  $b_1$ ), manufacturer data (for  $R_2$ ) and standard value from the literature (for  $b_2$ : [202]). It may be seen that method is able to estimate the thermal properties of the insulation system (sound area). In particular, the main parameter of interest,  $R_2$ , is only about 5% away from its reference value. This 5% difference is deemed reasonable despite the smaller value of the relative estimation uncertainty: below 2%. As presented at the end of this section, the uncertainty is probably underestimated.

As expected, the equivalent resistances  $R_2$  of the thermal bridges are smaller than that of the sound area (especially for TB 3). The estimated thermal effusivity  $b_2$  is also higher on thermal bridges because of the higher thermal inertia of metallic rails when compared to glass wool. The estimated properties of the first layer ( $R_1$  and  $b_1$ ) for each area are not equals (yet very close: the differences are smaller than the uncertainties). This justifies the use of the Two-step approach. For the calculation of thermal bridges transmittance coefficient  $\psi$ , only the values of the thermal resistances (especially  $R_2$ ) are required.

**Table 9.5.:** Summary of parameter estimation on sound area and thermal bridges (configurations 2, model  $A_2$ ).

	SA (ref)	SA	TB 1	TB 2	TB 3
$R_1$ ( $m^2 \cdot K \cdot W^{-1}$ )	0.05	$0.04 \pm 0.01$	$0.03 \pm 0.01$	$0.03 \pm 0.01$	$0.03 \pm 0.01$
$b_1$ ( $J \cdot K^{-1} \cdot m^{-2} \cdot s^{-1/2}$ )	420	$471 \pm 31$	$522 \pm 50$	$484 \pm 42$	$527 \pm 53$
<b><math>R_2</math></b> ( $m^2 \cdot K \cdot W^{-1}$ )	<b>3.12</b>	<b><math>3.05 \pm 0.05</math></b>	<b><math>2.33 \pm 0.04</math></b>	<b><math>2.13 \pm 0.03</math></b>	<b><math>1.50 \pm 0.01</math></b>
$b_2$ ( $J \cdot K^{-1} \cdot m^{-2} \cdot s^{-1/2}$ )	21	$38.1 \pm 3.5$	$65.8 \pm 2.2$	$71.7 \pm 2.4$	$67.2 \pm 4.7$

On this example, the two-layer model  $A_2$  (see Tab 8.6) was used because the external temperature is constant. In this model, temperature  $T_{in}$  between the insulation system and the building blocks is supposed constant during the active test (see Chap 8). This assumption is valid for the sound area, TB 1 and TB 2 (this was



**Figure 9.15.:** Comparison of measurements and model output after parameter estimation (model  $A_2$ ).

checked using thermocouples placed inside the wall). However, the metallic rail of TB 3 crosses the insulation layer entirely and is directly in contact with the third layer. Thus,  $T_{\text{in}}$  does not remain constant on TB 3. However, on the ROI used on thermal images for the extrapolation of surface temperature and heat flux, the thermal bridge itself only represents a limited area. Temperature differences shown in Fig 9.12 arise from an average over the thermal bridge and its surrounding where  $T_{\text{in}}$  is less affected. As a consequence, the assumption  $T_{\text{in}} = \text{constant}$  in model  $A_2$  is also deemed valid for TB 3. Results presented below prove that this model is able to correctly estimate the transmittance  $\psi$  of this thermal bridge.

It may be noted that the uncertainties given in Tab 9.5 come from the  $V_{\text{cor}}$  matrix of the inverse technique. Thus, random measurement noise is taken into account. Yet, measurement uncertainty of  $h$  cannot be propagated (with the current approach) and does not contribute to the  $R$  and  $\psi$  estimation uncertainties. Therefore, the latter may be underestimated here. Next steps would consist in exploring different potential approaches to take the uncertainty over  $h$  into account (such as Bayesian inferences [208] for instance).

## 9.2.2. Results for different configurations

The results obtained for all the active tests are summarized in Tab 9.6 as well as in Fig 9.16. The heat transfer coefficients, equivalent thermal resistances and thermal transmittances  $\psi$  are detailed. The model output, measurements and residuals for all the parameter estimations are plotted in Appendix F.1. In every configuration (except configuration 6), at least four active tests are performed following the pattern shown in Fig 9.11. For the first test,  $T_{\text{air,e}}$  is around the maximum of its sinusoid. It increases during the second test, is around its minimum during the third one, and decreases for the last test. These four regimes correspond to the four symbols  $\cap$ ,  $\nearrow$ ,  $\cup$  and  $\searrow$  used in Tab 9.6.

**Table 9.6.:** Estimations of thermal resistances and thermal bridge transmission coefficients for every experiment. Depending on the experiment,  $T_{\text{air,e}}$  is constant:  $-$ , or around a maximum:  $\cap$ , or increasing:  $\nearrow$ , or around a minimum:  $\cup$ , or decreasing:  $\searrow$ .

Conf	Exp	$T_{\text{air,e}}$	$h$ ( $\text{W}\cdot\text{m}^{-2}\cdot\text{K}^{-1}$ )	$R_1 + R_2$ ( $\text{m}^2\cdot\text{K}\cdot\text{W}^{-1}$ )				$\psi$ ( $\text{mW}\cdot\text{m}^{-1}\cdot\text{K}^{-1}$ )		
				SA	TB 1	TB 2	TB 3	TB 1	TB 2	TB 3
1	1	$-$	$10.1 \pm 0.6$	$3.09 \pm 0.14$	$2.20 \pm 0.10$	$1.97 \pm 0.08$	$1.45 \pm 0.03$	$29 \pm 6$	$41 \pm 6$	$114 \pm 7$
	2	$-$	$9.7 \pm 0.6$	$3.07 \pm 0.07$	$2.28 \pm 0.05$	$2.13 \pm 0.05$	$1.54 \pm 0.03$	$25 \pm 3$	$32 \pm 3$	$100 \pm 5$
	3	$-$	$9.7 \pm 0.7$	$3.16 \pm 0.11$	$2.33 \pm 0.08$	$2.11 \pm 0.06$	$1.55 \pm 0.03$	$27 \pm 4$	$38 \pm 4$	$110 \pm 6$
	4	$-$	$9.6 \pm 0.4$	$3.14 \pm 0.20$	$2.36 \pm 0.17$	$2.20 \pm 0.16$	$1.60 \pm 0.04$	$25 \pm 8$	$32 \pm 9$	$102 \pm 9$
	5	$-$	$10.3 \pm 0.8$	$3.07 \pm 0.08$	$2.20 \pm 0.05$	$2.01 \pm 0.04$	$1.49 \pm 0.02$	$29 \pm 3$	$39 \pm 3$	$107 \pm 5$
2	6	$-$	$9.6 \pm 0.4$	$3.06 \pm 0.11$	$2.29 \pm 0.09$	$2.24 \pm 0.09$	$1.51 \pm 0.03$	$24 \pm 5$	$27 \pm 5$	$104 \pm 6$
	7	$-$	$9.6 \pm 0.5$	$3.16 \pm 0.07$	$2.40 \pm 0.05$	$2.31 \pm 0.05$	$1.55 \pm 0.02$	$24 \pm 3$	$28 \pm 3$	$110 \pm 4$
	8	$-$	$9.5 \pm 0.4$	$3.09 \pm 0.06$	$2.36 \pm 0.04$	$2.28 \pm 0.04$	$1.53 \pm 0.02$	$23 \pm 2$	$27 \pm 3$	$105 \pm 4$
3	9	$\cap$	$9.4 \pm 0.5$	$3.02 \pm 0.12$	$2.18 \pm 0.09$	$2.07 \pm 0.08$	$1.41 \pm 0.03$	$27 \pm 5$	$33 \pm 5$	$110 \pm 6$
	10	$\nearrow$	$9.9 \pm 0.5$	$3.05 \pm 0.12$	$2.21 \pm 0.09$	$2.07 \pm 0.08$	$1.38 \pm 0.03$	$27 \pm 5$	$34 \pm 5$	$117 \pm 6$
	11	$\cup$	$9.5 \pm 0.5$	$3.04 \pm 0.14$	$2.18 \pm 0.10$	$2.00 \pm 0.09$	$1.36 \pm 0.04$	$28 \pm 6$	$37 \pm 6$	$119 \pm 8$
	12	$\searrow$	$9.6 \pm 0.3$	$3.05 \pm 0.07$	$2.24 \pm 0.05$	$2.07 \pm 0.04$	$1.40 \pm 0.02$	$26 \pm 3$	$34 \pm 3$	$115 \pm 4$
4	13	$\cap$	$9.5 \pm 0.4$	$2.92 \pm 0.14$	$2.11 \pm 0.11$	$1.91 \pm 0.09$	$1.35 \pm 0.04$	$26 \pm 6$	$36 \pm 6$	$106 \pm 8$
	14	$\nearrow$	$9.5 \pm 0.4$	$3.05 \pm 0.13$	$2.23 \pm 0.10$	$2.02 \pm 0.08$	$1.33 \pm 0.03$	$26 \pm 5$	$37 \pm 5$	$124 \pm 7$
	15	$\cup$	$9.3 \pm 0.4$	$3.24 \pm 0.10$	$2.41 \pm 0.09$	$2.21 \pm 0.07$	$1.47 \pm 0.04$	$27 \pm 5$	$37 \pm 5$	$132 \pm 7$
	16	$\searrow$	$9.8 \pm 0.5$	$2.97 \pm 0.08$	$2.18 \pm 0.06$	$2.04 \pm 0.06$	$1.41 \pm 0.02$	$25 \pm 3$	$32 \pm 4$	$105 \pm 5$
5	17	$\cap$	$10.3 \pm 0.8$	$3.06 \pm 0.10$	$2.11 \pm 0.07$	$1.95 \pm 0.06$	$1.32 \pm 0.04$	$32 \pm 4$	$41 \pm 4$	$128 \pm 7$
	18	$\cap$	$9.5 \pm 0.5$	$3.23 \pm 0.13$	$2.27 \pm 0.09$	$2.10 \pm 0.07$	$1.40 \pm 0.04$	$32 \pm 4$	$42 \pm 4$	$141 \pm 7$
	19	$\nearrow$	$9.7 \pm 0.6$	$3.06 \pm 0.13$	$2.23 \pm 0.09$	$2.06 \pm 0.11$	$1.53 \pm 0.04$	$27 \pm 5$	$35 \pm 5$	$101 \pm 6$
	20	$\nearrow$	$9.3 \pm 0.5$	$2.93 \pm 0.10$	$2.19 \pm 0.08$	$2.02 \pm 0.07$	$1.30 \pm 0.04$	$23 \pm 4$	$31 \pm 4$	$113 \pm 6$
	21	$\cup$	$9.7 \pm 0.7$	$2.99 \pm 0.06$	$2.25 \pm 0.04$	$2.11 \pm 0.04$	$1.45 \pm 0.02$	$23 \pm 2$	$30 \pm 2$	$102 \pm 4$
	22	$\cup$	$9.0 \pm 0.5$	$2.99 \pm 0.05$	$2.20 \pm 0.03$	$2.04 \pm 0.03$	$1.40 \pm 0.02$	$25 \pm 2$	$33 \pm 2$	$108 \pm 4$
	23	$\searrow$	$9.6 \pm 0.4$	$3.08 \pm 0.05$	$2.24 \pm 0.03$	$2.12 \pm 0.03$	$1.50 \pm 0.02$	$27 \pm 2$	$33 \pm 2$	$106 \pm 4$
	24	$\searrow$	$9.1 \pm 0.5$	$3.01 \pm 0.05$	$2.14 \pm 0.03$	$1.99 \pm 0.03$	$1.39 \pm 0.02$	$29 \pm 2$	$37 \pm 2$	$113 \pm 4$
6	25	$\cap$	$9.6 \pm 0.4$	$2.96 \pm 0.10$	$2.18 \pm 0.07$	$2.03 \pm 0.06$	$1.29 \pm 0.03$	$25 \pm 4$	$32 \pm 4$	$118 \pm 6$
	26	$\nearrow$	$9.6 \pm 0.5$	$2.98 \pm 0.12$	$2.32 \pm 0.09$	$2.17 \pm 0.08$	$1.27 \pm 0.04$	$20 \pm 5$	$27 \pm 5$	$123 \pm 7$
	27	$\searrow$	$9.5 \pm 0.4$	$2.95 \pm 0.05$	$2.19 \pm 0.04$	$2.16 \pm 0.04$	$1.45 \pm 0.02$	$24 \pm 2$	$26 \pm 2$	$97 \pm 4$
average			9.6	3.05	2.24	2.09	1.43	26	34	112
standard deviation			0.1	0.08	0.08	0.10	0.09	3	4	10

The measured heat transfer coefficient ranges from  $9.1$  to  $10.3 \text{ W}\cdot\text{m}^{-2}\cdot\text{K}^{-1}$  with a mean value of  $9.6 \text{ W}\cdot\text{m}^{-2}\cdot\text{K}^{-1}$ . These measurements are very reproducible since the relative standard deviation between active tests is only 1%.

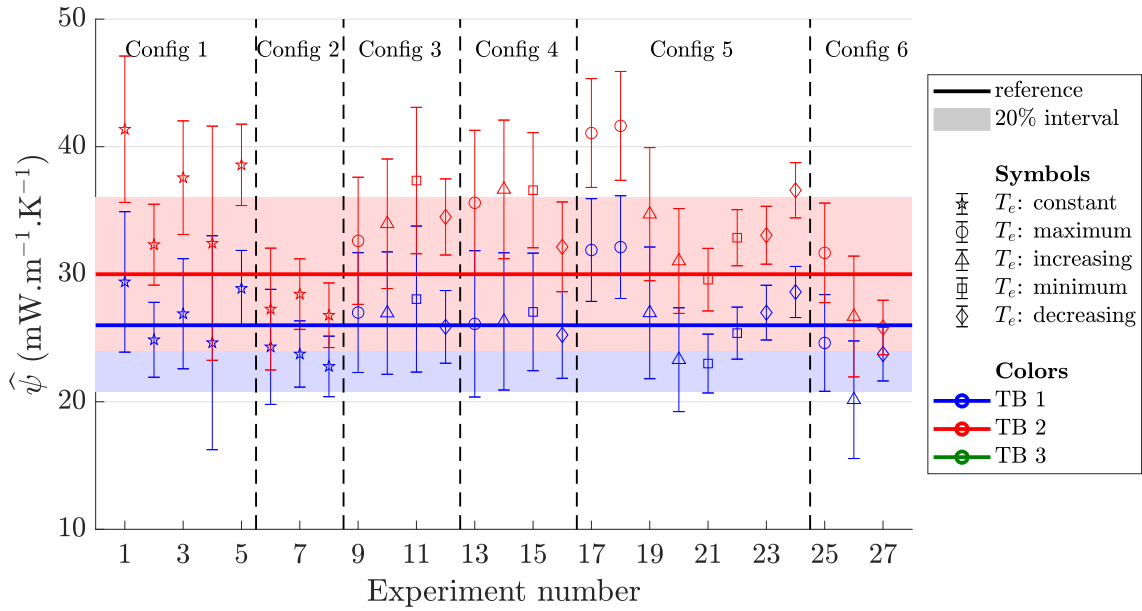
Thermal resistances given in Tab 9.6 are the sum  $R_1 + R_2$  of the first two layer resistances. For the sound area,  $R_1 + R_2$  corresponds to the resistance of the ther-

mal insulation system. For the thermal bridges, it corresponds to their equivalent resistance.

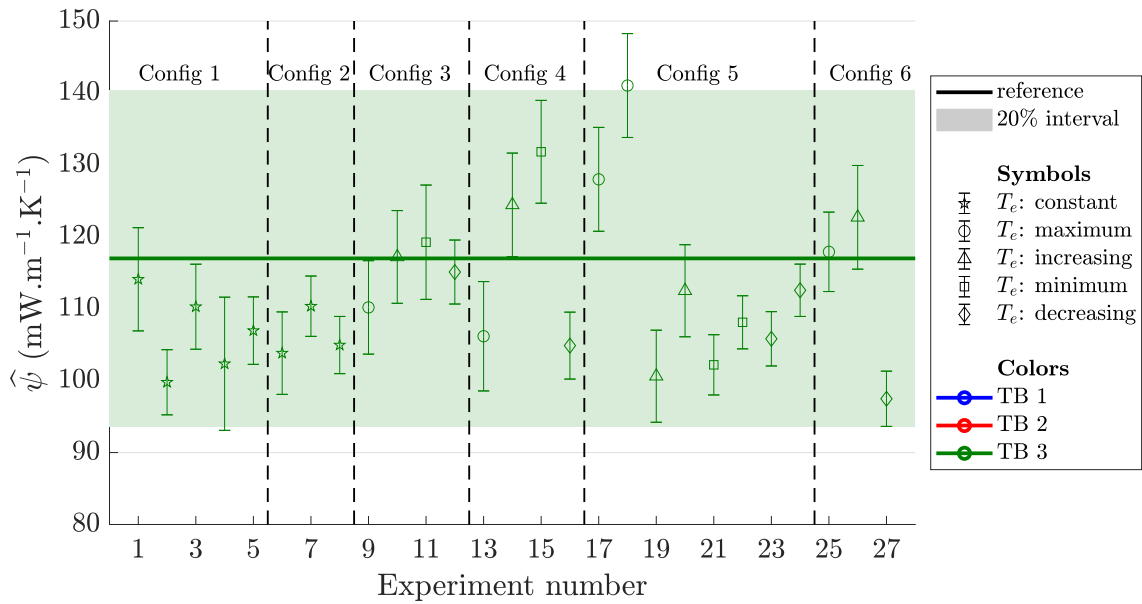
Model  $A_2$  was used for configurations 1 and 2 (constant external air temperature) whereas model  $AE_3$  was preferred for other configurations (varying external air temperature). This later model requires prior quantification of the thermal properties of the building blocks layer. This was done thanks to model  $H_1$  fed with external measurements. Please refer to Chap 8 for a presentation of these models. It may be seen that despite the variations in the external temperature, the thermal resistances are estimated with a good reproducibility: the standard deviation is between 0.08 and  $0.10 \text{ m}^2 \cdot \text{K} \cdot \text{W}^{-1}$ , depending on the zone considered. This corresponds to 2.6, 3.6, 4.8 and 6.3% for SA, TB 1, TB 2 and TB 3 respectively. These standard deviations are of the same magnitude of the individual estimation uncertainty predicted by the inverse method.

The thermal bridge transmission coefficients  $\psi$ , derived from these thermal resistances, are also estimated with a good reproducibility. The relative standard deviation is equal to 11% for TB 1 and TB 2 and 9% for TB 3. The individual uncertainties are of the same order of magnitude except for TB 3 for which they are smaller (about 5%). The estimated  $\psi$ -values are also in good agreement with steady-state results presented in Chap 6 (horizontal lines in Fig 9.16). Only the transmission coefficient of TB 2 is slightly over-estimated by the active method.

The results are rather independent of the magnitude of the external temperature variation. By including the external wall surface temperature  $T_{se}$  in the model, unsteady external conditions do not limit the applicability of the active method. The presence of a temperature gradient is not a limitation either. This is an illustration of the superimposition theorem: by subtracting the initial conditions, only variations in temperature and heat flux are accounted for. This active method would therefore be applicable with an external temperature either above or below the internal temperature. It is not limited to winter-time conditions. Yet, this analysis does not consider solar gains.



(a) TB 1 and TB 2.



(b) TB 3.

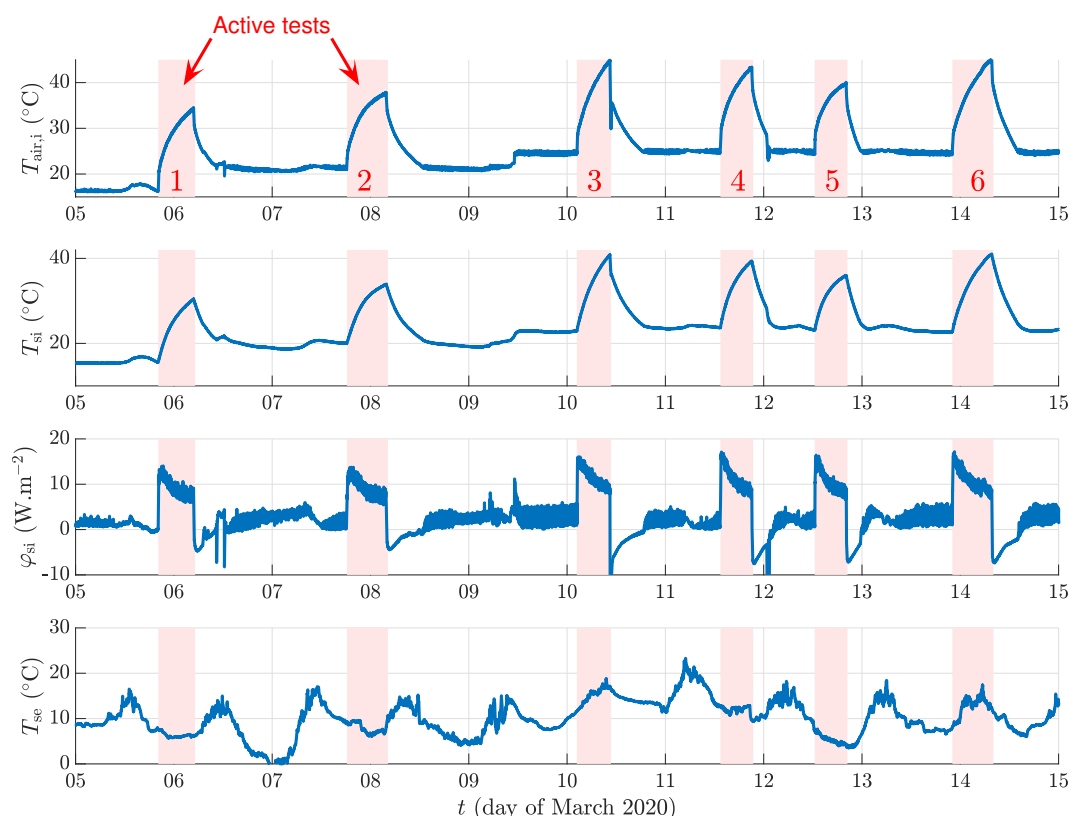
Figure 9.16.: Summary of estimated  $\psi$  coefficients for each thermal bridge.

### 9.2.3. Conclusion

The active method for the quantification of a thermal bridge  $\psi$ -value is validated in a climate chamber on the CEREMA setup. This load-bearing wall is equipped with a conventional internal insulation system made of glass wool. The metallic rails which hold the insulating materials generate structural thermal bridges. The active tests undertaken typically last 8 hours during which the indoor air temperature rises by about 15 K. The robustness of the method on this type of wall is assessed by performing 27 active tests in 6 different configurations simulating various weather configurations (up to 15 K of external temperature variation amplitude). The method shows a good repeatability and robustness to unsteady external temperature. The measured  $h$  coefficient (harmonic excitation method) is estimated to about  $9.6 \text{ W.m}^{-2}.\text{K}^{-1}$  with only 1% standard deviation between experiments. The surface temperature contrasts measured with IRT are between 0.2 and 0.5 K depending on the thermal bridge. The extrapolated temperatures on the thermal bridges are very similar but the differences between the extrapolated heat flux curves are much more noticeable. Estimated thermal bridge linear transmittances are less than 20% away from reference values derived from steady-state measurement, and majority of them are even below 10%. The measured  $\psi$ -values range from 26 to 112  $\text{mW.m}^{-1}.\text{K}^{-1}$  (in average), depending on the type of thermal bridge considered.

### 9.3. Results on SGR experiments

The active tests of the SGR experimental campaign are reminded in Fig 9.17. The internal air temperature  $T_{\text{air},i}$ , internal surface temperature  $T_{\text{si}}$ , internal surface heat flux  $\varphi_{\text{si}}$ , and external air temperature  $T_{\text{air},e}$  are plotted. Active tests number 3 and number 6 were carried out during day-time whereas the other four were performed by night. The internal air temperature is kept approximately constant between the tests: the set point temperature is between 17 and 25°C, depending on the experiment.



**Figure 9.17.:** Presentation of active measurements for the SGR experimental campaign. The active tests are highlighted in red.

#### 9.3.1. Detailed results on one example

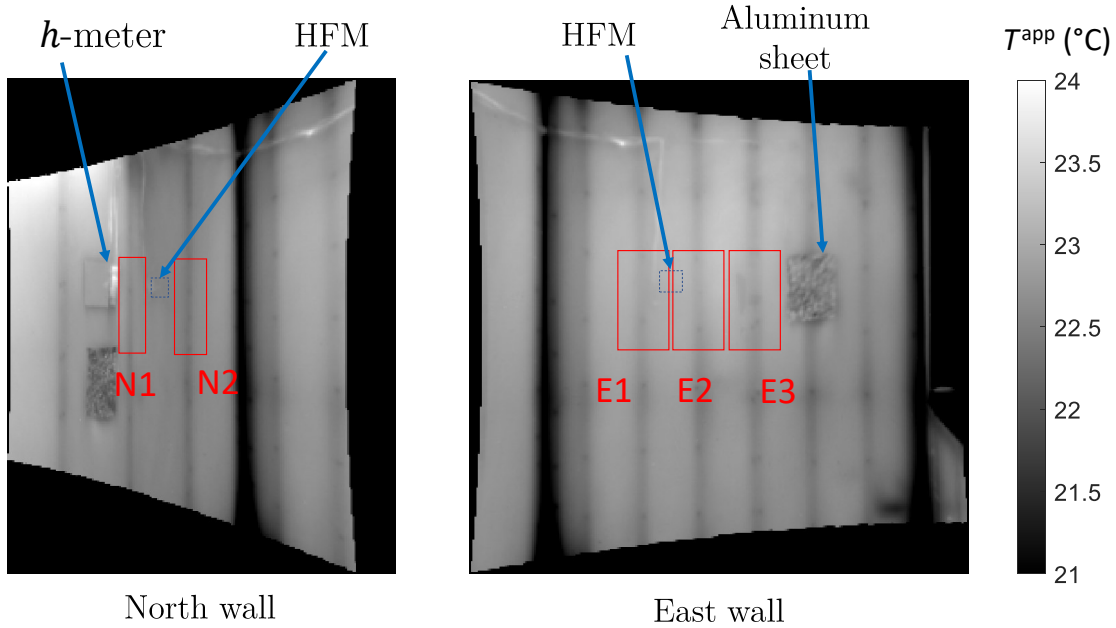
In this section, the results are presented in details for the example of Experiment 1.

##### 9.3.1.1. Temperature and heat flux extrapolation

Figure 9.18 shows an example of thermal images captured 4 h after the beginning of the considered active test. The ROIs of the studied thermal bridges, the HFMs and the  $h$ -meter (harmonic excitation method) were placed at the same altitude. The surface temperature between the thermal bridges is rather uniform: heat transfers

### 9.3. RESULTS ON SGR EXPERIMENTS

are 1D (even for thermal bridges of the East wall which are located only 30 cm away from each other). The apparent temperature on the thermal bridges is slightly smaller than that on the sound areas: temperature contrasts are very small. From these thermal images, the mean temperature difference  $\Delta T = T_{\text{si}}^{1\text{D}} - \overline{T_{\text{si}}^{\text{tb}}}$  (or temperature contrast) between a thermal bridge and the surroundings 1D zones are calculated. The width  $L_{\text{tb}}$  of the ROIs was set such that the surface temperature field is not affected by the thermal bridges outside these regions. In practice, this correspond to  $L_{\text{tb}}$  values around 25 cm.

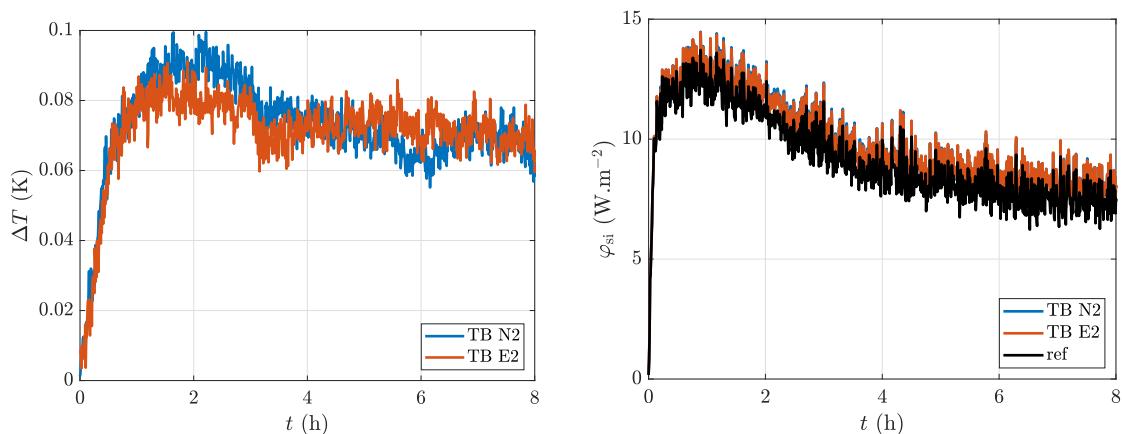


**Figure 9.18.:** Thermal images captured during an active test (Experiment 1, after 4 h of heating) and ROIs used for temperature and heat flux extrapolation. HFMs are the sound areas.

Figure 9.19a plots the temporal evolution of the surface temperature contrasts of thermal bridges N2 and E2. For clarity purposes, the curves of the other thermal bridges are not shown. These temperature differences are obtained from apparent temperature differences measured with the infrared camera. The two curves are very similar, which was expected given that all the thermal bridges are identical. It may be seen that the temperature differences due to the thermal bridges increase during the first hour of heating and then tends to stabilize (like for TB 1 and TB 2 of the CEREMA experimental campaign). The signals are not smooth at all: they suffer from random measurement noise as well as some low frequency disturbances probably due to variations in the external environment. This is due to the small SNR: the magnitude of the contrasts is below 0.1 K which is very small. In similar conditions, the temperature contrasts noted on the CEREMA setup were between 0.2 and 0.5 K, depending on the thermal bridge (see Fig 9.12). In addition, the curves of the extrapolated heat fluxes are very close, see Fig 9.19b (also expected: thermal bridges are identical). Again, the noise on the extrapolated heat fluxes is very much correlated because the noise induced by the correction term  $h \times \Delta T$  is negligible with respect to the noise on the measured heat flux  $\varphi_{1\text{D}}$  (about ten



times smaller). The heat transfer coefficient, required in the extrapolation process, is estimated to  $9.5 \pm 0.7 \text{ W.m}^{-2}.\text{K}^{-1}$  during this experiment (very similar to the values measured on the CEREMA setup).



(a) Temperature differences between thermal bridges and sound area.

(b) Extrapolated surface heat flux.

**Figure 9.19.:** Evolution of temperature difference and surface heat flux extrapolated from the sound area to thermal bridges N2 and E2 during an active test.

### 9.3.1.2. Parameter estimation

Direct model AIE<sub>2</sub> (internal and external corrections, see Chap 8) was used for the inverse method. The parameters  $\hat{\beta}$  estimated for the sound area (SA) and each studied thermal bridge are summarized in Tab 9.7. The first 10 min for the experiments were not analyzed for the parameter estimation. The corresponding model output  $\varphi_{\text{mo}}(\hat{\beta})$ , measurements  $\varphi$  and residuals are plotted in Fig 9.20. The residuals are unsigned and their magnitude correspond to the noise level: the model successfully fits the measurement data. The estimated equivalent thermal resistance  $R_2$  of the second layer (insulating material with or without metal rails) is smaller on the thermal bridges than on the sound area. However, this difference is small: it goes from 4.77 to about  $4.3 \text{ m}^2.\text{K.W}^{-1}$  (depending on the thermal bridge) which represents only a 10% reduction. The other parameters are not significantly affected by the presence of the thermal bridges. The transmittances  $\psi$  calculated from the estimated thermal resistances are also presented in Tab 9.7. Given the small differences in equivalent thermal resistance between the sound area and the thermal bridges (and the small SNR on surface temperature contrasts), the estimation uncertainty on  $\psi$  is very high: around 80%. The results are studied in further details in the next section, where several experiments are compared.

### 9.3.2. Results for all experiments

The method was applied similarly to the other experiments of the SGR campaign. Unfortunately, there was an issue with the infrared camera rotation system for

### 9.3. RESULTS ON SGR EXPERIMENTS

**Table 9.7.:** Summary of parameter estimation on the sound area and the thermal bridges (Experiment 1). The  $\psi$ -value is calculated from the estimated thermal resistances. The parameter of interest ( $R_2$ ) is in bold.

	$R_1$ ( $\text{m}^2.\text{K}.\text{W}^{-1}$ )	$b_1$ ( $\text{J}.\text{K}^{-1}.\text{m}^{-2}.\text{s}^{-1/2}$ )	<b><math>R_2</math></b> ( $\text{m}^2.\text{K}.\text{W}^{-1}$ )	$b_2$ ( $\text{J}.\text{K}^{-1}.\text{m}^{-2}.\text{s}^{-1/2}$ )	$\psi$ ( $\text{mW}.\text{m}^{-1}.\text{K}^{-1}$ )
SA (ref)	0.06	420	<b>5.15</b>	21	-
SA	0.05 $\pm$ 0.02	448 $\pm$ 71	<b>4.77</b> $\pm$ 0.24	25.1 $\pm$ 8.2	-
N1	0.06 $\pm$ 0.02	442 $\pm$ 63	<b>4.29</b> $\pm$ 0.19	24.6 $\pm$ 12.1	5.9 $\pm$ 4.1
N2	0.05 $\pm$ 0.02	459 $\pm$ 65	<b>4.17</b> $\pm$ 0.18	23.8 $\pm$ 14.2	6.7 $\pm$ 3.5
E1	0.06 $\pm$ 0.02	439 $\pm$ 58	<b>4.36</b> $\pm$ 0.21	26.9 $\pm$ 9.4	5.2 $\pm$ 4.3
E2	0.04 $\pm$ 0.02	512 $\pm$ 99	<b>4.31</b> $\pm$ 0.24	34.1 $\pm$ 5.7	4.9 $\pm$ 3.8
E3	0.05 $\pm$ 0.02	483 $\pm$ 73	<b>4.29</b> $\pm$ 0.20	27.7 $\pm$ 8.9	5.3 $\pm$ 3.7

experiments 3 and 6. Thus, the thermal bridges  $\psi$ -values could be estimated for experiments 1, 2, 4 and 5 only. The results are given in Tab 9.8. The corresponding model outputs, measurements and residuals are all presented in Appendix F.2.

There is a good reproducibility in the sense that the standard deviation between the four experiments (between 0.8 and 1.4  $\text{mW}.\text{m}^{-1}.\text{K}^{-1}$ , depending on the thermal bridge) is smaller than the estimation uncertainty (between 3.1 and 5.6  $\text{mW}.\text{m}^{-1}.\text{K}^{-1}$ ). In addition, the results are rather close to the reference values obtained in steady-state: the maximum difference is of 1.1  $\text{mW}.\text{m}^{-1}.\text{K}^{-1}$  which is about three time smaller than the measurement uncertainty.

However, as noted in the previous section, the measurement uncertainties are very high: they go from 60 to almost 100% of  $\psi$ , depending on the estimation. This is due to the small difference between the estimated equivalent thermal resistance of the thermal bridges and the sound area. In other words: the thermal bridges have a very small impact on the overall wall heat losses. This shows the limits of the proposed active method: the current experiments proved that it is not suitable for the measurement of such small thermal bridges.

Yet, the relevance of performing  $\psi$ -value measurements for such small thermal bridges is questionable. Indeed, another more sensible approach could be to include the thermal bridges in the overall wall  $U$ -value. Thus, the limitations of the present active method arise when there is no more need for a quantification of each thermal bridge individual performance.

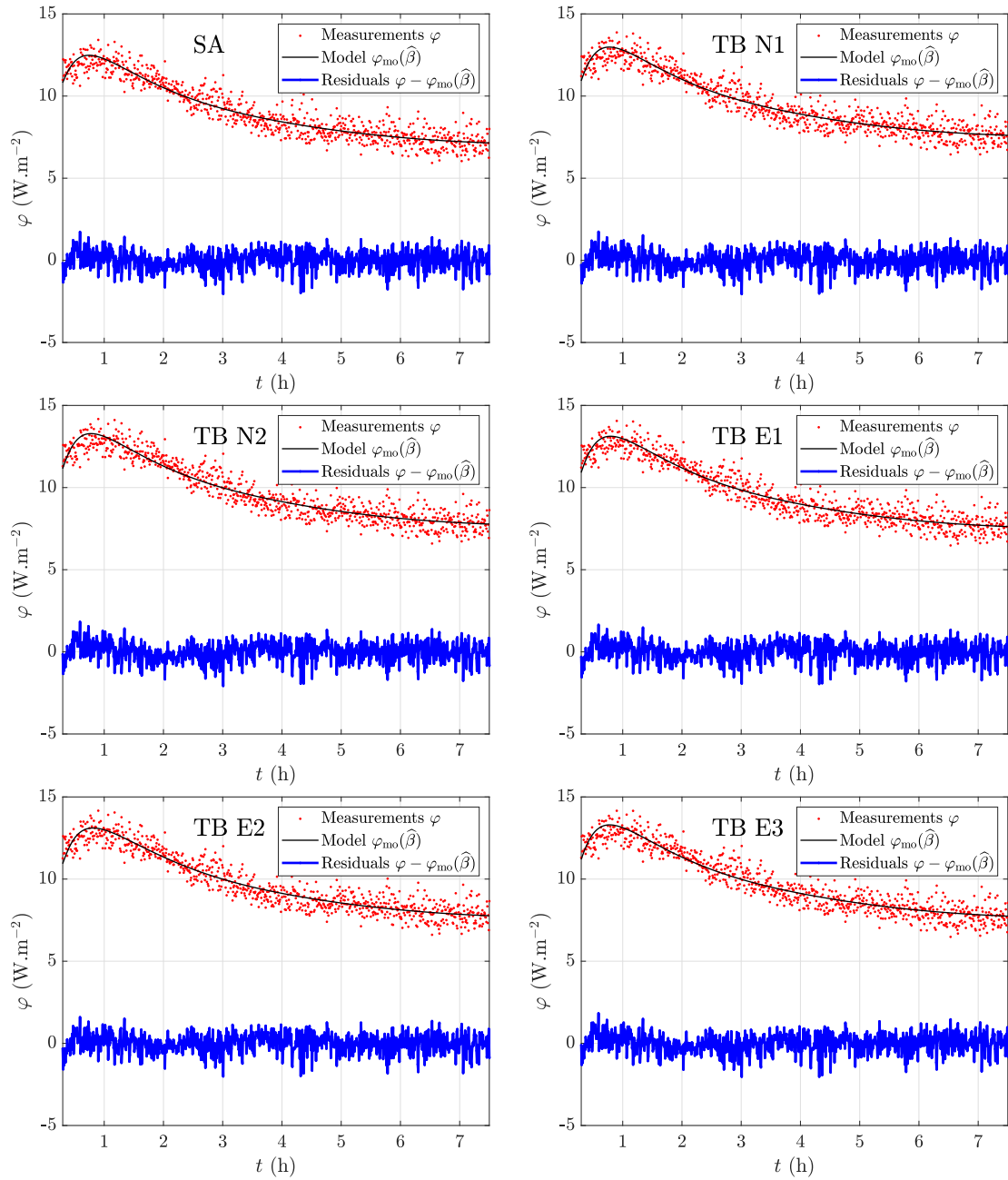
#### 9.3.3. Conclusion

Thanks to the SGR experimental campaign, the present active method for the characterization of thermal bridges could be tested *in situ*. The test cells has lightweight walls inside which metal rails generate thermal bridges. Four active tests are compared. The estimated equivalent thermal resistances of the thermal bridges are about 10% smaller than the resistance of the sound area. This leads to small thermal bridge transmission coefficients: 5  $\text{mW}.\text{m}^{-1}.\text{K}^{-1}$  and very high relative uncertainty of estimation: around 80%. The standard deviation of all the results (for

**Table 9.8.:** Summary of estimated  $h$  and  $\psi$  values for each studied thermal bridge and experiments 1, 2, 4 and 5. The reference values were obtained in steady-state (see Chap 8).

		Experiment				average	standard deviation	ref value
		1	2	4	5			
$h$ (W.m <sup>-2</sup> .K <sup>-1</sup> )		9.5 ±0.7	8.6 ±0.6	8.2 ±0.7	7.9 ±0.9	8.5	0.7	-
$\psi$	N1	5.9 ±4.1	3.7 ±3.6	4.1 ±4.3	6.7 ±4.5	5.1	1.4	4.1
	N2	6.7 ±3.5	5.0 ±3.1	6.5 ±4.1	3.7 ±3.7	5.5	1.4	5.0
	E1	5.2 ±4.3	4.2 ±3.8	3.4 ±4.8	5.8 ±5.6	4.6	1.1	5.7
(mW.m <sup>-1</sup> .K <sup>-1</sup> )	E2	4.9 ±3.8	3.9 ±3.1	5.7 ±3.6	4.8 ±3.9	4.8	0.8	4.3
	E3	5.3 ±3.7	3.5 ±3.3	6.0 ±3.9	5.4 ±4.1	5.1	1.1	4.7

the five studied thermal bridges and the four experiments) is lower: around 25%. Also, the estimated  $\psi$ -values are in rather good agreement with the reference values obtained in steady state: the relative difference is below 30%. As a conclusion, the present active method is able to estimate *in situ* the equivalent thermal resistance of a wall with a thermal bridge. However, it is not applicable for the estimation of  $\psi$ -values of thermal bridges which are as small as those in the SGR setup. This is not seen as a limitation because the presence of such small thermal bridges could be advantageously included in the overall  $U$ -value.



**Figure 9.20.:** Comparison of measurements and model output after parameter estimation (Experiment 1).

## 9.4. Conclusion

This chapter proposes an active method for the *in situ* measurement of (i) a non-homogeneous wall thermal resistance and (ii) thermal bridge transmission coefficients  $\psi$  in a building. It is a generalization of the method originally design for the characterization of a homogeneous wall presented in Chap 8. This method may be used on a non-homogeneous wall (with one or several thermal bridges) by working with space averages of the surface temperature and heat flux. This enables to estimate an equivalent thermal resistance. The surface temperature and heat flux fields on the non-homogeneous wall are measured by extrapolating contact measurements made on a nearby sound area. As presented in Chap 5, the extrapolation process is based on the quantification of surface temperature differences with infrared thermography and of the total heat transfer coefficient using a “*h*-meter”. A tabulated value may be assigned to the wall surface emissivity: temperature difference measurements are less sensitive to this quantity than absolute temperature measurements with IRT.

The method has the advantage of being almost non-intrusive: very few contact sensors are needed and they are not placed on thermal bridges but on a nearby zone. In addition, because only variations in surface heat fluxes and temperatures are analyzed, the method is applicable whatever the external temperature mean value. It may be either above or below the internal temperature. However, this method has several limitations. First, a sound area is required on the wall to fix a HFM: surface heat fluxes are extrapolated from this reference. If the distance between thermal bridges is not sufficient for the heat transfers to be 1D at least on one location of the wall, no reference heat flux contact measurement is possible. Second, the magnitude of external temperature variations should not be too large. This limitation is less restrictive as the CEREMA experimental campaign showed that the method is robust to a 15 K external temperature variation in 16 h (which simulates very fast weather variations) for the considered wall.

Third, this method is not applicable for external insulation systems. Indeed, the thermal load must take place on the side of the insulation layers to maximize sensitivity to the desired thermal resistance and to avoid lateral losses. As in the previous chapters, the main features of the method are summarized in Tab 9.9.

The method was validated on the CEREMA experimental campaigns. It showed a good reproducibility and a good agreement with steady-state measurements. The SGR measurements enabled to show the limits of the method. Indeed, the thermal bridges of this setup are very small, so the  $\psi$ -coefficients are estimated with a very high relative uncertainty. The present active method is therefore not adapted for the measurement such small  $\psi$ -values (around  $5 \text{ mW}\cdot\text{m}^{-1}\cdot\text{K}^{-1}$ ) on this type of lightweight highly insulated walls. For such small thermal irregularities (of defaults), it might be more sensible to include the heat losses due to thermal bridges in the overall wall  $U$ -value. In other words, the limitations of the present active method arise when there is no more need for a quantification of each thermal bridge individual performance.

**Table 9.9.:** Summary of active non-homogeneous wall characterization method.

Hypotheses	Equipment	Comments
<ul style="list-style-type: none"><li>• 1D heat transfers on a sound area</li><li>• small <math>\Delta T</math></li><li>• uniform <math>h</math> and <math>T_{op}</math></li><li>• uniform <math>\varepsilon</math></li></ul>	<ul style="list-style-type: none"><li>• temperature sensors</li><li>• heat flux meters</li><li>• <math>h</math>-meter</li><li>• acquisition system</li><li>• infrared camera</li></ul>	<p>Pros</p> <ul style="list-style-type: none"><li>• fast (4 to 6 hours)</li><li>• almost non-intrusive</li><li>• robust to varying external conditions (but influence of solar heat flux not investigated)</li><li>• <math>T_{op}</math> is not required</li></ul> <p>Cons</p> <ul style="list-style-type: none"><li>• requires a nearby sound area (the size of a HFM)</li><li>• needs to know <math>\varepsilon</math> (but a tabulated value is enough)</li><li>• not sensitive to thermal bridges with low transmission coefficients</li></ul>



# 10. Conclusion

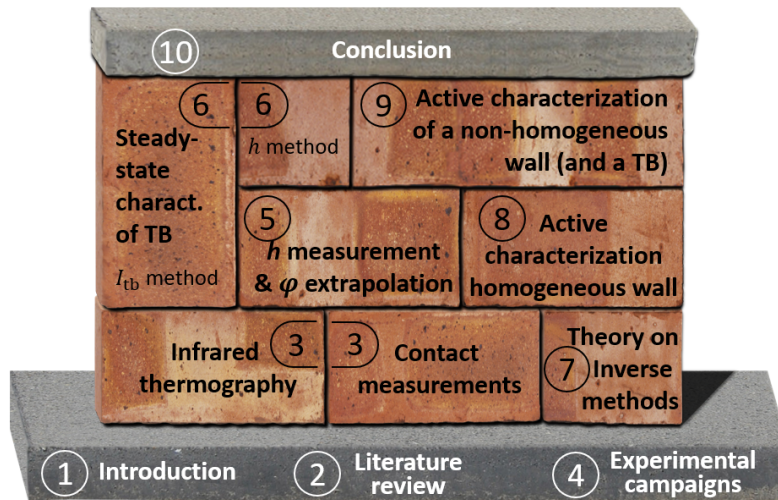


Figure 10.1.: Illustration of thesis plan.

## 10.1. Context and objectives

Thermal insulation of buildings is a cornerstone of the reduction of greenhouse gas emissions. When *in situ* measurements are performed, the results usually show some discrepancies with theoretical predictions. To assess this so-called “performance gap”, the contribution of each building element to the overall heat losses is needed. In particular, the heat losses due to thermal bridges are most of the time not well known. Aside from increasing the building energy demand, thermal bridges tend to alter the comfort of occupants and may cause mould growth issues. Today, there is a lack of fast and reliable methods for the *in situ* characterization of a wall or a thermal bridge.

Many methods were developed in the past decades for the *in situ* assessment of a wall thermal transmittance ( $U$ -value). Yet, the only standardized techniques are based on steady-state assumptions which are seldomly achieved in a building. As a consequence, they require a high and constant temperature difference between the interior and exterior environments. They also involve very long measurements to compensate for variations in the external temperature. The *in situ* characterization of a thermal bridge has been much less addressed in past studies. The only standards apply to numerical simulations in which the exact geometry and thermal properties



of each material must be known. The few measurements techniques applied *in situ* are once again based on a steady-state hypothesis.

In this context, the present thesis focused on the development of active methods for the assessment of the thermal performances of building envelope elements (thermal bridges and walls). In practice, they aim at quantifying the thermal resistance  $R$  (or the thermal transmittance  $U$ ) of a wall and the  $\psi$  or  $\chi$  coefficient of a thermal bridge. The active approach, consisting in applying an artificial thermal load to the wall and analyzing its transient response, enables to be much less demanding in terms of weather condition and measurement duration than steady-state methods.

## 10.2. Summary of developments

Here are summarized the main developments of the thesis. The presented methods were validated in laboratory conditions, in a climate chamber, as well as *in situ* thanks to four experimental campaigns. The walls tested were highly insulated (thermal resistance between 3 and 5.2 m<sup>2</sup>.K.W<sup>-1</sup>).

Some of the methods required the *in situ* measurement of the total heat transfer coefficient  $h$  on a building wall. Therefore, a study dedicated to this topic compared five different methods to measure this coefficient. Two of them are inspired from the literature and the other three were developed in this thesis. The heat transfer coefficient, coupled with infrared thermography, is useful to extrapolate the heat flux measured with a contact sensor at one specific location to the rest of the wall.

The thermal resistance  $R$  of a homogeneous wall was measured in steady-state following guidelines from existing standards. For the characterization of a thermal bridge, two steady-state methods were compared. The “ $I_{tb}$  method” is a variation of an already existing technique. It does not require the knowledge of the wall emissivity  $\varepsilon$  nor the total heat transfer coefficient  $h$  but relies on many assumptions which makes it only applicable indoor, in a well insulated building. The “ $h$  method”, which was developed in this thesis, is based on fewer assumptions: the air and mean radiant temperatures do not have to be equals. However, it needs the knowledge of both  $\varepsilon$  and  $h$ . These steady-state methods are well adapted to measurements in a controlled environment (laboratory, climate chamber, ...) and were useful to obtain reference values of the desired coefficients ( $R$ ,  $\psi$ ,  $\chi$ , ...). Active methods are more suited to *in situ* measurements.

An active method was first developed for the *in situ* measurement of a homogeneous wall thermal resistance  $R$ . It consists in rapidly heating the indoor air for a few hours thanks to electric fan heaters. This approach is easy to implement *in situ* and provides a rather uniform heating of the walls. The wall thermal properties are then estimated using an inverse method. The ideal operating conditions and direct model definition were thoroughly studied. Several model reduction steps were required to improve the well-posedness of the inverse problem. Both temperature and heat flux are measured on the wall surface (with contact sensors). This enables to remove the heat transfer coefficients from the unknown parameters to estimate and to avoid the very complex measurement of operative temperatures. White-box models and

black-box ARX models were compared. The white-box approach proved more robust to varying weather conditions. This method only takes a few hours (typically five, depending on the wall) and is applicable whatever the season and the weather. However, it is more complex to implement than a steady-state method. In addition, it is based on local measurements: the results might not be representative of the whole wall.

This last limitation was removed: the active method was extended to non-homogeneous walls and thermal bridges. The generalization was made by working with the space average of surface heat fluxes and temperatures. The thermal properties estimated by the inverse method become those of an equivalent homogeneous wall having the same thermal behavior than the real non-homogeneous wall. The surface heat flux and temperature fields were measured by extrapolating contact measurements thanks to the quantification of the total heat transfer coefficient  $h$  and infrared thermography (and knowledge of the wall emissivity  $\varepsilon$ ).

The main results of this thesis were published in scientific papers and presented in conferences. The corresponding references are summarized in Appendix G.

## 10.3. Limitations

The active methods developed in this thesis need the heat transfers to be 1D at least on one location of the wall. If no sound area can be found (because of too close thermal bridges or because of edge effects), no HFM can be implemented on the wall. Given that the surface heat flux field on a non-homogeneous wall (or a thermal bridge) is extrapolated from contact measurements, the developed active method is not applicable without a sound area. A solution would be to measure the absolute surface heat flux with IRT only. However, this requires knowledge of the mean radiant temperature, the wall emissivity, the convective heat transfer coefficient, and the average air temperature. This would increase the measurement uncertainties. Steady-state methods used for the characterization of a thermal bridge also require a sound area (for the calculation of the incidence factor mainly).

The measurement of temperature and heat flux fields on the surface of a non homogeneous wall (extrapolation procedure) lies on homogeneity assumptions. First, the wall infrared emissivity  $\varepsilon$  must be uniform. If the emissivity is not the same on the thermal bridge and the sound area, the measurement of true temperature differences with IRT is still possible but it is more complex. The measurement of the mean radiant temperature becomes compulsory and the uncertainties are higher. In addition, both the total heat transfer coefficient  $h$  and the operative temperature  $T_{op}$  are supposed uniform as well. This condition imposes the sound area to be close to the studied thermal bridge, preferably at the same altitude (because of air stratification). This limits the type of thermal bridge which may be characterized with the proposed methods.

It was also showed that the proposed method cannot estimate accurately the thermal transmittance of small thermal bridges. The  $\psi$  (or  $\chi$ ) coefficient is estimated from the difference in equivalent thermal resistance between a sound area and a

thermal bridge. If the relative difference between these resistances is small, then the uncertainty on the  $\psi$  (or  $\chi$ ) value will be high. As an example, for thermal bridges with a  $\psi$ -value around  $5 \text{ mW}\cdot\text{m}^{-1}\cdot\text{K}^{-1}$  inside a wall of thermal resistance higher than  $5 \text{ m}^2\cdot\text{K}\cdot\text{W}^{-1}$ , the estimation uncertainties were around 80%. The measurement method is therefore not relevant in this configuration. Yet, this limitations arises when the need for a quantification of each thermal bridge individual performance is questionable. Another maybe more sensible approach could be to include the thermal bridges in the overall wall  $U$ -value.

## 10.4. Next steps

In order to reduce the uncertainty on the estimated equivalent thermal resistance, one should try to reduce the measurement noise on the surface heat flux recorded by the HFM. This could be achieved by (i) using a bigger sensor (but a bigger sound area would be needed and the sensor might become more intrusive), (ii) using a different thermal load (the measurement noise was mainly due to air movements induced by the electric fan heaters). It would also be interesting to study the possibility to apply the inverse technique to measurements made during the free-cooling phase during which the signal to noise ratio is much better. This could significantly reduce the estimation uncertainties on the wall thermal resistance.

The camera used in this thesis had a coold sensors and thus a low sensitivity, but such sensors are expensive. Thus, the methods presented in this study (both steady-state and active ones) should be tested with a more affordable equipment, such as a microbolometer infrared camera.

The measurement methods developed should be validated on more types of walls. The  $U$ -value active measurement technique was validated on a load-bearing wall internally insulated and a lightweight insulated wall. Also, every wall had the same facing layer: a gypsum board. As it is, the method is hardly applicable to externally insulated walls. Indeed, the thermal load and the measurements must be made on the insulated side of the wall. Otherwise, lateral losses in the heavy layers would prevent the heat from probing the insulating material. In addition, the sensitivity to the insulation thermal resistance would be very low (ill-posed problem). Yet, it is not possible to heat up the external air by 20 degrees in a few hours: another type of thermal load would have to be used. Furthermore, outdoor measurements pose many practical problems. The application of the method to ventilated walls might be complicated as well.

The methods for the quantification of thermal bridge performances (both steady-sate and active techniques) should also be tested on more types of irregularities. In this thesis, material-related thermal bridges were studied (mainly mechanical systems to hold insulating materials). Linear and point irregularities could be characterized. However, the characterization of structural thermal bridges is more challenging. Given their high thermal inertia, their large dimensions, and because they may only be revealed by outdoor measurements.

In the objective of making the active methods applicable in most situations, it would be interesting to investigate the possibility to work with a cooling thermal load instead of a heating one. Indeed, in a warm climate or a warm season, it might not be sensible to heat up the internal air by 20 degrees. In theory, the protocol remains unchanged: a polynomial is fitted to the surface temperature measurements and the parameter estimation is performed on the internal surface heat flux. Neither the sign of this heat flux nor the shape of the temperatures imposes a limit to the method, as long as the signal to noise ratio is sufficient.

The  $h$  measurement methods developed in this thesis were only validated indoor. It would be interesting to apply them on outdoor surfaces. For most method, no specific difficulty is anticipated for an external application.

Finally, the quantification of the estimation uncertainties could be improved. Indeed, depending on the type of wall considered and the weather conditions, some parameters of the direct model might have to be supposed perfectly known. The values assigned to these parameters may be default or measured values. Either way, these parameters are known with non-null uncertainties. The latter cannot be propagated to the uncertainty on the estimated wall thermal resistance with the proposed inverse method. Furthermore, in the case of a non-homogeneous wall, the heat flux used for the estimation is extrapolated from contact measurements. The uncertainties due to this extrapolation process (mainly the measurement uncertainty on the heat transfer coefficient  $h$ ) are not taken into account in the calculation of the uncertainties on  $\psi$  and  $\chi$  coefficients. Bayesian inferences could be used to include these sources of uncertainties in the analysis. Within the Bayesian framework, every quantity is a random variable. In other words, it is not possible to allocate a perfectly known value to a quantity. This inaccessible single value is replaced by a probability density function defined by an expectancy and a covariance matrix.

The methods were applied in a research context. It would be interesting to automatize some calculations for the methods to be easily applicable in an industrial context. Further developments would be necessary to develop a more user-friendly program. For instance, it could be possible to choose the direct model among a list of predefined models.



# References

- [1] L. Gynther, B. Lappillone, and K. Pollier. Energy efficiency trends and policies in the household and tertiary sectors. *An analysis based on the ODYSSEE and MURE databases*, 2015.
- [2] Commissariat général au développement durable. Chiffres clés du climat France, Europe et Monde. 2019 (in French).
- [3] P. De Wilde. The gap between predicted and measured energy performance of buildings: A framework for investigation. *Automation in Construction*, 41:40–49, 2014, doi:<https://doi.org/10.1016/j.autcon.2014.02.009>.
- [4] D. Johnston, D. Miles-Shenton, and D. Farmer. Quantifying the domestic building fabric 'performance gap'. *Building Services Engineering Research and Technology*, 36(5):614–27, 2015, doi:<https://doi.org/10.1177/0143624415570344>.
- [5] A.C. Menezes, A. Cripps, D. Bouchlaghem, and R. Buswell. Predicted vs. actual energy performance of non-domestic buildings: Using post-occupancy evaluation data to reduce the performance gap. *Applied energy*, 97:355–364, 2012, doi:<https://doi.org/10.1016/j.apenergy.2011.11.075>.
- [6] A. Stafford, M. Bell, and C. Gorse. Building Confidence – A working paper. Report 008, The Centre for Low Carbon Futures, March 2012.
- [7] J.-P. Monchau, V. Feuillet, L. Ibos, and Y. Candau. Comparaison de méthodes de mesure de résistance thermique in-situ de parois de bâtiment: essais sur un immeuble d'habitation occupé. In *23ème Congrès annuel de la Société Française de Thermique*, 2015, (in French).
- [8] L. Ibos, J.-P. Monchau, V. Feuillet, and Y. Candau. A comparative study of in-situ measurement methods of a building wall thermal resistance using infrared thermography. In *Twelfth International Conference on Quality Control by Artificial Vision 2015*, volume 9534, page 95341I. International Society for Optics and Photonics, 2015.
- [9] D. Pajani. Thermographie du bâtiment - Diagnostic et applications. *Techniques de l'ingénieur*, R2743, 2014, (in French).
- [10] S. Farkh. Les ponts thermiques dans le bâtiment – Mieux les connaître pour mieux les traiter. Technical report, Centre Scientifique et Technique du Bâtiment (CSTB), 2014, (in French).
- [11] T.G. Theodosiou and A.M. Papadopoulos. The impact of thermal bridges on the energy demand of buildings with double brick wall constructions. *Energy and Buildings*, 40(0):2083–2089, 2008, doi:<https://doi.org/10.1016/j.enbuild.2008.06.006>.

- 
- [12] G. Evola, G. Margani, and L. Marletta. Energy and cost evaluation of thermal bridge correction in Mediterranean climate. *Energy and Buildings*, 43(9):2385–2393, 2011, doi:<https://doi.org/10.1016/j.enbuild.2011.05.028>.
- [13] A.B. Larbi. Statistical modelling of heat transfer for thermal bridges of buildings. *Energy and Buildings*, 37(0):945–951, 2005, doi:<https://doi.org/10.1016/j.enbuild.2004.12.013>.
- [14] X. Maldague. Theory and practice of infrared technology for nondestructive testing. *Ed. Wiley-Intersciences*, New York, 2001.
- [15] ISO 9869-1:2014. Thermal insulation – Building elements – In-situ measurement of thermal resistance and thermal transmittance – Part 1: Heat flow meter method. *International Standards Organisation*, 2014.
- [16] Les essentiels de l’habitat - Introduction à la thermique du bâtiment. *Saint-Gobain*, 2016, (in French).
- [17] L. Whale. Thermal Bridging Guide. *Zero Carbon Hub*, 2016.
- [18] ISO 14683:2007. Thermal bridges in building construction - Linear thermal transmittance - Simplified methods and default values. *International Standards Organisation*, 2007.
- [19] F. Asdrubali, G. Baldinelli, and F. Bianchi. A quantitative methodology to evaluate thermal bridges in buildings. *Applied Energy*, 97(0):365–73, 2012, doi:<https://doi.org/10.1016/j.apenergy.2011.12.054>.
- [20] F. Bianchi, A.L. Pisello, G. Baldinelli, and F. Asdrubali. Infrared Thermography Assessment of Thermal Bridges in Building Envelope: Experimental Validation in a Test Room Setup. *Sustainability*, 6(10):7107, 2014, doi:<https://doi.org/10.3390/su6107107>.
- [21] I. Nardi, D. Ambrosini, D. Paoletti, and S. Sfarra. Combining Infrared Thermography and Numerical Analysis for Evaluating Thermal Bridges In Buildings: A Case Study. *International Journal of Engineering Research and Applications*, 5(1):67–76, 2015.
- [22] G. Baldinelli, F. Bianchi, A. Rotili, D. Costarelli, M. Seracini, G. Vinti, F. Asdrubali, and L. Evangelisti. A model for the improvement of thermal bridges quantitative assesment by infrared thermography. *Applied Energy*, 211:854–864, 2018, doi:<https://doi.org/10.1016/j.apenergy.2017.11.091>.
- [23] D. Pajani. Surface équivalente d’irrégularité ou de défaut (Seid) et mesure du U par la méthode du Seid. In *Actes de la conférence Thermogram*, 2011, (in French).
- [24] T. Taylor, J. Counsell, and S. Gill. Combining thermography and computer simulation to identify and assess insulation defects in the construction of building façades. *Energy and Buildings*, 76:130–142, 2014, doi:<https://doi.org/10.1016/j.enbuild.2014.02.080>.
- [25] T.I Ward. *Assessing the effects of thermal bridging at junctions and around openings*. Number 1. 2006.

- [26] SAP 2012 – The Government’s Standard Assessment Procedure for Energy Rating of Dwellings. Technical Report version 9.92, Building Research Establishment (BRE), Watford, UK, October 2013.
- [27] ISO 10211:2017. Thermal bridges in building construction - Heat flows and surface temperatures - Detailed calculations. *International Standards Organisation*, (14683), 2017.
- [28] C.A. Balaras and A.A. Argiriou. Infrared thermography for building diagnostics. *Energy and Buildings*, 34(2):171–83, 2002, doi:[https://doi.org/10.1016/S0378-7788\(01\)00105-0](https://doi.org/10.1016/S0378-7788(01)00105-0).
- [29] A. Kylii, P.A. Fokaides, P. Christou, and S.A. Kalogirou. Infrared thermography (IRT) applications for building diagnostics: A review. *Applied Energy*, 134(0):531–49, 2014, doi:<https://doi.org/10.1016/j.apenergy.2014.08.005>.
- [30] E. Lucchi. Applications of the infrared thermography in the energy audit of buildings: A review. *Renewable and Sustainable Energy Reviews*, 82:3077–3090, 2018, doi:<https://doi.org/10.1016/j.rser.2017.10.031>.
- [31] I. Nardi, E. Lucchi, T. de Rubeis, and D. Ambrosini. Quantification of heat energy losses through the building envelope: A state-of-the-art analysis with critical and comprehensive review on infrared thermography. *Building and Environment*, 2018, doi:<https://doi.org/10.1016/j.buildenv.2018.09.050>.
- [32] B. Lehmann, K.G. Wakili, Th. Frank, B.V. Collado, and Ch Tanner. Effects of individual climatic parameters on the infrared thermography of buildings. *Applied Energy*, 110:29–43, 2013, doi:<https://doi.org/10.1016/j.apenergy.2013.03.066>.
- [33] S. Datcu, L. Ibos, Y. Candau, and S. Matteï. Improvement of building wall surface temperature measurements by infrared thermography. *Infrared physics & technology*, 46(6):451–467, 2005, doi:<https://doi.org/10.1016/j.infrared.2005.01.001>.
- [34] E. Barreira and V.P. de Freitas. Evaluation of building materials using infrared thermography. *Construction and building materials*, 21(1):218–224, 2007, doi:<https://doi.org/10.1016/j.conbuildmat.2005.06.049>.
- [35] ISO 13187:1999. Thermal Performance of Buildings - Qualitative Detection of Thermal Irregularities in Building Envelopes - Infrared method (ISO 6781:1983 Modified). *International Standards Organisation*, 1999.
- [36] S.M. Ocaña, I.C. Guerrero, and I.G. Requena. Thermographic survey of two rural buildings in Spain. *Energy and Buildings*, 36(6):515–523, 2004, doi:<https://doi.org/10.1016/j.enbuild.2003.12.012>.
- [37] N. Garcez, N. Lopes, J. de Brito, and J. Silvestre. System of inspection, diagnosis and repair of external claddings of pitched roofs. *Construction and Building Materials*, 35:1034–1044, 2012, doi:<https://doi.org/10.1016/j.conbuildmat.2012.06.047>.
- [38] A. Menezes, M.G. Gomes, and I. Flores-Colen. In-situ assessment of physical performance and degradation analysis of render-



- ing walls. *Construction and Building Materials*, 75:283–292, 2015, doi:<https://doi.org/10.1016/j.conbuildmat.2014.11.039>.
- [39] M. Fox, D. Coley, S. Goodhew, and P. De Wilde. Thermography methodologies for detecting energy related building defects. *Renewable and Sustainable Energy Reviews*, 40:296–310, 2014, doi:<https://doi.org/10.1016/j.rser.2014.07.188>.
- [40] M. Fox, D. Coley, S. Goodhew, and P. De Wilde. Time-lapse thermography for building defect detection. *Energy and Buildings*, 92:95–106, 2015, doi:<https://doi.org/10.1016/j.enbuild.2015.01.021>.
- [41] M. Fox, S. Goodhew, and P. De Wilde. Building defect detection: External versus internal thermography. *Building and Environment*, 105:317–331, 2016, doi:<https://doi.org/10.1016/j.buildenv.2016.06.011>.
- [42] ISO 6781-3:2015. Performance of buildings - Detection of heat, air and moisture irregularities in buildings by infrared methods - Part 3: Qualifications of equipment operators, data analysts and report writers. *International Standards Organisation*, 2015.
- [43] F. Asdrubali, G. Baldinelli, F. Bianchi, D. Costarelli, A. Rotili, M. Seracini, and G. Vinti. Detection of thermal bridges from thermographic images by means of image processing approximation algorithms. *Applied Mathematics and Computation*, 317:160–171, 2018, doi:<https://doi.org/10.1016/j.amc.2017.08.058>.
- [44] D. Costarelli and G. Vinti. Approximation by nonlinear multivariate sampling Kantorovich type operators and applications to image processing. *Numerical Functional Analysis and Optimization*, 34(8):819–844, 2013, doi:<https://doi.org/10.1080/01630563.2013.767833>.
- [45] I. Garrido, S. Lagüela, T. Arias, and J. Balado. Thermal-based analysis for the automatic detection and characterization of thermal bridges in buildings. *Energy and Buildings*, 158:1358–1367, 2018, doi:<https://doi.org/10.1016/j.enbuild.2017.11.031>.
- [46] J. Cereijo, S. Lagüela, D. Roca, J. Martínez, and H. Lorenzo. Automatic detection of thermal bridges in thermographic building inspections. In *40th IAHS World Congress on Housing, Sustainable Housing Construction*, 2014.
- [47] E. Grinzato, G. Cadelano, and P. Bison. Moisture map by IR thermography. *Journal of Modern Optics*, 57(18):1770–1778, 2010, doi:<https://doi.org/10.1080/09500341003731597>.
- [48] P.G. Bison, M.D. Bardeschi, E. G Grinzato, T. T Kauppinen, E. Rosina, and G. Tucci. Survey of facades based on thermal scanning: Palazzo della Ragione, Milan, Italy. In *Thermosense XVIII: An International Conference on Thermal Sensing and Imaging Diagnostic Applications*, volume 2766, pages 55–64. International Society for Optics and Photonics, 1996.
- [49] Z. Li, W. Yao, S. Lee, C. Lee, and Z. Yang. Application of infrared thermography technique in building finish evaluation. *Journal of Nondestructive Evaluation*, 19(1):11–19, 2000, doi:<https://doi.org/10.1023/A:1006612023656>.

- [50] S.S. de Freitas, V.P. de Freitas, and E. Barreira. Detection of façade plaster detachments using infrared thermography—A nondestructive technique. *Construction and Building Materials*, 70:80–87, 2014, doi:<https://doi.org/10.1016/j.conbuildmat.2014.07.094>.
- [51] J. Laranjeira, N. Simões, I. Simões, A. Tadeu, and C. Serra. Passive thermography evaluation of bonding defects in adhered ceramic tiling: experimental and in-situ assessments. In *12th International Conference on Quantitative InfraRed Thermography (QIRT 2014)*, Bordeaux, France, July 7-11 2014.
- [52] C. Ibarra-Castanedo, S. Sfarra, M. Klein, and X. Maldague. Solar loading thermography: Time-lapsed thermographic survey and advanced thermographic signal processing for the inspection of civil engineering and cultural heritage structures. *Infrared Physics & Technology*, 82:56–74, 2017, doi:<https://doi.org/10.1016/j.infrared.2017.02.014>.
- [53] E. Grinzato, V. Vavilov, and T. Kauppinen. Quantitative infrared thermography in buildings. *Energy and Buildings*, 29(1):1–9, 1998, doi:[https://doi.org/10.1016/S0378-7788\(97\)00039-X](https://doi.org/10.1016/S0378-7788(97)00039-X).
- [54] E. Grinzato, V. Vavilov, and T. Kauppinen. Quantitative infrared thermography technique in building finish evaluation. *Journal of Non-destructive Evaluation*, 12:9–11, 2000.
- [55] K. Kurita, M. Oyado, H. Tanaka, and S. Tottori. Active infrared thermographic inspection technique for elevated concrete structures using remote heating system. *Infrared Physics & Technology*, 52(5):208–213, 2009, doi:<https://doi.org/10.1016/j.infrared.2009.07.010>.
- [56] C. Maierhofer, R. Arndt, M. Röllig, C. Rieck, A. Walther, H. Scheel, and B. Hillemeier. Application of impulse-thermography for non-destructive assessment of concrete structures. *Cement and Concrete Composites*, 28(4):393–401, 2006, doi:<https://doi.org/10.1016/j.cemconcomp.2006.02.011>.
- [57] T. Taylor, J. Counsell, S. Gill, and G. Oakley. Assessing the severity of workmanship defects using thermography and 2-d and 3-d heat transfer models. In *Proc. of Sustainable Building Conference (SB13)*, Graz (Austria), September 2013.
- [58] R. Douguet, T.T. Ha, V. Feuillet, J. Meulemans, and L. Ibos. A novel experimental method for the in situ detection of thermal bridges in building envelopes based on active infrared thermography and singular value decomposition analysis. *The 14th Quantitative InfraRed Thermography Conference*, Berlin, Germany, 25 to 29 June 2018., doi:<https://doi.org/10.21611/qirt.2018.029>.
- [59] F. Asdrubali and G. Baldinelli. Thermal transmittance measurements with the hot box method: Calibration, experimental procedures, and uncertainty analyses of three different approaches. *Energy and buildings*, 43(7):1618–1626, 2011, doi:<https://doi.org/10.1016/j.enbuild.2011.03.005>.
- [60] ISO 8990:1996. Thermal insulation – Determination of steady-state thermal

- transmission properties – Calibrated and guarded hot box. *International Standards Organisation*, 1996.
- [61] American Society for Testing and Materials. ASTM C1363-05: Standard Test Method for Thermal Performance of Building Materials and Envelope Assemblies by Means of a Hot Box Apparatus. *West Conshohocken, PA*, 2005.
- [62] Interstate Standard of Russian Federation. GOST 26602.1-99, Windows and doors. Methods of determination of resistance of thermal transmission. 1999.
- [63] K. Martin, A. Campos-Celador, C. Escudero, I. Gomez, and J.M. Sala. Analysis of a thermal bridge in a guarded hot box testing facility. *Energy and Buildings*, 50:139–49, 2012, doi:<https://doi.org/10.1016/j.enbuild.2012.03.028>.
- [64] M. O’Grady, A.A. Lechowska, and A.M. Harte. Infrared thermography technique as an in-situ method of assessing heat loss through thermal bridging. *Energy and Buildings*, 135:20–32, 2017, doi:<https://doi.org/10.1016/j.enbuild.2016.11.039>.
- [65] S.W. Churchill and H. HS Chu. Correlating equations for laminar and turbulent free convection from a vertical plate. *International journal of heat and mass transfer*, 18(11):1323–1329, 1975, doi:[https://doi.org/10.1016/0017-9310\(75\)90243-4](https://doi.org/10.1016/0017-9310(75)90243-4).
- [66] M. O’Grady, A. A Lechowska, and A. M Harte. Quantification of heat losses through building envelope thermal bridges influenced by wind velocity using the outdoor infrared thermography technique. *Applied energy*, 208:1038–1052, 2017, doi:<https://doi.org/10.1016/j.apenergy.2017.09.047>.
- [67] I. Benko. Quantitative analysis of thermal bridges of structures through infrared thermographs. In *6th International Conference on Quantitative InfraRed Thermography (QIRT 2002)*, Dubrovnik (Croatia), September 2002.
- [68] R. Albatici and A.M Tonelli. Infrared thermovision technique for the assessment of thermal transmittance value of opaque building elements on site. *Energy and Buildings*, 42(11):2177–2183, 2010, doi:<https://doi.org/10.1016/j.enbuild.2010.07.010>.
- [69] E. Cuce and P.M. Cuce. The impact of internal aerogel retrofitting on the thermal bridges of residential buildings: An experimental and statistical research. *Energy and Buildings*, 116:449–54, 2016, doi:<https://doi.org/10.1016/j.enbuild.2016.01.033>.
- [70] A. Aïssani, A. Chateauneuf, J.-P. Fontaine, and Ph. Audebert. Quantification of workmanship insulation defects and their impact on the thermal performance of building facades. *Applied Energy*, 165:272–84, 2016, doi:<https://doi.org/10.1016/j.apenergy.2015.12.040>.
- [71] H. Heinrich and K. Dahlem. Thermography of low energy buildings. In *Proc. of International Conference on Quantitative InfraRed Thermography (QIRT 2000)*, Reims (France), July 2008.
- [72] L. Zalewski, S. Lassue, D. Rousse, and K. Boukhalfa. Experimental and numerical characterization of thermal bridges in prefabricated build-

- ing walls. *Energy Conversion and Management*, 51(12):2869–77, 2010, doi:<https://doi.org/10.1016/j.enconman.2010.06.026>.
- [73] F. Ascione, N. Bianco, R.F. De Masi, G. M. Mauro, M. Musto, and G.P. Vanoli. Experimental validation of a numerical code by thin film heat flux sensors for the resolution of thermal bridges in dynamic conditions. *Applied Energy*, 124:213–22, 2014, doi:<https://doi.org/10.1016/j.apenergy.2014.03.014>.
- [74] F. Ascione, N. Bianco, R.F. De Masi, F. de’Rossi, and G.P. Vanoli. Simplified state space representation for evaluating thermal bridges in building: Modelling, application and validation of a methodology. *Applied Thermal Engineering*, 61(2):344–354, 2013, doi:<https://doi.org/10.1016/j.applthermaleng.2013.07.052>.
- [75] J.E. Seem, S.A. Klein, W.A. Beckman, and J.W. Mitchell. Transfer function for efficient calculation of multidimensional transient heat transfer. *ASME Journal of Heat Transfer*, 111(0):5–12, 1989, doi:<https://doi.org/10.1115/1.3250659>.
- [76] A. Wrobel and T. Kisilewicz. Detection of thermal bridges - aims, possibilities and conditions. In *Proc. of 9th International Conference on Quantitative InfraRed Thermography (QIRT 2008)*, Krakow (Poland), July 2008.
- [77] C. Serra, A. Tadeu, N. Simões, and I. Simões. Simulation of heat diffusion in multi-layered construction systems for active IRT data analysis. In *Proc. of 12th International Conference on Quantitative InfraRed Thermography (QIRT 2014)*, Bordeaux (France), July 2014.
- [78] A. Tadeu and N. Simões. Three-dimensional fundamental solutions for transient heat transfer by conduction in an unbounded medium, half-space, slab and layered media. *Engineering Analysis with Boundary Elements*, 30(5):338–349, 2006, doi:<https://doi.org/10.1016/j.enganabound.2006.01.011>.
- [79] J. Kosny and E. Kossecka. Multi-dimensional heat transfer through complex building envelope assemblies in hourly energy simulation programs. *Energy and buildings*, 34(0):445–454, 2002, doi:[https://doi.org/10.1016/S0378-7788\(01\)00122-0](https://doi.org/10.1016/S0378-7788(01)00122-0).
- [80] J. Quinten and V. Feldheim. Dynamic modelling of multidimensional thermal bridges in building envelopes: Review of existing methods, application and new mixed method. *Energy and Buildings*, 110:284–93, 2016, doi:<https://doi.org/10.1016/j.enbuild.2015.11.003>.
- [81] K. Martin, C. Escudero, A. Erkoreka, I. Flores, and J.M. Sala. Equivalent wall method for dynamic characterisation of thermal bridges. *Energy and Buildings*, 55(0):704–14, 2012, doi:<https://doi.org/10.1016/j.enbuild.2012.08.024>.
- [82] O. Gutschker. LORD 3.2. *PASLINK European Economic Interest Grouping*, Brussels, Belgium, 2002.
- [83] C. Borgelt, G.G. Rodríguez, W. Trutschnig, M.A. Lubiano, M.A. Gil, P. Grzegorzewski, and O. Hryniewicz. *Combining Soft Computing and Statistical Methods in Data Analysis*, volume 77. Springer Science & Business Media, 2010.

- 
- [84] E. Kossecka and J. Kosny. Equivalent wall as a dynamic model of a complex thermal structure. *Journal of Thermal Insulation and Building Envelopes*, 20(3):249–268, 1997, doi:<https://doi.org/10.1177/109719639702000306>.
- [85] S. Carpenter. Advances in modeling thermal bridges in building envelopes. *Enermodal Engineering Limited. Kitchener, ON, Canada*, 2001.
- [86] F. Aguilar, J.P. Solano, and P.G. Vicente. Transient modeling of high-inertial thermal bridges in buildings using the equivalent thermal wall method. *Applied thermal engineering*, 67(1-2):370–377, 2014, doi:<https://doi.org/10.1016/j.applthermaleng.2014.03.058>.
- [87] A. Nagata. A simple method to incorporate thermal bridge effects into dynamic heat load calculation programs. In *International IBPSA Conference*, pages 817–822, 2005.
- [88] X. Xiaona and J. Yi. Equivalent slabs approach to simulate the thermal performance of thermal bridges in building constructions. *IBPSA, Proceedings Building Simulation*, pages 287–293, 2007.
- [89] J. Quinten and V. Feldheim. Mixed equivalent wall method for dynamic modelling of thermal bridges: Application to 2-D details of building envelope. *Energy and Buildings*, 183:697–712, 2019, doi:<https://doi.org/10.1016/j.enbuild.2018.11.004>.
- [90] S.A. Al-Sanea and M.F. Zedan. Effect of thermal bridges on transmission loads and thermal resistance of building walls under dynamic conditions. *Applied Energy*, 98:584–593, 2012, doi:<https://doi.org/10.1016/j.apenergy.2012.04.038>.
- [91] H. Viot, A. Sempey, M. Pauly, and L. Mora. Comparison of different methods for calculating thermal bridges: application to wood-frame buildings. *Building and Environment*, 93(0):339–348, 2015, doi:<https://doi.org/10.1016/j.buildenv.2015.07.017>.
- [92] D. Bienvenido-Huertas, J. Moyano, D. Marín, and R. Fresco-Contreras. Review of in situ methods for assessing the thermal transmittance of walls. *Renewable and Sustainable Energy Reviews*, 102:356–371, 2019, doi:<https://doi.org/10.1016/j.rser.2018.12.016>.
- [93] N. Soares, C. Martins, M. Gonçalves, P. Santos, L.S. da Silva, and J.J. Costa. Laboratory and in-situ non-destructive methods to evaluate the thermal transmittance and behavior of walls, windows, and construction elements with innovative materials: A review. *Energy and Buildings*, 182:88–110, 2019, doi:<https://doi.org/10.1016/j.enbuild.2018.10.021>.
- [94] M. Teni, H. Krstić, and P. Kosiński. Review and comparison of current experimental approaches for in-situ measurements of building walls thermal transmittance. *Energy and Buildings*, page 109417, 2019, doi:<https://doi.org/10.1016/j.enbuild.2019.109417>.
- [95] G. Ficco, F. Iannetta, E. Ianniello, F.R. Alfano, and M. Dell’Isola. U-value in situ measurement for energy diagnosis of existing buildings. *Energy and Buildings*, 104:108–121, 2015, doi:<https://doi.org/10.1016/j.enbuild.2015.06.071>.

- [96] L. Evangelisti, C. Guattari, and F. Asdrubali. Influence of heating systems on thermal transmittance evaluations: Simulations, experimental measurements and data post-processing. *Energy and Buildings*, 168:180–190, 2018, doi:<https://doi.org/10.1016/j.enbuild.2018.03.032>.
- [97] K. Gaspar, M. Casals, and M. Gangolells. Review of criteria for determining HFM minimum test duration. *Energy and Buildings*, 176:360–370, 2018, doi:<https://doi.org/10.1016/j.enbuild.2018.07.049>.
- [98] S.H. Kim, J.H. Kim, H.G. Jeong, and K.D. Song. Reliability field test of the air–surface temperature ratio method for in situ measurement of U-values. *Energies*, 11(4):803, 2018, doi:<https://doi.org/10.3390/en11040803>.
- [99] ISO 6946:2017. Building components and building elements - Thermal resistance and thermal transmittance - Calculation methods. *International Standards Organisation*, 2017.
- [100] D. Bienvenido-Huertas, R. Rodríguez-Álvaro, J.J. Moyano, F. Rico, and D. Marín. Determining the U-value of façades using the thermometric method: potentials and limitations. *Energies*, 11(2):360, 2018, doi:<https://doi.org/10.3390/en11020360>.
- [101] J.M. Andújar Márquez, M.A. Martínez Bohórquez, and S. Gómez Melgar. A new metre for cheap, quick, reliable and simple thermal transmittance (U-Value) measurements in buildings. *Sensors*, 17(9), 2017, doi:<https://doi.org/10.3390/s17092017>.
- [102] ISO 9869-2:2018. Thermal insulation – Building elements – In-situ measurement of thermal resistance and thermal transmittance – Part 2: Infrared method for frame structure dwelling. *International Standards Organisation*, 2018.
- [103] S. Kato, K. Kuroki, and S. Hagihara. Method of in-situ measurement of thermal insulation performance of building elements using infrared camera. In *6th International Conference on Indoor Air Quality, Ventilation & Energy Conservation in Buildings-IAQVEC*, 2007.
- [104] R. Madding. Finding R-values of stud frame constructed houses with IR thermography. *Proc., InfraMation 2008*, pages 261–277, 2008.
- [105] J.P. Holman. *Heat transfer, 8th edition*. McGraw Hill, 1997.
- [106] R.L. Earle and M.D. Earle. *Unit Operations in Food Processing*. 1983.
- [107] P.A. Fokaides and S.A. Kalogirou. Application of infrared thermography for the determination of the overall heat transfer coefficient (U-Value) in building envelopes. *Applied Energy*, 88(12):4358–4365, 2011, doi:<https://doi.org/10.1016/j.apenergy.2011.05.014>.
- [108] B. Tejedor, M. Casals, M. Gangolells, and X. Roca. Quantitative internal infrared thermography for determining in-situ thermal behaviour of façades. *Energy and Buildings*, 151:187–197, 2017, doi:<https://doi.org/10.1016/j.enbuild.2017.06.040>.

- 
- [109] B. Tejedor, M. Casals, M. Macarulla, and A. Giretti. U-value time series analyses: Evaluating the feasibility of in-situ short-lasting IRT tests for heavy multi-leaf walls. *Building and Environment*, 159:106123, 2019, doi:<https://doi.org/10.1016/j.buildenv.2019.05.001>.
- [110] B. Tejedor, E. Barreira, R. Almeida, and M. Casals. Thermographic 2D U-value map for quantifying thermal bridges in building façades. *Energy and Buildings*, page 110176, 2020, doi:<https://doi.org/10.1016/j.enbuild.2020.110176>.
- [111] R. Albatici, A.M Tonelli, and M. Chiogna. A comprehensive experimental approach for the validation of quantitative infrared thermography in the evaluation of building thermal transmittance. *Applied Energy*, 141:218–228, 2015, doi:<https://doi.org/10.1016/j.apenergy.2014.12.035>.
- [112] K. Watanabe. *Architectural Planning Fundamentals*. 1965.
- [113] G. Dall’O, L. Sarto, and A. Panza. Infrared screening of residential buildings for energy audit purposes: results of a field test. *Energies*, 6(8):3859–3878, 2013, doi:<https://doi.org/10.3390/en6083859>.
- [114] D. Bienvenido-Huertas, J. Bermúdez, J.J. Moyano, and D. Marín. Influence of ICHTC correlations on the thermal characterization of façades using the quantitative internal infrared thermography method. *Building and Environment*, 149:512–525, 2019, doi:<https://doi.org/10.1016/j.buildenv.2018.12.056>.
- [115] D. Bienvenido-Huertas, J. Bermúdez, J. Moyano, and D. Marín. Comparison of quantitative IRT to estimate U-value using different approximations of ECHTC in multi-leaf walls. *Energy and Buildings*, 184:99–113, 2019, doi:<https://doi.org/10.1016/j.enbuild.2018.11.028>.
- [116] D. Pajani. *La thermographie du bâtiment – Principes et applications du diagnostic thermique*. Eyrolles, 2012, (in French).
- [117] O. Gutschker. Parameter identification with the software package LORD. *Building and Environment*, 43(2):163–169, 2008, doi:<https://doi.org/10.1016/j.buildenv.2006.10.010>.
- [118] P.H. Baker and H. Van Dijk. PASLINK and dynamic outdoor testing of building components. *Building and Environment*, 43(2):143–151, 2008, doi:<https://doi.org/10.1016/j.buildenv.2006.10.009>.
- [119] M.J. Jiménez, B. Porcar, and M.R. Heras. Application of different dynamic analysis approaches to the estimation of the building component U value. *Building and Environment*, 44(2):361–367, 2009, doi:<https://doi.org/10.1016/j.buildenv.2008.03.010>.
- [120] A.H. Deconinck and S. Roels. Comparison of characterisation methods determining the thermal resistance of building components from onsite measurements. *Energy and Buildings*, 130:309–320, 2016, doi:<https://doi.org/10.1016/j.enbuild.2016.08.061>.
- [121] A.H. Deconinck and S. Roels. A maximum likelihood estimation of the thermal resistance of a cavity wall from on-site measurements. *Energy Procedia*, 78:3276–3281, 2015, doi:<https://doi.org/10.1016/j.egypro.2015.11.723>.

- [122] I. Naveros, P. Bacher, D.P. Ruiz, M.J. Jiménez, and H. Madsen. Setting up and validating a complex model for a simple homogeneous wall. *Energy and Buildings*, 70:303–317, 2014, doi:<https://doi.org/10.1016/j.enbuild.2013.11.076>.
- [123] P. Bacher and H. Madsen. Identifying suitable models for the heat dynamics of buildings. *Energy and Buildings*, 43(7):1511–1522, 2011, doi:<https://doi.org/10.1016/j.enbuild.2011.02.005>.
- [124] S. Rouchier. Solving inverse problems in building physics: An overview of guidelines for a careful and optimal use of data. *Energy and Buildings*, 166:178–195, 2018, doi:<https://doi.org/10.1016/j.enbuild.2018.02.009>.
- [125] P. Biddulph, V. Gori, C. A Elwell, C. Scott, C. Rye, R. Lowe, and T. Oreszczyn. Inferring the thermal resistance and effective thermal mass of a wall using frequent temperature and heat flux measurements. *Energy and Buildings*, 78:10–16, 2014, doi:<https://doi.org/10.1016/j.enbuild.2014.04.004>.
- [126] V. Gori, V. Marincioni, P. Biddulph, and C.A Elwell. Inferring the thermal resistance and effective thermal mass distribution of a wall from in situ measurements to characterise heat transfer at both the interior and exterior surfaces. *Energy and Buildings*, 135:398–409, 2017, doi:<https://doi.org/10.1016/j.enbuild.2016.10.043>.
- [127] V. Gori and C.A. Elwell. Estimation of thermophysical properties from in-situ measurements in all seasons: Quantifying and reducing errors using dynamic grey-box methods. *Energy and Buildings*, 167:290–300, 2018, doi:<https://doi.org/10.1016/j.enbuild.2018.02.048>.
- [128] L. De Simon, M. Iglesias, B. Jones, and C. Wood. Quantifying uncertainty in thermophysical properties of walls by means of Bayesian inversion. *Energy and Buildings*, 177:220–245, 2018, doi:<https://doi.org/10.1016/j.enbuild.2018.06.045>.
- [129] H. Madsen, P. Bacher, G. Bauwens, A.H. Deconinck, G. Reynders, S. Roels, E. Himpe, and G. Lethé. Thermal performance characterization using time series data-IEA EBC Annex 58 Guidelines. 2015.
- [130] L. Ljung. System identification: theory for the user. *PTR Prentice Hall, Upper Saddle River, NJ*, 1999.
- [131] G. Bauwens. *In situ testing of a building’s overall heat loss coefficient - Embedding quasi-stationary and dynamic tests in a building physical and statistical framework*. PhD thesis, KU Leuven, 2015.
- [132] M.J. Jiménez, H. Madsen, and K.K. Andersen. Identification of the main thermal characteristics of building components using MATLAB. *Building and Environment*, 43(2):170–180, 2008, doi:<https://doi.org/10.1016/j.buildenv.2006.10.030>.
- [133] M.J. Jimenez and H. Madsen. Models for describing the thermal characteristics of building components. *Building and Environment*, 43(2):152–162, 2008, doi:<https://doi.org/10.1016/j.buildenv.2006.10.029>.



- 
- [134] I. Naveros, C. Ghiaus, D.P. Ruiz, and S. Castano. Physical parameters identification of walls using ARX models obtained by deduction. *Energy and Buildings*, 108:317–329, 2015, doi:<https://doi.org/10.1016/j.enbuild.2015.09.021>.
- [135] E. Lambie and D. Saelens. The thermal resistance of retrofitted building components based on in-situ measurements. In *7th International Building Physics Conference*, 2018.
- [136] M. Senave, G. Reynders, P. Bacher, S. Roels, S. Verbeke, and D. Saelens. Towards the characterization of the heat loss coefficient via on-board monitoring: Physical interpretation of ARX model coefficients. *Energy and Buildings*, 195:180–194, 2019, doi:<https://doi.org/10.1016/j.enbuild.2019.05.001>.
- [137] M. Senave, G. Reynders, B. Sodagar, S. Verbeke, and D. Saelens. Mapping the pitfalls in the characterisation of the heat loss coefficient from on-board monitoring data using ARX models. *Energy and Buildings*, 197:214–228, 2019, doi:<https://doi.org/10.1016/j.enbuild.2019.05.047>.
- [138] E. Lambie, M. Senave, and D. Saelens. The co-heating test as a means to evaluate the efficiency of thermal retrofit measures applied on residential buildings. In *7th International Building Physics Conference*, pages 953–958, 2018.
- [139] D. Bienvenido-Huertas, J. Moyano, C.E. Rodríguez-Jiménez, and D. Marín. Applying an artificial neural network to assess thermal transmittance in walls by means of the thermometric method. *Applied energy*, 233:1–14, 2019, doi:<https://doi.org/10.1016/j.apenergy.2018.10.052>.
- [140] D. Bienvenido-Huertas, C. Rubio-Bellido, J.L. Pérez-Ordóñez, and J. Moyano. Optimizing the evaluation of thermal transmittance with the thermometric method using multilayer perceptrons. *Energy and Buildings*, 198:395–411, 2019, doi:<https://doi.org/10.1016/j.enbuild.2019.06.040>.
- [141] D. Bienvenido-Huertas, J.L. Pérez-Ordóñez, J. Moyano, and S. Seara-Paz. Towards an in-situ evaluation methodology of thermal resistance of basement walls in buildings. *Energy and Buildings*, 208:109643, 2020, doi:<https://doi.org/10.1016/j.enbuild.2019.109643>.
- [142] C. Roulet, J. Gass, and I. Marcus. In situ U-value measurement: reliable results in shorter time by dynamic interpretation of the measured data. *Thermal Performance of the Exterior Envelopes of Buildings III; ASHRAE Transactions: Atlanta, GA, USA*, pages 777–784, 1987.
- [143] G. Anderlind. Multiple regression analysis of in situ thermal measurements, Study of an attic insulated with 800 mm loose fill insulation. *Journal of Thermal Insulation and Building Envelopes*, 16(1):81–104, 1992, doi:<https://doi.org/10.1177/109719639201600109>.
- [144] G. Anderlind. *Dynamic Thermal Models: Two Dynamic Models for Estimating Thermal Resistance and Heat Capacity from in Situ Measurements*. Byggeforskningsrådet, 1996.
- [145] M.H.A. Larbi Youcef, V. Feuillet, L. Ibos, and Y. Candau. In situ quantitative diagnosis of insulated building walls using passive infrared ther-

- mography. *Quantitative InfraRed Thermography Journal*, pages 1–29, 2020, doi:<https://doi.org/10.21611/qirt.2012.302>.
- [146] R. Ricci, F. Ragnedda, A. Galatioto, S. Gana, L.A. Besalduch, and A. Fratolillo. Thermal properties of building walls: Indirect estimation using the inverse method with a harmonic approach. *Energy and Buildings*, 187:257–268, 2019, doi:<https://doi.org/10.1016/j.enbuild.2019.01.035>.
- [147] ISO 13786:2007. Thermal performance of building components–Dynamic thermal characteristics–Calculation methods. *International Organization for Standardization*, 2007.
- [148] Á. Lakatos. Comprehensive thermal transmittance investigations carried out on opaque aerogel insulation blanket. *Materials and Structures*, 50(1):2, 2017, doi:<https://doi.org/10.1617/s11527-016-0876-7>.
- [149] J. Meulemans, F. Alzetto, D. Farmer, and C. Gorse. QUB/e: A Novel Transient Experimental Method for in situ Measurements of the Thermal Performance of Building Fabrics. pages 115–127, 2017, doi:<https://doi.org/10.1007/978-3-319-50346-2-9>.
- [150] J. Meulemans. An assessment of the QUB/e method for fast in situ measurements of the thermal performance of building fabrics in cold climates. pages 317–326, 2019, doi:<https://doi.org/10.1007/978-3-030-00662-4-27>.
- [151] A. Rasooli, L. Itard, and C.I. Ferreira. A response factor-based method for the rapid in-situ determination of walls thermal resistance in existing buildings. *Energy and Buildings*, 119:51–61, 2016, doi:<https://doi.org/10.1016/j.enbuild.2016.03.009>.
- [152] G.P. Mitalas. Room thermal response factors. *ASHRAE Transaction*, 73, 1967.
- [153] A. Rasooli and L. Itard. In-situ rapid determination of walls’ thermal conductivity, volumetric heat capacity, and thermal resistance, using response factors. *Applied energy*, 253:113539, 2019, doi:<https://doi.org/10.1016/j.apenergy.2019.113539>.
- [154] Y. Yang, T.V. Wu, A. Sempey, J. Dumoulin, and J.C. Batsale. Short time non-destructive evaluation of thermal performances of building walls by studying transient heat transfer. *Energy and Buildings*, 184:141–151, 2019, doi:<https://doi.org/10.1016/j.enbuild.2018.12.002>.
- [155] M.H.A. Larbi Youcef, V. Feuillet, L. Ibos, Y. Candau, P. Balcon, and A. Filoux. Quantitative diagnosis of insulated building walls of restored old constructions using active infrared thermography. *Quantitative InfraRed Thermography Journal*, 8(1):65–87, 2011, doi:<https://doi.org/10.3166/qirt.8.65-87>.
- [156] K. Chaffar, A. Chauchois, D. Defer, and L. Zalewski. Thermal characterization of homogeneous walls using inverse method. *Energy and Buildings*, 78:248–255, 2014, doi:<https://doi.org/10.1016/j.enbuild.2014.04.038>.
- [157] H. Preston-Thomas. The international temperature scale of 1990 (ITS-90). *Metrologia*, 27(1):3, 1990, doi:<https://doi.org/10.1088/0026-1394/27/2/010>.

- 
- [158] IEC ISO and BIPM OIML. Guide to the Expression of Uncertainty in Measurement. *Geneva, Switzerland*, 122, 1995.
- [159] National Instruments. Note d'application 043 (in French). Technical report.
- [160] National Instruments. NI 9214 and TB-9214 Datasheet.
- [161] P. Thureau. Fluxmètres thermiques. *Techniques de l'ingénieur*, R2900v2, 1996, (in French).
- [162] H. Trethowen. Measurement errors with surface-mounted heat flux sensors. *Building and Environment*, 21(1):41–56, 1986, doi:[https://doi.org/10.1016/0360-1323\(86\)90007-7](https://doi.org/10.1016/0360-1323(86)90007-7).
- [163] M. Planck. *The theory of heat radiation*. Courier Corporation, 2013.
- [164] J. Taine, F. Enguehard, and E. Iacona. *Transferts thermiques - Introduction aux transferts d'énergie - 5e édition*. Dunod, 2014, (in French).
- [165] K.J. Havens and E.J. Sharp. *Thermal imaging techniques to survey and monitor animals in the wild: A methodology*. Academic Press, 2015.
- [166] L. Ibos and J. Meulemans. Infrared thermography: materials & buildings. In *METTI 7, Advanced Autumn School in Thermal Measurements & Inverse Techniques, 7th edition*, Porquerolles, France, 2019.
- [167] B. Rémy, Y. Souhar, and A. Degiovanni. Evolution des caméras thermiques et métrologie thermique. In *Conférence Thermogram'2011*, Châlons en Champagne, France, 2011, (in French).
- [168] L. Ibos, J.-P. Monchau, V. Feuillet, J. Dumoulin, P. Ausset, J. Hameury, and B. Hay. Investigation of the directional emissivity of materials using infrared thermography coupled with a periodic excitation. 2016.
- [169] ASTM. E1862-97 Standard Test Methods for Measuring and Compensating for Reflected Temperature Using Infrared Imaging Radiometers. *ASTM International West Conshohocken, PA*, 2010.
- [170] A. Bejan. *Convection heat transfer*. John Wiley & sons, 2013.
- [171] S. Datcu. *Quantification des déperditions thermiques des bâtiments par thermographie infrarouge*. PhD thesis, Université Paris XII - Val de Marne, 2002.
- [172] D. Scaramuzza, A. Martinelli, and R. Siegwart. A toolbox for easily calibrating omnidirectional cameras. In *2006 IEEE/RSJ International Conference on Intelligent Robots and Systems*, pages 5695–5701. IEEE, 2006.
- [173] A. François, L. Ibos, V. Feuillet, and J. Meulemans. Novel in situ measurement methods of the total heat transfer coefficient on building walls. *Energy and Buildings*, 219:110004, 2020, doi:<https://doi.org/10.1016/j.enbuild.2020.110004>.
- [174] A. François, L. Ibos, V. Feuillet, and J. Meulemans. In situ measurement of the heat transfer coefficient on a building wall surface: h-measurement device based on a harmonic excitation. *Entropie*, 2020, doi:<https://doi.org/10.21494/ISTE.OP.2020.0547>.

- [175] A. François, L. Ibos, V. Feuillet, and J. Meulemans. In situ measurement of the heat transfer coefficient on a building wall surface: h-measurement device based on a harmonic excitation. 2020, doi:<https://doi.org/10.25855/SFT2020-091>.
- [176] H.B. Awbi and A. Hatton. Natural convection from heated room surfaces. *Energy and buildings*, 30(3):233–244, 1999, doi:[https://doi.org/10.1016/S0378-7788\(99\)00004-3](https://doi.org/10.1016/S0378-7788(99)00004-3).
- [177] E. Dascalaki, M. Santamouris, C.A. Balaras, and D.N. Asimakopoulos. Natural convection heat transfer coefficients from vertical and horizontal surfaces for building applications. *Energy and Buildings*, 20(3):243–249, 1994, doi:[https://doi.org/10.1016/0378-7788\(94\)90027-2](https://doi.org/10.1016/0378-7788(94)90027-2).
- [178] S.E.G. Jayamaha, N.E. Wijesundera, and S.K. Chou. Measurement of the heat transfer coefficient for walls. *Building and Environment*, 31(5):399–407, 1996, doi:[https://doi.org/10.1016/0360-1323\(96\)00014-5](https://doi.org/10.1016/0360-1323(96)00014-5).
- [179] A. Hagishima and J. Tanimoto. Field measurements for estimating the convective heat transfer coefficient at building surfaces. *Building and Environment*, 38(7):873–881, 2003, doi:[https://doi.org/10.1016/S0360-1323\(03\)00033-7](https://doi.org/10.1016/S0360-1323(03)00033-7).
- [180] D.L. Loveday and A.H. Taki. Convective heat transfer coefficients at a plane surface on a full-scale building facade. *International Journal of Heat and Mass Transfer*, 39(8):1729–1742, 1996, doi:[https://doi.org/10.1016/0017-9310\(95\)00268-5](https://doi.org/10.1016/0017-9310(95)00268-5).
- [181] N. Ito. Field experiment study on the convective heat transfer coefficient on exterior surface of a building. *ASHRAE Trans. (United States)*, 78, 1972.
- [182] K.E.A. Ohlsson, R. Östin, and T. Olofsson. Accurate and robust measurement of the external convective heat transfer coefficient based on error analysis. *Energy and Buildings*, 117:83–90, 2016, doi:<https://doi.org/10.1016/j.enbuild.2016.01.040>.
- [183] K.E.A. Ohlsson, R. Östin, S. Grundberg, and T. Olofsson. Dynamic model for measurement of convective heat transfer coefficient at external building surfaces. *Journal of Building Engineering*, 7:239–245, 2016, doi:<https://doi.org/10.1016/j.jobe.2016.06.005>.
- [184] A.J.N. Khalifa and R.H. Marshall. Validation of heat transfer coefficients on interior building surfaces using a real-sized indoor test cell. *International Journal of Heat and Mass Transfer*, 33(10):2219–2236, 1990, doi:[https://doi.org/10.1016/0017-9310\(90\)90122-B](https://doi.org/10.1016/0017-9310(90)90122-B).
- [185] P. Wallentén. Convective heat transfer coefficients in a full-scale room with and without furniture. *Building and Environment*, 36(6):743–751, 2001, doi:[https://doi.org/10.1016/S0360-1323\(00\)00070-6](https://doi.org/10.1016/S0360-1323(00)00070-6).
- [186] E. Mayer. Measurement of the convective surface coefficient of heat transfer of man. *Room Vent*, 87, 1987.
- [187] S.R. Delaforce, E.R. Hitchin, and D.M.T. Watson. Convective heat transfer at internal surfaces. *Building and Environment*, 28(2):211–220, 1993, doi:[https://doi.org/10.1016/0360-1323\(93\)90054-7](https://doi.org/10.1016/0360-1323(93)90054-7).

- 
- [188] A.D. Irving, T. Dewson, G. Hong, and B. Day. Time series estimation of convective heat transfer coefficients. *Building and Environment*, 29(1):89–96, 1994, doi:[https://doi.org/10.1016/0360-1323\(94\)90056-6](https://doi.org/10.1016/0360-1323(94)90056-6).
- [189] B. Griffith, D. Turler, H. Goudey, and D. Arasteh. Experimental techniques for measuring temperature and velocity fields to improve the use and validation of building heat transfer models. Technical report, Lawrence Berkeley National Lab.(LBNL), Berkeley, CA (United States), 1998.
- [190] M. Davies, C. Martin, M. Watson, and C.N. Riain. The development of an accurate tool to determine convective heat transfer coefficients in real buildings. *Energy and Buildings*, 37(2):141–145, 2005, doi:<https://doi.org/10.1016/j.enbuild.2004.06.001>.
- [191] D. Maillet, S. André, J.C. Batsale, A. Degiovanni, and C. Moyne. *Thermal quadrupoles: solving the heat equation through integral transforms*. John Wiley & Sons Inc, 2000.
- [192] IEC BIPM, ILAC IFCC, and IUPAC ISO. IUPAP and OIML 2008 Guide to the Expression of Uncertainty in Measurement (GUM: 1995 with minor corrections) Bureau International des Poids et Mesures.
- [193] T. Metzger and D. Maillet. Multisignal Least Squares: Dispersion, Bias, and Regularization. In *Thermal Measurements and Inverse Techniques*, pages 613–632. CRC Press, 2011.
- [194] A. François, L. Ibos, V. Feuillet, and J. Meulemans. Building thermal bridge heat losses quantification by infrared thermography. Steady-state evaluation and uncertainty calculation. In *Journal of Physics: Conference Series*, volume 1343, page 012171. IOP Publishing, 2019.
- [195] A. François, L. Ibos, V. Feuillet, and J. Meulemans. Quantification par thermographie infrarouge des déperditions énergétiques d’une paroi de bâtiment liées aux ponts thermiques intégrés: essais en régime permanent et évaluation des incertitudes de mesure. In *27ème Congrès Français de Thermique SFT 2019*, 2019.
- [196] A. François, L. Ibos, V. Feuillet, and J. Meulemans. In situ measurement method for the quantification of the thermal transmittance of a non-homogeneous wall or a thermal bridge using an inverse technique and active infrared thermography. *Energy and Buildings*, 233:110633, 2021, doi:<https://doi.org/10.1016/j.enbuild.2020.110633>.
- [197] C.S.T.B. *Réglementation Thermique*. Ed. Centre Scientifique et Thermique du Bâtiment, Paris, FRANCE, 2012, (in French).
- [198] COMSOL Multiphysics. Comsol multiphysics user guide (version 4.3 a). *COMSOL, AB*, pages 39–40, 2012.
- [199] H. Stehfest. Algorithm 368: Numerical inversion of Laplace transforms [D5]. *Communications of the ACM*, 13(1):47–49, 1970, doi:<https://doi.org/10.1145/361953.361969>.

- [200] F.R. De Hoog, J.H. Knight, and A.N. Stokes. An improved method for numerical inversion of Laplace transforms. *SIAM Journal on Scientific and Statistical Computing*, 3(3):357–366, 1982, doi:<https://doi.org/10.1137/0903022>.
- [201] Juraj. Numerical Inversion of Laplace Transforms in Matlab, MATLAB Central File Exchange.
- [202] J.C. Jones and M. Wade. On the thermal diffusivity of insulating glass wool. *Journal of fire sciences*, 18(1):74–77, 2000, doi:<https://doi.org/10.1177/073490410001800104>.
- [203] D. Maillet, Y. Jarny, and D. Petit. Problèmes inverses en diffusion thermique - Modèles diffusifs, mesures, sensibilités. *Techniques de l'ingénieur*, be8265, 2018, (in French).
- [204] D. Maillet, Y. Jarny, and D. Petit. Problèmes inverses en diffusion thermique - Formulation et résolution du problème des moindres carrés. *Techniques de l'ingénieur*, be8266, 2018, (in French).
- [205] D. Maillet, Y. Jarny, and D. Petit. Problèmes inverses en diffusion thermique - Outils spécifiques de conduction inverse et de régularisation. *Techniques de l'ingénieur*, be8267, 2018, (in French).
- [206] D. Petit and D. Maillet. Techniques inverses et estimation de paramètres. Partie 1. *Techniques de l'ingénieur*, af4515, 2008, (in French).
- [207] D. Petit and D. Maillet. Techniques inverses et estimation de paramètres. Partie 2. *Techniques de l'ingénieur*, af4516, 2008, (in French).
- [208] J.V. Beck and K.J. Arnold. *Parameter Estimation in Engineering and Science*. Wiley Interscience, 1977.
- [209] J.V. Beck, B. Blackwell, and C. R. St Clair Jr. *Inverse heat conduction: Ill-posed problems*. Wiley Interscience, 1985.
- [210] Y. Bard. *Nonlinear Parameter Estimation*. Academic Press, Inc., New York, 1974.
- [211] M.N. Ozisik and H.R.B. Orlando. *Inverse Heat Transfer: Fundamentals and Applications*. Taylor & Francis, 2000.
- [212] H.R.B. Orlando, O. Fudym, D. Maillet, and R.M. Cotta. *Thermal measurements and inverse techniques*. CRC Press, 2011.
- [213] J. Hadamard. Lectures on Cauchy's Problem in Linear Partial Differential Equations, Yale Univ. Press. New Haven, 1923.
- [214] K. Levenberg. A method for the solution of certain non-linear problems in least squares. *Quarterly of Applied Mathematics*, 2(2):164–168, 1944, doi:<https://doi.org/10.1090/qam/10666>.
- [215] D.W. Marquardt. An algorithm for least-squares estimation of nonlinear parameters. *Journal of the society for Industrial and Applied Mathematics*, 11(2):431–441, 1963, doi:<https://doi.org/10.1137/0111030>.
- [216] J.J. Moré. The Levenberg-Marquardt algorithm: implementation and theory. In *Numerical analysis*, pages 105–116. Springer, 1978.

- [217] A.N. Tikhonov and V.Y. Arsenin. Solutions of ill-posed problems. *New York*, pages 1–30, 1977.
- [218] D.L.B. Jupp and K. Vozoff. Stable iterative methods for the inversion of geophysical data. *Geophysical Journal International*, 42(3):957–976, 1975, doi:<https://doi.org/10.1111/j.1365-246X.1975.tb06461.x>.
- [219] L. Ibos, J.-L. Bodnar, and Y. Candau. Caractérisation thermophysique de matériaux polymères en utilisant un signal d’excitation pseudo-aléatoire: méthode par conduction. In *23ème Congrès Français de Thermique SFT*, 2015, (in French).
- [220] A. François, L. Ibos., V. Feuillet, and J. Meulemans. Estimation of the thermal resistance of a building wall with inverse techniques based on rapid in situ measurements and white-box or ARX black-box models. *Energy and Buildings*, 226:110346, 2020, doi:<https://doi.org/10.1016/j.enbuild.2020.110346>.
- [221] A. François, L. Ibos, V. Feuillet, and J. Meulemans. Novel active method for the estimation of a building wall thermal resistance. In *E3S Web of Conferences*, volume 172, page 14008. EDP Sciences, 2020.
- [222] J.-P. Monchau. *Mesure d’émissivité pour la thermographie infrarouge appliquée au diagnostic quantitatif des structures*. PhD thesis, Université Paris Est, 2013, (in French).
- [223] S.E. Gustafsson. Transient plane source techniques for thermal conductivity and thermal diffusivity measurements of solid materials. *Review of scientific instruments*, 62(3):797–804, 1991, doi:<https://doi.org/10.1063/1.1142087>.
- [224] M. Gustavsson, E. Karawacki, and S.E. Gustafsson. Thermal conductivity, thermal diffusivity, and specific heat of thin samples from transient measurements with hot disk sensors. *Review of Scientific Instruments*, 65(12):3856–3859, 1994, doi:<https://doi.org/10.1063/1.1145178>.
- [225] M. Gustavsson and S.E. Gustafsson. On the use of transient plane source sensors for studying materials with direction dependent properties. In *Thermal Conductivity 26: Thermal Expansion 14: Joint Conferences, August 6-8, 2001, Cambridge, Massachusetts, USA*, page 367. DEStech Publications, Inc, 2005.
- [226] ISO 22007-2:2015. Plastics - Determination of thermal conductivity and thermal diffusivity - Part 2: Transient plane heat source (hot disc) method. *International Standards Organisation*, 2015.
- [227] Y. Jannot and Z. Acem. A quadrupolar complete model of the hot disc. *Measurement science and technology*, 18(5):1229, 2007, doi:<https://doi.org/10.1088/0957-0233/18/5/009>.
- [228] R. Coquard, E. Coment, G. Flasquin, and D. Baillis. Analysis of the hot-disk technique applied to low-density insulating materials. *International journal of thermal sciences*, 65:242–253, 2013, doi:<https://doi.org/10.1016/j.ijthermalsci.2012.10.008>.
- [229] Q. Zheng, S. Kaur, C. Dames, and R.-S. Prasher. Analysis and improvement of the hot disk transient plane source method for low thermal conductivity

- materials. *International Journal of Heat and Mass Transfer*, 151:119331, 2020, doi:<https://doi.org/10.1016/j.ijheatmasstransfer.2020.119331>.
- [230] B. Hay, J.R. Flitz, and J.C. Batsale. Mesure de la diffusivité thermique par la méthode flash. *Techniques de l'ingénieur*, R2955v1, 2004, (in French).





## A. Appendices of Chap 3

This section presents a few measurement methods used in the thesis to estimate in laboratory some material thermal and optical properties. The measurements were useful to run numerical simulations and to validate the *in situ* characterization methods.

### A.1. Emissivity (IR spectrometer)

#### A.1.1. Principle of the method

Emissivities were measured with an infrared spectrometer (FRONTIER<sup>®</sup> model, from Perkin-Elmer<sup>®</sup>) equipped with an integrating sphere (from Pike<sup>®</sup>). The device is shown in Fig A.1.

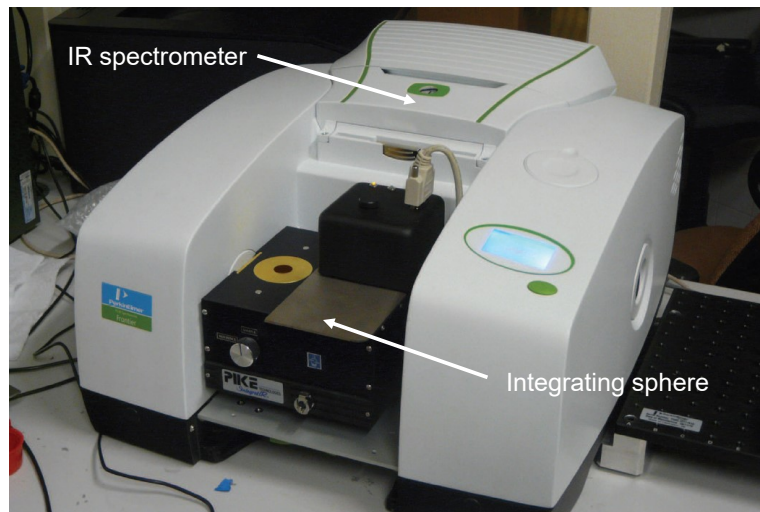


Figure A.1.: Photography of the IR spectrometer.

This equipment measures the spectral directional hemispherical reflectance  $\rho_\lambda$  between 2 and 20  $\mu\text{m}$  by comparison to a known reference (for more details, see [222], in French). This reference is a diffusing gold surface from SpectraGold<sup>®</sup>. Its reflectance  $\rho_\lambda^{\text{gold}}$  was measured by an independent method at the French National Metrology Institute (LNE: Laboratoire National de métrologie et d'Essais). It is given as a

polynomial in  $\lambda$ :

$$\rho_{\lambda}^{\text{gold}} = \sum_{k=0}^6 a_k \lambda^k \quad (\text{A.1})$$

where coefficients  $a_k$  are given in Tab A.1.

**Table A.1.:** Coefficients of  $\rho_{\lambda}^{\text{gold}}$ .

Coefficient	Value	Unit
$a_0$	0.90037	—
$a_1$	0.057132	$\mu\text{m}^{-1}$
$a_2$	-0.018875	$\mu\text{m}^{-2}$
$a_3$	0.002682	$\mu\text{m}^{-3}$
$a_4$	-0.00018431	$\mu\text{m}^{-4}$
$a_5$	0.0000060323	$\mu\text{m}^{-5}$
$a_6$	-0.000000075399	$\mu\text{m}^{-6}$

The emissivity measurement procedure consists in measuring five reflectances. Indeed, the characteristics of the gold sphere are modified by the presence of the sample. To overcome this limitation, a mirror inside the system can be moved in order to measure either the reflectance of the sample (position “Sample”, noted “S”), or the reflectance of the internal surface of the gold sphere (position “Reference”, noted “R”). The reflectance is measured with the sample in both positions, with a reference gold plate in both positions as well, and with no sample in position S (to remove background signal):

$$\rho_{\lambda} = \rho_{\lambda}^{\text{gold}} \frac{\frac{\rho_{\lambda}^{\text{sample}}|_{\text{S}} - \rho_{\lambda}^{\text{nothing}}|_{\text{S}}}{\rho_{\lambda}^{\text{sample}}|_{\text{R}} - \rho_{\lambda}^{\text{nothing}}|_{\text{S}}}}{\frac{\rho_{\lambda}^{\text{gold}}|_{\text{S}} - \rho_{\lambda}^{\text{nothing}}|_{\text{S}}}{\rho_{\lambda}^{\text{gold}}|_{\text{R}} - \rho_{\lambda}^{\text{nothing}}|_{\text{S}}}} \quad (\text{A.2})$$

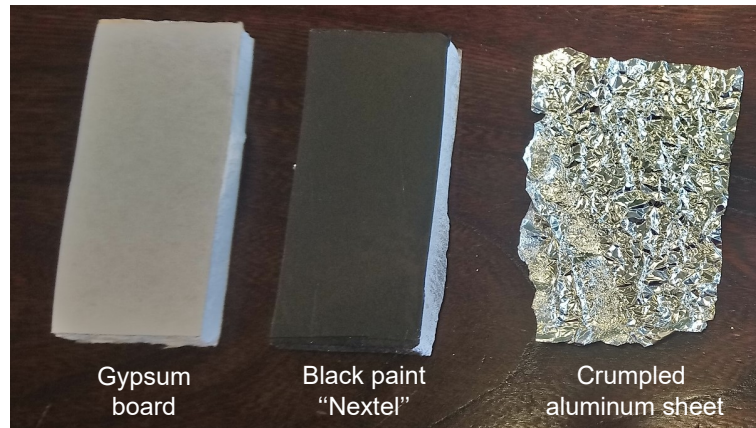
Finally, the desired emissivity is obtained from integration of the spectral emissivity  $\varepsilon_{\lambda} = 1 - \rho_{\lambda}$  over the desired spectral band  $\Delta\lambda$ :

$$\varepsilon_{\Delta\lambda} = \frac{\int_{\Delta\lambda} \varepsilon_{\lambda} \times I_{\lambda}^{\circ}(T) d\lambda}{\int_{\Delta\lambda} I_{\lambda}^{\circ}(T) d\lambda} \quad (\text{A.3})$$

This method works well for diffuse materials but is not able to estimate the emissivity of highly specular materials.

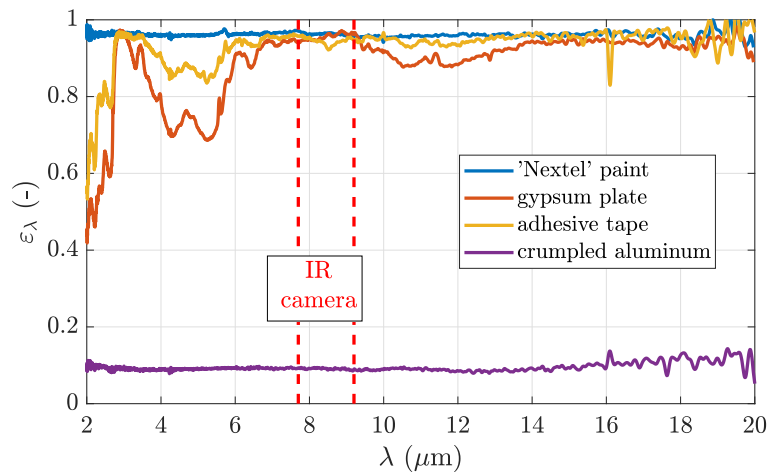
### A.1.2. Results: examples

Here are presented the results obtained on measurements of four materials: black Nextel<sup>®</sup> paint, a piece of gypsum board, some adhesive tape, and a crumpled sheet of aluminum. The samples are presented in Fig A.2. The gypsum board is made out of gypsum sandwiched between two sheets of cardboard. Thus, the optical properties measured are those of the cardboard. The aluminum sheet was crumpled because if not, reflection on the sample would be highly specular.



**Figure A.2.:** Samples used for emissivity measurements.

Figure A.3 plots the spectral emissivity measured on several materials between 2 and 20  $\mu\text{m}$  and Tab A.2 presents their emissivity between 7.7 and 9.2  $\mu\text{m}$ .



**Figure A.3.:** Example of measured spectral emissivities.

It may be observed that  $\varepsilon_\lambda$  is rather independent on  $\lambda$  on this interval for the “Nextel” paint and the crumpled aluminum sheet. The former is highly emissive whereas the latter is highly reflective. The spectral emissivity of the gypsum board and the adhesive tape are not as uniform but have a similar shape. However, in the spectral band of the IR camera (7.7-9.2  $\mu\text{m}$ ), the gypsum board, the adhesive tape and the “Nextel” paint have about the same spectral emissivity.

**Table A.2.:** Measured emissivity (7.7-9.2  $\mu\text{m}$ ).

Material	$\varepsilon$
“Nextel” paint	0.96
gypsum board	0.95
adhesive tape	0.94
crumpled aluminum	0.09

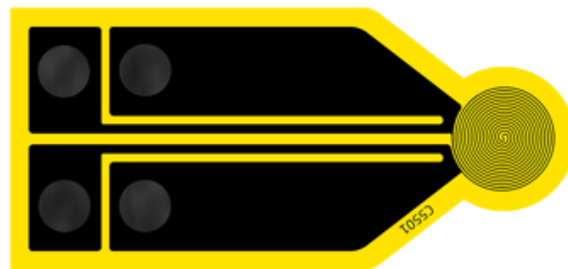
## A.2. Thermal conductivity and diffusivity (Hot Disk)

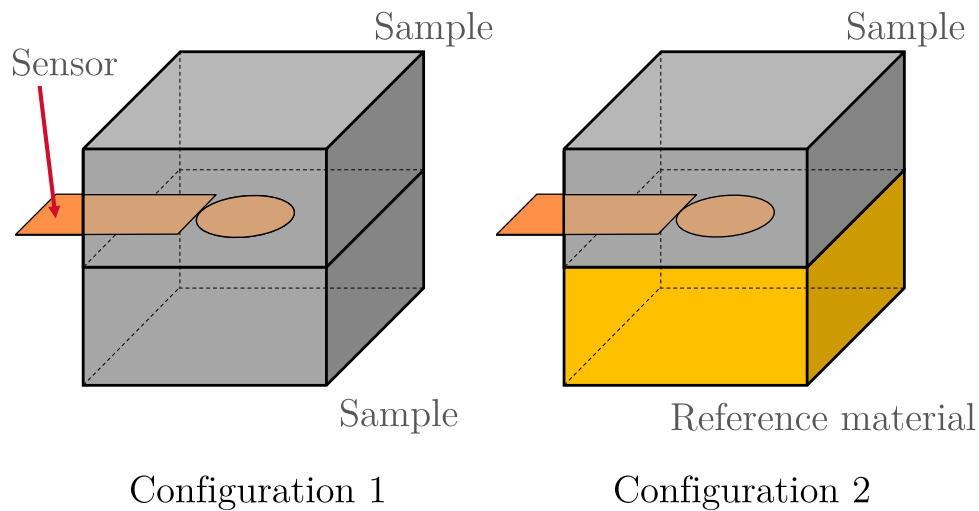
The Hot Disk Transient Plane Source (TPS) method [223] allows rapid characterization of thermal properties of materials in a single experiment. The thermal conductivity and diffusivity are estimated, and the specific heat may be calculated from the former two parameters. This method has the advantages of being absolute, with no need for repeated calibrations of standard samples. In addition, it is flexible and only requires one or two pieces of the sample to characterize with only a single flat surface. The method is applicable to most materials types, including thin samples [224] and non isotropic materials [225]. It is standardized in ISO 22007-2 [226] since 2008. Several authors pointed out the limitations of the method, especially for insulating materials [227, 228, 229].

### A.2.1. Principle of the method

The TPS method consists in feeding a probe with a constant power source in order to increase the temperature of a sample by a few degrees. The probe also measures the temperature elevation thanks to the recording of its electrical resistance with very accurate Wheastone bridge and voltmeter. The analysis of the temperature elevation (transient regime) allows determining both the thermal conductivity and the thermal diffusivity of the sample material. This is an inverse problem.

The probe is a double spiral covered with an electrical insulator, as presented in Fig A.4. It is inserted between two samples of the material to characterize or between one sample and one reference material of known thermal properties. These two configurations are illustrated in Fig A.5.

**Figure A.4.:** Example of a hot disk sensor.



**Figure A.5.:** Two configurations for measurement with the “Hot Disk”.

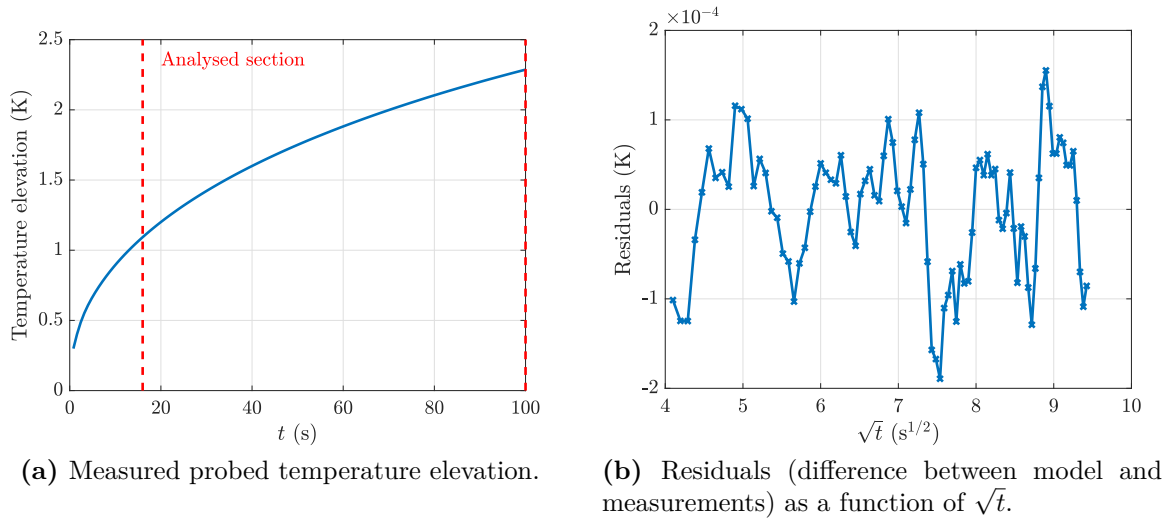
The operator must pay attention to a few points for the parameter estimation to be accurate:

- Probe size: the size of the probe depends obviously on the size of the sample but also on the size of the material features (such as beads in expanded polystyrene).
- Duration: a measurement time is chosen so as to allow the introduced heat to penetrate some distance into the sample, but not reach the outer bounds of the sample (for the semi-infinite medium hypothesis to remain valid). The duration of the experiment depends on the material thermal diffusivity. This criterion is valid for the analysis of bulk materials. The Hot Disk method is also able to study thin materials for which the duration criterion is different.
- Heating power: an appropriate power value is chosen so as to raise the temperature of the sample between 1 and 4°C. Highly thermally conducting materials will require higher power value than thermally insulating materials.

### A.2.2. Example of results

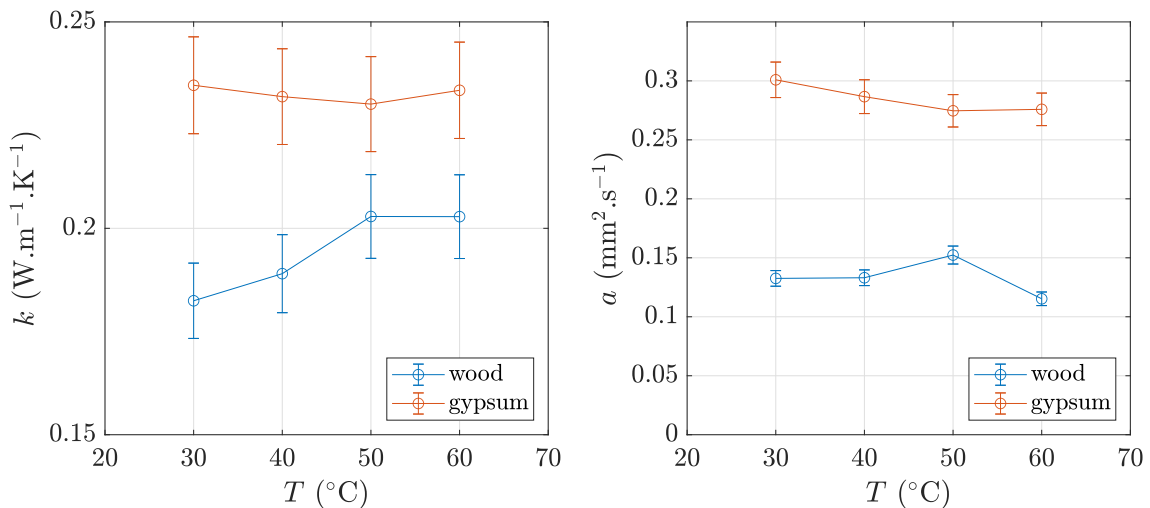
The Hot Disk equipment used is reference TPS 2500.

Figure A.6 plots the results obtained on one example. The probe has a 14.61 mm diameter and is sandwiched between two pieces of gypsum board. The first points ( $t < 15$  s) were removed because the measured temperature is too sensitive to the probe thermal capacity at the beginning of the experiment. The residuals are unsigned (flat) and of small magnitude ( $10^{-4}$  K) which shows that the model used successfully fits the data. On this example, the sample thermal conductivity and diffusivity are estimated to  $k = 0.23 \text{ W}\cdot\text{m}^{-1}\cdot\text{K}^{-1}$  and  $a = 0.28 \text{ mm}^2\cdot\text{s}^{-1}$ . According to the manufacturer, the estimated values are given with a 5% uncertainty.



**Figure A.6.:** Example of measured temperature and residuals after estimation of the sample material properties with the Hot Disk method.

It is also possible to measure a sample thermal characteristics as a function of temperature. Figure A.7 plots the measured  $k$  and  $a$  for two samples made of wood and gypsum. The sample were placed inside a regulated oven. It may be seen that the thermal properties of the wood and the gypsum are rather independent on the temperature between 30 and 60°C, except the wood conductivity which slightly increases with  $T$ .



**Figure A.7.:** Measured thermal conductivity  $k$  and diffusivity  $a$  as a function of temperature for two samples made of wood and gypsum.

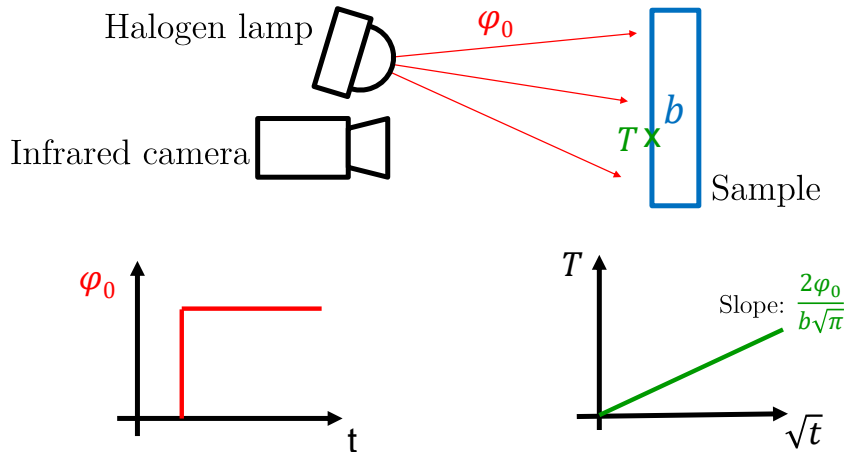
For lightweight materials, there is a module called “Low density - High insulating materials”. This module enables to take into account the thermal capacitance of the probe because this parameter is not negligible for such materials.

### A.3. Thermal effusivity (Photothermal method)

It was desired to measure in laboratory the thermal effusivity of some materials. Indeed, this quantity is estimated with inverse techniques (see Chap 8) so lab measurements could have available reference values. The photothermal method presented here was investigated because it is not intrusive easy to apply to large sample. The measurement were undertaken it CERTES laboratory.

#### A.3.1. Principle of the method

The optical method used is illustrated in Fig A.8. The surface of the sample is darkened with an emissive coating and is heated with a halogen lamp (500 W). The surface temperature is recorded by an infrared camera.



**Figure A.8.:** Description of the experimental setup used to characterize the thermal effusivity of materials.

The sample is supposed subject to a sudden constant heat flux  $\varphi_0$  (step). The experiment is supposed short enough for the exchanges with the environment to be negligible and for the sample to behave as a semi-infinite medium of thermal effusivity  $b$ . Given these assumptions, the surface temperature elevation is simply given by [164]:

$$T = \frac{2\varphi_0}{b\sqrt{\pi}}\sqrt{t} \quad (\text{A.4})$$

Therefore, the curve of  $T$  as a function of  $\sqrt{t}$  is a straight line of intersect 0. The ratio  $\frac{\varphi_0}{b}$  is worked out from the slope. The absorbed heat flux  $\varphi_0$  is hard to evaluate in practice as it depends on many parameters. It is simpler to estimate the sample effusivity from comparison to a reference material of known effusivity  $b_{\text{ref}}$ . The

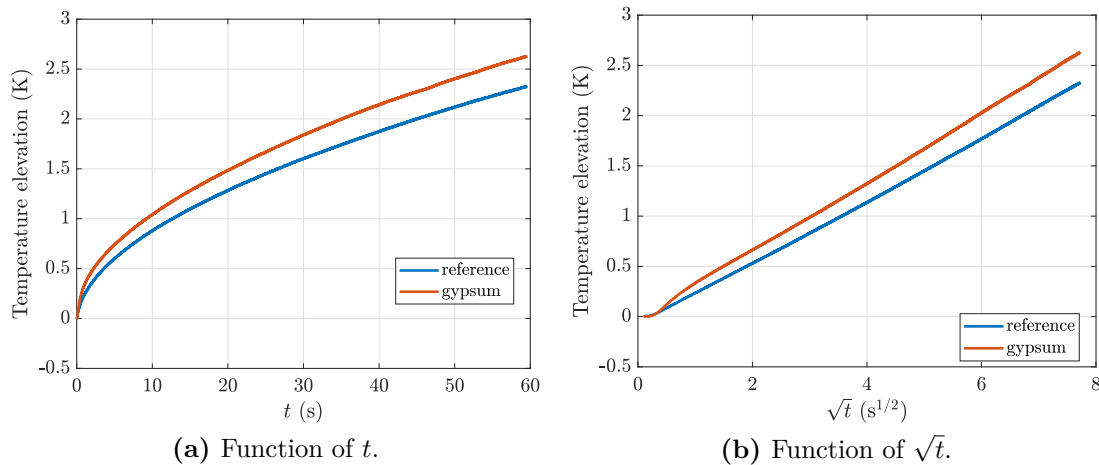


sample is swapped with the reference and the exact same experiment is performed (same position according to the lamps). The sample and the reference need to have the same emissivity (painted with the same paint for instance) so that  $\varphi_0$  is a constant. The ratio  $\frac{b}{b_{\text{ref}}}$  is derived from the two estimated ratios  $\frac{\varphi_0}{b}$  and  $\frac{\varphi_0}{b_{\text{ref}}}$ . Given that  $b_{\text{ref}}$  is known, the desired effusivity  $b$  can be estimated. Alternatively, the ratio  $\frac{b}{b_{\text{ref}}}$  could be derived from the intersect of the curve of  $\log(T)$  as a function  $\log(t)$ , which is also a straight line.

The reference material used in the experiments is a plastic plate of effusivity  $b_{\text{ref}} = 408 \text{ J.K}^{-1}.\text{m}^{-2}.\text{s}^{-\frac{1}{2}}$  [155].

### A.3.2. Results: examples

First, the method is used to determine the effusivity of a gypsum board. The heating time is set to 60 s. The temporal evolution of the surface temperature on the gypsum sample and on the reference plate are plotted in Fig A.9, as a function of  $t$  and  $\sqrt{t}$ .



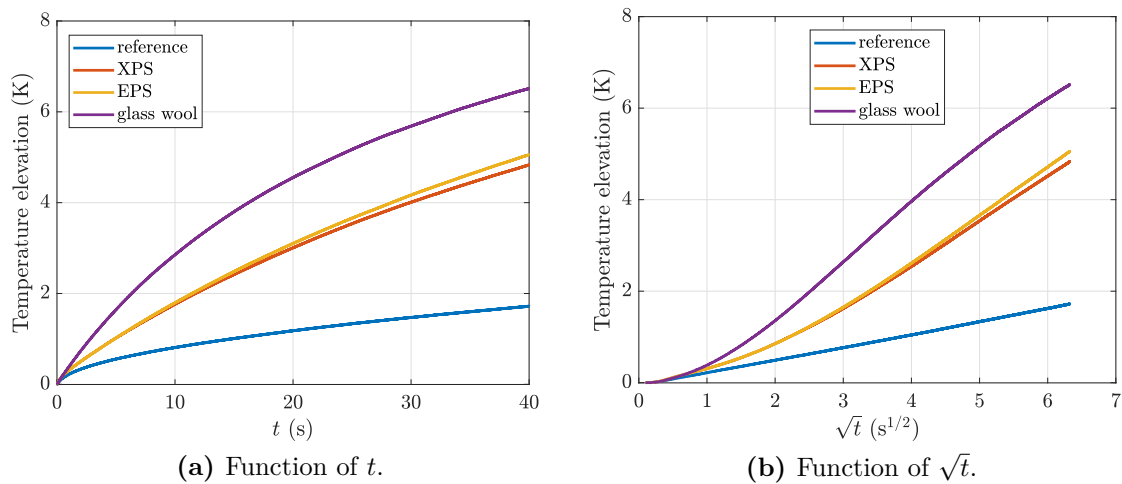
**Figure A.9.:** Surface temperature evolutions of the gypsum sample and the reference plastic plate as a function time and square root of time.

At short time,  $T$  is not quite proportional to  $\sqrt{t}$  because the halogen heating power is quite not constant during the first moments of the experiment. For  $t > 10$  s, the two curves are linear. The assumptions made to build the model defined in Eq A.4 are therefore valid. The estimated effusivity ratio is  $\frac{b}{b_{\text{ref}}} = 1.09$ . Thus, the gypsum effusivity is estimated to  $446 \text{ J.K}^{-1}.\text{m}^{-2}.\text{s}^{-\frac{1}{2}}$ . This result is in good agreement with the effusivity estimated from Hot Disk measurements on the same sample:  $428 \text{ J.K}^{-1}.\text{m}^{-2}.\text{s}^{-\frac{1}{2}}$ . The discrepancy between these two measurements is below 4% and is deemed acceptable. This is also in good agreement with standard material thermal properties given in the French Thermal Regulation RT2012 [197] corresponding to a gypsum effusivity between  $433$  and  $474 \text{ J.K}^{-1}.\text{m}^{-2}.\text{s}^{-\frac{1}{2}}$ .

However, this technique does not work for insulating materials. Three such materials were tested: glass wool, expanded polystyrene (EPS) and extruded polystyrene

## A.4. CONCLUSION

(XPS). The measurements are plotted in Fig A.10. The temperature elevation as a function of  $\sqrt{t}$  does not follow a straight line of zero intercept for any of these materials. This non-linear behavior was not due to the bigger temperature increase (between 5 and 7 K) on the insulating materials than on the reference (2 K). Indeed, the same experiment was undertaken on the reference with more heating power (so that the surface temperature increased by 6 K) but the model kept being valid. It is thought that the assumption of null heat losses is no longer valid for insulating materials. One possible explanation is that only a small amount of heat diffuses inside low effusivity materials during the experiment: most of the energy remains on the surface. The hypothesis of negligible heat exchanges may not be valid in these conditions. More complex models (including heat losses) were tried, but were not successful because of strong correlations between parameters.



**Figure A.10.:** Surface temperature evolutions of the insulating material samples and the reference plastic plate as a function time and square root of time.

As a conclusion, this photothermal method to determine the effusivity of materials is apparently not suited for low effusivity materials. Both the gypsum and the plastic samples worked well, while neither the glass wool, the polystyrene nor the cellular concrete worked.

## A.4. Conclusion

Several laboratory measurements and their limitations are presented in this section. They aim at measuring a material thermal properties (conductivity, diffusivity, effusivity and emissivity). The quantification of these quantities has several objectives. First, it enables to perform numerical simulations of the problem. These simulations are useful for the sizing of the experimental setup in the design phase. Second, the material thermal properties measured in laboratory may be used as references to validate the results of *in situ* measurements. Third, the value of the wall surface emissivity is required to quantify surface temperature differences with infrared

thermography. In addition, emissivity measurements are useful to select the best material to use in order to make HFMs as emissive as the wall.

## B. Appendices of Chap 5

### B.1. Type-A uncertainty calculation of the HE method

#### B.1.1. 5Amplitude and phase uncertainty of a Fourier transform

The Fourier transform of a  $N$ -point sequence  $x$  (temperature or heat flux measurement with time for instance) is given by:

$$FT(k) = \frac{1}{N} \sum_{n=0}^{N-1} x(n) \exp(-jk\beta_n) \quad (\text{B.1})$$

with  $\beta_n = 2\pi n/N$ . The number  $N$  is chosen such that a whole number of periods is analyzed. The real and imaginary parts of  $X$  are therefore:

$$\begin{cases} R(k) &= \frac{1}{N} \sum_{n=0}^{N-1} x(n) \cos(k\beta_n) \\ I(k) &= \frac{1}{N} \sum_{n=0}^{N-1} x(n) \sin(k\beta_n) \end{cases} \quad (\text{B.2})$$

The amplitude  $A$  and phase  $\zeta$  of the  $k$ -th harmonic are as follows:

$$\begin{cases} A(k) &= 2 \times \sqrt{R(k)^2 + I(k)^2} \\ \zeta(k) &= \arctan\left(-\frac{I(k)}{R(k)}\right) \end{cases} \quad (\text{B.3})$$

Let assume that each point of the  $x$  sequence is affected by an uncertainty  $u(x)$  (measurement noise). The uncertainty is propagated to  $R$  and  $I$ :

$$\begin{cases} u^2(R(k)) &= \sum_{n=0}^{N-1} \left(\frac{\partial R(k)}{\partial x(n)}\right)^2 u^2(x(n)) \\ u^2(I(k)) &= \sum_{n=0}^{N-1} \left(\frac{\partial I(k)}{\partial x(n)}\right)^2 u^2(x(n)) \end{cases} \quad (\text{B.4})$$

leading to:

$$\begin{cases} u^2(R(k)) &= \frac{1}{N^2} \sum_{n=0}^{N-1} \cos^2(k\beta_n) u^2(x) \\ u^2(I(k)) &= \frac{1}{N^2} \sum_{n=0}^{N-1} \sin^2(k\beta_n) u^2(x) \end{cases} \quad (\text{B.5})$$

For  $k \neq 0$ , it comes:

$$u^2(R(k)) = u^2(I(k)) = \frac{u^2(x)}{2N} \quad (\text{B.6})$$

Similarly, the uncertainties are propagated to the amplitude  $A$  and phase  $\zeta$ :

$$\begin{cases} u^2(A(k)) &= \frac{2u^2(x)}{N} \\ u^2(\zeta(k)) &= \frac{2u^2(x)}{NA^2(k)} \end{cases} \quad (\text{B.7})$$

### B.1.2. Uncertainty on $h$ calculation

The  $h$  value is obtained from the ratio of the heat flux and temperature Fourier transforms at the excitation frequency  $f$  (associated to the index  $k_f$ ):

$$\hat{h} = \Re \left( \frac{FT_\varphi(k_f)}{FT_T(k_f)} \right) \quad (\text{B.8})$$

with  $FT_\varphi$  and  $FT_T$  the Fourier transforms of  $\varphi$  and  $T$  respectively. Let  $FT_\varphi(k_f) = R_\varphi + jI_\varphi$  and  $FT_T(k_f) = R_T + jI_T$ . The previous equation becomes:

$$\hat{h} = \frac{R_\varphi R_T + I_\varphi I_T}{R_T^2 + I_T^2} = \frac{\text{Num}}{\text{Den}} \quad (\text{B.9})$$

with  $\text{Num} = R_\varphi R_T + I_\varphi I_T$  and  $\text{Den} = R_T^2 + I_T^2$ , the four partial derivatives of  $\hat{h}$  are given by:

$$\frac{\partial \hat{h}}{\partial R_\varphi} = \frac{R_T}{\text{Den}} \quad (\text{B.10})$$

$$\frac{\partial \hat{h}}{\partial I_\varphi} = \frac{I_T}{\text{Den}} \quad (\text{B.11})$$

$$\frac{\partial \hat{h}}{\partial R_T} = \frac{R_\varphi \text{Den} - 2R_T \text{Num}}{\text{Den}^2} \quad (\text{B.12})$$

$$\frac{\partial \hat{h}}{\partial I_T} = \frac{I_\varphi \text{Den} - 2I_T \text{Num}}{\text{Den}^2} \quad (\text{B.13})$$

The uncertainty of each of these parameters are given by Eq. B.6. Once again, the uncertainty propagation law is applied to derive the  $h$  measurement uncertainty  $u_h$ :

$$\begin{aligned} u^2(h) = & \frac{R_T^2}{\text{Den}^2} \frac{u^2(\varphi)}{2N} + \frac{I_T^2}{\text{Den}^2} \frac{u^2(\varphi)}{2N} + \frac{R_\varphi^2 \text{Den}^2 + 4R_T^2 \text{Num}^2 - 4R_T R_\varphi \text{DenNum}}{\text{Den}^4} \frac{u^2(T)}{2N} \\ & + \frac{I_\varphi^2 \text{Den}^2 + 4I_T^2 \text{Num}^2 - 4I_T I_\varphi \text{DenNum}}{\text{Den}^4} \frac{u^2(T)}{2N} \end{aligned} \quad (\text{B.14})$$

$$\begin{aligned} u^2(h) = & \frac{R_T^2 + I_T^2}{\text{Den}^2} \frac{u^2(\varphi)}{2N} \\ & + \frac{(R_\varphi^2 + I_\varphi^2) \text{Den}^2 + 4(R_T^2 + I_T^2) \text{Num}^2 - 4(R_T R_\varphi + I_T I_\varphi) \text{DenNum}}{\text{Den}^4} \frac{u^2(T)}{2N} \end{aligned} \quad (\text{B.15})$$

Substituting Num and Den by their expression:

$$u^2(h) = \frac{1}{R_T^2 + I_T^2} \frac{u^2(\varphi)}{2N} + \frac{(R_\varphi^2 + I_\varphi^2)}{(R_T^2 + I_T^2)^2} \frac{u^2(T)}{2N} \quad (\text{B.16})$$

Combining with Eq B.3:

$$u^2(h) = \frac{4}{A_T^2} \frac{u^2(\varphi)}{2N} + \frac{4A_\varphi^2}{A_T^4} \frac{u^2(T)}{2N} \quad (\text{B.17})$$

It comes:

$$u(h) = \sqrt{\frac{2}{N}} \frac{1}{A_T} \sqrt{u^2(\varphi) + \left(\frac{A_\varphi}{A_T}\right)^2 u^2(T)} \quad (\text{B.18})$$

with  $A_T$  and  $A_\varphi$  the temperature and heat flux amplitudes (see Eq. B.3). For given noise levels  $u(\varphi)$  and  $u(T)$ , the uncertainty on  $h$  decreases in  $1/\sqrt{N}$ .

This uncertainty may also be expressed in terms of the uncertainty over the amplitudes  $u(A_\varphi)$  and  $u(A_T)$  (see Eq. B.7):

$$u(h) = \frac{1}{A_T} \sqrt{u^2(A_\varphi) + \left(\frac{A_\varphi}{A_T}\right)^2 u^2(A_T)} \quad (\text{B.19})$$

# C. Appendices of Chap 6

## C.1. $\psi$ uncertainty calculation

Here are presented the equations used for the the calculation of the measurement uncertainty of  $\psi$  and  $\chi$  coefficients with the “ $I_{tb}$ ” method and the “ $h$ ” method.

### C.1.1. Partial derivatives for the “ $I_{tb}$ ” method

The partial derivatives of  $\psi$  (see Eq 6.5) are given by:

$$\frac{\partial\psi}{\partial L_{tb}} = U_{1D} (I_{tb} - 1) \quad (C.1)$$

$$\frac{\partial\psi}{\partial U_{1D}} = L_{tb} (I_{tb} - 1) \quad (C.2)$$

$$\frac{\partial\psi}{\partial I_{tb}} = U_{1D} L_{tb} \quad (C.3)$$

The partial derivatives of  $L_{tb}$  (see Eq 6.17) are given by:

$$\frac{\partial L_{tb}}{\partial N_{ref}} = -N_p \frac{L_{ref}}{N_{ref}^2} \quad (C.4)$$

$$\frac{\partial L_{tb}}{\partial L_{ref}} = \frac{N_p}{N_{ref}} \quad (C.5)$$

The partial derivatives of  $U_{1D}$  (see Eq 6.2) are given by:

$$\frac{\partial U_{1D}}{\partial \varphi} = \frac{\Delta T}{\varphi^2} U_{1D}^2 \quad (C.6)$$

$$\frac{\partial U_{1D}}{\partial \Delta T} = -\frac{U_{1D}^2}{\varphi} \quad (C.7)$$

The partial derivatives of  $I_{tb}$  (see Eq 6.15) are given by:



$$\frac{\partial I_{\text{tb}}}{\partial \Delta T_{\text{tb}}^{\text{app}}} = \frac{1}{\Delta T_{\text{1D}}^{\text{app}}} \quad (\text{C.8})$$

$$\frac{\partial I_{\text{tb}}}{\partial \Delta T_{\text{1D}}^{\text{app}}} = -\frac{\Delta T_{\text{tb}}^{\text{app}}}{(\Delta T_{\text{1D}}^{\text{app}})^2} \quad (\text{C.9})$$

The measurement uncertainty of  $\chi$  is obtained similarly.

### C.1.2. Partial derivatives for the “ $h$ ” method

The partial derivatives of  $\psi$  (see Eq 6.23) are given by:

$$\frac{\partial \psi}{\partial L_{\text{tb}}} = \frac{h}{\Delta T_{\text{sie}}} \frac{\Delta T_{\text{tb-1D}}^{\text{app}}}{\varepsilon} \quad (\text{C.10})$$

$$\frac{\partial \psi}{\partial h} = \frac{L_{\text{tb}}}{\Delta T_{\text{sie}}} \frac{\Delta T_{\text{tb-1D}}^{\text{app}}}{\varepsilon} \quad (\text{C.11})$$

$$\frac{\partial \psi}{\partial \Delta T_{\text{sie}}} = -\frac{L_{\text{tb}} h}{(\Delta T_{\text{sie}})^2} \frac{\Delta T_{\text{tb-1D}}^{\text{app}}}{\varepsilon} \quad (\text{C.12})$$

$$\frac{\partial \psi}{\partial \Delta T_{\text{tb-1D}}^{\text{app}}} = \frac{L_{\text{tb}} h}{\Delta T_{\text{sie}}} \frac{1}{\varepsilon} \quad (\text{C.13})$$

$$\frac{\partial \psi}{\partial \varepsilon} = -\frac{L_{\text{tb}} h}{\Delta T_{\text{sie}}} \frac{\Delta T_{\text{tb-1D}}^{\text{app}}}{\varepsilon^2} \quad (\text{C.14})$$

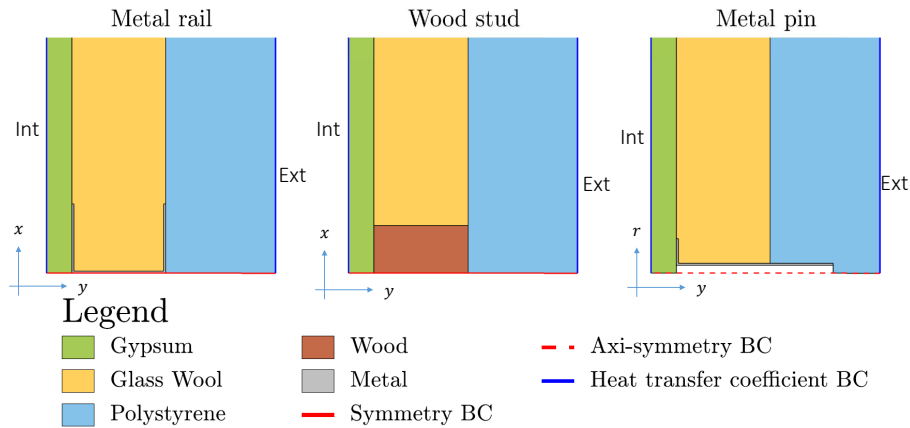
The measurement uncertainty of  $\chi$  is obtained similarly.

## C.2. Details on FE simulations (CERTES 1 setup)

This appendix presents the construction of the three 2D models of the thermal bridges included in the CERTES 1 setup.

### C.2.1. Geometry and boundary conditions

The three geometries are shown in Fig C.1. The whole computational domains span 0.5 m away from the thermal bridge: only a fraction of them is displayed here. Thanks to the symmetry of the problem, only half of the geometry is modeled. In addition to this symmetry condition on the bottom boundary, a heat transfer coefficient with a reference temperature set to the environment temperature is prescribed on either side of the domain. The internal (left-hand side) and external (right-hand side) superficial resistances are set respectively to 0.13 and 0.04 m<sup>2</sup>.K.W<sup>-1</sup>, according to ISO 14683 [18]. The upper boundary (not shown) is adiabatic. The difference between the internal and external environment temperatures is set arbitrarily to 1 K.



**Figure C.1.:** Parts of computational domains and boundary conditions of FE models (note: the computational domains are much taller: only a fraction of them is shown).

### C.2.2. Equations and numerical scheme

The 2D heat transfer equation in solid bodies is solved [198]:

$$\rho c_p \frac{\partial T}{\partial t} + \nabla \cdot q = Q \quad (\text{C.15})$$

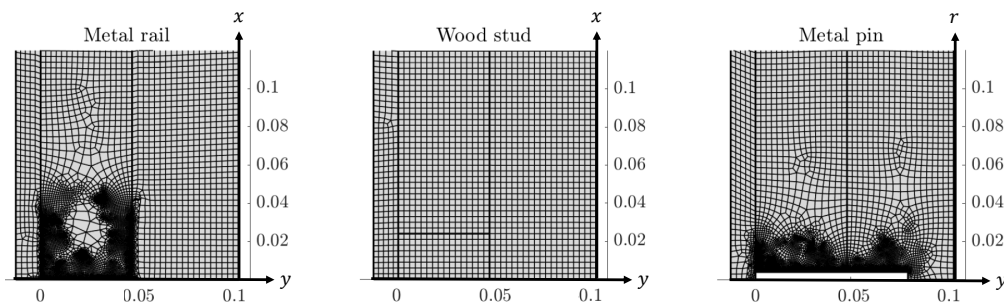
where

- $\rho$  is the density ( $\text{kg.m}^{-3}$ )
- $c_p$  is the specific heat capacity ( $\text{J.kg}^{-1}.\text{K}^{-1}$ )
- $T$  is the temperature (K)
- $q$  is the heat flux by conduction given by  $q = -k\nabla T$
- $k$  is the thermal conductivity ( $\text{W.m}^{-1}.\text{K}^{-1}$ )
- $Q$  is the internal heat sources ( $\text{W.m}^{-3}$ ), equal to zero in this study.

For transient simulations, the discretization scheme used is a Quadratic Lagrange whose tolerance is set to  $10^{-7}$ .

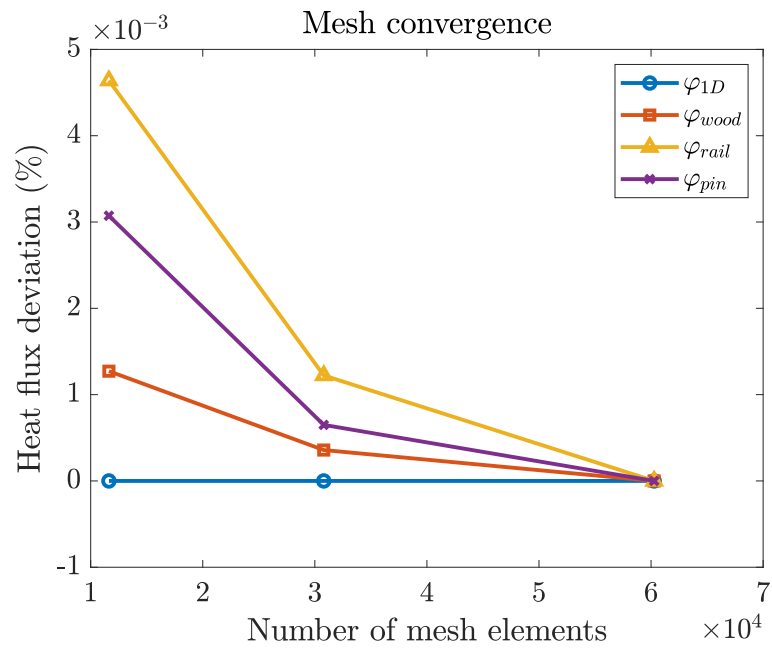
### C.2.3. Mesh

The meshes are visible in Fig C.2. Free quad cell are used, because of their simplicity of application. The grid is refined close to geometrical irregularities (in the metal rail and metal pin cases).



**Figure C.2.:** Meshes used in the FE simulations. Zoom on thermal bridge.

Each mesh contains around 10,000 elements. The convergence analysis shown in Fig C.3 proves the mesh-independency of the solution. The mean heat flux on the internal surface is calculated in steady-state with three different meshes from 10,000 to 60,000 elements. The finest mesh is taken as reference and the relative distance to it is calculated. The three meshes deliver almost identical results, the maximum deviation is lower than 0.01 %. Therefore, the mesh used is fine enough so that that the discretization does not to affect the results. A coarser mesh would also be suitable, but given the short computational time of simulations, there is no need to reduce the number of elements.



**Figure C.3.:** Mesh convergence: the internal surface heat flux is measured on several simulations of increasing mesh refinement and the simulation with the finest mesh is used as a benchmark.

### C.3. Detailed uncertainty analysis (CERTES 1 setup, “ $I_{tb}$ method”)

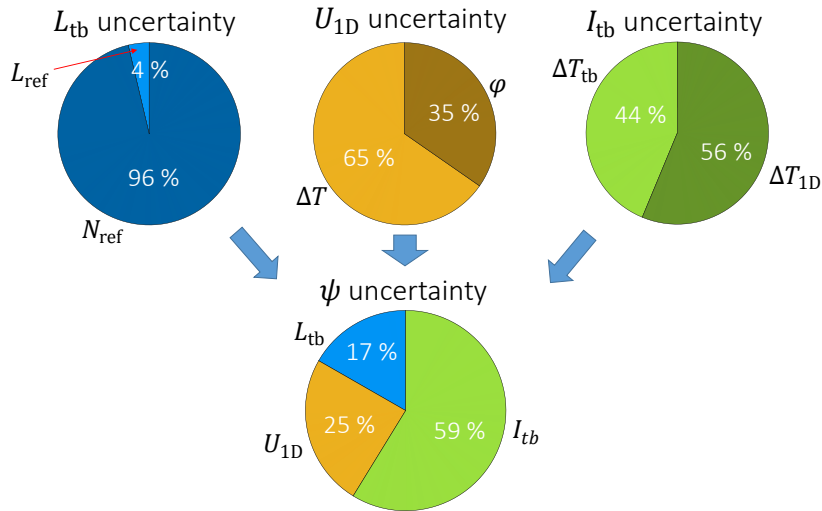
An analysis of the measurement uncertainties is carried out to identify the main sources of error. The numerical values of each parameter used in the uncertainty calculation are summarized in Tab C.1. The metal rail is taken as an example.

**Table C.1.:** Input data for  $\psi$  uncertainty calculation (metal rail).

$\psi$ (Eq 6.5)		
$L_{tb}$ (Eq 6.17)	$U_{1D}$ (Eq 6.2)	$I_{tb}$ (Eq 6.15)
$L_{ref} = 1200 \pm 1$ mm	$\varphi = 11.7 \text{ W.m}^{-1}.\text{K}^{-1} \pm 3\%$	$\Delta T_{tb}^{app} = 0.91 \pm 0.02$ K
$N_{ref} = 230 \pm 3$	$\Delta T = 31.4 \pm 0.5$ K	$\Delta T_{1D}^{app} = 0.52 \pm 0.02$ K

The relative contribution of each parameter to the measurement uncertainty on  $\psi$  and  $\chi$  is given in Fig C.4. For a quantity  $Y$  function of parameters  $\beta_i$ , each parameter relative contribution to  $u_Y$  is:  $|\frac{\partial Y}{\partial \beta_i} u_{\beta_i}| / \sqrt{\sum (\frac{\partial Y}{\partial \beta_i} u_{\beta_i})^2}$ .

It may be concluded that most of the measurement uncertainty comes from the calculation of the impact factor  $I_{tb}$ , that is to say from the measurement of the apparent temperatures  $T_{tb}^{app}$  and  $T_{1D}^{app}$ .



**Figure C.4.:** Relative uncertainty of each parameter in  $\psi$  coefficient calculation (metal rail).

# D. Appendices of Chap 7

## D.1. Details on the Levenberg-Marquardt algorithm

The minimization of cost junction  $J$  in the case of a non-linear direct model is based on a iterative procedure. The Levenberg-Marquardt algorithm was chosen to perform this identification for its robustness and stability. It uses a regularization process based on Tikhonov penalization [217]. This regularization enable the algorithm to converge even when the problem is rather ill-posed (when the determinant of the information matrix is close to zero). The algorithm works as follows:

Levenberg [214] suggested to add a penalization term in Eq 7.48:

$$\hat{\boldsymbol{\beta}}^{(k+1)} = \hat{\boldsymbol{\beta}}^{(k)} + \left( X^{(k)\text{T}} X^{(k)} + \mu^{(k)} D^{(k)} \right)^{-1} X^{(k)\text{T}} \left( \mathbf{y} - \mathbf{y}_{mo} \left( \hat{\boldsymbol{\beta}}^{(k)} \right) \right) \quad (\text{D.1})$$

where  $\mu$  is a damping factor and  $D$  a positive definite diagonal matrix (usually,  $D = I$ ). To ease notations, we introduce the parameter increments  $\boldsymbol{\delta}^{(k)} = \hat{\boldsymbol{\beta}}^{(k+1)} - \hat{\boldsymbol{\beta}}^{(k)}$  and  $\mathbf{r}^{(k)} = \mathbf{y} - \mathbf{y}_{mo} \left( \hat{\boldsymbol{\beta}}^{(k)} \right)$ . In addition, the  $(k)$  subscripts will now be omitted. Equation D.1 can therefore be written as:

$$\boldsymbol{\delta} = \left( X^{\text{T}} X + \mu I \right)^{-1} X^{\text{T}} \mathbf{r} \quad (\text{D.2})$$

Marquardt [215] used this algorithm on a normalized version of the problem. We define the normalized sensitivity matrix  $X^*$  such that:

$$X_{ij}^* = \frac{X_{ij}}{\| \mathbf{X}_j \|} \quad (\text{D.3})$$

Then, the Singular Value Decomposition (SVD) of the normalized sensitivity matrix is used:

$$X^* = U W V^{\text{T}} \quad (\text{D.4})$$

so that Eq D.2 becomes:

$$\boldsymbol{\delta}^* = \left( V (W^2 + \mu I) V^T \right)^{-1} X^T \mathbf{r} \quad (\text{D.5})$$

$$= V (W^2 + \mu I)^{-1} \mathbf{u} \quad (\text{D.6})$$

with  $\mathbf{u} = V^T X^T \mathbf{r} = W U^T$

The previous equation enables to work out  $\boldsymbol{\delta}^*$  from which  $\boldsymbol{\delta}$  is extracted:

$$\forall i \in \llbracket 1; n \rrbracket : \delta_i = \frac{\delta_i^*}{\|\mathbf{X}_j\|} \quad (\text{D.7})$$

This allows computing the parameter vector for the next iteration  $\hat{\boldsymbol{\beta}}^{(k+1)}$ . At every iteration, the damping factor  $\mu$  is increased or decreased depending on the evolution of the cost function  $J$ :

$$\text{if } J\left(\hat{\boldsymbol{\beta}}^{(k+1)}\right) > J\left(\hat{\boldsymbol{\beta}}^{(k)}\right), \text{ then } \mu^{(k+1)} = 10\mu^{(k)} \quad (\text{D.8})$$

$$\text{if } J\left(\hat{\boldsymbol{\beta}}^{(k+1)}\right) < J\left(\hat{\boldsymbol{\beta}}^{(k)}\right), \text{ then } \mu^{(k+1)} = \frac{1}{10}\mu^{(k)} \quad (\text{D.9})$$

As the algorithm converges, the value of the damping factor decreases. Convergence is deemed achieved when one of the following quantity becomes smaller than a predefined threshold: the cost function, the gradient of the cost function, the parameter increment or the relative parameter increment. When the damping factor  $\mu$  is very small, the Levenberg-Marquardt algorithm is equivalent to the Gauss-Newton method: convergence is rather fast but it requires to have initial values close to the optimum. However, when the damping factor is very large, the algorithm becomes equivalent to the gradient method which converges slowly but is more stable in case of initial conditions far away from the optimum. Thus, the Levenberg-Marquardt algorithm combines the advantages of the Gauss-Newton and the gradient methods.

## D.2. ARX MISO case

### D.2.1. Formulation

In the MISO case (Multiple Inputs, Single Output), the ARX formulation is written as:

$$\mathcal{A}(\boldsymbol{\beta}, q) y = \mathcal{B}(\boldsymbol{\beta}, q) u + \mathcal{C}(\boldsymbol{\beta}, q) v \quad (\text{D.10})$$

with  $\boldsymbol{\beta}$  the parameter vector:

$$\boldsymbol{\beta} = [a_1, \dots, a_{n_a}, b_0, \dots, b_{n_b-1}, c_0, \dots, c_{n_c-1}]^T \quad (\text{D.11})$$

$\mathcal{A}$ ,  $\mathcal{B}$  and  $\mathcal{C}$  are polynomials in the back-shift operator  $q$ . Their orders are  $n_a$ ,  $n_b - 1$  and  $n_c - 1$  respectively:

$$\mathcal{A}(\boldsymbol{\beta}, q) = 1 + a_1 q^{-1} + \dots + a_{n_a} q^{-n_a} \quad (\text{D.12})$$

$$\mathcal{B}(\boldsymbol{\beta}, q) = b_0 + b_1 q^{-1} + \dots + b_{n_b-1} q^{-n_b+1} \quad (\text{D.13})$$

$$\mathcal{C}(\boldsymbol{\beta}, q) = c_0 + c_1 q^{-1} + \dots + c_{n_c-1} q^{-n_c+1} \quad (\text{D.14})$$

Parameter  $n_k$  is set to zero.

### D.2.2. Estimation of a wall thermal resistance

The MISO formulation is interesting to include measurements of the external surface temperature  $\theta_{\text{se}}$ :

$$\begin{cases} y &= \varphi_{\text{si}} \\ u &= \theta_{\text{si}} \\ v &= \theta_{\text{se}} \end{cases} \quad (\text{D.15})$$

In this case, there is no explicit formulation of the wall thermal resistance from parameters  $a_i$ ,  $b_i$  and  $c_i$ . Indeed, two impedances are defined ( $\mathcal{Z}_{\text{si}}$  and  $\mathcal{Z}_{\text{se}}$ ) so two thermal resistances may be derived:



$$\widehat{R}_i = \mathcal{Z}_{si}(\beta, 1) = \frac{\mathcal{A}(\beta, 1)}{\mathcal{B}(\beta, 1)} \quad (\text{D.16})$$

$$\widehat{R}_e = \mathcal{Z}_{se}(\beta, 1) = \frac{\mathcal{A}(\beta, 1)}{\mathcal{C}(\beta, 1)} \quad (\text{D.17})$$

There is no relationship between these estimated resistances and the thermal resistances of each wall layer. In most studies dealing with this issue, these two estimations of  $R$  (or similarly HLC) are combined into a single value by a Lagrange weighting [120, 132, 135, 136]:

$$\widehat{R} = \lambda \widehat{R}_i + (1 - \lambda) \widehat{R}_e \quad (\text{D.18})$$

where the weighting factor  $\lambda$  is chosen to minimize the uncertainty on  $\widehat{R}$ :

$$\lambda = \frac{\text{Var}(R_e) - \text{Covar}(R_i, R_e)}{\text{Var}(R_i) + \text{Var}(R_e) - \text{Covar}(R_i, R_e)} \quad (\text{D.19})$$

This formulation has no physical meaning.

### D.2.3. Discussion of results

This procedure was tested but it turned out that the estimated value was very far from the reference and the associated uncertainty was very large. In addition, the algorithm is not stable: slightly changing the time horizon significantly changes the result. It is thought that the MISO formulation needs more data to converge than the SISO one because it has more parameters to determine. Indeed, the previous studies which successfully used this kind of MISO ARX models are all based on much longer measurement campaigns. Jiménez *et al.* [132] and Senave *et al.* [136] both used measurements recorded during 20 consecutive days to estimate a wall thermal resistance and a HLC respectively. Lambie and Saelens [135] performed two experimental campaigns of 15 and 35 days respectively (HLC estimation). Deconinck and Roels [120] used a dataset of 60 days and showed that a minimum of 20 days was required for their ARX method to give accurate results (thermal resistance estimation). In comparison to these durations, the present study deals with only 8 consecutive hours of measurement data which is almost two orders of magnitude shorter. From this perspective, implementing this model on more data (much longer experiments) might give better results but the present rapid method focuses on short measurements (i.e., less than 24 hours).

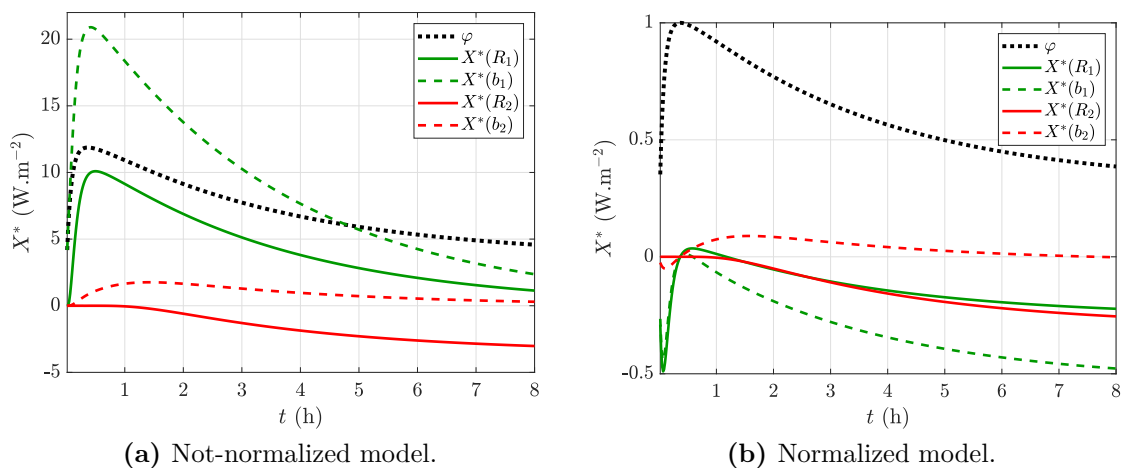
# E. Appendices of Chap 8

## E.1. Theoretical study: signal normalization

This appendix proposes a theoretical study about the normalization of signals for the estimation of a wall thermal resistance with a white-box model. Basically, in some cases, it is interesting to normalize the amplitude of the thermogram to estimate a thermal property from an active method. For instance, the estimation of a material thermal diffusivity with the flash method benefits from the normalization of the thermogram [230, 14]. It allows removing the amplitude of the pulse from the unknown parameter vector which makes the problem less ill-posed. However, as shown below, normalizing the measured heat flux in our case makes the inverse problem more ill-posed.

The test case presented in section 7.1.5 of Chap 7 is used (two-layer wall subjected to air heating). The problem has four unknown parameters  $R_1$ ,  $b_1$ ,  $R_2$  and  $b_2$  (thermal properties of the two layers).

The measured heat flux is normalized by its maximum value (which might be not straightforward to find on noisy signals), reached here after about half an hour of heating. Figure E.1 plots the reduced sensitivities for the not-normalized and the normalized models. At the maximum value, all the sensitivities collapse to zero. As a consequence, the reduced sensitivity coefficients look more correlated.



**Figure E.1.:** Reduced sensitivity coefficients of the non-normalized and normalized models.

This is confirmed by the analysis of the singular value of the reduced sensitivity matrix presented below.

Not-normalized model:

$$s = [1, 0.146, 0.040, 0.018] \quad (\text{E.1})$$

Normalized model:

$$s = [1, 0.130, 0.102, 6.6 \times 10^{-6}] \quad (\text{E.2})$$

These values are normalized by the first singular value. It may be seen that the last singular value of the normalized model is very close to zero: the information in the reduced sensitivity matrix is redundant. The normalized model has about three degrees of freedom whereas the not-normalized one has about four.

As a conclusion, the normalized problem is more ill-posed than the not-normalized one because of the appearance of strong correlations between parameters. In theory, the normalization enables to remove one parameter: the amplitude of the thermal load (here the amplitude of the internal air heating temperature). However, unlike the flash method, this amplitude was supposed known and not estimated so the normalization step does not remove any unknown parameter.

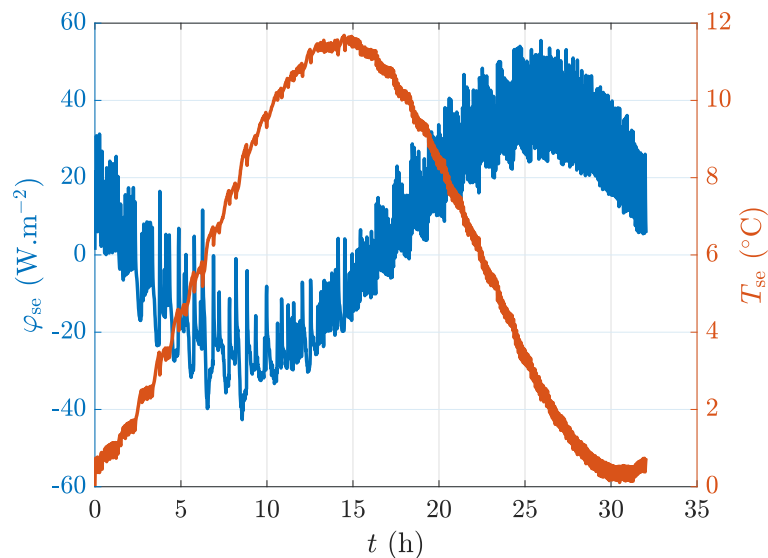
## E.2. CEREMA, estimation of $R_3$ & $b_3$ (concrete block thermal properties)

This section presents in details the estimation of the thermal properties  $R_3$  and  $b_3$  of the concrete layer of the CEREMA wall with model  $H_1$ . As exposed in section 8.3, this prior quantification of  $R_3$  and  $b_3$  from external surface measurements is required for the estimation of  $R_1$ ,  $b_1$ ,  $R_2$  and  $b_2$  with model  $AE_3$  (the problem is too-ill-posed for a simultaneous estimation of all six parameters).

Two methods are compared here. The first one (the “time-domain method”) follows the protocol presented in section 8.2 (white-box approach). A function of known Laplace transform is fitted to the input (the external surface temperature  $T_{se}$  here), and the external surface heat flux,  $\varphi_{se}$ , is the model output. In theory, it is applicable whatever the shape of  $T_{se}$ , as long as the amplitude is high enough to guarantee a decent SNR on the measurements.

The second method consists in working in the frequency domain given that  $T_{se}$  and  $\varphi_{se}$  are sinusoidal in the CEREMA experiments. This method is not meant to be applied *in situ* but is relevant in the current context of harmonic signals.

The methods are illustrated on measurements recorded during an experiment of configuration 5 (15 K amplitude of external air temperature oscillations). One oscillation period (32 h) is considered here, as shown in Fig E.2.



**Figure E.2.:** External surface measurements during one period (experiment of configuration 5).

### E.2.1. Time-domain method

Model  $H_1$  is defined as follows:

$$\widetilde{\varphi}_{\text{se}}(p) = Y(\boldsymbol{\beta}, p) \times \widetilde{T}_{\text{se}}(p) \quad (\text{E.3})$$

with

$$\boldsymbol{\beta} = [R_3 \ b_3] \quad (\text{E.4})$$

and  $Y$  the thermal admittance of the slab. From the thermal quadrupole formalism:

$$Y(\boldsymbol{\beta}, p) = \frac{C(\boldsymbol{\beta}, p)}{A(\boldsymbol{\beta}, p)} \quad (\text{E.5})$$

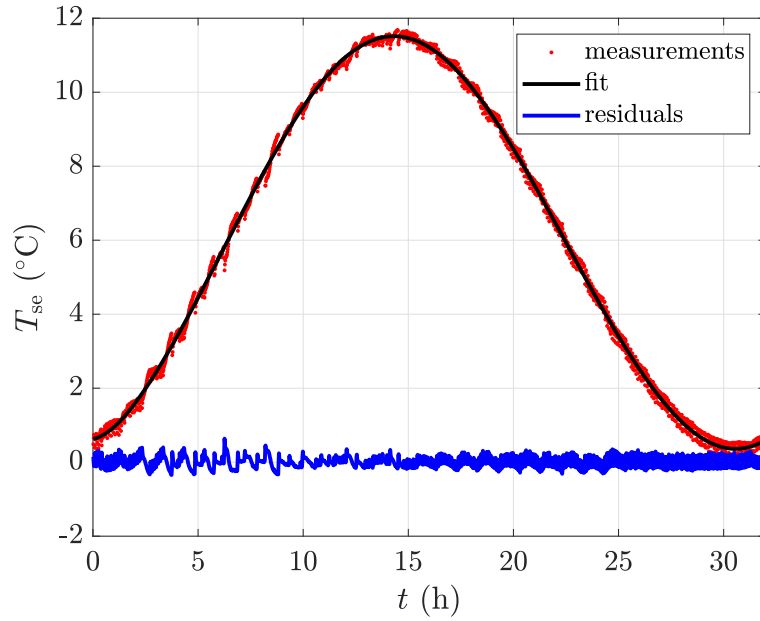
$$= b_3 \sqrt{p} \times \tanh(R_3 b_3 \sqrt{p}) \quad (\text{E.6})$$

A polynomial of order 7 is fitted to the measurements of  $T_{\text{se}}$ , as shown in Fig E.3. A polynomial was used to demonstrate that the method is not limited to sinusoidal signals. A temperature curve of any shape could be analyzed (provided it is “smooth” enough to fit a function to it). The reduced sensitivity coefficients and  $V_{\text{cor}}$  matrix calculated from the estimated parameters are presented in Fig E.4 and Tab E.1. The first twelve hours are not used in the inverse methods because the model needs time to develop from null initial conditions. The two parameters have a non-negligible reduced sensitivity and are not correlated with each other. The measurement noise used in the calculation of  $V_{\text{cor}}$  is estimated from the residual standard deviation:  $\sigma = 8 \text{ W.m}^{-2}$ . This is an order of magnitude higher than the measurement noise usually obtained ( $0.4 \text{ W.m}^{-2}$ ). This is due to the climate chamber regulation system. However, the magnitude of the measured heat flux (up to  $40 \text{ W.m}^{-2}$ ) is also higher than usual (up to  $12 \text{ W.m}^{-2}$ ). The high value of  $\sigma$  is also compensated by the simplicity of the model (only two parameters) and the high number of points (one per minute). In the end, the relative estimation uncertainties of  $R_3$  and  $b_3$  are of 2 and 1%, respectively.

**Table E.1.:**  $V_{\text{cor}}$  matrix (for  $\boldsymbol{\beta} = \widehat{\boldsymbol{\beta}}$  and  $\sigma = 8 \text{ W.m}^{-2}$ ).

	$R_3$	$b_3$
$R_3$	0.02	-0.81
$b_3$	-0.81	0.01

Figure E.5 plots the measured data alongside the model output after estimation of the parameters. The residuals looks unsigned. The independence of the results to



**Figure E.3.:** Fit of a polynomial function (order 7) to the external surface temperature  $T_{se}$ .

the initial parameter vector and time horizon was checked. The estimated thermal resistance and effusivity of the concrete block layer are  $\widehat{R}_3 = 0.28 \pm 0.01 \text{ m}^2 \cdot \text{K} \cdot \text{W}^{-1}$  and  $\widehat{b}_3 = 706 \pm 8 \text{ J} \cdot \text{K}^{-1} \cdot \text{m}^{-2} \cdot \text{s}^{-1/2}$ , respectively.

## E.2.2. Harmonic method

In this approach, the admittance is used in the frequency domain. The model  $Y_{mo}$  is given by Eq E.6 with  $p = j2\pi f_e$ :

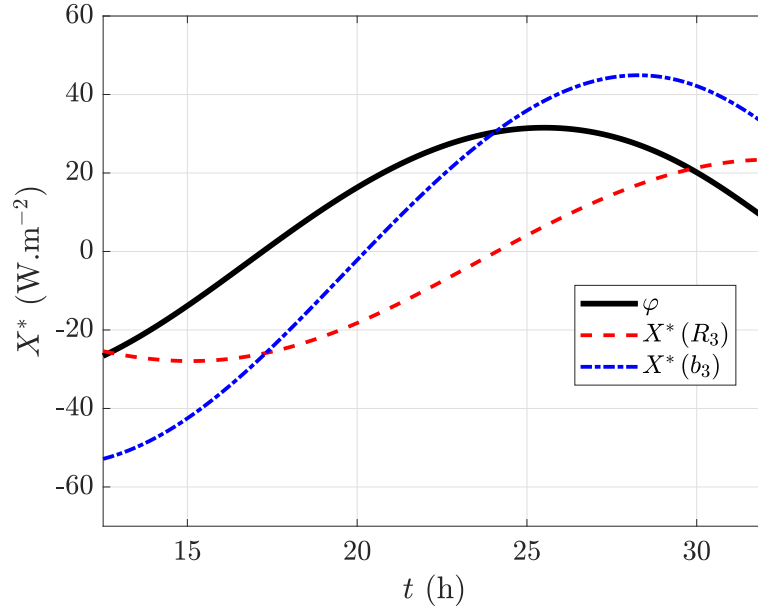
$$Y_{mo}(\beta) = b_3 \sqrt{j2\pi f_e} \times \tanh \left( R_3 b_3 \sqrt{j2\pi f_e} \right) \quad (\text{E.7})$$

with  $f_e$  the frequency of the oscillations ( $f_e = 1/[32 \text{ h}]$ ). The experimental impedance  $Y$  is derived from the measurements of  $\varphi_{se}$  and  $T_{se}$ :

$$Y = \frac{FT_\varphi(f_e)}{FT_T(f_e)} \quad (\text{E.8})$$

with  $FT_\varphi$  and  $FT_T$  the Fourier transforms of  $\varphi_{se}$  and  $T_{se}$ , respectively.

The estimated parameter vector is obtained from minimization of the difference between the experimental and theoretical admittances. In practice, the measurements



**Figure E.4.:** Reduced sensitivity coefficients (calculated for  $\beta = \hat{\beta}$ ).

and model vectors only have two elements: the real and imaginary parts of the admittance:

$$\mathbf{y} = [\text{Re}(Y), \text{Im}(Y)] \quad (\text{E.9})$$

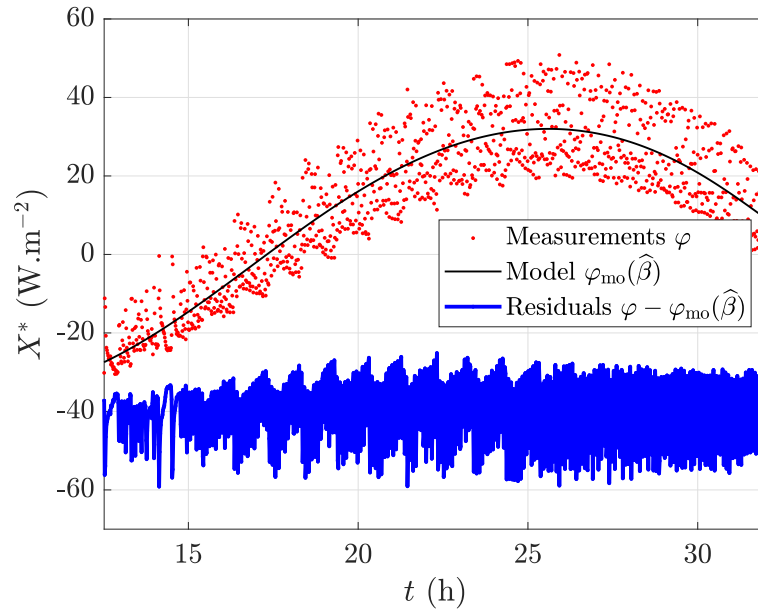
$$\mathbf{y}_{\text{mo}}(\beta) = [\text{Re}(Y_{\text{mo}}(\beta)), \text{Im}(Y_{\text{mo}}(\beta))] \quad (\text{E.10})$$

The cost function to minimize is:

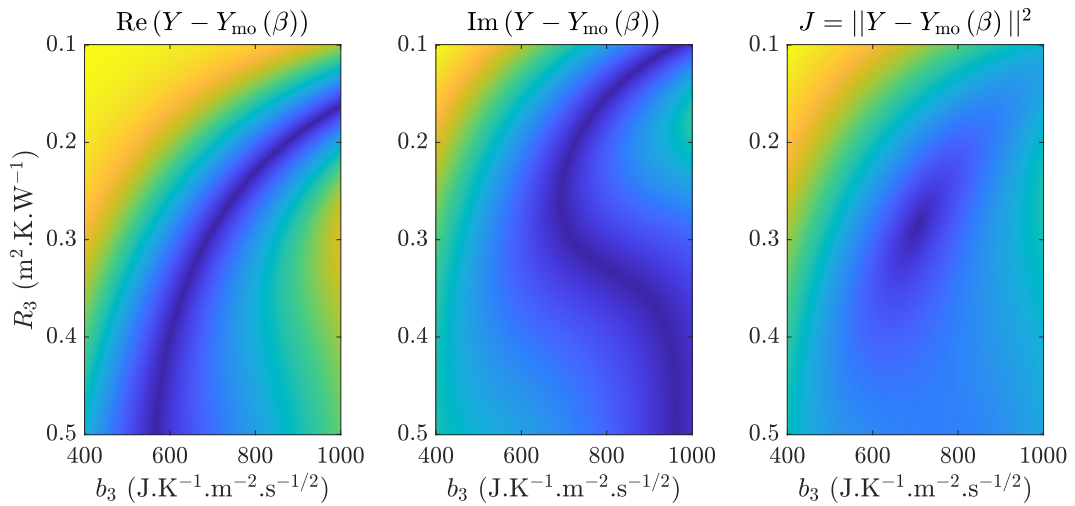
$$J(\beta) = (\mathbf{y} - \mathbf{y}_{\text{mo}}(\beta))^T (\mathbf{y} - \mathbf{y}_{\text{mo}}(\beta)) \quad (\text{E.11})$$

$$= \|Y - Y_{\text{mo}}(\beta)\|^2 \quad (\text{E.12})$$

The parameter space only has two dimensions:  $R_3$  and  $b_3$ . Therefore, it is interesting to plot the magnitude of the elements of  $\mathbf{y} - \mathbf{y}_{\text{mo}}(\beta)$  as well as the cost function in this space (see Fig E.6). It may be seen that the cost function  $J$  has a minimum around  $\beta = [0.30 \ 700]$ . The exact value of the optimum parameter vector is determined with the Levenberg-Marquardt algorithm. It comes  $\hat{\beta} = [0.28 \ 703]$ . These values are almost identical to the estimations with the time-domain approach.



**Figure E.5.:** Comparison model/measurements and residuals.



**Figure E.6.:** Elements of  $\mathbf{y} - \mathbf{y}_{\text{mo}}(\beta)$  vector and cost junction  $J$  plotted in the parameter space.



### E.3. CEREMA, impact of a bias on the values of $R_3$ and $b_3$ on the estimated thermal resistance

when the external temperature is not constant, the estimation of the thermal resistance of the insulation system of the CEREMA wall requires a prior quantification of parameters  $R_3$  and  $b_3$  (thermal properties of the building blocs layer). The estimation of  $R_1$ ,  $b_1$ ,  $R_2$  and  $b_2$  with model AIE<sub>3</sub> supposes  $R_3$  and  $b_3$  perfectly known. This appendix studies the impact of a bias on these two quantities on the estimated thermal resistance  $\widehat{R} = \widehat{R}_1 + \widehat{R}_2$ .

Four experiments of configuration 5 (maximum external temperature variation) are taken as example. They are number 17, 19, 21 and 23 (see Tab 8.11). They were chosen because they represent the four pattern of  $T_{\text{air,e}}$  variation (around a maximum:  $\cap$ , or increasing:  $\nearrow$ , or around a minimum:  $\cup$ , or decreasing:  $\searrow$ ).

We define the relative bias  $\delta(Y)$  of a quantity  $Y$  by:

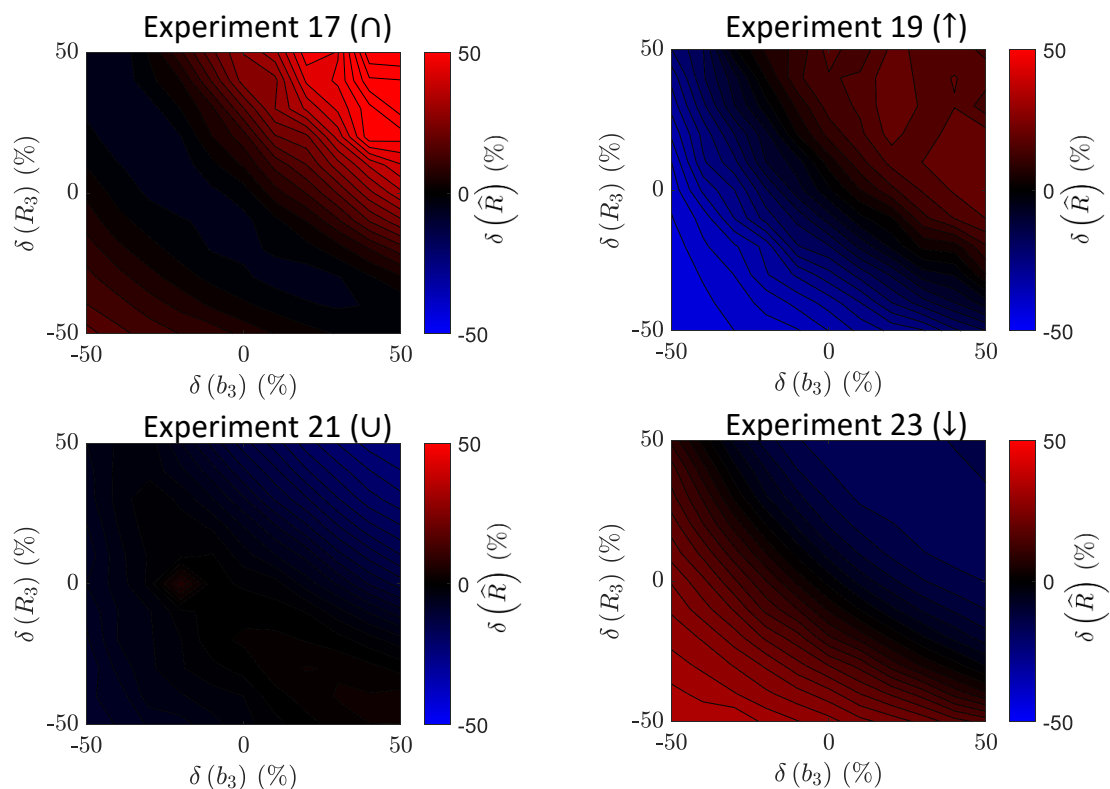
$$\delta(Y) = \frac{Y - Y^{\text{ref}}}{Y^{\text{ref}}} \quad (\text{E.13})$$

with  $Y^{\text{ref}}$  a reference values. The reference values assigned to  $R_3$  and  $b_3$  are the values estimated by model H<sub>1</sub> (see Appendix E.2) and used in section 8.3.4:  $R_3^{\text{ref}} = 0.28 \text{ m}^2.\text{K}.\text{W}^{-1}$  and  $b_3^{\text{ref}} = 708 \text{ J}.\text{K}^{-1}.\text{m}^{-2}.\text{s}^{-1/2}$ . The reference value of  $\widehat{R}^{\text{ref}}$  is obtained from estimation of the unknown parameters of model AIE<sub>2</sub> with  $R_3 = R_3^{\text{ref}}$  and  $b_3 = b_3^{\text{ref}}$  (it therefore depends on the experiment).

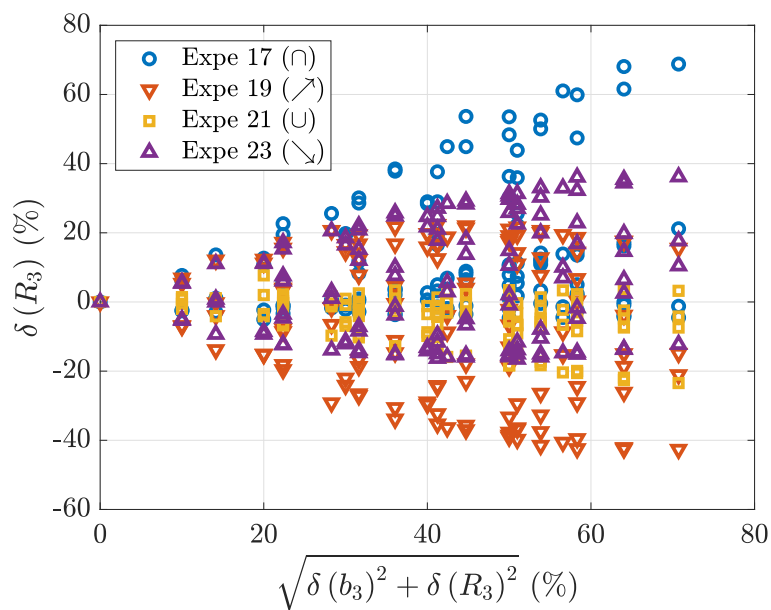
Figure E.7 plots  $\delta(\widehat{R})$  as a function of  $\delta(R_3)$  and  $\delta(b_3)$ . The same results are also summarized in Fig E.8. It may be seen that bias on  $\widehat{R}$  induced by as bias on  $R_3$  and  $b_3$  depends on the experiment. Overall, the biases are of the same order of magnitude: a bias of 50% on the thermal properties of the load bearing layer may generate a bias up to 50% on the estimated thermal resistance  $\widehat{R}$ . As a consequence, attention must be paid to the estimation of  $R_3$  and  $b_3$  as they have direct impact on  $\widehat{R}$ .

E.3. CEREMA, IMPACT OF A BIAS ON THE VALUES OF  $R_3$  AND  $B_3$  ON THE ESTIMATED THERMAL RESISTANCE

---



**Figure E.7.:** Isocontours of relative bias on  $\hat{R}$  as a function of relative bias on  $R_3$  and  $b_3$  for experiments 17, 19, 21 and 23.



**Figure E.8.:** Summary of relative biases on  $\hat{R}$  as a function of relative bias on  $R_3$  and  $b_3$  for experiments 17, 19, 21 and 23.

## E.4. CEREMA experiments, residuals after parameter estimation

This appendix compares the measurements and direct model outputs after parameter estimation for each experiment of the CEREMA experimental campaign. Measurements are performed on the sound area in order to estimate the thermal resistance of the wall thermal insulation system.

For each experiment except number 1, 4 and 6, the time horizon used for the inverse method goes from 10 min to 6 h. Experiments 1, 4 and 6 had to be stopped prematurely for practical reasons after only 5 or 4 h. However, on these three cases, those shorter durations were enough to estimate the desired thermal resistance. It may also be noted that experiment 11 suffers from a small disturbance before 2 h of measurements. This however does not impact the accuracy of the parameter estimation.

The residuals are unsigned which is an indicator of the quality of the inverse method.

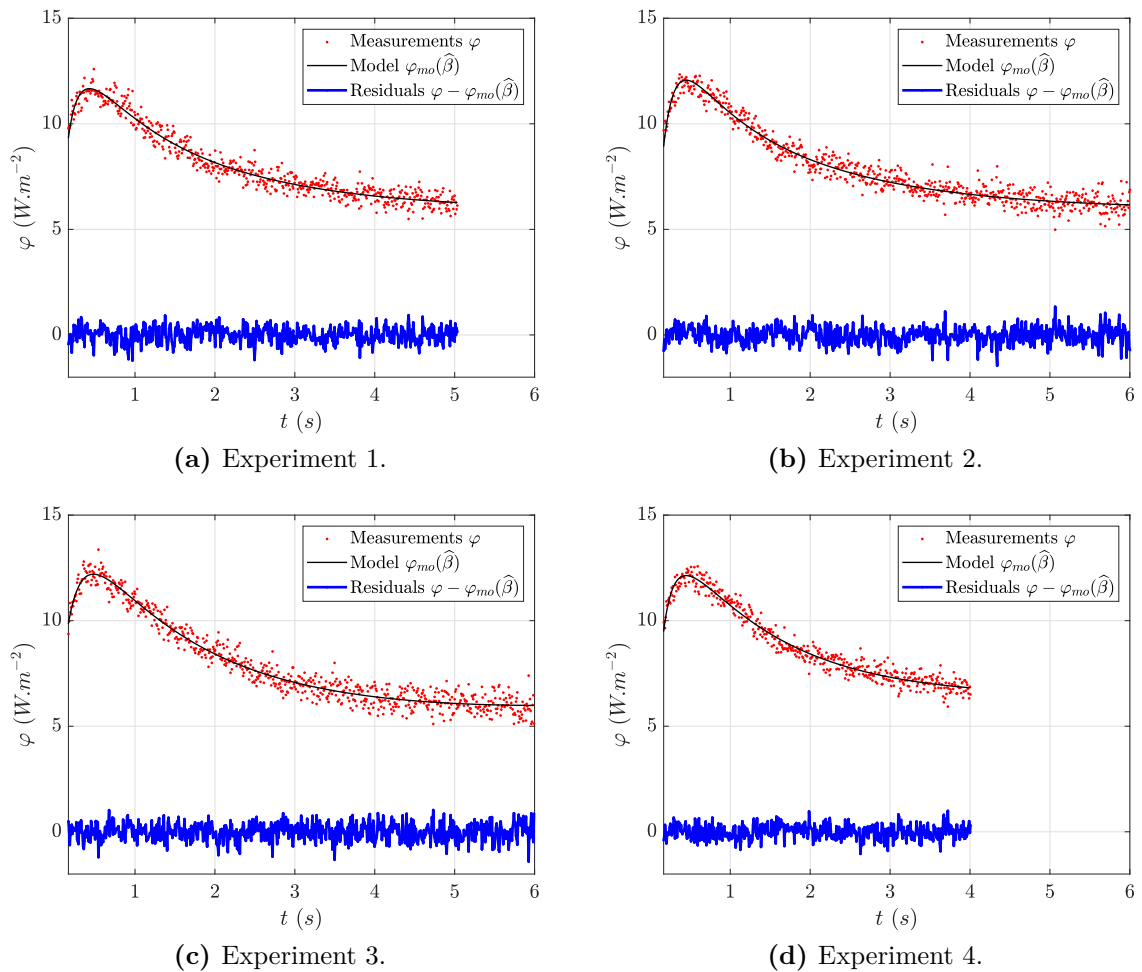


Figure E.9.: Configuration 1, model A<sub>2</sub>, 1/2.

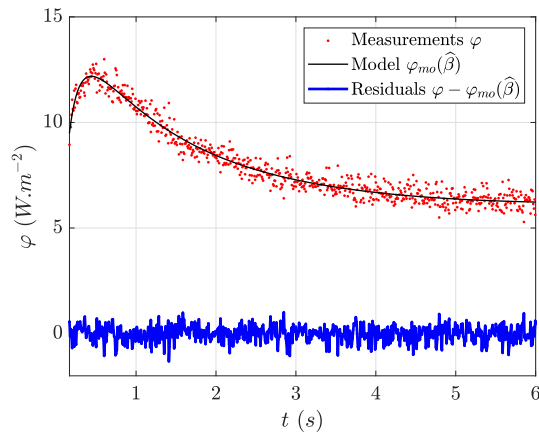
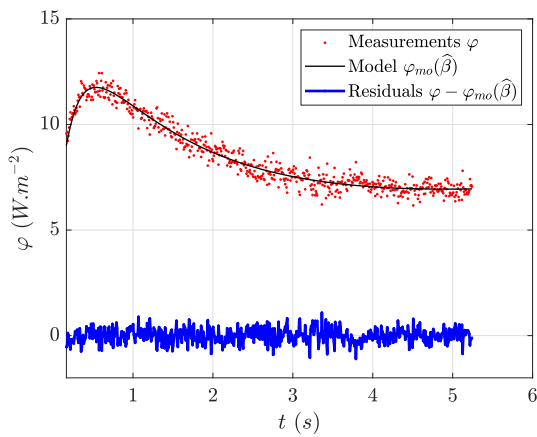
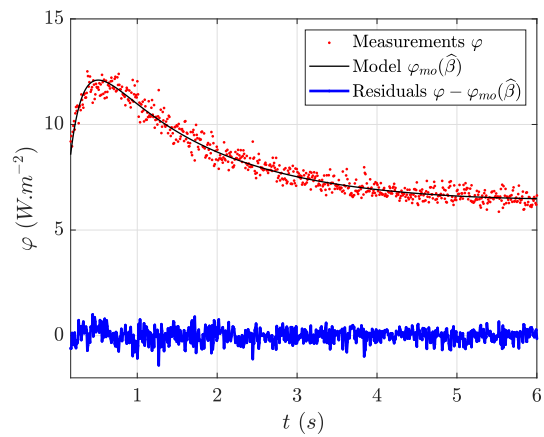


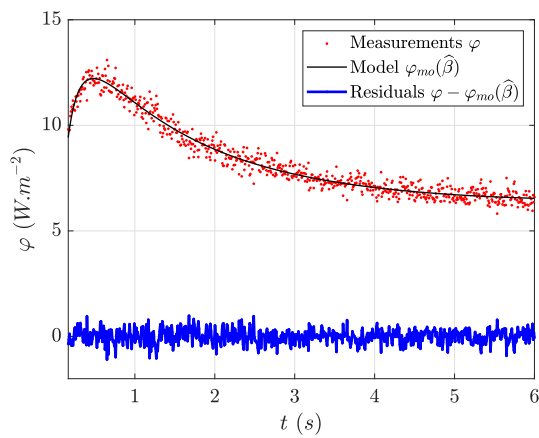
Figure E.10.: Configuration 1, model  $A_2$ , 2/2 (Experiment 5).



(a) Experiment 6.

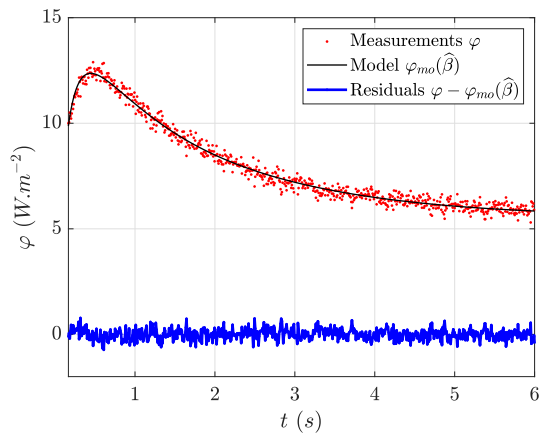


(b) Experiment 7.

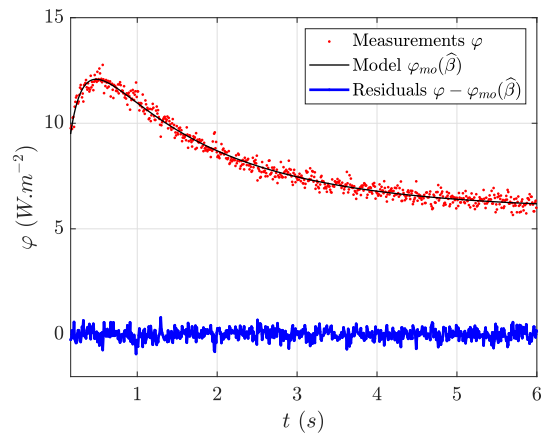


(c) Experiment 8.

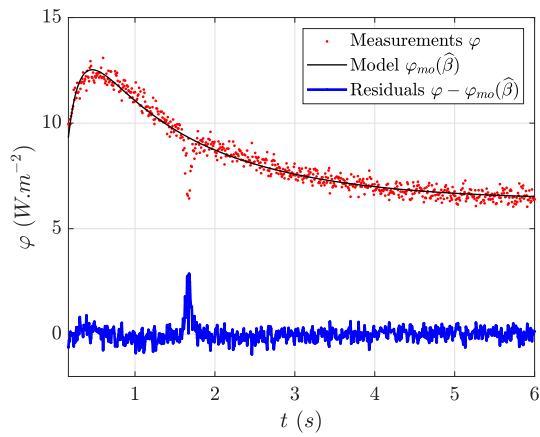
Figure E.11.: Configuration 2, model  $A_2$ .



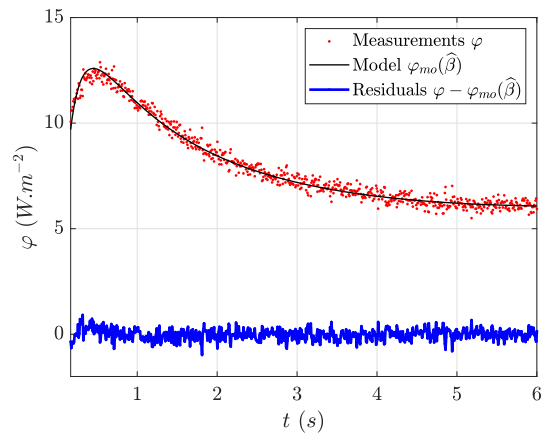
(a) Experiment 9.



(b) Experiment 10.



(c) Experiment 11.

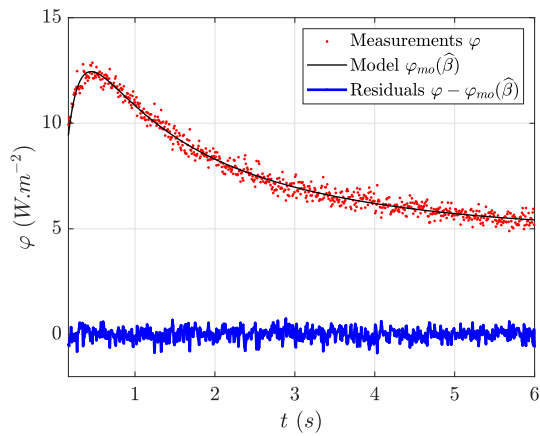


(d) Experiment 12.

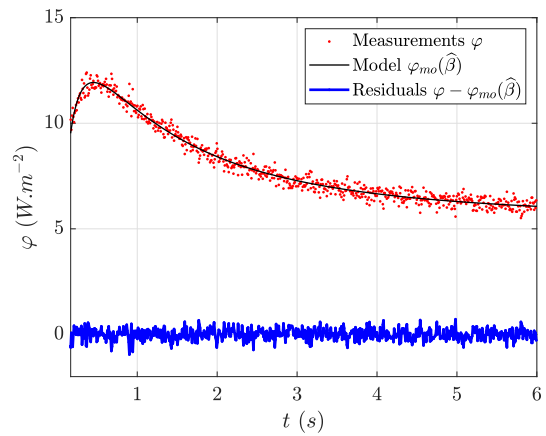
Figure E.12.: Configuration 3, model AE<sub>3</sub>.

#### E.4. CEREMA EXPERIMENTS, RESIDUALS AFTER PARAMETER ESTIMATION

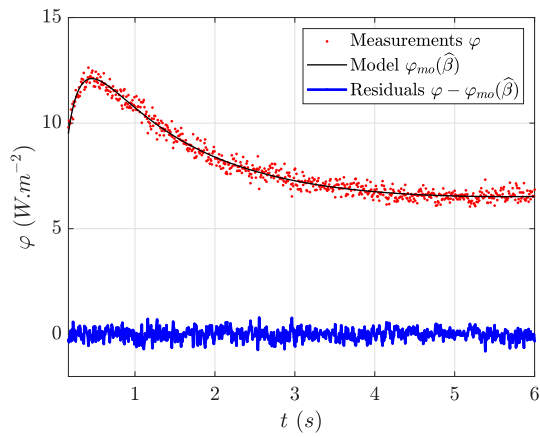
---



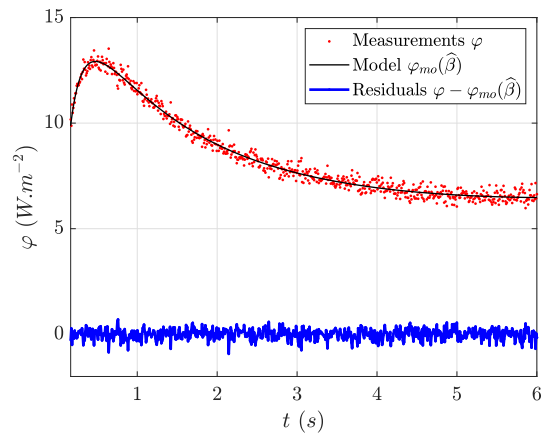
(a) Experiment 13.



(b) Experiment 14.

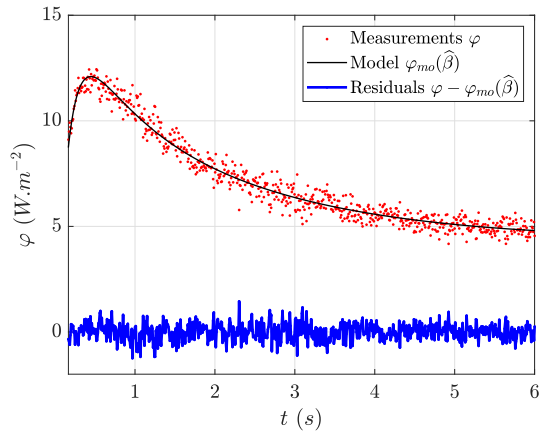


(c) Experiment 15.

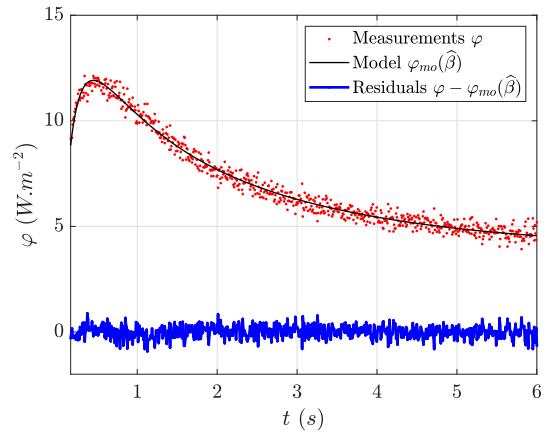


(d) Experiment 16.

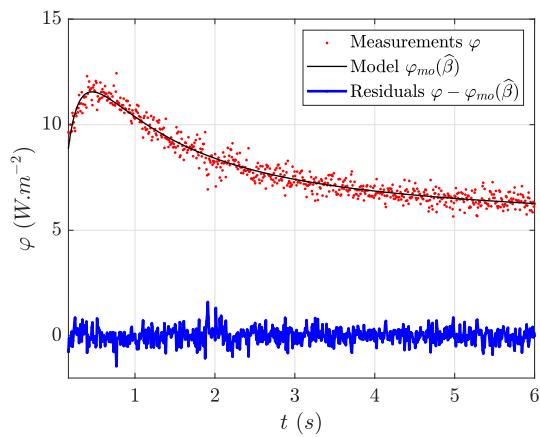
**Figure E.13.:** Configuration 4, model AE<sub>3</sub>.



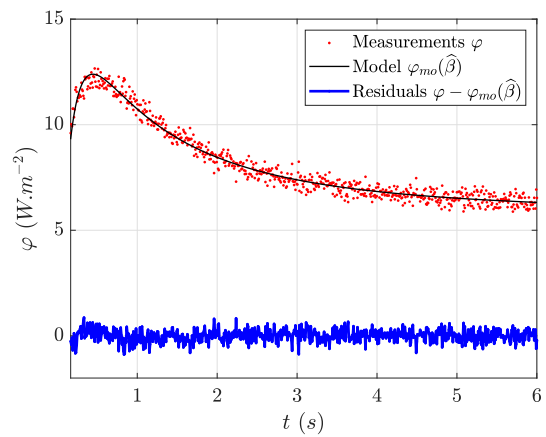
(a) Experiment 17.



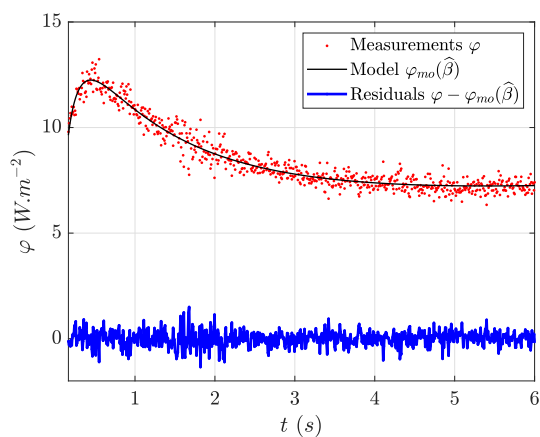
(b) Experiment 18.



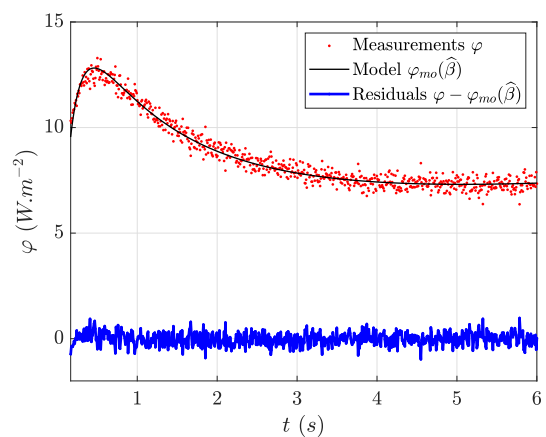
(c) Experiment 19.



(d) Experiment 20.



(e) Experiment 21.



(f) Experiment 22.

Figure E.14.: Configuration 5, model AE<sub>3</sub>, 1/2

#### E.4. CEREMA EXPERIMENTS, RESIDUALS AFTER PARAMETER ESTIMATION

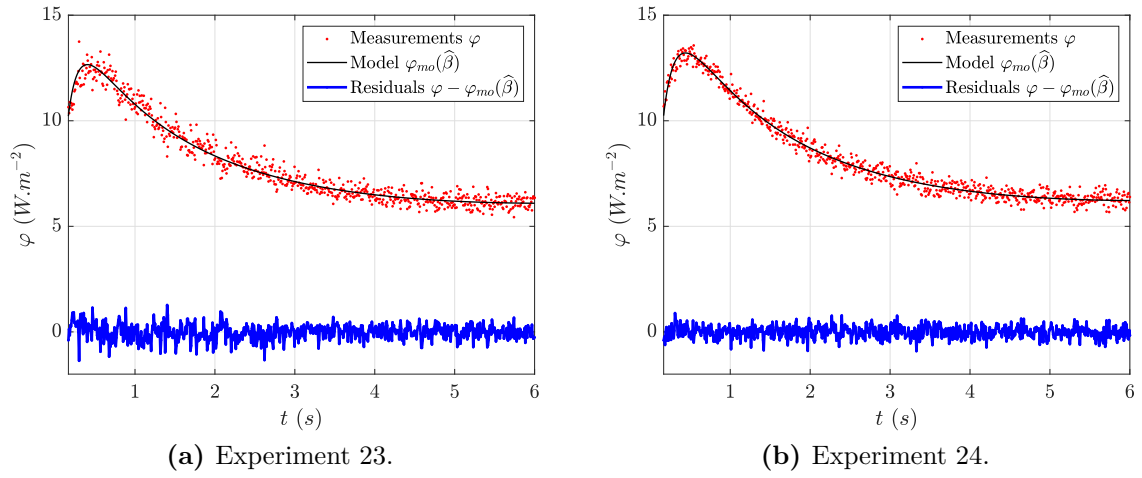


Figure E.15.: Configuration 5, model  $AE_3$ , 2/2.

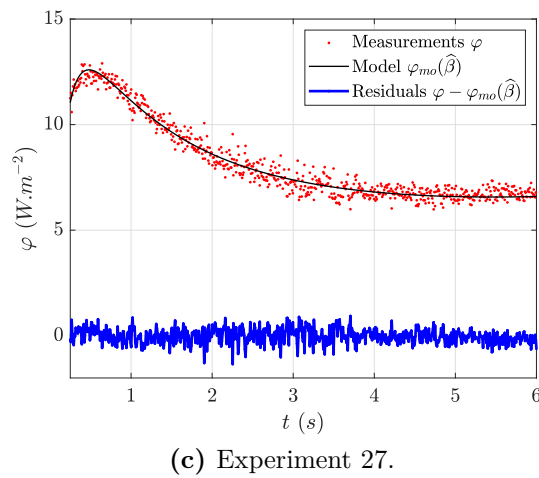
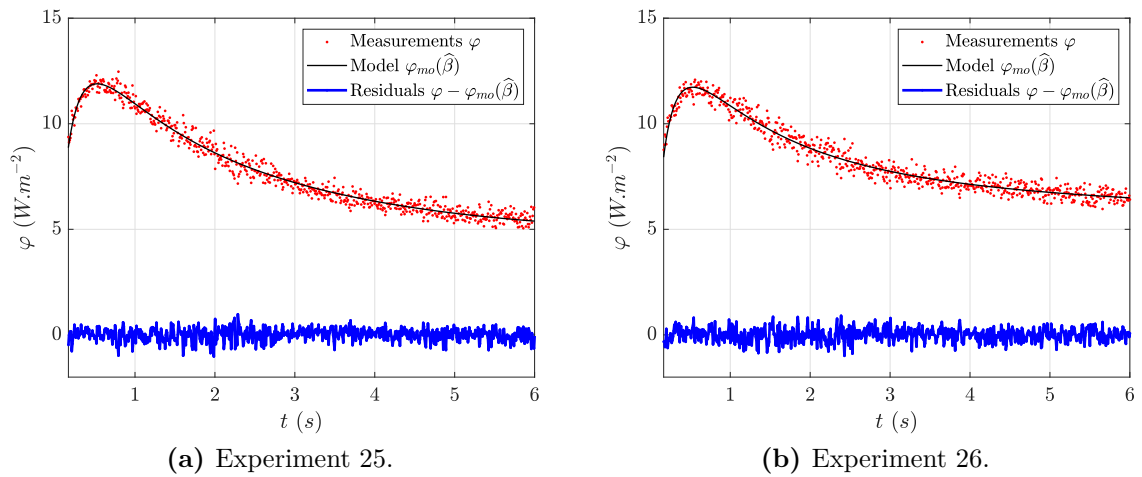


Figure E.16.: Configuration 6, model  $AE_3$ .



## E.5. SGR, residuals after parameter estimation

This appendix presents the residuals obtained after parameter estimation on the active measurements of the SGR experiments. The results of model AIE<sub>2</sub> are presented here (internal and external correction). The residuals are rather unsigned. They are not as good as with the CEREMA experiments because the measurements were made *in situ*, not in a climate chamber.

There is a small disturbance on the measured heat flux at the beginning of Experiment 5. This does not prevent the estimated thermal resistance to be close to the reference value (the sensitivity to  $R_2$  is almost null at the beginning).

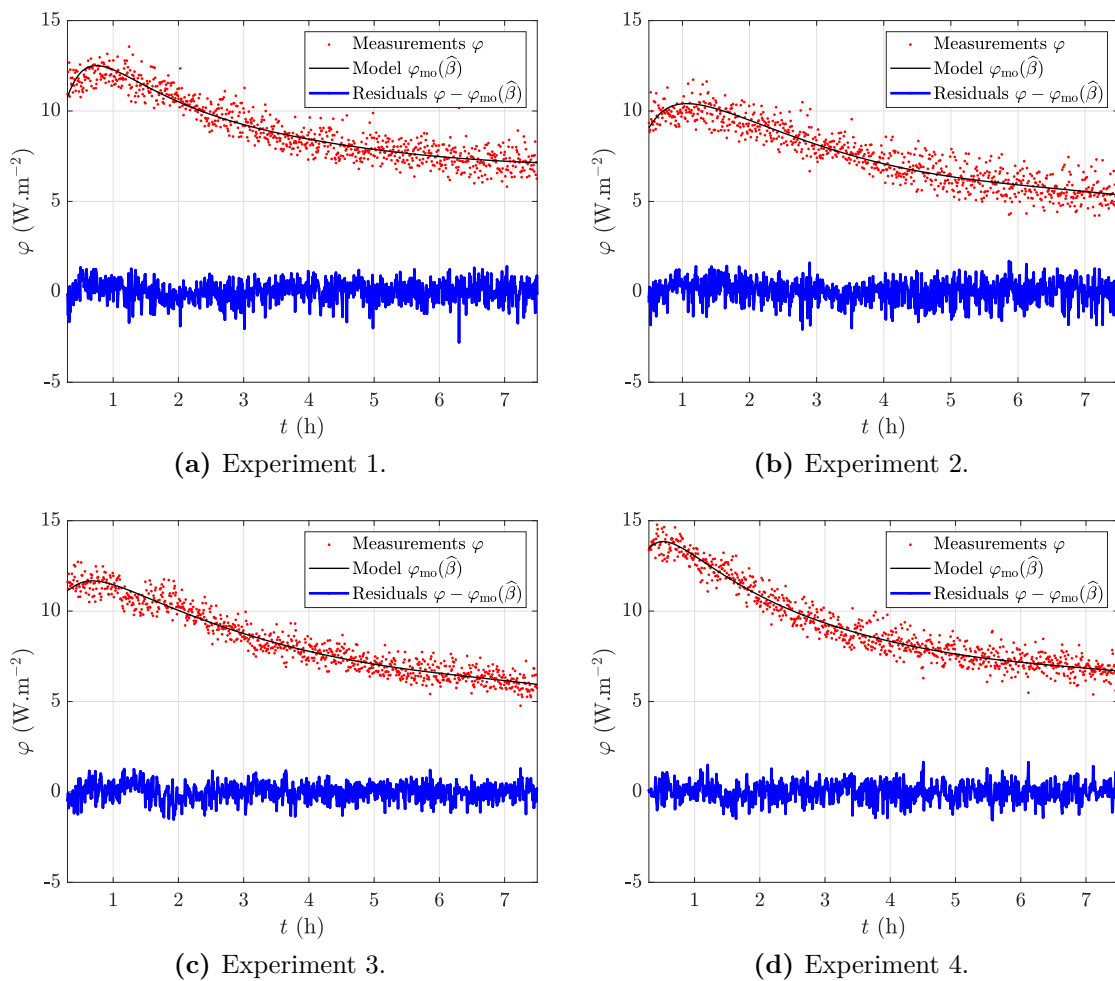


Figure E.17.: SGR experiments (1 to 4).

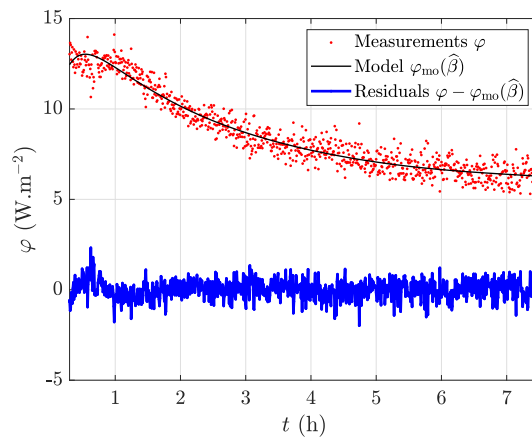


Figure E.18.: SGR Experiment 5.



# F. Appendices of Chap 9

## F.1. CEREMA experiments, residuals after parameter estimation

This appendix presents the measurements, model output and residuals after parameter estimation for each thermal bridge and all experiments of the CEREMA experimental campaign. The shorter experiments and the small disturbance on the measured heat flux noted sometimes were discussed in Appendix E.4.

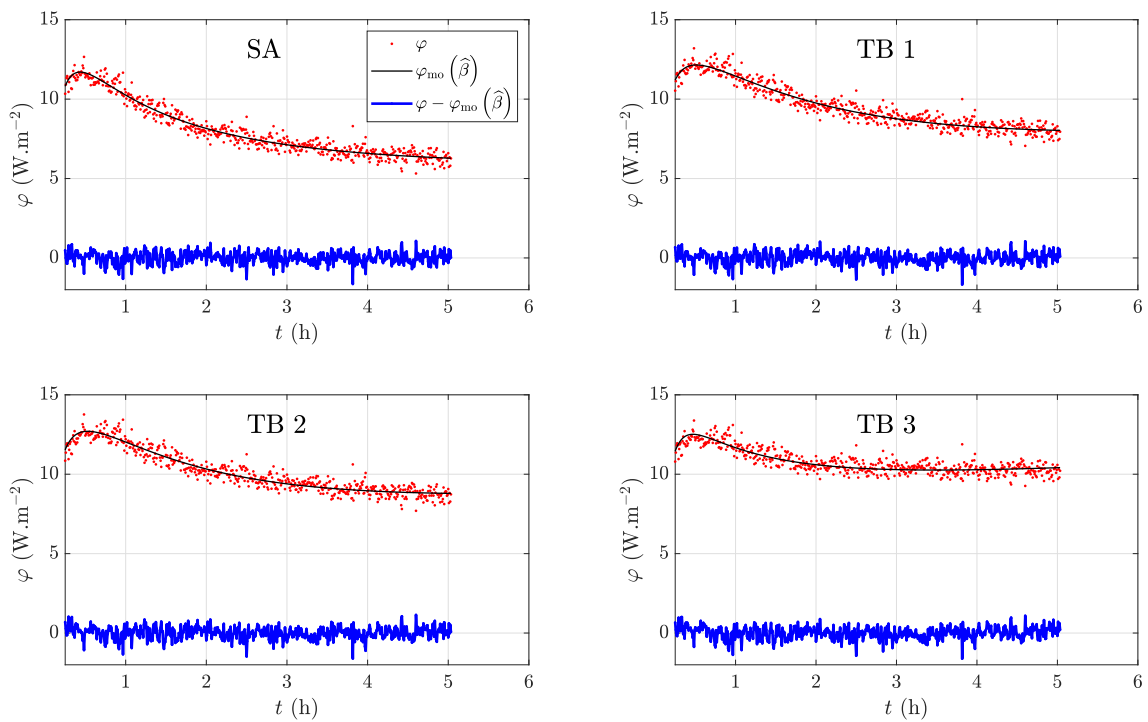
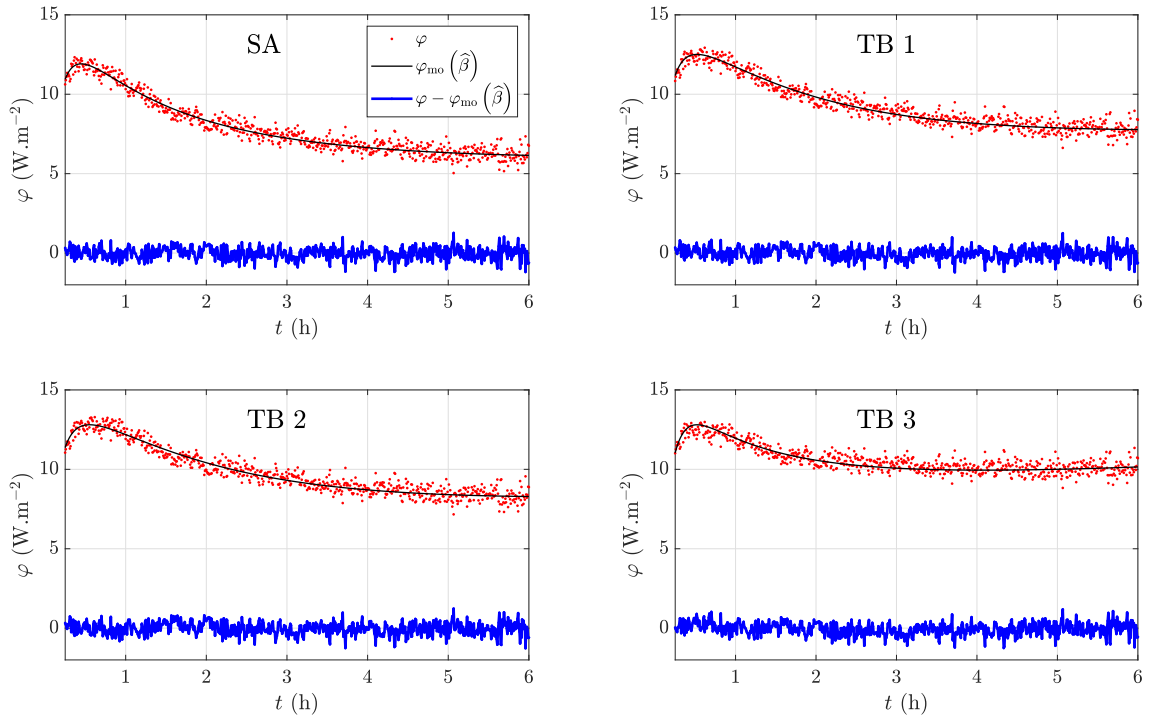
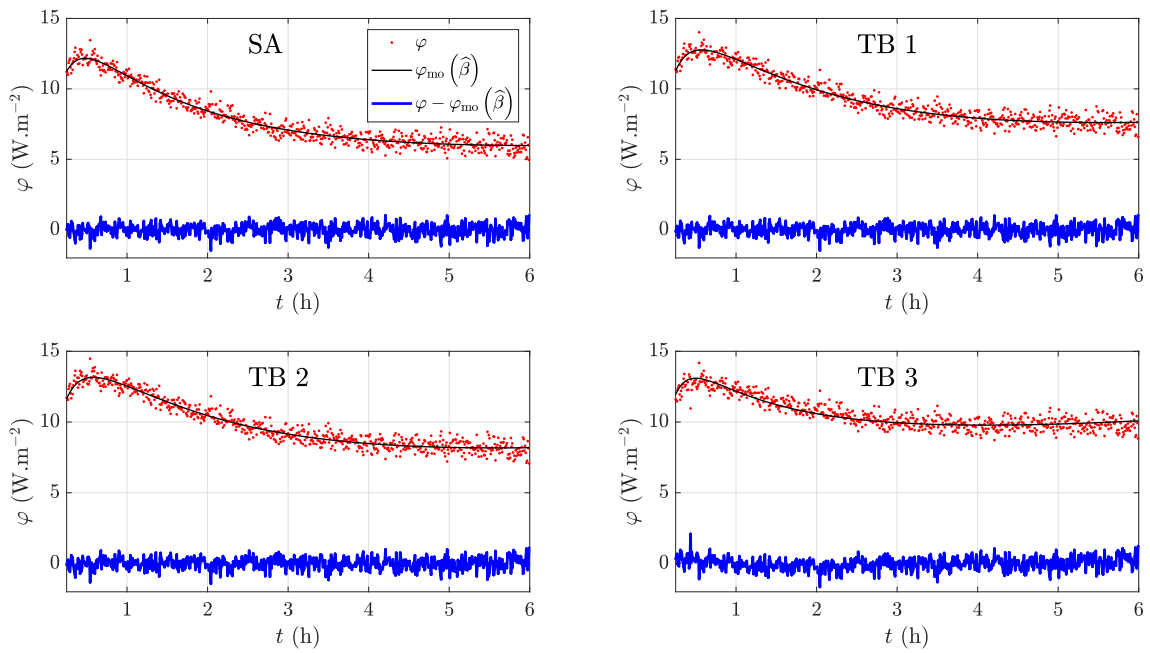


Figure F.1.: Experiment 1: configuration 1, model  $A_2$ .



**Figure F.2.:** Experiment 2: configuration 1, model  $A_2$ .



**Figure F.3.:** Experiment 3: configuration 1, model  $A_2$ .

# F.1. CEREMA EXPERIMENTS, RESIDUALS AFTER PARAMETER ESTIMATION

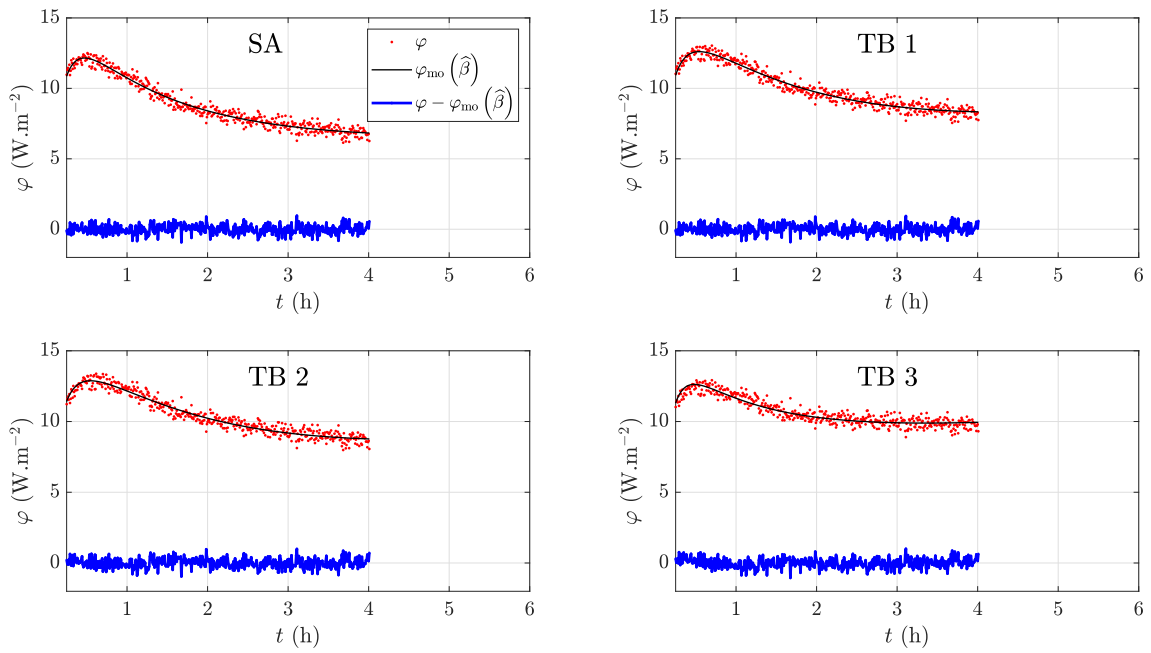


Figure F.4.: Experiment 4: configuration 1, model  $A_2$ .

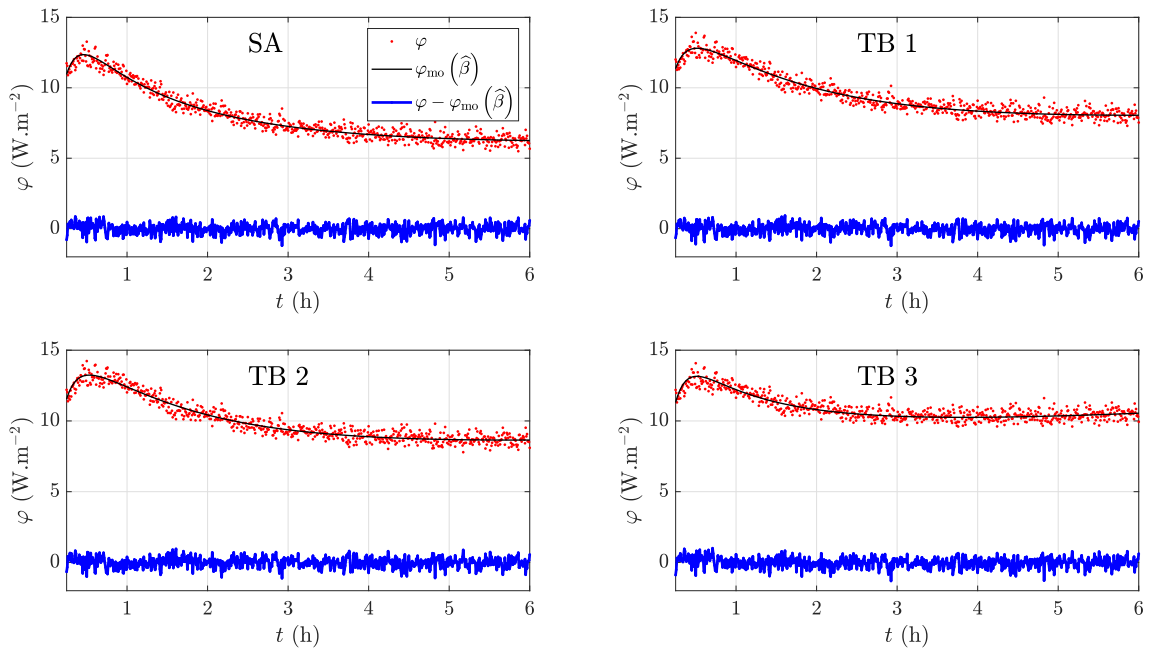
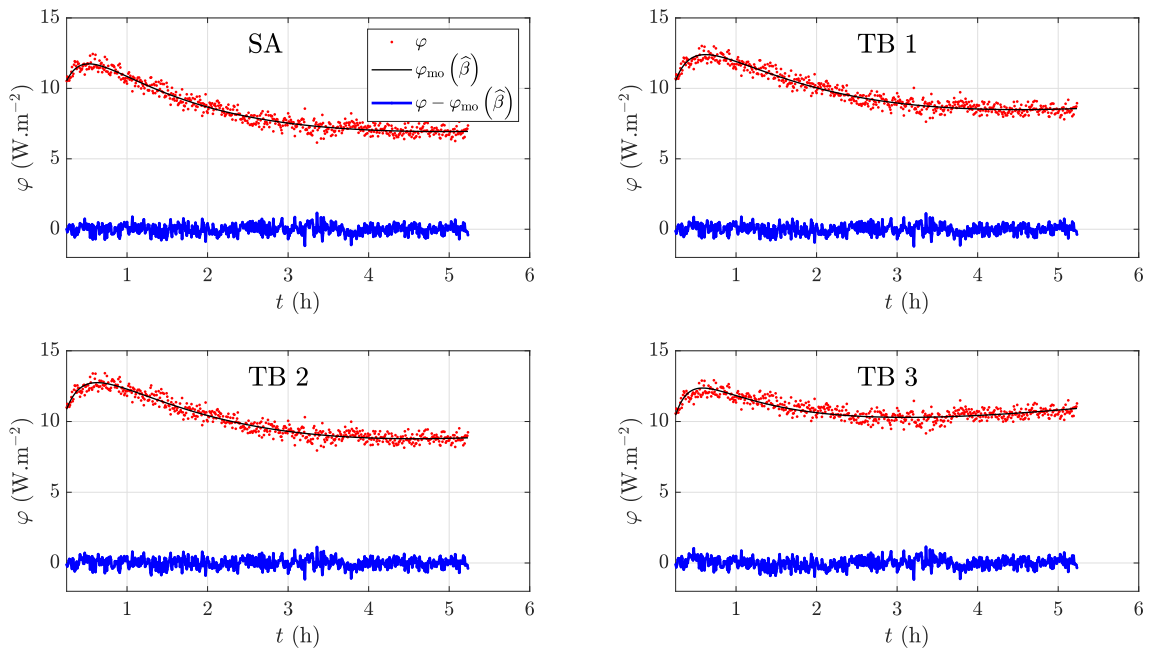
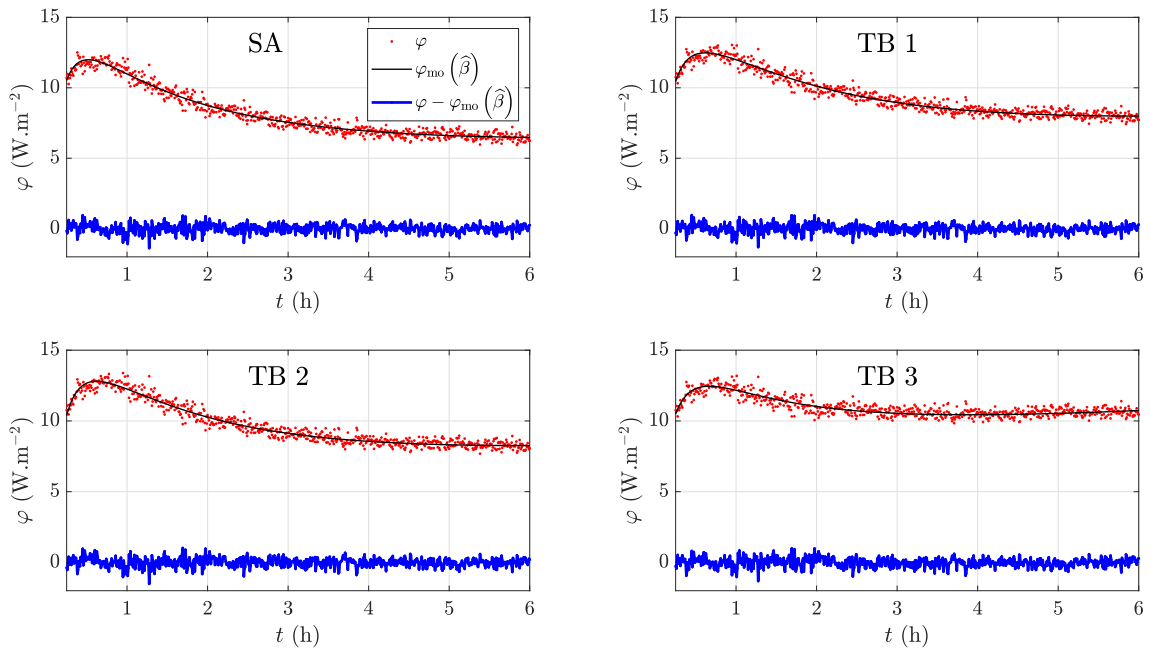


Figure F.5.: Experiment 5: configuration 1, model  $A_2$ .



**Figure F.6.:** Experiment 6: configuration 2, model A<sub>2</sub>.



**Figure F.7.:** Experiment 7: configuration 2, model A<sub>2</sub>.

F.1. CEREMA EXPERIMENTS, RESIDUALS AFTER PARAMETER ESTIMATION

---

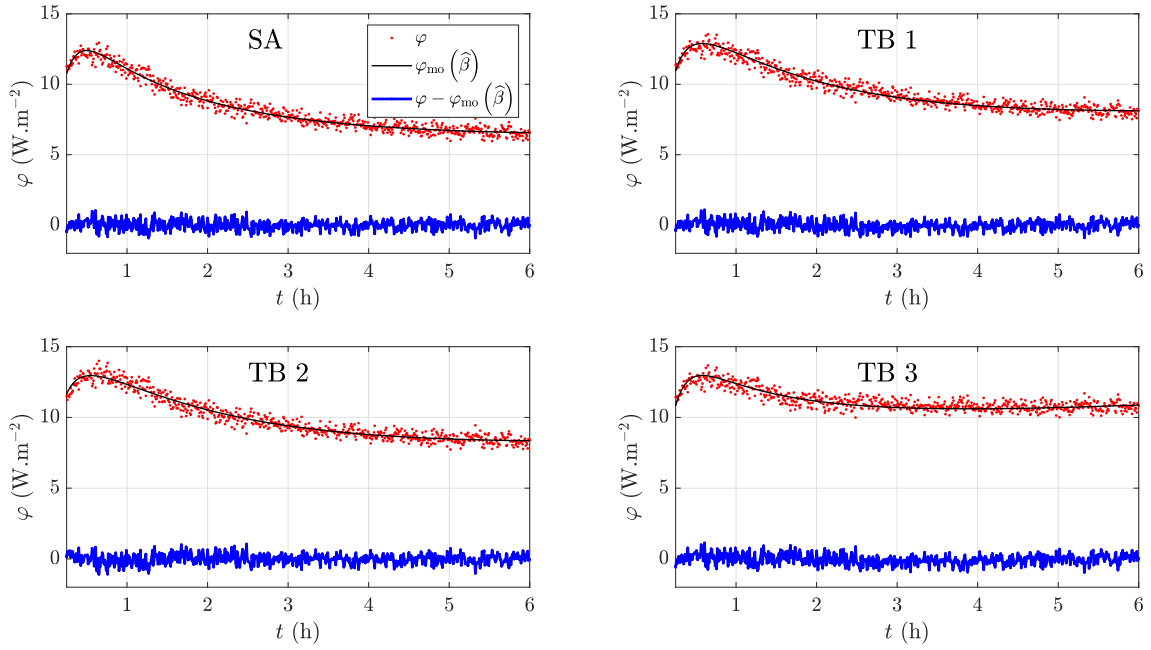


Figure F.8.: Experiment 8: configuration 2, model  $A_2$ .

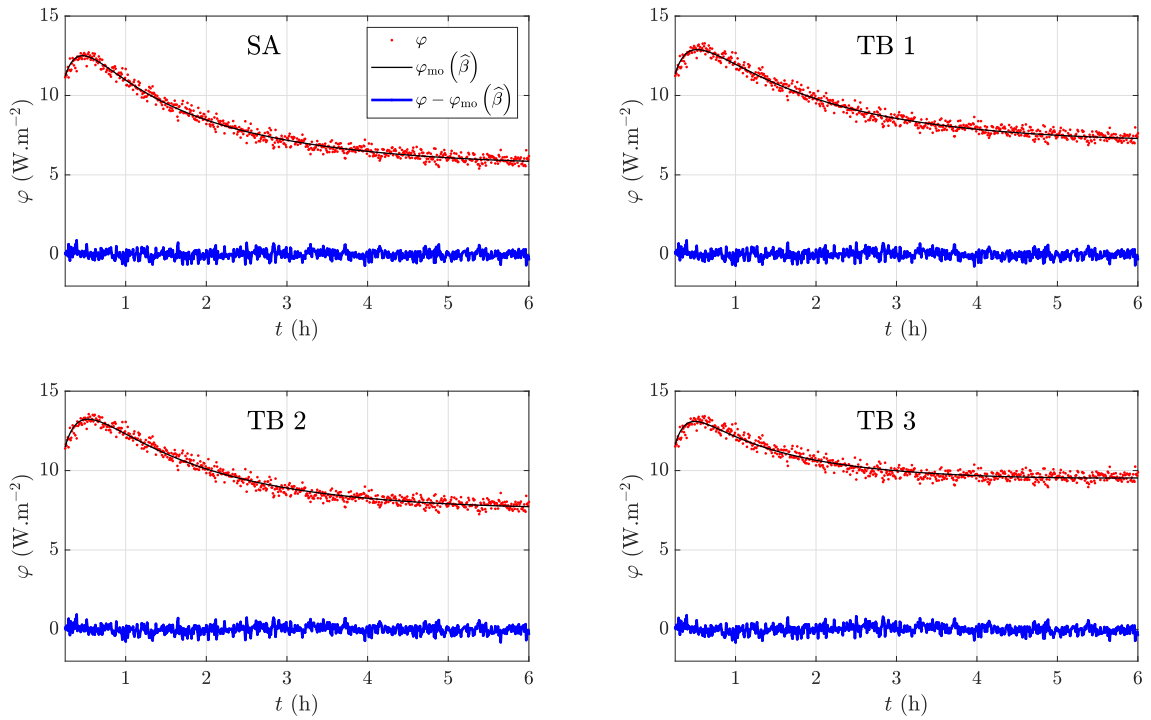


Figure F.9.: Experiment 9: configuration 3, model  $AE_3$ .



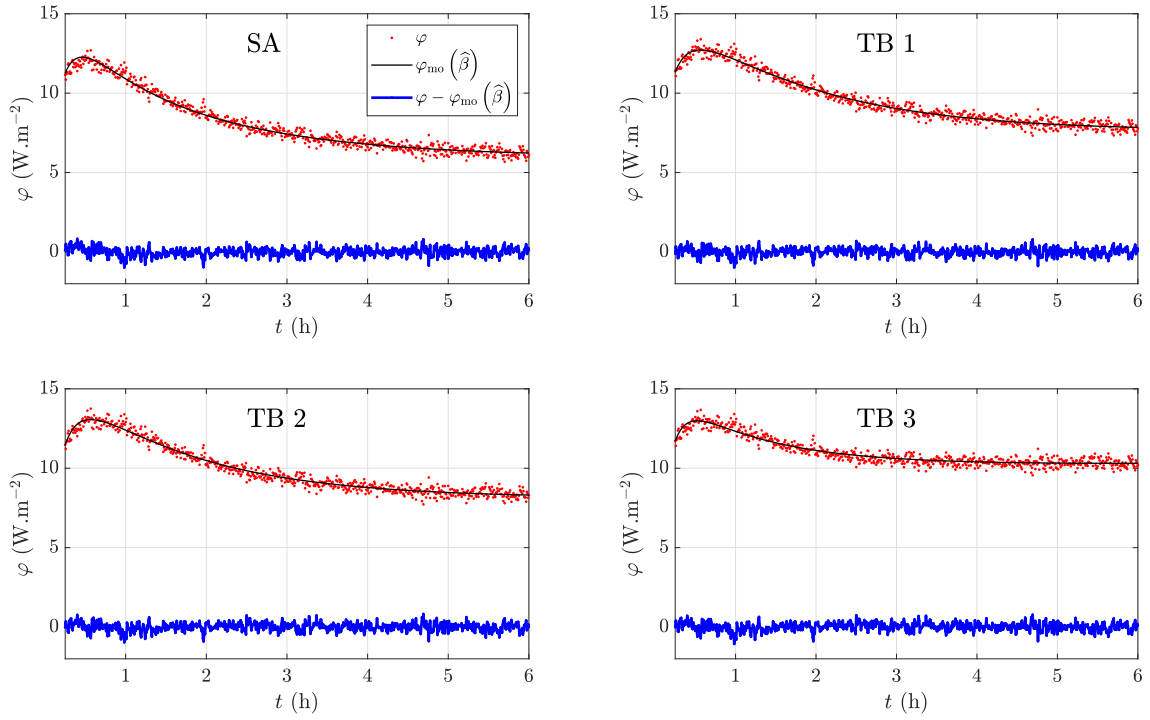


Figure F.10.: Experiment 10: configuration 3, model  $AE_3$ .

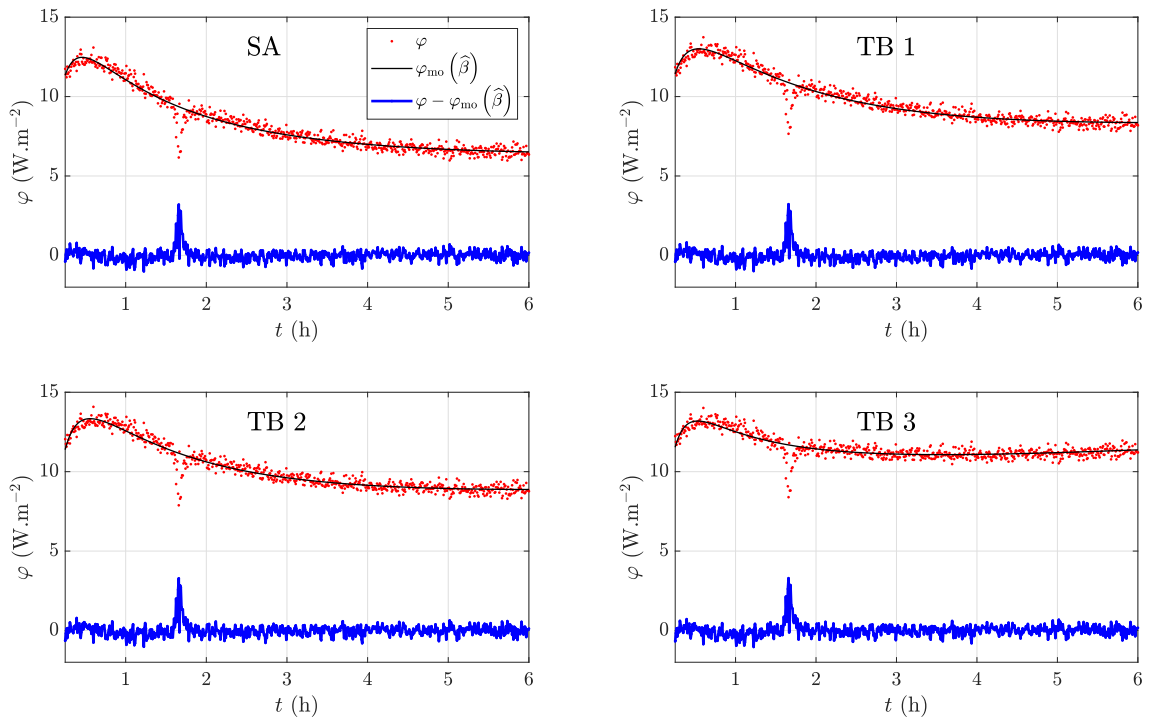


Figure F.11.: Experiment 11: configuration 3, model  $AE_3$ .

F.1. CEREMA EXPERIMENTS, RESIDUALS AFTER PARAMETER ESTIMATION

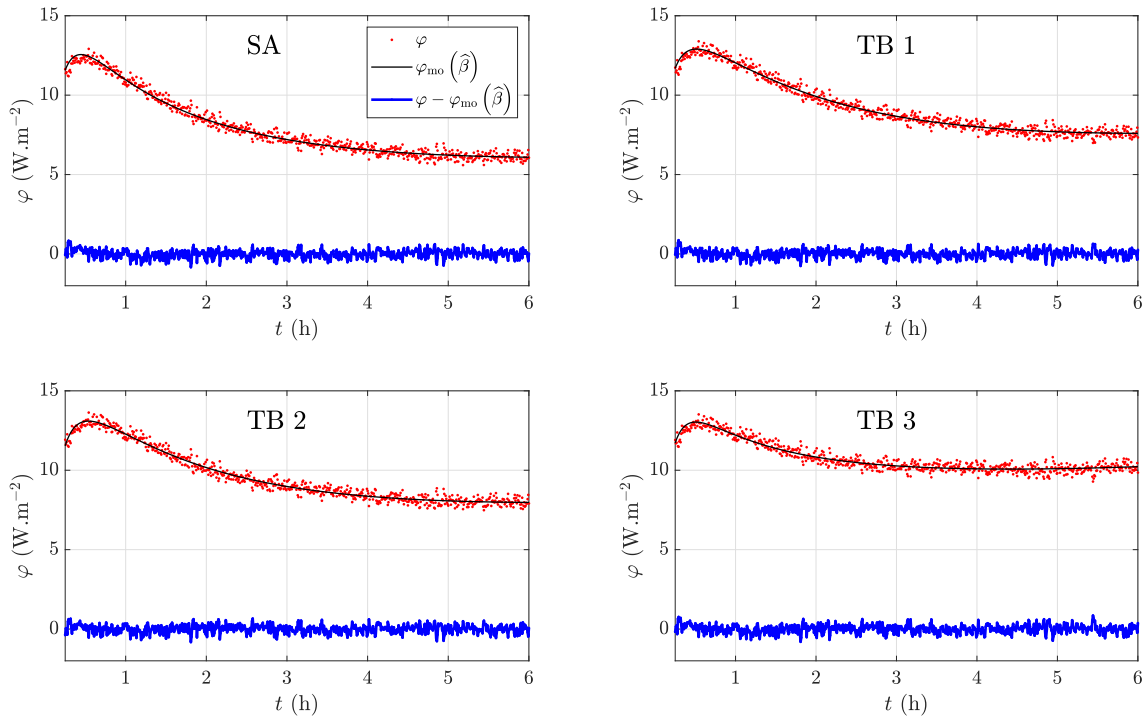


Figure F.12.: Experiment 12: configuration 3, model AE<sub>3</sub>.

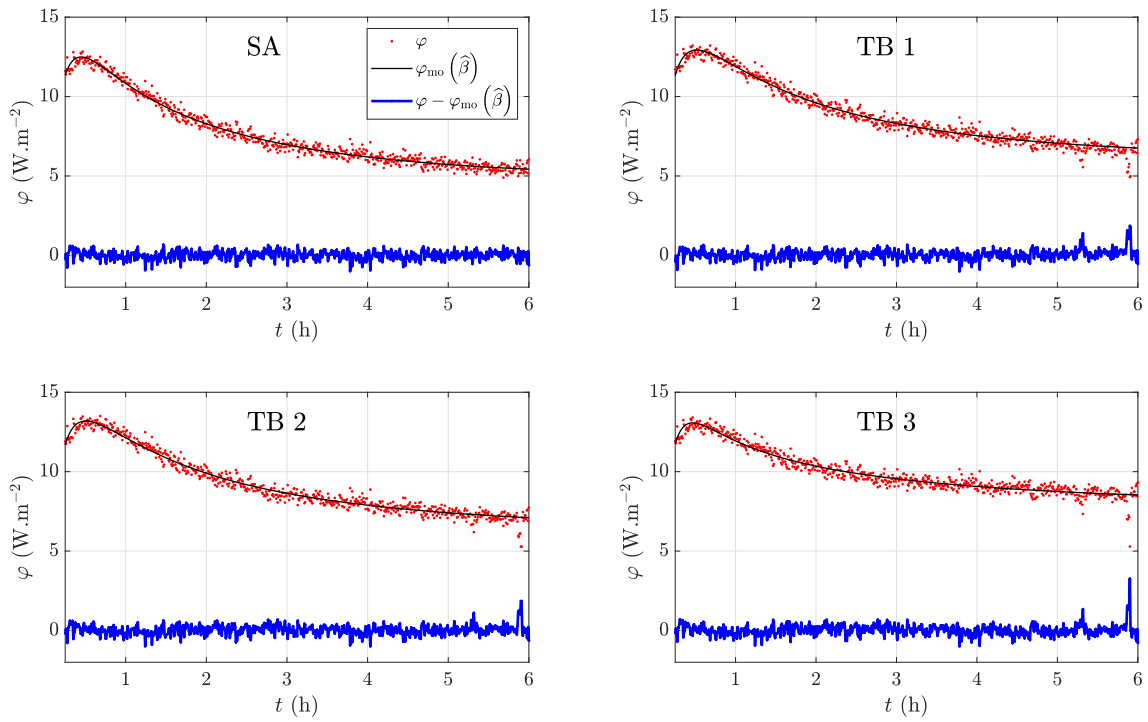


Figure F.13.: Experiment 13: configuration 4, model AE<sub>3</sub>.

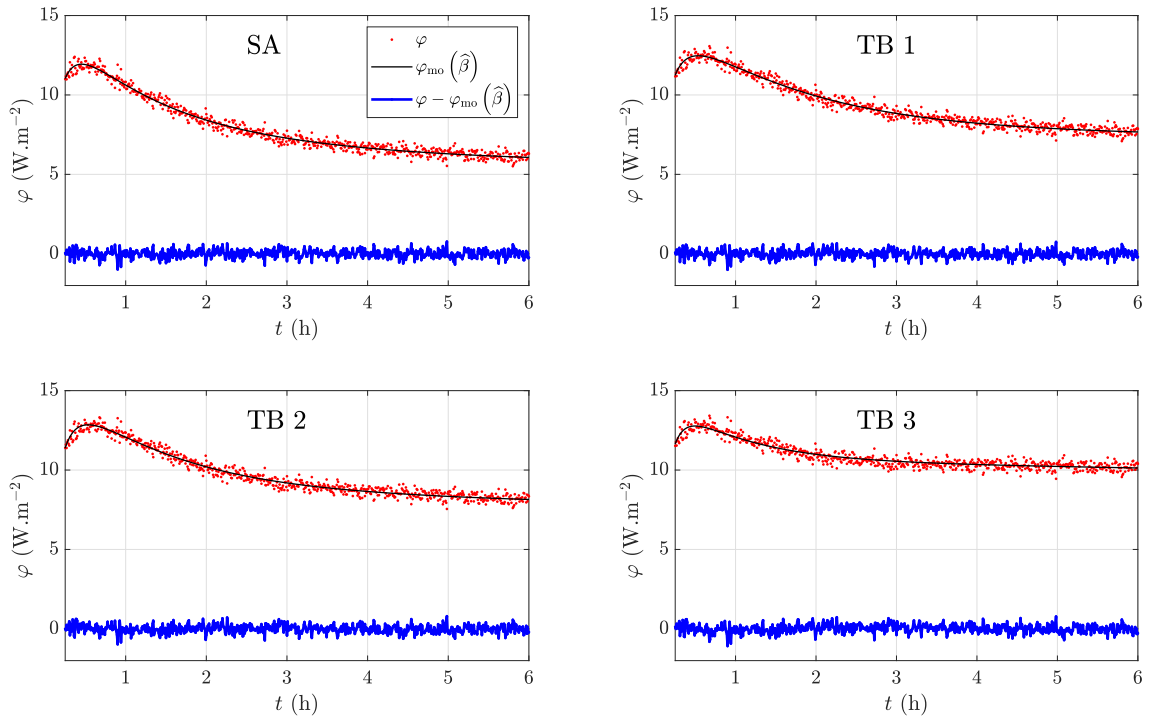


Figure F.14.: Experiment 14: configuration 4, model  $\text{AE}_3$ .

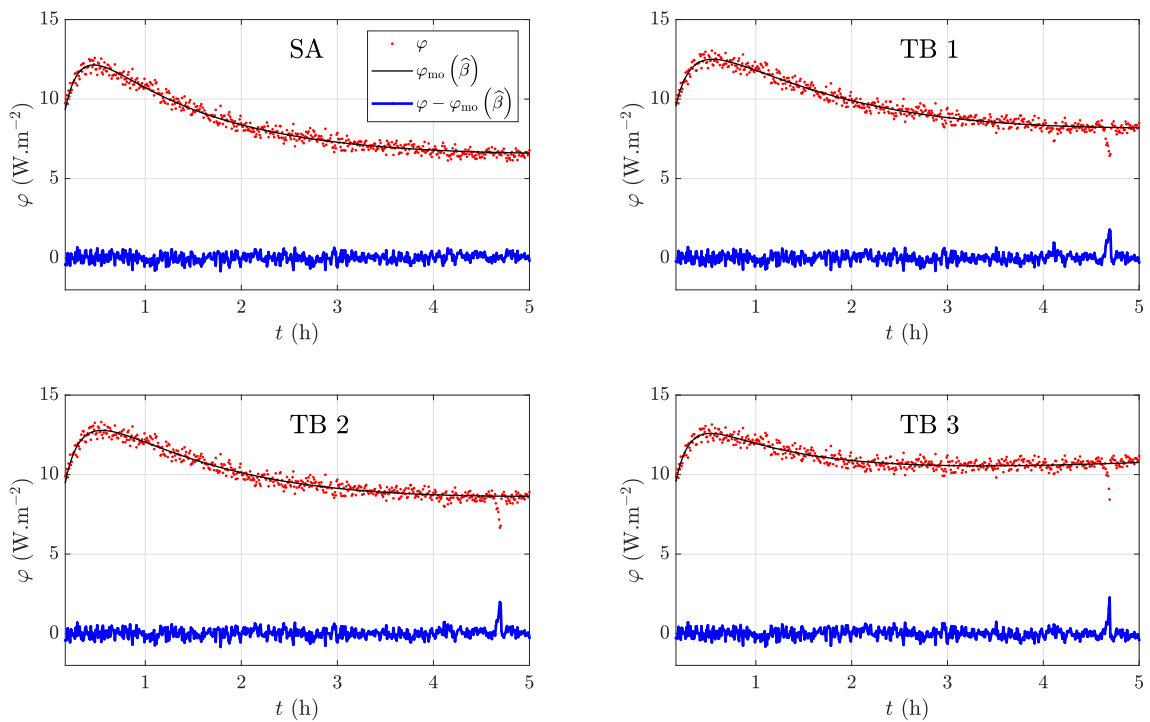


Figure F.15.: Experiment 15: configuration 4, model  $\text{AE}_3$ .

F.1. CEREMA EXPERIMENTS, RESIDUALS AFTER PARAMETER ESTIMATION

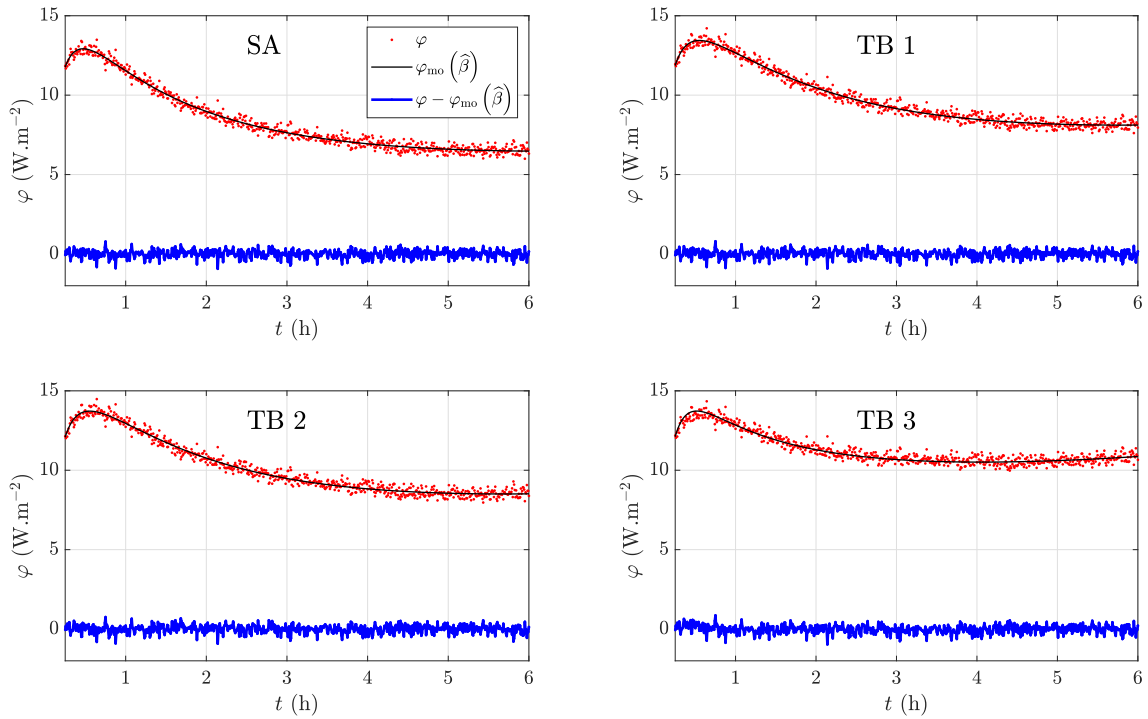


Figure F.16.: Experiment 16: configuration 4, model AE<sub>3</sub>.

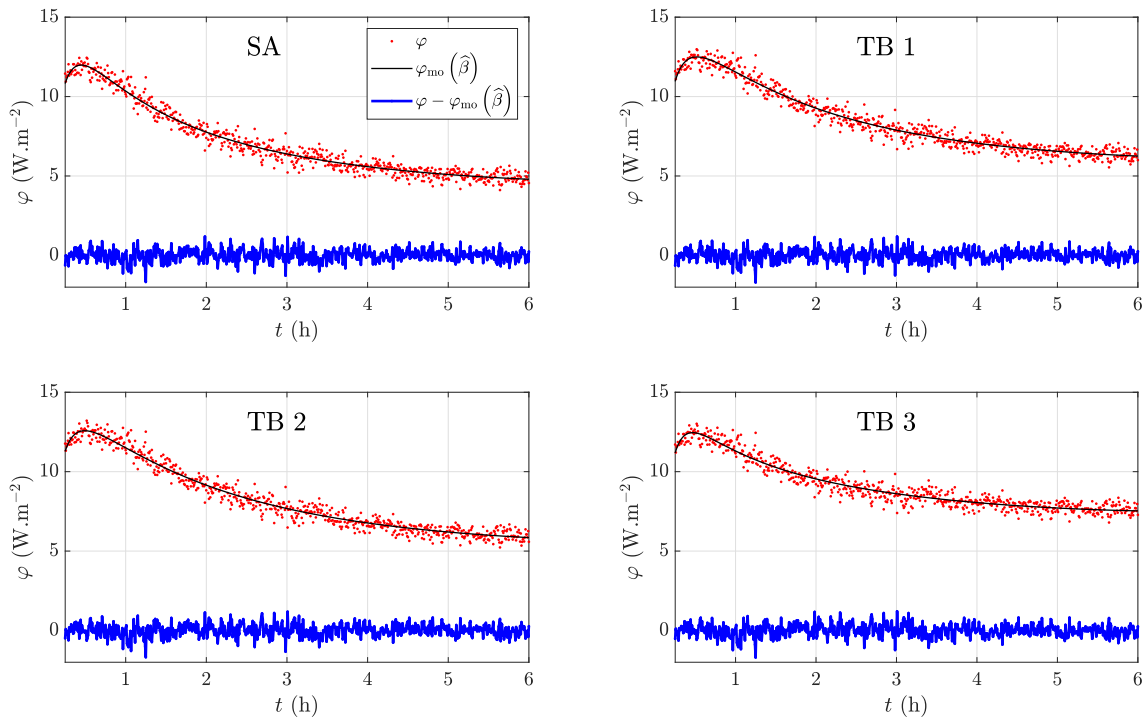


Figure F.17.: Experiment 17: configuration 5, model AE<sub>3</sub>.

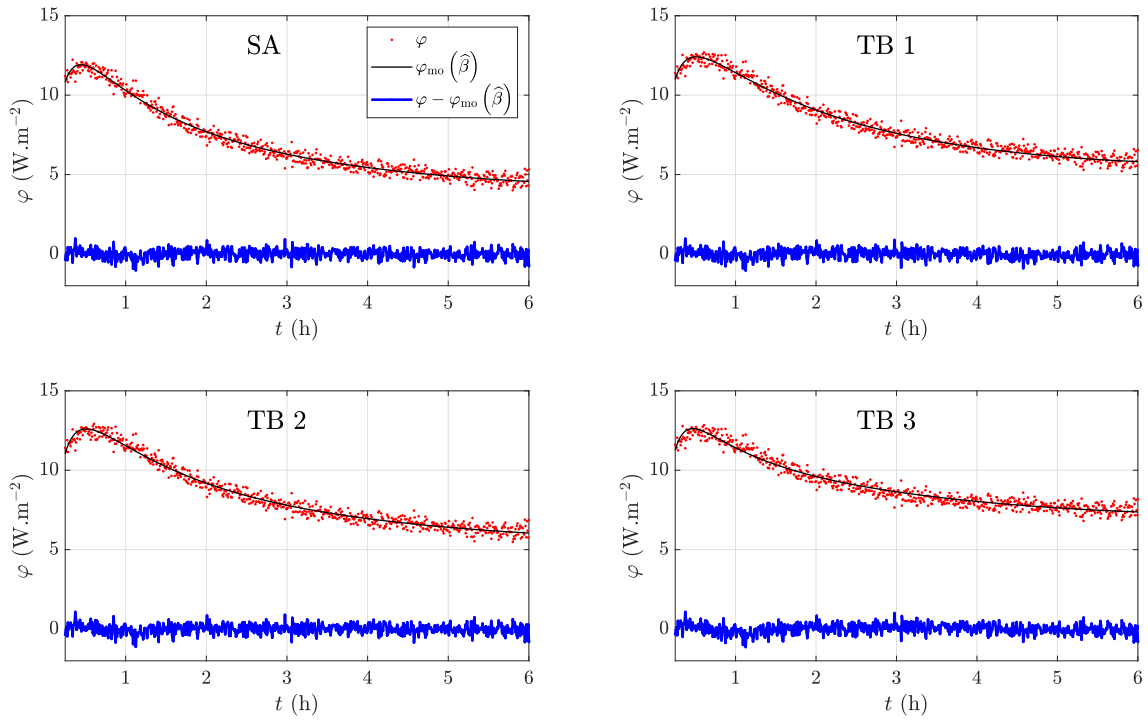


Figure F.18.: Experiment 18: configuration 5, model  $\text{AE}_3$ .

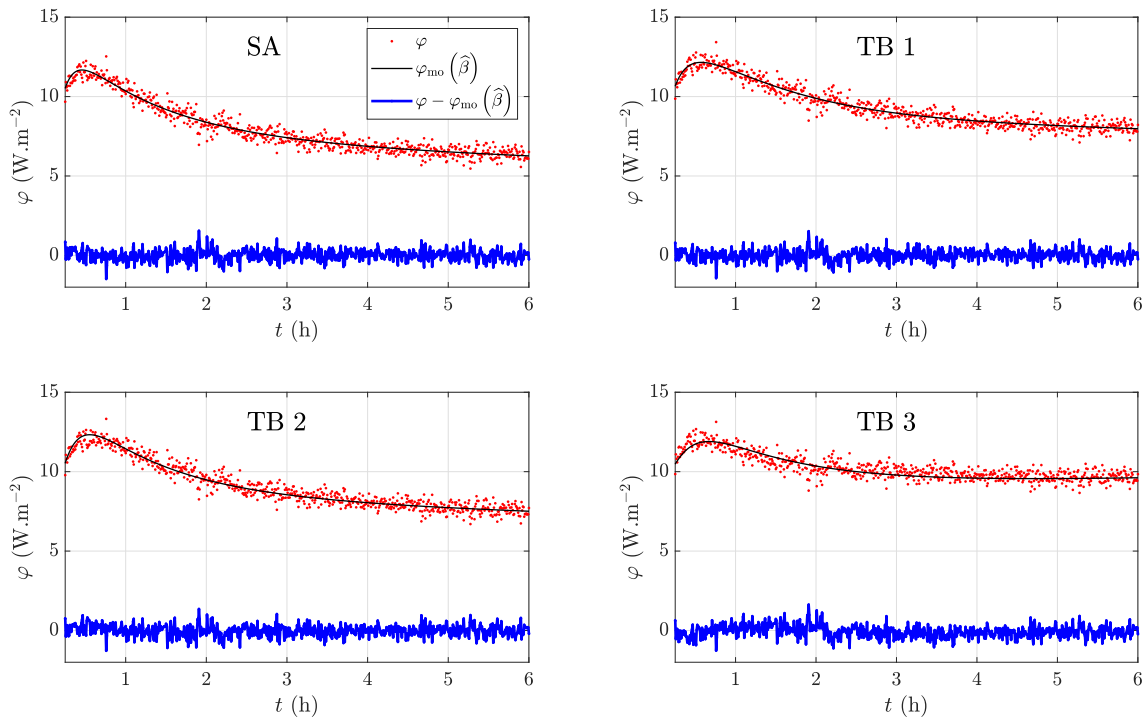


Figure F.19.: Experiment 19: configuration 5, model  $\text{AE}_3$ .

F.1. CEREMA EXPERIMENTS, RESIDUALS AFTER PARAMETER ESTIMATION

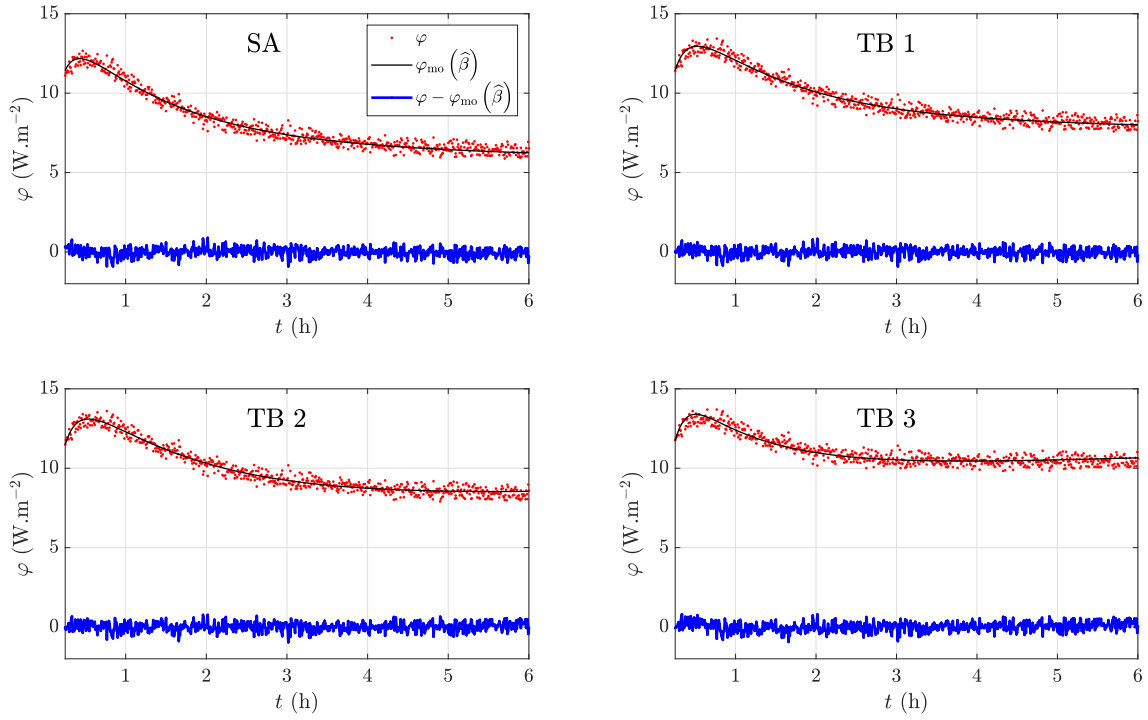


Figure F.20.: Experiment 20: configuration 5, model  $AE_3$ .

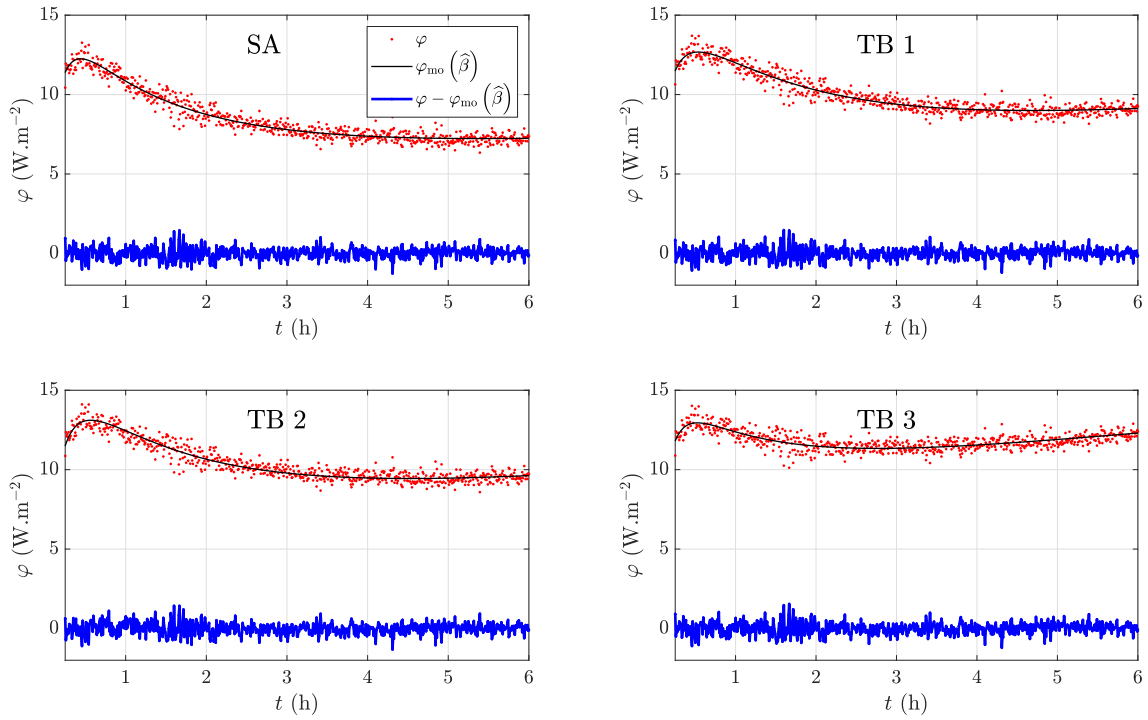


Figure F.21.: Experiment 21: configuration 5, model  $AE_3$ .

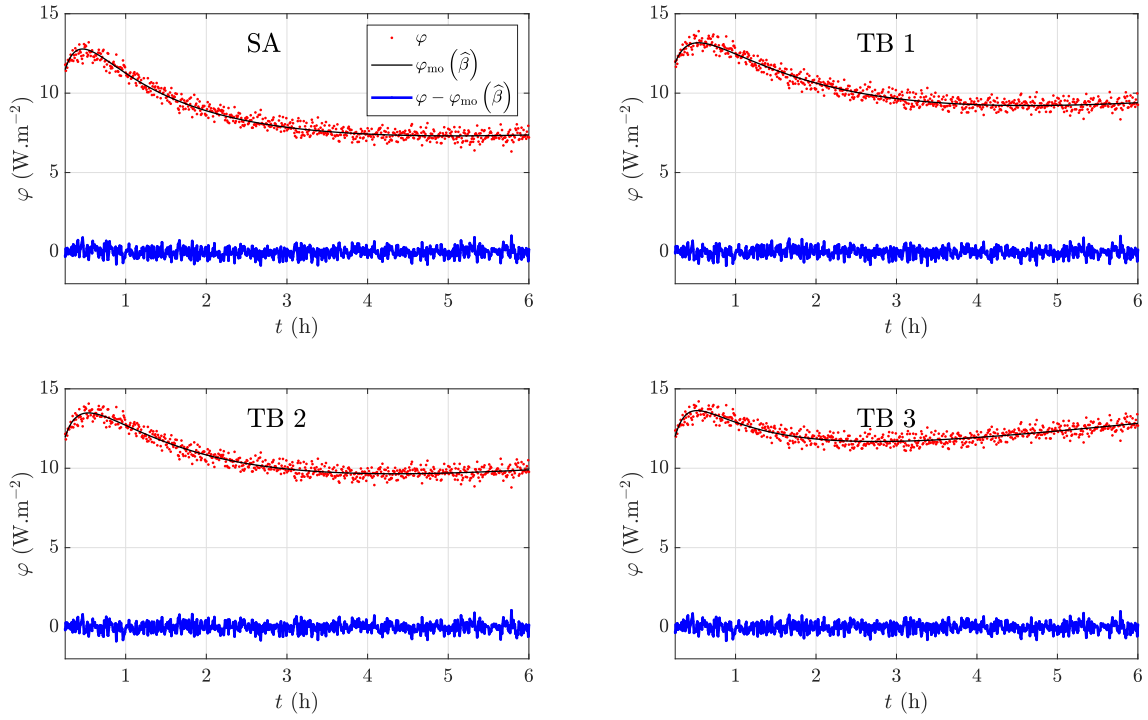


Figure F.22.: Experiment 22: configuration 5, model  $AE_3$ .

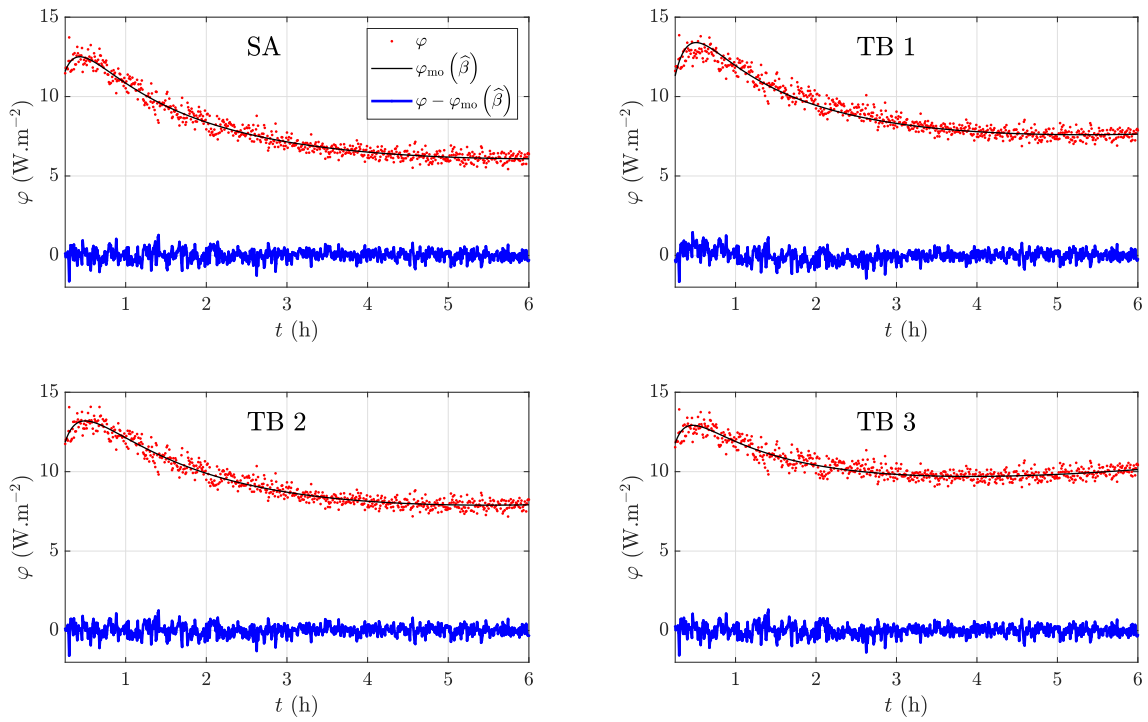


Figure F.23.: Experiment 23: configuration 5, model  $AE_3$ .

# F.1. CEREMA EXPERIMENTS, RESIDUALS AFTER PARAMETER ESTIMATION

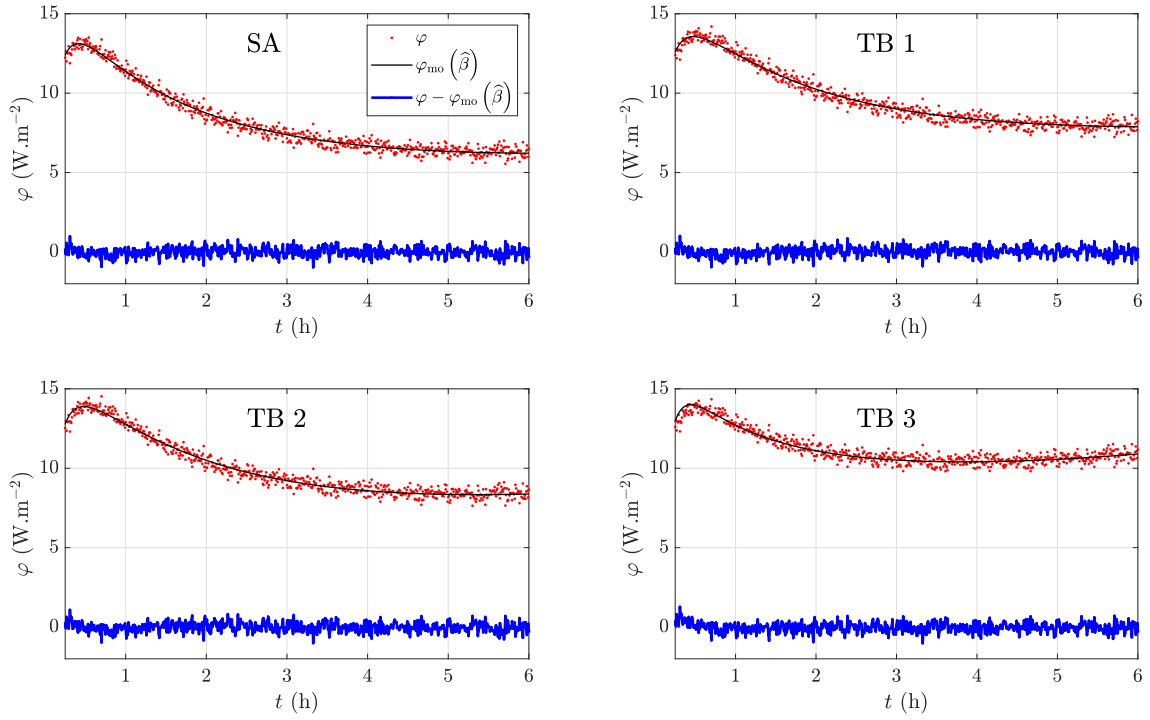


Figure F.24.: Experiment 24: configuration 5, model AE<sub>3</sub>.

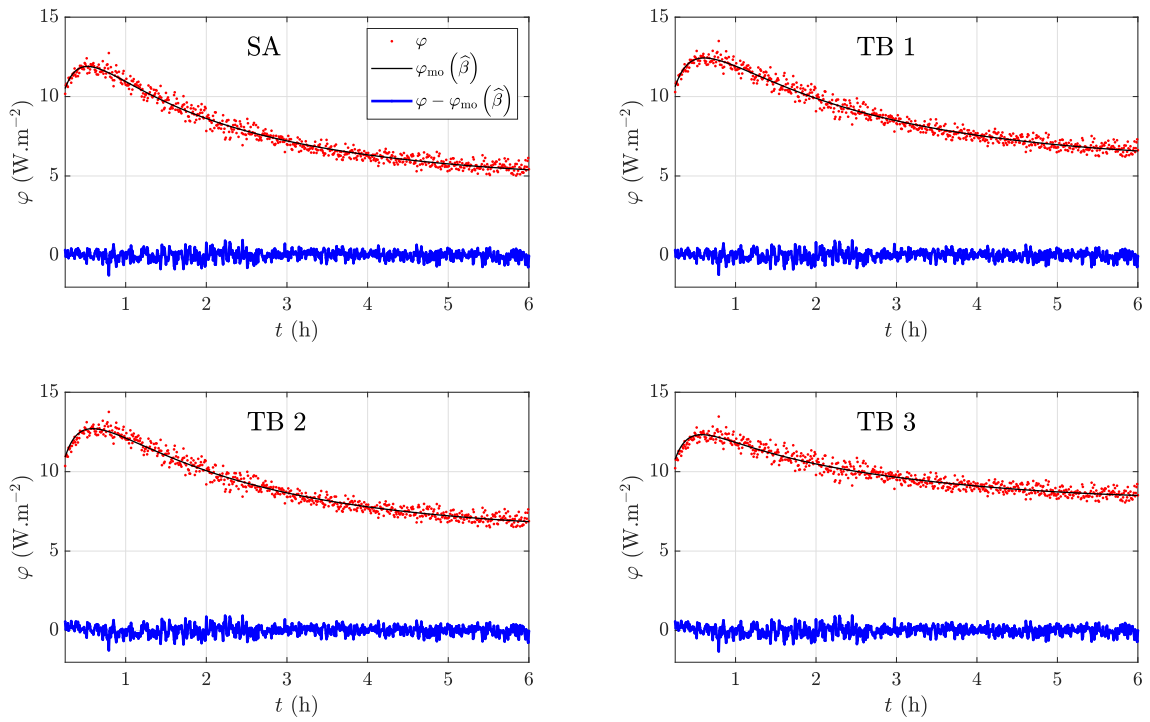


Figure F.25.: Experiment 25: configuration 6, model AE<sub>3</sub>.



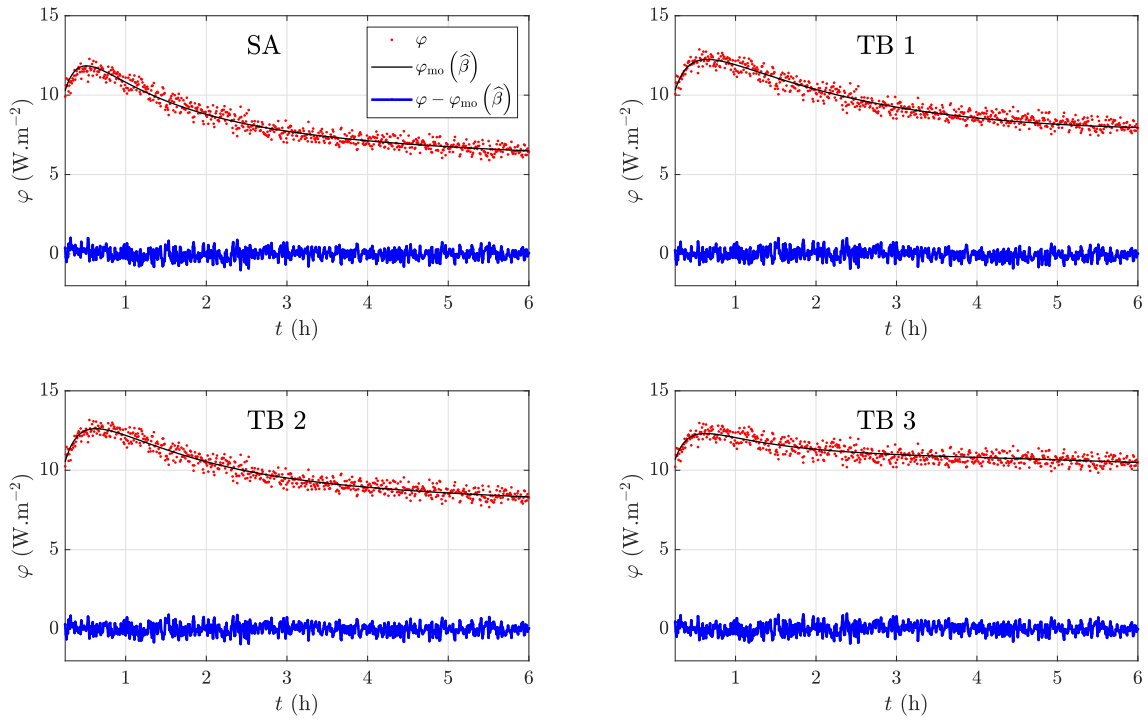


Figure F.26.: Experiment 26: configuration 6, model AE<sub>3</sub>.

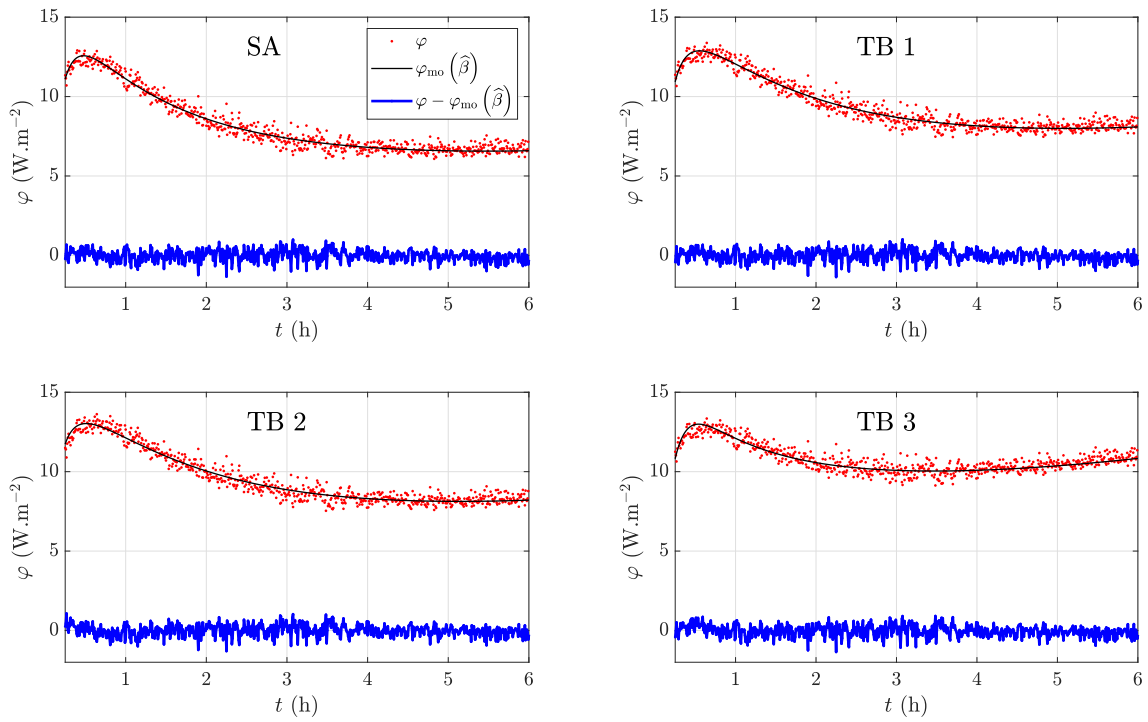


Figure F.27.: Experiment 27: configuration 6, model AE<sub>3</sub>.

## F.2. SGR experiments, residuals after parameter estimation

This appendix presents the measurements, model outputs and residuals after parameter estimation for each thermal bridge and experiments 1, 2, 4 and 5 of the SGR experimental campaign. The residuals are unsigned, except during the first hour of experiment 5 where there is a small disturbance on the heat flux measurements. Overall, the residuals are not as good as with the CEREMA experiments because the measurements were made *in situ*, not in a climate chamber.

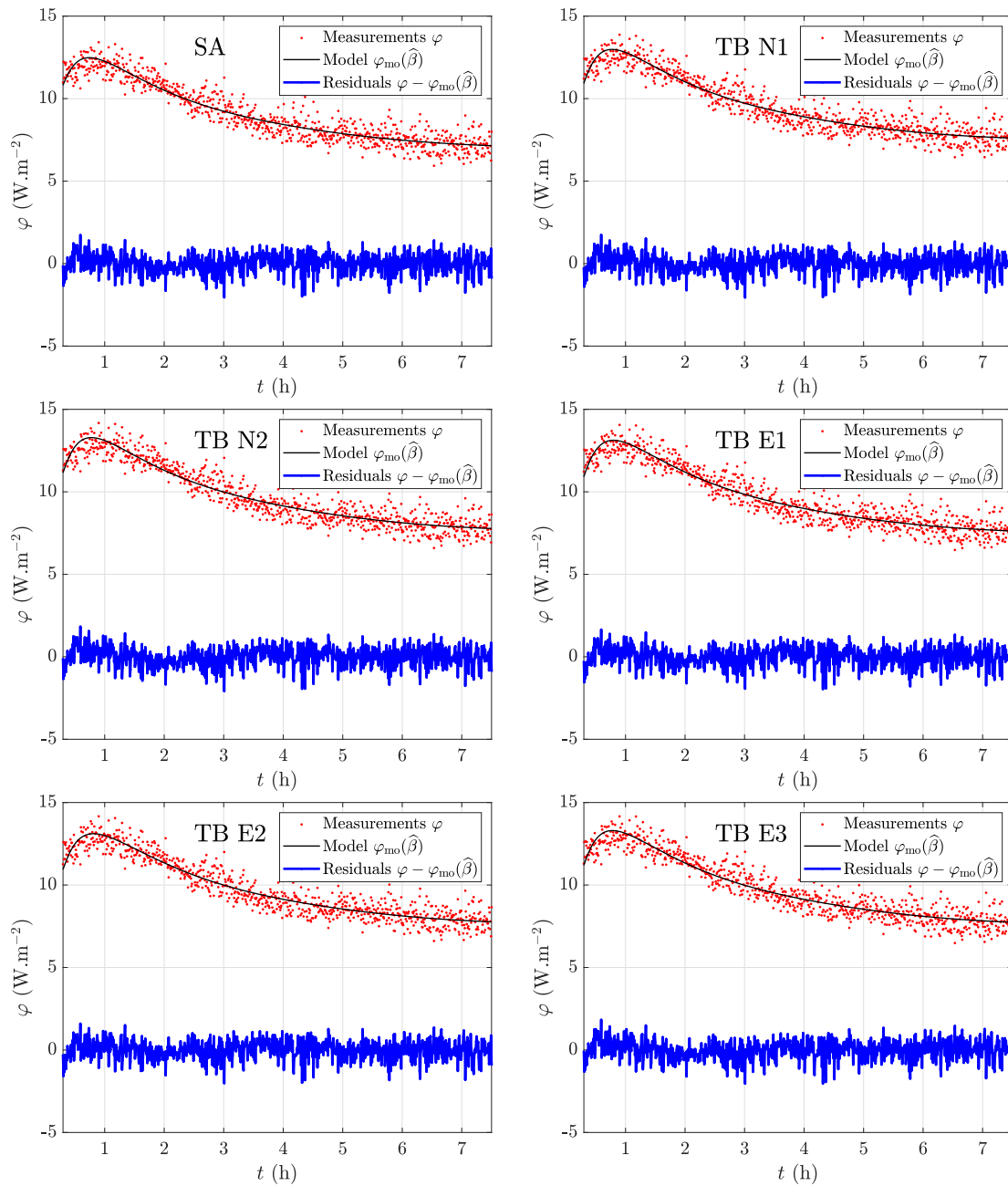
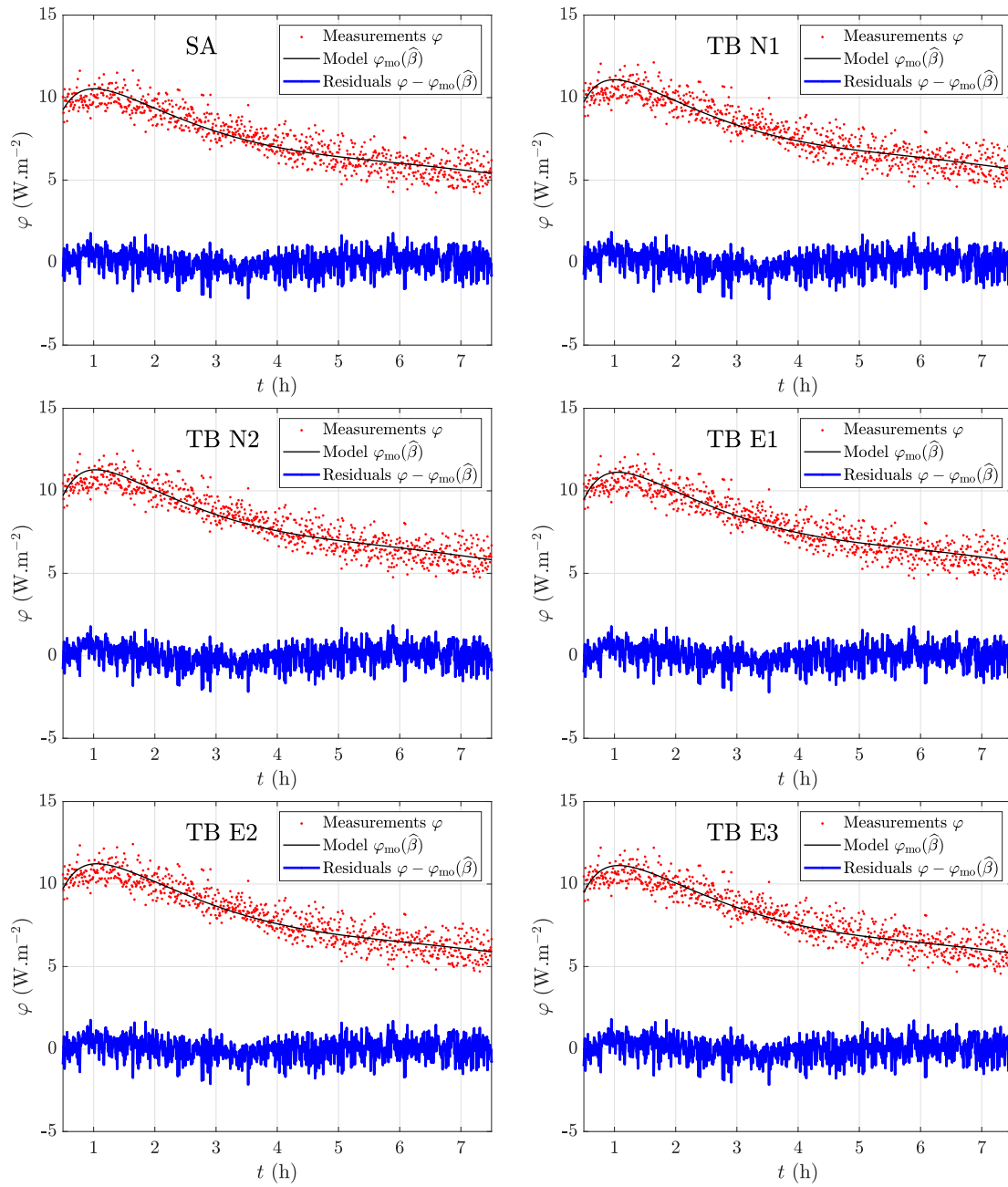


Figure F.28.: Experiment 1, model AIE<sub>2</sub>.

Figure F.29.: Experiment 2, model AIE<sub>2</sub>.

F.2. SGR EXPERIMENTS, RESIDUALS AFTER PARAMETER ESTIMATION

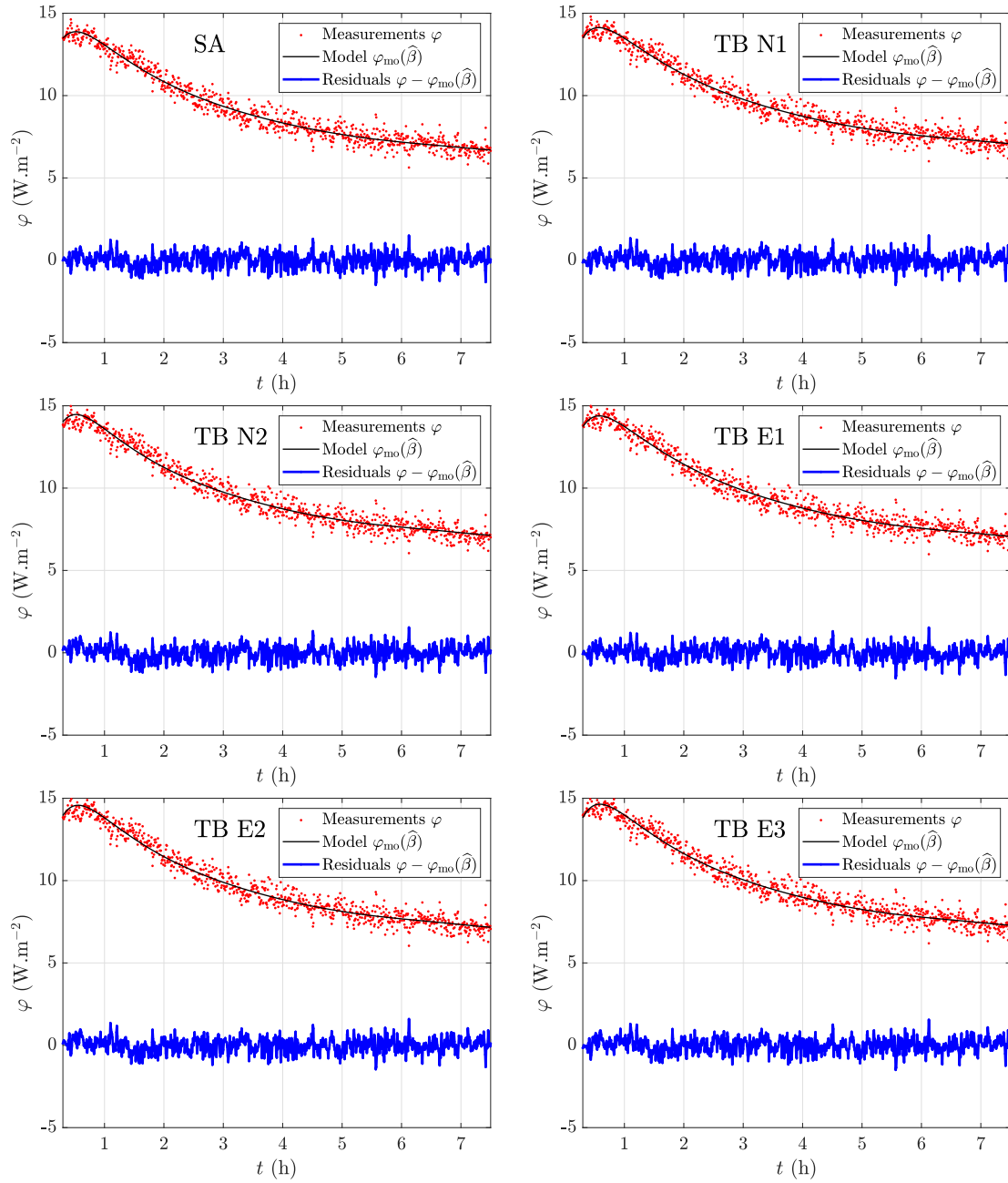
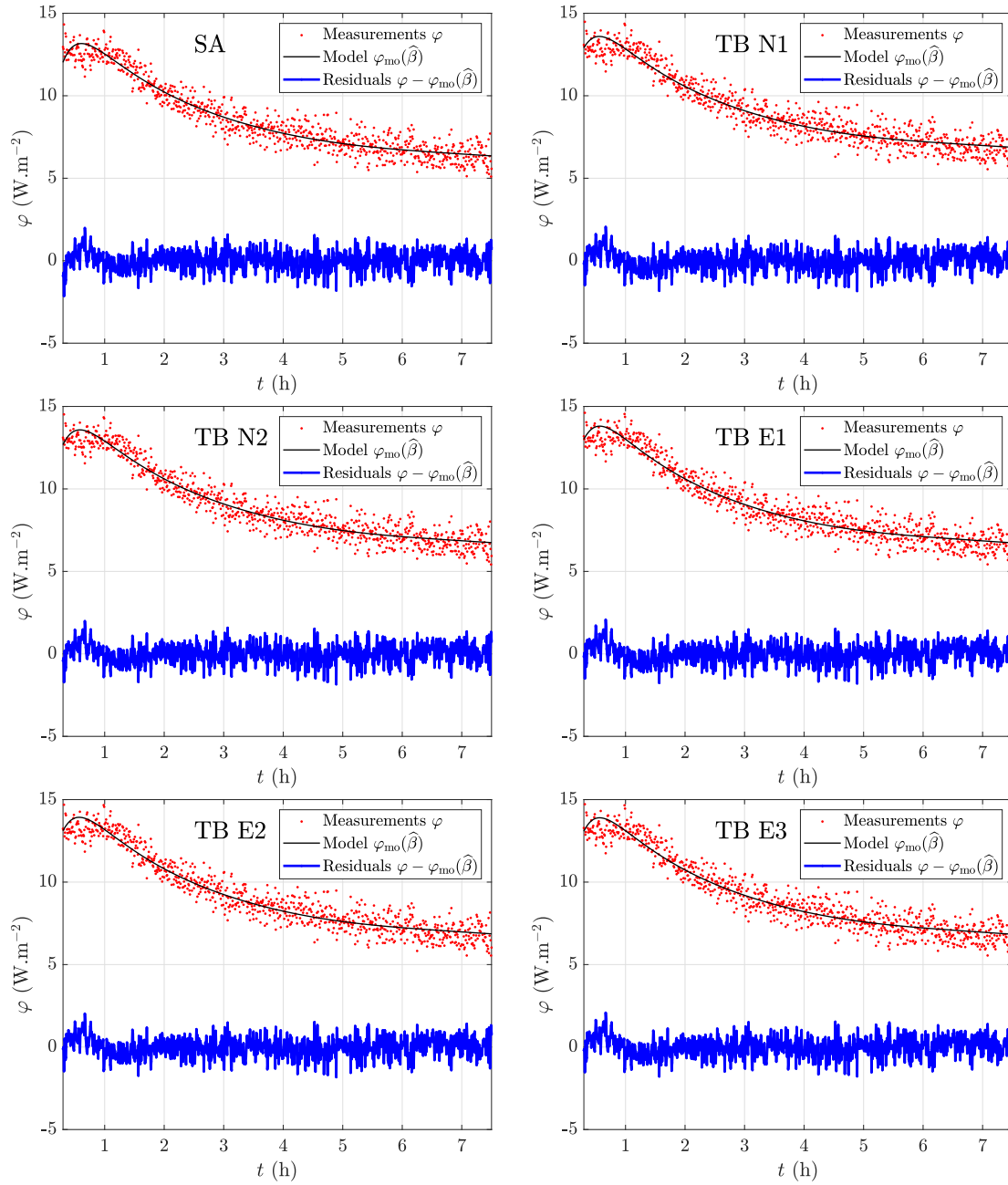


Figure F.30.: Experiment 4, model AIE<sub>2</sub>.

Figure F.31.: Experiment 5, model AIE<sub>2</sub>.

## G. Appendix: Personal references

The main results of this thesis were published in scientific papers and presented in conferences. Please find below the corresponding references.

### G.1. Scientific papers

- [173] A. François, L. Ibos, V. Feuillet, and J. Meulemans. Novel *in situ* measurement methods of the total heat transfer coefficient on building walls, *Energy and Buildings*, 219:110004, 2020. DOI: [10.1016/j.enbuild.2020.110004](https://doi.org/10.1016/j.enbuild.2020.110004)
- [174] A. François, L. Ibos, V. Feuillet, and J. Meulemans. *In situ* measurement of the heat transfer coefficient on a building wall surface: h-measurement device based on a harmonic excitation. *Entropie*, 2020. DOI: [10.21494/ISTE.OP.2020.0547](https://doi.org/10.21494/ISTE.OP.2020.0547)
- [220] A. François, L. Ibos, V. Feuillet, and J. Meulemans. Estimation of the thermal resistance of a building wall with inverse techniques based on rapid *in situ* measurements and white-box or ARX black-box models. *Energy and Buildings*, 226:110346, 2020. DOI: [10.1016/j.enbuild.2020.110346](https://doi.org/10.1016/j.enbuild.2020.110346)
- [196] A. François, L. Ibos, V. Feuillet, and J. Meulemans. *In situ* measurement method for the quantification of the thermal transmittance of a non-homogeneous wall or a thermal bridge using an inverse technique and active infrared thermography, *Energy and Buildings*, 233:110633, 2021. DOI: [10.1016/j.enbuild.2020.110633](https://doi.org/10.1016/j.enbuild.2020.110633)

### G.2. International conferences

CISBAT 2019 – International Scientific Conference 4-6 September 2019, EPFL Lausanne, Switzerland

- [194] A. François, L. Ibos, V. Feuillet, and J. Meulemans. Building thermal bridge heat losses quantification by infrared thermography. Steady-state evaluation and uncertainty calculation. *Journal of Physics: Conference Series*, volume 1343, page 012171, 2019. DOI: [10.1088/1742-6596/1343/1/012171](https://doi.org/10.1088/1742-6596/1343/1/012171)

NSB 2020 – 12th nordic symposium on building physics, 7-8 September 2020, Tallinn, Estonia

- [221] A. François, L. Ibos, V. Feuillet, and J. Meulemans. Novel active method for the estimation of a building wall thermal resistance, E3S Web of Conferences, 172:14008, 2020. DOI: [10.1051/e3sconf/202017214008](https://doi.org/10.1051/e3sconf/202017214008)

### G.3. National conferences

SFT 2019: Annual congress of the French society of thermal sciences, 3-6 June 2019, Nantes, France

- [195] A. François, L. Ibos, V. Feuillet, and J. Meulemans. Quantification par thermographie infrarouge des déperditions énergétiques d’une paroi de bâtiment liées aux ponts thermiques intégrés : essais en régime permanent et évaluation des incertitudes de mesure, 27ème congrès Français de Thermiques SFT, Nantes, 2019 (in French). URL: <https://hal.archives-ouvertes.fr/hal-02403709>

SFT 2020: Annals of the French society of thermal sciences (annual 2020 congress postponed to 2021 because of covid-19 pandemia).

This paper was selected for the “Biot-Fourier award” of the conference for its quality and originality.

- [175] A. François, L. Ibos, V. Feuillet, and J. Meulemans. *In situ* measurement of the heat transfer coefficient on a building wall surface: h-measurement device based on a harmonic excitation. Annales de la Société Française de Thermiques, 2020. DOI: [10.25855/SFT2020-091](https://doi.org/10.25855/SFT2020-091)